Transactions of the ASME

EDITORIAL STAFF
Editor, J. J. JAKLITSCH, JR.
Production Editor, STELLA ROBINSON
Editorial Production Asst. BETH DARCHI
Associate Editors
Air Pollution Control H. E. HESKETH
Diesel and Gas Engine Power F. PEKAR
Gas Turbine A. J. WENNERSTROM
Power D. T. BERUBE
Solar Energy F. KREITH
Energetics M. L. SAVITZ
Fuels C. R. PELLEY
Nuclear Engineering P. W. IANNI

POLICY BOARD, COMMUNICATIONS
Chairman and Vice-President I. BERMAN
Members-at-Large
J. E. ORTLOFF
J. W. LOCKE
M. J. RABINS
W. J. WARREN
Policy Board Representatives
Basic Engineering, F. LANDIS
General Engineering, A. A. SEIREG
Industry, R. K. HAMPTON
Power, R. E. REDER
Research, G. P. COOPER
Codes and Stds., L. L. ELDER
Nom. Com. Rep., S. ROGACKI

Business Staff
345 E. 47th St.
New York, N. Y. 10017
(212) 644-7789
Mng. Dir., Publ., C. O. SANDERSON

OFFICERS OF THE ASME
President, CHARLES E. JONES
Exec. Dir. & Sec'y, ROGERS B. FINCH
Treasurer, ROBERT A. BENNETT

Journal of Engineering for Power (ISSN 0022-0825) is edited and published quarterly at the offices of The American Society of Mechanical Engineers, United Engineering Center, 345 E. 47th St., New York, N. Y. 10017. ASME-TWX No. 710-581-5267, New York. Second Class postage paid at New York, N.Y., and at additional mailing offices.

CHANGES OF ADDRESS must be received at Society headquarters seven weeks before they are to be effective. Please send old label and new address.

PRICES: To members, $25.00, annually; to nonmembers, $50.00. Single copies, $15.00 each. Add $1.50 for postage to countries outside the United States and Canada.

STATEMENT from By-Laws. The Society shall not be responsible for statements or opinions advanced in papers or . . . printed in its publications (B 13, Par. 4).

COPYRIGHT © 1980 by the American Society of Mechanical Engineers. Reprints from this publication may be made on condition that full credit be given the TRANSACTIONS OF THE ASME—JOURNAL OF ENGINEERING FOR POWER, and the author, and date of publication be stated.

INDEXED by the Engineering Index, Inc.

Journal of Engineering for Power

Published Quarterly by The American Society of Mechanical Engineers
VOLUME 102 • NUMBER 3 • JULY 1980

513 Production of Photovoltaic Devices (79-SOL-8)
R. McGinnis

518 Designing Reliability into High-Effectiveness Industrial Gas Turbine Regenerators (79-GT-199)
S. J. Valentino

524 Account of Film Turbulence for Predicting Film Cooling Effectiveness in Gas Turbine Combustors (79-GT-200)
G. J. Sturgess

535 Mean Velocity and Decay Characteristics of the Near and Far Wake of a Compressor Rotor Blade of Moderate Loading (79-GT-202)
A. Ravindranath and B. Lakshminarayana

549 Ongoing Development of a Low Emission Industrial Gas Turbine Combustion Chamber (79-GT-203)
V. M. Sood and J. R. Shekleton

555 An Approximate Analysis of Fondation Stresses in Horizontal Pressure Vessels (79-NE-1)
Krishna P. Singh and V. K. Luk

558 Simplified Inelastic Analysis in Helical Coil Heat Exchanger Design (79-NE-2)
C. E. Richard

563 An IHX Design for Pool Type LMFBR System Application (79-NE-3)
D. D. DeFur

568 A High Reliability Straight Tube LMFBR System Generator Design (79-NE-4)
A. H. Spring and D. DeFur

573 Fiber Reinforced Metals in Turbine Blades (79-GT/Isr-1)
L. O. K. Larsson and R. Warren

579 The Behavior of a Closed-Cycle Gas Turbine with Time Dependent Operating Conditions (79-GT-Isr-2)
K. Bammert and H. Poesentrup

584 The Flow and Film Cooling Effectiveness Following Injection through a Row of Holes (79-GT/Isr-6)
N. W. Foster and D. Lampard

589 Plasma-Spray Coating Processes: Physico-Mathematical Characterization (79-GT/Isr-8)
B. Gal-Or

594 Matching of Turbocomponents Described by the Example of Impeller and Diffuser in a Centrifugal Compressor—Part I: Aerothermodynamic Coupling of Impeller and Diffuser. Part II: Optimized Stage Efficiency of a Centrifugal Compressor (79-GT/Isr-9)
K. Bammert, M. Rautenberg, and W. Wittekindt

601 The Film Cooling Effectiveness of Double Rows of Holes (79-GT/Isr-10)
W. O. Afejuku, N. Hay, and D. Lampard

607 A Fiber-Optic Laser-Doppler Probe for Vibration Analysis of Rotating Machines (79-GT/Isr-11)
R. A. Cookson and P. Bandyopadhyay

613 Conceptual Examination of Gas Phase Particulate Formation in Gas Turbine Combustors (79-GT/Isr-12)
A. S. Kesten, J. J. Sangiovanni, and P. Goldberg

619 An Analysis of Three-Dimensional Flow in a Centrifugal Impeller (79-GT/Isr-13)
C. Bosman

626 Application of Viscous Analysis to the Design of Jet Exhaust Powered Lift Installations (79-GT/Isr-15)
E. Tjonneland and S. F. Birch

632 A Blade-to-Blade Solution of the Flow in a Centrifugal Compressor Impeller with Splitters (79-GT/Isr-17)
A. Goulas

638 Interferometrically Measured Aerodynamic Forces on a Vibrating Turbine Blade Group (79-WA/GT-1)
Z. Kovats

(*Continued on page 606*)

Downloaded 03 Jun 2010 to 171.66.16.159. Redistribution subject to ASME license or copyright; see http://www.asme.org/terms/Terms_Use.cfm

646 The Prediction of Sauter Mean Diameter for Gas Turbine Fuel Nozzels of Different Types (79-WA/GT-5)
H. C. Simmons

653 Effects of Nonuniform Passages on Compact Heat Exchanger Performance (79-WA/GT-9)
R. K. Shah and A. L. London

660 Techniques for the Thermal/Hydraulic Analysis of LMFBR Check Values (79-WA/NE-4)
S. M. Cho and R. S. Kane

666 Laboratory Combustibility Testing of Solid Fuel (79-WA/Fu-1)
E. C. Winegartner and C. J. Lin

672 Characterization and Combustion of SRC II Fuel Oil (79-WA/Fu-2)
W. Downs, S. J. Vecci, J. A. Barsin, and W. C. Rovesti

679 Some Results of the Wetting and Adherence of Synthetic Coal Ash Droplets on Steel (79-WA/Fu-3)
A. K. Moza, L. G. Austin, and R. E. Tressler

684 Further Development of an Advanced Low-NO_x Combustion System and its Potential Application to Coal-Fired Utility Boilers (79-WA/Fu-4)
T. M. Sommers, S. A. Johnson, and G. D. Lindstrom

692 Composition and Microstructure of a Furnace Ash Deposit from a Coal-Fired Utility Boiler (79-WA/CD-1)
R. R. Fessler, A. J. Skidmore, H. R. Hazard, and J. P. Dimmer

698 Corrosion and Deposits from Combustion of Solid Wastes—Part VII: Coincineration of Refuse and Sewage Sludge (79-WA/CD-2)
H. H. Krause, P. W. Cover, W. E. Berry, and R. A. Olexsey

706 The Influence of Liquid Film Thickness on Airblast Atomization
N. K. Rizk and A. H. Lefebvre

711 The Base Pressure Problem in Transonic Turbine Cascades (78-GT-120)
C. H. Sieverding, M. Stanislas, and J. Snoeck

719 Waste Heat Disposal to Air with Mechanical and Natural Draft—Some Analytical Design Considerations
Ali Montakhab

728 Status of Centrifugal Impeller Internal Aerodynamics—Part I: Inviscid Flow Prediction Methods
D. Adler

738 Status of Centrifugal Impeller Internal Aerodynamics—Part II: Experiments and Influence of Viscosity
D. Adler

Announcements

747 Information for Authors

625 Call for papers

Downloaded 03 Jun 2010 to 171.66.16.159. Redistribution subject to ASME license or copyright; see http://www.asme.org/terms/Terms_Use.cfm

R. McGinnis
Manager,
Solar Operations,
Motorola,
Phoenix, Ariz.

Production of Photovoltaic Devices

This paper will provide a broad overview of present and future activities important for the production of Photovoltaic modules. First, the current methods for production will be reviewed, then a study of the techniques for further development will lead to an attempt to describe the factory of the future for Photovoltaic device production. The paper will look at the issues and technologies for the conversion from high purity quartz to silicon substrates and will then analyze processes from substrates to finished solar cells, and finish by reviewing the concepts for the manufacturing of the Photovoltaic modules.

Introduction

The need for a reusable nonpolluting source of energy is widely recognized, as is the fact that photovoltaic devices meet that need very well. The heart of the issue is economics. The cost of this form of energy must approach the cost of conventional energy sources as rapidly as possible so that it may start to displace conventionally generated power.

The available market for Photovoltaic devices is determined by the market elasticity and the rate of acceptance of these devices into ever widening areas of application. Fig. 1 shows a range of price elasticity variation which is consistent with the numerous market studies that have been accomplished over the past year. When the costs are high, the applications are restricted to very remote sites or very low power requirements; as the costs come down, larger and more centralized applications become economic. Even at one dollar/watt, the market ranges from 100 million to one billion dollars per year, worthy of careful consideration. The key task of research, development and manufacturing groups is to bring costs down so the market may generate the demand to impact our energy mix.

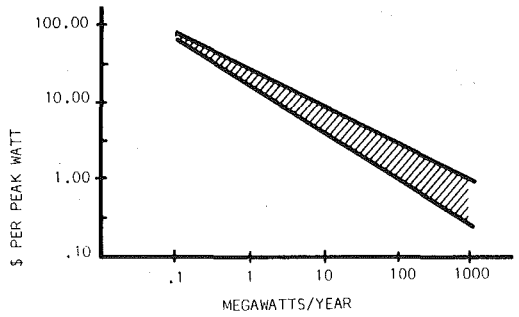


Fig. 1 Sales price of solar modules

Functional Division of Costs

There are four major manufacturing functions required for silicon solar cell modules:

1 Conversion of quartz (SiO_2) to pure silicon,
2 formation of silicon into sheets,
3 conversion of the sheet of silicon into solar cells by junction formation and contact application,
4 encapsulation and mechanical mounting of the cells into modules.

An analysis of the 1976 costs (near the starting point of major terrestrial solar activity) and the DOE 1985 goal is shown in Fig. 2 [1].

The impact of even a major photovoltaic industry will not be very heavy upon the conversion of SiO_2 to metallurgical grade Si (98 percent pure) as the large market for this product is in silicone sealers, oils and the alloying of metals. From that point on, however, there are cost reductions which must reach an aggregate of 20:1 to achieve the

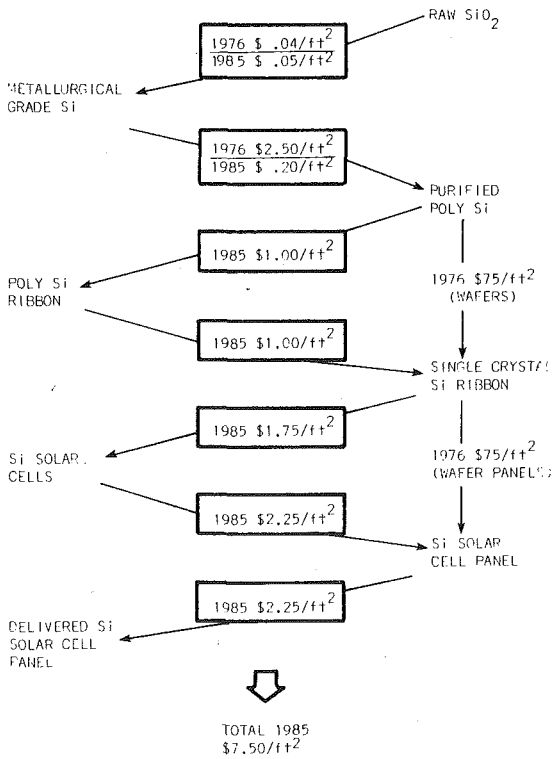


Fig. 2 Silicon solar cell panels: major production steps 1976 and 1985

Contributed by the Solar Energy Division and presented at the Gas Turbine Conference and Exhibit and Solar Energy Conference, San Diego, California, March 12–15, 1979 of THE AMERICAN SOCIETY OF MECHANICAL ENGINEERS. Manuscript received at ASME Headquarters December 8, 1978. Paper No. 79-SOL-8.

Copyright © 1980 by ASME
Downloaded 01 Jun 2010 to 171.66.16.58. Redistribution subject to ASME license or copyright; see http://www.asme.org/terms/Terms_Use.cfm

long term goal of 50 cents/peak watt.

From Quartz to Pure Silicon

The historical background of silicon purification which is shown in Table 1 dates back less than forty years, with the interest in ultra pure silicon occurring in the past twenty years.

The current process for manufacturing semiconductor grade (which is also used on virtually all the current solar applications) is shown in Fig. 3 along with the current costs. In order to achieve the more than seven times reduction called for in the flow chart, the cost of the pure Si must be brought under 10 dollars/Kg, and sawing kerf losses must be eliminated.

There are a number of different approaches which are possible, but there are five promising approaches (Table 2) to achieving the <10 dollars/Kg polysilicon cost goal. All of these programs are fully or partially funded by the DOE.

One of the more interesting, totally new, methods is the use of the reaction of SiF_4 with metallurgical grade silicon to form SiF_2. This is then polymerized to $(SiF_2)_X$ polymer chains which are subsequently heated up to form homologues which are finally harvested to provide pure silicon and additional SiF_4 gas which is recycled. The purpose of the process is to remove the impurities from the 98 percent pure metallurgical grade silicon and raise the purity to the order of five nines pure. Fig. 4 shows the primary impurities at the various steps in the process. This process has been costed out at under 8 dollars/Kg which is well within the 10 dollars required in the division of costs. A complete description of the process is given in [2].

Formation of the Silicon Sheet

Sunlight provides a great deal of total energy on the earth, but it is quite diffuse. Peak sunlight intensity is about 100 W/ft^2. Generation of megawatts of power, therefore, calls for large areas of silicon (with concentrating systems, some of the silicon area can be traded for reflector or refractor area, but there are other problems). The concern here is for the low cost production of large surface areas of silicon.

The Czochralski (Cz) method of silicon sheet generation requires these steps: (1) Place chunks of polysilicon into a pure quartz crucible and raise the temperature to the melting point of the silicon. (2) Place a seed crystal into the melt and slowly withdraw the seed. The silicon will attach to the seed and maintain its crystallographic orientation while it freezes into a solid. Single crystal ingots of 5 in. dia and 50 in. length are routinely grown in this way. (3) The crystals are centerless, ground to a specified diameter and an identification (and orientation) flat is frequently ground in as well. (4) The crystals are then cut into slices with ID diamond saws or slurry wire saws, and chemically etched to remove the damaged silicon near the surface. Even in the most advanced process, 50 to 60 percent of the silicon is lost through kerf and etching. Despite these significant process losses inherent in the Cz process, there are many who believe this technology could be pushed into the cost range required to meet the long range cost goals. Multiple recharges of a single crucible and very fine kerf wire sawing are the main areas for cost reduction.

There is a major research and development effort underway to replace the Cz process with alternate methods that do not waste such a large percentage of the material in the course of manufacture. All of these programs share the objective of making the sheets rectangular. (Cz crystals grow round and must be cut to get rectangular shapes). The two targets that these programs must hit are low cost, high purity and low defect density (for at this stage of the game, certain forms of crystal defects, as well as large impurity inclusions, can degrade solar cell performance).

Table 1 Historical background of the development of pure Si

1940	• Leached powdered silicon
1949	• Zinc reduction of silicon tetrachloride
	• Decomposition of silicon tetraiodide
Mid	• Pyrolytic decomposition of silane
1950's	• Hydrogen reduction of trichlorosilane
	• Siemens: hydrogen reduction of trichlorosilane on a silicon filament

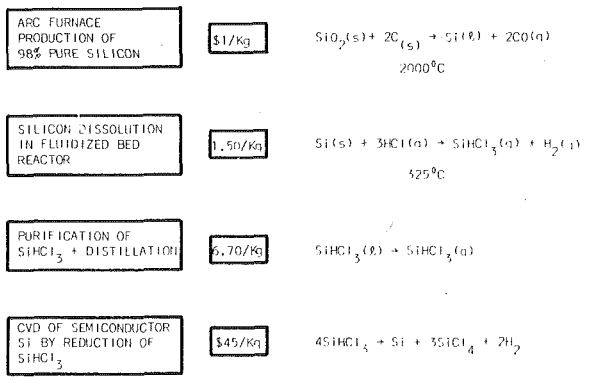


Fig. 3 Present process for manufacturing polycrystalline semiconductor and solar silicon

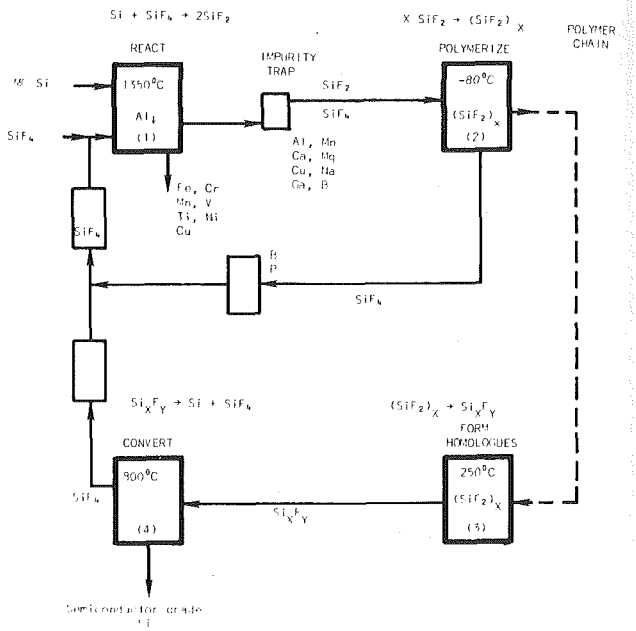


Fig. 4 Silicon Tetrafluride purification process flow and impurity removal distribution

Table 2 Low cost polysilicon programs

Method	Scale Up Status	Energy Payback	Contractor
Catalyzed reaction of hydrogen and silicon tetrachloride with metallurgical silicon to form trichlorosilane thence silane.	100 ton (M)/yr plant in design.	9 mo.	Union Carbide
Zinc reduction of silicon tetrachloride.	50 ton (M)/yr plant in design.	13 mo.	Batelle
Silicon tetrafluoride purification of metallurgical grade silicon.	8 ton (M)/yr plant nearly designed.	3 mo.	Motorola
Sodium reduction of silicon tetrachloride in 3500°K plasma arc reactor	No experimental verification of reactor yet.	14 mo.	Westinghouse
Increased purity of materials in a conventional silicon dioxide arc furnace.	Now testing in a 27 ton (M)/yr arc reactor	10 mo.	Dow-Corning

Downloaded 01 Jun 2010 to 171.66.16.58. Redistribution subject to ASME license or copyright; see http://www.asme.org/terms/Terms_Use.cfm

Table 3 Comparison of sheet growth methods

Process Description	To Achieve Continuous Growth	To Achieve High Through-Put	Best Growth Rate Demonstrated	Problems/ Features
EFG: Si pulled from melt by capillary slot thence ribbon.	Replenishment of Si in melt.	Multiple ribbons for melt.	37 cm^2/min	Die contamination of ribbons/ several years of experience.
RTR: Poly ribbon deposited, ribbon recrystallized by swept laser.	Continuous poly feedstock.	Side-by-side ribbons.	55 cm^2/min	Complex mechanical design/high purity achievable.
CAST: Si pulled from melt by capillary slot and ribbon pulled.	Replenishment of liquid.	Very wide (5″) ribbons.	30 cm^2/min	Contamination of ribbons/very wide ribbons.
WEB DENDRITIC: Si melted dendrites seeded ribbon pulled dendrites removed.	Replenishment of liquid.	Multiple pullers.	12 cm^2/min	Dendrites must be removed/good ribbon quality.

A listing of the sheet process under development, and some of the important comparisons, are shown in Table 3.

The RTR Process is one of the methods under development. In using a laser in a controlled atmosphere to recrystallize polysilicon ribbon, it shows the greatest promise for low defect density and, consequently, high cell performance [3]. In this approach, a polysilicon ribbon (which can be formed in the harvesting step of the SiF_4 process or by CVD from low cost silane) is passed through a laser beam as shown in Fig. 5. The resultant ribbon is single (or large grain polycrystalline). The thin ribbons can be processed "reel to reel" as the silicon is flexible when it has a thin cross-section. Ribbons have been grown at a rate of 55 cm^2/min. which is the fastest of all the development methods.

Solar Cell Fabrication

While most of the silicon technology came out of the semiconductor industry, the solar cell fabrication technology has evolved from the first cells put into orbit through the years as part of space technology. Most of the current manufacturers of terrestrial solar cells came from that industry.

Every solar cell requires a PN junction and a method of making electrical contact with both sides of that junction. Many advanced cells have, in addition to the basic elements, such attributes as antireflection coatings, textured surfaces, junction edge insolation, back surface field diffusions and others. In every case there is a trade-off between cell efficiency and cell (or module) cost, with the higher efficiency cells usually requiring more complex or critical process parameters.

A typical process sequence for a current terrestrial solar cell is shown in Fig. 6.

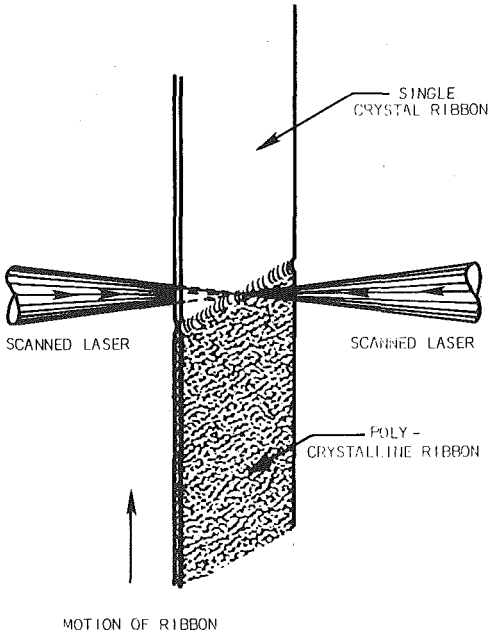


Fig. 5 Ribbon-to-ribbon (RTR) process for growing single crystal silicon from polycrystalline ribbon feedstock

This type of process, using good quality silicon will have a mean efficiency of about 13 percent (solar cell efficiency is electric power out/light power in). The junction formation step in the process is the N^+ diffusion into a P type wafer (P^+ diffusion into N type wafers also works well). This diffusion step is time consuming and difficult to automate, although quite controllable. A recent development in the semiconductor industry is ion implantation. With this technology, the desired impurities are accelerated and implanted into the silicon rather than by the surface reduction and solid state method. Studies [4] have shown that ion implantation promises to be more cost effective as a high volume process than diffusion. Fig. 7 is a possible advanced ion implant process.

This process will yield solar cells with a mean efficiency of 15–16 percent. The major factor preventing the large scale use of such a process today is the need for development of the high throughput special purpose ion implant machines.

Module Fabrication

Once you get past the high initial g forces, and other than the radiation problems, the environment in space is quite benign compared to the terrestrial environment. Moisture, salt spray, smog, ozone, ultraviolet radiation, animals, vandals, ice, snow, wind and hail are among the hazards a solar module must survive on earth. Much of the early packaging of solar cells was almost an afterthought of the total design, and many of the early problems with solar modules were due to encapsulation failures.

The keys to module design are high reliability and long life in the terrestrial environment, and low manufacturing cost. The latter must include low material and labor costs. A current production design which holds some promise for the future uses a glass superstrate with the solar cells bonded to the glass with polyvinyl buturate (PVB). This is the same material used to laminate automobile safety glass which,

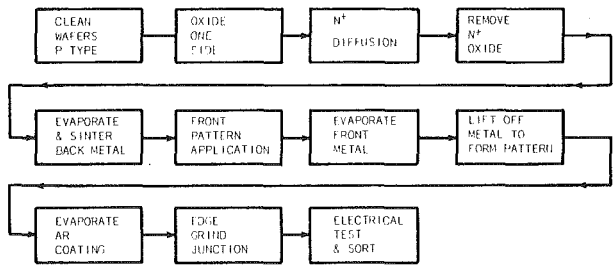


Fig. 6 Typical current solar cell process

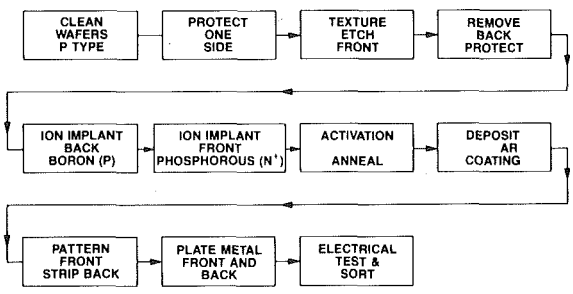


Fig. 7 Advanced ion implant solar cell process

Downloaded 01 Jun 2010 to 171.66.16.58. Redistribution subject to ASME license or copyright; see http://www.asme.org/terms/Terms_Use.cfm

in this application, has shown excellent long term weathering properties. One of the most reliable module designs shown in Fig. 8 uses a glass front and a stainless steel back pan and surrounding stainless steel bezel. The solar cells are interconnected with a copper kapton interconnect and can be arranged into any series parallel configuration. This module has a predicted MTBF of greater than 50 years based on test data.

The manufacturing process for modules varies greatly with the various designs. However, they all have in common:

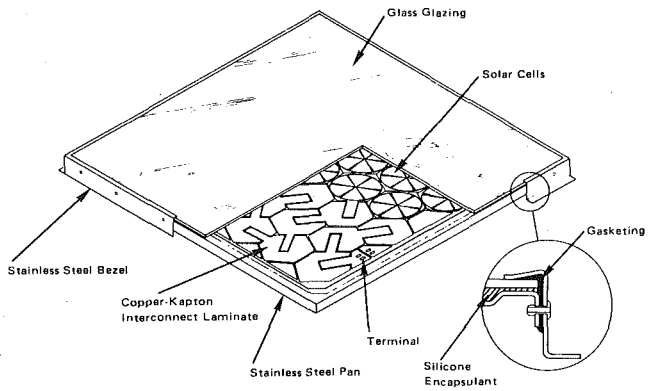


Fig. 8 Solar photovoltaic module section showing construction details and internal arrangement of cell interconnection

1 interconnection of one cell to another,
2 electrical connection of the cells to the outside,
3 attachment to the substrate or superstrate,
4 moisture sealing,
5 electrical test and sorting.

The high volume manufacturing line will probably be continuous, but with the operation sequences depending on specific designs.

Factory of the Future

The various trends that have been discussed lead toward some ideas as to what the factory of the future might look like. However, some important questions must be answered before the factory can be planned.

1 How large should it be?
2 What parts of the process will be centralized in the factory?
3 Will certain market areas require an indigenous manufacturing facility?
4 How important is the cost of land, power, labor and shipping?
5 What is the relative importance of capital and consumable costs?

A major cost of the factory is the overhead cost. This includes such elements as engineering, factory overhead, management, personnel, security, taxes, insurance, etc. Most of these costs are fixed or semi-fixed; therefore, on this basis, the factory should be made as large as possible. Only variable cost items such as shipping, labor cost increases, and market reasons would lead you toward decentralizing.

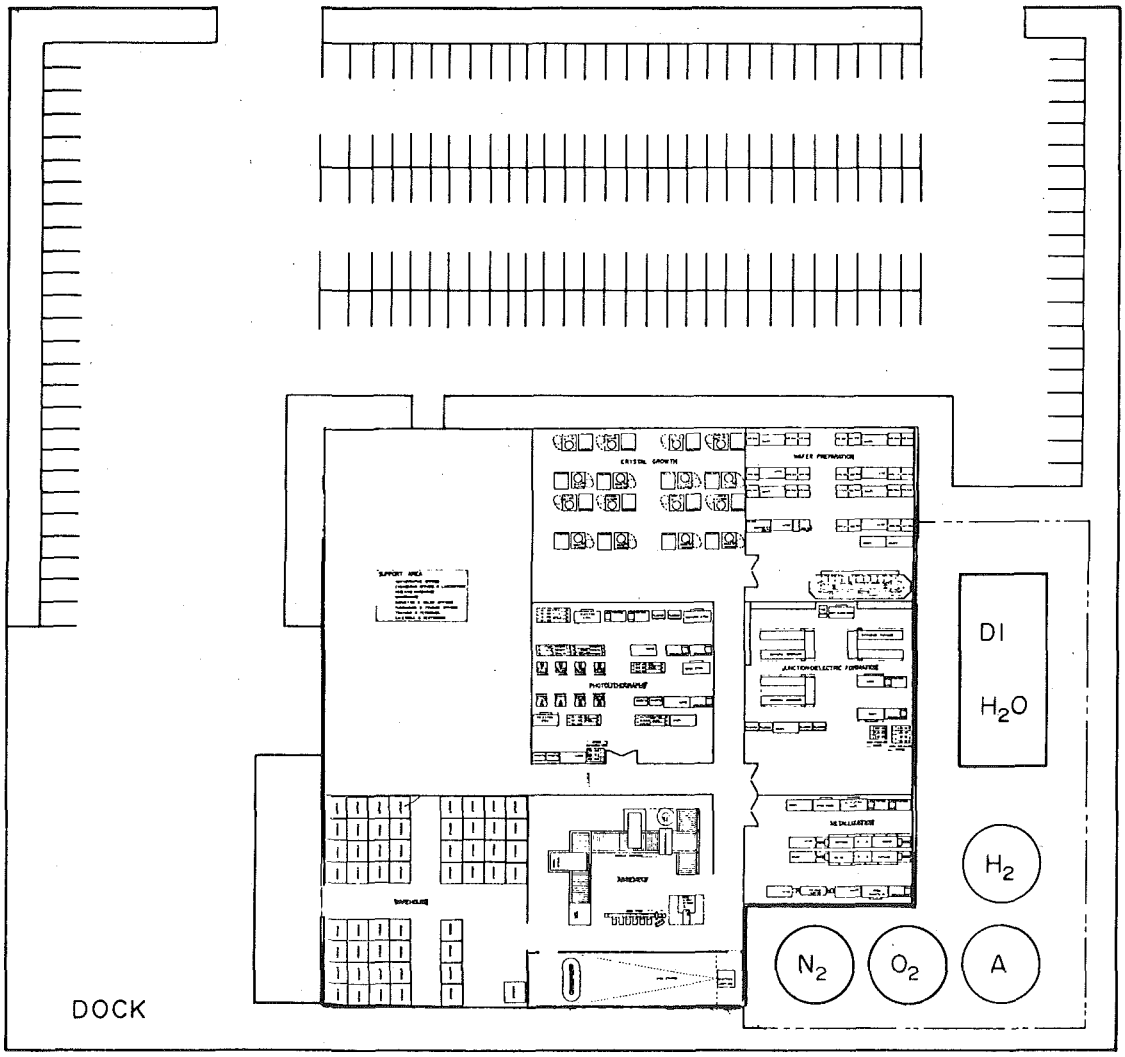


Fig. 9 Facility layout, including parking and support facilities, of sample 5 megawatt annual production factory

Downloaded 01 Jun 2010 to 171.66.16.58. Redistribution subject to ASME license or copyright; see http://www.asme.org/terms/Terms_Use.cfm

A 15–20 megawatt per year plant appears to be a reasonable unit size for at least the next 6–8 years.

Full integration of the process from polysilicon growth through finished solar module is an important feature. Shipping costs and overhead costs must be kept to a minimum. The integration also implies one profit center, eliminating the profit chain which occurs when a product moves through several manufacturers. The pocket electronic calculator is an example of the success enjoyed by those who are fully integrated and the failure of many who were not. Many of the largest markets for photovoltaic devices in the next decade will be outside of the U.S., many in countries which are striving to develop an industrial base. The laws and policies in these countries require a high local manufacturing content in products sold there. This will lead to the indigenous module assembly plant. This plant will use cells manufactured at the large centralized plant described before and other module components (particularly glass and metal parts) which are manufactured locally. Eventually, as volumes in these countries grow large enough, a fully centralized plant will be built.

Land, power, labor and shipping costs are the primary site variables which must be balanced and optimized. A sunny location is not needed as efficient module testing requires the use of light simulators which essentially duplicate the spectrum from the sun. A low cost power, labor and land site close to module component suppliers and major customers is the best site.

As production volumes grow and equipment utilization improves, the consumable items (e.g., pure water, masking materials, process chemicals, and factory supplies) begin to dominate the cost picture. The production processes developed for these high volume products must greatly minimize the costs for these types of items.

The layout [5] of a large plant is shown in Fig. 9.

Conclusion

Solar module manufacturing processes in use today have evolved from the semiconductor and space solar cell technologies. In order to achieve significant energy displacement with photovoltaic modules, these costs must be reduced by a factor of twenty or more, and these cost reductions must occur across the full spectrum of manufacturing processes. A great deal of research and development is taking place in all of these important areas now.

The factory of the future will be a large, fully integrated facility with a series of market region indigenous module manufacturing locations. The factory will be located so as to minimize fixed and variable costs. I believe that photovoltaic technology will successfully penetrate our energy market and such plants will be an important part of the American scene.

References

1 Lesk, I. A., "Invited: Solar Energy for Residential Use," *Proceedings of the 8th Conference (1976 International) on Solid State Devices,* Tokyo, 1976; *Japanese Journal of Applied Physics,* Vol. 16 (1977) Supplement 16-1, pp. 417–421. (Revised)

2 Ingle, W. M., Chev, R., Thompson, S., Rosler, R., Jackson, J., Technical Quarterly Report No. 9, JPL/DOE, Contract No. 954442, April 1978.

3 Baghdadi, A., Gurtler, R. W., Legge, R. N., Ellis, R. J., and Sopori, B. L., "The Impact of Defects on the Photovoltaic Potential of RTR Silicon Ribbon," *Thirteenth IEEE Photovoltaic Specialists Conference-1978,* pp. 363–369.

4 Grenon, L. A. and Coleman, M. G., "Silicon Solar Cells, A Manufacturing Cost Analysis," *Thirteenth IEEE Photovoltaic Specialists Conference 1978,* pp. 236–251.

5 Pryor, R. A., Grenon, L. A., Coleman, M. G., Final Report, Phase I of the Automated Array Assembly Task of the Low Cost Silicon Solar Array Project, JPL Contract No. 954363, pp. 209.

Downloaded 01 Jun 2010 to 171.66.16.58. Redistribution subject to ASME license or copyright; see http://www.asme.org/terms/Terms_Use.cfm

S. J. Valentino
Project Engineer,
Heat Transfer and Cryogenic Systems,
AiResearch Manufacturing Company of California,
Torrance, CA

Designing Reliability into High-Effectiveness Industrial Gas Turbine Regenerators

The increased demand for fuel conservation has provided the impetus for higher efficiency in the design of gas turbines and their operation. To conserve more fuel, regenerators must operate at higher temperatures and pressures, and must experience frequent on-off cycles. The design concept, methodology, and full-scale testing leading to the final design of the regenerator will be presented. Particular emphasis will be given to the importance of meaningful testing of both the regenerator and materials used. The necessity of having materials data, in the as-processed condition versus catalog data, for reliable design, is also presented.

Introduction

Increases in operating temperatures and pressures in industrial gas turbines, combined with frequent start/stop cycles, have placed new demands on regenerators—demands that require new design concepts and technology to achieve reliability.

To improve gas turbine efficiency for fuel conservation, high-performance regenerators must operate in the temperature range of 1000 to 1200°F (538 to 649°C) and with an effectiveness between 81 and 90 percent. These conditions impose severe material and design requirements. Most regenerators operating today were designed for continuous duty at temperatures below 1000°F (538°C) and an effectiveness of 81 percent or less. This comparatively benign requirement permitted the use of low-alloy steel without too much concern for fatigue life of the equipment or excessive high-temperature corrosion.

The new operating methods require that the regenerator operate at higher temperatures and withstand thousands of starting and stopping cycles without leakage or excessive repair. A review of the history of existing units has shown that such equipment has not been able to withstand such duty.

This paper addresses the measures necessary to ensure a reliable regenerator design that can withstand the high temperatures and many start and stop cycles—conditions encountered in high-efficiency operation on pipeline applications. While the design of a regenerator for high-temperature applications requires careful consideration of many design areas, this discussion will concentrate on only three areas: (1) structural analysis of the heat exchanger core—the part of the regenerator that must withstand the higher temperatures and cyclic duty, (2) materials data and material selection, and (3) the comprehensive test program to demonstrate the reliability of the regenerator.

Regenerator Design. The design and performance features of this regenerator have been well described in earlier ASME publications [1, 2]. These features are briefly summarized here and in various other sections of this paper because of their effect on the unit's reliability.

Contributed by the Gas Turbine Division of The American Society of Mechanical Engineers for presentation at the Gas Turbine Conference and Exhibit and Solar Energy Conference, San Diego, Calif., March 12–15, 1979. Manuscript received at ASME Headquarters January 17, 1979. Paper No. 79-GT-199.

The basic regenerator shown in Figs. 1 and 2 is designed for a 15,000 hp (11.8×10^6 w) gas turbine and for air and gas flows of 80 to 125 lb/s (36.3 to 56.7 kg/s).[1] A modular design is used, with the basic regenerator comprising two shippable halves. In fact, for gas turbine engines of lower power and lower flow, only one of these halves is necessary. Engines of power ratings higher than 15,000 hp can be accommodated by adding more half modules or another regenerator. The plate-fin regenerator cores are furnace-brazed modules, comprising alternating layers of air and gas fins. Each core weighs about 5000 lb. Six cores are welded together in a six-pack configuration to make up half the regenerator (Fig. 2). Bellows expansion joints connect the six-pack to air piping flanges that are rigidly attached to the regenerator case. The six-pack is supported within the case with flexible Inconel straps. During high-temperature operation, these straps and bellows allow unrestrained growth of the cores relative to the case. The regenerator cores are stainless steel. The internally insulated case is made from structural steel. The basic regenerator weighs 50 tons (45,350 kg) and has overall dimensions of 15.4 ft (4.69 m) in height, 11.3 ft (3.44 m) in the gas flow direction, and 17.2 ft (5.24 m) in length.

The regenerator is designed to operate for 120,000 hr and 5000 cycles without scheduled repairs; however, manways provide access into the air plenums for inspection, on-site maintenance, and internal repair. Damaged areas can be weld-repaired or air passages can be blanked off in the event the damaged area is not accessible. The unit is designed to operate with an exhaust gas temperature up to 1100°F (593°C). Growth potential to 1200°F (649°C) or higher is anticipated with the same overall design concept and material system.

The regenerator shown in Fig. 1 is designed for a horizontal exhaust gas flow installation. A regenerator configured for a vertical exhaust gas flow is similar in all pertinent details.

Materials Data Program

For a manufacturer to guarantee the life and reliability of his product, it is essential that the properties of his materials be absolutely known. In this case, data on the yield strength and creep rupture limits of stainless steel (particularly when processed by brazing and tempering for high-temperature and cyclical applications such as

[1] Protected by U.S. Patent No. 4073340 and others pending.

Copyright © 1980 by ASME
Downloaded 01 Jun 2010 to 171.66.16.58. Redistribution subject to ASME license or copyright; see http://www.asme.org/terms/Terms_Use.cfm

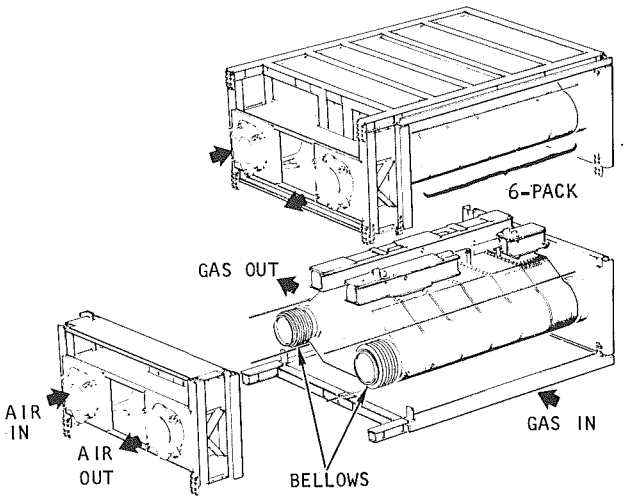


Fig. 1 Regenerator design features

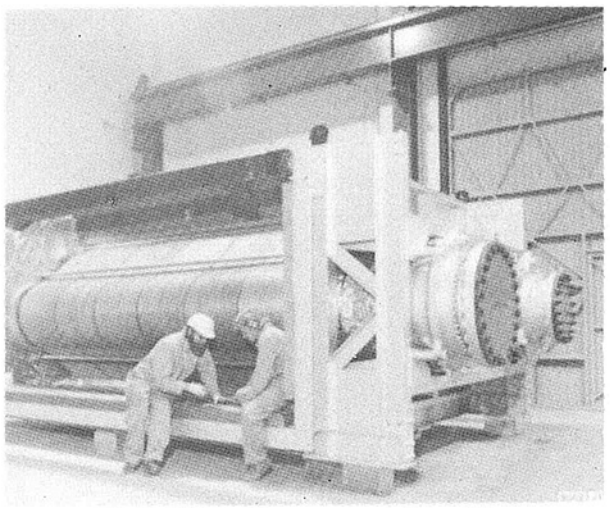


Fig. 2 High-performance regenerator module

regenerators) were either nonexistent, incomplete, or generally suspect. This is probably because of the wide variety of processes and the extensive testing and analysis necessary to obtain these data. The result is that material properties for a given application are either of little interest to other companies, or conversely, of great interest and therefore highly proprietary.

In its own test program, AiResearch subjected many samples of regenerator materials to both short- and long-term tests. Fig. 3 shows specimens of AISI 409 stainless steel that were tested for creep strength. From such tests, a statistical base is derived, which is then converted into usable engineering data such as the well-known Larson-Miller parameter (LMP).

Using the data from the test program and the LMP relationship, a typical creep life for one of the regenerator AISI 409 elements was determined to be 8.7 million hours. This value provides a more than adequate margin for long-term reliability. It should be noted that the LMP for this element is for a particular process of AISI 409 stainless steel, and will vary for other processes. Similar data were derived for other materials and processes.

In selecting materials for the regenerator core, a number of factors were considered: mechanical properties, oxidation and corrosion resistance, weldability, formability, brazeability, and cost. It was particularly important to consider the nature of the duty cycle. For example, high-temperature cyclic duty in a coastal (salt-laden) air environment imposes greater requirements for corrosion protection than does a less demanding, continuous duty cycle under clean air and clean fuel conditions. Chloride corrosion posed particularly difficult problems since practically all candidate regenerator alloys are susceptible to some form of attack in chloride environment. Of the

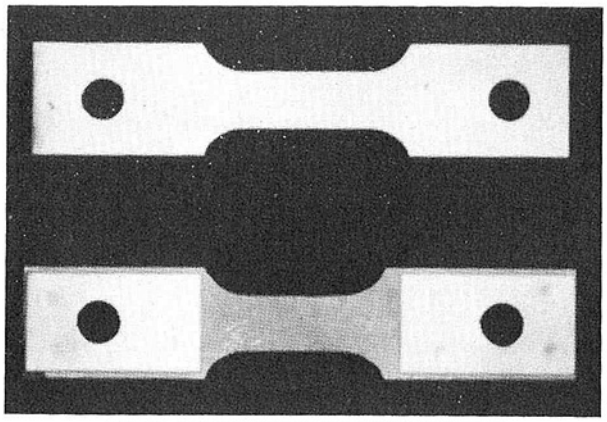


Fig. 3 409 material creep strength specimen

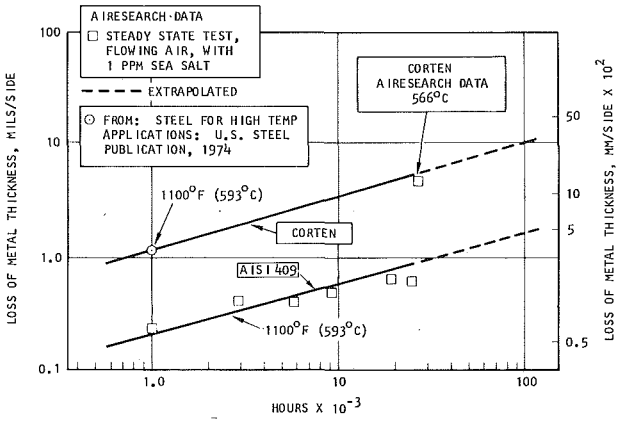


Fig. 4 Oxidation rates of regenerator steels

stainless steels, the most serious attack occurs in Type-300 austenitic stainless steels such as 304, 316, etc. In these steels, chlorides are known to cause both stress corrosion cracking [3, 4] and intergranular corrosion or oxidation [5] at elevated temperatures, any of which could lead to a failure under pressure.

Accordingly, the ferritic 400-Type stainless steels were selected as the basic alloy system for this regenerator. These materials are resistant to both stress corrosion cracking and intergranular corrosion [3–5]. Of the ferritic stainless steels evaluated, AISI 409 was chosen for the core because of its excellent properties of corrosion resistance at high temperatures. Over 30,000 hr of materials testing at high temperatures (1100°F or 593°C) in a salt-laden atmosphere has proven the validity of the choice. (See Fig. 4.)

Experience has shown that AISI 409 stainless steel has corrosion properties, particularly pitting resistance, which excel over those of some of the more highly alloyed grades. This is largely attributed to the titanium stabilization. Various other factors such as strength and fabricability were studied in the materials test program. These are ranked in Table 1.

To achieve an optimum design, it becomes necessary to balance strength against corrosion/oxidation resistance. Since many of the stress considerations are based on thermal gradients and only minimally depend on section size, the tendency is to select the low-chromium, higher-strength materials and make sufficient design allowances for loss of metal thickness during the intended service life of the unit.

To insure reliability, an in-house specification is used to control 409 chemistry for mechanical properties and for optimum behavior during brazing, such as surface wetting and flow, grain size control, etc.

Structural Analysis of the Regenerator

Because no other industrial regenerator had been designed to meet such high temperatures, pressures, and cyclic loads, every detail of the heat exchanger was analyzed. An extensive analytical effort was undertaken to evolve a heat exchanger that combined high effec-

Downloaded 01 Jun 2010 to 171.66.16.58. Redistribution subject to ASME license or copyright; see http://www.asme.org/terms/Terms_Use.cfm

*Table 1 Candidate ferritic stainless steel alloys**

AISI No.	Percentage Cr	Percentage Mo	Stabilizer	High-Temperature Strength	Fabricability
405 DR**	13	0	Al	4	3
409	11	0	Ti	1	1
410	12	0	None	1	4
430	18	0	None	5	4
434	18	1	None	4	4
436	18	1	Cb	3	2-3
439**	18	0	Ti	5	1
444L**	18	2	Ti	2	1
18-2**	18	2	Cb	2	1

*Ranked by most desirable property, i.e., a rating of 1 indicates the highest strength, weldability, and formability.

**Vendor codes, not AISI designations.

tiveness, good producibility, and the ability to withstand the startup and shutdown thermal cycles of industrial gas turbines without requiring special starting procedures. To insure reliability, a design life of 120,000 operating hr and 5000 start-stop cycles over the full range of temperature and pressure was established.

By way of comparison, many high-temperature heat exchangers have been developed to withstand 50,000 cycles of thermal stresses induced by aircraft turbine engines—most with thermal ramps much more severe than those of industrial turbines. The comprehensive digital computer programs used to analyze the effects of temperature, pressure, and cyclic loads on these heat exchangers were employed to design the industrial regenerator. These analyses were added to the metallurgical properties determined by actual test.

The design process is an iterative one. Once detailed analysis pinpoints areas subject to creep rupture from pressure or thermal stresses and cyclic fatigue, design changes are made. The new design is then reanalyzed to confirm that the potential failure point has been eliminated.

Steady-State Stresses. A finite-element model of the core was constructed to determine stress levels arising from high-temperature, steady-state operations. Steady-state pressure and temperature levels typical of growth engines have been used in sizing manifolds, bellows, and cores for 120,000 hr of operation with the engine operating at ambient temperature conditions from −60 to 120°F (−51.1 to 48.9°C). Thus, for present-day engines, a considerable margin exists. Finite-element models were used extensively to determine thermal and pressure stress levels. Fig. 5 is a finite-element model of the regenerator core.

Transient Thermal Stresses. A rigorous finite-element stress analysis of the core assembly was performed using data derived from the materials test program. Fig. 6 shows a typical output plot of stress distribution at a particular time. Auxiliary models are constructed to determine stress concentration factors and more detailed information about local stress fields. The entire range of operation (startup, steady-state operation, and shutdown) is analyzed to determine the stresses to be used in low-cycle fatigue analysis. For this analysis, a survey of industrial engine transients was made and the most severe conditions were chosen for the thermal stress design.

Once stress history of the most critically stressed areas was determined, a low-cycle fatigue analysis of these areas was performed. The program used to analyze the stress history incorporates all of the material constants found from ongoing materials test programs. This program computes low-cycle fatigue with creep interaction. In the core, the stress-strain cycle starts at zero, and then goes negative due to compression; after some plasticity, the stress-strain curve reaches tension as the core achieves temperature uniformity. Creep relaxation then takes place as the regenerator operates at steady state. During shutdown and subsequent start, another loop occurs until stabilization takes place; that is, the amount of plastic deformation in compression exactly matches creep relaxation.

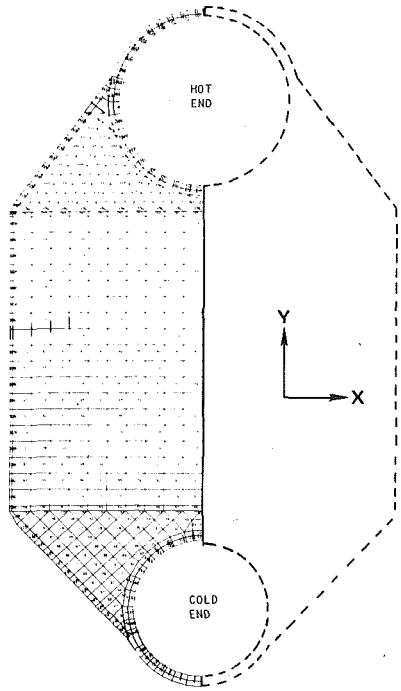


Fig. 5 Finite-element model of heat exchanger core

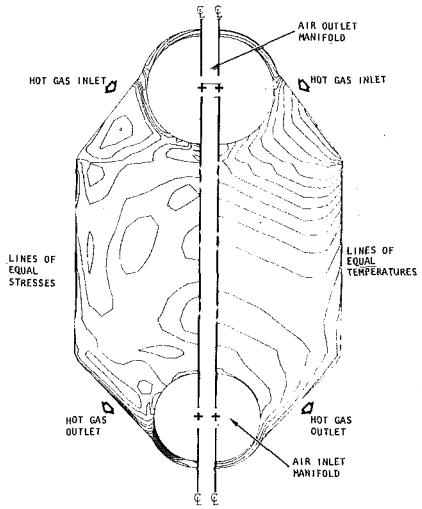


Fig. 6 Typical isostress map

Fig. 7 shows the stress history of an element in the heat exchanger matrix. The "allowable stress" curve represents the variation of allowable stress as the metal heats up through the operating cycle. The lower curve shows the imposed stress from the startup transient through steady-state operation and shutdown. The shaded region is where material creep relaxation and plastic strain occur. Note that material gauges must be properly matched to avoid a thick-to-thin thermal mismatch where the cusp of the transient stress level would readily exceed the allowable limit and result in cyclic fatigue failure.

Life calculations are based on the total strain range produced by material elastic-plastic behavior with creep interaction. Life is calculated by linearly summing the damage incurred in each cycle due to creep stress relaxation and total strain range.

Stresses relax asymptotically with time. Creep damage is directly proportional to the stress relaxed. Most of creep damage occurs in the first 24 hours of a cycle (see Fig. 8). To insure design integrity, 5000 cycles of 24 hr duration were used to accumulate the 120,000 hr of operation. A computer model for a 24 hr cycle was used to analyze the life of the unit.

Downloaded 01 Jun 2010 to 171.66.16.58. Redistribution subject to ASME license or copyright; see http://www.asme.org/terms/Terms_Use.cfm

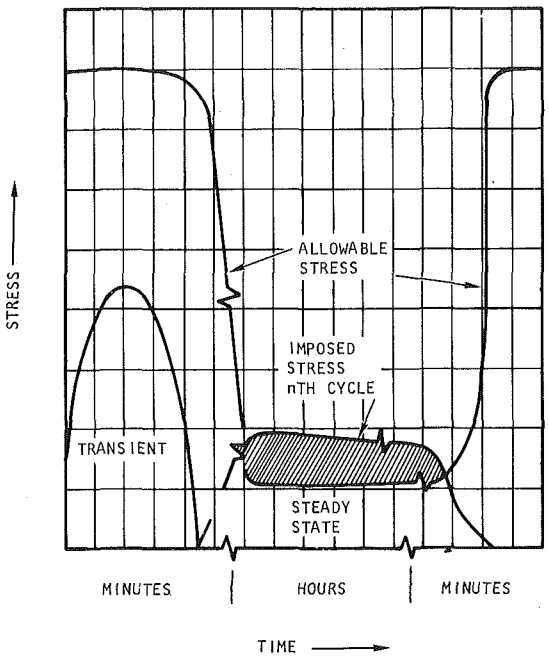


Fig. 7 Stress history

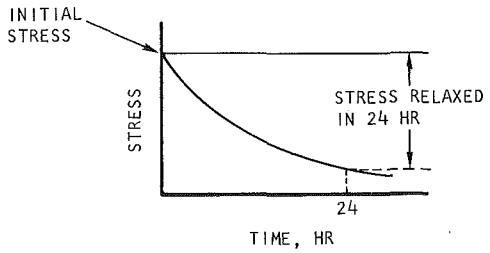


Fig. 8 Time-dependent relaxation of an initial stress

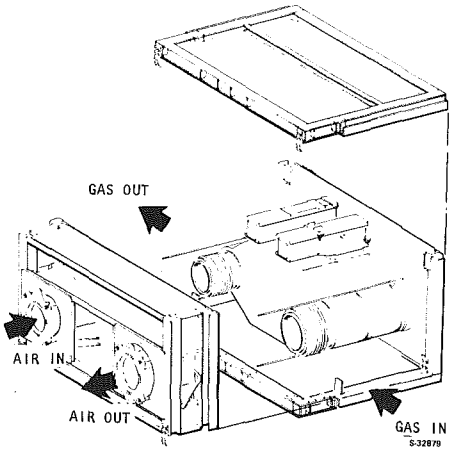


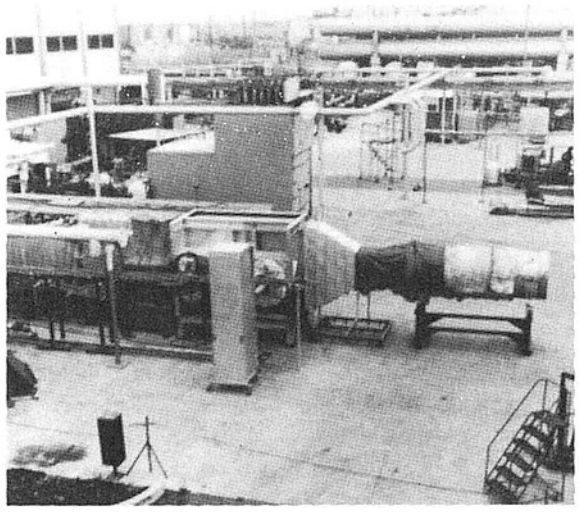
Fig. 9 Two-core laboratory test model

These techniques, when coupled with tests to establish materials data and the effects of manufacturing processes, yield a design optimized for thermal performance and efficient use of materials.

Reliability Demonstration

Despite the accuracy of analytical techniques and materials data, good engineering practice, especially in the design of high-performance regenerators, requires a comprehensive test program. Often such reliability tests can uncover potential problem areas not isolated by analysis.

The first cores fabricated from production tooling were used to verify performance and life predictions of the regenerator. These test modules included the front and rear panels, piping flanges, hanger system, tie rods, bellows, insulation, and gas seals, as shown in Fig. 9. The test setup is illustrated in Fig. 10. To insure the integrity of the basic design, various tests were necessary. The primary areas, together with the critical parameters, are shown in Fig. 11.



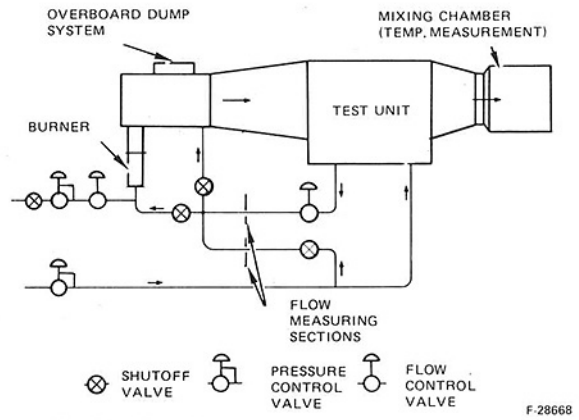


Fig. 10 Setup for performance and thermal cycle testing

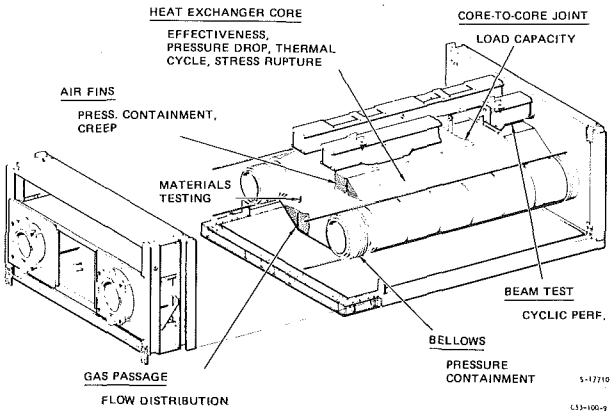


Fig. 11 Critical design areas covered by test program

Performance Requirements. Prior to starting the life-cycle test, the regenerator cores were subjected to performance testing. The test cores were designed for an 83.5 percent thermal effectiveness, including margins for fouling and manufacturing tolerance. The performance test results for heat transfer and pressure drop of two-core assembly are shown in Table 2. These results provide an accurate indication of performance of a complete regenerator. Only overall gas and airflow distribution of larger assemblies are not laboratory-simulated. However, care is taken to minimize these gas and air distribution effects. Table 2 shows the close correlation of calculated and measured performance, substantiating the analytical tools used in design.

Life-Cycle Tests. The thermal cycle test, which is a measure of

Downloaded 01 Jun 2010 to 171.66.16.58. Redistribution subject to ASME license or copyright; see http://www.asme.org/terms/Terms_Use.cfm

Table 2 Performance requirements

Performance	Calculated	Test Results
Effectiveness, percent	83.5	83.4
Pressure drop		
Air, in. Hg	2.81 (71.37 mm Hg)	2.73 (69.37 mm Hg)
Gas, in. H_2O	5.85 (10.93 mm Hg)	5.01 (9.35 mm Hg)

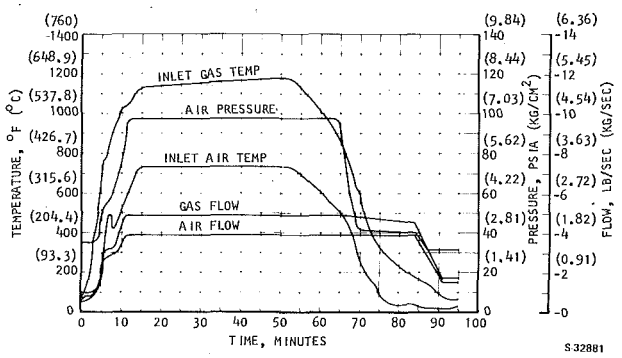


Fig. 12 Regenerator accelerated test transient

potential regenerator life, is a repetitive series of cycles. Each cycle lasts approximately 95 min and simulates the gas and compressed air flows, temperatures, and pressures of the regenerator during the gas turbine startup and shutdown. Thermal cycle tests are a critical part of the demonstration program, particularly where cyclic operation is anticipated. By overstress testing, many years of cyclic operation can be compressed into a few months of accelerated testing. The accurate simulation of turbine startup operation is an art in itself, and requires sophisticated equipment and techniques.

The accelerated test transient is shown in Fig. 12. Note that the test includes not only the maximum rate start anticipated, but a significant overtemperature condition at steady state. In this way, the combined effect of cyclic fatigue and creep damage were accelerated.

In accelerated life tests, the metal must reach the steady-state temperature and be held there long enough to induce the material creep characteristics. For this test, the metal temperature in the critical areas was held at 1150°F (621°C)—well above normal operating temperature—to effect the accelerated test conditions. Simply running the cycle up and down without overtemperature and adequate hold time does not provide a realistic test of the material and the unit. The test regenerator accumulated 1000 full startup and shutdown cycles with no evidence of leakage—the equivalent of 20 to 25 years of pipeline duty.

Pressure Containment in Fin Panels. A variety of tests were conducted to verify the life predictions and structural adequacy of the high-pressure, air-side heat transfer matrix. These tests, run at room temperature and elevated temperatures as high as 1100°F (593°C), included burst tests, short- and long-term high-temperature creep rupture testing, and post-test metallurgical examination. The adequacy of the design is illustrated by the following:

- Nominal design condition: 148 psig (10.4 kg/cm^2) at 1030°F (554°C)
- Room temperature burst test: 3470 psig (244 kg/cm^2)
- High temperature burst test: 2460 psig (173 kg/cm^2) at 1100°F (593°C)

Fig. 13 shows a typical test panel both before and after a pressure containment test. This test demonstrated the strength characteristics of the fin and the braze joints. It is of importance to note that it was the parent material that failed, having been stressed beyond its ultimate strength, and that the braze joints are still intact. A series of similar panel tests, in which the panels were intentionally burst, established the necessary statistical design data for a reliable design. The nominal design was for 120,000 hr of operation. Test results at nominal operating conditions indicate an operating life expectancy in exesss of 500,000 hr of pressure containment.



Fig. 13(*a*) Before pressure test

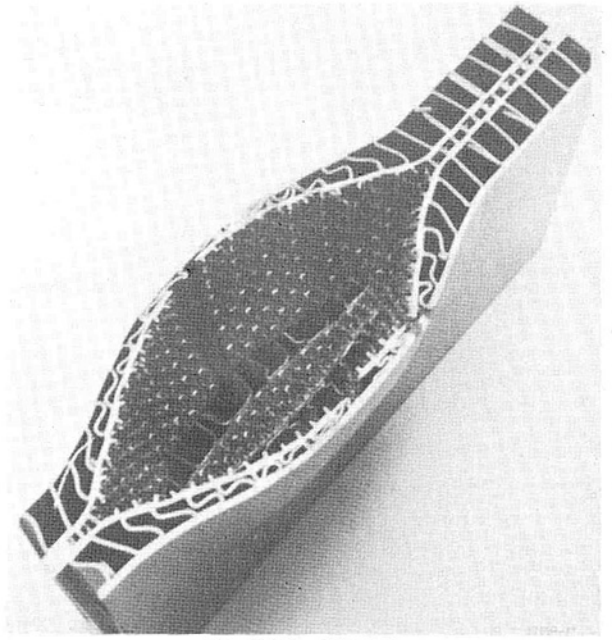


Fig. 13(*b*) After test

Fig. 13 Fin panel pressure containment test

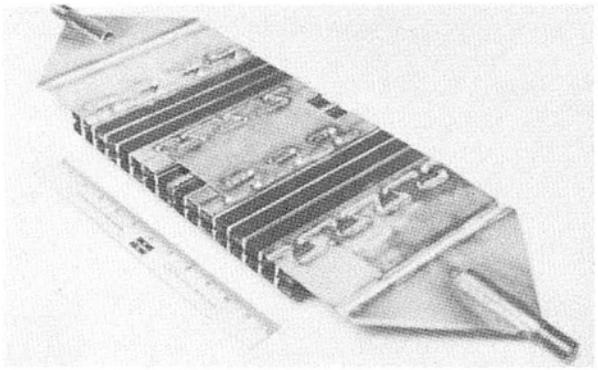


Fig. 14 Core-to-core joint test specimen

Core-to-Core Joint Structure Test. Fig. 14 shows the joint that connects the individual cores in a six-pack assembly. The objectives of this test were to (1) evaluate structural adequacy of the joint at operating conditions, and (2) determine the load capacity of the joints. This joint must withstand a load of 2650 lb (1202 kg) at operating conditions. The test value of 6000 lb (2722 kg) shows a very adequate design margin.

Bellows Pressure Containment Test. The structural integrity of the bellows joints is important because (1) they connect the high-pressure air inlet and outlet plenums to the piping flanges, and (2) they serve to isolate the regenerator cores from external structure loads. For these reasons, the material selection and the design are such that elastic behavior results during operation. Thus, a room temperature test, with a correction for high-temperature operation, is adequate to demonstrate structural integrity. Fig. 15 shows the setup used to test the pressure containment capability of the bellows. The design criteria for the bellows are 155 psig (10.9 kg/cm^2) at 1000°F (537.8°C). The test result was 430 psig (30.2 kg/cm^2) burst at room temperature, or the equivalent of 380 psig (26.7 kg/cm^2) at 1000°F (537.8°C).

Downloaded 01 Jun 2010 to 171.66.16.58. Redistribution subject to ASME license or copyright; see http://www.asme.org/terms/Terms_Use.cfm

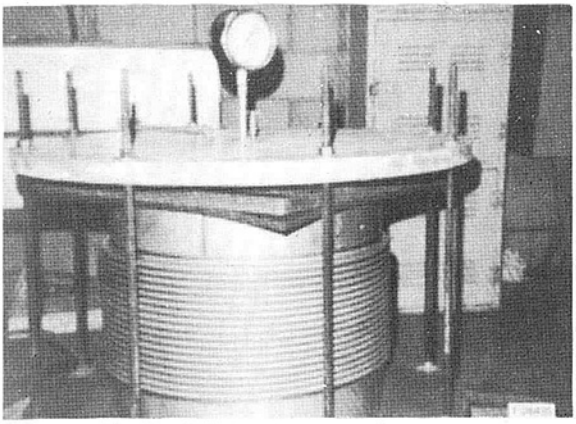


Fig. 15 Bellows pressure containment test

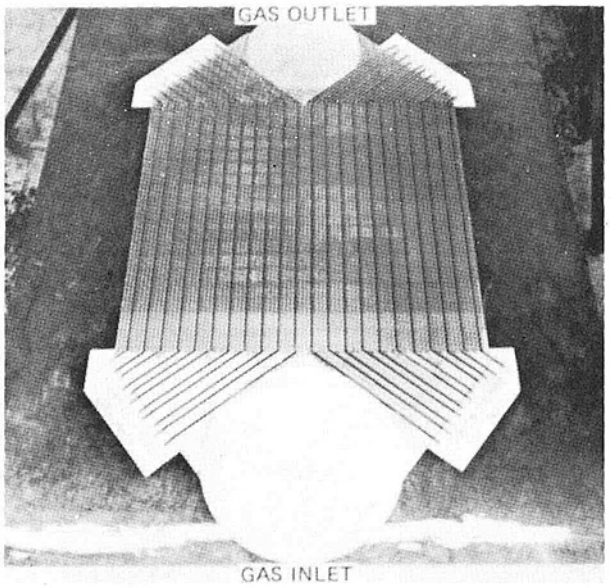


Fig. 16 Core gas-side passage flow distribution

Sliding Pad Test. One end of the core support beam, which is the load-carrying member for the regenerator cores, is free to move as its temperature and length change relative to the cold outer structure to which it is attached. In the regenerator installation, the sliding or free end of the beam is supported by a bolster extending out from the case. A prelubricated bearing between the two is a Meehanite iron pad impregnated with a high-temperature lubricant. The beam was then loaded to a value of 430 psi (30 kg/cm^2), the scheduled load. The unit is designed for 5000 cycles operation. Six thousand 1 in. (2.54-cm) stroke cycles were run at 850°F (454°C). At the end of the test, no galling or excessive wear was visible. Additional testing at a 50 percent overload of 660 psi (46.4 kg/cm^2) was also run without appreciable wear.

Core Gas-Side Passage Flow Distribution. The flow distribution in the gas-side passages is most critical. Unless care is taken in the design of manifolds, ducting, and plenums, maldistribution of flow in the regenerator core can significantly degrade the performance. For this reason, a test program was conducted to compare measured and predicted flow distribution in these programs; a test panel is shown in Fig. 16. The test and predicted values correlated within the test tolerances.

Production Test. To insure the reliability of production units, each core is hydrostatically pressure-tested to a level of 550 psig (36.7 kg/cm^2). This test is performed after the core is brazed and prior to assembly into a heat exchanger module.

The final assembly of the regenerator module is pressure-tested to 230 psig (16.2 kg/cm^2). Maximum allowable leakage is 0.1 percent of the flow at operating conditions.

Summary

In summary, regenerators used in conjunction with modern industrial gas turbines must be specifically designed to meet higher temperatures and duty cycles in order to insure long-term reliability. Accurate materials data, analytical techniques, and design concepts previously used in high-technology applications are mandatory to produce equipment for such applications. Today's regenerators must have:

- High cyclic life capability—5000 full start/stop cycles
- Stainless steel construction for high-temperature operation and corrosion resistance
- Design and fabrication procedures that allow a long operational life of 120,000 hr without repair.

Once the design has been completed, the only true proof of reliability is a comprehensive test program that duplicates the operation and environment of the intended applications.

References

1 O'Reilly, W. J., *"A High-Effectiveness Regenerator Design Concept,"* ASME Paper No. 78-GT-78, 1978.

2 Parker, K. O., *Selection of a High-Efficiency Regenerator for Pipeline Gas Turbines,* ASME Paper No. 77-GT-39, 1977.

3 American Society of Testing and Materials, *Stress Corrosion Cracking of Metals—A State of the Art,* ASTM STP518, 1972.

4 American Society of Testing and Materials, *Localized Corrosion—Cause of Metal Failure,* ASTM STP516, 1972.

5 Pickering, H. W., Beck, F. H., and Fontana, M. G., "Rapid Intergranular Oxidation of 18-8 Stainless Steels by Oxygen and Dry Sodium Chloride at Elevated Temperatures," *Trans. ASM,* Vol. 53, 1961, pp. 793–803.

Downloaded 01 Jun 2010 to 171.66.16.58. Redistribution subject to ASME license or copyright; see http://www.asme.org/terms/Terms_Use.cfm

G. J. Sturgess
Senior Research Engineer,
Turbine Durability and Combustion,
United Technologies Corporation,
Pratt & Whitney Aircraft Group,
Commercial Products Division,
East Hartford, Conn.
Mem. ASME

Account of Film Turbulence for Predicting Film Cooling Effectiveness in Gas Turbine Combustors

The paper deals with a small but important part of the overall gas turbine engine combustion system and continues earlier published work on turbulence effects in film cooling to cover the case of film turbulence. Film cooling of the gas turbine combustor liner imposes certain geometric limitations on the coolant injection device. The impact of practical film injection geometry on the cooling is one of increased rates of film decay when compared to the performance from idealized injection geometries at similar injection conditions. It is important to combustor durability and life estimation to be able to predict accurately the performance obtainable from a given practical slot. The coolant film is modeled as three distinct regions, and the effects of injection slot geometry on the development of each region are described in terms of film turbulence intensity and initial circumferential non-uniformity of the injected coolant. The concept of the well-designed slot is introduced and film effectiveness is shown to be dependent on it. Only slots which can be described as well-designed are of interest in practical equipment design. A prediction procedure is provided for well-designed slots which describes growth of the film downstream of the first of the three film regions. Comparisons of predictions with measured data are made for several very different well-designed slots over a relatively wide range of injection conditions, and good agreement is shown.

Introduction

The liners of gas turbine combustion chambers are commonly film cooled by tangential injection of cooling air along their flame-side surfaces from one or more injection devices placed axially in the liner to form individual circumferential panels.

Many experimental data have been published concerning film cooling effectiveness along single panels. Almost all of these data have been concerned with idealized injection geometries consisting of a thin-lipped slot fed with remotely-metered coolant though a smooth convergence. However, the practical injection geometry typically consists of coolant metering in some form, usually circular holes, immediately feeding a small chamber formed by the liner wall and a short lip of substantial thickness arranged to discharge the coolant rearwards, tangential to the cooled wall. This type of injection geometry results in substantial film turbulence. Attempts to predict liner temperatures with correlations derived from film effectiveness measurements made with idealized geometries always underestimate by unacceptably large amounts.

The amount of data published for more realistic injection slot geometries is extremely limited. Some work on thick slot lips has been published [1], and on actual combustor geometries, e.g., [2–6], but the results have not been presented in systematic form suitable for use in equipment design. Recommendations for predicting film effectiveness from practical injection slots have been made [7, 8], but these recommendations do not enable distinctions to be made between slots of different design, or, they involve guessing a suitable value of a mixing coefficient. The problem is frequently addressed in the industry by building a model of the proposed slot and measuring its effectiveness directly in a rig or, by building a combustor containing the proposed slot, testing it to measure liner temperatures with thermocouples and/or temperature sensitive paints, and then back-calculating film effectiveness assuming the heat fluxes about the liner wall can be reliably estimated. Neither procedure is very satisfactory, nor useful for preliminary design work.

Failure to recognize that different designs of practical injection slot can produce very different film effectiveness levels can lead to serious design mistakes and subsequent combustor development problems. In earlier times such mistakes could be corrected without much difficulty by adding more cooling air to overcome the design deficiencies. However, with modern engine operating temperature levels the limitations of the available liner materials are being approached so that the margin for error is much reduced. Furthermore, the need to produce low engine exhaust emissions of carbon monoxide, unburned hydrocarbons, oxides of nitrogen and smoke for social acceptance of the engine and for compliance with Federal and State regulations means close control of the combustor stoichiometry distribution is necessary. This can severely limit the amount of air available for cooling and may determine regions of the combustor where air can or cannot be added in large quantities. Furthermore, the expense of protracted development testing and extended field problems is be-

Contributed by the Gas Turbine Division of THE AMERICAN SOCIETY OF MECHANICAL ENGINEERS and presented at the Gas Turbine Conference and Exhibit and Solar Energy Conference, San Diego, CA, March 12–15, 1979. Manuscript received at ASME Headquarters January 17, 1979. Paper No. 79-GT-200.

Copyright © 1980 by ASME
Downloaded 01 Jun 2010 to 171.66.16.58. Redistribution subject to ASME license or copyright; see http://www.asme.org/terms/Terms_Use.cfm

coming prohibitive. It is, therefore, necessary to be able to predict the film effectiveness achieveable in a combustor from a particular practical injection slot, so that the preliminary design is fundamentally capable of achieving combustor durability goals in service with minimum expenditure of cooling air and with economic development testing along the way to certification of the engine.

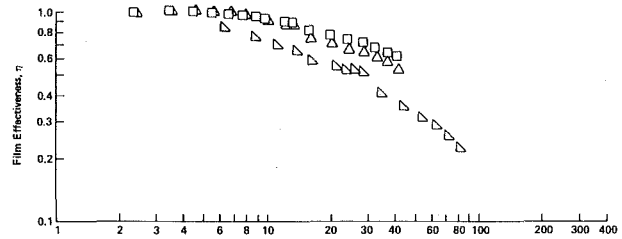
Difference between Idealized Slots and Practical Slots

It has been stated that practical slots have increased rates of decay of film effectiveness compared to idealized slots. This is illustrated in Fig. 1 which is a plot of film effectiveness η, defined as the normalized adiabiatic wall temperature, against the simple correlation group $x/(Ms)$ for three slots. Two are clean slots with remote coolant metering and a smooth convergence to the discharge plane while the third is a practical slot of the type described above. The second of the clean slots had a turbulence grid placed in the convergence about the same distance from the coolant discharge plane as the metering holes of the practical slot. Film turbulence intensities were measured at mid-slot height in the discharge plane of each slot using the hot-wire anemometer; mainstream turbulence intensity $u'_{\text{rms}}/\overline{u}$, at the slot outlet plane was measured as being less than 3 percent. All three slots had thick lips so the effects observed are only associated with the film turbulence. The length scale of the film turbulence was about the same in the latter two cases, and was equal to the pitch of the metering holes in the practical slot. The measurements were made in a facility described in [13].

It can be seen that film effectiveness is decreased as film turbulence intensity is increased. At a typical design value of $x/(Ms)$ of 25, (typical for the rear of combustors), the degradation in effectiveness for the practical slot over the ideal slot is down to 0.50 from 0.75. This is the difference in practice between acceptable combustor liner durability and failure through over-temperature.

Fig. 1 suggests that the film effectiveness decreases as the ratio of slot outlet area A_s, to slot inlet area A_H, increases. That this is indeed so for practical slots is demonstrated in Fig. 2 at two values of $x/(Ms)$, the lower value of which, 6.5, is an appropriate design value for combustor primary zones. The only geometric variable in these slots was A_s/A_H which was achieved by varying metering port diameter and outlet area while preserving lip thickness to slot outlet height ratio. The major difference between idealized slots and practical slots is that practical slots always have a value of A_s/A_H greater than unity.

A generalized practical slot is illustrated in Fig. 3; a particular practical slot may contain all or merely some of the features shown. Cooling air is admitted to the slot through a series of circular metering holes or racetrack slots, which may be arranged as a single row or a double row if impingement cooling of the lip is desired. The metered cooling air enters a "plenum" chamber formed by the cooled wall and the lip, in order for individual air-jets to lose as much of their identity as possible prior to being exposed to the hot combustion gases. The plenum chamber may be of constant cross-sectional area, (or constant annular height), or may have a convergence such that D/s is greater than unity. The lip will have finite thickness δ_W, to resist bending, and may have mechanical support through posts or other means. The slot flow path may be folded so that the jet mixing length inside the slot L', becomes long. An almost infinite variety of dimensions such as δ_W/s, D/s, L'/s, A_s/A_H, p/d, etc., can be used in combination so that each engine slot is usually individual with its own performance. The method of construction used for the slot may influence the geometric features that can be used in a particular design.



Symbol	δ_W/s	M	Re_s	$\left(\frac{u'_{rms}}{\overline{u}}\right)_m$%	$\left(\frac{u'_{rms}}{\overline{u}}\right)_c$%	A_s/A_H	Comment
□	0.604	0.89	8,058	<3	3	<1.0	Clean Slot
△	0.604	0.87	8,064	<3	9	<1.0	Clean Slot With Grid
▷	0.433	0.69	3,700	<3	19	3.39	Practical Slot

Fig. 1 Demonstration of effectiveness degradation with increasing film turbulence

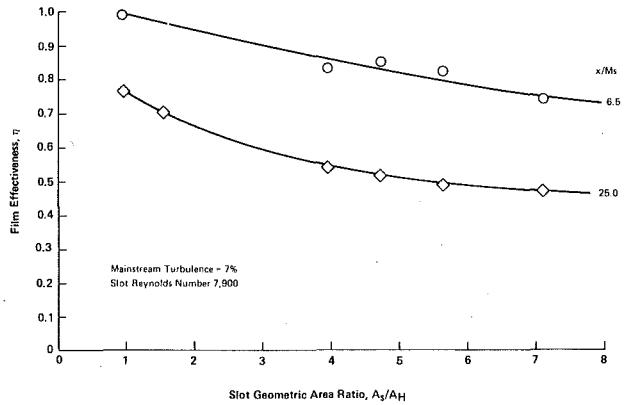
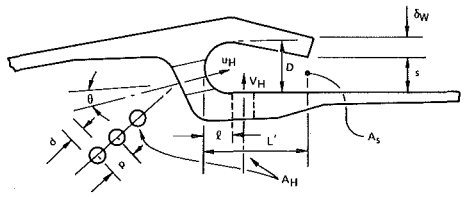


Fig. 2 Effect of slot area ratio on film development



δ_W – Lip Trailing-Edge Thickness
s – Slot Outlet Height
A_s – Slot Outlet Area, (Geometric)
u_H – Coolant Velocity from Axial Holes
V_H – Coolant Velocity from Normal Holes
A_H – Total Coolant Metering Area, (Geometric)
θ – Angle of Axial Metering Holes to Cooled Wall
D – Height of Mixing Chamber at Coolant Inlet
d – Metering Port Diameter
p – Metering Port Pitch, (Axial/Normal, Indexed p/2)
L' – Mixing Chamber Length
ℓ – Downstream Position of Leading-Edge of Impingement Metering Port in Mixing Chamber

Fig. 3 Geometric description of practical slot

Relationship of Film Turbulence to Slot Area Ratio A_s/A_H

Film effectiveness for an otherwise fixed slot geometry has been demonstrated in Fig. 2 to depend on the slot area ratio A_s/A_H. It also appears from Fig. 1 that the effect of A_s/A_H is one of increasing the film turbulence.

Nomenclature

A_E = slot overall effective area
A_H = metering port geometric area
A_0 = slot outlet effective area
A_s = slot geometric outlet area
C_d = discharge coefficient applied to metering ports
C_F = flow coefficient applied to slot outlet passage
M = slot blowing ratio, $(\rho_c\overline{u}_c)/\rho_m u_m)$
Pr = Prandtl number
PTB = mainstream turbulence intensity, percent
Re_s = slot Reynolds number, $\rho_c\overline{u}_c s/\mu_c$
T_c = coolant temperature
T_m = mainstream temperature
T_{sad} = adiabatic wall temperature
s = slot height at outlet
$\overline{u}$ = mean axial velocity component
$\overline{u}_c$ = mean coolant velocity at slot outlet
u'_{rms} = root mean square value of fluctuating axial velocity component
x = distance downstream from injection plane
x_{pH} hydrodynamic potential core length
x_{pT} = thermal potential core length
x_{pTurb} = thermal potential core length with mainstream turbulence
y = distance normal to cooled wall
z = lateral distance across slot outlet
η = film effectiveness, $(T_m - T_{sad})/(T_m - T_c)$
μ_c = coolant viscosity
μ_m = mainstream viscosity

Downloaded 01 Jun 2010 to 171.66.16.58. Redistribution subject to ASME license or copyright; see http://www.asme.org/terms/Terms_Use.cfm

For conventional grid turbulence, which to first order is independent of grid Reynolds number provided it is high enough, the level of turbulence is determined by N/d and the decay depends on x/N, where N and d are defined in Fig. 4 and x is the axial distance downstream from the grid. The grid blockage area B, which is defined as the difference between total and open areas, divided by the total area is,

$$B = 1 - \left(1 + \frac{d}{N}\right)^{-2} \tag{1}$$

For a slot, B and A_s/A_H are linked by,

$$A_s/A_H = (1 - B)^{-1} \tag{2}$$

Thus, the slot turbulence intensity may be related to an equivalent grid turbulence through,

$$A_s/A_H = \left(1 + \frac{d}{N}\right)^2 \tag{3}$$

and its decay through x/p, where p is the pitch of the metering ports.

Fig. 4 tracks the measured decay of film turbulence at mid-slot height generated by a practical film cooling slot. The turbulence intensity is plotted as a function of x/p, the downstream distance from the slot lip divided by the coolant metering port pitch. For this slot the value of L'/p is 3 and A_s/A_H is 3.65. Also shown in the figure are the grid turbulence decay characteristics of Baines and Peterson [9] for a square mesh of square bars, the square bar case being appropriate for comparison with the sharp-edged slot metering holes. Data are given for N/d of 1.5 and 2.0. For the practical slot the equivalent N/d is 1.1, obtained using equation (3). The turbulence intensity level and decay rates for the grids and the practical slot are very similar.

Measurements using a hot-wire anemometer were made of the mid-slot height turbulence intensity at the slot outlet plane for four different practical slots. These data are presented in Fig. 5 and show that film turbulence increases with the slot area ratio A_s/A_H. Also shown on the plot of Fig. 5 are lines representing Marek and Tacina's measurements [10] for a drilled-plate turbulence grid at dimensionless distances L/p in the range of L'/p for the practical slots. The agreement with the practical slot data is convincing.

It can be seen from Figs. 4 and 5 that the effect of slot area ratio A_S/A_H greater than unity is to introduce turbulence into the film just as if a turbulence grid had been introduced into the slot.

Using Fig. 5, the data of Fig. 2 for an $x/(Ms)$ of 25 have been replotted to show the dependency of practical slot film effectiveness on the turbulence intensity generated in the film by the slot itself. This is shown in Fig. 6 where effectiveness decreases linearly with increasing film turbulence intensity. The penalty of producing a practical device from the idealized case is clearly demonstrated, and has led to the description of idealized slots and practical slots as being respectively, clean and dirty, [7], by drawing on the analogy with an aircraft in its cruise and landing configurations.

Equations have been derived [11, 12], to describe film effectiveness from a practical slot that account for film turbulence effects by introducing an empirical area ratio term A_0/A_E, where A_0 is the outlet area and A_E is the overall effective area of the slot. These equations also permit account to be taken of slot lip thickness and film exit radial velocity profile, as well as mainstream turbulence. Direct substitution of A_s/A_H for A_0/A_E in these equations with the existing entrainment and profile constants did not yield uniformly good predictions of film effectiveness. An additional effect appeared to be present to a degree which depended on the individual slot geometry, and which was not accounted for in the equations.

Slot Effective Area

The less than successful film effectiveness prediction attempts using the geometric A_s/A_H directly prompted the questions: If effective area A_E is not equal to the metering area, what is it?

Applying axial conservation of momentum for incompressible flow to the general slot shown in Fig. 7, and assuming constant pressure mixing of the film and mainstream at the slot outlet yields the relationship,

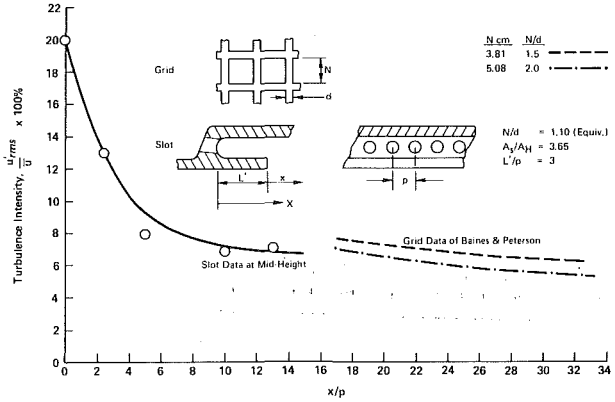


Fig. 4 Comparison of grid and slot-generated turbulence decay

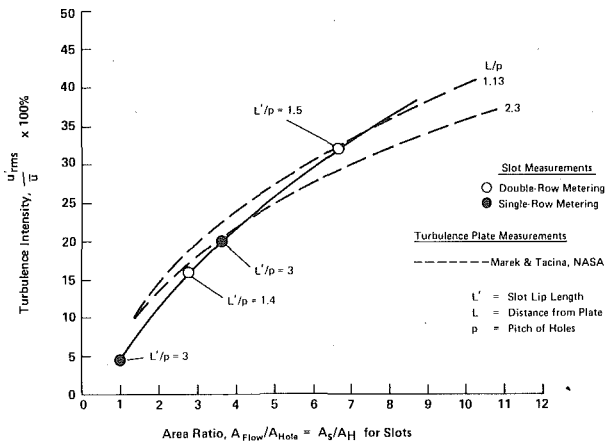


Fig. 5 Relationship of slot exit plane turbulence to area ratio

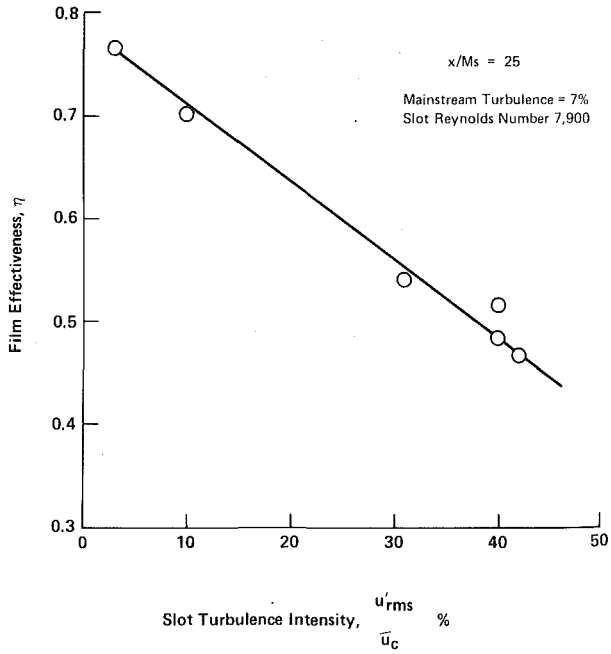


Fig. 6 Effect of slot turbulence on film effectiveness

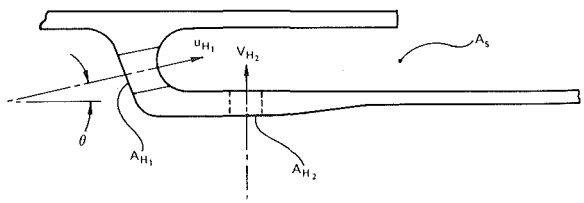


Fig. 7 Metering port definitions

Downloaded 01 Jun 2010 to 171.66.16.58. Redistribution subject to ASME license or copyright; see http://www.asme.org/terms/Terms_Use.cfm

$$\frac{A_0}{A_E} = \frac{A_s}{(1+\lambda)A_{H_1}}\left[1 + 2\left(\frac{A_{H_1}}{A_s}\right)^2 (1+\lambda)^2 - 2\frac{A_{H_1}}{A_s}\cos\theta\right]^{1/2} \quad (4)$$

where,

λ = ratio of normal to axial coolant mass flows at the metering

In writing equation (4) the assumption has been made that V_{H_2} is equal to U_{H_1}, so that λ reduces to the area ratio A_{H_2}/A_{H_1}. This is not entirely general since the slot axial holes will normally be fed with total pressure and the radial holes will be fed with static pressure in a typical combustion chamber. It is, however, valid for many of the rig experiments commonly made.

Examination of equation (4) shows that θ has a small effect at all conditions, λ has a relatively small effect for values above 0.5, and, that A_s/A_H has a large effect.

Equation (4) implies a diffusion of the individual coolant jets from the metering holes to completely fill the slot mixing chamber by the outlet plane. Therefore, the static pressure inside the slot should be below that inside the combustor. Using equation (4) for a single-row metering slot, it can be shown that,

$$(p_{combustor} - p_{slot}) = \rho u_H^2 \left[\frac{A_H C_{d_H}\cos\theta}{A_s}\left(\frac{A_H C_{d_H}}{A_s}\right)^2\right] \quad (5)$$

where a positive value of $(p_{\text{combustor}} - p_{\text{slot}})$ confirms diffusion of the jets. Fig. 8 compares equation (5) with some experimental data from a slot with single-row metering. It can be seen that the difference in static pressure between the combustor and the slot is indeed positive so that jet-diffusion is present, but that the amount of diffusion is much less complete than that indicated by equation (5). The implication of this observation is that the slot does not "run full," i.e., that a flow coefficient C_F, should be applied to A_s. Confirmation of this is obtained from measurements of the velocity profiles obtained at the exit from practical slots. Fig. 9 shows radial velocity profiles measured in a practical slot with A_s/A_H equal to 5.65, and with two values of metering port angle θ. Profiles are shown in line with and between coolant metering holes. Fig. 10 gives the circumferential velocity profile at mid-slot height for the 10 deg slot. It can be seen that marked velocity profiles, both radially and circumferentially, exist in a practical slot, and the slot does not run full at discharge due to this incomplete diffusion of the individual coolant jets within the lip lengths consistent with durable designs.

It is apparent that in equation (4), the following should be used.

$$A_{H_1} = A_{H_1} C_{d_{H_1}} \quad (6a)$$

$$A_{H_2} = A_{H_2} C_{d_{H_2}} \quad (6b)$$

$$A_s = A_s C_F \quad (6c)$$

where C_d and C_F are discharge coefficients and a flow coefficient respectively.

The Well-Designed Slot

It is also apparent from Figs. 9 and 10 that equation (4), even with substitution of equation (6), is not likely to provide a sufficiently general description of all possible practical slots. Furthermore, film decay rates are influenced not only by the metering-generated turbulence, but also by the circumferential non-uniformities in the film at its discharge, which will change the initial entrainment rates into the film. These difficulties could be solved by increasing the lip length L' a sufficient amount to cause the circumferential non-uniformities to be mixed-out internally by diffusion of the individual coolant jets. Unfortunately, considerations of durability of the unsupported slot lip preclude such approaches. Mechanically supported lips may be made long enough for the individual jets to be mixed out internally, but the lip supports themselves introduce flow distrubances. A non-uniform initial film is, therefore, a feature of practical slots.

It can be illustrated that other features of the slot besides A_s/A_H influence effectiveness through the initial uniformity of the film. An example is given in Fig. 11, which shows the influence of coolant metering port pitch to diameter ratio. For otherwise fixed geometry, including A_s/A_H, the value of pitch to diameter ratio was increased.

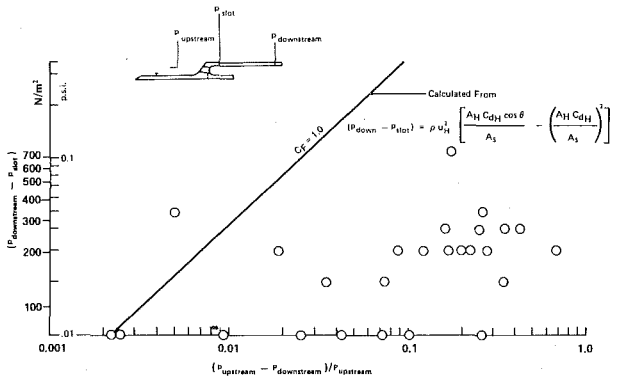


Fig. 8 Demonstration of static pressure depression under slot lip and that coolant jets are not fully diffused at discharge

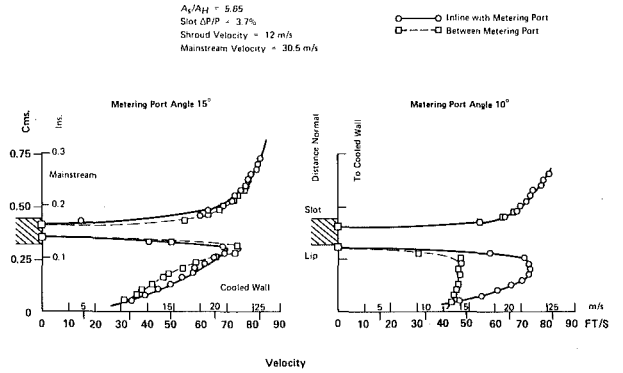


Fig. 9 Normal velocity profiles at discharge from a practical cooling slot

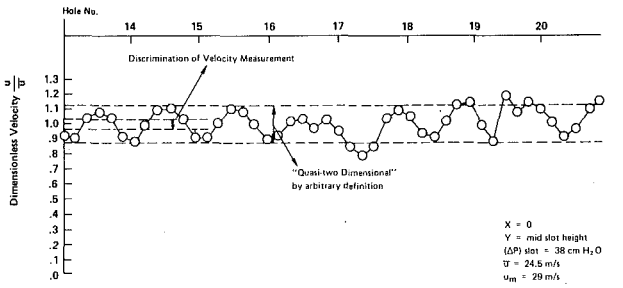


Fig. 10 Cooling slot outlet velocity traverse

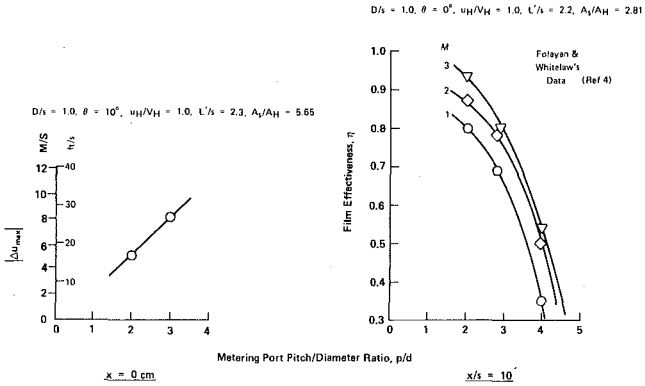


Fig. 11 Demonstration of a single slot geometry variable on film lateral uniformity and downstream effectiveness

At the outlet plane of the slot, the slot mid-height circumferential velocity profile shows an increase in the maximum difference between a velocity peak in line with jets and the adjacent velocity trough between the jets. These measurements were obtained over a circumferential run of slot extending over several tens of coolant metering ports. At a downstream distance the increased entrainment resulting from increasing the port spacing is translated into reduced effectiveness, as the data taken from Folayan and Whitelaw [4] show. Note the dramatic fall-off in film effectiveness at all blowing ratios M, for

Downloaded 01 Jun 2010 to 171.66.16.58. Redistribution subject to ASME license or copyright; see http://www.asme.org/terms/Terms_Use.cfm

a doubling in p/d, and compare it with that in Fig. 2 for A_s/A_H variations. Fig. 11 brings out the design importance of the slot mixing chamber visible in Fig. 3. Careful design of the mixing chamber permits the slot lip to be shortened for a significant improvement in lip durability at no penalty in film effectiveness. This is illustrated in Fig. 12 where the same performance is achieved with a slot having an internal mixing length only 40 percent that of the other slot, but with a sophisticated mixing chamber design.

Other of the dimensions shown in Fig. 3 exert considerable influence on film effectiveness. Some of these are described in Fig. 13, being respectively, axial metering port angle θ, plenum chamber dimension D/s, and the ratio of axial coolant flow to radial flow in a two-row metering system. Fig. 14 shows the effect of position of the radial-flow cooling in a two-row metering system. These figures together can explain the performance achievements evident in Fig. 12. (N. B.: It should be noted that in addition to the circumferential profile the slot exit radial profile is also affected by changes in the mixing chamber dimensional arrangements. Fig. 9 shows for example, how the radial profile is affected by axial coolant port angle θ. The major effect of such radial profile changes is in the potential core region of the film [11]. It is not intended to discuss the potential core in the present paper.)

To fulfill its function adequately, a slot must not produce a film which decays rapidly when exposed to the hot combustion gases. To insure this is avoided a slot must be well-designed, which implies low film turbulence generation and low initial entrainment rates. Only well-designed slots are useful in equipment design.

The foregoing data suggests that a well-designed slot should have as long and thin a lip as is commensurate with satisfying structural requirements, a low value of A_s/A_H, metering ports as close together as possible, a convergence in the mixing chamber, and, nearly all the total coolant flow admitted "axially" but with such an angle as to "splash" off the slot lip. Manufacturing and structural constraints prohibit simultaneous achievement of all of these desirable features. For example, metering hole p/d values much less than 2–3 are subject to cracks linking holes and causing failure of the parts in service; the

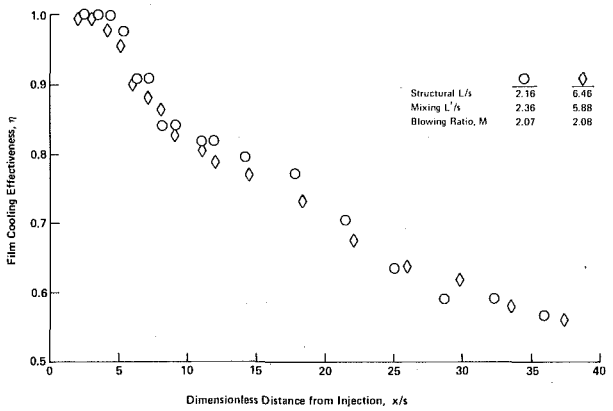


Fig. 12 Reduction of lip length due to sophisticated mixing chamber design

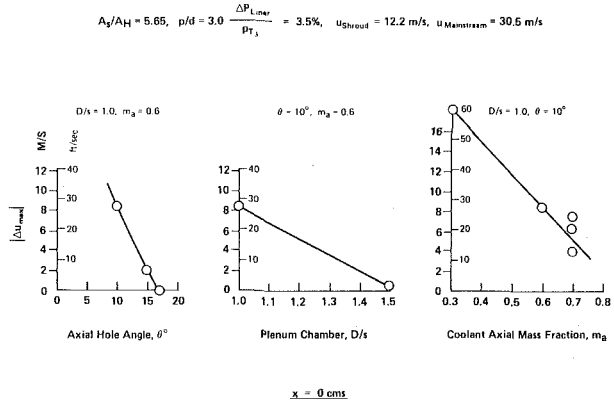


Fig. 13 Effect of slot mixing chamber variables other than A_s/A_H on film uniformity

minimum value of θ depends on the type of slot construction, i.e., machined or fabricated, and on whether the metering ports are made in detail or assembly of the part, etc. The extreme sensitivity of film effectiveness to the slot details can lead to manufacturing tolerance problems. These constraints have led to the appearance of the so-called folded, or indirect metering, slot which is designed to de-sensitize the film to slot mixing chamber details. Generally, however, cost considerations limit the wide use of such devices. Fortunately, it does not appear necessary to incorporate all the desirable slot characteristics simultaneously in a single slot in order to achieve adequate performance.

The dramatic effects shown in Figs. 11, 13, and 14 for relatively small changes in single geometric variables of the slot mixing chamber suggest that even smaller changes in several of these variables together, might permit achievement of the same degree of coolant jet internal mixing. A slot having such a combination of features that could be manufactured easily and cheaply, while maintaining a high level of film effectiveness, would be a well-designed slot. It is, however, necessary to define such a slot quantitatively.

Description of a Well-Designed Slot

The exit velocity profile from a practical geometry slot can be described as follows:

$$\psi = \left(\frac{u_{\max} - u_{\min}}{\overline{u}}\right) \tag{7}$$

where,

$$[\overline{u}]\, y = \left[\frac{\int_{z_1}^{z_2} u\,dz}{(z_2 - z_1)}\right]_y \tag{8}$$

and,

$u_{\max}$ = axial velocity crest
$u_{\min}$ = axial velocity trough
} in a circumferential-section of profile,

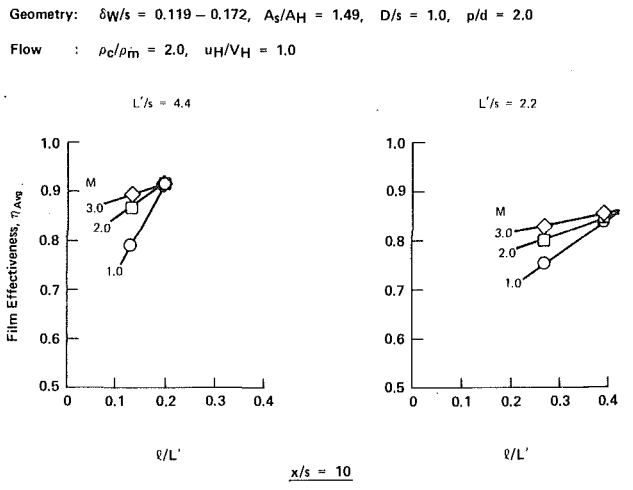
y = radial position in slot outlet at which the considered circumferential profile exists.

z = circumferential distance at radial position y

The considered profile is at the slot exit plane.

Considering a simple slot with a single row metering and no plenum chamber, the term ψ can be shown to be related to the mixing chamber design through:

1 expansion of the metered jets, represented by the area ratio $d^2/(sp)$
2 wall drag through jet impingement, related to dL'



(Based on Data of Ref. 4)

Fig. 14 Effect of impingement hole position in mixing chamber

Downloaded 01 Jun 2010 to 171.66.16.58. Redistribution subject to ASME license or copyright; see http://www.asme.org/terms/Terms_Use.cfm

3 jet interaction, through p/d

These can be combined to give,

$$\lambda = f_1\left(\frac{ps}{dL'}\right) \tag{9}$$

The limits of this expression are,

$d = s$ and $p = 0$ (straight through slot) $\psi = 0$, i.e., perfect internal mixing

$L' = 0$ (no lip) $\psi = \infty$, i.e., zero internal mixing

$d = s$, $p = 0$, $L' = 0$ (no slot) ψ indeterminate.

For good internal mixing and a uniform initial film, the group $ps/(dL')$, termed MIX, tends toward zero.

The term MIX takes different forms according to the geometry of the cooling slot; two further examples are given below:

1 single row of rectangular or racetrack metering ports of height b and length ℓ, pitched p apart, no plenum,

$$\psi = f_2\left[\frac{ps(\ell + b)}{2\ell bL'}\right] \tag{10}$$

2 double row of circular metering ports d_1 and d_2 diameters, equally pitched p apart with $p/2$ indexing between rows, no plenum,

$$\psi = f_3\left[\frac{ps(d_1 + d_2)}{L'(d_1^2 + d_2^2)}\right] \tag{11}$$

Similar expressions for different slot geometries are readily obtained.

In order to use expressions (9–11) for design purposes, it is necessary to obtain the functional dependencies f_1, f_2 and f_3 and to set a limiting value on ψ.

The limiting value set on ψ is somewhat arbitrary. Quasi-two-dimensional flow was defined as being twice the estimated discrimination of the velocity measurement in the experimental velocity profiles when expressed in the form of equation (8). This gave a definition of quasi-two-dimensional flow as,

$$0.89 \leqslant \frac{u}{\bar{u}} \leqslant 1.11 \tag{12}$$

where u = local axial velocity at position y

This definition was tested by measuring the circumferential variation in film effectiveness of a slot which satisfied the ψ-criteria set up. It proved to be satisfactory in that average film effectiveness at a downstream distance equivalent to a typical combustor panel length was sufficiently high, and lateral variations in effectiveness were insignificant.

The individual functions $f_1, f_2, f_3 \ldots f_n \ldots$ were not determined directly. Rather, values of MIX which satisfied expression (12) were obtained for several mixing chamber designs to yield the general criteria:

$$\text{for slots with } D/s = 1.0, \quad \text{MIX} \leqslant 0.9 \tag{13}$$

$$\text{for slots with } D/s = 1.5 \quad \text{MIX} \leqslant 1.3 \tag{14}$$

Between the two D/s values, a linear relationship for MIX is appropriate; values of D/s greater than 1.5 were not tested and values less than unity are not used because they result in unstable films. Note that the effect of a "plenum" chamber, $D/s > 1.0$, is to improve the mixing by permitting a higher MIX value for satisfaction of the two-dimensional definition. The approach outlined was chosen since it is simpler to use in design work, and covers most cases likely to be considered with the exception of folded (indirectly-metered) slots.

To test the validity of the MIX group the data from Fig. 2 for an $x/(Ms)$ value of 25 were replotted against the MIX form for that particular slot geometry, and the result is shown in Fig. 15. The maximum allowable MIX from statement 13 is shown on the plot; the slot had D/s equal to unity. Also shown on the plot are indications of lipless slot effectiveness levels at $x/(Ms)$ of 25 for both double and single-row metering: These values occur at a MIX-value of infinity.

It can be seen that at large MIX values the data are becoming asymptotic to the lipless-slot values of effectiveness. When MIX is reduced effectiveness increases very rapidly as the recommended maximum MIX is approached; thereafter, the rate of increase is considerably reduced. It is concluded that for MIX values greater than that recommended, entrainment of mainstream into the film due to initial non-uniformity dominates the film degradation process, and that for MIX values less than that recommended film turbulence dominates the film decay. The maximum value chosen for MIX in statement 13 is seen to be a good one. The curve of Fig. 15 is not universal. The levels of film effectiveness at a given $x/(Ms)$ also depend on the slot lip thickness, slot mean radial velocity profile at exit, and the mainstream turbulence.

A further test of MIX was made using the data of Folayan and Whitelaw [4], and this is presented in Fig. 16 for several blowing ratio values and a dimensionless distance from injection of ten slot heights. The data cover several plenumless mixing chamber and slot designs. The recommended maximum general value of MIX for plenumless slots can be seen to provide a good definition of the geometric arrangements beyond which film effectiveness suffers a severe decline.

It may be concluded, therefore, that the parameter MIX provides a good assessment of slot mixing chamber design. Slots which satisfy the MIX-criteria will be well-designed, by definition. It is important to remember that well-designed means well-designed in respect of two-dimensionality of the film; such a slot may not perform well due to poor choice of other design parameters, such as lip thickness, slot height and blowing ratio. However, well-designed slots are amenable to reliable and consistent calculation using equations (4) and (6). For given lip thickness, slot height and blowing ratio, a well-designed slot will, of course, outperform a poorly designed slot.

Flow Coefficient Information for Well-Designed Slots

As has been shown, if practical consideration is limited to well-designed slots which satisfy the appropriate MIX criteria, the required values of A_0/A_E for such slots can be calculated accurately from equation 4 together with equation (6) only. In equation (6) informa-

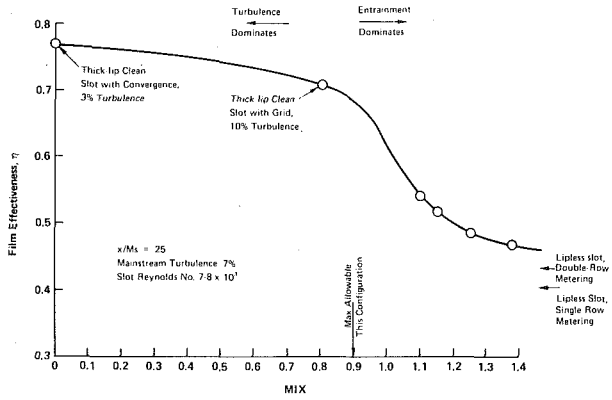


Fig. 15 Effects of film turbulence and non-uniformity on effectiveness described by mix criterion

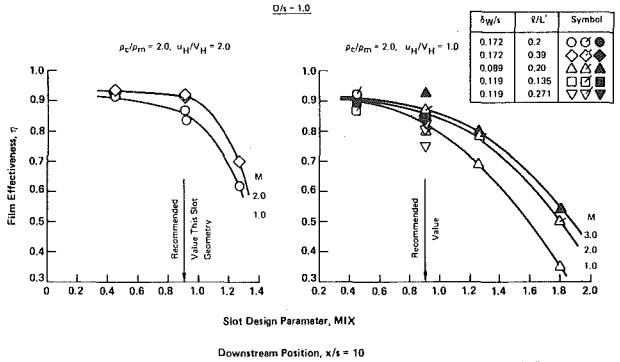


Fig. 16 Assessment of mix-criterion against Whitelaw's data [4] for a plenumless slot design family

Downloaded 01 Jun 2010 to 171.66.16.58. Redistribution subject to ASME license or copyright; see http://www.asme.org/terms/Terms_Use.cfm

tion on metering hole discharge coefficients $C_{d_{H_1}}$ and $C_{d_{H_2}}$ and on the slot flow coefficient C_F is required.

Considerable information on metering hole discharge coefficients is available in the literature, However, care should be exercised to ensure account is taken of metering hole length-to-diameter ratio, the hole Reynolds number and, the technique used to form the holes in the slot, all of which can affect the discharge coefficient.

Information on suitable flow coefficients for slots is not readily available. It can be shown that the rate of spread of a confined jet decreases as the pressure drop across the slot increases. Therefore, C_F will not be a constant for a given geometry, but will tend to decrease as the coolant mean exit velocity based on continuity, $\overline{u}_c$, increases. This is due to the radial and circumferential profiles becoming more peaked. Fig. 9 indicates that even for well-designed slots the value of C_F at any particular $\overline{u}_c$ will depend to some extent on the slot geometry through the mean radial velocity profile.

Theoretical prediction of mean radial and circumferential velocity profile development within slots was not really practical. Recourse was, therefore, made to measurements of C_F from experimental velocity profiles obtained from a number of practical slots.

Experimental data may be examined in the following terms. The flow coefficient is defined as

$$C_F = 1 - \overline{B} \tag{15}$$

where the slot outlet blockage $\overline{B}$ is defined,

$$\overline{B} = \frac{\int_{z_1}^{z_2} B_{\text{Local}} dz}{(z_2 - z_1)} \tag{16}$$

For a two-dimensional test piece of type used in the experiments, the local blockage due to the local radial velocity profile is given by,

$$B_{\text{Local}} = \left[\frac{(\delta^*_{\text{Lip}} + \delta^*_{\text{Wall}})}{s}\right]_z \tag{17}$$

where the displacement thicknesses are given by,

$$\delta^* = \int_0^{\delta} (1 - u/u_{\max}) dy$$

and δ is defined as the distance from the surface to the point of 99 percent of the maximum velocity in the profile. Equation (17) can be computed from the measured radial velocity profiles at a number of lateral stations across the slot outlet plane. These values when substituted into equation (16) provide the integrated blockage $\overline{B}$, which can be used in equation (15) to yield the slot flow coefficient.

Analysis of some well-designed slots in this fashion resulted in the curve shown in Fig. 17. This figure shows C_F decreases from unity with increasing $\overline{u}_c$, to an asympotic value of 0.4 – 0.5, as was expected. The spread in the data is attributed to the peakiness of the profiles, and this can be associated with the axial metering hole angle θ, and/or the existence of a plenum chamber formed by bending-in the slot-lip. The effect appears not to be due to just impingement of coolant on the slot lip since double-row metering, which has deliberate impingement cooling of the slot lip, did not necessarily produce lower values of C_F provided that the axial hole angle θ was not excessive.

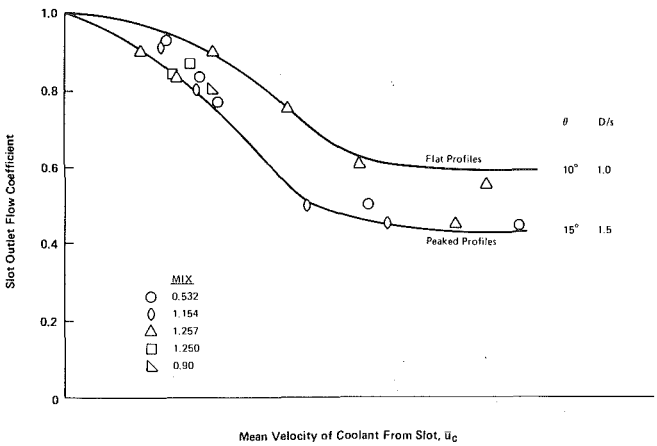


Fig. 17 Measured slot flow coefficients for some well-designed practical slots

Comparison of Film Effectiveness Predictions with Measurement

It has been shown that the film effectiveness from practical geometry injection slots depends on the entrainment of mainstream into the film due to nonuniformities in the emerging film and on turbulence generated in the film by the slot, It has also been shown that for a class of slots described as well-designed, these effects can be described downstream of the initial region of the film by an area ratio A_0/A_E which can be related to the slot mixing chamber geometry in simple fashion through equation (4). It is necessary now to demonstrate that use of equation (4) together with equation (6) and Fig. 17, enables accurate predictions of film effectiveness to be made for practical film cooling slots.

Experimental data from three very different practical slots were used. The slots are described in Table 1.

These slots can be seen to be very different from each other: A1 and A2 have moderately thick lips, short plenumless mixing chambers with double-row metering, and differ from each other in axial metering hole angle, area ratio and flow split; B3 has a thick lip, moderately long plenum mixing chamber and single-row metering.

The film effectiveness measurements from these slots were made in an incompressible flow, atmospheric pressure, two-dimensional facility provided with a mainstream turbulence grid such that the turbulence intensity $u'_{\text{rms}}/\overline{u}$ at the plane of injection was 7 percent. The coolant was electrically heated over the mainstream temperature so that the film effectiveness could be found from an array of wall thermocouples set in an adiabatic wall; measured effectivenesses used in the comparisons are based on the average of several lateral wall thermocouples at each downstream position.

The predictions of effectiveness were made using the model and equations presented in [11] and [12]. These equations are as follows:

$$\text{Potential core region:} \quad \eta = 1.0 \tag{18a}$$

$$\text{Transition region:} \quad \eta = 1 - CS_{N_2}^D \tag{18b}$$

where,

$$S_{N_2} = [(x - x_{p\,\text{Turb}})/(Ms) \cdot (\text{Re}_s \cdot \mu_c/\mu_m)^{-0.15} \cdot A_0/A_E] \tag{18c}$$

$$C = 0.12 + 0.0040\ \text{PTB} \tag{18d}$$

$$D = 0.65 - 0.0028\ \text{PTB} \tag{18e}$$

$$\text{Main region:} \quad \eta = \eta_T (S_{N_{2T}}/S_{N_2})^F \tag{18f}$$

where,

$$\eta_T = 1 - CS_{N2T}^D \tag{18g}$$

$$S_{N_2} = [1/(C + CD/E)]^{1/D} \tag{18h}$$

$$E = 0.8 + 0.008\ \text{PTB} \tag{18i}$$

Table 1 Geometric descriptions of study slots

Slot	A1	A2	B3
Parameter			
θ, rad.	0.174	0.262	0.262
s, cms.	0.635	0.635	0.381
D/s	1.0	1.0	1.33
$\delta W/s$	0.36	0.36	0.60
(p/d) axial	3.0	3.0	1.99
(p/d) radial	3.67	3.0	—
indexing	p/2	p/2	—
coolant split, axial/radial	60/40	50/50	100/0
A_s/A_H	5.65	4.74	4.804
L'/s	2.6	2.6	3.78

Downloaded 01 Jun 2010 to 171.66.16.58. Redistribution subject to ASME license or copyright; see http://www.asme.org/terms/Terms_Use.cfm

and where,

$$x_{p\text{Turb}} = x_{pT}(1.17 - 0.327\ \text{PTB})^{0.263} \tag{18j}$$

$$x_{pT} = x_{pH} \cdot \text{Pr} \tag{18k}$$

The hydrodynamic potential core length x_{pH} was calculated according to the method given in [13]. For practical slots the calculation of x_{pH} involves an assessment of the coolant mean radial velocity profile at the outlet plane. Presently this has been limited to a peak-to-mean velocity description. Such a simplistic approach yields sufficiently accurate predictions of x_{pH} for the present purposes. More accurate predictions are possible with a more sophisticated description of this profile. Detailed discussion of the potential core calculations are omitted for the sake of brevity. For the calculations to be presented the term A_0/A_E in equation (18c) was obtained from equation (4) using equation (16) together with Fig. (17) for C_F values. The blowing ratio M and the slot Reynolds number were based on the coolant mean exit velocity $\bar{u}_c$ from conservation of mass.

The comparisons are shown in terms of effectiveness variations with distance downstream from the injection plane. The comparisons presented have been selected to demonstrate the success in predicting the performance of the different slots and over a wide range of injection conditions for one of these slots.

Fig. 18 compares predictions with measured data for two different slots, B3 and A2 from Table 1, at about the same blowing ratio M. The MIX values for the two slots are shown and it can be seen that B3 is a well-designed slot according to the definition, but that A2 does not quite qualify. The Reynolds number difference between the two tests is mainly due to the slot height difference of the slots. It can be seen that the effectiveness is well-predicted for both slots over the whole range of the data with the predictions being inside the uncertainty band of the data in each case. The predictions illustrate the nature of the model, showing the potential core of unity effectiveness followed by a region of relatively rapid decay which corresponds to the transition region, and finally the main region of less rapid decay. In both cases the potential core is well-predicted despite the simple velocity profile description used.

In Figs. 19–23 inclusive, the comparisons are for slot A1 which is just a well-designed slot over a range of injection conditions from extremely low blowing ratios to very high values. To cover this range of M it was necessary to vary both coolant velocity and mainstream velocity as indicated on each figure. The figures are arranged in order of increasing M. During the course of the series of tests, which were not performed in the order presented, some difficulty was experienced with the wall thermocouples in the region of 5 to 15 cms from the injection plane. This is evidenced by an increased scatter in the averaged values of the data, an increased uncertainty band, and missing data points on some of the figures.

Fig. 19 is for blowing ratio of 0.431. It can be seen that the prediction underestimates the performance of the slot by an amount that increases with increasing distance from injection. The potential core length prediction again seems reasonable. The failure of the method at very low blowing ratios is characteristic for practical slots when M is less than about 0.5, but not for clean slots [12]. It is believed this

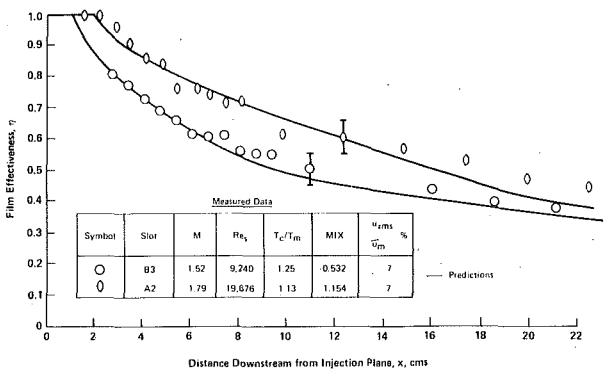


Fig. 18 Comparison of predictions with data for two different practical slot geometries

failure is associated with the accuracy of the value for C_F at low $\bar{u}_c$. In gas turbine combustor practice blowing ratios below 0.5 are not recommended or usually used becasue of the weak nature of the film which results.

When the blowing ratio is increased above 0.5, as in Fig. 20 where M is 0.87, the predictions improve considerably. Out to 8 cms from injection, the predictions are within the uncertainty of the data. From a practical point of view this is more than adequate as gas turbine combustor panels are seldom longer than this in scaled length. Potential core is once again predicted quite well. In the main region of the film, where the predictions underestimate the slot performance, the rate of film decay is correctly predicted. The underestimation of absolute value is caused by an incorrect prediction of the end of the transition region.

For blowing ratios around 1.5 Fig. 18 is typical of the prediction accuracy achieved, which is good over the whole range of x.

In Fig. 21 the blowing ratio is increased to 2.38. Prediction is within the data uncertainty over the whole range of distance. It does appear that the potential core length in this case is underpredicted, but it is difficult to be certain due to the data scatter.

Fig. 22 is for a blowing ratio of 3.28. Potential core length is well predicted but the transition region performance is apparently overestimated. However, the main region is well predicted in both absolute value and rate of decay. This test was performed immediately prior to the clear identification of the thermocouple problems described above. It is tempting to regard the data in the transition region as being suspicious because the region of disagreement is confined to readings from thermocouples which subsequently gave trouble.

At a blowing ratio of 4.13 Fig. 23 shows the predictions clearly overestimating the slot performance from about 3 cms downstream, although the final rate of decay does seem well-predicted. It appears that the potential core is overestimated, as is the initial rate of film decay. Failure of the method at some point as M is increased was to be expected. This is so because the method is based on a modified boundary layer analysis [11] which becomes increasingly inapproriate as the film approaches a pure wall-jet condition. In practice gas turbine combustor slots are seldom operated with blowing ratios over 3.

Discussion

It has been demonstrated that the film effectiveness performance of practical geometry injection slots is less than that of the idealized slot even when lip thickness effects are accounted for. It also has been shown that this degradation in performance is associated with two separate effects which derive from metering of the coolant and design of the slot internal passage following the metering. A film turbulence arises from the coolant metering with the intensity being determined by the blockage introduced into the coolant flow and the length scale being related to the metering port pitch. The effect is extremely close to that of grid turbulence. The second effect is one of increased initial entrainment rates into the emerging film due to circumferential non-uniformities. Circumferential non-uniformities are introduced into the film by incomplete internal diffusion of the metered coolant jets. This diffusion is controlled by the design of the slot mixing chamber, which is itself constrained by practical considerations of manufacturing ease and cost and durability in service. It is not presently possible to calculate the complete and accurate development of circumferential and radial velocity or mass-velocity profiles at the slot outlet plane, and it is, therefore, impossible to reliably calculate the effectiveness performance of all slots. However, it has been shown that a limiting value of a certain combination of slot design parameters delineates between entrainment-dominated and turbulence-dominated film decay. Thus, a class of slots is geometrically defined as well-designed. For such slots, the film turbulence can be accounted for through an area ratio term into which profile-development effects can be incorporated by means of an empirical flow coefficient.

Good predictions of well-designed slot film effectiveness can be made over wide ranges of geometric and blowing variables. The limitations on accuracy appear to be determined by the limitations of the basic model used, rather than on the way film turbulence is accounted

Downloaded 01 Jun 2010 to 171.66.16.58. Redistribution subject to ASME license or copyright; see http://www.asme.org/terms/Terms_Use.cfm

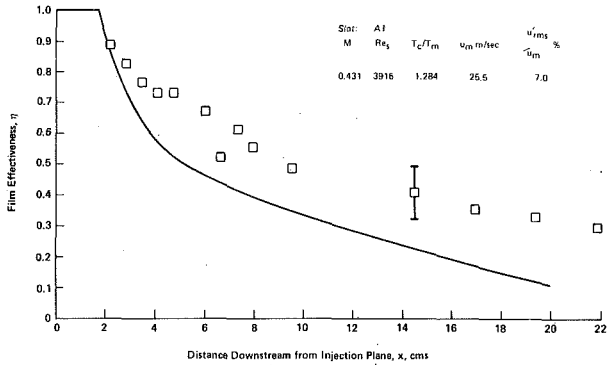


Fig. 19 Comparison of prediction with data for a single slot at low blowing ratio

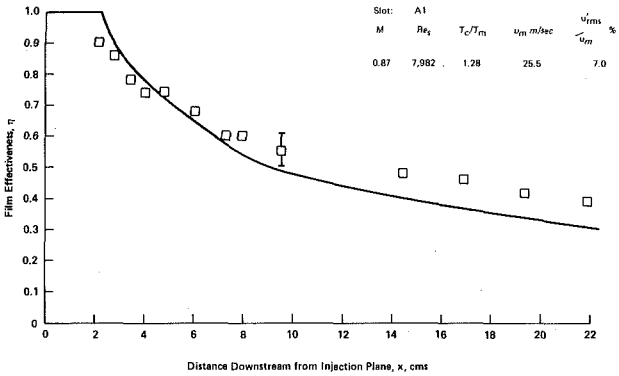


Fig. 20 Comparison of prediction with data for a single slot at intermediate blowing ratio

for. From a user's point of view, all practical ranges of injection condition are accurately predicted. The film cooling model developed over a number of years, now permits complete account to be taken of slot height, lip thickness, film turbulence, mainstream turbulence, and injection conditions. Within the constraints described above, prediction accuracy is determined only by how well the problem boundary conditions in the combustor can be defined.

From considerations of design, slot height, lip thickness and blowing ratio must be chosen to satisfy the particulars of the application in the usual fashion, but a means is now available to assess how well these choices are translated into hardware through application of the MIX criterion. Figs. 11, 15, and 16, for example, illustrate quite dramatically the penalties of a poor translation of operating conditions into hardware. They also imply that when designing a slot the manufacturing tolerances should be given careful attention. In addition, when testing practical slot designs in experimental facilities, the hardware should always be inspected and the measured values used in assessing the results of testing.

Film turbulence and initial profiles exert an effect on development of the hydrodynamic potential core. These effects have been accounted for in the calculations shown in Fig. 18–23, but have not been described in detail. Since calculation of the potential core is not a simple procedure, these details were omitted for brevity. This does not detract from the comparisons of measured data and predictions since the nature of the model is clearly revealed in the figures.

Although the present paper provides a pragmatic phenomenological handling of the film turbulence and initial entrainment, more detailed work is required to determine the complete effects of turbulence length scale on the film [12] and the nature of its relationship to the metering port design. Systematic variation of the mixing chamber parameters to complete the somewhat cursory study described in Figs. 11, 13 and 14 would be desirable. More work on the folded, or indirectly-metered, slot is needed.

Conclusions

The following conclusions can be reached:

1 Practical geometry slots will have a lower film effectiveness at identical injection conditions than idealized slots with the same slot height and lip thickness.

2 The degradation of film effectiveness is due to film turbulence generated by the coolant metering system, and to high initial entrainment rates into the film which arise from circumferential or spanwise nonuniformities resulting because of incomplete diffusion of the individual coolant jets within the body of the slot.

3 Domination of film turbulence or nonuniformities in the film decay is determined by a combination of slot mixing chamber dimensions termed MIX.

4 A limiting value can be assigned to MIX beyond which entrainment due to nonuniformities dominates film decay. Slots within the MIX limits are described as well-designed.

5 The performance of well-designed slots is quasi-two-dimensional, and is amenable to satisfactory calculation as the film turbulence can be described through an area ratio term.

6 The fall-off in film effectiveness once the limiting MIX is exceeded, i.e., the slot is no longer well-designed, is extremely rapid as MIX is increased. Only well-designed slots should be considered for engine use.

7 When a slot is designed for engine use the production tolerances associated with the chosen manufacturing technique should be

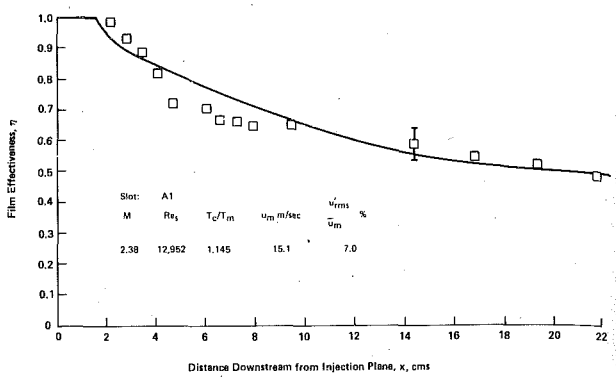


Fig. 21 Comparison of prediction with data for a single slot at high blowing ratio

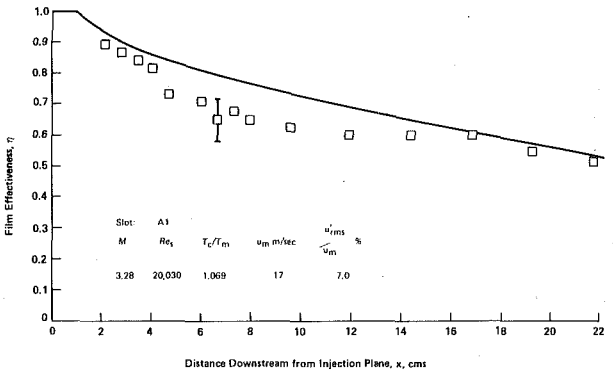


Fig. 22 Comparison of prediction with data for a single slot at high blowing ratio

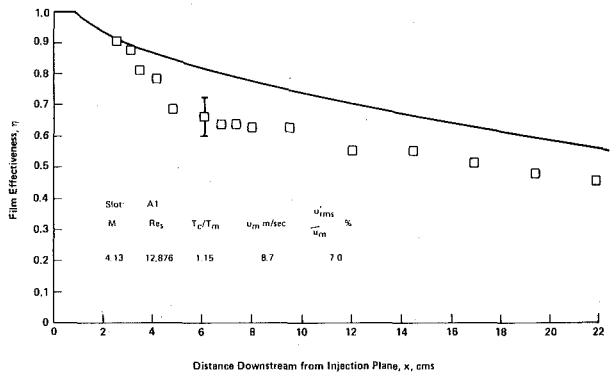


Fig. 23 Comparison of prediction with data for a single slot at high blowing ratio

Downloaded 01 Jun 2010 to 171.66.16.58. Redistribution subject to ASME license or copyright; see http://www.asme.org/terms/Terms_Use.cfm

checked against the appropriate MIX criterion to ensure that the slot remains well-designed even with the worse tolerance stack-up allowable.

8 When rig data are being compared to assess the performance of candidate slot designs, or when rig data are to be compared with predictions, it is important to inspect the test pieces and only use measured dimensions in any comparisons or calculations.

References

1 Sivasegarem S. and Whitelaw, J. H., "Film-Cooling Slots: The Importance of Lip Thickness and Injection Angle," Imperial College Report EHT/TN/6, Oct. 1967.

2. Nina, M. N. R. and Whitelaw, J. H., "The Effectiveness of Film-Cooling with Three-Dimensional Slot Geometries," Imperial College Report EHT/TN/A/24, July 1970.

3. Rastogi, A. K. and Whitelaw, J. H., "The Effectiveness of Three-Dimensional Film-Cooling Slots—I. Measurements," *Int. J. Heat Mass Transfer*, Vol. 16, 1973, pp. 1665–1681.

4. Folayan, C. O. and Whitelaw, J. H., "The Effectiveness of Combined Tangential and Normal Film-Cooling Slots with Finite Lip," ASME Paper 76-HT-30, presented at ASME-AIChE Heat Transfer Conference, St. Louis, Mo. Aug. 1976.

5. Nobbs, K. W. and Rice, P. B., "The Performance of Splash Impingement Cooling Devices," Cranfield Institute of Technology, CoA Memo No. 146, Jan. 1968.

6. Tabakoff, W. and Ravuri, R., "Film Cooling Effectiveness for Combustion Chambers," AIAA Paper 75-162, presented at AIAA 13th Aerospace Sciences Meeting, Pasadena, Jan. 1975.

7. Ballal, D. R. and Lefebvre, A. H., "A Proposed Method for Calculating Film-Cooled Wall Temperatures in Gas Turbine Combustion Chambers," ASME Paper 72-WA/HT 24.

8. Juhasz, A. J. and Marek, C. J., "Combustor Liner Film Cooling in the presence of High Free-Stream Turbulence," NASA TN D-6360, 1971.

9. Hinze, J. O., *Turbulence—An Introduction to Its Mechanism and Theory*, McGraw Hill, New York 1959, p. 216.

10. Marek, C. J. and Tacina, R. R., "Effect of Free-Stream Turbulence on Film Cooling," NASA TN D-7958, June 1975.

11. Sturgess, G. J., "Correlation of Data and Prediction of Effectiveness from Film-Cooling Injection Geometries of a Practical Nature," *Proceedings of Cranfield International Symposium Series Vol. 11, Combustion and Heat Transfer in Gas Turbine Systems*, Edit. E. R. Norster, Pergamon Press, 1971, pp. 229–250.

12. Sturgess, G. J. and Lenertz, J. E., "Account of Mainstream Turbulence for Predicting Film Cooling Effectiveness in Gas Turbine Combustors," ASME Paper No. 77-HT-10, Aug. 1977.

13. Sturgess, G. J., "Wall Cooling by Gaseous Injection for a High Performance Combustion System," Ph.D. Thesis, University of Technology, Loughborough, England, 1970.

APPENDIX

Overall Effective Area of Film Cooling Slots. Consider the general film cooling slot shown in Fig. 7 which has two rows of coolant metering. Let λ be the ratio of normal to axial coolant mass flow rates entering the slot. If constant density and a plenum chamber feed to the slot is assumed then,

$$\lambda = A_{H_2}/A_{H_1} \tag{A1}$$

Conservation of mass yields,

$$\dot{m}_s = (1 + \lambda)\rho A_{H_1} u_{H_1}$$

so that,

$$\frac{u_s}{u_{H_1}} = \frac{A_{H_1}}{A_s}(1 + \lambda) \tag{A2}$$

Applying conservation of axial momentum,

$$p_s A_s - p_{H_1} A_{H_1} \cos\theta - p_0(A_s - A_{H_1}\cos\theta) = \iint \rho_{H_1} u^2 \cos\theta \, dA_{H_1} - \iint \rho_s u^2 dA_s$$

With perfect internal mixing, uniform entry and unchoked metering ports such that pressure on slot upstream face p_0 is equal to p_{H_1}, this gives,

$$p_s A_s - p_{H_1} A_{H_1} \cos\theta - p_{H_1}(A_s - A_{H_1}\cos\theta) = \dot{m}_{H_1} u_{H_1} \cos\theta - \dot{m}_s u_s$$

Upon algebraic manipulation this reduces to,

$$(p_s - p_{H_1}) = \rho u_{H_1}^2 \left[\frac{A_{H_1}}{A_s}\cos\theta - \left(\frac{A_{H_1}}{A_s}\right)^2 (1 + \lambda)^2\right] \tag{A3}$$

Now, the total pressure in holes H_1 is equal to the slot exit total pressure plus the losses in total pressue due to coolant jet expansion, turning and mixing within the slot.

i.e., $$P_{H_1} = p_s + \Delta P_{\text{Loss}}$$

Hence,

$$p_{H_1} + 1/2\rho u_{H_1}^2 = p_s + 1/2\rho u_s^2 + \Delta P_{\text{Loss}}$$

or,

$$(p_s - p_{H_1}) = 1/2\rho(u_{H_1}^2 - u_s^2) - \Delta P_{\text{Loss}}$$

Substituting from equation (A2) this becomes,

$$(p_s - p_{H_1}) = 1/2\rho u_{H_1}^2 \left[1 - \left(\frac{A_{H_1}}{A_s}\right)^2 (1 + \lambda)^2\right] - \Delta P_{\text{Loss}} \tag{A4}$$

Equating equations (A3) and (A4) and rearranging gives,

$$\frac{\Delta P_{\text{Loss}}}{1/2\rho u_{H_1}^2} = 1 + \left(\frac{A_{H_1}}{A_s}\right)^2 (1 + \lambda)^2 - 2\frac{A_{H_1}}{A_s}\cos\theta \tag{A5}$$

If the dynamic head in the flow feeding the metering ports is small the driving force for coolant flow through the complete slot is the difference between this shroud total pressure and the combustor static pressure. Furthermore, if there is constant pressure mixing of film cooling air with the combustor flow at the slot outlet plane, the combustor static pressure can be replaced by the slot outlet static pressure p_s. Finally, if it is assumed that there is no loss in total pressure in feeding the metering ports the overall driving force for both sets of ports is $(P_{H_1} - p_s)$.

From the expression for total pressures through the slot with substitution from equation (A5) for the losses,

$$(P_{H_1} - p_s) = 1/2\rho \left\{u_s^2 + u_{H_1}^2 \left[1 + \left(\frac{A_{H_1}}{A_s}\right)^2 (1 + \lambda)^2 - 2\frac{A_{H_1}}{A_s}\cos\theta\right]\right\} \tag{A6}$$

An expression for slot flow can be obtained from the orifice equation as,

$$\dot{m}_s = A_E[2\rho(P_{H_1} - p_s)]^{1/2}$$

since

$$A_H/A_{\text{Shroud}} \to 0$$

Substituting in this equation the expression above for $\dot{m}_s$ and equation (A6) for the driving force yields,

$$\frac{(1 + \lambda)^2 A_{H_1}}{A_E^2} = \left(\frac{u_s}{u_{H_1}}\right)^2 + \left[1 + \left(\frac{A_{H_1}}{A_s}\right)^2 (1 + \lambda)^2 - 2\frac{A_{H_1}}{A_s}\cdot\cos\theta\right]$$

Introducing equation (A2) into this gives,

$$\frac{(1 + \lambda)A_{H_1}}{A_E} = \left[1 + 2\left(\frac{A_{H_1}}{A_s}\right)^2 (1 + \lambda)^2 - 2\cdot\frac{A_{H_1}}{A_s}\cdot\cos\theta\right]^{1/2} \tag{A7}$$

Now

$$(1 + \lambda)A_{H_1} = \left(1 + \frac{A_{H_2}}{A_{H_1}}\right)A_{H_1} = A_{H_1} + A_{H_2} = A_H$$

and since A_0 is equivalent to A_s,

$$A_0/A_E = \frac{A_H}{A_E}\cdot\frac{A_s}{A_s} = \left[\frac{(1 + \lambda)A_{H_1}}{A_E}\right]\left[\frac{A_s}{(1 + \lambda)A_{H_1}}\right] \tag{A8}$$

Hence, from equation (A7) and identity (A8),

$$A_0/A_E = \frac{A_s}{(1 + \lambda)A_{H_1}}\left[1 + 2\left(\frac{A_{H_1}}{A_s}\right)^2 (1 + \lambda)^2 - 2\cdot\frac{A_{H_1}}{A_s}\cdot\cos\theta\right]^{1/2} \tag{A9}$$

Downloaded 01 Jun 2010 to 171.66.16.58. Redistribution subject to ASME license or copyright; see http://www.asme.org/terms/Terms_Use.cfm

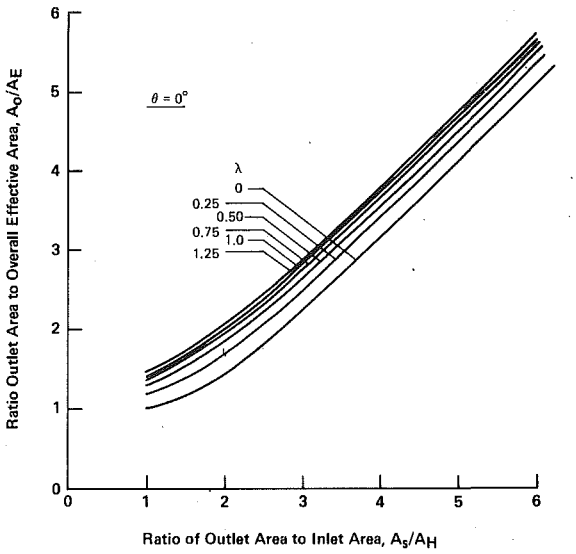


Fig. A1 Effect of flow split on effective area for single row and double row-in-parallel metered film cooling slots

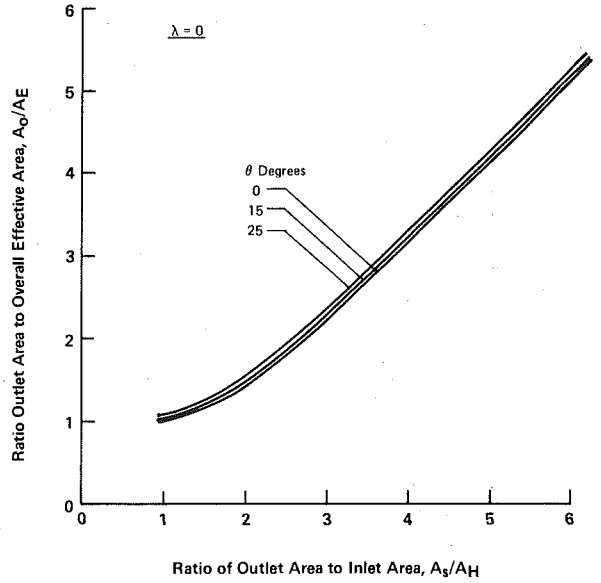


Fig. A3 Effect of metering port angle on effective area for single row metered film cooling slots

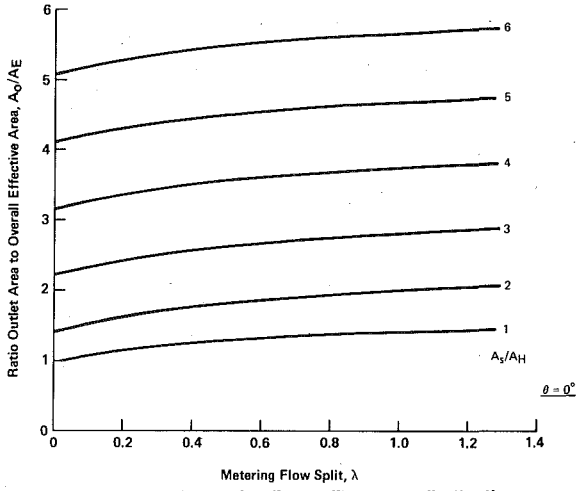


Fig. A2 Effect of metering flow split on overall effective area

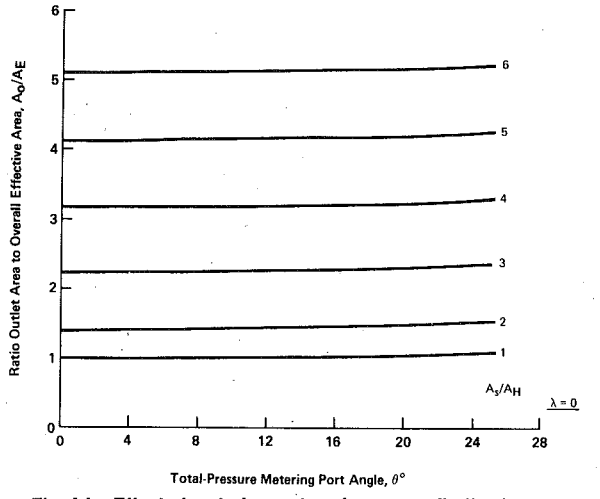


Fig. A4 Effect of metering port angle on overall effective area

Equation (A9) appears as equation (4) in the main body of the paper.

Variations of equation (A9) for different slot geometries exist as follows:

1 Single row metering with total pressure-fed holes at angle θ: $\lambda = 0$, $A_{H_1} = A_H$ and equation (A9) reduces to,

$$A_0/A_E = \frac{A_s}{A_H}\left[1 + 2\left(\frac{A_H}{A_s}\right)^2 - 2\frac{A_H}{A_s}\cos\theta\right]^{1/2} \quad \text{(A10)}$$

2 Single row metering with total pressure fed holes parallel to slot flow:

$\lambda = 0$, $A_{H_1} = A_H$, $\theta = 0$, $\cos\theta = 1$

$$A_0/A_E = \frac{A_s}{A_H}\left[1 + 2\left(\frac{A_H}{A_s}\right)^2 - 2\frac{A_H}{A_s}\right]^{1/2} \quad \text{(A11)}$$

3 Double row metering with total pressure fed holes parallel to slot flow:

$\theta = 0$, $\cos\theta = 1$

$$A_0/A_E = \frac{A_s}{(1+\lambda)A_{H_1}}\left[1 + 2\left(\frac{A_{H_1}}{A_s}\right)^2 (1+\lambda)^2 - 2\frac{A_{H_1}}{A_s}\right]^{1/2} \quad \text{(A12)}$$

(N.B.: For a total/static fed coolant mass flow split of 60/40, $\lambda = 0.667$. For a split of 50/50, $\lambda = 1.0$; and for a split of 70/30, $\lambda = 0.428$.

Fig. A1 shows the effects of flow split λ on slot effective area for single row and double row metering. It is desirable to design with A_s/A_H close to unity and in this range addition of the second row of metering has a significant effect on A_0/A_E. However, constrained by combustor manufacturing techniques and thermal severity in operation most practical slots fall in the range $2 \lesssim A_s/A_H \lesssim 4$, where the effect is small compared to A_s/A_H changes. Fig. A2 is a crossplot from Fig. A1 and shows this more dramatically.

The effects of port angle for single row metering are illustrated in Figs. A3 and A4. The effect is again small.

Downloaded 01 Jun 2010 to 171.66.16.58. Redistribution subject to ASME license or copyright; see http://www.asme.org/terms/Terms_Use.cfm

A. Ravindranath
Graduate Assistant.

B. Lakshminarayana
Professor of Aerospace Engineering.

Department of Aerospace Engineering,
The Pennsylvania State University,
University Park, PA 16802

Mean Velocity and Decay Characteristics of the Near and Far-Wake of a Compressor Rotor Blade of Moderate Loading

This paper reports the experimental study of the three-dimensional characteristics of the mean velocity in the wake of a moderately loaded compressor rotor blade. The measurements were taken with a three-sensor hot-wire probe rotating with the rotor. The wake was surveyed at several radial and axial stations. The loading was found to have substantial effect and this was reflected not only in the axial and tangential components, but also in the radial component. The radial velocities were found to be high very near the trailing-edge and this exhibits the characteristics prevalent in a trailing vortex system. The static pressures across the wake were measured using a direction insensitive spherical head static-stagnation pressure probe. The static pressure was found to be higher inside the wake. These and other measurements are reported and correlated in this paper.

Introduction

The flow through a compressor rotor blade row is very complex and deviates considerably from the two-dimensional flow field because of a number of phenomena including vortex shedding, variation in spanwise circulation, radial flow in the boundary-layers, hub and annulus-wall boundary-layer growth, etc. The boundary-layer on the blades is shed out from the pressure and suction surfaces, and they combine very near the trailing-edge to form the viscous wake referred to as the rotor-wake. Study of the rotor-wake should yield a comprehensive understanding of the flow and acoustic field induced by this phenomena, which is essential to progress in reducing the noise, losses, and in improving the mechanical and aerodynamic performance of rotors.

The rotor-wakes, which represent the flow field downstream of the rotor, are not only influenced by upstream flowfield conditions but are also controlled by such parameters as blade spacing, solidity, hub-tip ratio, blade loading, distance from the blade trailing edge, and Centrifugal and Coriolis forces induced by curvature and rotation. These effects make the flow highly three-dimensional, which introduces many complications in the experimental and theoretical investigations of the rotor wake.

This paper reports some results of a comprehensive investigation of the wake of such a moderately loaded compressor rotor conducted at the Turbomachinery Laboratory of the Pennsylvania State University. The immediate objectives of the program include a thorough experimental investigation of the flow ahead of, within, and downstream of the rotor. In the present paper two aspects of the study will be discussed: a detailed study in the trailing-edge region outside the hub and annulus-wall boundary layers, and a description of the flow field in the near-wake region.

Contributed by the Gas Turbine Division of The American Society of Mechanical Engineers and presented at the Gas Turbine Conferences and Exhibit and Solar Energy Conference, San Diego, Calif., March 12–15, 1979. Manuscript received at ASME Headquarters January 3, 1979. Paper No. 79-GT-202.

The general structure of the rotor-wakes was studied by Raj and Lakshminarayana [1] and Reynolds, et al. [2]. These data were taken from a lightly loaded axial flow fan at Penn State. In the above studies it was realized that loading has a considerable effect on the nature of the mean velocities and turbulence quantities inside the wake. It was also noted that the annulus- and hub-wall boundary-layers affect the development and decay of rotor wakes near the wall regions and that the wake behavior in the trailing edge region is quite different from that in the near or far-wake regions. This investigation was undertaken to study these effects, and thereby provide the acousticians and the aerodynamicists with the nature of the flow very near the blade trailing-edge, near-wake and far-wake region of a moderately loaded compressor blade. This information is essential for the prediction of the noise levels, optimum rotor-stator spacing, and losses in a compressor. In this paper only the wake data outside the annulus and hub-wall boundary-layers will be presented.

Experimental Equipment and Procedure

The experiments described in this paper were conducted using the axial-flow compressor facility at the Department of Aerospace Engineering, the Pennsylvania State University. The measurement procedure used was similar to the one described in [2]. A tri-axial hot-wire probe rotating with the rotor was used to measure the characteristics of the rotor-wake. A modified version of the traverse gear used in [3] was employed for traversing the probe across the wake, while the rotor was in motion.

Description of the Facility. The axial-flow compressor facility used in this investigation is shown in Fig. 1. The general description of the stage is given in [4] and the operating characteristics in [5]. At a fixed rotor speed the operating conditions can be varied by a throttle located downstream of the auxiliary fan. To remove dust and other particles from the flow which enters the test section a large dust screen was placed around the bellmouth inlet.

The rotor with 21 cambered and twisted blades is housed between an inlet guide vane (IGV) assembly and a stator assembly. The IGV has a swirl distribution varying linearly from zero at the hub to 0.3

Copyright © 1980 by ASME

Downloaded 01 Jun 2010 to 171.66.16.58. Redistribution subject to ASME license or copyright; see http://www.asme.org/terms/Terms_Use.cfm

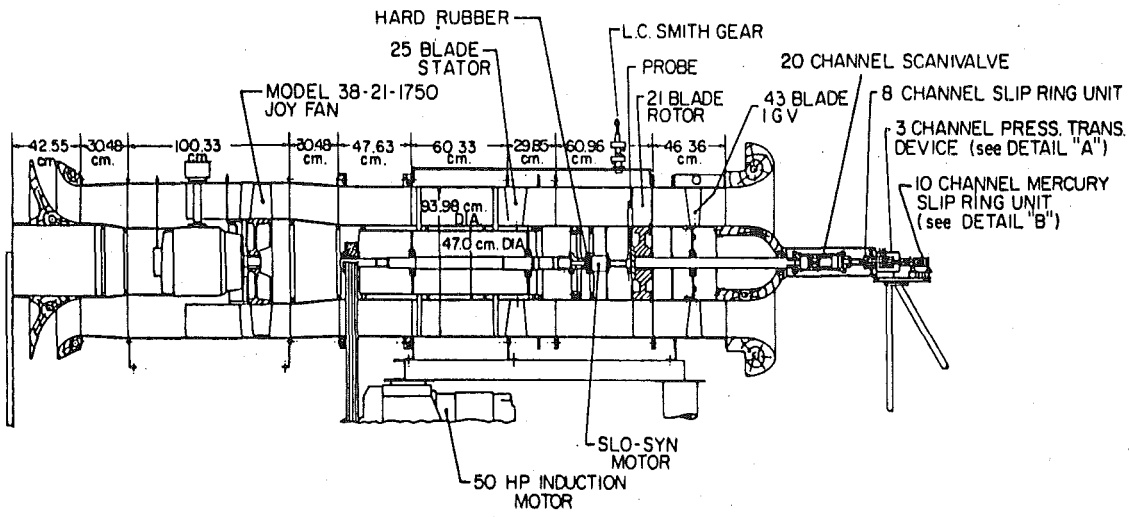


Fig. 1 PSU axial flow compressor facility

Table 1 Wake Measuring Stations

R	Chord m(inch)	Axial Location From Trailing Edge Z						Inlet Turbulence
0.9595	0.150(5.90)	0.0104	0.0417	0.124	0.240	0.458		
0.9324	0.147(5.80)	0.0104	0.0412	0.125	0.250	0.458		0.5% (Axial
0.8615	0.141(5.56)	0.0104	0.0417	0.125	0.208	0.417	0.625	Intensity/
0.7973	0.137(5.40)		0.03125	0.146	0.229	0.375	0.563	Axial Vel.)
0.7297	0.134(5.26)	0.0104	0.0208	0.1354	0.219	0.354	0.5313	
0.6581	0.130(5.12)			0.1146	0.240	0.458	0.6875	
0.5676	0.128(5.02)			0.125	0.308	0.458	0.6563	

U_t at the tip and the IGV trailing edge is located about 1.8 rotor chords upstream of the rotor leading edge at mid-radius. The rotor tip diameter is 0.9322 m (36.700 in.) with a hub to tip ratio of 0.5. The rotor tip clearance is 2.26×10^{-3} m (0.089 in.). The rotor is driven by a variable speed 37.3 kw (50 hp) motor. The rotor was operated at 1066 rpm and the speed is measured by a photocell attached to the rotor shaft. The inlet axial velocity before the inlet guide vanes is approximately 96 ft/s at the operating flow coefficient of 0.56 (based on blade tip speed).

All measurements reported in this paper were carried out behind the rotor at various axial and radial distances and are tabulated in Table 1. The blade profiles are of modified NACA 65-010 basic profile with a circular arc camber. The blade has a varying stagger angle and blade chord along the radius and the details are given in [4]. The rotor was operated at a flow coefficient of 0.56 and the performance curve for the compressor with its operating point is shown in Fig. 2. This operating point was chosen to provide a reasonable stall margin as well as good efficiency.

Rotating Probe Traverse Mechanism. The rotating probe traverse mechanism used in [3] was modified to suit the requirements for the rotor-wake measurements. This new traverse gear achieves the objectives of the gear used in [2] in a much simpler fashion.

Fig. 3 shows the main features of the new gear. It has a SLO-SYN motor of 225 in-oz torque driving a 3.81×10^{-2} m (1.5 in.) dia shaft

Nomenclature

A_n = Fourier cosine coefficient
B_n = Fourier sine coefficient
C = blade chord
$C_p = (p - p_1)/\frac{1}{2}\rho U_t^2$
C_{pT} = total pressure coefficient $(P_{01} - P)_{rel}/\frac{1}{2}\rho U_t^2$
C_D = section drag coefficient
i = incidence of inlet flow with rotor blade in relative (rotating) frame of reference
L_s, L_p = wake width at half the depth on rotor blade suction and pressure surface of the wake, respectively
$L = 2(L_s + L_p)/S$ = sum of the characteristic length on the pressure and suction surfaces normalized by semi-blade spacing
n = number of coefficients in the Fourier series
P = stagnation pressure
p = static pressure
R = radius ratio = (r/r_t)
r = local radius
(r, θ, z) = rotating cylindrical coordinate system
S = blade spacing
U_t = blade tip speed
u_{d_N} = normalized velocity defect = $u_d/u_{d_c} = (u_{max} - u)(u_{max} - u_{min})$
u_{max} = maximum velocity in the wake
u_{min} = minimum velocity in the wake
u = velocity at any point in the wake
W_r, W_θ, W_z = relative velocity in the radial, tangential and axial directions
W = relative total velocity
w_θ, w_z = defects in tangential and axial velocities in relative frame of reference
Y = tangential distance
$(2Y/S)$ = tangential distance normalized by half the blade spacing ($Y = 0$ at the wake center)
Z = axial distance from blade trailing edge normalized by rotor blade chord
$\bar{\phi}$ = mass averaged flow coefficient $(\overline{W}_z/U_t)$
$\bar{\psi}$ = mass averaged stagnation pressure rise coefficient (normalized by $\frac{1}{2}\rho U_t^2$)
Ω = speed of rotation of rotor blade
η_s, η_p = wake transverse distance normalized by L_s and L_p, respectively
θ_L = distance between the centerline and the location where $u_d = u_{d_c}/2$
β = outlet air angle
$\bar{\eta}$ = rotor efficiency (Euler) = $\bar{\psi}/\bar{\psi}_{Euler}$

Subscripts

c = value at the wake center
d = defect (difference between free stream and wake value)
0 = value at wake edge/stagnation property
m/max = maximum value in the wake
t = value at rotor tip
1 = value at inlet (passage averaged)
min = minimum value
TE = values at the trailing edge

Superscript

— = average value

Downloaded 01 Jun 2010 to 171.66.16.58. Redistribution subject to ASME license or copyright; see http://www.asme.org/terms/Terms_Use.cfm

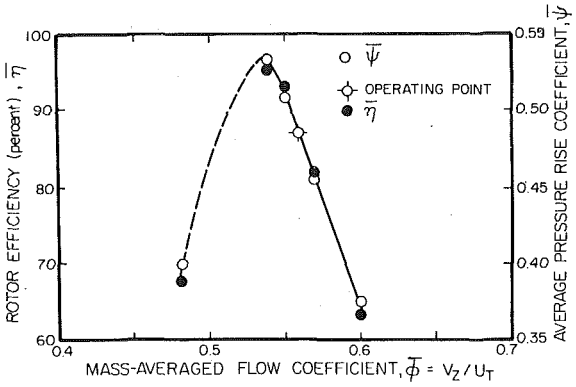


Fig. 2 PSU axial-flow compressor rotor performance curve

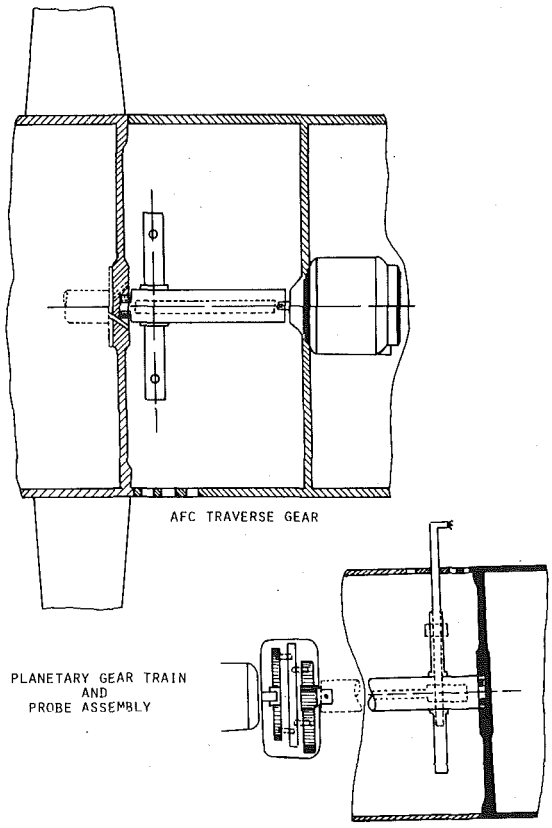


Fig. 3 Rotating probe traverse mechanism

through a palnetary reduction gear train. The gear train steps down (1.8 deg/step) circumferential stepping to (0.09 deg/step). The shaft carries a rider which can be traversed axially. The rider in turn carries a pair of mounting blocks which can be used to hold the probe. These mounting blocks give the probe two degrees of freedom; (1) rotation about the probe axis; this motion is used to align the hot-wire sensors in any desired direction; (2) movement in the radial direction; the probe can be traversed from hub-to-tip of the machine.

The probe holder, the stepping motor, and the probe are mounted inside the rotating hub of the machine. The probe which is located behind the blade row traverses in a slot in the hub. The motor is powered and controlled by a stationary traverse indexing device through an eight-channel brush slip-ring unit. The traverse unit and the probe are locked, except when indexed. Though the circumferential traverse can be accomplished when the rotor is rotating, the radial and axial motions have to be accomplished manually when the rotor is stationary.

Probes, Instrumentation and Data Transmission System. A tri-axial hot-wire probe, similar to that used in [1] and [2] was employed for all velocity measurements reported in this paper. The probe has been found to measure the three components of velocity and turbulence intensities accurately. The probe sensors were built out

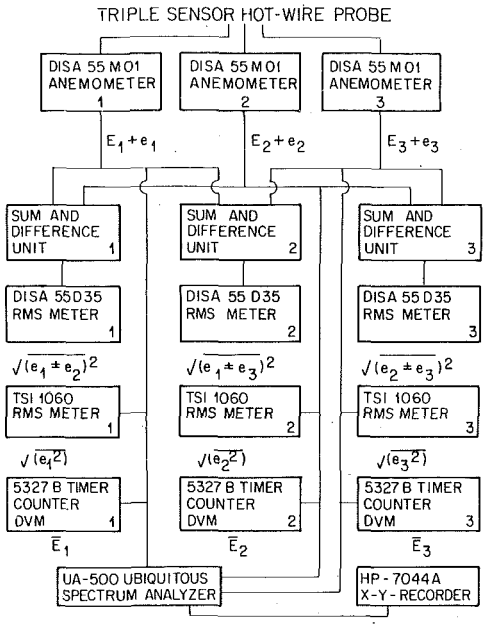


Fig. 4 Schematic of instrumentation for rotating hot-wire measurement

of tungsten wire and had a length to diameter ratio of 270. The sensor resistances were around 5 ohms. The probe calibrations are corrected for the variations of temperature and aging of the wire. The effect of rotation on heat transfer properties of the wire was found to be negligible [6]. The signals from the rotating hot-wire, rotating with the rotor, was taken through a ten channel slip-ring unit to a stationary data-processing system which was similar to the one employed in [1] and [2].

To evaluate the accuracy of the hot-wire measurements and to find the static pressure gradients across the wake a spherical head static-stagnation pressure probe was rotated with the rotor. The probe was found to be fairly insensitive (within ±20 deg) to the large pitch or yaw angles that were encountered in the three-dimensional flow in the wake. The probe consists of 0.3175 cm (1/8 in.) sphere with trips mounted on the sphere to stabilize the wake region. The wake pressure and the total pressure were measured to evaluate the static pressure upstream of the sphere. A complete description of the probe is given in [7]. The probe is calibrated in a known uniform flow and, therefore, the calibration would include the aerodynamic interference effects. But the errors due to the probe immersed in shear gradients are not included.

Fig. 4 illustrates the instrumentation used with the tri-axial hot-wire probe. The choice of the instrumentation was made such that the raw data from the experiment could be used directly in the data processing program developed by Gorton and Lakshminarayana [8]. Consistent with the assumptions made in [8], a streamline coordinate system was chosen and the hot-wire axis was aligned along the blade stagger. The data was then transformed to the r-θ-z coordinate system where the r-direction is in the direction of the machine radius, z in the axial direction, and θ in the tangential direction.

Experimental Data and Interpretation

Rotating hot-wire measurements were made to study the rotor-wake characteristics in the trailing-edge, near and far-wake regions. Trailing-edge region is defined as the region very close to the blade trailing-edge where the radial velocities show trends similar to that of a trailing vortex system; a near-wake is defined as the region where the defects in velocity are of the same order of magnitude as the free-stream velocity. Far wake is defined as the region where velocity defects are very small. With these measurements, the mean velocity and turbulence characteristics of the rotor-wake were found. Similarity rules and decay laws were established for the mean velocities. Static-pressure variations across the wake were also measured. In this paper only the mean velocity characteristics of the rotor-wake outside the annulus- and hub-wall boundary-layers are presented. The tur-

Downloaded 01 Jun 2010 to 171.66.16.58. Redistribution subject to ASME license or copyright; see http://www.asme.org/terms/Terms_Use.cfm

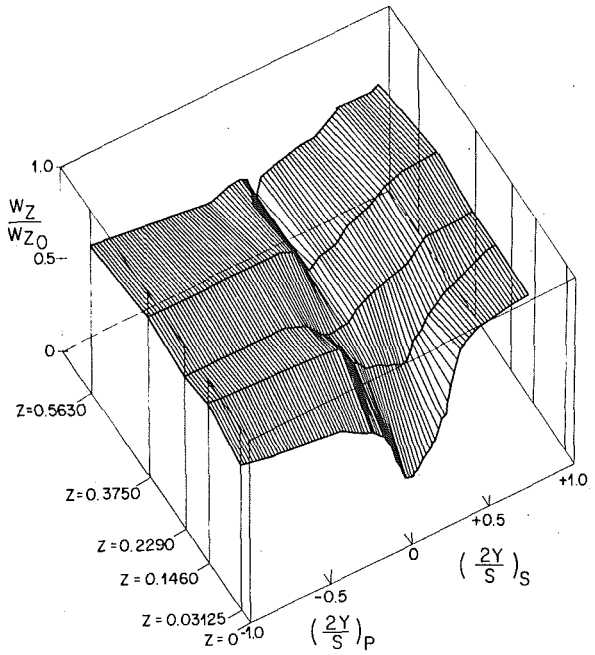


Fig. 5 Three-dimensional plot of axial velocity profiles, $R = 0.7973$, $\phi = 0.56$

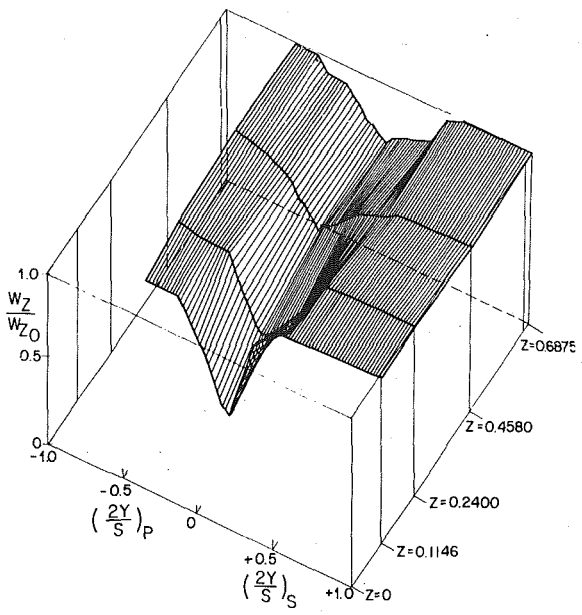


Fig. 6 Three-dimensional plot of axial velocity profiles, $R = 0.6581$, $\phi = 0.56$

bulence data and data inside the annulus and hub-wall boundary layers will be presented and interpreted in a subsequent paper.

Mean Velocity Profiles. All velocities discussed in this section are relative velocities and are normalized by the corresponding free-stream axial velocity, unless otherwise specified. The data at three radial locations, $R = 0.7973$, 0.7297 and 0.6581, are presented in this paper.

Axial Velocity. Variations of axial velocity across the wake and at various downstream locations for the radii $R = 0.7973$ and $R = 0.6581$ are shown as a three-dimensional plot in Figs. 5 and 6. The tangential distance is normalized by the blade spacing.

Fig. 7 shows the variations of the axial velocity profiles for the radius $R = 0.7297$. The wake profiles are asymmetrical about the wake center indicating differential growth of the boundary layers on the two surfaces of the blade. This is true at all the radii (Figs. 5–7) and near the trailing edge region. Because of wake spreading and mixing with free-stream as well as interchange of momentum and energy on either side of the wake, the wake will become nearly symmetrical at far downstream locations.

In the trailing-edge region, for the radius $R = 0.7297$, the wake defect is 0.88 which reduces to 0.2 at $Z = 0.5313$. For the wake at $R = 0.7973$, a defect of 0.71 at $Z = 0.03125$ reduces to 0.24 at $Z = 0.5625$. As the hub wall is approached the decay rate decreases as shown at the radius $R = 0.6581$ (Fig. 6) where a defect of 0.66 at $Z = 0.1146$ reduces to 0.33 at a Z location of 0.6875. The same trend is observed even when the annulus-wall boundary-layer is approached. So the wakes decay differentially in the radial direction.

Not only is the decay different at each radius so are the velocity profiles. Because of radial transport of mass, momentum, and energy, wakes at the hub are expected to be thinner gradually increasing towards the tip. But in the present case the wakes at lower radius are as thick as those at higher radii. The probable reason for this is that the drag coefficient at the root is higher than that at tip due to larger turning, and this may offset the effect discussed earlier and yield results contrary to what is expected. Also, axial velocity profiles show a lower value of the free stream on the pressure side and higher value on the suction side. This is a consequence of the existence of pressure gradients (inviscid effects) across the passage immediately downstream of the trailing-edge. This effect is less pronounced beyond $Z = 0.045$.

The variation of the tangential gradients of axial component of velocity indicate the changes in profile shape downstream of the rotor.

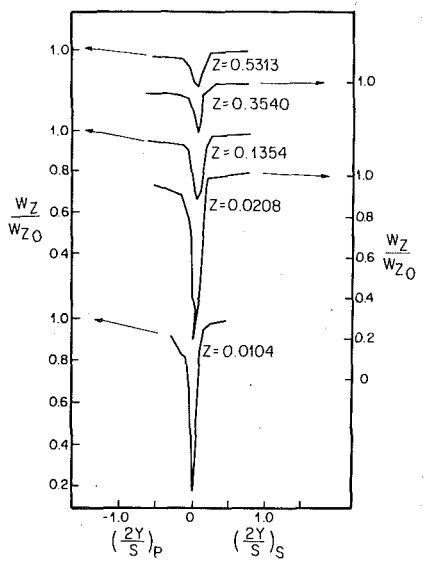


Fig. 7 Axial velocity profiles, $R = 0.7297$, $\phi = 0.56$

For the wake in the trailing-edge region the gradients are very large and can be clearly seen in Fig. 7. This characteristic for the wake results from the development of the flow as it moves over the rotor blade and transforms into the wake at the trailing-edge from a boundary-layer. In the far-wake region the gradient becomes considerably smaller because of wake spreading and mixing with the free-stream. The steep gradient in the trailing-edge region represents highly unstable and developing flow conditions. There is another interesting feature that can be observed in the trailing-edge region. Here the pressure-surface boundary-layer is slightly thicker than the suction-surface boundary layer (Figs. 5–7). One probable cause of this is that radial inward velocities on the pressure surface (reported later) will cause a larger accumulation of boundary-layer on the pressure-surface compared to that on the suction-surface. Exact cause of this phenomena is not known. Measurements presently carried out to determine the boundary-layer characteristics near the trailing-edge ($z < 0$) should provide an explanation of this phenomena. As the wake travels downstream the radially inward velocities decrease, and beyond 0.15 chord downstream, we have only radially outward flow (as discussed later). The wake shows a tendency to become symmetrical further downstream under these conditions.

Downloaded 01 Jun 2010 to 171.66.16.58. Redistribution subject to ASME license or copyright; see http://www.asme.org/terms/Terms_Use.cfm

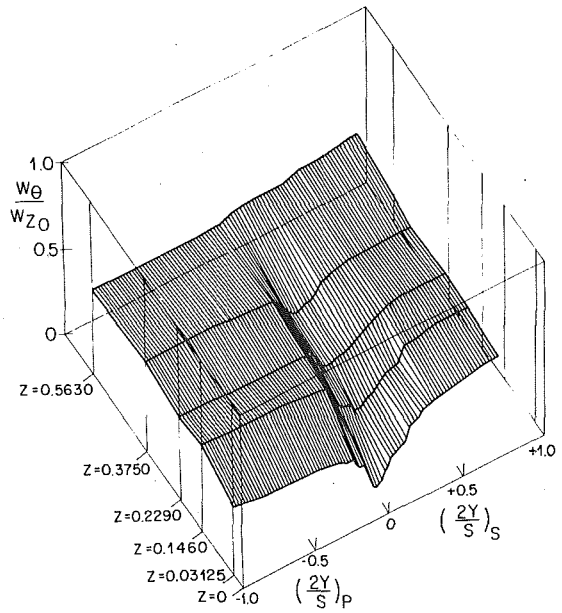


Fig. 8 Three-dimensional plot of tangential velocity profiles, $R = 0.7973$, $\phi = 0.56$

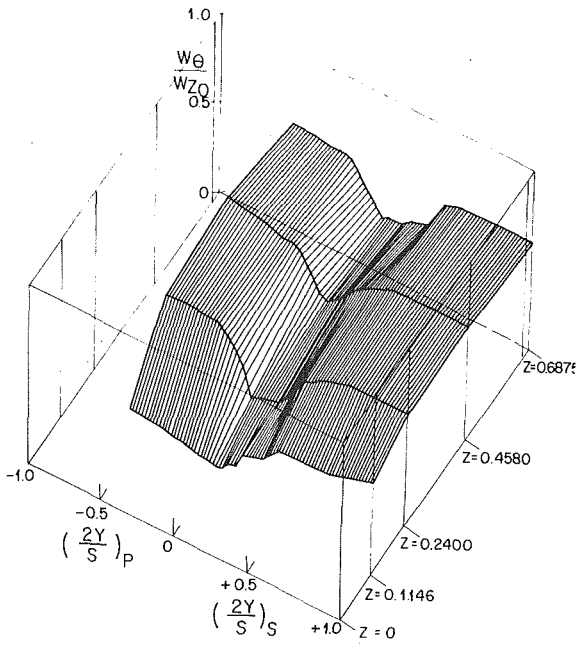


Fig. 9 Three-dimensional plot of tangential velocity profiles, $R = 0.6581$, $\phi = 0.56$

The effect of blade loading can be observed in the near-wake plots of Fig. 7. The wakes become highly unsymmetrical because of loading and is noted by comparing Fig. 7 with Figs. 4 and 5 of [2]. From [2] we note that the wake becomes approximately symmetrical at 0.271 chord downstream where as in Fig. 7 for the present case the wake still tends to be asymmetrical at half-a-chord downstream. Thus the effect of blade loading is to sustain the asymmetry to a much larger extent downstream of the blade trailing-edge.

Blade loading not only makes the profiles asymmetrical, it also increases the velocity defect and slows down the decay rate. Thus at mid-radius, comparing Fig. 7 with Figs. 4 and 5 of [2] we note that at about the same Z location (say $Z = 0.0208$) a heavily loaded blade gives much deeper wake compared to that of a lightly loaded blade used in [2]. The decay of the heavily loaded rotor-wake is much slower with a defect of 0.16 at half-a-chord downstream compared to that of a lightly loaded rotor-wake where the defect is 0.2 at $Z = 0.271$.

Relative Tangential Velocity. Figs. 8 and 9 show the three-dimensional plot of relative tangential velocity for the radii $R = 0.7973$ and $R = 0.6581$ while Fig. 10 shows the tangential velocity variation with downstream distance for the radius $R = 0.7297$.

In general, the tangential velocity defects were found to be greater than axial velocity defects. At $R = 0.7297$ and $Z = 0.0104$ the defect is almost 0.9 W_{θ_0} dropping off to about 0.2 W_{θ_0} in half-a-chord downstream. The same type of trend is observed for the other radii $R = 0.7973$ and 0.6581. The tangential velocities profiles are also asymmetrical because of differential growth of boundary-layers on the two surfaces.

The variation of the decay of tangential velocity defect in the radial direction show an interesting trend. At $R = 0.7973$ and at a downstream location of 0.5630 chords the defect in tangential velocity is 0.13 and this defect continuously increases towards the hub. Probable cause for this is the larger turning near the hub and hence increased drag coefficient. Furthermore, the presence of hub wall boundary layer and secondary flow may produce this effect. As the defect is large near the lower radius as compared to higher radius, the decay rate is correspondingly slower at the lower radius. But compared to axial velocity, the tangential velocity defect decays much more rapidly. Loading not only increases the defect and asymmetry, but it also slows down the decay. Comparison of Fig. 10 with Figs 6 and 7 of [2] will confirm this argument. Tangential velocities also show considerable asymmetry in the trailing-edge and near-wake regions. Blade loading does make a significant contribution to the asymmetry and its effect persists up to half-a-chord downstream.

Tangential velocities are greatly influenced by the radial component

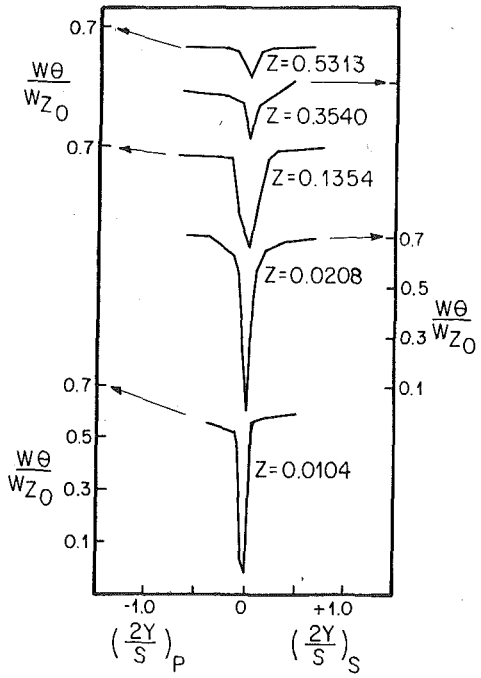


Fig. 10 Tangential velocity profiles, $R = 0.7297$, $\phi = 0.56$

of velocities. In the trailing-edge and near-wake regions for $R = 0.7297$, it is observed that there are very large radial velocities and a small component of negative relative tangential velocities. This implies that the absolute and relative velocities are in the same direction and that there is a very large change in angle in these regions.

Radial Velocities. Radial velocities are caused by an imbalance in the radial pressure gradients and the centrifugal forces. Physically at either surface of the trailing-edge of a compressor rotor blade, the radial velocities must be zero while the maximum radial outward velocities occur slightly away from the blade surface. This was confirmed by measurements on an inducer blade by Lakshiminarayana, et al. [9]. Raj and Lakshminarayana [1] and Reynolds, et al. [2] measured the radial velocity profiles in the wakes from a lightly loaded rotor. The behavior of the radial velocities were very much different in these cases compared to that of [9]. In the present case radial ve-

Downloaded 01 Jun 2010 to 171.66.16.58. Redistribution subject to ASME license or copyright; see http://www.asme.org/terms/Terms_Use.cfm

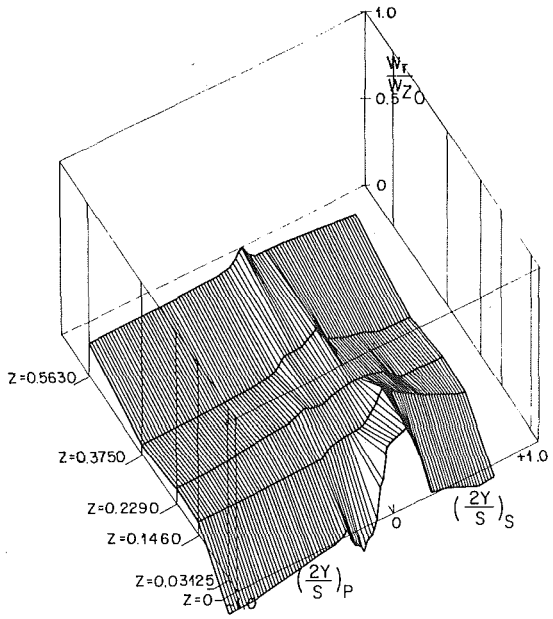


Fig. 11 Three-dimensional plot of radial-velocity profiles, $R = 0.7973$, $\phi = 0.56$

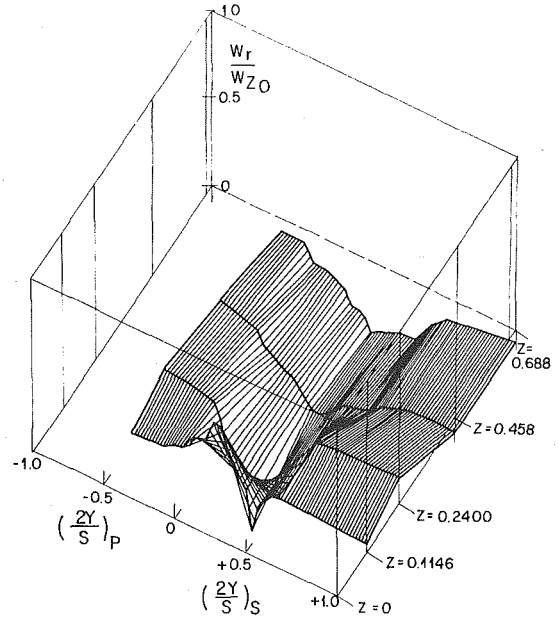


Fig. 12 Three-dimensional plot of radial-velocity profiles, $R = 0.6581$, $\phi = 0.56$

locity profiles for the radii $R = 0.7973$ and 0.6581 are shown as three-dimensional plots in Figs. 11 and 12, respectively, while Fig. 13 shows the radial velocity variation with downstream distance for $R = 0.7297$.

As mentioned earlier the radial velocities are caused by an imbalance of centrifugal forces and the radial pressure gradients inside the wake. Depending on which of the above forces dominates, there will be a radially inward or outward flow. Very near the trailing-edge there might be one other reason why a radially inward or outward flow exists. A trailing vortex system associated with the circulation might give a radially inward flow on one side and radially outward flow on the other side of the blade. Referring to Fig. 13 we note that at the wake center as well as in the free stream we have nearly zero radial velocity and radially inward flow near the pressure-surface and radially outward flow near the suction side. This situation is possible if the trailing vortex dominates the flow in the trailing-edge region while the boundary-layer flow dominates the flow in the near and far-wake regions. This complex flow phenomenon is not fully understood and a knowledge of the flow on the blades (blade boundary-layer) could assist in explaining the nature of the flow. Further experiments in this region along with flow visualization studies have been planned with a view towards better understanding and interpretation of this data.

In the near and far-wake region we have a radially outward flow with the maximum velocity occurring slightly away from the wake center and towards the suction-surface. This flow phenomena can be explained on the basis of the earlier concept of imbalance between the centrifugal forces and radial pressure gradients.

The nature of radial velocities differs condiderably in the radial direction. Wall constraints imposed on the flow near the tip would force the flow to have an inward direction [9]. In addition, secondary flow and tip leakage flow would greatly influence the nature of flow in this region. Consequently, we will have mostly radial inward flow at these locations. So the radial velocities would be maximum near the mid-radius decreasing in magnitude towards the tip of the machine (Figs. 11–13). Far downstream, the radial velocity is inward at $R = 0.6581$ and outward at $R = 0.7973$ and 0.7297.

Very near the trailing edge, for $R = 0.7297$, the maximum radial velocity (W_r/W_{z_0}) is 0.7 dropping to about 0.2 in half-a-chord downstream. The decay of the radial velocity seems to follow the same trend as that of the axial and the tangential velocities. The magnitude of radial velocity seems to follow the same trend as that of the axial and the tangential velocities. The magnitude of radial velocity for the

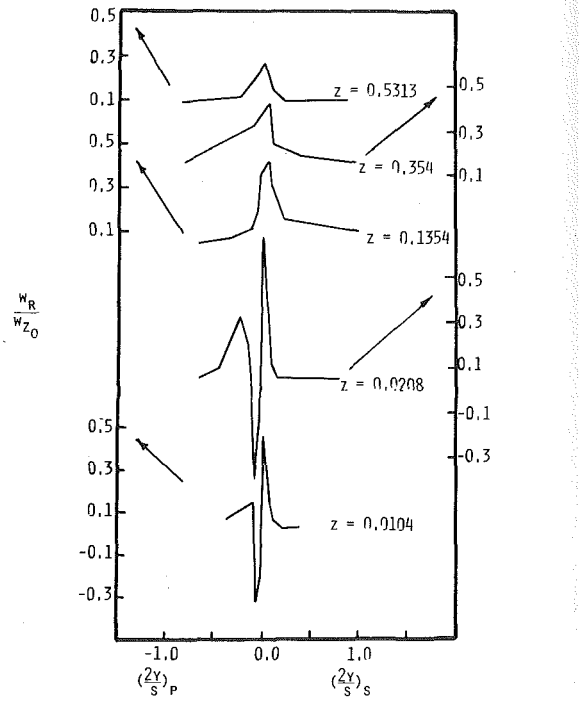


Fig. 13 Radial velocity profiles, $R = 0.7297$, $\phi = 0.56$

other two radii $R = 0.7973$ and 0.6581 is considerably less, being consistent with the reasoning mentioned earlier.

The large radial component of velocities indicates the highly three-dimensional nature of the rotor-wake. The radially inward or outward flow in the wake will result in an increased dissipation of energy. The spread of the radial velocity profile downstream of the blade is not as marked as in the case of axial or the tangential component of velocity.

The effect of blade loading on the radial velocities can be discerned by comparing the results of this paper with those of [2]. The radial velocities are dependent on the pressure gradient, centrifugal forces and Coriolis forces arising due to rotation and the strength of the trailing vortex. All these effects increase with increased blade loading. Referring to Fig. 13, it can be noted that for this blading at $R = 0.7297$

Downloaded 01 Jun 2010 to 171.66.16.58. Redistribution subject to ASME license or copyright; see http://www.asme.org/terms/Terms_Use.cfm

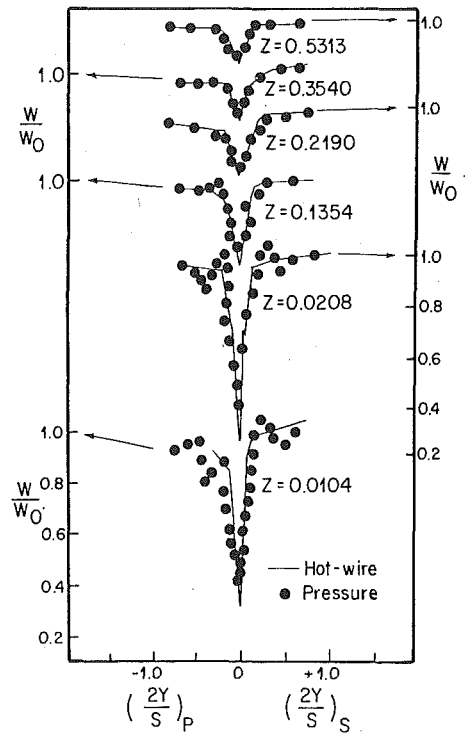


Fig. 14(*a*) Total relative velocity profiles, $R = 0.7297$, $\phi = 0.56$

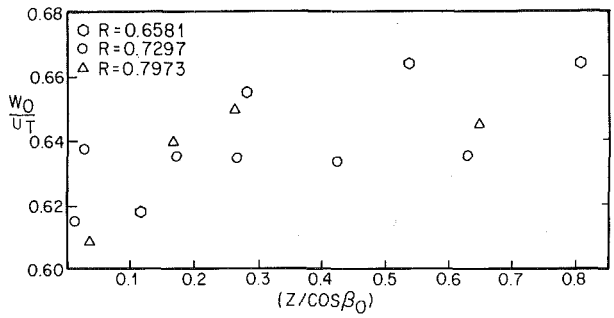


Fig. 14(*b*) Free-stream relative velocity variation with streamwise distance

and at $Z = 0.5313$ the magnitude of the maximum radial velocity is nearly 0.2, while for a lightly loaded rotor used in [1] and [2] the radial velocities have dropped to a value of around 0.1 even at 0.2 chords downstream. So the effect of loading is to induce higher radial velocities, and these decay at a slow rate.

Total Mean Relative Velocity. The total mean relative velocity which is the resultant of the axial, tangential and radial velocities is shown plotted in Fig. 14(*a*) for $R = 0.7297$. A comparison of the velocities derived from the hot-wire and static-stagnation pressure probe is also shown. The velocities are normalized by the corresponding free-stream velocity and the abscissa represents the tangential distance as a fraction of blade spacing with Y equal to zero at the wake centerline. A maximum wake defect of 0.8 at $Z = 0.0104$ reduces to about 0.2 at $Z = 0.5313$. The data seem to confirm that the velocities are very low at the blade trailing edge and the defect decays very rapidly in this region ($0 < Z < 0.13$). In the case of the rotor-wakes, this is probably the closest station to the trailing-edge ($Z = 6.25 \times 10^{-2}$ in. or 1.588×10^{-1} cm) where measurements are available. Furthermore, the defects measured are larger than any reported so far. The asymmetry in the velocity profiles, which arises due to differential growth of boundary-layers and the effect of loading in sustaining the asymmetry to beyond half-a-chord downstream can also be observed in Fig. 14(*a*).

Velocity derived from the hot-wire and the pressure measurements

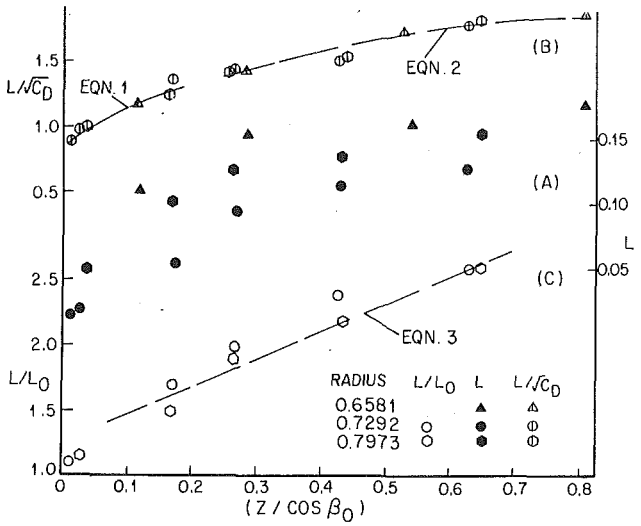


Fig. 15 Variation of semi-wake-width with downstream distance

are shown plotted in Fig. 14(*a*). The agreement between the two measurements beyond $Z = 0.1354$ is very good indicating pressure measurements are as accurate as hot-wire measurements. In the trailing-edge and near-wake measurements there is slight discrepancy between the two measurements. The pressure measurements do show the inviscid effects which are not reflected in the hot-wire measurements. A point of concern is that the velocity measured by hot-wire is greater than that measured by the pressure probe and the difference between the two is as much as 10 percent at the wake center. Although the spatial resolution of the hot-wire is better than that of the pressure probe it is not possible to assume that the hot-wire has better accuracy than the pressure probe. Two most probable errors at the trailing edge location are (1) wall vicinity effects in the case of pressure probe and (2) distortion of cooling characteristics of the wire because of vicinity of the wall. No attempt is made in this paper to evaluate the relative merits of the two systems in the near-wake and trailing-edge region as the source of error is not properly understood.

The variation of the free stream total velocity (W_0) with downstream distance is shown in Fig. 14(*b*). The free stream velocity increases by 5 percent in the trailing edge region $0 < Z < 0.2$. Beyond this region, the variation is negligibly small at all radii.

Wake-Width Variation. The variation of the semi-wake width normalized by blade spacing is shown in Fig. 15(*a*) for the radii $R = 0.7973$, 0.7297 and 0.6581. The wake-width increases rapidly in the trailing-edge region and then the growth becomes very gradual in the near- and far-wake region. As the interchange of energy, mass and momentum is continuous on the two sides of the wake as the wake travels downstream, the growth should also be continuous, and this behavior is observed in Fig. 15(*a*), which is consistent with those observed in the isolated airfoil and cascade wake studies. The wake-width varies considerably in the radial direction. It increases towards the hub and annulus-wall which is due to the complex interaction of the wake, hub- or annulus-wall boundary-layer, secondary flow (tip vortex in the annulus-wall case).

Wake-width, besides other factors, depends on the aerodynamic properties of the blade, and this should vary with radius in conformity with the variation of the drag coefficient. Normalizing the wake-width, as a function of C_D, should collapse all the points on to a single curve. Fig. 15(*b*) shows this correlation, where $C_D{}^{-0.5}$ has been used as the normalizing parameter. A functional dependency for the growth of wake-width ($L/\sqrt{C_D}$) was tried as a function of the downstream distance. An equation of the type, $L/\sqrt{C_D} = K(Z/\cos\beta_0 - Z_0/\cos\beta_0)^n$ can be used to represent the present data quite accurately. The constant (K) and the exponent (n) take on different values in the near- and far-wake regions and are found to be (Fig. 15(*b*)

$$\text{Near Wake: } L/\sqrt{C_D} = 1.34\,(Z/\cos\beta_0 + 0.83)^{2.39}$$
$$0.01 < Z/(\cos\beta_0) < 0.2 \qquad (1)$$

Downloaded 01 Jun 2010 to 171.66.16.58. Redistribution subject to ASME license or copyright; see http://www.asme.org/terms/Terms_Use.cfm

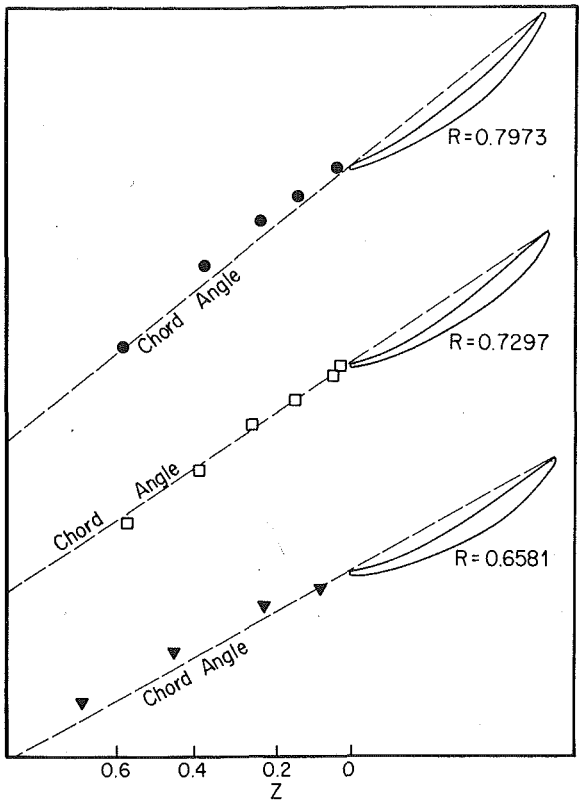


Fig. 16(*a*) Curvature of rotor wake centerline in relative frame of reference

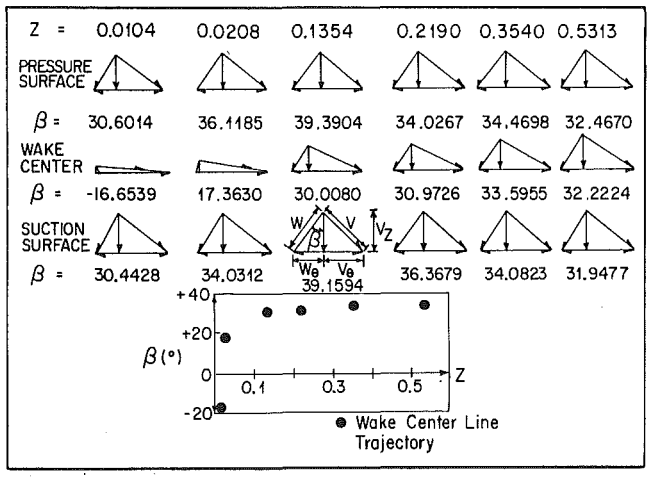


Fig. 16(*b*) Velocity triangles and flow angle variation, $R = 0.7297$, $\phi = 0.56$

$$\text{Far Wake: } L/\sqrt{C_D} = 0.833(Z/\cos\beta_0) + 1.302$$
$$0.25 < Z/(\cos\beta_0) < 0.8 \qquad (2)$$

Fig. 15(*c*) shows the plot of wake-width normalized by L_0, the corresponding initial value at the first station. The wake spread can now be represented by the equation

$$L/L_0 = A_4(Z/\cos\beta_0) + A_5 \quad 0.05 < Z/\cos\beta_0 < 0.7 \qquad (3)$$

where the constants are found to be (Fig. 15(*c*)) $A_4 = 3.293$, $A_5 = 1.0$. L_0 is the value of L at the trailing edge. These constants may vary depending on the type of blade row.

Wake Curvature and Flow Angle Variation. Wake curvature, which is the locus of the wake center line is shown plotted in Fig. 16(*a*), for the radii $R = 0.7273$, 0.7297 and 0.6581. The curvature of the rotor-wake is appreciable in the trailing-edge region and is negligibly small in the near- and far-wake regions. As seen from Fig. 16(*a*) the wake curvature is towards the suction-surface of the blade in the near- and far-wake regions and the path is coincident with the blade outlet angle in the trailing-edge region. The radius of curvature of the wake is found to be high at higher radius decreasing towards the hub where the trend of the curvature changes.

Curvature can also be thought of as the variation in flow angle at

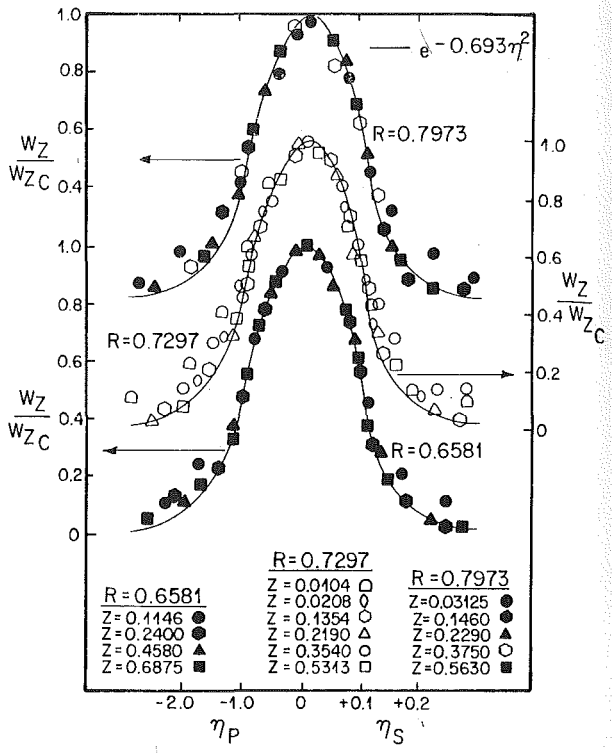


Fig. 17 Axial velocity profile similarity

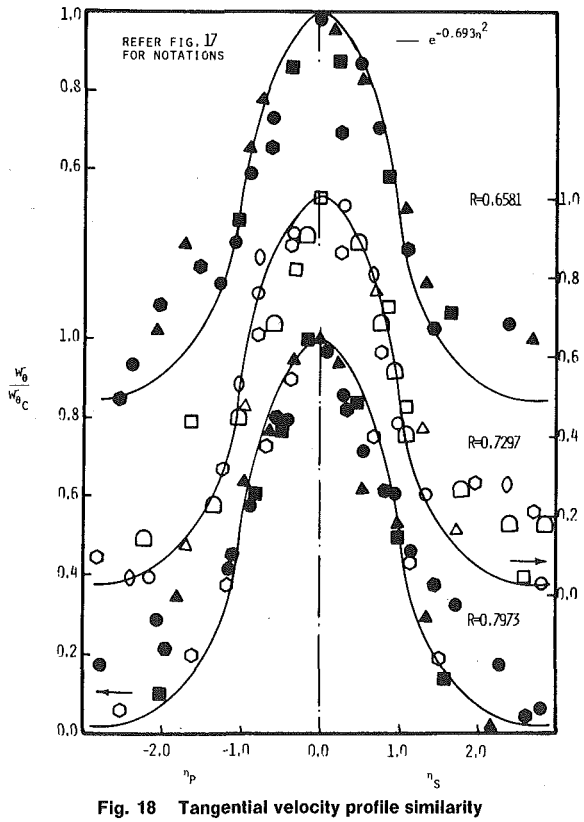


Fig. 18 Tangential velocity profile similarity

Downloaded 01 Jun 2010 to 171.66.16.58. Redistribution subject to ASME license or copyright; see http://www.asme.org/terms/Terms_Use.cfm

the wake center with downstream distance. The flow angle can be calculated from the velocity triangles at each of the downstream locations. This plot is shown in Fig. 16(b). In the trailing-edge region the flow is still developing where the trailing vortex system may dominate the wake. As the axial component of velocity is very small and the radial velocities are large, the flow deflection is quite considerable resulting in small negative tangenetial relative velocities. This implies that the relative and the absolute velocities will be in the same direction. As the wake travels downstream the tangential relative velocity reverses its sign and becomes positive. The reversal of tangential velocity in its direction introduces a large angle variation which is reflected in the wake curvature in the trailing-edge region. Beyond $Z = 0.1354$ the flow angle variation is very small and consequently the curvature of the wake is also small.

The effect of loading is to increase the curvature of the wake and is noted by comparing Fig. 16 with Fig. 10 of [2].

Similarity of Velocity Profiles. Experimental evidence has shown that similarity exists for the mean velocity profiles. Raj and Lakshminarayana [1] have shown that these velocity components follow the Gaussian profile given by $e^{-0.693\eta^2}$. Raj and Lakshminarayana [1] and Reynolds, et al. [2] examined this for a lightly loaded fan blade. In this section the same is tried for a heavily loaded compressor blade.

Axial and Tangential Velocity Profiles. Maximum velocity defect was used as the nondimensionalizing velocity scale for the local velocity defect. The wake width at half the wake depth was taken as the characteristic length scale. Corresponding values L_s and L_p were taken for the pressure- and suction-surfaces of the wake. Using this technique, similarity was examined for the axial and tangential velocity profiles and are shown in Figs. 17 and 18. It is seen that the similarity does exist even in the case of a heavily loaded blade following the Gaussian distribution given by $e^{-0.693\eta^2}$. As seen from Figs. 17 and 18, the discrepancy from the Gaussian curve for the wake in the trailing-edge region can be attributed to the fact that we are not only dealing with the wake but are also dealing with the trailing vortex system out of the trailing-edge of the blade. There is a substantial scatter from the Gaussian curve, in the outer regions of the flow. The discrepancy is marked particularly for a heavily loaded blade (compare Figs. 17 and 18 with Figs. 11 and 12 of [2]). Townsend's [11] approach of inclusion of an intermittancy factor into the Gaussian law in the form

$$\frac{U_d}{U_{d_c}} = \exp\left\{-C_1\eta^2\left[1+\frac{1}{3}\left(\frac{\eta}{\eta_1}\right)\right]^4\right\} \tag{4}$$

might yield better results. Here U_d is the velocity defect, C_1 and η_2 are constants.

Radial Velocity Profiles. Radial velocities show two different trends, one trend in the trailing-edge region and the other in the near- and far-wake regions. For the far-wake region the similarity is quite good and is plotted in Fig. 19(a). The maximum radial outward velocity is taken as the normalizing velocity. The similarity for the wakes for $R = 0.6581$, 0.7297, and 0.7973 is quite good except for the scatter in the outer regions of flow. This indicates that even the radial velocities follow the trend of the Gaussian function.

The radial velocities in the trailing-edge region exhibits two different types of velocity distribution with radially inward flow on the pressure side and radially outward flow on the suction side of the wake. Here again maximum radial velocity defect was used as the normalizing velocity (on the suction-surface the absolute magnitude of the velocities were considered). The plots are shown in Fig. 19(b). The agreement with the Gaussian distribution is fairly good. It has to be realized that at these Z-locations we are not only dealing with the boundary-layer flow but also trailing vortex system. Similarity for such a complex flow phenomena has not been proven before and this is a first step in that direction. It is quite probable that the Townsend's approach might yield a better correlation with the experimental data.

Decay of Velocity Defects. Decay of axial and tangential velocities are shown plotted in Fig. 20(a).[1] Since the free stream velocities on the pressure and suction side are different it is argued that the two velocity defects decay differentially. This is clearly seen at the three radii $R = 0.7973$, 0.7297, and 0.6581. The variations between the two surfaces are small.

The general trend observed for the decay of the defect in axial and tangential velocity is that they decay very rapidly in the trailing-edge

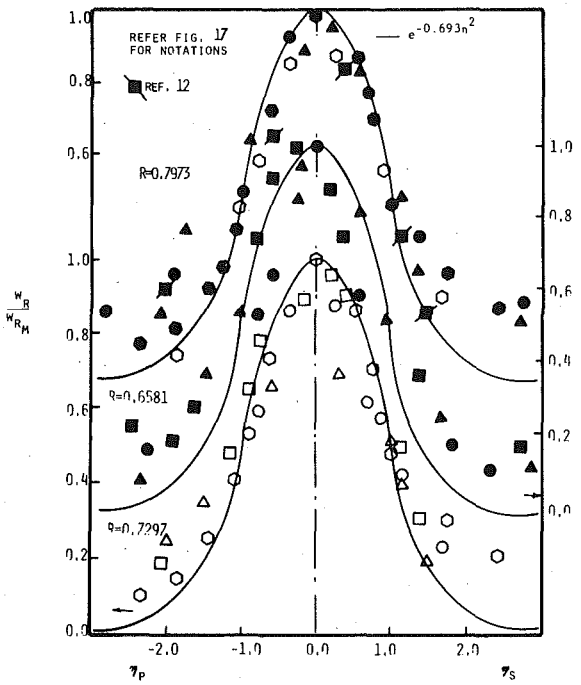


Fig. 19(a) Radial velocity profile similarity (far-wake region)

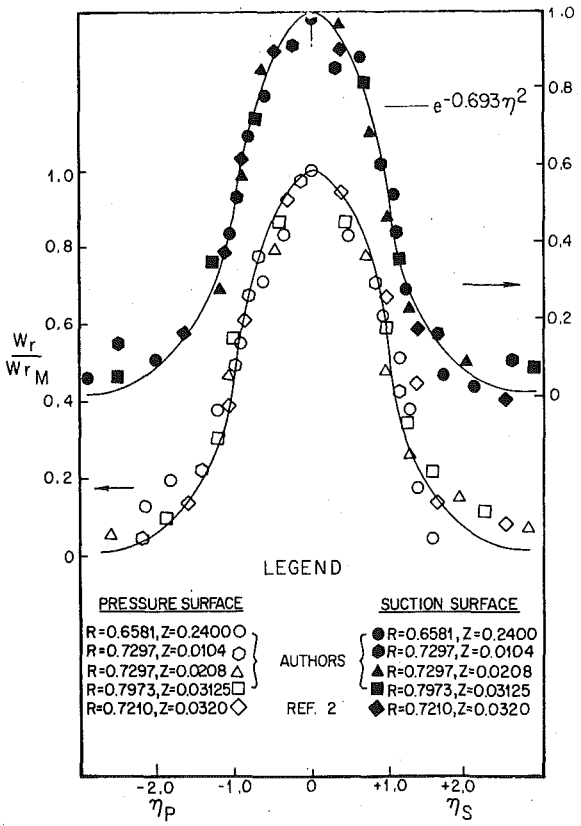


Fig. 19(b) Radial velocity profile similarity (near-wake region)

[1] In all the plots showing the decay characteristics, the decay quantity is plotted against $Z/\cos\beta_0$, since this quantity represents the streamwise distance from the trailing edge.

Downloaded 01 Jun 2010 to 171.66.16.58. Redistribution subject to ASME license or copyright; see http://www.asme.org/terms/Terms_Use.cfm

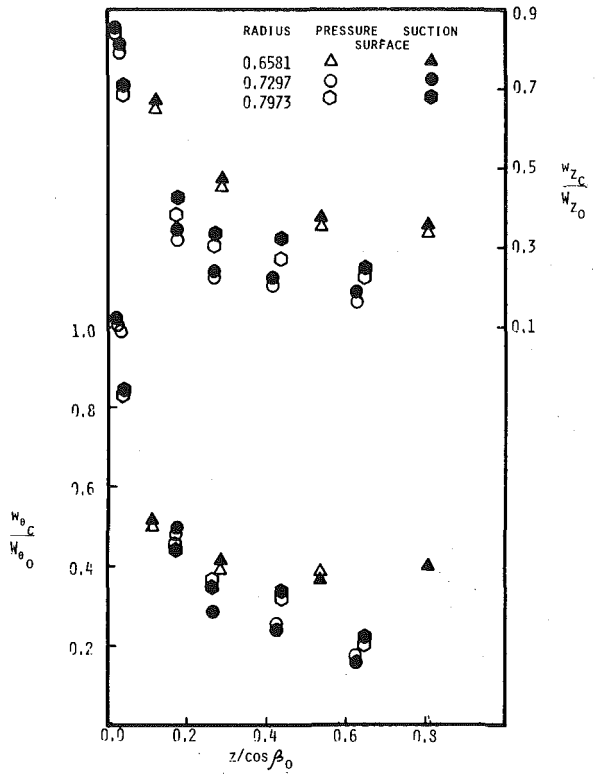


Fig. 20(*a*) Decay of axial and tangential velocity defects with streamwise distance

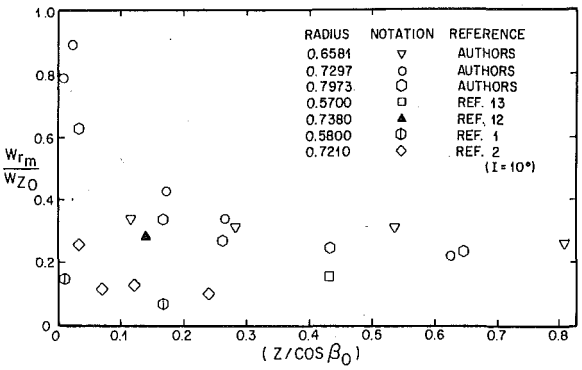


Fig. 20(*b*) Decay of maximum radial velocity with streamwise distance

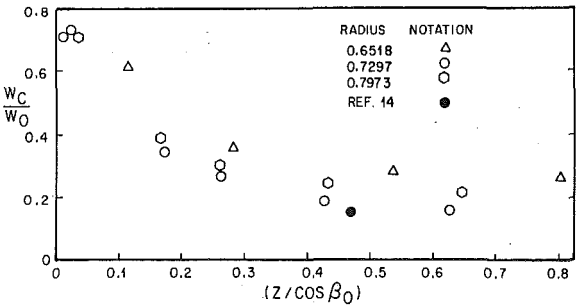


Fig. 20(*c*) Decay of total relative velocity with streamwise distance

region and the decay tends to be less rapid in the near- and far-wake regions. The very rapid decay in the trailing-edge region is attributed to very large turbulence intensities, the pressure gradients, and three dimensional effects. The tangential velocity defect decays much more rapidly than the axial velocity defect. The contributing factor to the very rapid decay of the tangential velocities is the radical component of velocity as well as the radial distribution of free stream tangential and axial velocities [10].

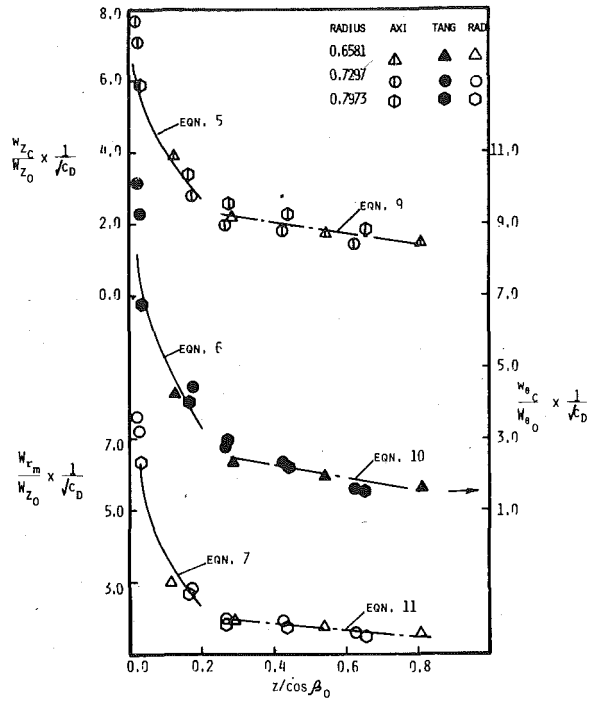


Fig. 21 Correlation of three components of velocity defects

The decay of the maximum radial velocity at the three radii are shown in Fig. 20(*b*). It is clear that the decay is extremely rapid in the trailing-edge region and slows down considerably in the near- and far-wake regions. Even at 0.6 chords downstream it is seen that there is a significant radial velocity component. This not only indicates that the decay of radial velocities is less rapid compared to the defect in axial and tangential velocities but also reflects the radial migration of flow in the rotor-wakes. The very rapid decay in the trailing-edge region can be attributed to not only the high turbulence intensities but also the decay of the trailing-vortex system which dominate the flow in this region. Also plotted in Fig. 20(*b*) are the data on the maximum radial velocity from other sources [1, 2, 12, 13]. Comparison of the data from various sources indicates the effect of blade loading on the radial velocity. Higher blade loading induces larger radial velocities. The data in [1, 2] and [13] correspond to low blade loading, the authors at moderate loading and those of [12] are at higher Mach numbers.

The decay of the total relative velocity, which is the resultant of axial, tangential and the radial velocity components is shown plotted in Fig. 20(*c*). Some very interesting features are noted in the total velocity decay which was not reflected in the axial and tangential velocity decay. For the radius $R = 0.7297$ and at $Z = 0.0104$ the non-dimensionalized defect in total velocity is 0.69 which increases to 0.735 at $Z = 0.0208$ and from then on it monotonically decays to a value of 0.13 at half a chord downstream. The data of [14] for a transonic rotor also follow the trend of the authors' data (Fig. 20(*c*)). The decay of the total velocity conforms more closely to the decay of the axial velocity. It is seen that at half-a-chord downstream, the defect in total velocity (w/W_0) is of the same order as that of axial velocity defect (w_{zc}/W_{z0}) while the tangential velocity defect ($w_{\theta}c/W_{\theta_0}$) is much less than either the axial or the total velocity.

The initial wake characteristics differ considerably with radius and hence the decay rates are also different. The main controlling factor in the development of a wake is the section drag coefficient of the blade element. So normalizing the decay by the drag coefficient should collapse all the data points onto a single decay curve. This plot is shown in Fig. 21 where $\sqrt{C_D}$ has been used as the normalizing parameter. It is evident that the decay data correlate well with $\sqrt{C_D}$.

The functional dependency of the defects in axial and tangential velocities, and the radial velocity with streamwise distance ($Z/\cos\beta_0$) is tried as shown in Fig. 21. The functional relationship for the decay

Downloaded 01 Jun 2010 to 171.66.16.58. Redistribution subject to ASME license or copyright; see http://www.asme.org/terms/Terms_Use.cfm

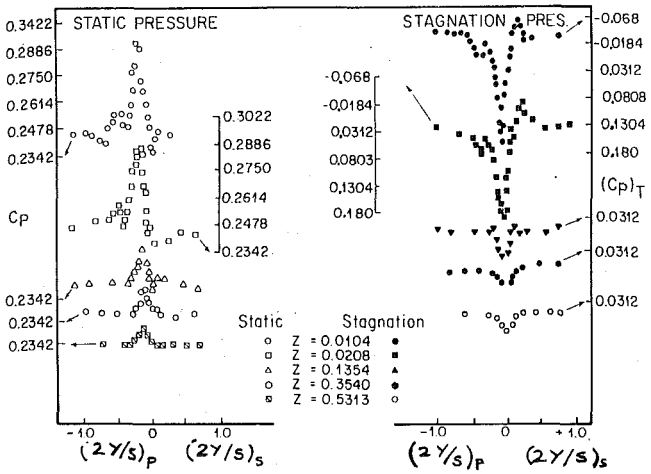


Fig. 22 Static and stagnation pressure variation across the wake

of the axial and tangential velocity defect as well as radial velocity can be represented in the trailing-edge and near-wake region in the form

$$\frac{w_c}{W_0\sqrt{C_D}} = K_1\left(\frac{Z - Z_0}{\cos\beta_0}\right)^n$$

where the values of K_1, Z_0 and n take different values for the three component of velocities. These relationships for the data presented in Fig. 21 are given by (in the near-wake region)

$$\frac{w_{z_c}}{W_{z_0}}\frac{1}{\sqrt{C_D}} = 0.592(Z/\cos\beta_0 + 0.35)^{-2.39}$$

$$\text{For } 0.03 < (Z/\cos\beta_0) < 0.2 \tag{5}$$

$$\frac{w_{\theta_c}}{W_{\theta_0}}\frac{1}{\sqrt{C_D}} = 0.778(Z/\cos\beta_0 + 0.35)^{-2.39}$$

$$\text{For } 0.03 < (Z/\cos\beta_0) < 0.2 \tag{6}$$

$$\frac{(W_r)_{\max}}{W_{z_0}}\frac{1}{\sqrt{C_D}} = 0.566(Z/\cos\beta_0 + 0.35)^{-2.39}$$

$$\text{For } 0.03 < (Z/\cos\beta_0) < 0.2 \tag{7}$$

In the region $0.2 < (Z/\cos\beta_0) < 0.8$ the decay of the radial velocity and defects in axial and tangential velocities were found to vary linearly with Z and can be represented by a general equation of the type

$$\frac{w_c}{W_0} = K_2(Z/\cos\beta_0)^{-1} + K_3 \tag{8}$$

where again the constants K_2 and K_3 take different values for the three different velocity components and are as follows:

$$\frac{w_{z_c}}{W_{z_0}}\frac{1}{\sqrt{C_D}} = 0.39(Z/\cos\beta_0)^{-1} + 0.984$$

$$\text{For } 0.2 < (Z/\cos\beta_0) < 0.8 \tag{9}$$

$$\frac{w_{\theta_c}}{W_{\theta_0}}\frac{1}{\sqrt{C_D}} = 0.221(Z/\cos\beta_0)^{-1} + 1.492$$

$$\text{For } 0.2 < (Z/\cos\beta_0) < 0.8 \tag{10}$$

$$\frac{W_{r_{\max}}}{W_{z_0}}\frac{1}{\sqrt{C_D}} = 0.221(Z/\cos\beta_0)^{-1} + 1.20$$

$$\text{For } 0.2 < (Z/\cos\beta_0) < 0.8 \tag{11}$$

The decay rates as represented by the above equations are shown plotted in Fig. 21. It is seen that the data correlate quite well with these expressions.

Static Pressure Variations across the Wake. In order to get a complete understanding of the flow in the wake, time averaged static-stagnation surveys were done in a relative frame of reference. A spherical head static-stagnation pressure probe built at Penn State

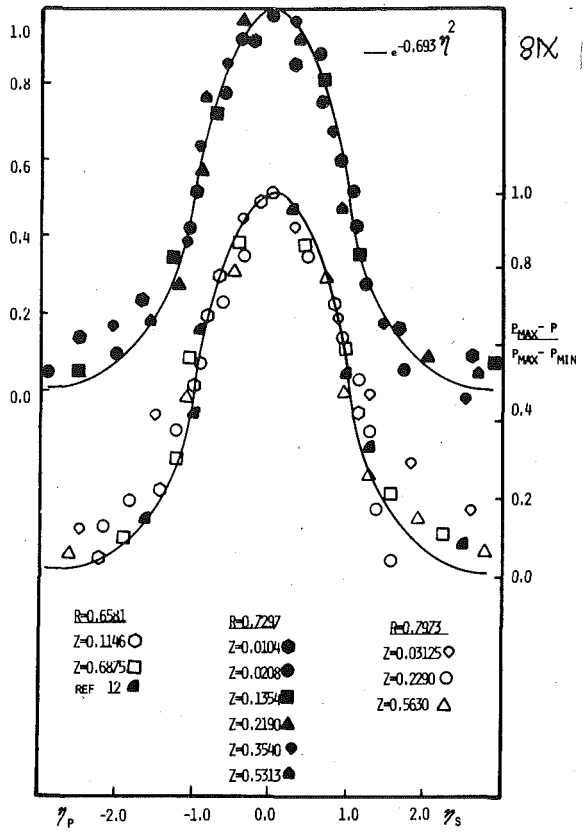


Fig. 23 Static-pressure profile similarity for the wake

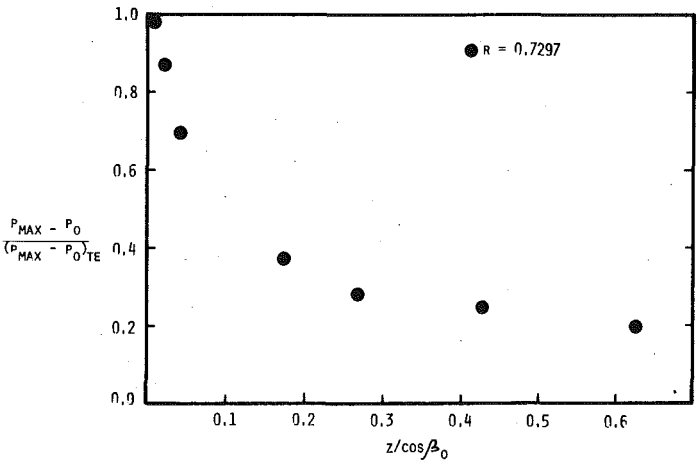


Fig. 24 Decay of the difference in static pressure with downstream distance

and described earlier was employed for all the pressure surveys reported in this section. Variation of static pressure rise coefficient (C_p) across the wake of the rotor is shown plotted in Fig. 22. Some of the traditional models of an inviscid core flow plus a viscous wake appear in these plots. Static pressure not only varies across the wake, but also in the wake edge near trailing edge due to the inviscid effects, which is not reflected in the stagnation pressure plots. In the trailing-edge region the static pressure variation across the wake is as large as 40 percent which drops off to about 5 percent in half-a-chord downstream. The measurement seems to confirm the trend observed by Thompkins and Kerrebrock [12] who have reported a 25 percent variation in static pressure across the wake at 10 percent of the axial chord downstream of a transonic rotor. In the present case the first measurement station is very close to the trailing-edge and very large static pressure gradients were measured. However, the data must be reviewed with some caution. As reported earlier, the pressure probes

Downloaded 01 Jun 2010 to 171.66.16.58. Redistribution subject to ASME license or copyright; see http://www.asme.org/terms/Terms_Use.cfm

are subjected to wall vicinity effects and also the large angle variations reported earlier would adversely affect the values in the trailing-edge region.

As seen from Fig. 22, the static pressure increases towards the wake center and that the peak pressure lie outside the center of the wake towards the pressure surface. It is also observed that the minimum stagnation pressure and the maximum static pressure are off-set by a small tangential distance. At this point it is difficult to comment whether the error arises from the spatial error of the static-stagnation ports or whether it is because of the nature of the flow itself. Further analysis in understanding this flow situation is being pursued.

It is logical to assume that similarity exists in pressure profiles as with velocity profiles. The plot of such a similarity is shown in Fig. 23. The data seem to follow the Gaussian distribution fairly closely and only in the outer regions of the flow do we see substantial discrepancy from the curve $e^{-0.693\eta^2}$. This might be due to interference effects or the effect of the inviscid region located just outside the "wake" region. The data due to Thompkins and Kerrebrock [12] also seem to show the existence of similarity (Fig. 23) in static pressure distribution.

Experimental evidence indicates that the static-pressure increases at the wake center and as the wake travels downstream this difference decreases. For the data presented for $R = 0.7297$, the ratio of the static pressure at the wake center to the corresponding static pressure in the free-stream decays rather rapidly in the trailing-edge region and the decay is markedly slow in the near and far-wake regions. This very rapid decay at the trailing-edge regions is attributed to the very rapid decay in velocity defect and turbulence intensity.

The existence of pressure gradients across the wake can be understood by examining the equation of motion in a rotating coordinate system in a direction normal (n) to the streamlines (s). The equation can be approximately written as

$$-\frac{1}{\rho}\frac{\partial p}{\partial n} \approx 2\Omega W_r \cos\beta - \frac{W_s{}^2}{R_c} - \frac{\partial}{\partial n}\overline{(w'^2{}_n)} \tag{12}$$

where n is the direction normal to streamline, W_s is the streamwise velocity, R_c is the radius of curvature of the streamline and $\overline{w'^2}_n$ is the turbulent fluctuation in n direction. It is evident from the above equation that, in addition to Coriolis and Centrifugal forces, the gradient of turbulent intensity in the n direction has an appreciable influence on the pressure gradient $\partial p/\partial n$. In the wake center, near the trailing-edge region, the turbulence intensity terms dominate and hence the static pressure gradients can exist even in the absence of curvature (R_c). Qualitative analysis of this effect is given by Reynolds [15].

The decay of the maximum static pressure difference across the wake ($p_{max} - p_0$), shown in Fig. 24, is rapid in the trailing edge region and reaches nearly the free stream values within half-a-chord downstream.

Fourier Decomposition of Rotor-Wake. In the aerodynamic and aeroacoustic analysis of rotors it is convenient to represent the wake velocities in terms of the Fourier series. This representation is possible because the velocity distributions are periodic and continuous. The velocity defect at a position (r, θ, z) can be represented as

$$u_{d_N}(r, \theta, z) = A_0 + \sum_{n=1}^{\infty}\left[A_n(r, z)\cos\frac{n\theta}{\theta_L} + B_n(r, z)\sin\frac{n\theta}{\theta_L}\right] \tag{13}$$

This type of representation was tried for the data of [1] and [2] and for the present data. The method is based on the recursive technique of Ralston [16]. In the analysis, the velocity defect is normalized by the wake centerline defect and all the angles by the angle at half the wake-width.

From the Fourier series we know that,

$$A_n = \frac{\epsilon_n}{2\pi}\int_0^{2\pi}\frac{u_d}{U_{d_N}}\cos\frac{n\theta}{\theta_L}\,d(\theta/\theta_L) \tag{14}$$

where: ϵ_n = Neumann's factor (=1 for $n = 0$; = 2 for $n > 0$)

2π = interval of integration (in the analysis only the wake portion is considered) for θ/θ_L. Value of θ/θ_L at the wake center is π and at edges 0 and 2π.

A_0 represents the average value across the wake and since the defect is normalized by the corresponding wake centerline defect, A_0 should approximately remain constant with downstream distance. This is shown plotted in Fig. 25 for the data from [1] and for the present case for the radii $R = 0.7973$, 0.7297 and 0.6581. Data of [1] is at zero loading. The effect of loading is clearly seen in these plots. Higher the loading, higher is the defect and correspondingly larger values of A_0.

The harmonic content in the wake is represented by the Fourier cosine coefficients and the asymmetry of the wake by Fourier sine coefficients. The first coefficient (A_1) is shown plotted in Fig. 25. As normalized velocity defects were used in the analysis the values of B_n were found to be very small indicating the axisymmetric nature of the

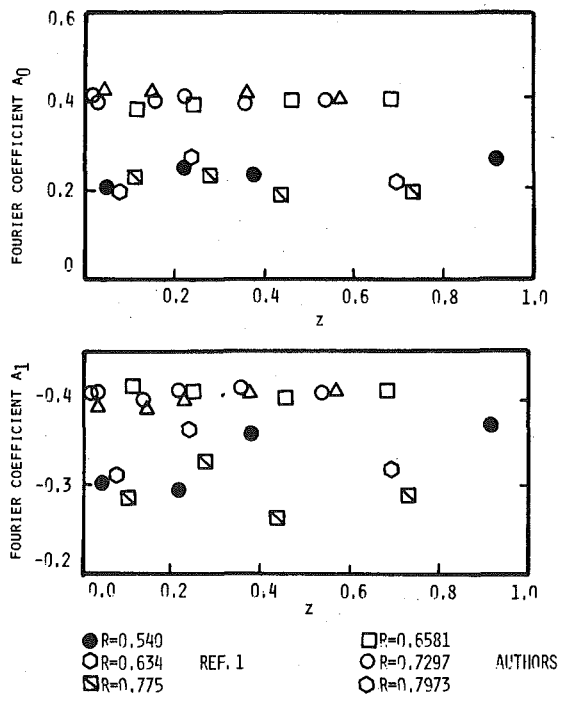


Fig. 25 Variation of Fourier coefficient A_0 and A_1 with downstream distance

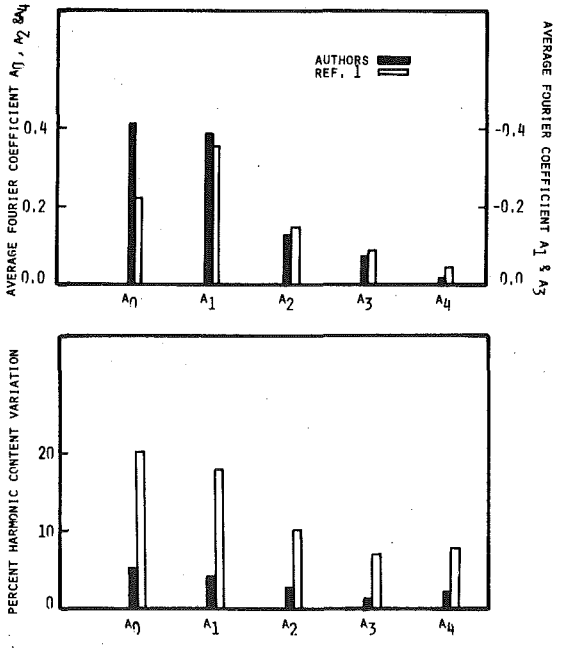


Fig. 26 Average Fourier coefficients and scatter of harmonic content in rotor-wake

Downloaded 01 Jun 2010 to 171.66.16.58. Redistribution subject to ASME license or copyright; see http://www.asme.org/terms/Terms_Use.cfm

normalized wake. The average values of the harmonics are shown in Fig. 26 for the authors' data. Fig. 26 shows the plot of the scatter in the first four coefficients for the data under consideration. The Fourier curve correlated quite well with the data when the first four coefficients were considered in the analysis, with the correlation coefficient for the entire wake being about 0.998.

Conclusions

The measurements reported in this paper represent the first set of data in the trailing-edge region of a moderately-loaded compressor rotor blade. The results reveal the highly three-dimensional nature of the rotor-wake, with radial velocities dominating the flow in the trailing-edge region. It is also seen that the effect of loading has a substantial influence on the wake width and the decay of the velocity defect. Some of the major conclusions of the present investigation are:

1 In the trailing-edge region the radial velocities are found to be very large and are influenced by the trailing-vortex system. Large velocity defects are measured in the trailing edge region.

2 Higher blade loading results in not only higher velocity defect but also slows down the decay rate. Tangential velocities are found to decay much more rapidly in the trailing-edge region than the other velocity components. In the far-wake region the decay of all the three components of velocities are of the same order. Decay laws are presented for all the velocity components.

3 The wake curvature is considerable in the trailing-edge region and beyond 0.2 chords downstream the relative flow angle variation as well as curvature of the wakes become very small.

4 The variation of the wake width with downstream distance is found to be very rapid in the trailing-edge region. In the near- and far-wake the growth is slow.

5 Mean velocity profiles in the trailing-edge and near-wake regions are unsymmetrical and tend to become symmetrical in the far-wake region. The effect of loading has been found to sustain the asymmetry to a much longer downstream distance as compared to a lightly loaded case investigated earlier. All the components of velocity become symmetrical and similar when the defect is normalized by its value at the wake center and the lengths by corresponding length scale. All the similarity profiles follow the Gaussian function given by $e^{-0.693\eta^2}$. The wake profiles are also represented by Fourier series. The magnitude of the coefficients decrease rapidly, with the first three coefficients being the dominant ones.

6 Static-pressure in the wake is found to increase towards the wake center. The decay of static-pressure difference across the wake is found to be rapid in the trailing-edge region and it slows down in the far-wake region. The static-pressure profiles also exhibit the similarity, except in the trailing-edge region, and the similarity follows the Gaussian distribution, $e^{-0.693\eta^2}$. The discrepancy in the trailing-edge region from the Gaussian might be due to the complex interactions of the boundary-layer flow and the trailing-vortex systems.

7 The wake decay and wake-width differ in the radial direction. The main controlling factor seems to be the section-drag coefficient of the blades. The width as well as the decay correlate well with $\sqrt{c_d}$.

Acknowledgments

This work was supported by the National Aeronatuics and Space Adminstration, through the grant NSG 3012, with M. F. Heidmann as the technical monitor. The authors wish to acknowledge G. Kane and J. Rishell for their aid in experimental set-up and S. Kovacic for his help in data processing.

References

1 Raj, R. and Lakshminarayana, B., "Three-Dimensional Characteristics of Turbulent Wakes Behind Rotors of Axial-Flow Turbomachinery," ASME JOURNAL OF ENGINEERING FOR POWER, Vol. 98, April 1976, pp. 218–228.

2 Reynolds, B., Lakshminarayana, B., and Ravindranath, A., "Characteristics of the Near-Wake of a Compressor or Fan Rotor Blade," *AIAA Journal*, Vol. 17, 1979, pp. 959–967.

3 Anand, A. K. and Lakshminarayana, B., "Three Dimensional Boundary Layer in a Rotating Helical Channel," ASME *Journal of Fluids Engineering*, Vol. 97, No. 2, June 1975, pp. 197–210.

4 Smith, L. H., Jr., "Three-Dimensional Flow in an Axial-Flow Turbomachinery," (contract AF 33(616)-152) ADC Technical Report 55-348. Vol. II, Johns Hopkins University, March 1956.

5 Lakshminarayana, B. and Sitaram, N., "Axial-Flow Compressor Facility With Unique Instrumentation for Relative Flow Measurement," (in preparation) 1979.

6 Hah, C. and Lakshminarayana, B., "Effect of Rotation on a Rotating Hot-Wire," *Journal of Physics, E.: Scientific Instruments*, Vol. 11, Oct. 1978, pp. 999–1001.

7 Ravindranath, A., "Wake Characteristics of a Moderately Loaded Compressor Rotor Blade," M.S. Thesis, Department of Aerospace Engineering, The Pennsylvania State University, 1979.

8 Gorton, C. A. and Lakshminarayana, B., "A Method of Measuring the Three-Dimensional Mean-Flow and Turbulence Quantities Inside a Rotating Turbomachinery Passage," ASME JOURNAL OF ENGINEERING FOR POWER, Vol. 98, No. 2, 1976, pp. 137–146.

9 Lakshminarayana, B., Jabbari, B., and Yamaoka, H., "Turbulent Boundary-Layer on a Rotating Helical Blade," *Journal of Fluid Mechanics*, Vol. 51, Part 3, 1972, pp. 545–569.

10 Lakshminarayana, B., "The Nature of Flow Distortions Caused by Rotor Blade Wakes," AGARD CP-177, Sept. 1975.

11 Townsend, A. A., "Measurements in the Turbulent Wake of a Cylinder," *Proceedings of the Royal Society, London, Series A*, Vol. 190, May 1947, pp. 551–561.

12 Thompkins, W. T. and Kerrebrock, J. L., "Exit Flow From a Transonic Compressor Rotor," AGARD CP-177, 1975.

13 Kool P., EdRuyck, J., and Hirsch, C. H., "The Three-Dimensional Flow and Blade Wake in an Axial Plane Downstream of an Axial Flow Compressor Rotor," ASME Paper No. 78-GT-66, 1978.

14 Dunker, R. J., Strinning, P. E., and Weyer, H. B., "Experimental Study of the Flow Field Within a Transonic Axial Compressor Rotor by Laser Velocity and Comparison with Through-Flow Calculations," ASME Paper No. 77-GT-28, 1977.

15 Reynolds, B., "Characteristics of Lightly Loaded Fan Rotor Blade Wakes," M.S. Thesis, Department of Aerospace Engineering, The Pennsylvania State University, 1978.

16 Ralson, H., *Numerical Methods for Digital* Computers, Chapter 24, Wiley, New York, 1960.

Downloaded 01 Jun 2010 to 171.66.16.58. Redistribution subject to ASME license or copyright; see http://www.asme.org/terms/Terms_Use.cfm

normalized wake. The average values of the harmonics are shown in Fig. 26 for the authors' data. Fig. 26 shows the plot of the scatter in the first four coefficients for the data under consideration. The Fourier curve correlated quite well with the data when the first four coefficients were considered in the analysis, with the correlation coefficient for the entire wake being about 0.998.

Conclusions

The measurements reported in this paper represent the first set of data in the trailing-edge region of a moderately-loaded compressor rotor blade. The results reveal the highly three-dimensional nature of the rotor-wake, with radial velocities dominating the flow in the trailing-edge region. It is also seen that the effect of loading has a substantial influence on the wake width and the decay of the velocity defect. Some of the major conclusions of the present investigation are:

1 In the trailing-edge region the radial velocities are found to be very large and are influenced by the trailing-vortex system. Large velocity defects are measured in the trailing edge region.

2 Higher blade loading results in not only higher velocity defect but also slows down the decay rate. Tangential velocities are found to decay much more rapidly in the trailing-edge region than the other velocity components. In the far-wake region the decay of all the three components of velocities are of the same order. Decay laws are presented for all the velocity components.

3 The wake curvature is considerable in the trailing-edge region and beyond 0.2 chords downstream the relative flow angle variation as well as curvature of the wakes become very small.

4 The variation of the wake width with downstream distance is found to be very rapid in the trailing-edge region. In the near- and far-wake the growth is slow.

5 Mean velocity profiles in the trailing-edge and near-wake regions are unsymmetrical and tend to become symmetrical in the far-wake region. The effect of loading has been found to sustain the asymmetry to a much longer downstream distance as compared to a lightly loaded case investigated earlier. All the components of velocity become symmetrical and similar when the defect is normalized by its value at the wake center and the lengths by corresponding length scale. All the similarity profiles follow the Gaussian function given by $e^{-0.693\eta^2}$. The wake profiles are also represented by Fourier series. The magnitude of the coefficients decrease rapidly, with the first three coefficients being the dominant ones.

6 Static-pressure in the wake is found to increase towards the wake center. The decay of static-pressure difference across the wake is found to be rapid in the trailing-edge region and it slows down in the far-wake region. The static-pressure profiles also exhibit the similarity, except in the trailing-edge region, and the similarity follows the Gaussian distribution, $e^{-0.693\eta^2}$. The discrepancy in the trailing-edge region from the Gaussian might be due to the complex interactions of the boundary-layer flow and the trailing-vortex systems.

7 The wake decay and wake-width differ in the radial direction. The main controlling factor seems to be the section-drag coefficient of the blades. The width as well as the decay correlate well with $\sqrt{c_d}$.

Acknowledgments

This work was supported by the National Aeronatuics and Space Adminstration, through the grant NSG 3012, with M. F. Heidmann as the technical monitor. The authors wish to acknowledge G. Kane and J. Rishell for their aid in experimental set-up and S. Kovacic for his help in data processing.

References

1 Raj, R. and Lakshminarayana, B., "Three-Dimensional Characteristics of Turbulent Wakes Behind Rotors of Axial-Flow Turbomachinery," ASME JOURNAL OF ENGINEERING FOR POWER, Vol. 98, April 1976, pp. 218–228.

2 Reynolds, B., Lakshminarayana, B., and Ravindranath, A., "Characteristics of the Near-Wake of a Compressor or Fan Rotor Blade," *AIAA Journal*, Vol. 17, 1979, pp. 959–967.

3 Anand, A. K. and Lakshminarayana, B., "Three Dimensional Boundary Layer in a Rotating Helical Channel," ASME *Journal of Fluids Engineering*, Vol. 97, No. 2, June 1975, pp. 197–210.

4 Smith, L. H., Jr., "Three-Dimensional Flow in an Axial-Flow Turbomachinery," (contract AF 33(616)-152) ADC Technical Report 55-348. Vol. II, Johns Hopkins University, March 1956.

5 Lakshminarayana, B. and Sitaram, N., "Axial-Flow Compressor Facility With Unique Instrumentation for Relative Flow Measurement," (in preparation) 1979.

6 Hah, C. and Lakshminarayana, B., "Effect of Rotation on a Rotating Hot-Wire," *Journal of Physics, E.: Scientific Instruments*, Vol. 11, Oct. 1978, pp. 999–1001.

7 Ravindranath, A., "Wake Characteristics of a Moderately Loaded Compressor Rotor Blade," M.S. Thesis, Department of Aerospace Engineering, The Pennsylvania State University, 1979.

8 Gorton, C. A. and Lakshminarayana, B., "A Method of Measuring the Three-Dimensional Mean-Flow and Turbulence Quantities Inside a Rotating Turbomachinery Passage," ASME JOURNAL OF ENGINEERING FOR POWER, Vol. 98, No. 2, 1976, pp. 137–146.

9 Lakshminarayana, B., Jabbari, B., and Yamaoka, H., "Turbulent Boundary-Layer on a Rotating Helical Blade," *Journal of Fluid Mechanics*, Vol. 51, Part 3, 1972, pp. 545–569.

10 Lakshminarayana, B., "The Nature of Flow Distortions Caused by Rotor Blade Wakes," AGARD CP-177, Sept. 1975.

11 Townsend, A. A., "Measurements in the Turbulent Wake of a Cylinder," *Proceedings of the Royal Society, London, Series A*, Vol. 190, May 1947, pp. 551–561.

12 Thompkins, W. T. and Kerrebrock, J. L., "Exit Flow From a Transonic Compressor Rotor," AGARD CP-177, 1975.

13 Kool P., EdRuyck, J., and Hirsch, C. H., "The Three-Dimensional Flow and Blade Wake in an Axial Plane Downstream of an Axial Flow Compressor Rotor," ASME Paper No. 78-GT-66, 1978.

14 Dunker, R. J., Strinning, P. E., and Weyer, H. B., "Experimental Study of the Flow Field Within a Transonic Axial Compressor Rotor by Laser Velocity and Comparison with Through-Flow Calculations," ASME Paper No. 77-GT-28, 1977.

15 Reynolds, B., "Characteristics of Lightly Loaded Fan Rotor Blade Wakes," M.S. Thesis, Department of Aerospace Engineering, The Pennsylvania State University, 1978.

16 Ralson, H., *Numerical Methods for Digital* Computers, Chapter 24, Wiley, New York, 1960.

DISCUSSION

T. H. Okiishi[2]

The results presented in this paper undoubtedly represent a great deal of effort. Hot-wire and flow field pressure measurements in the relative frame of reference in a turbomachine require much skill and patience.

As mentioned by the authors, detailed information about turbomachine blade wake development is important for competently calculating blade flow field interaction effects. Recent developments in measuring equipment and procedures, including the system described in this paper, are resulting in the accumulation of this kind of data. It is interesting to consider wake development, as these authors have done, in a research compressor with the blade rows spaced rather far apart. However, when turbomachine blade rows are placed more closely together several important phenomena can occur. Walker and Oliver [17] observed that the exit flow of a rotor can be affected by the potential flow field of the downstream stator row. Several investigators [17–23] have noted that chopped and transported blade wakes can appreciably affect the chopping blade wake flow. Interaction noise levels [24, 25] and stage efficiencies [26, 27, 28] have been observed to increase with decrease in blade row gap. In view of these considerations, gap width should be an important variable in studies like the one described in this paper.

It would be of interest to know if the authors analyzed the variation of the higher harmonic Fourier coefficients A_2, A_3 and A_4 with downstream distance. This kind of information would be useful for determining what portion of the harmonic content of the developing wake is significant at various distances downstream from the trailing

[2] Professor, Mechanical Engineering Department, Iowa State University, Ames, Iowa 50011

Copyright © 1980 by ASME

Downloaded 01 Jun 2010 to 171.66.16.58. Redistribution subject to ASME license or copyright; see http://www.asme.org/terms/Terms_Use.cfm

edge of the wake producing blade. Lowson [29] and Homicz, et al. [30] suggested that immediately behind a blade, all harmonics of the wake velocity profile are important but at larger distances downstream only the first harmonic is significant.

Additional References

17 Walker, G. J. and Oliver, A. R. "The Effect of Interaction Between Wakes from Blade Rows in an Axial-Flow Compressor on the Noise Generated by Blade Interaction," ASME JOURNAL OF ENGINEERING FOR POWER, 241–248 1972, pp. 241–248.

18 Smith, L. H., Jr. "Wake Dispersion in Turbomachines," ASME *Journal of Basic Engineering,* 1966, pp. 688–690.

19 Kerrebrock, J. L. and Mikolajozak, A. A. "Intra-Stator Transport otor Wakes and its Effect on Compressor Performance," ASME JOURNAL OF ENGINNERING FOR POWER, 1970, pp. 359–368.

20 Lockhart, R. C. and Walker, G. J. "The Influence of Viscous Interactions on the Flow Downstream of an Axial Compressor Stage," *Proceedings of the 2nd International Symposium on Air Breathing Engines,* 1974.

21 Schmidt, D. P. and Okiishi, T. H. "Multistage Axial-Flow Turbomachine Wake Production, Production, Transport, and Interaction," *AIAA Journal* 15, 1977, pp. 1138–1145.

22 Wagner, J. H., Okiishi, T. H., and Holbrook, G. J. "Periodically Unsteady Flow in an Embedded Stage of a Multistage Axial-Flow Turbomachine," ASME *Journal of Engineering for Power,* Vol. 101 1979, pp. 42–51.

23 Gallus, H. E., Lambertz, J. and Wallman, T. "Blade Row Interaction in an Axial-Flow Subsonic Compressor Stage," ASME Paper No. 79-GT-92, 1979.

24 Lowson, M. V. "Reduction of Compressor Noise Radiation," *The Journal of the Acoustical Society of America,* Vol. 43, No. 1, 1968, pp. 37–50.

25 Lumsdaine, E. and Chrng, J. G. "Influence of Blade Characteristics on Axial Flow Compressor Noise," AIAA Paper No. 1976, pp. 76–570.

26 Smith L. H., Jr. "Casing Boundary Layers in Multistage Axial-Flow Compressors" in *Flow Research on Blading,* L. S. Dzung, Ed., Elsevier Publishing Company, New York, 1970.

27 Kramer, J. J., Hartmann, M. J., Leonard, B. R., Klapproth, J. F. and Sofrin, T. G. "Fan Noise and Performance," in *Aircraft Engine Noise Reduction,* NASA SP-311, 1972.

28 Mikolajczak, A. A. "The Practical Importance of Unsteady Flow," in *Unsteady Phenomena in Turbomachinery,* AGARD-CP-177, 1976.

29 Lowson, M. V. "Reduction of Compressor Noise Radiation," *The Journal of the Acoustical Society of America,* Vol. 43, No. 1, 1968, pp. 37–50.

30 Homicz, G. F., Ludwig, G. R. and Lordi, J. A. "Theoretical and Experimental Studies of Discrete-Tone Rotor-Stator Interaction Noise," in *Proceedings of the AIAA 2nd Aero-Acoustics Conference,* 1975.

Author's Closure

The authors wish to thank Professor Okiishi for the discussion of the paper. Though some compressors have small inter stator-rotor spacing, there are many fan stages (e.g., JT9D, CF6, RB211, etc.) which have two to three chord spacing between the rotor and the stator. It is of interest to know how the wakes develop and decay with such large spacing. Once the mechanism of decay of the wake and its contribution to the acoustic levels are understood at such large spacings, it is possible to effectively study the wake behavior at smaller spacing and account for the potential interaction with the downstream stator.

The authors have analyzed the variation of higher Fourier coefficients up to A_7 and have found for the two sets of rotors [1, 2] that the predominant harmonics are up to A_5 in the trailing-edge and near-wake regions and only the first two in the far-wake region.

Downloaded 01 Jun 2010 to 171.66.16.58. Redistribution subject to ASME license or copyright; see http://www.asme.org/terms/Terms_Use.cfm

V. M. Sood
Engineering Specialist,
Combustion Systems

J. R. Shekleton
Engineering Staff Specialist,
Combustion Systems

P.O. Box 80966,
Solar Turbines International,
San Diego, CA 92138

Ongoing Development of a Low Emission Industrial Gas Turbine Combustion Chamber

Experiments were performed in laboratory- and full-scale combustors to test the feasibility of meeting proposed EPA emission standards. It was found that by uniformly mixing gaseous fuel and primary zone air prior to combustion and burning fuel leanly (equivalence ratio <1.0), it was possible to meet the proposed emission standards in an industrial gas turbine. The characteristic narrow range of flame stability obtained with lean premix combustion necessitated the use of fuel staging or variable geometry to handle the operational range of the engine. Fuel staging was selected for its relative simplicity. Consequently, EPA proposed emission standards were met only over a narrow range covering the engine operation at and near the design point. Experiments on small scale models of various sizes operated with gaseous and liquid fuels showed that, contrary to expectation, NO_x production from a lean premix combustion system is independent of the system pressure in the pressure range investigated (1 atm to 16 atm). The desirability of high combustor inlet temperature and pressure for premixing was indicated. Despite the complexities of premixing fuel and air, such a combustion system, in addition to meeting the proposed emission standards, offers advantages such as easing of combustor wall cooling problems, improved combustor exit temperature distribution, and freedom from exhaust and primary zone smoke.

Introduction

The emission of pollutants from industrial plants in the USA are being controlled to maintain or improve the existing air quality of the regions in which these plants are located. In order that the gas turbines manufactured by Solar Turbines International may be used in these plants, Solar has conducted research and development on various methods of controlled combustion to reduce the emission of pollutants such as oxides of nitrogen (NO_x), carbon monoxide (CO), and smoke. This work culminated in the design and development of a liquid and a gas fueled combustor for a 3500 horsepower industrial gas turbine, incorporating features aimed at producing low emissions. Development is continuing. This paper describes the progress made to date.

Design Requirements

The following emission levels at the engine design point were chosen as design goals.

Based on 15 percent O_2 in Exhaust

Fuel Type	NO_x ppmv	CO ppmv	Smoke (Percent Opacity)
Natural Gas	75	215	0
Liquid Fuel	75	215	0

The NO_x design goal is the same as the Environmental Protection Agency NO_x limit [1]. The CO design goal was chosen to limit the toxicity of the exhaust and to avoid fuel wastage due to combustion inefficiency. Because of the use of exhaust heat recovery on this engine, a goal of zero smoke in the exhaust was set in order to minimize the possibility of fouling the heat exchanger surfaces. In addition, there are the usual important criteria for a successful industrial combustor, such as cost, reliability, life, temperature distribution, pressure loss, and flame stability. The engine used for these investigations was a recuperative version of the Solar simple-cycle Centaur.

A schematic of the engine is shown in Fig. 1. In the simple-cycle version of the Centaur engine an annular combustor is used. In the recuperated version, this was replaced by a single can combustor, as shown in Fig. 2. The design point conditions for the combustor are:

- Air Flow — 15.88 kg/s
- Air Pressure — 786 kPa
- Air Inlet Temperature — 700 K
- Turbine Inlet Temperature — 1145 K

The engine was to be dual fuel, operating on hydrocarbon fuels either gaseous or liquids, not heavier than No. 2 diesel fuel.

Design Approach

Theory. CO and NO_x design point emission data for a number of different simple-cycle engines, having conventional combustors operating at sea level, have been examined by Lipfert [2]. These, together with the emission data from gas turbine engines manufactured by Solar Turbines International, showed that carbon monoxide was within the chosen goals in all cases while the oxides of nitrogen were not. The oxides of nitrogen increased with the engine pressure ratio. The correlation between the oxides of nitrogen and engine pressure ratio can be expressed by the following equation:

$$NO_x = 0.693 \times R^{1.17}$$

where NO_x is in grams/kilogram fuel and R is the engine pressure ratio.

Contributed by the Gas Turbine Division of The American Society of Mechanical Engineers and presented at the Gas Turbine Conference and Exhibit and Solar Energy Conference, San Diego, Calif., March 12–15, 1979. Manuscript received at ASME Headquarters January 17, 1979. Paper No. 79-GT-203.

Copyright © 1980 by ASME

Downloaded 01 Jun 2010 to 171.66.16.58. Redistribution subject to ASME license or copyright; see http://www.asme.org/terms/Terms_Use.cfm

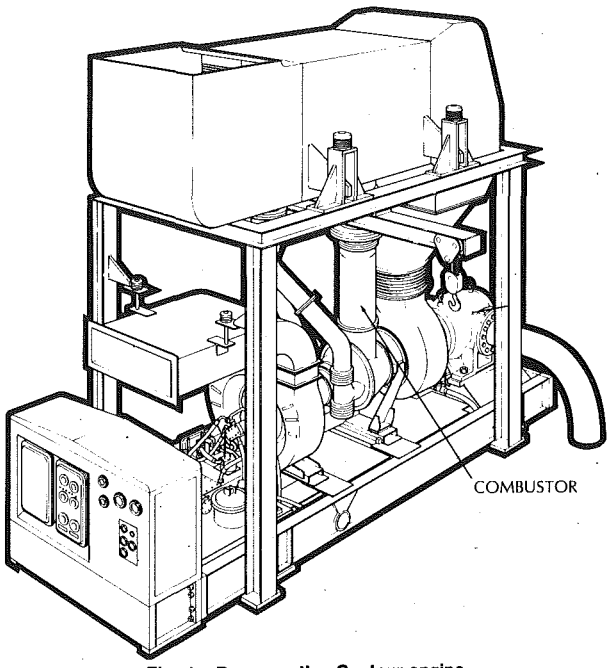


Fig. 1 Recuperative Centaur engine

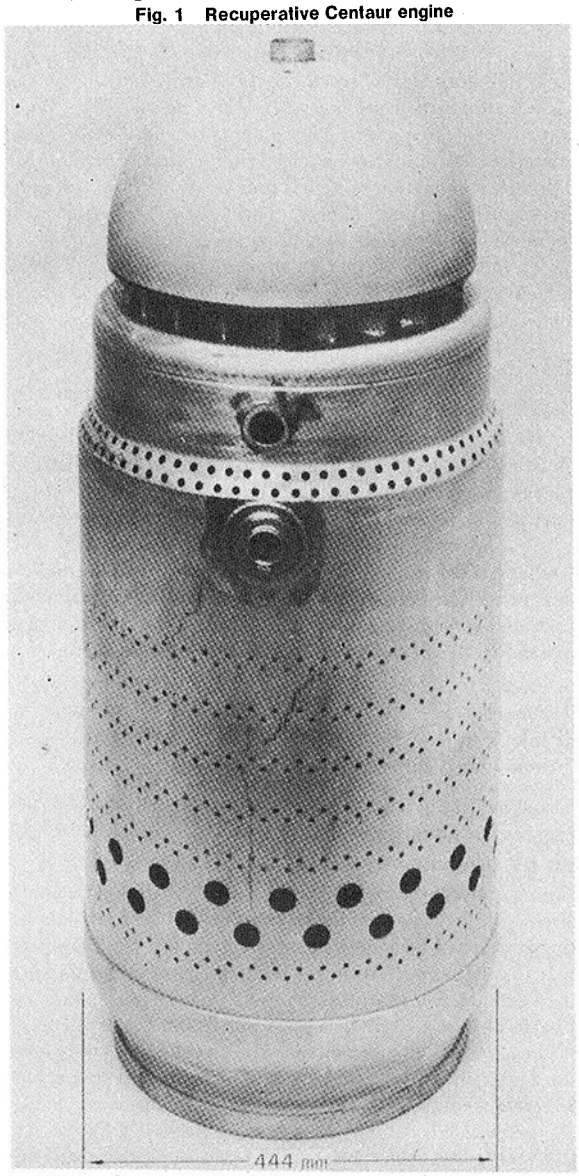


Fig. 2 Can combustor for the recuperative Centaur engine

The exponent of engine pressure ratio in the equation above takes into account the combined effect of combustor inlet temperature and pressure on NO_x production. The recuperative Centaur engine could not meet the NO_x emission goal using a conventional combustor, as its pressure ratio was too high. In addition, its combustor inlet temperature was higher than that of a simple-cycle engine of equivalent pressure ratio, and this would further raise the NO_x.

It is generally accepted that NO_x production is a result of reaction at high temperature [3–5]. (These are only a few of the references on the subject.) In a conventional combustor, the processes of fuel-air mixing and reaction proceed simultaneously, resulting in locally high reaction temperatures even if the average reaction temperature is kept low by design. Because of the dominant increase of reaction rate with air pressure, being proportional to $P^{1.8}$ [6] in a perfectly stirred reactor, compared to the mixing rate, being proportional to $P^{1.0}$ [7], these locally high reaction temperatures increase still further when the operating pressure of the combustor is raised. Thus, in any combustor in which fuel-air mixing and reaction proceed simultaneously, a significant effect of operating pressure on NO_x production is to be expected. But this is a simplistic view; in actual practice, the operating air pressure has additional influence on NO_x production due to its effect on fuel atomizer characteristics, fuel evaporation rates, and droplet burning. The approach chosen was to completely evaporate and homogeneously mix fuel with excess air prior to reaction. A fuel-lean premix combustor has a poor lean flameout limit and would not provide a sufficient range of stable combustion for operating a gas turbine. Variable geometry and two-stage fuel injection were the alternatives chosen to handle the off-design engine operation.

Combustor Design

Various methods of flame stabilization, such as recessed wall, bluff body, opposed jets, impinging jets, and vortex flow, were examined from the point of view of their suitability for the low emissions combustor. The vortex method was selected as it has been extensively studied, offers controlled combustion by controlling fuel-air mixing, and results in a simple variable geometry design. Although an axially generated vortex was considered, a radially generated one was chosen because of its simpler variable geometry mechanism.

A radial vortex can combustor, as shown in Fig. 3, was designed. Conventional cooling and dilution design techniques were used. The combustor is unusual in that nearly half the total combustor airflow passes through the swirl vanes into the flame zone. Using premix fuel injection, the fuel-air ratio could be controlled by adjustment of the swirl vanes. As an alternate to premix, a two-stage fuel injection system was used. The aim was to run the engine on a conventional diffusion flame fuel injection system at lower power levels and transfer to premix fuel injection only at design point power. The diffusion flame fuel was injected at the inner periphery of the vortex flow. The resultant low density hot core that results from ignition serves to impede the mixing of fuel and air because of the centrifugal force field that occurs in a vortex flow. Thus, even with a large amount of excess air in the flame zone, the unmixed fuel-air provides a considerably better lean flameout limit than that obtained with the premix fuel injection system. This method of fuel injection was named "stratified charge."

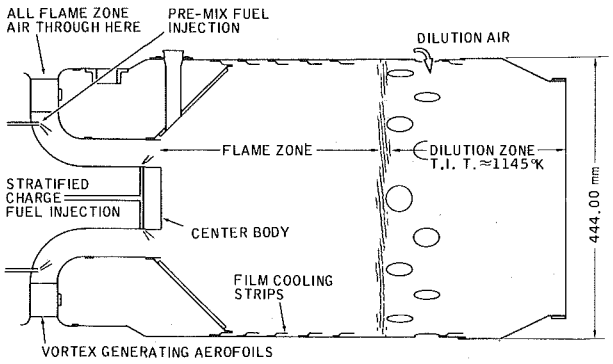


Fig. 3 Cross-section of the recuperative Centaur can combustor

Downloaded 01 Jun 2010 to 171.66.16.58. Redistribution subject to ASME license or copyright; see http://www.asme.org/terms/Terms_Use.cfm

Development Process

The development of the recuperative Centaur combustor was carried out in four phases:

- Scaled primary zone tests at atmospheric and high pressures
- Combustor development at atmospheric pressure
- Combustor development on the engine
- Development of a variable geometry combustor at atmospheric pressure

Primary Zone Tests

Full Scale Model—Premix Fuel Injection. A schematic of the full scale uncooled primary zone model of the vortex combustor is shown in Fig. 4. Tests were carried out at the design point combustor inlet temperature of 700 K, at ambient pressure, keeping the combustor $\Delta P/P_{t_{in}}$ constant. Test results obtained with natural gas are shown in Fig. 5. It is seen that, using natural gas, it is possible to meet the proposed emission goals if the primary zone is operated between 1490 and 2100 K. Below 1490 K, the carbon monoxide emission goal is exceeded. Above 2100 K, the emission characteristic for oxides of nitrogen becomes very steep and this temperature is, therefore, considered as the practical high limit of primary zone temperature for a low emission system. The narrow low emission operational range obtained could not be improved by modifying the fuel injection system and is considered a characteristic of premix combustion.

Full Scale Model—Stratified Charge Fuel Injection. The full scale model was tested with the stratified charge fuel injection system using natural gas. Excellent lean flameout limit and light-off performance were obtained. NO_x emission was high as expected from a diffusion flame. JP4 and No. 2 diesel fuels had a good lean flameout limit at combustor inlet temperatures above 500 K only. At lower combustor inlet temperatures, corresponding to engine light-off, the light-off performance of the system was inadequate, as it resulted in very poor combustion efficiency. As the liquid fuel starting capability on the recuperative Centaur was not an immediate customer requirement and as it was apparent that there were considerable improvements possible in the liquid fuel injection system, the primary zone design was considered as acceptable for the full scale vortex combustor.

Small Scale Model A—Premix Fuel Injection. Because of the limited air facilities, a small scale combustor of radial vortex design (Fig. 6) was designed with a view to testing the effect of operating variables, primarily combustor inlet temperature and pressure. Tests at the design point air inlet temperature of 700 K, and with combustor inlet pressures of 186, 345, and 648 kPa, were carried out at constant combustor pressure loss, $\Delta P/P_{t_{in}}$) using No. 2 diesel fuel. The emission characteristics are shown in Fig. 7.

The effect of combustor operating pressure on NO_x production is small and no definite trend is seen with pressure. The CO characteristic is common to all the pressures. The lean limit is also found to be independent of the combustor operating pressure. Noteworthy is the narrow range of stable low emissions combustion obtained with a premix flame. The lack of significant effect of pressure on NO_x emissions has also been observed from lean premixed propane-air flames by Roffe and Venkataramani [8]. Their experiments covered a range of pressures from 507 to 3040 kPa and combustor inlet temperatures above 727 K.

Tests were also done with natural gas and JP4 fuel. Emissions of carbon monoxide were identical to those obtained with No. 2 diesel fuel. Emissions of NO_x were somewhat lower. The combustor inlet pressure effects were similarly random and small.

Small Scale Model A—Stratified Charge Fuel Injection. Tests were also conducted using the stratified charge fuel injection as shown in Fig. 6. At atmospheric pressure and a combustor inlet temperature of 700 K, a typical result for No. 2 diesel is shown in Fig. 8. Results are based on the emissions measurements at the primary zone exit and not downstream of the combustor dilution zone as in the previous tests. Noteworthy is the wide range of flame stability despite the high excess of air in the primary zone. Tests with natural gas gave similar results with a somewhat better lean flameout limit. Tests at light-off conditions (an air inlet temperature of approximately 300 K) were satisfactory with gas but unacceptable with No. 2 diesel fuel. A solu-

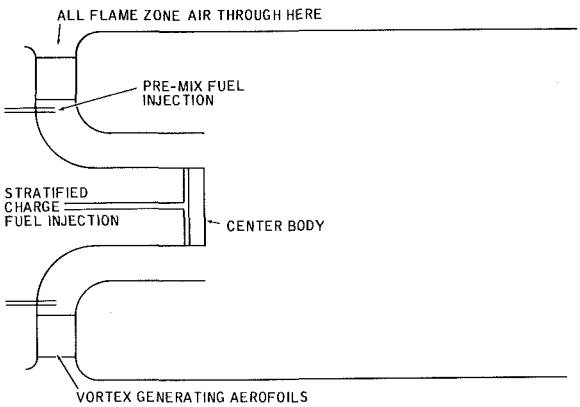


Fig. 4 Schematic of the recuperative Centaur full scale primary zone model (uncooled)

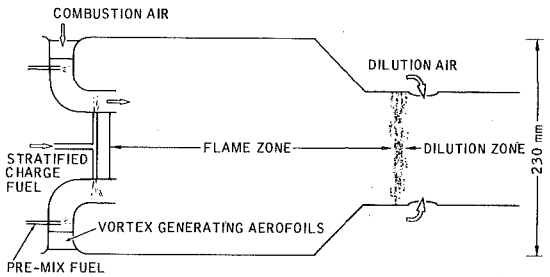


Fig. 6 Schematic of primary zone Model A

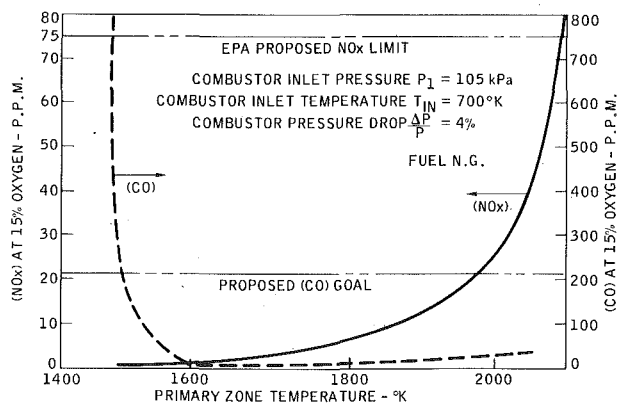


Fig. 5 Emissions characteristics of the recuperative Centaur full scale primary zone model operating on premix fuel injection system

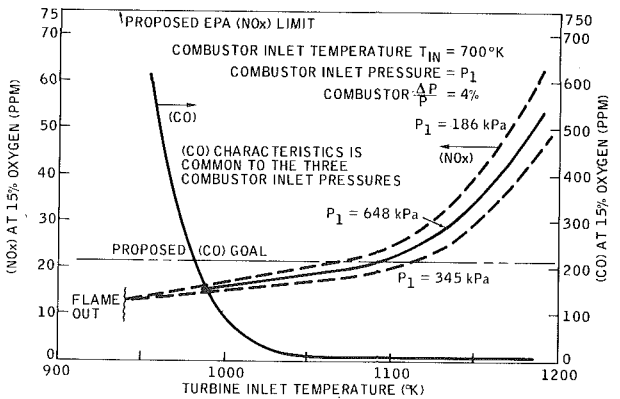


Fig. 7 Emissions characteristics of primary zone Model A operating on premix fuel injection system with No. 2 diesel fuel

Downloaded 01 Jun 2010 to 171.66.16.58. Redistribution subject to ASME license or copyright; see http://www.asme.org/terms/Terms_Use.cfm

tion was not necessary for the recuperative Centaur, as gas is used for starting and liquid fuels are used only after the recuperator has warmed up.

Small Scale Model B—Premix Fuel Injection. To study the effect of operating pressure on the premix emission characteristics at pressures higher than 648 kPa, a small scale Model B (Fig. 9), still smaller than the small scale Model A, was designed. The combustor performance at an air inlet temperature of 710 K and combustor inlet air pressures of 641 and 1413 kPa using No. 2 diesel fuel is shown in Fig. 10. The higher combustor exit temperatures are due to less dilution air in Model B to conserve air supply and thus permit higher air pressure tests. Pressure effects on flame performance are very low as in the case of small scale Model A. Tests were also conducted at a combustor inlet air temperature of 600 K. After only a short period of running, a large amount of carbonaceous deposits was found in the premix duct, due to incomplete vaporization of heavier fractions in the diesel fuel. Such deposits did not occur when using JP4 fuel at the same combustor inlet temperature. Tests showed that these deposits increased greatly with reduced combustor air inlet temperatures, and a minimum air temperature of at least 700 K was required to avoid deposits with No. 2 diesel fuel. This appeared to rule out the use of variable geometry with diesel fuels, unless some means of keeping the premix duct passages clean were adopted.

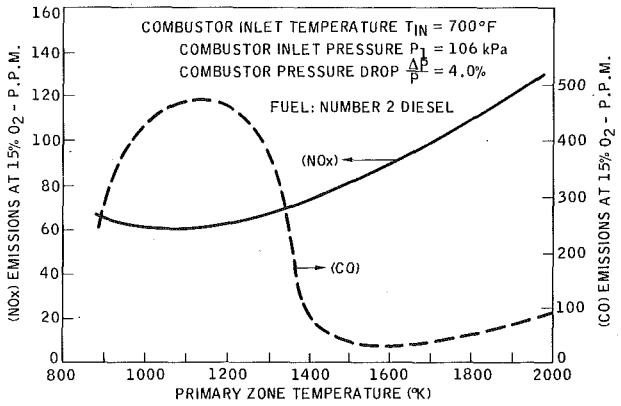


Fig. 8 Emissions characteristics of primary zone Model A operating on stratified charge fuel injection system with No. 2 diesel fuel

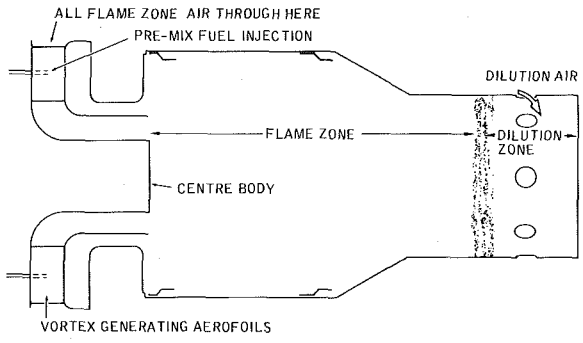


Fig. 9 Schematic of primary zone Model B

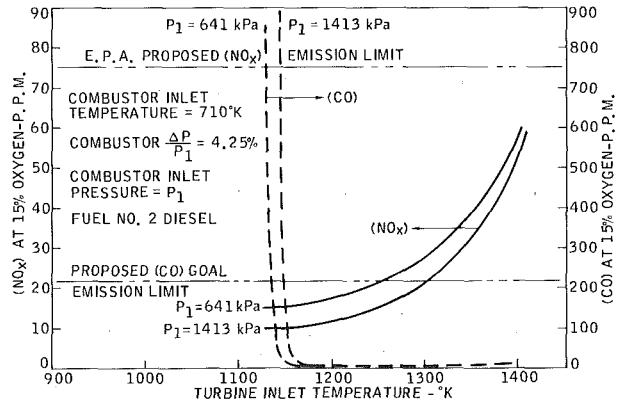


Fig. 10 Emissions characteristics of primary zone Model B operating on premix fuel injection system with No. 2 diesel fuel

Combustor Development at Atmospheric Pressure

Stratified Charge Fuel Injection System. Tests with a stratified charge fuel injection system using natural gas indicated that the combustor of Fig. 3 had excellent lean flameout limit and light-off characteristics. It produced a poor temperature distribution, with hot core at the combustor axis caused by insufficient penetration of the dilution jets. The combustor wall cooling airflow was also found to be excessive. The center body was, however, being adequately cooled by the gaseous fuel and presented no problems. The problem of the hot core was readily resolved by reducing the number of dilution holes from twenty to eight and changing their shape from round to elongated (Fig. 11), keeping the effective area of the dilution flow constant. This had a detrimental effect on light-off performance and the lean flameout limit of the combustor caused by the suction upstream of the dilution air by the vortex-induced low pressure region at the combustor axis. The light-off performance and the lean flameout limit were restored by introducing a small amount of pilot fuel (two percent). This fuel caused a patch of luminosity in front of the center body but the bulk of the flame remained transparent blue. Following this, the cooling airflow was reduced, and the combustor primary zone vanes adjusted to obtain acceptable performance to meet engine requirements.

Because of the complexity of a reliable liquid fuel pilot and because of no light-off requirements with liquid fuels, a liquid fuel pilot was not used. Also, when using liquid fuels, the center body had to be impingement-cooled with the combustor inlet air to keep it within the temperature limit for long life. Running on stratified charge with various fuels, such as JP4, kerosene, and No. 2 diesel, resulted in transparent blue flames of low luminosity, and consequently the combustor cooling developed on gaseous fuel was found to be adequate. Temperature distribution similar to that obtained with natural gas was achieved and exhaust smoke was completely absent.

Premix Fuel Injection System. The modified natural gas combustor of Fig. 11 was tested on premix fuel injection using natural gas. It was found that the combustor gave low NO_x emissions but produced CO levels that were consistently above the limit both at design point and at higher conditions. In view of the excellent low emission performance of the full scale primary zone models, this problem was thoroughly investigated. Tests were carried out by blanking off cooling and dilution airflow of the combustor each in turn and by examining CO emissions. This investigation confirmed that the high CO was being caused to some extent by the cooling airflow but mainly by the suction upstream of the dilution air into the primary zone by the vortex-induced reverse flow along the combustor axis. This was confirmed by flow visualization using cotton tufts.

To overcome this problem, the dilution zone of the combustor was redesigned. As shown in Fig. 12, the penetration of the main dilution flow is kept low by design, and the plunged dilution tubes are used to eliminate the hot core that results from the low penetration of dilution jets. The emission performance of this combustor at the facility-limited air inlet temperature of 600 K and at ambient pressure is shown in Fig. 13. It is clear from the curves that low emissions of NO_x and CO can be obtained at the engine design point and that the primary zone airflow should be reduced to extend the low emissions operational range to engine power levels lower than the design point. Consequently, the primary zone vanes were manually adjusted to reduce the airflow to the primary zone.

Combustion Development on the Engine

Stratified Charge Fuel Injection. The combustor of Fig. 11 was tested on the engine. The engine exhaust was smokeless. The flame, when viewed through the quartz viewing windows, seemed identical to that at atmospheric pressure. The combustor wall temperatures measured on the engine were found to be identical to those obtained on the rig at atmospheric pressure. The turbine inlet temperature

Downloaded 01 Jun 2010 to 171.66.16.58. Redistribution subject to ASME license or copyright; see http://www.asme.org/terms/Terms_Use.cfm

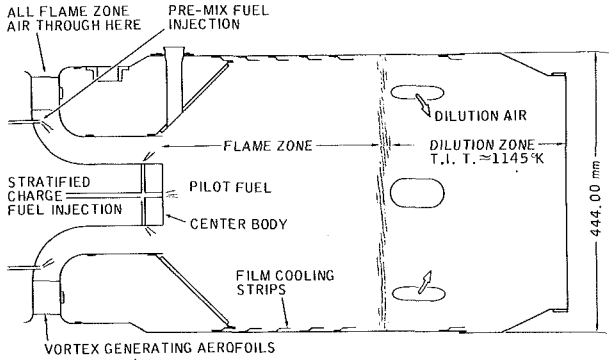


Fig. 11 Cross-section of the stratified charge recuperative Centaur combustor after development

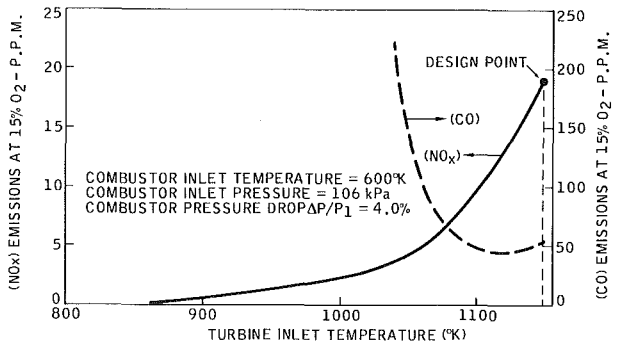


Fig. 13 Emissions characteristics of the recuperative Centaur low emissions combustor on natural gas fuel

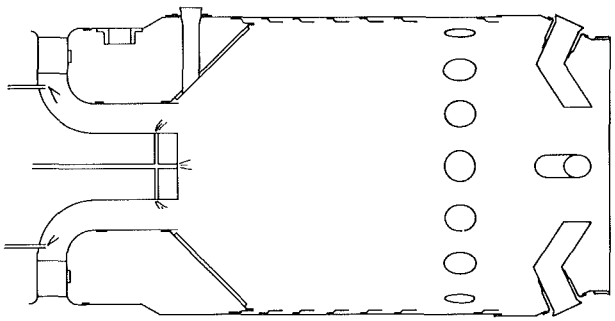


Fig. 12 Cross-section of the recuperative Centaur low emissions combustor

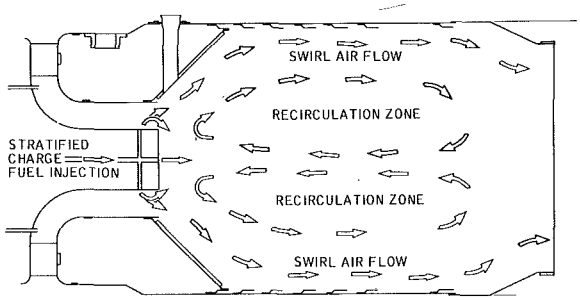


Fig. 14 Airflow diagram for recuperative Centaur can combustor

distribution was excellent, with a 1171 K hot spot when the average turbine inlet temperature was 1145 K.

Performance with distillate liquid fuels was also satisfactory. All the fuels tested (JP4, kerosene, and No. 2 diesel) produced temperature distributions at the combustor exit that were similar to that obtained with natural gas. The engine exhaust was free of carbon particles. Measurements with a Vonbrand smoke meter showed a zero smoke number even with No. 2 diesel fuel. The combustor wall temperatures were, on the average, only 30 K higher than those measured with natural gas. The flame was found to be of low luminosity throughout the primary zone except in front of the center body where fuel was entrapped in the recirculation zone (Fig. 14). After approximately 700 hours of testing on natural gas and 300 hours of testing on liquid fuel, the combustor was placed in service.

Premix Fuel Injection System. The combustor of Fig. 12 was tested on the premix fuel injection system using natural gas at the engine design point, and the following emissions, based on 15 percent oxygen in the exhaust, were obtained:

NO_x (ppmv)	CO (ppmv)	H/C (ppmv)	Smoke (percent opacity)
36.0	9.2	2	0

Turbine inlet temperature hot spots and wall temperatures were identical to previous engine tests with stratified charge natural gas, and smoke was entirely absent. Flame was transparent blue throughout the primary zone. Lean flameout limit was poor, however. Successful automatic fuel transfers from stratified charge to premix fuel injection system and vice versa to handle the operational range of the engine were demonstrated.

Even on light liquid fuels, such as JP4, performance on premix was entirely unsatisfactory. It was apparent, on viewing through the quartz windows, that flow separation was occurring on the inner edge of the vortex flow within the premix section. This resulted in ignition within the premix section at higher power conditions and tests had to be aborted to prevent center body burnout. Visual flame observations did, however, show a transparent light blue flame identical to that obtained with gas. The commencement of ignition at the edge of the center body was readily observable as, the flame being transparent, white hot molten particles of metal were seen exiting the flame zone. Future development is aimed at insuring stable aerodynamics in the premix zone with particular attention to the avoidance of flow separation.

Variable Geometry Combustor Development at Atmospheric Pressure. Following successful demonstration of low emissions on the engine using natural gas, a variable geometry mechanism, shown in Fig. 15, was designed. With this mechanism, the combustor primary zone airflow can be controlled by controlling the position of swirl vanes. The emission characteristics of the combustor at a combustor inlet temperature of 700 K and constant $\Delta P/P$ with high (I), medium (II), and low (III) primary zone airflows are shown in Fig. 16. It shows the considerable gains in low emissions operational range obtained by use of variable geometry. In view of the experience of premature ignition of liquid fuels at the edge of the center body, thought to be caused by flow separation, the variable geometry combustor will be modified by changing the premix duct geometry before it is tested on the engine.

Summary

Premix of natural gas with excess air, as a practical means of getting low emissions, appears feasible. Some increase in cost and complexity of the combustor fuel injection system and fuel control system beyond the current state of the art is to be expected. With No. 2 diesel fuel, reliable premix could not be obtained unless the combustor inlet air temperature was at least 700 K. This requires a simple-cycle engine pressure ratio of at least 16:1 or a recuperative cycle of somewhat lower pressure ratio.

In a combustor having excess air in the flame zone, either with premix or stratified charge fuel injection, the wall cooling problems are much less severe than in conventional systems. Stratified charge fuel injection appears particularly attractive, as not only can a simple film cooling scheme be used, but also much development can be carried out at atmospheric pressure. Formidable problems of light-off and combustion efficiency at engine idle on liquid fuels are yet to be resolved.

Downloaded 01 Jun 2010 to 171.66.16.58. Redistribution subject to ASME license or copyright; see http://www.asme.org/terms/Terms_Use.cfm

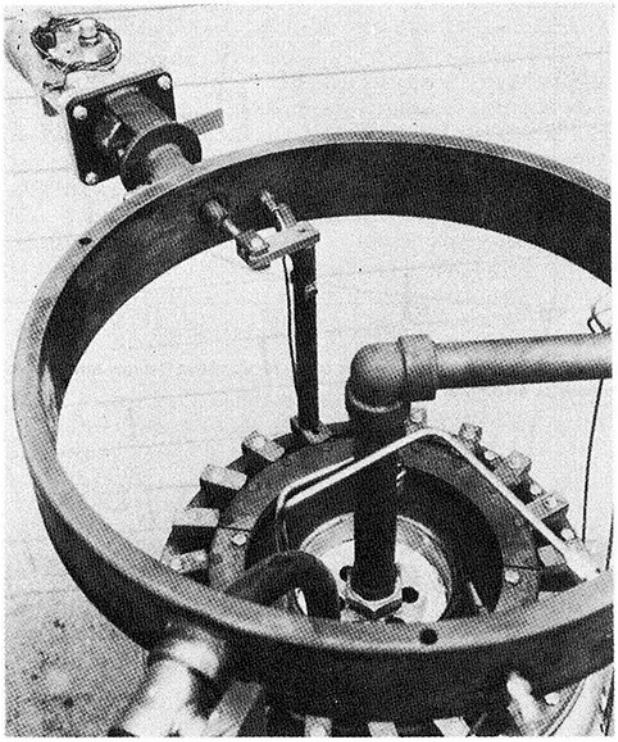


Fig. 15 Recuperative Centaur variable geometry combustor

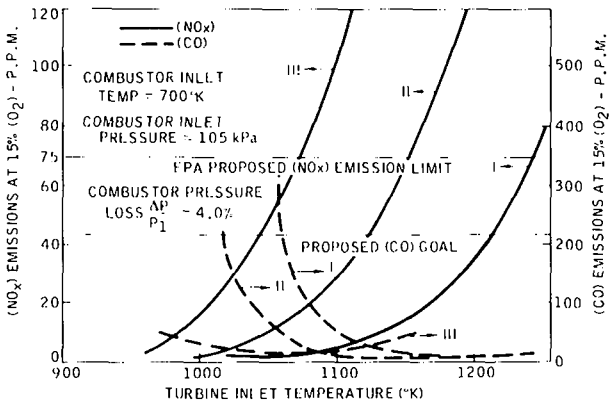


Fig. 16 Emissions characteristics of the variable geometry combustor

References

1 Anonymous, "Standards of Performance for New Stationary Sources, Stationary Gas Turbines," Environmental Protection Agency, Federal Register, Monday, Oct. 3, 1977.

2 Lipfert, F. W., "Correlation of Gas Turbine Emissions Data," ASME Paper No. 72-GT-60.

3 Fenimore, C. P., et al., "Formation and Measurements of Nitrogen Oxides in Gas Turbines," ASME Paper No. 70-WA/GT-3.

4 Shahed, S. M. and Newhall, H. K., "Kinetics of Nitric Oxide Formation in Propane-Air and Hydrogen-Air Diluent Flames," *Combustion and Flame*, Vol. 17, 1971, pp. 131–137.

5 Singh, P. P., et al., "Formation and Control of Oxides of Nitrogen Emissions from Gas Turbine Combustion Systems," ASME Paper No. 72-GT-22.

6 Longwell, J. P. and Weiss, M. A., "High Temperature Reaction Rates in Hydrocarbon Combustion," *Ind. Eng. Chem.* Vol. 47, 1955, pp. 1634–1643.

7 Lefebvre, A. H., "Theoretical Aspects of Gas Turbine Combustion Performance," CoA report Aero No. 163, The College of Aeronautics, Cranfield, 1966.

8 Roffe, G. and Venkataramani, K. S., "Emission Measurements for a Lean Premixed Propane/Air System at Pressures up to 30 Atmospheres," NASA CR-159421.

Downloaded 01 Jun 2010 to 171.66.16.58. Redistribution subject to ASME license or copyright; see http://www.asme.org/terms/Terms_Use.cfm

Krishna P. Singh
Chief Engineer,
Mem. ASME

V. K. Luk
Stress Analyst.

Joseph Oat Corporation
2500 Broadway
Camden, NJ 08104

An Approximate Analysis of Foundation Stresses in Horizontal Pressure Vessels

Saddle supports of horizontally mounted pressure vessels, when subject to seismic and mechanical loads, interact with the foundation in a highly non-linear manner. The maximum foundation concrete pressure, and hold-down bolt stresses are important design considerations which often govern the vessel support geometry. A method is given herein to determine the foundation stresses due to arbitrary imposed loadings. The solution procedure lends itself easily to automated computation—a highly desirable feature—since most nuclear equipment has to be analyzed for a large number of loading conditions.

1 Introduction

In this paper, a method to determine the interfacial concrete pressure, and the foundation bolt stresses for saddle supported pressure vessels is given. The saddle supports of a pressure vessel may be subjected to a variety of loads in its operating life. These loads may be broadly divided into two categories:

1 Time invariant loads; e.g., the operating weight of the equipment, and its attached appurtenances.
2 Time variant loads; e.g., wind loads, inertia loads, forces due to seismic disturbances; reactions transmitted through the nozzles from constrained thermal expansion (contraction) of connecting pipe lines; etc.

The invariant loads are fairly simple to analyze because they are directed vertically downwards and hence produce only a uniform compressive stress on the foundation. Zick [1] gives a comprehensive method, appropriate to a pressure vessel designer, of saddle support design for invariant loads. Variant loads, on the other hand, are more difficult to treat. These loads arise from a host of reasons, and may act coincidentally in numerous combinations. Hence, it is necessary to develop a general formalism for solution which may be computerized to examine the stresses resulting from each conceivable combination. Hence attention is focussed here on determining the stresses in the foundation bolts, and the peak concrete bearing pressure due to an arbitrary set of loadings applied to the pressure vessel. The solution procedure is readily amenable to automation.

A typical pressure vessel supported on two saddles is shown in Fig. 1. One of the two support base plates has slotted holes to accommodate thermal expansion of the shell. We will identify the two supports as "fixed support" and "slotted support."

In Section 2, the support reactions are expressed in terms of the imposed loads. Explicit formulae to correlate the foundation stresses to the support reactions are given in Section 3. Section 4 includes an illustrative example, and a brief discussion of the method is contained in Section 5.

2 Determination of Support Reactions

To facilitate analysis, all the imposed loads are resolved along the three coordinate axes as shown in Fig. 1. The origin of the coordinate system, 0, is located on the vessel centerline midway between the supports. The loads are identified as F_x, F_y and F_z acting along the x, y and z directions. The moments are similarly identified as M_x, M_y and M_z with subscripts indicating their axes in accordance with the conventional "right hand screw rule." As stated before, one saddle has slotted holes (elongated in the x-direction) to accommodate longitudinal thermal expansion of the vessel. To fix ideas, the slotted support is assumed to be located on the positive x-axis and the fixed support is located on the negative x-axis. The slotted support is idealized as a frictionless roller in the x-direction. The fixed support is

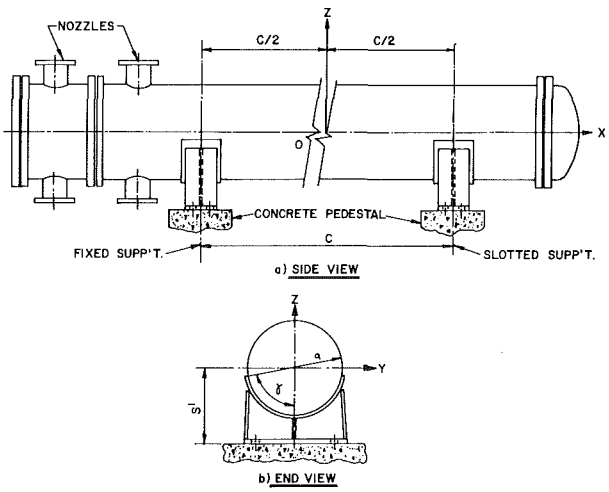


Fig. 1 A saddle supported heat exchanger

Contributed by the Nuclear Engineering Committee and presented at the Pressure Vessel and Piping Conference, San Francisco, California, June 25–29, 1979 of THE AMERICAN SOCIETY OF MECHANICAL ENGINEERS. Manuscript received at ASME Headquarters March 19, 1979. Paper No. 79-NE-1.

Copyright © 1980 by ASME
Downloaded 01 Jun 2010 to 171.66.16.58. Redistribution subject to ASME license or copyright; see http://www.asme.org/terms/Terms_Use.cfm

assumed to have its both ends "built-in." This assumption is generally conservative for calculating the foundation stresses. Furthermore, it is realistic to assume that the axial thrust, F_x, is resisted by the saddle through a uniformly distributed shear load over the entire circumferential extent of the saddle. Invoking the above assumptions, the foundation reactions and moments can be readily determined by appealing to static equilibrium; as follows:

$$R_{11} = F_x \tag{1}$$

$$R_{12} = 0.5\,F_y - \frac{M_z}{c} \tag{2}$$

$$R_{13} = \frac{F_x(s' - .5s) + M_y}{c} + 0.5\,F_z \tag{3}$$

$$R_{22} = 0.5\,F_y + \frac{M_z}{c} \tag{4}$$

$$R_{23} = -\frac{F_x(s' - .5s) + M_y}{c} + 0.5\,F_z \tag{5}$$

$$M_{12} = \frac{F_x s}{2} + \frac{M_Y}{2} \tag{6}$$

$$M_{11} = M_{21} = -\frac{F_y s'}{2} + \frac{M_x}{2} \tag{7}$$

$$M_{22} = \frac{F_x s}{2} + \frac{M_y}{2} \tag{8}$$

where

$$s = s' - \frac{a \sin\gamma}{\gamma}$$

In the foregoing equations, R_{ij} denotes the reaction and M_{ij} denotes the moment applied on the foundation by the saddle base plate. The first subscript, $i = 1$ (or 2), indicates that the reaction acts at the fixed (or slotted) support; and the second subscript, j (1, 2 or 3), indicates its direction (x, y or z). s' is the height of the x-y plane (Fig. 1); γ is the semi-saddle angle, a is the shell outer radius, and c is the distance between support centerlines.

Equations (1–8) give the support reactions as explicit functions of the imposed loads. The next step in the analysis is to develop the relationship between these reactions, and the foundation interfacial concrete pressure and bolt stresses. It suffices to find expressions for concrete pressure due to loadings in one plane, viz., reactions R_{13} and moments M_{12} acting in the x-z plane; since effects of loadings in the other vertical plane can be obtained in a similar manner.

3 Foundation Stresses

A typical base plate is shown in Fig. 2. The base plate is of rectangular shape with a number of bolt lines. In a general case, let there be n bolt lines parallel to the y-axis. The distance of i-th bolt line from the right edge of the plate is denoted by b_i, $i = 1, n$. Let a moment M_{12} ($= M$) and vertical thrust R_{13} ($= -W$) be applied on the foundation. The concrete base is assumed to be linearly elastic. Noting that the concrete surface is tensionless, and the bolts are effective only in tension, it is necessary to determine the neutral axis. Assuming the base plate to be rigid, the load distribution on the foundation typically looks like Fig. 2 (b). Let d denote the distance of the neutral axis from the right edge and p denote the maximum pressure on concrete. Then, if

$$b_{j+1} \geq d > b_j,\ j = 0, n \tag{9}$$

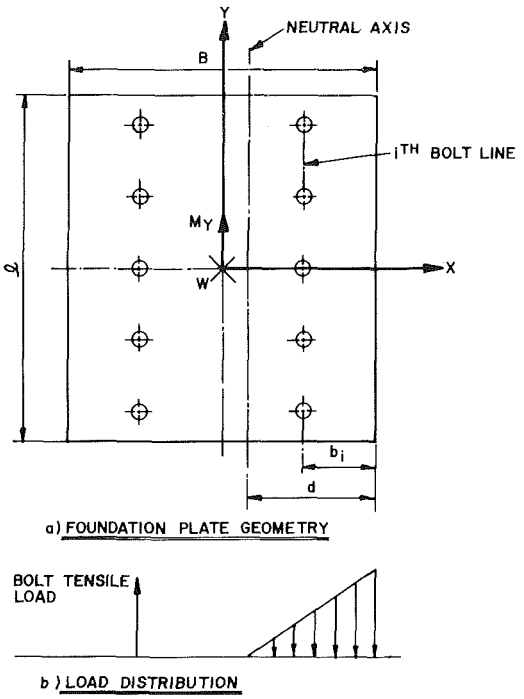


Fig. 2 Applied loadings on a rectangular base plate

where $b_0 = 0$, and $b_{n+1} = B$, then vertical force equilibrium requires

$$W = \frac{pd\ell}{2} - \frac{pNA}{d}\sum_{i=j+1}^{n}(b_i - d) \tag{10}$$

Furthermore, moment equilibrium requires

$$M + W(d - 0.5B) = \frac{p\ell d^2}{3} + \frac{pNA}{d}\sum_{i=j+1}^{n}(b_i - d)^2 \tag{11}$$

In the preceding equations, A is the gross tensile stress area available in one bolt line[1] and N is the ratio of the Young's modulus of bolt material to that of concrete. For common structural bolting material—e.g., A325 or A307—and common grades of concrete, N varies from 10 to 15.

The following dimensionless quantities are introduced:

$$\rho_i = \frac{b_i}{B} \tag{12a}$$

$$\rho = \frac{d}{B} \tag{12b}$$

$$\theta = \frac{NA}{\ell B} \tag{12c}$$

$$p^* = \frac{p}{\Lambda} \tag{12d}$$

[1] Tensile stress area, A', of a bolt of nominal diameter D, is defined in the *Manual of Steel Construction* [2] as $A' = \pi/4(D - .9743/n')^2$ where n' = number of threads per inch.

Nomenclature

A = bolt tensile stress area in one bolt line
a = outer radius of shell
B = width of base plate
b_i = distance of i-th bolt line (Fig. 2)
c = distance between support centerlines
d = distance of the neutral axis
F_x, F_y, F_z = applied load vectors
ℓ = length of saddle base plate
M = applied moment
M_x, M_y, M_z = applied moment vectors
M_{ij} = moment at i-th support in the j-th direction
M^* = dimensionless moment
N = ratio of Young's moduli
n = number of bolt lines
p = peak concrete pressure
p^* = dimensionless peak concrete pressure
R_{ij} = reaction at i-th support in the j-th direction
s' = height of centerline
W = vertical load
W^* = dimensionless vertical load
γ = semi-saddle angle
Λ = nondimensionalized pressure
ρ = dimensionless distance of neutral axis
σ_n = maximum bolt tensile stress

Downloaded 01 Jun 2010 to 171.66.16.58. Redistribution subject to ASME license or copyright; see http://www.asme.org/terms/Terms_Use.cfm

$$W^* = \frac{W}{\Lambda \ell B} \tag{12e}$$

$$M^* = \frac{M}{\Lambda \ell B^2} \tag{12f}$$

Where Λ is an arbitrary nondimensionalizing pressure. Equations (10) and (11) cast in terms of the dimensionless variables become:

$$W^* = \frac{\rho p^*}{2} - \theta p^* \sum_{i=j+1}^{n} \frac{1}{\rho}(\rho_i - \rho) \tag{13}$$

$$M^* + W^*(\rho - .5) = \frac{\rho^2}{3} p^* + \theta p^* \sum_{j+1}^{n} \frac{1}{\rho}(\rho_i - \rho)^2 \tag{14}$$

where

$$\rho_j \le \rho \le \rho j + 1, j = 0, n \tag{15}$$

Equations (13) and (14) are combined to yield the following nonlinear equation in terms of ρ only:

$$(0.5\rho^2 - \theta\alpha)[M^* + W^*(\rho - 0.5)] - W^*\left(\frac{1}{3}\rho^3 + \theta\beta\right) = 0 \tag{16}$$

where

$$\alpha = \sum_{i=j+1}^{n} (\rho_i - \rho) \tag{17}$$

$$\beta = \sum_{i=j+1}^{n} (\rho_i - \rho)^2 \tag{18}$$

Equation (16) is solved for ρ subject to the inequality (15) by using the linear interpolation technique through the method of secants.

The value of Λ seems to directly affect the convergence of solutions. As a general rule, keeping Λ below the anticipated value of peak concrete pressure ensures convergence.

Having thus determined the location of neutral axis, the peak interfacial concrete pressure p is directly obtained from equation (14). The maximum bolt tensile stress is given by

$$\sigma_n = \frac{1}{d} Np(b_n - d) \tag{19}$$

It is obvious from physical considerations that solution for equation (16) within the physically meaningful range ($0 \le \rho \le 1$) can be found only for a limited range of values of W and M. Beyond this range, a neutral axis may not exist. Instead, one of the following two conditions may obtain:

1 Edging. For large values of M, and relatively small W, the entire base plate lifts off the foundation and presses the concrete on one of its edges. This situation will occur when ρ in equation (16) approaches zero. Accordingly, the following relation between M and W will correspond to the onset of edging:

$$M = \frac{W(0.5B\Sigma b_i - \Sigma b_i^2)}{\Sigma b_i} \tag{20}$$

It should be realized that the aforementioned equation is a necessary, but not a sufficient, condition for edging occurrence.

It can be shown that the maximum stress in the bolts for edging condition is given by

$$\sigma_n = \frac{b_n(M - 0.5WB)}{A\Sigma b_i^2} \tag{21}$$

The maximum concrete pressure is mathematically infinite.

2 Complete Compression. This case exists when the overturning moment is small relative to the vertical load W. It can be shown that the pressure distribution is trapezoidal; and its extremal magnitudes are given by

$$p = \frac{W}{B\ell} \pm \frac{3M}{\ell B^2} \tag{22}$$

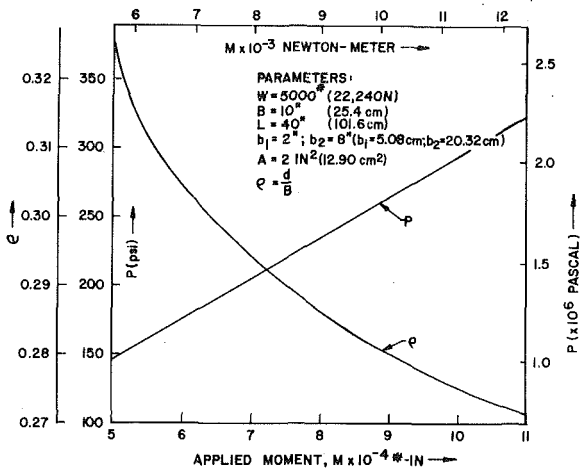


Fig. 3 Variation of ρ and p with applied moment

It should be noticed that from equations (21), in order that tension may exist in all the bolts, the following condition must be satisfied,

$$W^* < 2M^* \tag{23}$$

Furthermore, in order that some concrete be in compression, it is required that (via equation (22))

$$W^* > 3M^* \tag{24}$$

It can be shown that equation (24) is a necessary and sufficient condition for complete compression.

4 An Example

Consider the case of foundation base plate with an applied vertical load W = 5,000# (22,240N) and a variable overturning moment which ranges from 50,000# in. (5,650N-m) to 110,000# in. (12,430N-m). The geometric parameters are B = 10 in. (0.254m); ℓ = 40 in. (1.016m); n = 2; b_1 = 2 in. (0.0508m); b_2 = 8 in. (0.2032m); A = 2 sq. in. (1.29×10^{-3}m^2).

The maximum concrete pressure p, and neutral axis parameter ρ are calculated, and plotted as functions of the applied moment in Fig. 3.

5 Discussion

A method to determine the maximum interfacial concrete pressure, and foundation bolt tension in a rectangular base plate subject to vertical loads and overturning moments is given. The method is particularly useful in designing saddle supported heat exchangers. It is shown that, within a limited range of applied loadings, there exists a neutral axis which can be determined by solving one nonlinear equation in ρ subject to a set of inequality constraints.

References

1 Zick, L. P., "Stresses in Large Horizontal Cylindrical Pressure Vessels on Two Saddle Supports," *Pressure Vessel and Piping; Design and Analysis*, Vol. 2, ASME, New York, 1972, pp. 959–970.

2 *Manual of Steel Construction*, American Institute of Steel Construction, Seventh Edition, New York, 1970, pp. 1265.

Downloaded 01 Jun 2010 to 171.66.16.58. Redistribution subject to ASME license or copyright; see http://www.asme.org/terms/Terms_Use.cfm

C. E. Richard
Staff Engineer,
General Atomic Company,
P.O. Box 81608,
San Diego, CA 92138

Simplified Inelastic Analysis in Helical Coil Heat Exchanger Design[1]

A simplified, inelastic analysis of helical coil tubing for high-temperature applications is described. Elastically calculated operating stresses are compared with inelastic estimates of allowable cyclic creep/fatigue stresses. The technique of simplifying and analyzing the operating cycles to determine acceptable creep damage levels has general application. The allowable stresses represent the greatest uncertainty in the method, and tests are required to improve their accuracy. A method of utilizing short-time test data to determine allowable stresses for reactor lifetimes of 30 to 40 years is proposed.

Introduction

Simplified inelastic analyses of critical components are required in the conceptual and preliminary phases of high-temperature heat exchanger design to establish concept feasibility and to estimate structural envelope requirements. This paper uses helical coil tubing parameters for typical gas-cooled reactor steam generators to develop structural design equations. Although an integrated heat transfer and structural effort is necessary owing to the interaction of the performance and geometry variables, this paper emphasizes only structural considerations. The assumed operating cycle, which is typical of a gas-cooled reactor power plant, causes oscillatory thermal stresses, which are the major tube cyclic stresses. Simplified elastic analyses are used to estimate these operating stresses, and allowable limits on these stresses are based on simplified inelastic analysis of cyclic stress histories associated with assumed reactor operations. The approach followed in this method is to determine the allowable cyclic strain, or stress, range for a given number of cycles. These analytically determined stresses are the major uncertainty in this simplified method. Consequently, substantiating tests must be accomplished. In addition, a test method is needed which can supply acceptable data in about a year or less and yet permit extrapolation to design lifetimes of 30 to 40 years.

Design Procedure

An iterative process, shown in Fig. 1, is required to size the tubing and the overall steam generator structure or substructure. First, thermal conditions and geometry including tube diameter are selected. Tube wall thickness based on estimated temperatures is computed using allowable primary load stresses for either internal or external pressure; hoop stress generally determines thickness for internal pressure designs. Heat transfer calculations are performed to determine associated metal temperatures and to set the tube spacings which satisfy performance requirements. Wall thickness is revised based on these temperatures, and the process is continued until consistent geometry and temperatures are achieved (for primary stresses).

When the heat transfer and structural iteration is completed, cyclic stresses (discussed in the next section) are compared with allowable creep/fatigue values. If the maximum cyclic stress equals the allowable stress, the design is considered to be acceptable and cannot be improved without changing the initial design conditions. If the maximum cyclic stress is less than the allowable stress, tube diameter increases

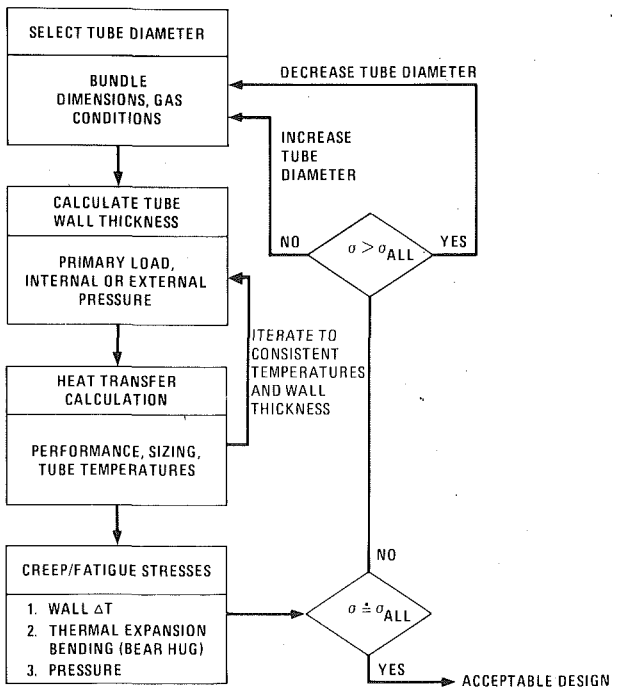


Fig. 1 Simplified tube design procedure

[1] This work was supported in part by U. S. Department of Energy Contract EY-76-C-03-0167, Project Agreement No. 65.

Contributed by the Nuclear Energy Committee and presented at the Pressure Vessel and Piping Conference, June 25–29, 1979, San Francisco, California, of THE AMERICAN SOCIETY OF MECHANICAL ENGINEERS. Manuscript received at ASME Headquarters March 26, 1979. Paper No. 79-NE-2.

Copyright © 1980 by ASME

Downloaded 01 Jun 2010 to 171.66.16.58. Redistribution subject to ASME license or copyright; see http://www.asme.org/terms/Terms_Use.cfm

are possible; this is generally advantageous from a cost standpoint. If the cyclic stress exceeds the allowable stress, it is necessary to reduce the tube diameter.

Tube Operating Stresses

The critical combination of tube creep/fatigue stresses occurs on the outside wall surface at or near support plates. The stresses are axial or longitudinal. The individual stress components arise due to plate and tube differential radial thermal expansion, temperature gradients across the tube wall thickness, and differential pressure loading.

Fig. 2(*a*) shows a typical helical coil tube bundle arrangement. Plates required for weight or seismic support or prevention of undesirable tube vibration are also shown. The plates restrain tube coil radial expansion, which causes tube bending stress (sometimes referred to as "bear hug" stress). The equation for estimating this stress is

$$\sigma = KE\alpha\Delta T, \tag{1}$$

where K depends on plate fixity and geometry, E is the tube material elastic modulus, α is the instantaneous thermal expansion coefficient, and ΔT is the temperature difference between the tube and the plate. This is a bending stress across the tube section and is derived for a ring with point supports [1]. For analytical purposes, this stress is assumed to be strain controlled, although in later design stages the effects of load control must be considered.

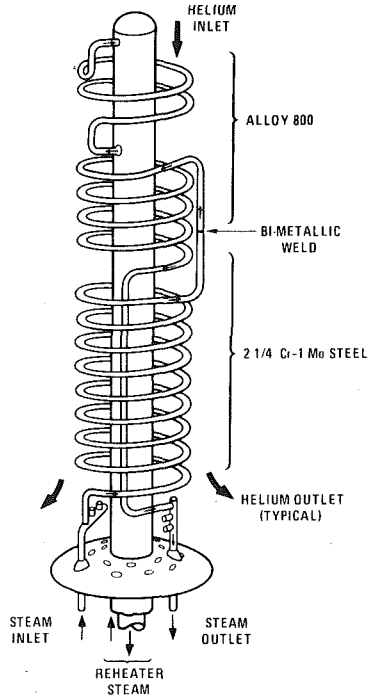


Fig. 2(*a*) Overall component location and tube routing

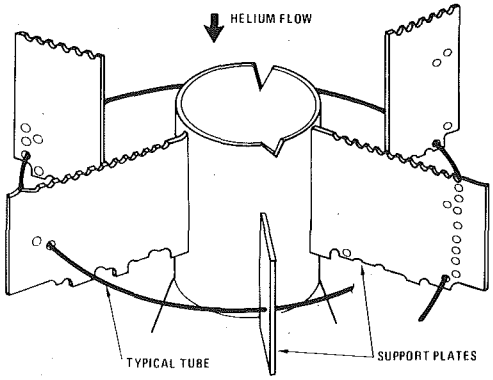


Fig. 2(*b*) Plate details

Fig. 2 Heat exchanger arrangement

Helium flow, which is parallel to the coiled tubing axis, induces temperature gradients through the wall thickness, and the resulting stress can be calculated with sufficient accuracy as follows:

$$\sigma = E\alpha\Delta T/2(1-\nu), \tag{2}$$

where ΔT is the difference across the tube wall, and ν is Poisson's ratio. This stress is strain controlled.

These two thermal stresses (equations (1) and (2)) plus axial pressure stress combine in the axial direction to give the maximum cyclic stress on the tube cross section. The equation for axial pressure stress in thick wall tubes [1] is

$$\sigma = (p_i a^2 - p_0 b^2)/(b^2 - a^2), \tag{3}$$

where p_i and p_0 are internal and external pressure, respectively, and a and b are the inside and outside radii, respectively. This pressure stress is much lower than the thermal stresses, and although it is load controlled, it also is considered to be strain controlled in this analytical procedure. Fig. 3 illustrates these operating stresses and shows typical relative magnitudes.

Cyclic Nature of Stresses/Allowable Stresses

Heat exchangers for power plant applications are subjected to temperature and pressure oscillations related to power output and maintenance requirements. The associated operating stresses are therefore cyclic in nature. In a helium-gas-cooled reactor the stress histories depend on the heat exchanger helium inlet temperature histories. Fig. 4 shows typical helium temperature oscillations during a full week of reactor operation in which the plant power output is set according to demand. In this weekly cycle (also called the power-following cycle), the plant is at 25 percent of full rated power on

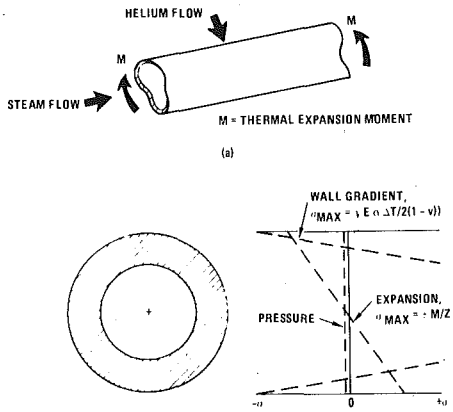
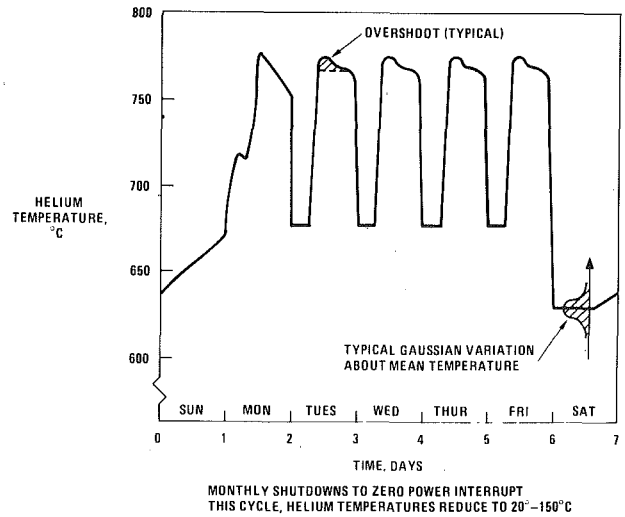


Fig. 3 Tube loads (*a*) tube conditions (*b*) section operating stresses (axial)



MONTHLY SHUTDOWNS TO ZERO POWER INTERRUPT
THIS CYCLE, HELIUM TEMPERATURES REDUCE TO 20°–150°C

Fig. 4 Typical weekly cycle

Downloaded 01 Jun 2010 to 171.66.16.58. Redistribution subject to ASME license or copyright; see http://www.asme.org/terms/Terms_Use.cfm

weekends and oscillates between 100 percent during the day and 50 percent at night during weekdays. Plants which are exclusively operated at full power except for shutdowns are referred to as base-loaded plants. (Shutdowns also occur in load-following plants but are not shown in Fig. 4.)

Allowable stress ranges are computed for each operating cycle assuming strain-controlled loadings. The cycles are characterized by sustained power outputs (holds) at constant strain with relatively rapid transitions. Creep damage is the predominant damage mechanism at the temperatures of interest. This damage, D, may be estimated for the sustained holds according to ASME Code recommendations [2],

$$D = \sum_i t_i/t_{i,r}, \tag{4}$$

where t_i is the time at a stress level i, and $t_{i,r}$ is the minimum time to rupture of the material at the same stress. Relaxed stresses and associated creep damage during the holds are computed in increments, and the stress range which gives a damage of unity is the allowable stress for that cycle (the required 1.1 factor on stress [2] is included). Assuming a stress-free state for the start of the first cycle, the material is usually loaded (or strained) into the plastic zone during the first load application. However, to have an acceptable stress range for design lives on the order of 40 years, repetitive plasticity (hysteresis) cannot occur. Fatigue damage is usually negligible.

For analysis of the weekly power cycle, the Fig. 4 helium variation was approximated by the block diagram in Fig. 5(a). Each step in the cycle has an associated strain (approximately proportioned to reactor power), temperature, and time duration. Analysis of such cycles has shown that the extreme power conditions will govern stress history and the associated accumulated creep damage. Intermediate power levels consume elapsed time without adding significantly to total damage because stresses are low and/or times are short. Furthermore, if the time steps are regrouped as shown in Fig. 5(b), the computation yields the same accumulated creep damage. This grouping is possible because acceptable stresses for long life operations are small and little relaxation occurs after the cycle stabilizes. Stresses during the week in the equivalent two-step cycle are shown in Fig. 5(c). After initial relaxation or shakedown, a stable cycle develops in which stresses (and relaxation) are alternately tensile and compressive. The resulting stress-strain cycle for 25 to 100 percent power changes (after stabilization) is also illustrated in Fig. 6. In this long-life application, the acceptable stress ranges, between power extremes, are small and transition loadings are elastic. Hence, the stress range is approximately constant. Furthermore, the creep damage fraction associated with initial shakedown is small compared to that accumulated after stabilization. The total damage is, therefore, relatively insensitive to starting stresses, and is predominantly governed by the stress or, equivalently, the strain range between the 25 and 100 percent power extremes. With such two-power-level cases, an accurate relation can be developed between acceptable stress range, the difference in the two stresses, and a desired range of temperatures. This is accomplished by analyzing a series of stress ranges at each of several desired temperatures spanning the operating range of interest. The stress range in the series giving a total accumulated creep damage equal to unity is the allowable stress range. A 1.1 factor on stress range is also included to satisfy the requirements of [2].

Base-loaded (monthly) cycles are characterized by excursions between 0 and 100 percent power. Shutdown, or zero power, occurs at low temperatures, and thus no creep relaxation takes place. Maximum operating temperatures occur at 100 percent power and at constant applied strain. This is a stress-strain cycle with a single hold time at elevated temperature. When plasticity occurs on shutdown, high stresses are repeatedly regenerated at 100 percent power; otherwise the cycle is essentially a single relaxation with elastic unloading at monthly intervals. Calculations of creep damage during cycles with plasticity have shown that typical heat exchanger materials have unacceptable accumulated creep damage. (Fg. 6 shows cycles with and without repetitive plastic strain after initial shakedown.) An allowable stress range which avoids such repetitive plasticity ensures that excessive damage does not occur. Therefore, for this monthly cycle, the total allowable stress range is set equal to the material low-temperature proportional limit plus 0.9 times the high-temperature rupture stress for the desired operating time.

Based on these two operating cycles (weekly and monthly), calculations were performed to determine allowable stress ranges for 2-1/4 Cr − 1 Mo steel and Alloy 800H for a 32 year life (assumes 80 percent availability during a 40 year design life). Fig. 7(a) summarizes the calculations for 2-1/4 Cr − 1 Mo steel. For temperatures below about 400°C, the standard $3S_m$ low-temperature code limit is incorporated for simplicity; fatigue rather than creep usually governs life. The base-loaded, or monthly, cycle provides a larger stress range than the weekly cycle, particularly at high temperatures. Fig. 7(b) shows a similar curve for Alloy 800H. The reference [2] allowable creep/fatigue stress for Alloy 800H for these two operating cycles is also shown for comparison in Fig. 7(b). (Stress and strain are essentially equivalent for elastic material behavior.) This limiting stress for elastic analysis is less than or equal to the current method results, as it should be for less detailed analysis.

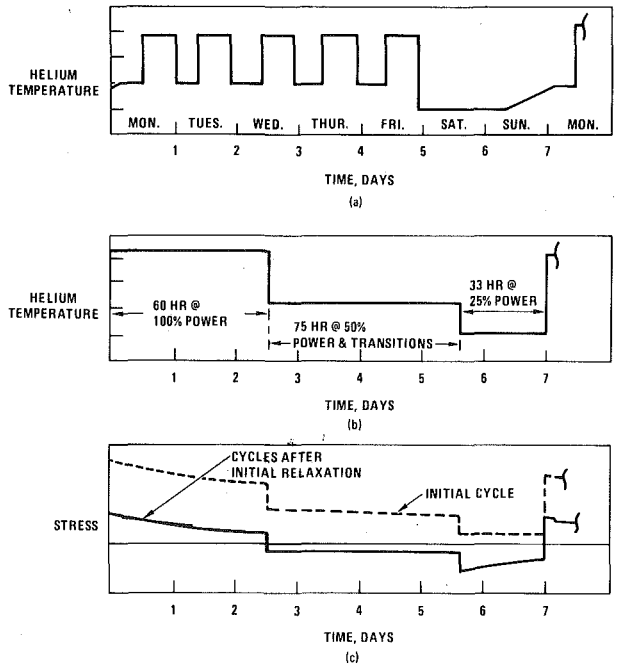


Fig. 5 Weekly power cycle, associated analysis cycle, and stress variations (a) weekly power cycle (b) equivalent cycle for damage calculations (c) stress-time history for (b)

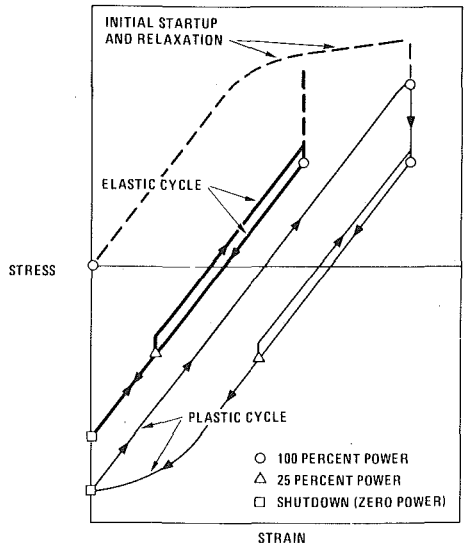


Fig. 6 Stress-strain cycles due to high-temperature gas-cooled reactor power changes

Downloaded 01 Jun 2010 to 171.66.16.58. Redistribution subject to ASME license or copyright; see http://www.asme.org/terms/Terms_Use.cfm

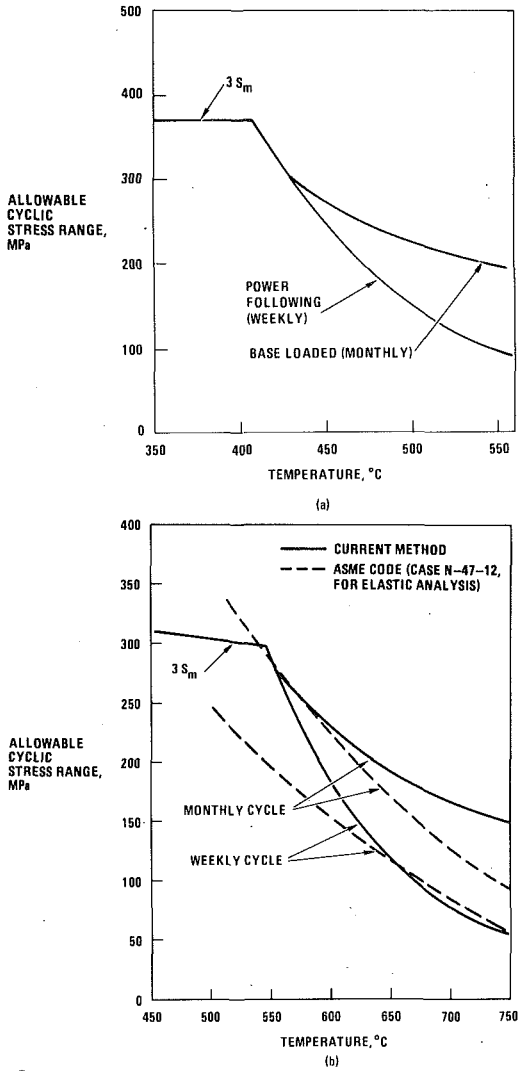


Fig. 7 Comparison of analysis method and ASME creep/fatigue allowable stresses (*a*) 2-1/4 Cr − 1 Mo steel (*b*) alloy 800H

Test Verification

It is desirable to obtain test data which would substantiate the design curves. The startup to maximum power cycle (a strain cycle with a single hold time at maximum applied strain) has been tested. However, strain ranges have generally equaled or exceeded 0.5 percent while 0.2 percent or less is estimated for a practical design. Hence, fatigue damage contributed the largest damage fraction, making it difficult to isolate the creep-related damage fraction. Test cycles for the weekly and monthly design curves are shown in Fig. 8. Families of design curves (such as those shown in Fig. 9(*a*)) of strain range versus cycle to failure are needed for the applicable operating temperature ranges. Curves of strain range versus cycle to failure can be extrapolated from high-strain-range, short-life tests to low-strain, long-life operating conditions. However, it is necessary to limit test strain ranges so that an acceptable cycle can be maintained (i.e., one *without excessive fatigue damage*). Small strain ranges, preserving the desired stress-strain cycle, must have hold times of 1 to 5 min to limit test times to less than one year. Consequently, hold times must also be extrapolated, since typical weekly and monthly hold times are of the order of 10 and 1000 hours, respectively. The proposed method of achieving hold time extrapolation is to conduct strain cycling tests with various hold times so that stress histories can be determined; no specimen failure occurs during testing. Based on the inferred damage per cycle (using equation (4)) in the short hold time failure tests, damage per cycle can be computed from these stress histories. The families of curves shown in Fig. 9(*b*) can then be generated. An example extrapolation of damage per cycle as a function of hold time is shown in Fig. 10. The stress histories were determined at hold times

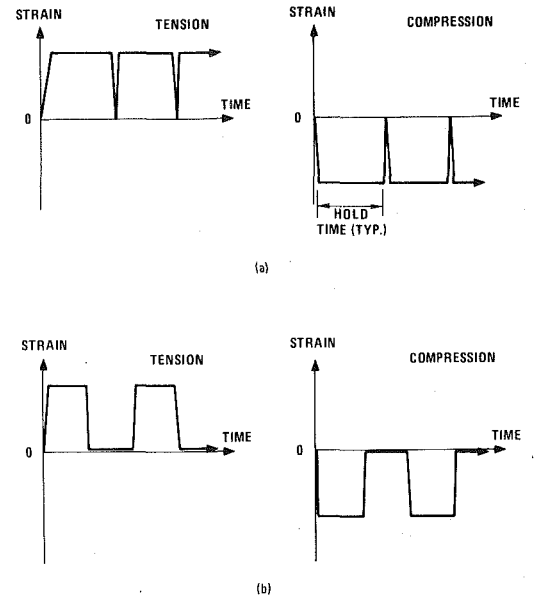


Fig. 8 Strain-time histories for two reactor operating cycles (*a*) base-loaded (monthly) cycle (*b*) load-following (weekly) cycle

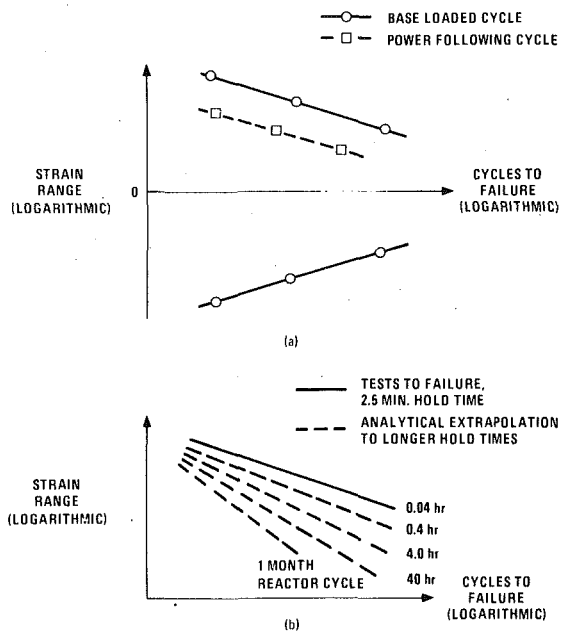


Fig. 9 Creep/fatigue data reduction (*a*) failure test results at a single test temperature (*b*) use of stress histories to predict life at longer hold times

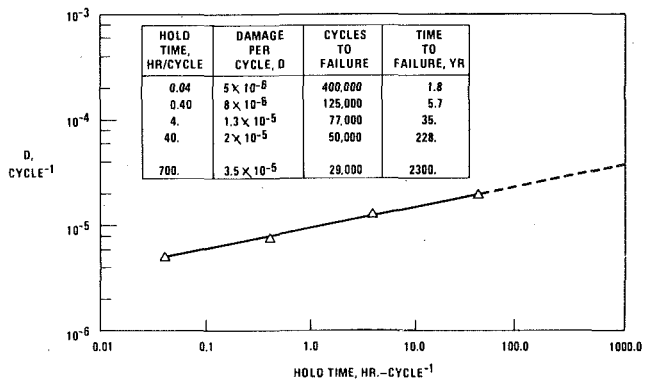


Fig. 10 Estimated creep/fatigue damage per cycle (650°C)

Downloaded 01 Jun 2010 to 171.66.16.58. Redistribution subject to ASME license or copyright; see http://www.asme.org/terms/Terms_Use.cfm

of 0.04, 0.4, 4.0, and 40 hours. The damage computed at each of these times is shown in Fig. 10 and provides a reasonably straight-line logarithmic extrapolation to the desired 700 hour hold time. The predicted cycles to failure are also shown in Fig. 10 and decrease from 400,000 to 29,000 for hold times of 0.04 to 700 hours per cycle. The test times to failure would, however, increase from 1.8 years to essentially unlimited specimen life. Such test times are clearly unrealistic; however, the design strain ranges could be of the same order of magnitude as those of the test, since allowable ranges are calculated using minimum creep rupture properties and include a 1.1 safety factor on stress.

Concluding Remarks

A tube design procedure which emphasizes simplified structural analyses is described for preliminary and conceptual heat exchanger designs. Elastically calculated operating stresses are compared with the allowable creep/fatigue stresses currently derived from simplified inelastic analysis. Because of a lack of supporting test data, the allowable stresses are less accurately known than the operating stresses. Improvements of the method can only be realized by increasing our knowledge of the material creep/fatigue behavior for low strain ranges and long-life design requirements. A test method is proposed which is designed to reduce uncertainties associated with extrapolation of strain and hold times so that acceptable long-life predictions can be derived from short-time test data.

Acknowledgments

The author is grateful for the helpful comments and suggestions given by Mr. M. Lasarev and Mr. R. H. Ryder of General Atomic Company.

References

1 Roark, R. J., *Formulas for Stress and Strain,* McGraw-Hill, New York, 1965.

2 ASME Code Case N-47-12, Nov. 21, 1977.

Downloaded 01 Jun 2010 to 171.66.16.58. Redistribution subject to ASME license or copyright; see http://www.asme.org/terms/Terms_Use.cfm

D. D. DeFur
Senior Design Engineer
Combustion Engineering, Inc.
911 West Main Street,
Chattanooga, TN 37403

An IHX Design for Pool Type LMFBR System Application

This paper presents the design of a 500 MWt Intermediate Heat Exchanger (IHX) for application in a multi-zone pool-type Liquid Metal Fast Breeder Reactor System. The primary feature around which this design was developed is the ability to function under all steady-state and transient conditions without the need for a distinct mechanical feature to accommodate differential thermal expansion between the tube bundle and shell. This is accomplished by using thermal baffles and judiciously adjusting the ratio of shell length in contact with the hot and cold pools of the multi-zone reactor. Thus, the component shell is maintained at a higher temperature than the tube bundle and the tubes are basically tension members. Under certain transient conditions the tubes heat up and become compression members but are not loaded to the point of buckling. A secondary, but not less significant, feature is the low primary side pressure drop and good flow distribution offered by this design. (Multi-zone reactor systems have no hard piping between the IHX outlet and primary pump inlet; therefore, the relatively small differential head of sodium between the two pools is the only driving element which causes flow through the primary side of the IHX. For this reason, a low primary side pressure drop is essential). To accomplish this, the primary sodium flows through the tube side of the component where the flow channel is simple and unimpeded by tube supports or other restrictions. Secondary flow distribution, through the shell side of the unit, can be adjusted as required since a higher pressure drop can be tolerated.

Introduction

The design presented in this paper is a shell and tube counterflow heat exchanger designed for use as an intermediate heat exchanger (IHX) for application in a multi-zone sodium cooled pool type liquid metal fast breeder reactor system. The design was developed during 1977–78 by Combustion Engineering, Inc., under contracts to the Electric Power Research Institute (EPRI). The reactor system is rated at 3000 MWt (1000 MW gross electric) and requires six of the IHX components; therefore, the IHX has been designed as a 500 MWt unit.

Functionally, the IHX is the interfacial device between the radioactive primary sodium, which serves as the core coolant medium, and the nonradioactive intermediate sodium, which serves as a heat transport medium. As shown in Fig. 1, the IHX is physically located within the reactor such that heat can be extracted while maintaining the entire inventory of radioactive materials within the confines of the reactor vessel. (The intermediate sodium is at a slightly higher pressure than the primary sodium such that any leakage will be into the reactor vessel).

The multi-pool reactor concept provides no hard piping for the primary sodium either to or from the IHX. The pumps force primary fluid from the lower or cold pool, through the reactor core, into the upper or hot pool. Since the only driving head causing primary flow through the IHX is the relatively small elevation differential between the two respective pools, the IHX design must offer low resistance to primary sodium flow. Thus, a major design objective was to provide a relatively small primary side pressure drop with uniform flow distribution.

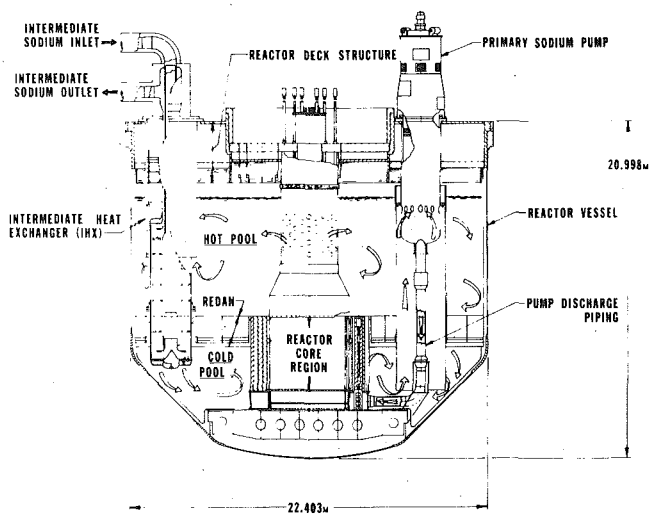


Fig. 1 Pool type liquid metal fast breeder reactor layout

Contributed by the Nuclear Energy Committee and presented at the Pressure Vessel Piping Conference, June 25–29, 1979, San Francisco, California of THE AMERICAN SOCIETY OF MECHANICAL ENGINEERS. Manuscript received at ASME Headquarters March 26, 1979. Paper No. 79-NE-3.

Copyright © 1980 by ASME
Downloaded 01 Jun 2010 to 171.66.16.58. Redistribution subject to ASME license or copyright; see http://www.asme.org/terms/Terms_Use.cfm

Most heat exchanger designs, regardless of their intended application, incorporate some distinct mechanical device for accommodating differential thermal espansion between the tube bundle shell and tube bundle. Bent tubes and bellows joints are among the most common devices found within IHX designs. The concept presented in this paper, however, circumvents the need for such a device by judiciously utilizing the environment to permit the use of a continuous shell with no bellows joints and straight tubes within the tube bundle. The avoidance of using bent tubes simplifies component manufacturing procedures and subsequent inspection and repair of units which have been in service, and the avoidance of utilizing a bellows joint negates the necessity for continuously monitoring for bellows failures and increases the overall reliability and availability of the plant.

IHX Design Description

The IHX can be generally described as a vertically oriented, top supported, shell and tube, counterflow heat exchanger. As shown in Fig. 1, the IHX is attached to and supported from the upper surface of the reactor cover structure (deck). The component extends downward through the hot pool through an opening in the pool separator structure (redan) and terminates in the cold pool. Sodium flow circuits through the component are as follows:

- Primary sodium enters the tube side of the IHX by flowing from the hot pool upward through the annulus formed between the tube bundle shell and support skirt and into the inlet plenum above the upper tubesheet. The fluid then enters the tubes and flows downward through the length of the tube bundle giving up heat through the tube walls and exists directly into the cold pool below the lower tubesheet.
- Intermediate sodium, returning from the steam generators through a closed, piped loop, enters the IHX through the 762 mm (30 in.) dia central downcomer pipe. After making an essentially isothermal passage through the downcomer to the lower extremity of the tube bundle, the fluid is guided radially outward in crossflow by flow baffles into the shell side of the component. The fluid then begins to flow upward receiving heat through the tube walls from the counterflowing primary sodium. After having traversed the entire length of the tube bundle and having reached the upper region of the tube bundle, the flow is guided radially inward in crossflow by flow baffles to the riser annulus formed between the 1067 mm (42 in.) riser and 762 mm (30 in.) downcomer pipes. After passing upward through the outlet plenum, the flow is directed back to the steam generators.

Fluid flow rates and temperatures are as tabulated below:

	Primary Sodium	Intermediate Sodium
Mass Flow Rate-Kg/s	2495	2772
(lbm/hr × 10^6)	(19.8)	(22.0)
Inlet Temperature °C	468	285
(°F)	(875)	(545)
Outlet Temperature °C	311	427
(°F)	(591)	(800)

With the above described flow arrangement, primary and intermediate side pressure drops have been calculated to be 17.2 kPa (2.5 psi) and 103.4 kPa (15.0 psi), respectively. As stated in the introduction, the multi-zone pool type liquid metal fast breeder reactor system dictates a low primary side pressure drop with uniform attendant flow distribution. The above stated values of pressure drop are acceptable and as the computer flow code output demonstrates in Fig. 2, the primary side flow distribution is uniform within an acceptable margin. The results of intermediate side flow distribution analyses are not available for this publication; however, the higher allowable pressure drop range would permit the incorporation of flow distribution devices as necessary to rectify any maldistribution problems which might arise.

The total dry weight of the IHX assembly is approximately 208 t (230 tons). As shown in Fig. 3, the unit extends downward approximately 15 m (50 ft) from the top of the support flange to the lower

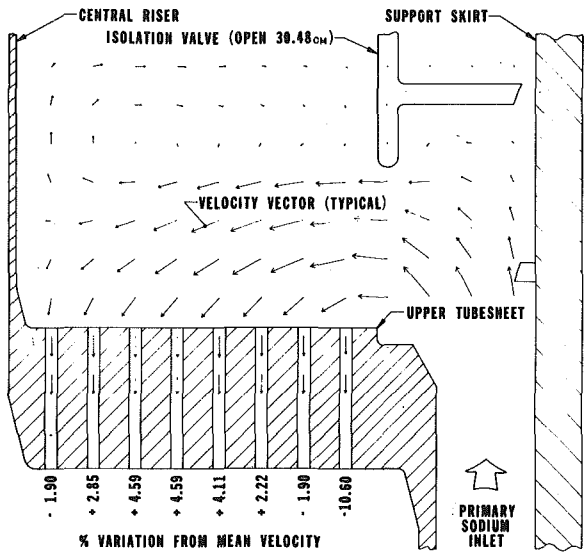


Fig. 2 Primary inlet flow distribution

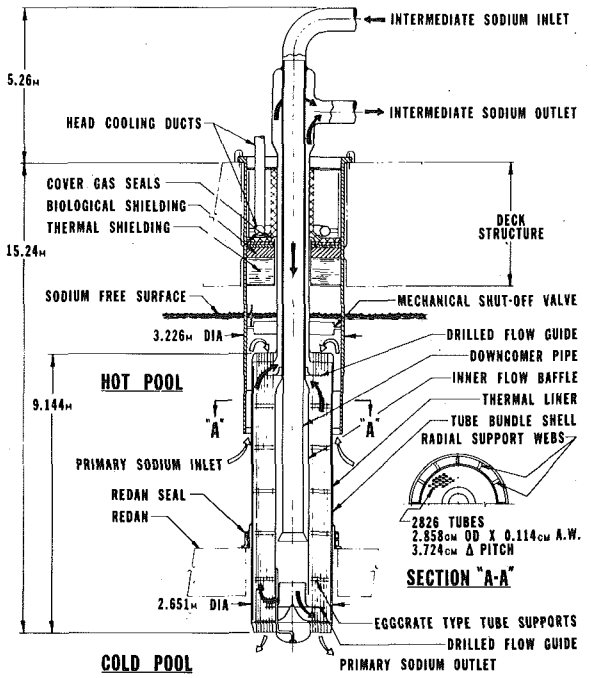


Fig. 3 Elevation view of IHX

surface of the lower tubesheet and upward approximately 5 m (17 ft) to the upper extremity of the intermediate sodium inlet pipe. Thus, the overall length of the IHX is approximatley 20 m (67 ft). Extreme diameters are 3658 mm (144.00 in.), 3226 mm (127.00 in.), and 2651 mm (104.38 in.) for the support flange, the support skirt, and the tube bundle shell, respectively. The dimension over the tubesheets is 9144 mm (30 ft, 0 in.) and the heated length of the tubes is 8534 mm (28 ft, 0 in.). The tube bundle is comprised of 2826 tubes placed in a triangular array with a center to center pitch of 37.24 mm (1.466 in.). There are 366 surplus tubes in the tube bundle to allow for contingencies in manufacturing, inaccuracies in the heat transfer correlations, tube wall tolerance adversities, tube plugging, and other uncertainties. The tubes are a nominal 28.58 mm (1.125 in.) OD with an average wall thickness of 1.14 mm (0.045 in.).

Except for the drilled flow guides in the inlet and outlet regions, all tube supports are of the eggcrate type manufactured from rectangular bars 3.18 mm (0.125 in.) in thickness. There are eight of these tube supports located approximately 940 mm (37 in.) apart, along the length of the tube bundle. The 25.4 mm (1.0 in.) thick thermal liner

Downloaded 01 Jun 2010 to 171.66.16.58. Redistribution subject to ASME license or copyright; see http://www.asme.org/terms/Terms_Use.cfm

and the 12.7 mm (0.5 in.) thick flow shroud encase the outer and inner peripheries of the tube bundle as closely as feasible; however, there are still regions where the triangular pitch tube bundle peripheries do not match well with the adjacent circular members. Thus, close fitting seal plates are provided at each tube support elevation to force peripheral fluid back into the tube bundle for mixing. These plates preclude gross, straight through sodium streaming or bypass of the heating surfaces of the tubes. (It should be noted that such problems with streaming are not unique to this design but are generic to all triangular pitch tube bundle designs.)

Both tubesheets are 304.8 mm (12.00 in.) thick and have the 38.1 mm (1.50 in.) thick cylindrical tube bundle shell welded to them at the tubesheet midplane. The tube-to-tubesheet joint is made by explosively expanding the tubes into the tubesheet holes and welding the tubes to the tubesheet on the primary sodium side.

The weight of the entire lower assembly consisting of the tube bundle, the tube bundle shell, the thermal liner, the flow shroud, the tube supports, the tubesheets, the downcomer and riser pipes, etc., is transmitted into the lower portion of the support skirt by 12 38.1 mm (1.50 in.) radial webs which bridge across the primary sodium inlet annulus as shown in Section A-A of Fig. 3. Thus loads of every origin (i.e., dead weight, vertical seismic, and horizontal seismic) are transmitted through the 109.5 mm (4.31 in.) thick support skirt into the deck. Vertical loads are taken at the mechanical joint at the top of the deck and horizontal loads are taken as a couple within the thickness of the deck.

The deck plug region is comprised of numerous thicknesses of plate stock. There is a total of approximately 720 mm (28.25 in.) of steel in this area. The thin lowermost plates, 40 pieces 2.5 mm (0.10 in.) in thickness spaced 19.1 mm (0.75 in.) apart, are reflective thermal insulation. Above the thermal insulation are three other plates for biological shielding: one piece 330 mm (13.00 in.) and, two 108 mm (4.25 in.). The uppermost, or cover plate, is 50.8 mm (2.00 in.) thick. The reactor cover gas seal is located at the upper face of the uppermost 108 mm (4.25 in.) plate. This location was chosen because of accessibility for seal inspection. There is a cooling system above the cover gas seal to remove heat from the upper region of the support skirt. Air from the containment building environment is drawn down through a duct to a distribution ring just above the cover gas seal. After passing into the annular cooling riser provided, the air rises and picks up heat from the inner diameter of the support skirt. The heated air exits the plug region through a 9 m (30 ft) chimney. Thermal insulation is provided around the intermediate sodium riser pipe and across the cover gas seal region to limit heat losses in these areas.

The design includes a mechanical valve assembly in the primary sodium inlet region. The purpose of this value is to stop primary sodium flow and thereby isolate the IHX for removal or during certain transient conditions where the IHX might be damaged if flows are permitted to continue. The valve is driven by a number of ball screw actuators coupled to a single electric gear motor.

A spring loaded piston ring type seal is provided at the top surface of the redan to prevent short circuit flow from the hot pool to the cold pool. This design accommodates the relative motions due to differential thermal expansion between the deck and redan as well as the 36.6 mm (1.44 in.) deflections which will exist during a seismic event. The entire seal assembly is attached to and is removable with the IHX for ease of inspection and repair.

There are several noteworthy points pertaining to fabricability, inspectability, maintainability, and reliability which are associated with the simplicity of this design. These are summarized briefly as follows:

- The design features primary sodium flow through the tube side of the component and there are no heads or other hindrances to limit direct access to the tubesheets. This simplifies decontamination procedures; provides for more direct inspection and repair of tube-to-tubesheet welds; and, greatly simplifies tube replacement.
- The straight tube design, while more difficult to analyze, is much easier and less costly to fabricate than a bent tube design. In addition, since bend regions are difficult to support, many bent tube designs have a lower ratio of heat transfer length to actual tube length than does the straight tube design.
- The design avoids the use of bellows joints and floating heads, while bellows joints do provide a conservative approach to dealing with the tube bundle shell to tube bundle differential thermal expansion problem, they are within themselves rather fragile members and require constant surveillance for failures and reduce the overall reliability and availability of the component.

The entire IHX is designed and fabricated to the requirements of Section III, Class 1 of the ASME Boiler and Pressure Vessel Code for Nuclear Components, including Code Case 1592. Materials of construction are Type 304, Stainless Steel throughout the design.

Maintenance and Repair

Hot standby conditions for the pool system for which this IHX was designed were defined as being at 204°C (400°F). Remote maintenance and repair in a sodium environment at this temperature is not believed to be realistically achievable; therefore, it has been assumed that a unit in need of repair would be removed from the reactor vessel and be decontaminated prior to being repaired utilizing currently available techniques. The procedure for accomplishing removal and reinstallation of an IHX is basically as outlined below:

- The reactor would be brought to the 204°C (400°F) hot standby condition.
- The intermediate side of the IHX would be emptied of its contents utilizing the drain line provided.
- A heated cask with an appropriate floor valve attached would be positioned over the IHX and the unit would be lifted from the reactor vessel after having been cut out of the intermediate loop and disconnected from the reactor deck.
- Utilizing the cask as a temporary containment, the IHX would then be moved to a repair area where it would be cooled to room temperature and be decontaminated.
- Repair work would be accomplished utilizing state of the art techniques.
- The IHX would then be repositioned on the reactor deck, preheated to 204°C (400°F), and be lowered back into the reactor vessel.
- After reattaching the IHX to the deck and welding the intermediate sodium piping back into place, the intermediate side of the component would be refilled and the unit would be placed back into an operational state.

Design Justification

As with any novel or out of ordinary design, there are questions which must be addressed concerning the design's ability to function under all normal and abnormal operating conditions under which it is expected to operate. With this design, which features straight tubes with no floating heads or bellows joints, the primary questions allude to the possibility of tube or tube bundle shell buckling under transient conditions. This is certainly a viable area within the design to question and has therefore been rigorously analyzed under all known operational conditions to verify that the design will not fail to function properly.

It is by no coincidence that the tube bundle shell is positioned partially in contact with the hot pool and partially in contact with the cold pool. It is this placement and selection of the proper ratio of shell length contacting the two respective pools that afford this design the ability to function with no bent tubes or bellows joints. By protecting the shell from the cooler intermediate sodium flow and by flowing the primary fluid through the tube side of the unit, it is possible to cause the unit to operate between the compressive limits of the tube bundle and tube bundle shell.

The following paragraphs define the compressive limits between which the unit must operate, list the transient conditions for which the design has been analyzed, and demonstrate that the unit operates between these specified limits.

Throughout the remaining portions of this paper frequent reference will be made to the tube bundle shell to tube bundle temperature

Downloaded 01 Jun 2010 to 171.66.16.58. Redistribution subject to ASME license or copyright; see http://www.asme.org/terms/Terms_Use.cfm

differential (ΔT). This temperature differential is defined as follows:

$\Delta T = \overline{T}_{\text{Shell}} - \overline{T}_{\text{Tube Bundle}}$

where, $\overline{T}_{\text{Shell}}$ = Mean shell temperature averaged along the entire length of the shell

and, $\overline{T}_{\text{Tube Bundle}}$ = Mean temperature of a typical tube within the tube bundle averaged along the entire length of the tube bundle

Acceptable Limits of ΔT

Structural analyses based upon the tube bundle shell thickness, tube sizes, tube support spacing, and other geometric parameters have shown that tube bundle shell buckling will occur at a ΔT of +98.3°C (+177°F) and that the tube bundle will buckle at a ΔT of −32.2°C (−58°F). Thus, these values become the short term allowable limits between which the IHX must remain functional. When material creep and racheting effects are considered in determining long term allowable limits for ΔT values, it has been found that the bounding values reduce to +88.9°C (+160°F) and −22.2°C (−40°F), respectively. Thus, for steady state operation or other long term operating conditions, ΔT must be between the long term limits; and, during transient conditions, ΔT must be between the short term limits.

Even though subsequent paragraphs will demonstrate that the design functions comfortably between these limits, it should be pointed out that buckling of either element would not result in a catastrophic event. Buckling would be of the strain controlled type where axial deflection would be limited to the thermally-induced strain; therefore, there is no danger of gross collapse of either a single tube or the entire unit. To substantiate this fact, crude buckling tests were performed imposing axial deflections up to 6.35 cm (2.5 in.), and order of magnitude greater than is possible in an operational unit, and no indications of loss of tube integrity were found. It should be noted, however, that buckled tubes could contact one another and if left uncorrected for an extended period of time could leak due to mechanical wear.

Steady-State Operation

After having analyzed the design for several selected harsh transient conditions, and after comparing the value of ΔT produced by each to the calculated short term allowable range of ΔT, the position of the shell relative to the redan was set as shown in Fig. 3. Thus, at the normal operating steady-state design point to value of ΔT is +41.1°C (+74°F). This falls comfortably away from the two long term limits; therefore, no creep or material racheting problems should exist.

Transient Conditions with Highest Potential for Buckling

After having analyzed the design for the entire gamut of transients shown in Table 1, the conditions attendant with the inadvertent opening of a relief valve on a steam generator being fed by the intermediate sodium from the IHX (transient number 6 in Table 1) was determined to impose the worst possible compressive loading condition on the tube bundle shell. As shown in the ΔT versus time curve of this transient, Fig. 4, a peak positive ΔT valve of +82.2°C (+148°F) occurs. It should be pointed out that even though this value is significantly below the allowable buckling limit of +93.8°C (+177°F), this value assumes perfect pool stratification beginning immediately after the transients starts. It is known that some degree of mixing will exist within the pool and therefore the value of ΔT from Fig. 4 is somewhat conservative.

On the other end of the spectra, it was determined that the conditions attendant with an inadvertent water side isolation and dump of a steam generator loop being fed by the IHX (transient number 4 in Table 1) imposed the worst possible compressive loads on the tube bundle. As shown in Fig. 5, the lowest negative value of ΔT is −23.9°C (−43°F). Again, this value falls comfortably short of the allowable shell buckling limit of −32°C (−58°F).

Table 1 List of transients

Transient Number	Description
1	The reactor is tripped from full power with normal decay heat and assuming perfect mixing in the hot pool (no stratification).
2	The reactor is tripped from full power with normal decay heat and assuming no mixing in the hot pool (stratification).
3	Loss of power to one intermediate pump with the affected loop being isolated from the system by closing the isolation valve. Plant continues operation at 5/6 of full power.
4	The inadvertent waterside isolation and dump of a steam generator loop resulting in a reactor trip.
5	The inadvertent opening of a steam generator outlet relief valves resulting in a reactor trip with no stratification.
6	The inadvertent opening of a steam generator's outlet relief valves resulting in a reactor trip with stratification.
7	The inadvertent dump of intermediate loop sodium with the affected loop being isolated by closing the isolation valve. The plant is then shut down.

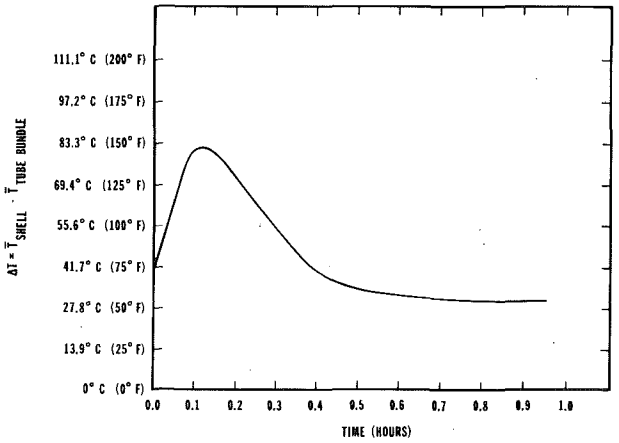


Fig. 4 ΔT response for transient number 6; stratified, inadvertant opening of steam generator outlet relief valve

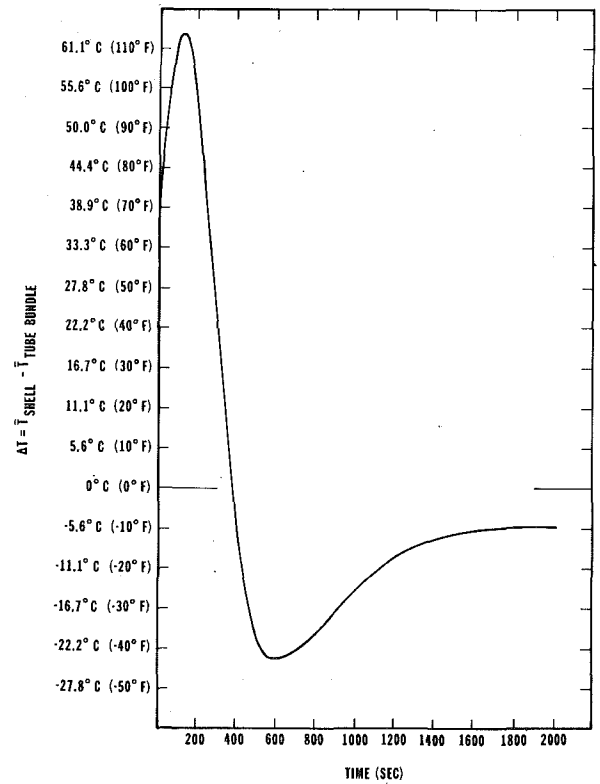


Fig. 5 ΔT response for transient number 4; inadvertent waterside isolation and dump of steam generator loop

Downloaded 01 Jun 2010 to 171.66.16.58. Redistribution subject to ASME license or copyright; see http://www.asme.org/terms/Terms_Use.cfm

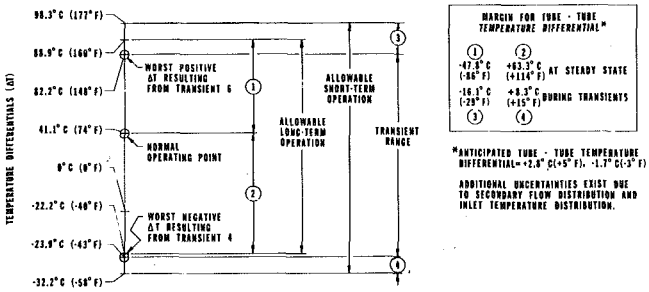


Fig. 6 Design justification summary

Summary

Fig. 6 provides a graphic summary of the design justification. As noted in that figure, the "worst case" transients are sufficiently within the allowable ΔT range to allow a significant margin to prevent individual tube buckling as a result of tube to tube temperature differentials.

Acknowledgments

The author is grateful to Combustion Engineering, Inc. and the Electric Power Research Institute for allowing the publication of this paper. In addition, appreciation is extended to the following individuals who actively participated in the project from which this design emerged:

R. B. Creek, Senior Design Engineer, (Responsible for conceptual design layouts and design assistance).

D. R. Dodson, Senior Designer/Draftsman, (Responsible for drafting and other graphic support).

A. W. Lubkowitz, Senior Analytical Engineer, (Responsible for thermal analyses and transient evaluation).

M. G. Sowers, Senior Analytical Engineer, (Responsible for hydraulic and flow distribution evaluation).

J. E. Wilson, Analytical Engineering Supervisor, (Responsible for structural analyses).

Downloaded 01 Jun 2010 to 171.66.16.58. Redistribution subject to ASME license or copyright; see http://www.asme.org/terms/Terms_Use.cfm

A. H. Spring
Engineering Supervisor.

D. D. DeFur
Senior Design Engineer.

Combustion Engineering, Inc.
911 West Main Street,
Chattanooga, TN 37403

A High Reliability Straight Tube LMFBR Steam Generator Design

Straight-tube counterflow steam generators for LMFBR applications have been proposed, tested, fabricated and operated with varying degrees of success. A new embodiment of the straight-tube concept is described which incorporates a number of unique features which contribute to high reliability and availability. These features include a replaceable bellows for accommodation of differential thermal expansion between shell and tubes and a redundant, crevice-free tube-to-tubesheet joint design. The design can also easily incorporate single-wall or double-wall tubes. Single and double-wall tube versions are described whose thermal and geometric size are based on anticipated manufacturing limitations. The results of scoping tests of the tube-to-tubesheet welds are described which provide positive indications of the soundness of the weld design.

Introduction

Straight-tube counterflow heat exchangers for LMFBR steam generator applications have been proposed, tested, fabricated and operated with varying degrees of success. Notable examples are the EBR-II Steam Generator [1] and the SNR Proto-type [2]. The principal concerns in the development of such designs have been related to providing an appropriate means for accommodating differential thermal expansion between the tube bundle and component shell, as well as between tubes within the tube bundle. The choice of tube-to-tubesheet weld configuration has also been shown to have a strong influence on component reliability with a secondary impact on available fabrication approaches. Control of differential thermal expansion can be achieved by utilizing mechanical devices (e.g., a bellows expansion joint in the shell [2], bent tubes, etc.) or in some cases [3], through careful attention to steady-state and transient operating conditions. In the design for EBR-II [1], the shell was thermally elongated during tubing installation so that the tubes were in compression at room temperature and hence a relaxed stress state was achieved under operating conditions. For tube-to-tube differential expansion, prediction or experimental verification of flow and temperature maldistributions are necessary to determine the integrity of a straight-tube design. The SNR [2] design represents an example where proto-typical testing revealed unacceptable temperature variations across the tube bundle due to excessive bypass flow at the tube bundle periphery.

In the discussion to follow, a straight-tube steam generator design is presented which incorporates a replaceable bellows expansion joint in the component shell for accommodating differential thermal expansion between the tube bundle and shell. Other features include a crevice-free tube-to-tubesheet joint which is readily adaptable to either a single-wall or double-wall tube arrangement.

Design Description

In order to illustrate the concept and describe the constraints imposed on configuration definition, the thermal design conditions listed in Table 1 were used as the basis for design. The conditions are representative of large-scale LMFBR plant steam generator design conditions. The tube bundle geometry (tube size, tube pitch, heated length, and number of tubes) was selected on the basis of the parametric studies and subject to the constraints listed in Table 2. Within these constraints the general approach was to choose a minimum number of maximum length tubes and hence minimize the required

Table 1 Thermal design conditions

Power Per Loop, MWt	1050
Sodium Side	
Superheater Inlet Temp, °C	510
Flow Rate, kg/s	4956.2
Water Side	
Superheater outlet temp, °C	485
Superheater outlet pressure, MPa	16.96
Flow Rate, kg/s	499.7
Evaporator Type	Once-through

Table 2 Assumed tube bundle configuration constraints

Constraint	*Explanation*
Heated Length < 22m	Fabricability and tubing availability
Bundle Diameter < 2.6m	Tubesheet thickness and forging availability
Sodium Velocity < 9m/s	Erosion considerations
Steam Velocity < 36m/s	Erosion considerations
Tube Spacing > 1.3cm	Access for tube-to-tubesheet welding

Contributed by the Nuclear Energy Division and presented at the Pressure Vessels and Piping Conference, June 25–29, 1979, San Francisco, California of THE AMERICAN SOCIETY OF MECHANICAL ENGINEERS. Manuscript received at ASME Headquarters March 23, 1979. Paper No. 79-NE-4.

Copyright © 1980 by ASME

Downloaded 01 Jun 2010 to 171.66.16.58. Redistribution subject to ASME license or copyright; see http://www.asme.org/terms/Terms_Use.cfm

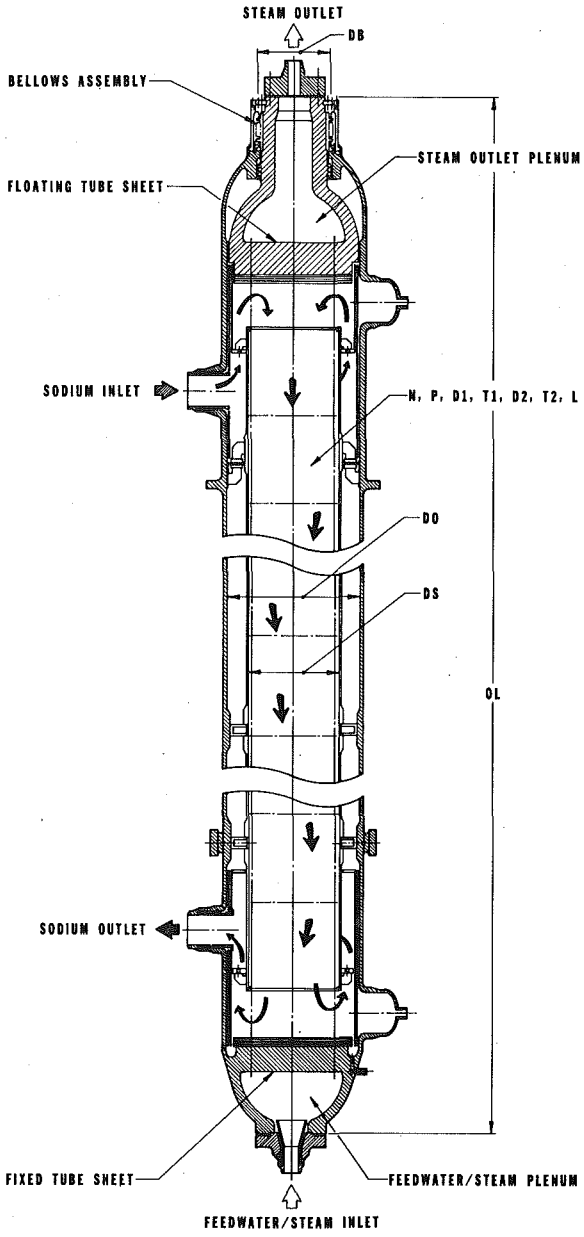


Fig. 1 Steam generator elevation

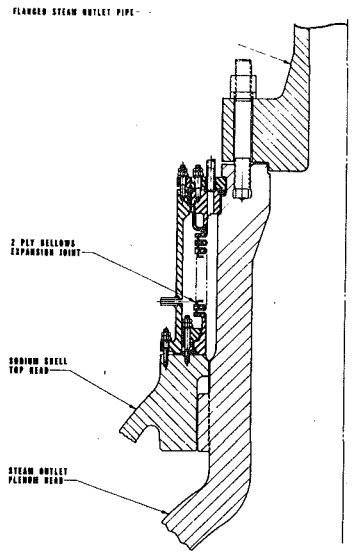


Fig. 2 Bellows expansion joint

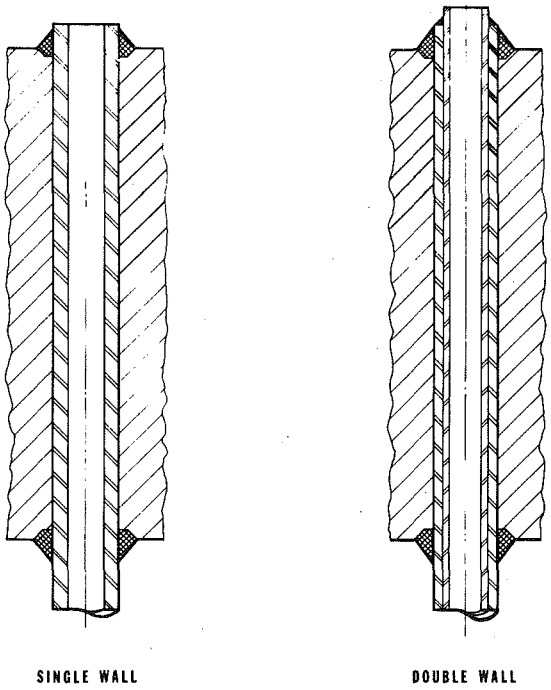


Fig. 3 Tube-to-tubesheet weld

Table 3 Steam generator dimensional details

	Superheater		Evaporator	
	Single Wall	Double Wall	Single Wall	Double Wall
Thermal rating, MW	155	155	185	185
Number per loop	2	2	4	4
Overall length (*OL*), m	25.16	26.21	24.89	26.19
Shell outside diameter (*DO*), m	1.83	2.49	1.72	2.51
Shroud outside diameter (*DS*), m	1.29	1.86	1.18	1.92
Number of tubes (*N*)	663	1378	894	1985
Tube material	2¼ Cr − 1 Mo	2¼ Cr − 1 Mo	2¼ Cr − 1 Mo	2¼ Cr − 1 Mo
Outer tube outside diameter (*D*1), mm	22.2	25.4	19.1	22.2
Outer tube wall thickness (*T*1), mm	4.7	4.4	3.2	3.2
Inner tube outside dia (*D*2), mm	—	16.5	—	15.9
Inner tube wall thickness (*T*2), mm	—	2.3	—	2.3
Tube pitch (*P*) (triangular), mm	42.5	44.5	34.9	38.1
Heated length (*L*), m	21.3	21.3	21.3	21.3
Bellows diameter (*DB*), m	0.9	0.9	0.9	0.9

Downloaded 01 Jun 2010 to 171.66.16.58. Redistribution subject to ASME license or copyright; see http://www.asme.org/terms/Terms_Use.cfm

number of tube-to-tubesheet welds. This approach tends to reduce fabrication cost and increase component reliability.

Based on the selected tube bundle configuration, mechanical design layouts for both single-wall and double-wall tube configuration were developed. Fig. 1 illustrates the overall layout with dimensional details for the two cases listed in Table 3. The configurations selected require four evaporators and two superheaters to provide a loop output of 1050 MWt. Some of the more significant design features, indicated in Fig. 1, are as discussed below:

Bellows Expansion Joint. A bellows expansion joint is located at the top of the steam generator to accommodate thermal growth differentials between the shell and the tube bundle during steady-state and transient operating conditions. (Additional detail of the bellows region is shown in Fig. 2.) This particular location, as opposed to a mid-shell location for the bellows, offers three distinct advantages. First, a reasonable bellows diameter is achievable, second, bellows replacement can be accomplished with minimum effort and, third, potential loss of sodium inventory due to a bellows failure is minimized. These advantages more than offset concerns relative to the higher temperature environment found in the upper extremity of the component.

Tube-to-Tubesheet Weld. The tube-to-tubesheet attachment for both the single-wall and double-wall versions of the steam generator are depicted on Fig. 3. This attachment consists of redundant "J-Groove" configuration welds on either side of the tubesheet. The J-Groove weld geometry is commonly applied in boiler and pressure vessel fabrication and in this application is designed as a multi-pass weld with filler wire added to give a throat dimension 1.5 to 2 times the tube wall thickness. While the redundant nature of the welds obviously raises some questions of thermal restraint, testing and analysis to determine feasibility and potential failure modes have been performed (see Section 3). The redundant weld geometry performs two functions. First, it requires failure of either two welds or a single weld and the tube wall (between tubesheets) before a sodium water reaction could result from a tube-to-tubesheet attachment failure. The double-wall configuration shown in Fig. 3 is generically the same as the single-wall design except that a back-up boundary (the second tube wall) is added to further minimize the likelihood of a sodium water reaction occurring as a result of tube failure away from the tube-to-tubesheet attachment region. Second, this configuration provides a crevice-free sodium side weld joint. This feature is viewed by many as being a mandatory feature of sodium heated steam generators.

Fabrication Approach. The bellows expansion joint and tube-to-tubesheet weld configuration described contribute primarily to the general reliability and ruggedness of the design. In addition, the tube-to-tubesheet weld configuration allows a simplified assembly approach relative to other candidate weld configurations (e.g., a

Table 4 Test conditions for thermal cycles

Specimen	T (°C)	Number of Cycles
A	94	2000
B	222	2000
Severe Umbrella Transient	18	1854

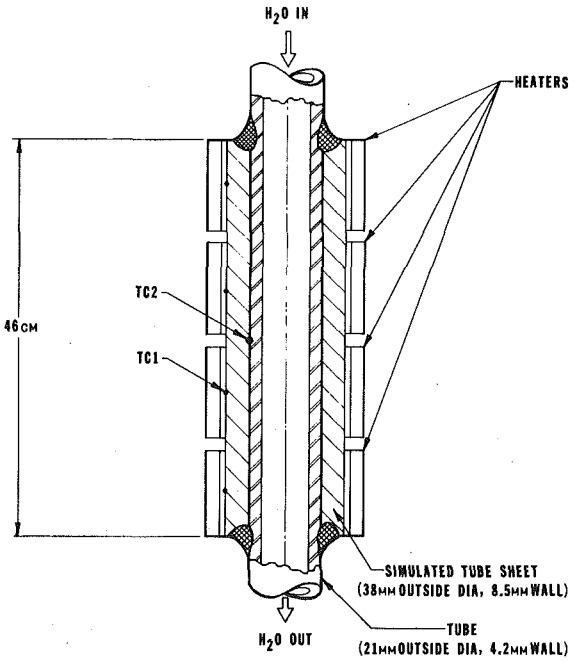


Fig. 4 Tube-to-tubesheet weld test section

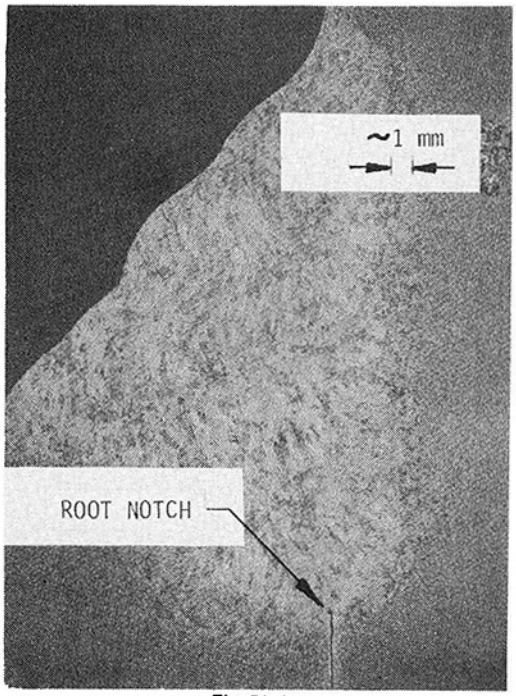


Fig. 5(a)

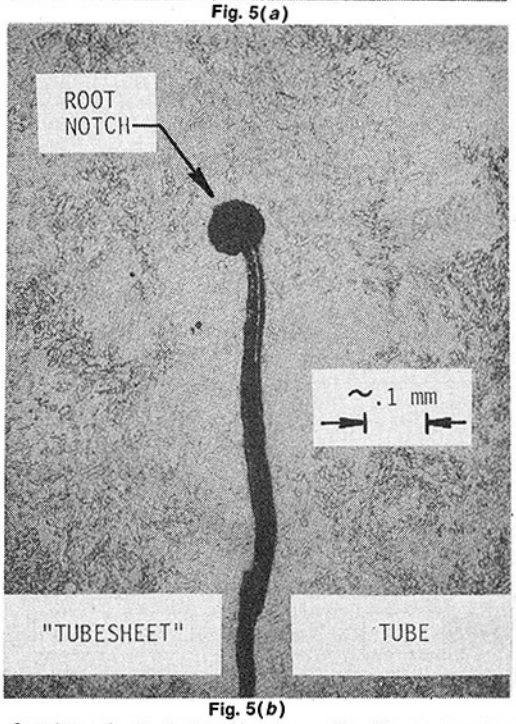


Fig. 5(b)

Fig. 5 Specimen A—typical weld cross section No. 1 after thermal cycling

Downloaded 01 Jun 2010 to 171.66.16.58. Redistribution subject to ASME license or copyright; see http://www.asme.org/terms/Terms_Use.cfm

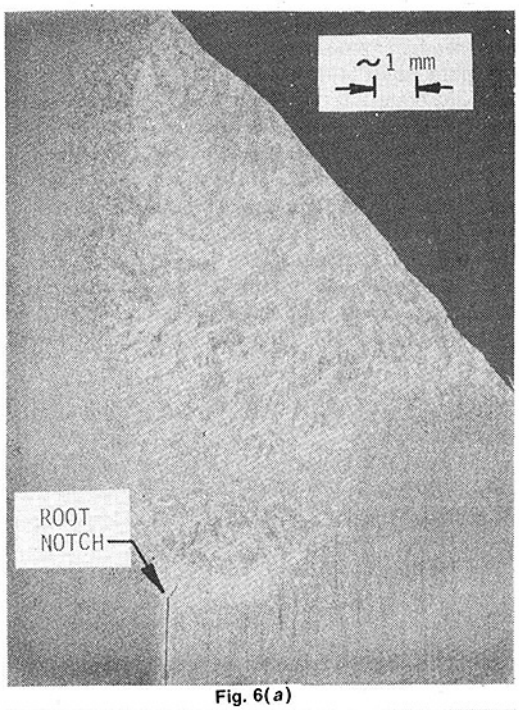


Fig. 6(*a*)

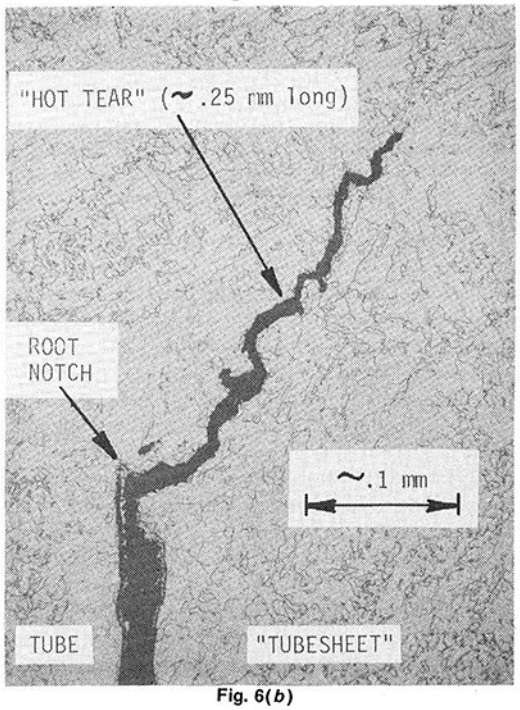


Fig. 6(*b*)

Fig. 6 Specimen A—typical weld cross section No. 2 after thermal cycling

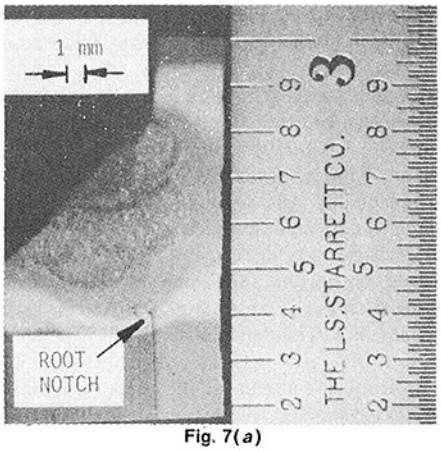


Fig. 7(*a*)

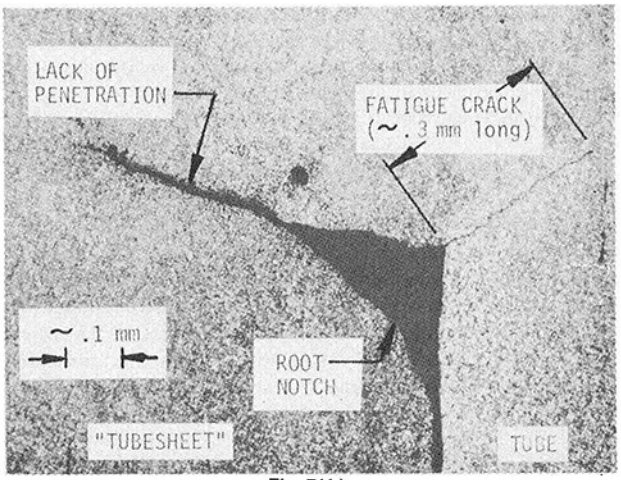


Fig. 7(*b*)

Fig. 7 Specimen B—typical weld cross section No. 1 after thermal welding

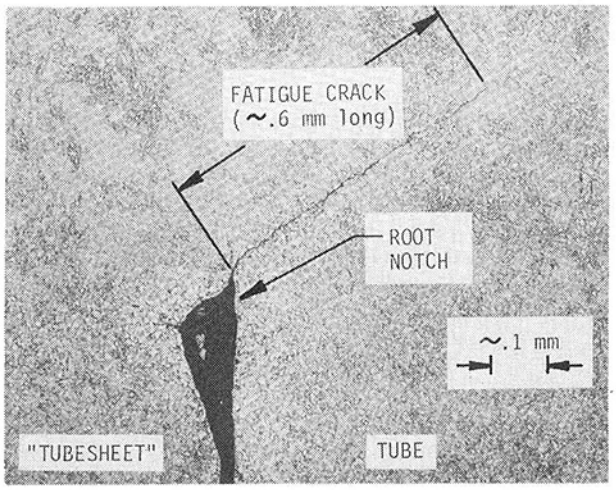


Fig. 8 Specimen B—typical weld cross section No. 2 after thermal cycling

bore-side butt weld or a back side corner weld). This arrangement permits complete assembly of the tube support structure prior to tubing installation; thus, the tubing process is accomplished by inserting the tubes directly through the tubesheets and support structure. Special welding equipment and inspection techniques are required for producing the sodium side tube-to-tubesheet welds. However, the tube pitch has been defined to allow the use of currently procurable automated welding equipment. Inspection of the tube-to-tubesheet joints by source radiographic techniques is considered feasible.

Tube-to-Tubesheet Weld Thermal Shock Test Results

The redundant nature of the tube-to-tubesheet weld suggests that thermal transients may complicate the demonstration of adequate structural integrity or introduce undesirable failure modes in service. Thermal shock tests of the tube-to-tubesheet weld were performed with the objective of demonstrating the mode of failure of the weld. Table 4 lists the test conditions and provides a comparison to conditions which are anticipated under the most adverse service transient conditions. The temperature difference (ΔT) is the maximum difference between the thermocouples $TC1$ and $TC2$ during each cycle. $TC1$ is located on the outside of the simulated tubesheet. $TC2$ is lo-

Downloaded 01 Jun 2010 to 171.66.16.58. Redistribution subject to ASME license or copyright; see http://www.asme.org/terms/Terms_Use.cfm

cated on the tube surface (see Fig. 4). It should be noted that the test conditions were much more severe than the anticipated service conditions.

Three test sections (see Fig. 4) were fabricated and subjected to cyclic thermal shocks. In order to provide a conservative test, the welds were performed manually in such a way that defects could be anticipated in the root notch region. As such, the welds do not exhibit normal production quality. After testing, the specimens were dissected and subjected to metallographic examination. Fig. 5(*a*) shows a section typical of the welds for Specimen A, and Fig. 5(*b*) shows a magnification of the weld root region of the same specimen. No evidence of fatigue crack initiation was observed. Figs. 6(*a*) and 6(*b*) show similar sections of Specimen A. The defect observed in Figs. 6(*a*) and 6(*b*) is interpreted as a "hot tear" generated during the welding process and does not indicate evidence of fatigue crack initiation.

Figs. 7(*a*) and 7(*b*) show a typical weld section from Specimen B. A defect is noted at the weld root in Fig. 7(*a*) and on closer examination, Fig. 7(*b*) shows evidence of fatigue damage. The crack propagates into the tube wall (not the weld). Fig. 8 shows another weld section of Specimen B with similar crack propagation behavior. The severity of the imposed test conditions was also indicated by the formation of fatigue cracks on the inside surface of the tubes.

The third specimen was subjected to thermal shocks of similar severity to Specimen B. The results show the same crack initiation and propagation behavior as noted for Specimen B.

Conclusions and Recommendations

A steam generator design has been described which incorporates design features that contribute to high reliability without excessive cost penalties. The straight-tube, straight-shell construction reflects a philosophy of design simplicity and minimal stress on the critical sodium-to-water boundary. The bellows expansion joint is located so as to minimize the consequences of failure and is designed for replacement, if necessary. The tube-to-tubesheet weld is relatively insensitive to operator or process shortcomings and allows for simplified "through the tubesheet" tubing operations.

The feasibility of the tube-to-tubesheet weld configuration has been demonstrated by thermal shock tests which show that fatigue damage is unlikely for very conservative conditions. In addition, under very severe conditions, failure modes were observed which would not lead to a breach of the sodium-water boundary.

A significant uncertainty for any straight-tube configuration relates to flow and temperature maldistributions which may cause differential thermal expansion between tubes. Clearly, testing and analysis is recommended to develop appropriate inlet and outlet configurations. This problem is being addressed in on-going development programs.

Acknowledgment

The permission of Combustion Engineering, Inc. to present the paper is gratefully acknowledged. Also recognized are the conceptual design contributions of R. B. Creek and the welding expertise of C. T. Ward.

References

1 Bishop, E. C., et al, "Historical Perspective of the Development and Operation of LMFBR Steam Generator in the U. S. Including Problems Associated with Development and Operational Experience of the EBR-II and Fermi Steam Generators," *Proceedings of the US/USSR Seminar on the Development of Sodium-Cooled Fast Breeder Reactor Steam Generators*, Dec. 2–4, 1974, ERDA-32.

2 de Haas van Dorsser, A. H. and Mausbeck, H., "SNR Coolant System Components," *Proceedings of 1976 ASME–ANS International Conference on Advanced Nuclear Energy Systems*, March 14–17, 1976.

3 DeFur, D. D., "An IHX Design for Pool-Type LMFBR System Application," to be presented at the ASME Joint Pressure Vessel and Piping Conference, June 25–29, 1979, Paper No. 79-NE-3.

Downloaded 01 Jun 2010 to 171.66.16.58. Redistribution subject to ASME license or copyright; see http://www.asme.org/terms/Terms_Use.cfm

L. O. K. Larsson
New Technology Department,
Volvo Flygmotor AB,
Dept. 328L,
S-461 01 Trollhatten,
Sweden

R. Warren
Department of Engineering Metals,
Chalmers University of Technology,
S-402 20 Goteborg,
Sweden

Fiber Reinforced Metals in Turbine Blades

Composites of tungsten wire reinforced stainless steel were prepared by a specially developed fabrication method based on hot isostatic pressing. This composite system was chosen as a convenient model material. Its mechanical properties were investigated to provide a basis for the evaluation of the potential advantages and possible difficulties to be expected in the application of such material to turbine blades. Results obtained so far suggest that composites based on W-alloy wires show considerable promise as blade materials for very high service temperatures. Further research effort is required, particularly on fiber/matrix interaction, thermal fatigue and to optimize the properties of the reinforcement wire.

1 Introduction

The performance and efficiency of the gas turbine engine is a direct function of the maximum cycle temperature. This is the prime motivation behind the continuous search for turbine blade materials capable of operating at even higher temperatures. Considerable improvements in the properties of super-alloys have been achieved during recent years by using conventional metallurgical strengthening techniques, such as solid solution strengthening, precipitation and dispersion hardening, grain refining, directional solidification, etc. The use of superalloys for turbine blade materials is, however, currently limited to a material temperature of approximately 980°C if they are to have reasonable life times; and improvements in the temperature capability appear to have reached an upper limit. The increasing gap between the highest metal temperature allowed and the gas inlet temperatures for which the engines are being designed is made possible by advanced blade cooling. However, the complexity of the cooling system and the increased need for cooling air are also limiting factors in the development of efficient, high temperature gas turbines. There is therefore a strong need for new types of materials which can withstand high temperatures.

The potential of refractory wire reinforced oxidation resistant and ductile metals for turbine applications has been the subject of investigation at a number of laboratories [1–8]. The most commonly studied reinforcements are wires of tungsten alloys, such as W-2 percent ThO_2, W-Hf-C, W-Re and doped W, in matrices of Ni and Co-base superalloys and Fe-base alloys. Significant improvements in high temperature creep properties, compared to conventional superalloys, have been demonstrated. The selection of material combinations are limited by many factors, such as fiber-matrix interaction, thermal expansion missmatch and the fabrication process used.

The main objective of the present work was to investigate the high temperature properties of tungsten wire reinforced metals and thereby provide the basis for an evaluation of the potential advantages and limitations of such materials in turbine blades in an advanced turbojet engine. A composite fabrication method, based on hot isostatic pressing, was developed and an experimental study was made of the mechanical properties of a model composite system consisting of stainless steel matrix reinforced with W-2 percent ThO_2 and doped lamp wires. The implications of their use in a planned advanced engine has also been investigated.

2 Experimental Details

2.1 Material. The reinforcements selected for study were a W-2 percent ThO_2 wire of 0.295 mm dia supplied by Metallwerk Plansee, Reutte, Austria and a doped lamp wire of 0.315 mm dia supplied by the Luma Lamp Co of Stockholm. Both were commercial, well-characterized wires with good creep strength. However, it should be emphasised that neither was optimized with respect to use in composites. In the following discussions allowance should also be made for possible variations in properties from batch to batch.

Stainless steel of AISI type 304 was selected as matrix in the composite. Fe-base matrices can in some respects be expected to have superior compatibility behavior with tungsten wires as compared with Ni-base matrices [9]. Though it doesn't have the most ideal high-temperature properties, this matrix was chosen because it was readily available in suitable form and, at the same time, provides a convenient model of Fe-base solid-solution matrices.

2.2 Composite Fabrication. A new method for the fabrication of wire reinforced metal-matrix composites was developed [9]. The fabrication of tensile and creep specimens will be described briefly here. The matrix was obtained in the form of small-diameter tubing, with inner diameter of about 0.4 mm and outer diameters between 0.6 and 0.7 mm. This was used to clad the reinforcement wire. The clad wire was cut into lengths corresponding to the intended specimen length and parallel bundles of these lengths were packed as tightly as possible by hand into stainless steel container tubes of 4 mm ID and 10 mm OD. After evacuation and sealing the containers were com-

Contributed by the Gas Turbine Division and presented at the Israel Joint Gas Turbine Conference and Exhibition, Haifa, Israel, July 9–11, 1979 of THE AMERICAN SOCIETY OF MECHANICAL ENGINEERS. Manuscript received at ASME Headquarters March 30, 1979. No. 79-GT/Isr-1.

Copyright © 1980 by ASME
Downloaded 01 Jun 2010 to 171.66.16.58. Redistribution subject to ASME license or copyright; see http://www.asme.org/terms/Terms_Use.cfm

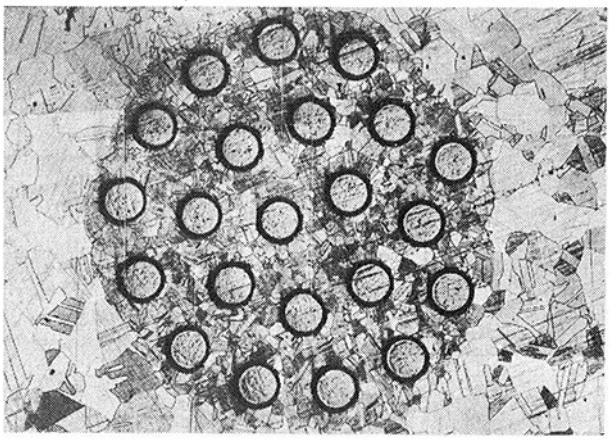


Fig. 1 Cross-section of the tungsten/stainless steel composite as fabricated

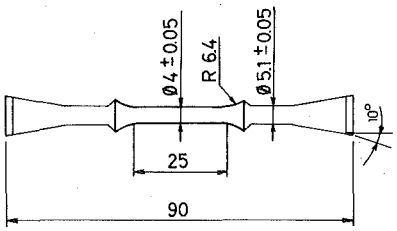


Fig. 2 Composite specimen for tensile and creep tests

pacted by hot isostatic pressing (HIP) for approximatively 1 hr at 1000°C, 170 MPa and 3 hr at 1180°C, 190 MPa using argon as pressing medium. The composites as produced attained full density; the fibers were undamaged and uniformly distributed, Fig. 1.

The rods resulting from the HIP-process had an external diameter of about 9.8 mm and a central composite core of 3 mm dia. These were centerless ground to give tensile and creep test specimens with conical ends and with shoulders for the support of a strain gauge (Fig. 2). The fiber ends were protected by including end-plugs of stainless steel in the container tubes. The fiber content could be varied widely by changing the dimensions of the matrix tubes and composites were produced with fiber volume fractions between about 20 and 50 percent.

A reaction layer was found to form between wire and matrix during the HIP-process [9] (Fig. 3). It had a thickness of approximately 12 μm and an approximate composition: 55 wt percent W, 33 percent Fe, 9 percent Cr and 3 percent Ni.

By the process described turbine blade airfoils that are close to final dimensions can be produced. Fig. 4 shows a cross section of a prototype to a composite airfoil consisting of stainless steel reinforced by tungsten wires.

2.3 Testing. The short-term tensile behavior of the composites was studied between RT and 950°C in air using standard testing equipment. Creep experiments were carried out at 900 and 950°C in air in a M Nickel Co/H Wiggin and Co testing rig. The creep strain was recorded continuously by means of rods suspended from the shoulders on the specimen, their relative motion being monitored with two differential transformers.

The RT tensile properties of the uncombined W wire and matrix material were measured with a standard (INSTRON) testing machine. Their strength and creep properties at elevated temperatures were measured in a creep machine, specially designed for the testing of wires [10]. In all cases the temperature was measured to ±10°C with thermocouples placed close to the specimen.

3 Results and Discussions

3.1 Tensile Tests. The tensile strengths of composites containing nominal tungsten contents of 20 and 30 v/o are shown as a function of temperature in Fig. 5. The figure includes both the results

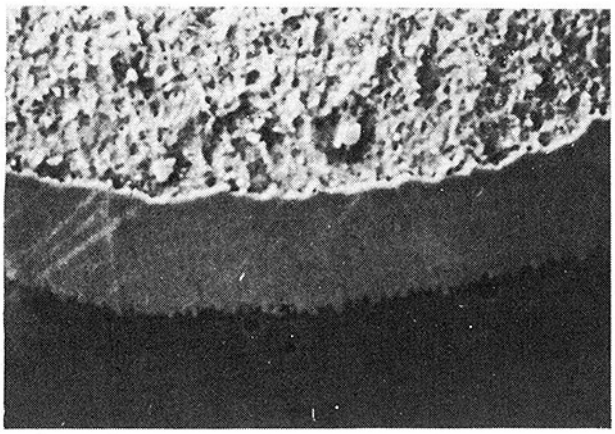


Fig. 3 Reaction layer formed between wire and matrix during the consolidation process

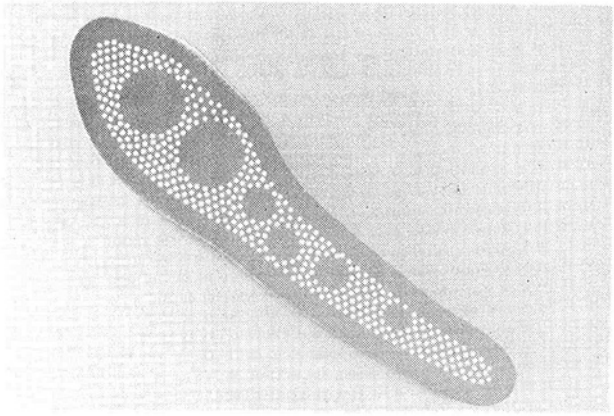


Fig. 4 Cross-section of a tungsten wire reinforced stainless steel model turbine blade

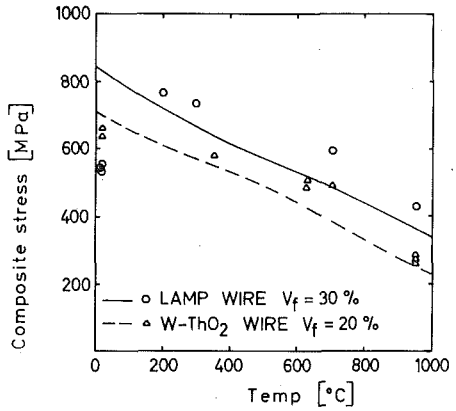


Fig. 5 Tensile strengths versus temperature of composites measured experimentally and estimated on the basis of as received wire strengths

of experimental measurements and strengths predicted from the uncombined wire strengths using a simple rule of mixtures (ROM). In the composites, variable deviations from the nominal contents occurred, e.g., as a result of machining away portions of some wires during specimen preparation. To allow convenient comparison, the strengths were adjusted to correspond to the nominal composition, again using the ROM.

The predicted composite strengths were obtained on the basis of the equation:

$$\sigma_c = \sigma_{fu} V_f + \sigma_m^* (1 - V_f) \quad (1)$$

where

σ_c = composite tensile strength, σ_{fu} = wire tensile strength, and σ_m^* = stress in the matrix at the breaking strain of the wires.

Downloaded 01 Jun 2010 to 171.66.16.58. Redistribution subject to ASME license or copyright; see http://www.asme.org/terms/Terms_Use.cfm

A detailed analysis shows that because of the relatively small fracture strain of the wires and the low work hardening rate of the matrix, $\sigma_m{}^*$ can to a good approximation be set equal to the yield stress.

At temperatures above 300–400°C the composites had somewhat higher strengths than predicted. This could partly be due to the solution hardening of the matrix by W. The brittle reaction layer might also contribute to the composite strength in special circumstances [11, 12].

Below 200°C the composite strengths fell below the predicted strength, the effect being particularly marked in the 30 v/o composites reinforced with lamp wire. This can be attributed to an effective embrittlement of the wire. Thermal expansion differences between the phases in such composites can create significant internal stresses [13]. These can be sufficient to result in premature micro-cracking in the reaction layer (Fig. 6). Below the ductile-brittle transition temperature (DBTT) of the wire such cracks can be expected to act as stress raisers and cause a drastic reduction in wire strength. During fabrication at 1180°C it is quite possible that sufficient recovery occurred in the wire to raise its DBTT to around 200°C [14].

These results can also be discussed in terms of V_c, the critical volume fraction of fibers, that must be exceeded to obtain fiber strengthening of the matrix. V_c is given by the equation:

$$V_c = \frac{\sigma_{mu} - \sigma_m{}^*}{\sigma_{fu} - \sigma_m{}^*} \tag{2}$$

where σ_{mu} = ultimate tensile strength for the matrix. Fig. 7 shows V_c for the composite as a function of temperature, based both on the wire tests and on fiber properties derived from the composite tests. From this it is clear that reinforcement is achieved with relatively low volume fraction of wire. Reinforcement becomes particularly effective above 700°C.

3.2 Creep Properties. Composite creep tests were carried out at 900 and 950°C. The specimens had fiber contents ranging from about 18 to 35 volume percent and were tested at stress levels from 60 to 250 MPa. Typical strain vs. time curves are shown in Fig. 8. The secondary or steady state creep rates for composites containing nominal 20 volume percent fibers are plotted in Fig. 9. Small corrections of the stress were made using the rule of mixtures to allow for small variations in volume fraction. Predicted curves of creep rate, based on wire tests, are also shown in the figure. The model used, for the estimation of creep properties, assumes that the strain rate is similar in the matrix and the fibers, and that the creep process in both constituents follows a power low of the type

$$\dot{\epsilon} = K\sigma^n \tag{3}$$

The composite stress can be estimated, as a function of the creep properties of the constituents, by the rule of mixtures [15]:

$$\sigma_c = K_1 V_f \dot{\epsilon}_c{}^{1/n} + K_2(1 - V_f) \cdot \epsilon_c{}^{1/m} \tag{4}$$

where K_1; n and K_2; m are constants for fiber and matrix, respectively.

For lamp wires the composite creep rates are seen to be in good agreement with the rates predicted on the basis of wire tests. The W-2 percent ThO_2 wire reinforced composite can withstand somewhat higher stresses than predicted for a given strain rate.

For the few results obtained, good agreement was also found be-

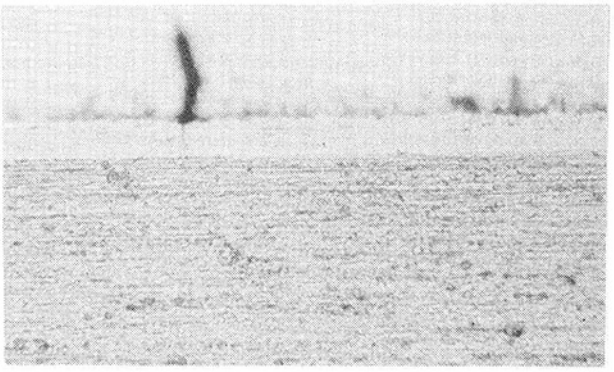


Fig. 6 Cracks in the reaction layer of the as fabricated composites

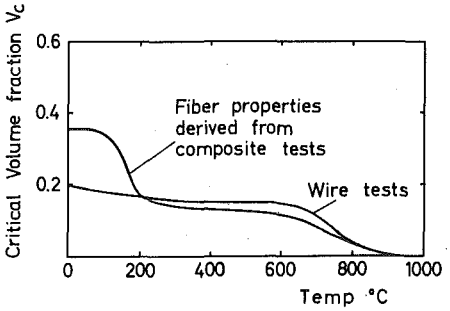


Fig. 7 Critical fiber volume fraction versus temperature for tungsten fiber reinforced stainless steel

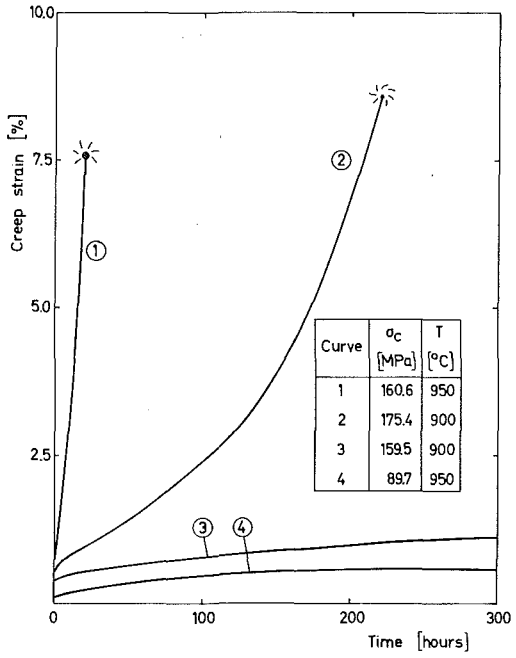


Fig. 8 Typical strain versus time curves for composites tested at 1175 and 1225 K

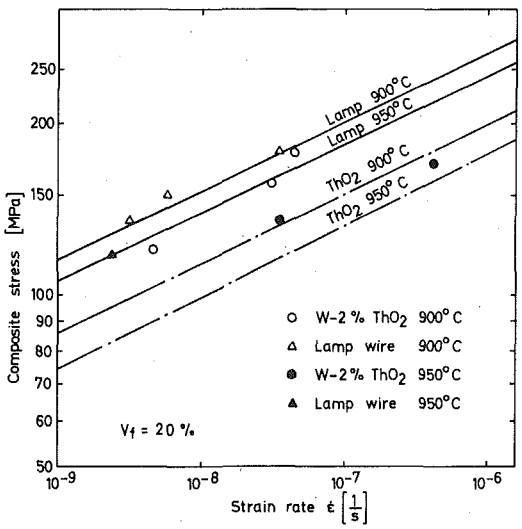


Fig. 9 Predicted and measured secondary creep rates of 20 v/o reinforced S/S composites as a function of stress and temperature. The predicted creep properties are based on tests on single, as-received wires

Downloaded 01 Jun 2010 to 171.66.16.58. Redistribution subject to ASME license or copyright; see http://www.asme.org/terms/Terms_Use.cfm

tween the composite stress versus rupture life behavior and the behavior predicted by a rule of mixtures from single wire tests. Our primary interest was an investigation of secondary creep and therefore many of the tests were not run to rupture. However, in creep tests on both composites and single wires a rough correlation between creep strain and rupture was observed. Namely, the creep rupture time was equal to the time to cause 3 ± 0.5 percent strain at the secondary strain rate.

It is often convenient to present creep data in a so-called Larson-Miller diagram. The Larson-Miller parametric equation relates the fracture or deformation time t to a function of stress $f(\sigma)$ and the temperature T by means of a constant K:

$$\log t = \frac{f(\sigma)}{T} - K \tag{5}$$

In fact, K is dependent on stress, for instance, but is frequently taken to be 20.

The stress to cause 3 percent secondary creep strain versus combined time and temperature for composite and wire tests are plotted in a Larson-Miller diagram (Fig. 10). As indicated above, this figure gives a close representation of rupture life behavior.

If the strength of the matrix at a particular value of the L-M parameter, P, is known, the stress borne by the fibers can be calculated with a rule of mixtures. In fact, above 900°C the creep resistance of the stainless steel is very low compared to that of the reinforcement and the load-carrying contribution of the matrix in the present tests can be considered to be very low. Assuming that the reinforcement bears the entire load, the stress on the wire was calculated and found to agree well with the tests on uncombined wires. On a similar basis, the creep properties of single wires were used to predict the creep behavior of composites having various volume fraction of reinforcement and the predicted curves are included in Fig. 10.

The good agreement between the observed and predicted results indicate that the wire properties are not seriously affected by fabrication or the presence of the matrix. The evident long-term and high-temperature compatibility of this wire/matrix combination may possibly be attributed to the reaction layer acting as a built-in barrier layer. In other composite systems, particularly those with certain nickel alloy matrices, the compatibility is often found to be poor. To reduce loss in strength during fabrication or long-term service as a result of such processes as recrystallization, it is sometimes necessary to deposit a barrier coating on the wire before fabrication [8]. In the present composites the microcracks observed in the reaction layer do not affect the creep properties of the composite. During creep their growth into the wire appears to be held up after a few micron penetration (Fig. 11).

3.3. The Potential Mechanical Properties of Optimal Composites. For turbine blade material the creep properties are of primary importance. The results presented above and those of previous studies show that, if a suitable fabrication is used and diffusion-based interactions between wire and matrix can be avoided, the composite creep behavior is determined largely by the creep properties and the volume content of the reinforcement. As will be discussed later, the matrix influences many important composite properties, but it contributes little to the high-temperature strength. It is therefore clear that efforts should be made to optimize the properties of reinforcement wires and to hinder their degradation in the matrix by, e.g., recrystallization or dissolution. A number of factors affecting fiber/matrix interactions have been studied with a view to limiting degradation, e.g.:

- *Matrix alloy composition*—increasing the tungsten content of the matrix has been shown to significantly reduce the interaction between W-wires and superalloy matrices [5]. Fe-base alloys seem to be more compatible than Ni-base alloys with tungsten. This can be explained at least partly by the lower solubility of W in Fe and by the fact that Fe is less active in promoting the recrystallization of tungsten [9].
- *The temperature (and time) involved in fabrication*—these, of course, should be kept as low as possible to minimize interaction prior to service. As well as requiring a relatively low temperature HIP minimizes mechanical damage to the fibers during fabrication.
- *The presence of a diffusion-barrier layer between fiber and matrix introduced either by prior fiber-coating or by in situ reaction*—for example, a 4 μm thick coating of HfC or HfN has been shown to be an effective diffusion barrier [8]. The reaction layer formed during fabrication in the present study probably also contributes to the observed high-temperature stability.
- *Fiber diameter*—the absolute depth of interaction of a given process is relatively insensitive to fiber diameter. Consequently, with increasing fiber diameter the proportion of unaffected fiber increases. The desirability of larger diameter in this respect is, however, offset by the fact that fiber strength generally increases with decreasing diameter and a compromise must usually be sought.

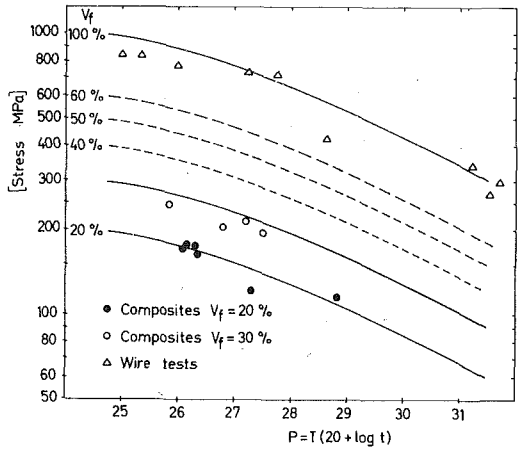


Fig. 10 Larson-Miller Parameter Curve for creep rupture and 3 percent strain with secondary creep rate for composites and single wires

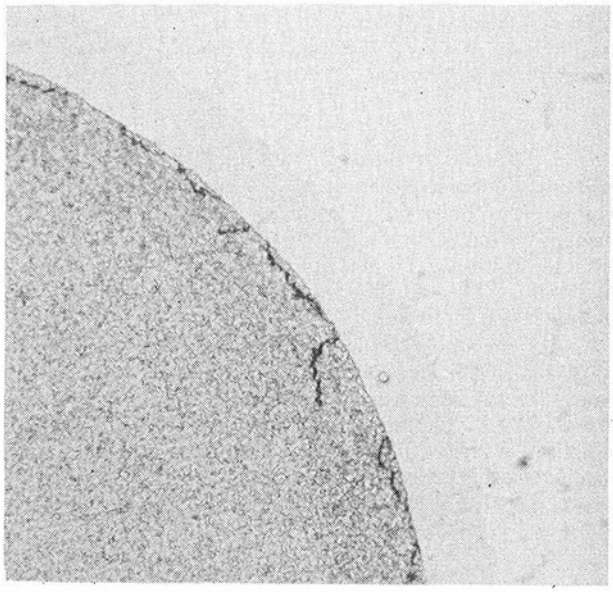


Fig. 11 Cracks in the reaction layer which have propagated into the fibers during a creep test, 630x

Considering the importance of the reinforcement in determining the composite creep behavior, it is clear that there is a need for the development of wire optimized for use in composites. Examples of specially developed wires with excellent creep strength are those of the alloys W-Hf-C and W-Re-Hf-C, in which precipitated HfC significantly improves the high-temperature strength over that of conventional wires [17].

The availability of such advanced wires is, limited however, and the majority of investigations of creep that have been reported are for composites containing more conventional wires, not optimized for use in composites. It is therefore difficult to predict the full potential

Downloaded 01 Jun 2010 to 171.66.16.58. Redistribution subject to ASME license or copyright; see http://www.asme.org/terms/Terms_Use.cfm

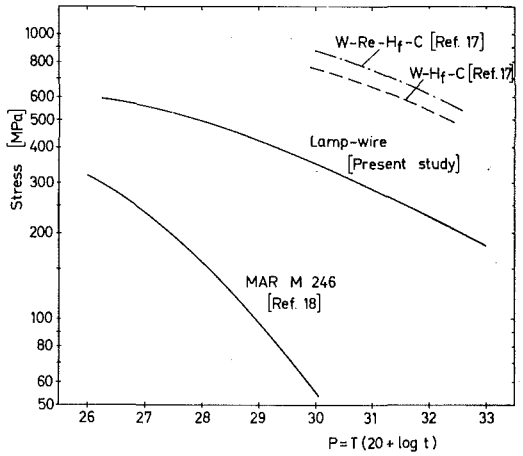


Fig. 12 Predicted Larson-Miller rupture curves for composites containing 60 v/o wire, comparing the lamp wire of the present study with advanced W-alloy reinforcement. The curve for a typical unreinforced superalloy is also included

of W-reinforced composites. In Fig. 12 the creep-rupture behavior is predicted, for composites containing 60 vol percent reinforcement, in terms of Larson-Miller plots. Curves are given based on the system of the present study as well as on the results reported by the NASA group for advanced alloy wires [17]. The curve for a superalloy (MAR M 246) [18] is included for comparison. The predictions are made assuming that the matrix bears no stress and that the wire properties are not affected by incorporation in the matrix.

The composites are clearly superior to the conventional superalloy, particularly at high temperature. At a stress level of 250 MPa, which is typical for the "critical section" of a turbine blade, inspection of the curves shows that, for a given rupture life, the temperature of a composite containing conventional lamp wire could be increased by about 200°C over that of the superalloy. Similarly, at a given temperature, a considerable increase in life is predicted.

In the above comparison no account is taken of the very high density of tungsten (19,4 g/cm^3) compared to that of superalloys (approximately 8,3 g/cm^3). The stresses in a rotating blade increase in proportion to the density and this would, of course, reduce the temperature advantage quoted above. A 50 percent increase in the stress level, for example, would reduce the temperature advantage to about 100°C. However, the density effect can be reduced by modifications in design and fabrication of the composite blade. For example, the fibre content can be varied along the blade to tailor the strength to that needed, the blade section near the base can be reduced compared to that of a superalloy blade because of the improved strength.

The roles of the matrix in this type of composite are complex and many conflicting factors have to be considered in the selection of a suitable matrix and in the prediction of the composite behavior. Some of the more important factors and requirements are:

- *Metallurgical compatibility with the fibers*—as discussed above with respect to tungsten wires.
- *Oxidation resistance*—the problems of oxidation and corrosion are considerable in turbine blade applications. There are probably few matrix alloys that have both adequate compatibility with the fibers and adequate oxidation resistance. Alloys of the M Cr Al Y type have shown promise in this respect [7]. An alternative is to use a compatible matrix in combination with a protective surface coating. Any system must not only be intrinsically oxidation resistant but also provide effective protection for oxidation-sensitive fibers.
- Sufficient *shear strength* for stress transfer to the reinforcement
- *Ductility* for good impact resistance
- *Suitability for the fabrication process used*—the fabrication process often dictates the matrix to be available in a specific form, e.g., powder, foil or, as in the method described here, small diameter tubing. Other process requirements such as formability, weldability, machinability may also be decisive.
- *Thermal fatigue properties*—during service the temperature of a blade fluctuates considerably and good thermal fatigue properties are essential for the blade material. In composites, the difference in thermal expansion of the constituent phases causes additional internal stresses. These can be very high and sufficient to cause early failure [13]. The effect has proved a great obstacle in the use of high-temperature composites. Typical superalloys have mean coefficients of thermal expansion in the range 14×10^{-6} to 17×10^{-6} (m/m C; 0–1000°C) while for tungsten alloys the coefficients are about 5×10^{-6} m/m °C. To minimize the effect a matrix with as low thermal expansion and as good thermal fatigue properties as possible should be chosen.

4 Composite Application in Advanced Gas-Turbine Blades

All aircraft and industrial gas-turbine manufactures wish to increase the engine cycle temperatures in order to improve the specific power output for a given machine size or decrease the specific fuel consumption. A combination of an increased pressure ratio and a higher turbine inlet temperature (TIT) give this performance improvement. Temperature improvements have so far been achieved mainly by material substitution or improved blade cooling techniques.

The required effectiveness of blade cooling can be expressed as

$$\xi = \frac{T_G - T_B}{T_G - T_C} \tag{6}$$

where T_G is the gas temperature, T_B is the allowable material temperature and T_C the temperature of the cooling air. The required cooling mass flow is given by:

$$\dot{m} = K \cdot \frac{\xi}{1 - \xi} \tag{7}$$

where K is a function of heat transfer, blade geometry and the efficiency of the cooling system used.

Equations (6) and (7) imply that if the gas temperature (T_G) increases, the required cooling effectiveness (ξ) increases and consequently a greater cooling air flow ($\dot{m}$) is required. A higher cycle pressure ratio cause a higher cooling air temperature, T_C, which also increases the required cooling effectiveness and again additional cooling flow is needed. On the other hand a small increase of the allowable material temperature reduce the cooling effectiveness and diminishes the required cooling flow significantly.

The introduction of fiber reinforced metals with improved creep properties will make it possible to take a considerable step upwards in blade temperature. Furthermore, since the composites can withstand higher stresses, the blade section can be reduced which means less aerodynamic loss. Thus, the turbine designer would be given the opportunity to make significant improvements in the performance of a gas-turbine engine. Optimum use of the material can offer:

- Increased turbine inlet temperature
- Higher temperature of the cooling air, allowing a greater total pressure ratio
- Reduced cooling flow
- Simplified cooling system
- Increased turbine aerodynamic efficiency

To illustrate the advantages of composite blades in an advanced gas-turbine their use in a projected research aero-engine with a turbine inlet temperature of 1800 K and a total pressure ratio of 25 is considered. The turbine consists of one high pressure stage and two low pressure stages. The required turbine cooling flow has been estimated for the case of blades made of superalloy and fiber reinforced metal respectively.

The heat transfer coefficient between the hot gas and the blade surface is calculated for each stage by aerodynamic considerations. Suitable cooling systems are suggested and their efficiencies are estimated. The allowed material temperature, T_B, is predicted from stress calculations on the blade in combination with the property data of Section 3. The parameters used and the required cooling air flow are shown in Table 1.

Downloaded 01 Jun 2010 to 171.66.16.58. Redistribution subject to ASME license or copyright; see http://www.asme.org/terms/Terms_Use.cfm

Table 1 Estimated cooling flow requirement in an advanced jet engine. The total pressure ratio is 25 which gives T_c = 820 K

Material	Par	HP S	HP R	LP1 S	LP1 R	LP2 S	LP2 R	$\Sigma\dot{m}$
Superalloy	T_G[K]	1800	1740	1450	1440	1315	1310	
T_B = 1250 K	K	0.055	0.053	0.086	0.068	0.132	0.108	
	$\dot{m}$ [percent]	7	6	4	3	2	1.5	23.5
Composite	T_G[K]	1800	1760	1450	1440	1315	1315	
T_B = 1450 K	K	0.048	0.036	–	–	–	–	
	$\dot{m}$ [percent]	3	2	–	–	–	–	5

When superalloy blades are used the required cooling flow is roughly a quarter of the total flow but only 5 percent for composite blades. It must be concluded that it would be impossible to use superalloy blades at such a high temperature level. Compared to superalloy the composites have potential for operating at 150 to 250°C higher temperatures. It may thus be possible to use a simple cooling system at this higher operating temperature and thereby gain the benefit of the simpler blade design and a lower cooling flow requirement. Furthermore, aft stages of the turbine might be operated without cooling because of the higher temperature operating limit of the composites. This can reduce cooling air flow requirements, engine complexity and weight, and increase engine performance.

However, the use of composite materials is not without its challenges to the turbine designer. The components must be designed to utilize the directional properties of the composite. At the same time their special disadvantages must be circumvented. Tungsten wires are extremely sensitive to oxidation and must be protected against contact with hot gas. Relatively little information has been obtained regarding the oxidation resistance of composites to combined exposure to erosive gas streams and cyclic temperatures.

The possibility of using composites with an advanced film-cooling system is doubtful but a convection system might be possible. Complex air-cooled blades have a high ratio of transverse to longitudinal stresses which might be a limiting criterion in a composite blade.

To minimize the effect of the high density of tungsten wires they should be concentrated in the most loaded part of the blade. At the same time the fiber content in any part of the blade should preferably not fall below the critical volume fraction, which can be relatively high (Fig. 7).

The blade root attachments are in a complex stress state and here an adequate longitudinal shear strength is important. Uniaxial composites usually have a low axial shear strength, but a possible solution is to combine a composite airfoil with a superalloy attachment by welding or hot isostatic pressing.

5 Concluding Remarks

The present study demonstrates that tungsten wire reinforced stainless steel composites have favorable high temperature mechanical properties. Fabricating the composite by a method based on HIP does not significantly affect the properties of the reinforcement wire. The good wire/matrix compatibility in this system can be associated at least partly with the formation of a stable reaction layer between wire and matrix. Creep tests on single uncombined wires and composites have shown that the composite properties can be estimated from the data of the constituents by a rule of mixture. However, test data is limited and must continue to be generated to identify the full potential and limitations of these materials.

The improvement in properties over those of conventional superalloys used for turbine blades promise significant improvement in the efficiency of turbine engines.

Further improvements in the properties of this type of composite can be expected as a result of further research on wire/matrix compatibility and of optimisation of reinforcement wire alloys.

Acknowledgments

This work was made possible by the financial support of the Swedish Board of Technical Development (STU) and Air Material Department (AMD). The authors also extend their thanks to the ASEA High-Pressure Laboratory, Robertsfors, Sweden, for carrying out the hot isostatic pressing.

References

1 Harris, B., and Ellison, E. G., "Creep and Tensile Properties of Heavily Drawn Tungsten Wire," *Trans ASM*, Vol 59, 1966, pp. 744–754.

2 Morris, A. W. H., and Burwood-Smith, A. "Fibre Strengthened Nickel-base Alloy," *AGARD—CP-73-71*, Paper 19, 1971.

3 Dean, A. V., "The Reinforcement of Nickel-Base Alloys with High-Strength Tungsten Wires," *Journal of the Institute of Metals*, Vol. 95, 1967, pp. 79–86.

4 Petrasek, D. W., and Signorelli, R. A., "Stress-Rupture Strength and Microstructural Stability of Tungsten—Hafnium—Carbon—Wire—Reinforced Superalloy Composites," *NASA TN D-7773*, Oct., 1974.

5 Ahmad, I., and Barranco, J. M., "Reinforced Cobalt Alloy Composite for Turbine Blade Application," *SAMPE Quarterly*, April 1977, pp. 38–49.

6 Grünling, H. W., "Preparation and Properties of Tungsten—Wire Reinforced Ni-Cr 80–20," *NASA TT F-16*, p. 275, 1975.

7 Brentnall, W. D., and Moracz, D. J. "Tungsten Wire—Nickel Base Alloy Composite Development," *TRW NASA* CR-135021, March 1976.

8 Mazzei, P. J., Vandrunen, G. and Hakim, M. J., "Powder Fabrication of Fibre-Reinforced Superalloy Turbine Blades," *AGARD CP-200*, Paper SC7-1, 1976.

9 Warren, R., Andersson, C. H., and Larsson, L. O., "Fiber/Matrix Interactions in a W-wire Reinforced Stainless Steel Composite," Submitted for publication in *Composites*.

10 Warren, R., et al., "The Effect of Nickel Coatings on the Creep of Tungsten Wire," *Proc VII International Congress Rheology*, Gothenburg, 1976.

11 Umakoshi, Y., and Yamane, T., "Contribution of the Interfacial Reaction to the Strength of Molybdenum and Tungsten Fiber-reinforced Composites," *Trans JIM*, Vol 17, 1976, pp. 25–34.

12 Friedrich, E., Pompe, W., and Kopjou, I. M. "The Influence of Brittle Boundary Layers on the Strength of Fibrous Metallic Composites," *J of Mat Sci*, 9, 1974, pp. 1911–1916.

13 Larsson, L. O. K., "Thermal Stresses in Metal Matrix Composites," *Proc of ICCM 2* Toronto, 16–20, April 1978.

14 Comerford, M. F., "Effects of Annealing Temperature and Surface Finish on the Ductile—Brittle Transition in Wand W-3 Re Wires," *Proc 2nd Int Conf on Mech Behavior of Materials*, Fed of Mat Soc, Boston, Mass 1976.

15 McDanels, D. L., Signorelli R. A. and Weeton J. W., "Analysis of Stress-Rupture and Creep Properties of Tungsten-Fiber-Reinforced Copper Composites," *NASA TND-4173*, Sept 1967.

16 Signorelli, R. A., "Review of Status and Potential of Tungsten-Wire-Superalloy Composites for Advanced Gas Turbine Engine Blades," *NASA TM X-2599*, Sept 1972.

17 Petrasek, D. W., "High-Temperature Strength of Refractory-Metal Wires and Consideration for Composite Applications," *NASA TN D-6881*, Aug 1972.

18 Wood, J. R., "Long-Time Creep Rupture Properties and Elevated Temperature Stability of D-979," *Proc. Third Int symp Superalloys*, Seven Springs, Penn, Sept 12–15, 1976.

Downloaded 01 Jun 2010 to 171.66.16.58. Redistribution subject to ASME license or copyright; see http://www.asme.org/terms/Terms_Use.cfm

K. Bammert
Professor.
Institute for Turbomachinery,
and Gasdynamics,
University of Hanover,
Hanover,
Germany

H. Poesentrup
Maschinenfabrik Augsburg-Nuernberg AG,
New Technology Division,
Munich,
Germany

The Behavior of a Closed-Cycle Gas Turbine with Time Dependent Operating Conditions

The closed-cycle gas turbine can be applied in thermal power stations using fossil, nuclear or solar energy. Here the behavior of the closed-cycle gas turbine plant under time dependent operating conditions is particularly important. A theoretical model was developed which unlike previously applied methods also considers the transient processes in the heat exchanging units, the heat transfer between the working medium and the internally insulated hot-gas pipes, and the condition of the blading. For examination of the model, measurements were taken on a closed-cycle air turbine. The results of the calculation made for comparison with the test results show the reliability of the calculation model. There is conformity of the measured speeds of the turbo group and of the pressures, temperatures and mass flows of the cycle with the theoretical values until a new steady-state condition is reached.

Introduction

Closed gas turbines have been employed for many years for converting fossil fuels into electrical current and heat [1, 2]. Further promising applications present themselves for this type of conversion system in conjunction with helium-cooled, high-temperature reactors or with solar tower plants using air or helium as a working fluid. The gas turbine process attains excellent efficiencies at elevated operating temperatures, which do not necessarily entail as high pressures as the steam process. The efficiency of the closed gas turbine almost remains constant over a wide operating power range. The heat to be dissipated also occurs at a comparatively high temperature range so that it can either be utilized for further purposes (e.g., desalination of sea water) or can be dissipated relatively easily in dry cooling towers.

One of the preconditions for designing closed gas turbine plants is the preparation of sufficient data and reliable methods of calculation with respect to the behavior of operating conditions that vary with time. Knowledge of the transient behavior of gas turbine plants is essential not only for reasons of safety, but also for the design of the control system and the appraisal of the anticipated loads on the machines and components arising from temperature and pressure fluctuations.

A theoretical model has therefore been developed which permits the examination of transient operational processes at acceptable computation times without neglecting any significant parameters. The method has been applied to an existing plant and checked by comparison with measured and calculated values [3].

Theoretical Model

Schematic of Operating Circuit. Fig. 1 is a schematic of the circuit of a closed gas turbine plant. It corresponds to that plant on which the experimental investigations were carried out. The air is precompressed in the low-pressure compressor (a), recooled in the intermediate cooler (b′, b) and compressed to the upper process pressure in the high-pressure compressor (c). In recuperator (d), the compressed air absorbs part of the heat contained in the expanded air escaping from the turbine (f) before flowing into heater (e). Heat is again extracted from the expanded air in the precooler (g′, g) so that the air again reaches the temperature prevailing at the low-pressure compressor, thus completing the cycle. Some of the waste heat is removed from the circuit in the "heating parts" b′ and g′ of the coolers and utilized in a municipal heating system.

The bypass is also shown in the diagram. It constitutes one of the most important means of controlling operation and is used primarily whenever rapid changes are necessary. In this case part of the working fluid is removed from the circuit behind the high-pressure compressor and is fed in again behind the turbine without having performed work. The bypass has proved very effective and very quick in controlling the plant. The alternative method of varying the gas inventory and

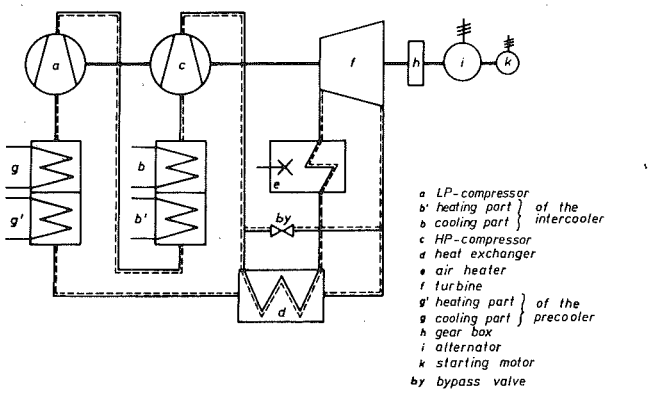


Fig. 1. Circuit diagram of a closed-cycle gas turbine

Contributed by the Gas Turbine Division and presented at the Israel Joint Gas Turbine Conference and Exhibition, Haifa, Israel, July 9–11, 1979, of THE AMERICAN SOCIETY OF MECHANICAL ENGINEERS. Manuscript received at ASME Headquarters April 2, 1979. Paper No. 79-GT/Isr-2.

Copyright © 1980 by ASME
Downloaded 01 Jun 2010 to 171.66.16.58. Redistribution subject to ASME license or copyright; see http://www.asme.org/terms/Terms_Use.cfm

with it the pressure level and the mass of circulating working fluid is, in comparison, relatively slow in taking effect.

Pressure and Pressure Gradients. Since approximately the same pressure prevails between any two turbomachines in the circuit, it is expedient to observe the respective representative mean pressure values and their gradients for these sections. For examining major malfunctions such as a line rupture, however, this representation is too simplified.

If we compute the amount of heat transferred to or removed from the gas in the individual components of the circuit, that is to say we take the transient behavior of the assemblies and lines into account, the mean pressure gradients for the section between any two machines can be determined directly. To do so we apply the energy equation which, neglecting the influence of gravity, can be expressed for any section in the form:

$$\frac{d}{dt}\left[\bar{\rho}\cdot V\cdot\left(c_v\cdot\overline{T}+\frac{\overline{v}^2}{2}\right)\right]_s=\Delta\left[\dot{m}\cdot\left(c_p\cdot T+\frac{v^2}{2}\right)\right]+\dot{Q} \tag{1}$$

The overlined quantities are mean values in the given section. The left side of the equation is a statement of the change in energy content of the section in question (subscript S). The first term of the right side expresses the quantities of energy carried by the inflowing and outflowing gases, the second term the sum of the heat energy supplied and withdrawn per unit time.

Neglecting the relatively small kinetic energy of the gases, we arrive at the equation

$$\frac{dp_s}{dt}=\left[(\dot{m}\cdot T)_{\text{in}}-(\dot{m}\cdot T)_{\text{out}}+\sum_i\frac{\dot{Q}_i}{c_{pi}}\right]_s\cdot\frac{R}{\sum_i\frac{V_{si}}{\varkappa_i}} \tag{2}$$

for the mean gradient of the pressure in the given section. The first two terms enclosed in brackets represent the quantities and temperatures flowing into and out of the section. They can be determined from the momentary course of the temperatures by applying the equation for the performance of the machines. Those quantities with the subscript i must be taken and added up for the individual elements of the section. In this way the variability of the specific heat and of the isentropic exponent is taken into account. One element is always understood to be one pipe or one apparatus of the section under consideration.

Thus the equation for calculating the pressure gradients in a given section is available. The difficulty lies in the calculation of the heat energy (Q_i) supplied and withdrawn. This calculation involves knowing the wall and gas temperatures as well as the rate of flow for each individual element of the circuit. Thus a continuity based program is important.

Flow Channels. A given element, e.g., a pipe in the circuit, can be represented by the model of a flow channel depicted in Fig. 2. The channel has an overall reference length $\xi = 1$ and is divided into N subdivisions of the finite length $\Delta\xi$. One subdivision contains the quantity μ at pressure p and temperature T. Quantity $\dot{m}_{\text{in}}$ at temperature T_{in} flows into the subdivision, whereas quantity $\dot{m}_{\text{out}}$ at temperature T_{out} flows out. The quantity of heat $\dot{Q}$ is supplied to the working fluid per unit time. In addition, quantity $\dot{m}'$, distributed

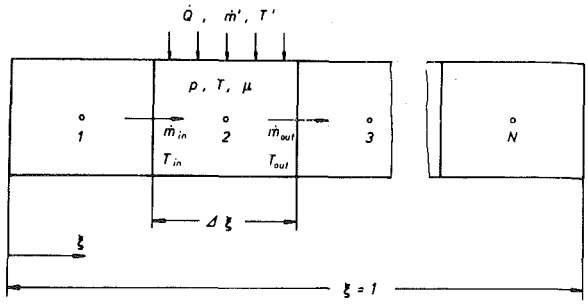


Fig. 2 Schematic of a flow channel

uniformly along the length, can be supplied through the walls with the temperature T'. This is the case, for example, if the flow channel is surrounded by a porous insulating material out of which gas flows into the channel in the case of a pressure drop in the channel.

Again neglecting the changes in kinetic energy and assuming that the state variables of the fluid are constant across the cross-section of the channel, we derive the equations

$$\frac{\partial T}{\partial t}=\frac{1}{\mu}\cdot\left[\frac{V\cdot\Delta\xi}{R}\cdot\frac{dp}{dt}-T\cdot\frac{\partial\mu}{\partial t}\right] \tag{3}$$

with

$$\frac{\partial\mu}{\partial t}=\frac{\frac{V\cdot\Delta\xi}{R\cdot\varkappa}\frac{dp}{dt}-\frac{\dot{Q}}{c_p}-\dot{m}'\cdot(T'-T)+\left(\frac{\dot{m}'}{2}+\dot{m}_{\text{in}}\right)\cdot\frac{\partial T}{\partial\xi}\cdot\Delta\xi}{T+\frac{\partial T}{\partial\xi}\cdot\frac{\Delta\xi}{2}} \tag{4}$$

The rate of change of the state variables of the working fluid in the circuit can be computed with equations (2–4) whenever the initial values are known.

Since the walls of the flow channels do not possess an infinitely large heat capacity, the transient processes also effect changes in the wall temperature. For this reason, the respective gradients must be calculated for each wall section.

In simple pipes a good approximation can be achieved by assuming that the pipes can be regarded as being adiabatic with respect to their environment. As a rule, pipes conveying hot gases are well insulated in order to prevent heat losses. The wall temperatures of pipes conveying cold gas deviate so little from the temperature of the environment that no appreciable heat exchange can take place.

This, however, does not hold true in the case of the heat exchange units where heat transfer on the external walls of the pipes must also be taken into account; specifically, heat transfer either to the working fluid of another flow channel in the heat exchanger or to the cooling water in the cooler, in which case the change of the temperature of the water must also be considered.

Turbomachines. The behavior of a closed gas turbine plant with transient operating states is largely determined by the operating behavior of the turbomachines. Sufficiently accurate information pertaining to the behavior of the turbomachines is therefore of vital importance.

In order to keep computation time to a minimum, it is expedient

Nomenclature

c_p, c_v = specific heat capacity at constant pressure or constant volume
h = lift of bypass valve
$\dot{m}$ = mass flow
n = alternator speed
P = power at terminals
p = pressure
$\dot{Q}$ = heat flux
R = gas constant
T = temperature (absolute)
t = time
V = volume
v = velocity
Δ = difference
$\varkappa$ = isentropic exponent
μ = mass of working medium in a subsection of a flow channel
ξ = related coordinate
ρ = density
overbars designate mean values

Subscripts

by = bypass
i = counting index
in = entering
hci = high pressure compressor inlet
hco = high pressure compressor outlet
hgp = hot gas pipe
hi = heater inlet
lci = low pressure compressor inlet
or = orifice
out = leaving
pci = precooler inlet
S = section
ti = turbine inlet
to = turbine outlet

Downloaded 01 Jun 2010 to 171.66.16.58. Redistribution subject to ASME license or copyright; see http://www.asme.org/terms/Terms_Use.cfm

to derive the behavior of the machines at each operating point from performance characteristics determined either from measurements or from more complicated calculations based on reliable methods. For the turbine performance characteristics we employed the method proposed by Bammert and Twardziok [4]. The performance characteristics of the axial-flow compressor are described by equations derived from measurements taken on very similar machines. The effect of the heat exchange between the working fluid and the wetted machine parts was approximated by using replacement heat exchangers in front of and behind each machine.

Results of the Experimental and Theoretical Investigations

Description of Plant Tested. First, the main parameters of the plant under consideration should be stated. The plant is designed for a maximum electrical power rating of 13.75 MW and can supply up to 27.9 MW of thermal energy to a heating system. At the design point the inlet pressure is 32.4 bar and the maximum temperature 983 K. The air enters the low-pressure compressor at 303 K and 7.8 bar. The turbo set has a single shaft and a rated rotational speed of 6643 rpm.

The location of measuring points is depicted in Fig. 3. Pressure and temperature of the circulating air were measured in front of and behind each machine and each component. An orifice gage was installed in the line between the high-pressure compressor and the heat exchanger for determining the mass flow. The mass flow through the bypass was measured by means of eight pitot-tubes. In addition, the lift of the bypass valve was measured. Finally, the generator output and rotational speed were determined.

Test with Sudden Load Release. The most pronounced changes of the circuit values and the steepest gradients occurred during load releases. The measured values are shown by solid lines and the computed values by points in Fig. 4. In this test the generator was disconnected from the power network when operating at an output of 10.5 MW, i.e., 84 percent of the rated output. The surge of surplus power causes an immediate acceleration in the rotational speed of the turboset. Just 0.1 s after the speed begins to increase, the bypass valve begins to open. The mass of working fluid flowing through the bypass increases rapidly and attains its maximum value after only approximately 0.5 s. At this point the value is more than twice as great as the mass of working fluid circulating in the circuit at the beginning of the test. The mass flow through the orifice gage downstream from the branch-off of the by-pass line also drops rapidly and even becomes negative for nearly 2 s.

Owing to the rapid opening of the bypass valve the rotational speed attains its maximum value after about 1.5 s and remains below 10 percent overspeed. Whenever the rotational speed drops, the speed regulator closes the bypass valve again completely for short periods of time. Ultimately, these processes approach a steady state which is reached after about 2.5 periods of oscillation of the rotational speed.

The significant changes in pressure and temperature take place in

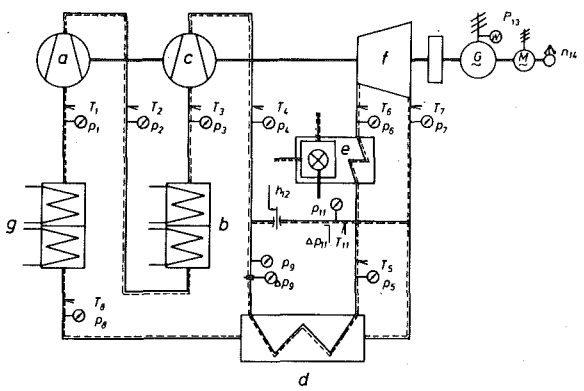


Fig. 3 Instrumentation stations of the investigated closed-cycle gas turbine

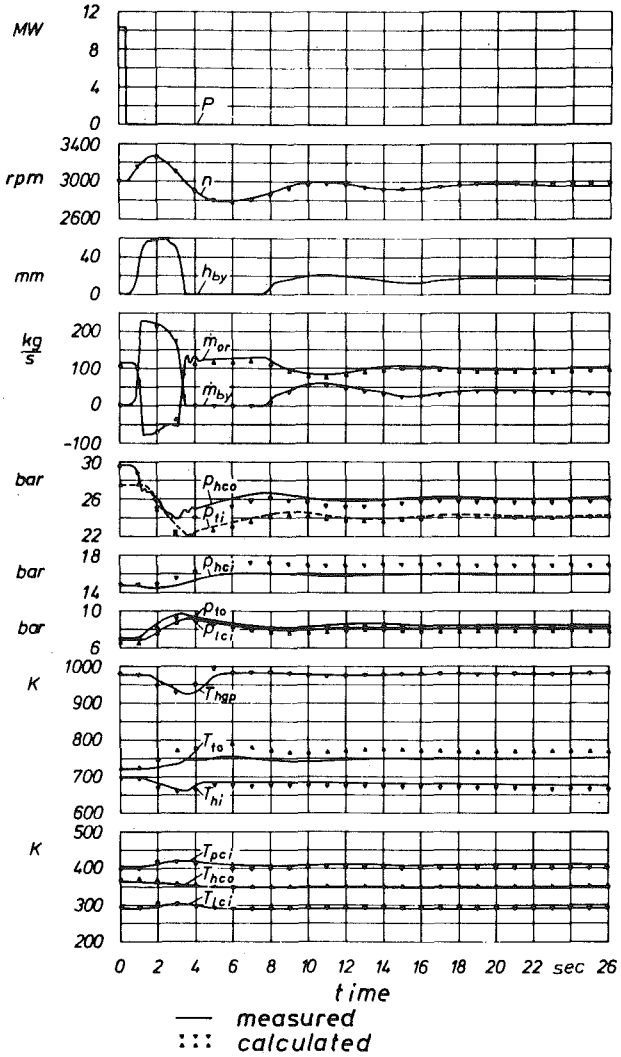


Fig. 4 Load release, comparison measurement-calculation

the first few seconds. Details are difficult to see in this illustration and are therefore depicted in the individual figures that follow.

Based on separately calculated stationary initial states, only the course of the generator ouptut, i.e., the load surge, and the measured lift of the bypass valve were known for calculating the load release. Considering the number of interrelated factors, the agreement between measured and calculated values can be regarded as very good. The measured course of the rotational speed (which can be regarded as the systems response to the outside, whereas the other processes take place internally within the circuit) is reproduced very well by the calculation. The agreementis not limited to the first few seconds but extends up to the new stable state.

In Fig. 5 the measured and calculated values of the mass flow through the orifice gage and the bypass line are again shown. The agreement is also very good during very sharp changes and the backflow phase at the orifice gage. The brief oscillations of the mass flow at the orifice gage are due to factors related to the inertia of mass of the flowing air. Their influence on the process as a whole can, however, be neglected.

Fig. 6 shows the course of several pressure readings for the first 12 seconds of the load-release test. The measuring point for the pressure at the high-pressure compressor output is located near the branch-off of the bypass line and therefore yields especially pronounced changes. Furthermore, influences arising from the inertia of mass of the flowing air are appreciable. The mean rate of pressure drop and recovery is in excellent agreement with predicted values. This applies with even greater accuracy to the pressure at the turbine inlet. Several components and long pipes are located between this measuring point and the branch-off of the bypass line, resulting in smoother transitions.

Downloaded 01 Jun 2010 to 171.66.16.58. Redistribution subject to ASME license or copyright; see http://www.asme.org/terms/Terms_Use.cfm

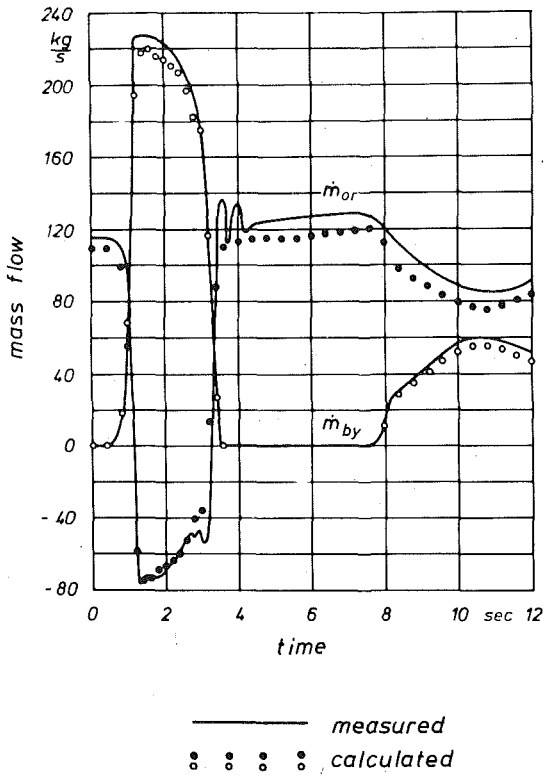


Fig. 5 Mass flows after load release

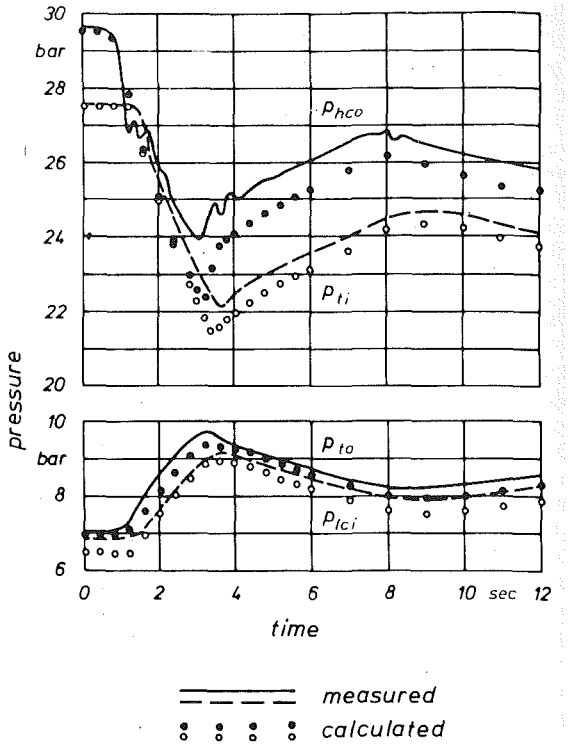


Fig. 6 Pressures after load release

On the plant tested the stream in the bypass line joins the large volume of the heat exchanger on the low-pressure side. There are therefore no abrupt pressure changes to be noted at the measuring point located at the turbine outlet and the low-pressure compressor inlet. The pressure gradients coincide well with the calculations.

Fig. 7 shows the measured and calculated processes for several temperatures in the circuit. The brief drops and/or rises in temperature during periods of greatest pressure change are especially noticeable. With regard to the temperature in the hot-gas line in front of the turbine, this phenomenon has been attributed to the influence of cooler gas flowing out of the insulation in the case of a pressure drop in the hot gas line. This explanation, however, does not account for a similar change in the heater input temperature, much less for the temperature increase on the low-pressure side of the circuit. These temperature changes are caused by the expansion or compression of the air.

The rise in temperature at the turbine output is also caused by a drop in the expansion ratio and therefore of the enthalpy gradient in the machine. With the sole exception of the turbine output temperature the calculated temperature course tallies very well with the measured values. Slight shifts in time occur which are due to the delayed reaction of the thermoelements.

The curves show that the assumption frequently made that the outlet temperatures of the heat exchanging components change only slightly yields excellent approximation. The assumption, however, may not be extended to apply to the quantity of heat transmitted within the components.

Fig. 8 gives the course of the thermal power transmitted in the heat exchanger during a load release. It can be seen that pronounced changes occur within a very short time. On the high-pressure side the direction of heat flow even reverses for short periods. As shown earlier, a reversed flow occurs briefly on the high-pressure side. In this way heated air comes in contact with cooler parts of the heat-transmitting surfaces and gives off some of its heat. The marked changes in the quantity of heat transferred to or withdrawn from the working fluid have a substantial effect on the course of the pressures in the circuit and further reinforce the pressure changes brought about by the bypass stream.

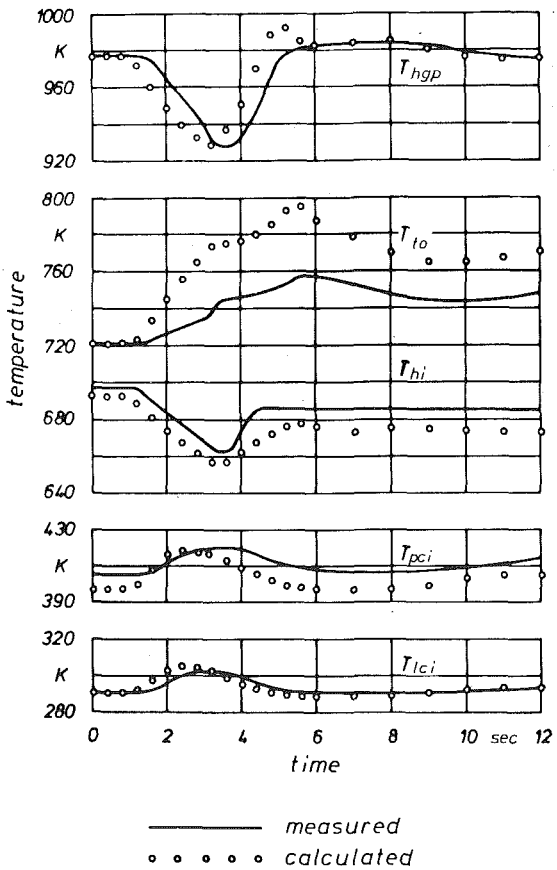


Fig. 7 Temperatures after load release

Downloaded 01 Jun 2010 to 171.66.16.58. Redistribution subject to ASME license or copyright; see http://www.asme.org/terms/Terms_Use.cfm

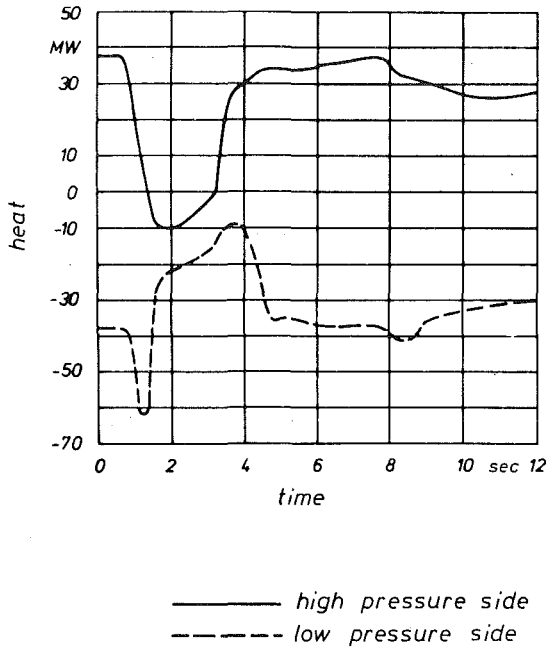


Fig. 8 Heat exchange in the recuperator

Summary

In order to study the behavior of a closed gas turbine plant having operational states that change with time, a theoretical model was developed that takes into account the transient behavior of the components. The heat exchange between the working fluid and the walls of the lines is considered as well.

In order to test the model, measurements were performed on a closed air turbine. The results of the test, the most important of which are presented, confirm the reliability of the computation method. The calculations coincide well with the measured rotational speed. Pressures, temperatures, and mass flow are also predicted accurately. The agreement of the measured and calculated values extends almost up to the establishment of a new stable state.

References

1 Bammert, K., and Groschup, G., "Status Report on Closed-Cycle Power Plants in the Federal Republic of Germany," ASME JOURNAL OF ENGINNEERING FOR POWER, Vol. 99, No. 1, 1977, pp. 37–46.

2 Bammert, K., and Deuster, G., "Operating Experiences with the Oberhausen Helium Turbine Power Plant," Presented at the 22nd ASME Gas Turbine Conference, Philadelphia, PA, March 28, 1977

3 Bammert, K., and Pösentrup, H., "The Behavior of a Closed-Cycle Gas Turbine with Time Dependent Operating Conditions," *VDI-Forschungsheft* 588, 1978, pp. 1–36.

4 Bammert, K., and Twardziok, W., "Stationary Operational Behavior of Gas Turbines Driven by Conventional and Nuclear Energy," *Atomkernenergie*, Vol. 11, No. 5/6, 1966, pp. 185–204.

Downloaded 01 Jun 2010 to 171.66.16.58. Redistribution subject to ASME license or copyright; see http://www.asme.org/terms/Terms_Use.cfm

N. W. Foster
D. Lampard

Department of Mechanical Engineering,
University of Nottingham,
NG7 2RD, England

The Flow and Film Cooling Effectiveness Following Injection through a Row of Holes

Using a mass transfer technique, detailed studies have been made of the effectiveness and flow downstream of a row of holes in the flat floor of a wind tunnel. The effects of variation of injection angle, upstream boundary layer, and hole spacing are described, and an assessment of the relative aerodynamic penalties is made. A small injection angle is shown to give the best cooling effectiveness at low blowing ratio while large injection angles are best at high blowing rates. Increasing the upstream boundary layer thickness reduces the effectiveness due to enhanced lateral mixing and film dilution. Small hole spacings give improved lateral coverage and alleviate jet lift-off effects.

1 Introduction

The film cooling of rotor blades has become common in gas turbines in recent years, and the high stress levels in these components have dictated the use of discrete holes, rather than slots, to eject the coolant through the blade surface. The effectiveness of the cooling provided by a row of holes is dependent upon a very large number of parameters including the ratios of injectant velocity and density to the mainstream levels, the injection angle, the hole spacing to diameter ratio, and the boundary layer thickness upstream of the injection point.

Because of the range of these parameters encountered in practice, it is usual to study the effects of only one or two in any particular investigation. Further, only the effectiveness has commonly been measured, and in some cases this has been an average value measured across a number of holes. The data thus obtained give no direct information about the flow which results in the measured levels of effectiveness and is of limited value therefore in the development of models to predict effectiveness. Flow measurements also permit some evaluation of the aerodynamic penalties which arise from the choice of a particular configuration and flow rate.

The results presented in this paper include both detailed effectiveness and flow data. Emphasis is given to the effects of injection angle, upstream boundary layer thickness and hole-spacing to diameter ratio.

2 Experimental Method and Ranges of Parameters Studied

A mass transfer technique was used in which a mixture of a dense refrigerant vapor (Freon 12) with air was injected into an airstream. Both injectant and mainstream were at ambient temperature and the proportion of Freon in the injectant was adjusted to give a nominal injectant to mainstream density ratio of 2, corresponding to that in many modern gas turbine blade cooling situations. The correct simulation of density ratio is important as the effectiveness increases with this parameter, as found by Goldstein, et al. [1], the present authors [2, 3], and Pedersen, et al. [4].

The Freon was thoroughly mixed with air from the laboratory compressed air supply using a chamber containing successively high and low pressure drop orifice systems and gauzes. The mixture then passed to a plenum chamber which contained further gauze screens.

The injectant was introduced through long tubes set in a section of the flat floor of an open return wind tunnel (see Fig. 1). This section could be traversed in a cross-stream direction so that only a single line of sampling tappings of 0.67 mm bore was needed in a fixed section of the floor downstream of the injection station to permit a complete survey of the surface. Most traverses were conducted behind the central injection hole, but surveys were also made at points close to the outer edge of the injection array to confirm two-dimensionality of the effectiveness distribution. A pitot tube was used to check that the total pressures of the injectant jets were uniform. Measurements within the upstream boundary layer, or the cooling film could be undertaken using a micrometer screw traverse fixed to the tunnel roof. Most boundary layer traversing was done with a hot wire probe, although a flattened pitot probe was used for the thickest layer. A flat nosed total pressure probe, and an isokinetic sampling probe were used for traverses within the films.

The tunnel floor boundary layer was bled off, and a trip wire of 0.75 mm dia sited at 42 mm from the leading edge to provide a turbulent upstream boundary layer. Interchangeable roof contours provided for varying degrees of acceleration over a boundary layer development length upstream of the injection station. In this way, a range of boundary layer thicknesses could be obtained. The upstream boundary layer was measured at points 1 mm upstream of the injection holes on, and 110 mm either side of, the center line. These mea-

Contributed by the Gas Turbine Division and presented at the Israel Joint Gas Turbine Conference and Exhibition, Haifa, Israel, July 9–11, 1979, of THE AMERICAN SOCIETY OF MECHANICAL ENGINEERS. Manuscript received at ASME Headquarters April 4, 1979. Paper No. 79-GT/Isr-6.

Copyright © 1980 by ASME

Downloaded 01 Jun 2010 to 171.66.16.58. Redistribution subject to ASME license or copyright; see http://www.asme.org/terms/Terms_Use.cfm

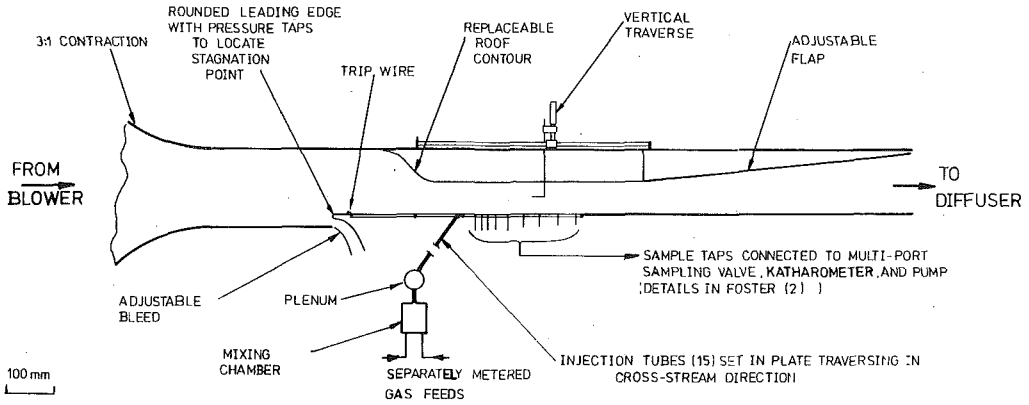


Fig. 1. Diagram showing the test section of the wind tunnel

Table 1 Main test parameters

Hole diameter, D	:	2.27 mm
Hole spacing	:	usually $3D$ $1.25D$, $2.5D$, $3.75D$, $5D$ used to study effect of spacing.
Injection angle	:	90 deg, 55 deg, or 35 deg
Injectant : Mainstream density ratio, ρ_j/ρ_∞	:	2
Range of blowing parameter, M	:	0.5 to 2.5
Mainstream velocity	:	25 m/s
Upstream boundary layer thickness, δ^*	:	0.16 D except for tests on effect of boundary layer thickness variation
Pressure gradient	:	Zero

surements confirmed that the boundary layer was two-dimensional and turbulent, although not in equilibrium as the shape factor varied from about 1.3 for the thickest boundary layer to 2.42 for the thinnest.

Gas samples were drawn through a simple katharometer for all concentration measurements. The film cooling effectiveness was then calculated from the ratio of concentrations in the local (wall) sample, c_ω, to that in the injectant, c_j i.e., $\eta = c_\omega/c_j$.

This can be shown to be equivalent to an adiabatic wall effectiveness following Pedersen, et al. [4].

Checks on the resolution of the gas analysis and repeatibility of results were conducted which indicated confidence limits for effectiveness of ± .02. i.e., in this paper, an effectiveness of n percent may be regarded as $(n \pm 2)$ percent.

The ranges of the main test parameters are given in Table 1. With the exception of the tests of Section 4, the upstream boundary layer displacement thickness was 0.16 diameters, and with the exception of those of section 5, the hole spacing was 3 diameters for the results reported here.

3 The Effect of Injection Angle

These tests were performed with a spacing-to-diameter ratio of 3, and a thin upstream boundary layer ($\delta^*/D = 0.16$). The results are presented in terms of spanwise averaged effectiveness in Fig. 2 for low and medium blowing rates. The most striking features are the change in form of the curves for 35 and 55 deg injection between the two blowing rates, and the reversal of the order of merit of the injection

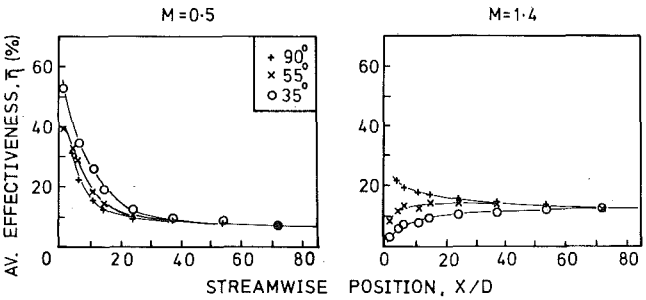


Fig. 2 Variation of spanwise averaged effectiveness with distances from the injection point for two blowing rates and three injection angles

angle. Far from the injection point, $\bar{\eta}$ becomes independent of injection angle, but this distance increases with the blowing rate.

The change in the form of the $\bar{\eta}$ distribution with blowing rate for the shallower injection angles can be explained by jet "lift off." The tendency for the emergent jets to become detached from the surface at elevated blowing rates is well-known. What then happens is that the region beneath the jet is ventilated by the mainstream, and a low effectiveness occurs. Subsequently, the jet spreads and mixes with the mainstream and re-attaches to the surface. Although the 90 deg injection angle leads to a higher jet trajectory, the jets spread more rapidly than for shallow injection angles, and coalesce closer to the injection point.

The spanwise averaged effectiveness is derived, of course, from the

Nomenclature

c = concentration (by mass)
D = injection hole diameter
M = blowing rate: $(\equiv \rho_j u_j/\rho_\infty u_\infty)$
S = injection hole spacing
u = velocity
x = streamwise coordinate; origin is hole center
y = coordinate normal to surface
z = cross-stream (spanwise) coordinate
η = effectiveness
$\bar{\eta}$ = spanwise (i,e., cross-stream) averaged effectiveness
ρ = density
δ^* = displacement thickness:

$$\left(\equiv \int_0^\infty \left(1 - \frac{\rho u}{\rho_\infty u_\infty}\, dy\right)\right)$$

θ = momentum thickness:

$$\left(\equiv \int_0^\infty \frac{\rho u}{\rho_\infty u_\infty}\left(1 - \frac{u}{u_\infty}\right) dy\right)$$

Subscripts

j = injectant (jet)
∞ = mainstream
ω = wall ($y = 0$)

Downloaded 01 Jun 2010 to 171.66.16.58. Redistribution subject to ASME license or copyright; see http://www.asme.org/terms/Terms_Use.cfm

cross-stream (spanwise) distribution of effectiveness. It depends strongly on the lateral spreading rate of the jets and on the spacing-to diameter ratio of the holes. Fig. 3 compares distributions for the three angles at $M = 1.4$ and an immediate impression of the relative strength of the mixing can be obtained by looking at the first station, $x/D = 6.5$, where near-zero values are obtained between the holes for 35 deg injection, while 90 deg injection gives a minimum level of about 50 percent of its maximum.

Fig. 3 also gives an indication of the speed with which the three films mix out. The cross-stream distribution has become uniform by 23.8 diameters for 90 deg injection and by 37.3 diameters, the 55 deg distribution is approximately uniform. This is also the point at which the two $\bar{\eta}$ distributions begin to agree (Fig. 2). For 35 deg injection, however, uniformity is still incomplete at 54.6 diameters.

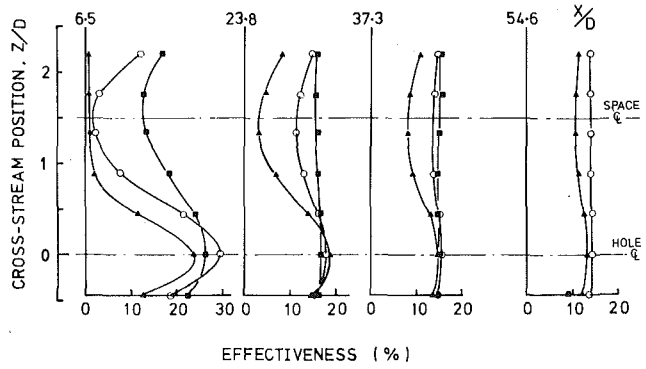


Fig. 3 Variation of local effectiveness with injection angle and position for $M = 1.4$ (▲ 35 deg injection angle; ○ 55 deg injection angle; ■ 90 deg injection angle)

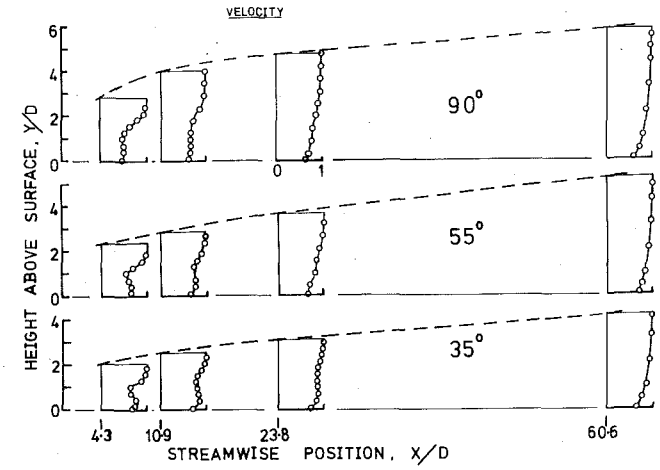


Fig. 4(*a*) Velocity profiles, u/u_∞

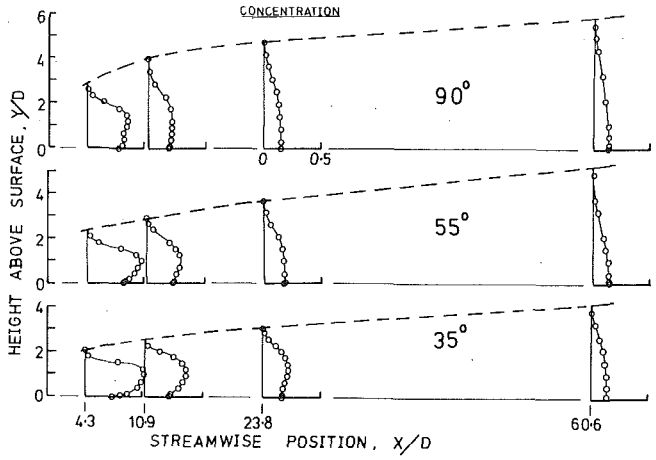


Fig. 4(*b*) Concentration Profiles, c/c_j, measured in the plane of a hole center. (Blowing rate, $M = 1.4$; --- Approximate position of edge of film)

Evidence of film non-uniformity at large distances for 35 deg injection is also present in velocity and concentration profiles measured in the films above the surface (Figs. 4(*a*), 4(*b*)), and has also previously been recorded by Liess and Carnell [5] at this injection angle for a comparable spacing to diameter ratio, at a lower blowing rate (0.85), and over a shorter measurement section.

The approximate location of the film boundaries in the measuring plane are also indicated in Fig. 4. The growth rates are clearly very different for the three angles, particularly in the initial twenty diameters. Jet lift-off is seen most clearly in the concentration profiles, Fig. 4(*b*), where prominent maxima are visible in the initial profile, especially for 35 and 55 deg injection. Comparison with Fig. 3 at $x/D = 23.8$ indicates that achievement of a uniform cross-stream distribution of effectiveness is roughly coincident with the disappearance of the concentration maximum and the occurrence of a near-zero concentration gradient close to the wall.

In interpreting the velocity profiles, it should be remembered that although the blowing rate is high, the velocity ratio is only 0.7 because of the high density ratio. The presence of the jet structure is therefore indicated by a depression in the velocity in the near-wall region.

The persistence of the jet structure is a function of blowing rate, as seen in Fig. 5 for normal injection. At $M = 2.4$, a slight maximum is still present above the wall. The rapid increase in the film thickness with blowing rate can be ascribed to the increasing penetration of the jet into the mainstream, as it is accompanied by a movement of the maximum concentration point away from the wall at $x/D = 4.3$.

It is clearly desirable to validate the present results by direct comparison with those of other investigators. Unfortunately, not only is geometric similarity necessary, but also, as mentioned in Section 2, the density ratio must be identical. This latter condition severely limits the comparative data, but fortunately, Pedersen, et al. [4] have used an identical geometry and density ratio. It also happens that the displacement thickness for their tests is 0.16 diameters as here. A comparison of results from the present series of tests with those estimated from [4] is given in Fig. 6. Only small differences are observed for the spanwise averaged and center line effectiveness in Fig. 6(*a*) and the spanwise distributions in Fig. 6(*b*) are also seen to be closely similar. It should be noted that the data of [4] in Fig. 6(*b*) are for a location 11.16 diameters downstream of the hole centre, while the position for the present data is 10.86 diameters. Further, although the boundary layer displacement thicknesses are the same in terms of hole diameter, the momentum thicknesses are almost certainly not.

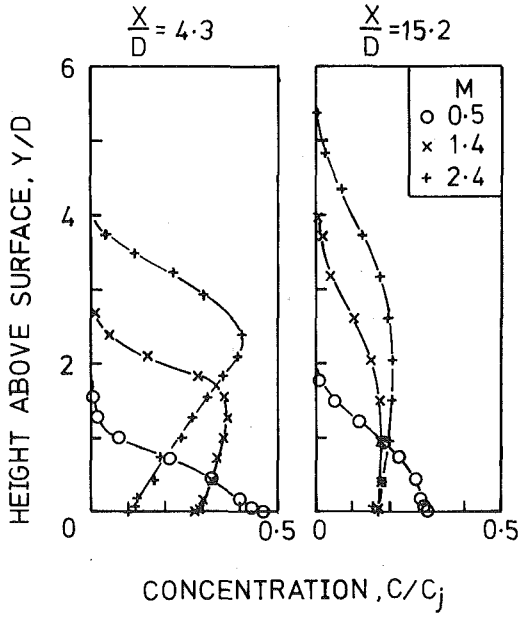


Fig. 5 Vertical distribution of concentration in the plane of a hole center for 90 deg injection

Downloaded 01 Jun 2010 to 171.66.16.58. Redistribution subject to ASME license or copyright; see http://www.asme.org/terms/Terms_Use.cfm

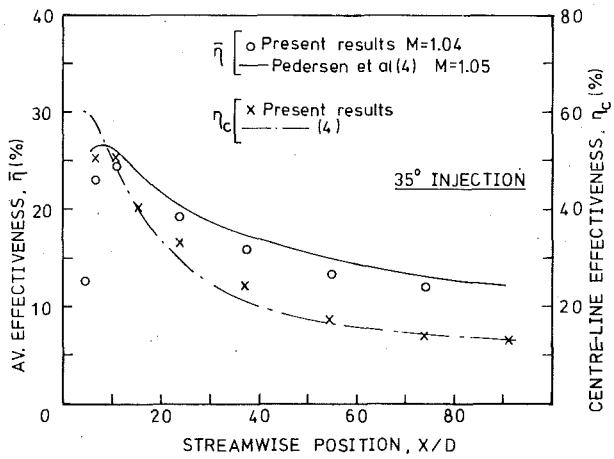


Fig. 6(*a*) Spanwise averaged and center line effectiveness

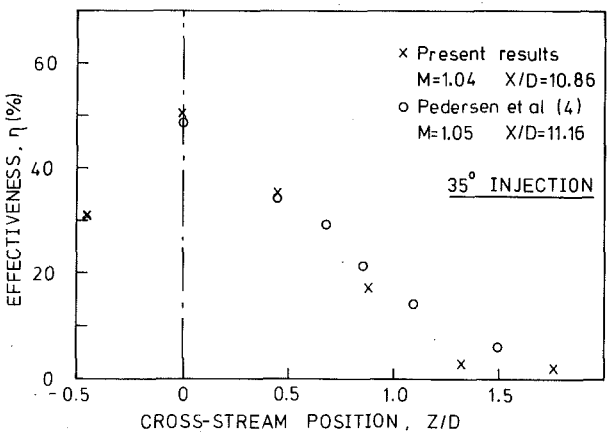


Fig. 6(*b*) Cross stream distribution of effectiveness

Fig. 6 Comparison of results for 35 deg injection with those of Pedersen, et al. [4]

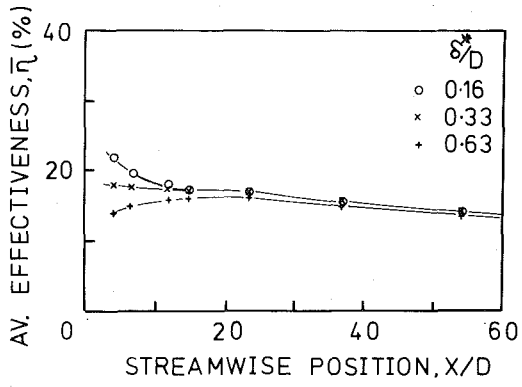


Fig. 7 Effect of upstream boundary layer thickness on spanwise averaged effectiveness for 90 deg injection at $M = 1.4$

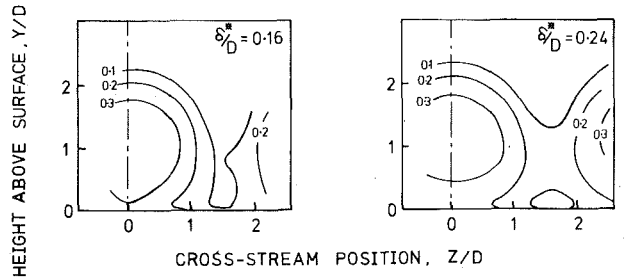


Fig. 8 Concentration contours in a vertical plane at $x/d = 4.3$ for two boundary layer thicknesses at $M = 1.4$, and 90 deg injection angle

These two factors probably account for the slightly higher effectiveness at $z = 0$, and slightly lower effectiveness at $z = 1.5D$ of the present results.

The observed three-dimensionality of the films has important consequences for the design of film cooling systems. The low effectiveness in the inter-hole region for shallow injection angles means that large spanwise temperature gradients can occur which may result in unacceptable stresses. Mixing is increased and three-dimensionality reduced as the injection angle approaches 90 deg: the severity of lift-off effects is also reduced, permitting higher blowing rates to be used. Wall conduction and internal blade cooling will, of course, mean that the spanwise temperature non-uniformity will be less than that of the effectiveness.

4 The Effect of Upstream Boundary Layer Thickness

A reduction in the cooling effectiveness with increasing upstream boundary layer thickness has been reported by Liess [6] and by Eriksen and Goldstein [7]. The results of the present investigation confirm this and are typified by Fig. 7 in which the effectiveness, $\bar{\eta}$, is plotted for three boundary layer thicknesses. The effect close to the injection point is strong, but has almost disappeared within 20 diameters.

Eriksen and Goldstein [7] suggested that a possible explanation for the observed behavior is the greater "force" encountered by the emergent jet in the presence of a thin boundary layer which results in the jet being turned parallel to the wall in a shorter distance.

Examination of concentration contours measured above the surface at $x/D = 4.3$, Fig. 8, does not confirm this hypothesis. There appears to be no measurable difference between the heights of the concentration profiles in the upper part of the jet on the jet center line. It should be noted that, although the displacement thicknesses differ by a factor of 1.5, the corresponding variation in momentum thicknesses was much bigger, about 2.7, and it is this which is most likely to control the jet deflection.

The major differences occur in Fig. 8 below the jet centers, and between the jets. Rather more cross-stream diffusion has occurred in this region with the thicker boundary layer, and the increased dilution leads to a lower effectiveness. It appears, then, that it is a decrease in the mixing between the jet and the mainstream rather than an increase in the jet deflection which results in an improvement in the effectiveness as the boundary layer thickness diminishes.

5 The Effect of Injection Hole Spacing

Studies of the effect of hole spacing have been reported for shallow injection angles by Liess and Carnell [5] and by Metzger, et al. [8, 9]. In [5], three spacings of 2.22, 3.33 and 4 diameters were used and in [8] and [9] two spacings of 1.55, 1.71.

In the present work, a 90 deg injection angle was used at spacings of 1.25, 2.5, 3.75 and 5 diameters in addition to the "standard" 3 diameters used in the remainder of the work. The smallest spacing, in common with those used by Metzger, et al. [8, 9] is too small to be employed in practice, but provides a "limiting condition" as the flow approaches that for slots. In fact, difficulties were initially encountered in the experiments at high blowing rates with the smallest spacing because the jets were found to coalesce almost immediately to form a detached coolant sheet which, because the row of holes did not fully span the tunnel, could be ventilated beneath from its ends. The resultant flow was far from two-dimensional with a large variation in effectiveness between the row center and ends. False side walls were fitted at the ends of the row extending over 100 diameters in the stream direction and this variation was thus eliminated.

Fig. 9 shows the cross-stream variation in effectiveness at 6.5 diameters from the row for spacings of 2.5, 3.75, and 5 diameters and for blowing rates of 0.5 and 2.4.

At the low blowing rate, little variation is seen in the center line effectiveness as the spacing varies; the primary variation is in the inter-hole region where near zero levels occur at the largest spacing indicating that the jets have not yet merged. The spacing of 1.25 diameters gave a nearly uniform cross stream distribution with a value approximately double that at the center line for the other spacings.

Downloaded 01 Jun 2010 to 171.66.16.58. Redistribution subject to ASME license or copyright; see http://www.asme.org/terms/Terms_Use.cfm

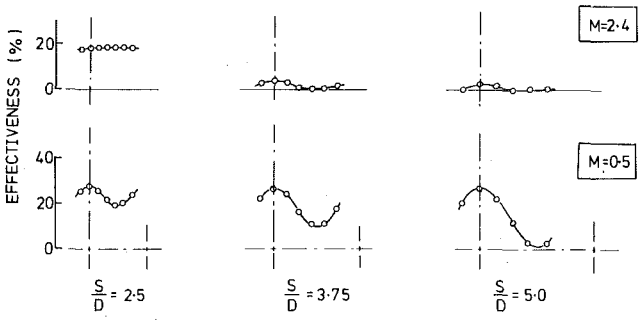


Fig. 9 Cross-stream variation in effectiveness for three hole spacings and two blowing rates ($x/D = 6.35$)

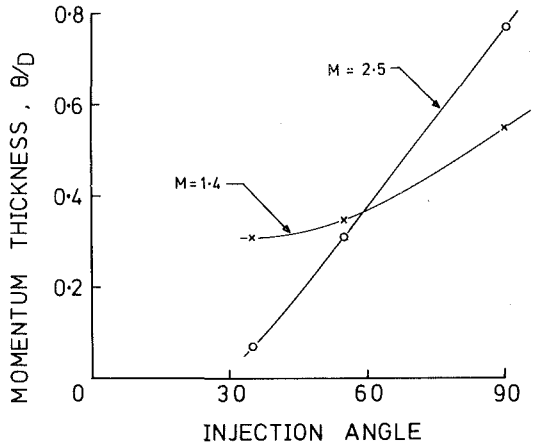


Fig. 10 Variation in momentum thickness of film with injection angle (at $x/D = 60.6$)

At the higher blowing rate of Fig. 9, it seems that the spacing of 2.5 diameters is sufficiently small for the jets to coalesce and inhibit the penetration of the mainstream with the result that a uniform level of effectiveness is observed; the distributions at the wider spacings are much less uniform and at very low levels.

From the design viewpoint, it is clearly desirable to use a small spacing to diameter ratio to insure good uniformity of the effectiveness at low blowing rates, and to alleviate lift-off effects at high blowing rates. If the coolant flow rate and blowing rate are specified, the hole diameter must, of course, be reduced with the spacing-to-diameter ratio.

The results presented in Fig. 9 are for a point close to the injecting row. Far downstream, the effectiveness was found to vary inversely with the row spacing for blowing rates less than 1.4. This indicates a direct dependence upon the coolant flow per unit span.

6 Aerodynamic Penalties

It is not possible to predict from the present measurements the penalties that will be incurred in any particular installation as an injudicious choice of injection angle, blowing rate or row position can result in the precipitation of flow separation with consequential large scale modification to the flow pattern. What we can do is to examine the momentum thicknesses of the films far from the injection point where they have become two-dimensional and use this as an indication of the relative momentum deficiencies which will occur in the blade wakes and thus as a measure of relative drags.

In Fig. 10, the momentum thickness at 60.6 diameters from the row is plotted as a function of injection angle for two blowing rates. It can be seen that the momentum thickness reduces with the injection angle for both blowing rates, but the decrease is much sharper at the high blowing rate. Whereas the momentum thickness increases with blowing rate for 90 deg injection, it decreases for 35 deg injection: in fact, at $M = 2.5$, the momentum thickness at 60 diameters is virtually the same as for the boundary layer immediately upstream of the row.

Conclusions

1 Shallow injection angles give the highest spanwise averaged effectiveness at small blowing rates and large injection angles at high blowing rates.

2 The cross-stream (spanwise) distribution of effectiveness is more uniform for large injection angles than for small angles.

3 An increase in the upstream boundary layer thickness produces a reduction in the effectiveness due to increased lateral mixing in the near-wall region rather than an increase of jet penetration into the mainstream.

4 The use of a small spacing-to-diameter ratio gives improved lateral coverage at all blowing rates, and alleviates lift-off effects at high blowing rates.

5 The momentum thickness far downstream of the injection point reduces with the injection angle, and also with the blowing rate for shallow injection angles.

Acknowledgments

This work was carried out in the Department of Mechanical Engineering at the University of Nottingham and funded by a grant from the Science Research Council. The use of the facilities, and the financial support are gratefully acknowledged.

References

1 Goldstein, R. J., Eckert, E. R. G., and Burggraf, F., "Effect of Hole Geometry and Density on Three Dimensional Film Cooling," *International Journal of Heat and Mass Transfer*, Vol. 17, 1974, pp. 595–607.

2 Foster, N. W., "Film Cooling of Gas Turbine Blades," Ph.D. Thesis, University of Nottingham, 1976.

3 Foster, N. W. and Lampard, D., "Effects of Density and Velocity Ratio on Discrete Hole Film Cooling," *AIAA Journal*, Vol. 13, No. 8, Aug. 1975, pp. 1112–1114.

4 Pedersen, D. R., Eckert, E. R. G., and Goldstein, R. J., "Film Cooling with Large Density Differences Between the Mainstream and the Secondary Fluid Measured by the Heat-Mass Transfer Analogy," ASME JOURNAL OF HEAT TRANSFER, Vol. 99, 1977, pp. 620–627.

5 Liess, C., and Carnell, J., "Application of Film Cooling to Gas Turbine Blades," *High Temperature Turbines*, AGARD CP 73-71, 1971, pp. 23.1–23.9.

6 Liess, C., "Film Cooling with Ejection from a Row of Inclined Circular Holes—An Experimental Study for the Application to Gas Turbine Blades," Von Karman Institute Tech. Note 97, March 1973.

7 Eriksen, V. L. and Goldstein, R. J., "Heat Transfer and Film Cooling following Injection through Inclined Circular Tubes," ASME JOURNAL OF HEAT TRANSFER, Vol. 16, May 1974.

8 Metzger, D. E. and Fletcher, D. D., "Surface Heat Transfer Immediately Downstream of Flush, Non-Tangential Injection Holes and Slots," A.I.A.A. Paper No. 69-523, 1969.

9. Metzger, D. E., Biddle, J. R. and Warren, J. M., "Evaluation of Film Cooling Performance on Gas Turbine Surfaces," *High Temperature Turbines*, AGARD CP 73-71, 1971, pp. 24.1–24.7.

Downloaded 01 Jun 2010 to 171.66.16.58. Redistribution subject to ASME license or copyright; see http://www.asme.org/terms/Terms_Use.cfm

B. Gal-Or

Professor.
Dept. of Aeronautical Engineering,
Technion-Israel Institute of Technology,
Turbo and Jet-Engine Laboratory,
Haifa, Israel

Plasma-Spray Coating Processes: Physico-Mathematical Characterization

Approximate characterization of the complicated dynamics of plasma-spray coating processes may be useful in obtaining optimal coatings. The usual industrial method of obtaining such a characterization by experimental trial-and-error procedures may be more time-wasting and costly than a combined procedure of analysis and trial-and-error. This paper describes such an approximate analysis and presents the results in a simple graphical form. Thus, by using a few simplified differential equations which describe the fluid dynamics, temperature and velocity distributions as well as the degree of evaporation of the injected powder in the plasma jet, we illustrate our method for the specific case of spraying molybdenum particles in argon as the carrier gas. The results indicate the various limitations associated with major operating variables such as particle size, relative mass flow rates of gas and particles, plasma temperatures, and distances from the plasma gun. Evaporation losses of the powder are given in Fig. 7.

Presentation of the Problem

Ceramic and metal coatings by plasma spraying processes are characterized by a high-temperature electric arc concentrated and stabilized in the controlled atmosphere of a non-oxidizing gas flowing through a subsonic or supersonic nozzle. As the gas passes through the arc it may reach temperatures of 20,000 to 30,000°F or beyond. Consequently, the gas is accelerated to subsonic or supersonic velocities. At these temperatures the gas (usually A, N_2, He, H_2 or their combinations) is ionized to form a plasma jet emerging from the nozzle. Cold, small, solid particles ("powder") of the materials to be coated are then injected into the flowing hot plasma. Entering the plasma jet the particles are heated, wholly or partially melted, and are finally impacted on the (cold) workpiece to produce an adherent coating which solidifies on impact. The process has been extensively used by the gas-turbine and other industries to produce coatings of a wide range of high-melting-point materials (i.e., refractory metals, such as W, Ta, or Mo, as well as ceramics such as Al_2O_3, ZrO_2 or magnesium zirconate, carbides—e.g., WC—borides, nitrides, etc.). The coatings are applied for such purposes as thermal barriers (in combustors, after-burner liners, nozzles, etc.) and as corrosion resistance, wear resistance, abrasive finishes, bearing surfaces and composite materials. The application of various ceramic coatings to engine combustors and to after-burner liners of modern jet engines has proved effective, since it allows an increase in flame temperature (and consequently of thrust), or a substantial increase in the lifetime of these components.

Advantages of the plasma spraying coating process include: (1) a wide range of materials for coatings (in particular high-melting point materials); (2) a low degree of oxidation (due to the inert atmosphere of the carrier gas); (3) a minimal workpiece deformation; and (4) a possibility for application to relatively low melting point materials (the workpiece remains relatively cold during coating). The flame spraying method uses a somewhat similar idea in applications which, however, are normally limited to lower melting-point coating materials than those used in plasma sprays. This is due to the lower temperature obtainable with flames as compared with the plasma.

By controlling the dynamics of plasma spraying one can vary the porosity in the resulting coating as well as its adhesive strength to the substrate. To arrive at predetermined goals the determination of optimum operating conditions for each specific application is required. The main problem involved here is the fact that porosity and adhesion depend on many factors: from nozzle to surface distance, to the distribution of particle and gas velocities in the jet, from the average size and size distribution of the injected particles, to the type of gas, plasma temperature, type of nozzle, etc. While an increasing number of technical reports have, during the last decade or so, reported a considerable amount of empirical data on this process, there has been as yet no systematic analysis of the fluid dynamic, heat and mass transfer processes involved during this complicated process.

One of the more advanced analyses in this field, written by Surov and Babrov [3] is still quite limited in being restricted to some simple considerations of the velocity distribution in the spray-coated jets without giving any systematic analysis of the heat transfer, evaporation rates and size distribution involved.

The objective of this paper is, therefore, to outline a simplified,

Contributed by the Gas Turbine Division and presented at the Israel Joint Gas Turbine Conference and Exhibition, Haifa, Israel, July 9–11, 1979, of THE AMERICAN SOCIETY OF MECHANICAL ENGINEERS. Manuscript received at ASME Headquarters April 2, 1979. Paper No. 79-GT/Isr-8.

Copyright © 1980 by ASME

Downloaded 01 Jun 2010 to 171.66.16.58. Redistribution subject to ASME license or copyright; see http://www.asme.org/terms/Terms_Use.cfm

one-dimensional analysis of this process and to demonstrate how the results may be utilized to characterize a specific application. (Extension of this method to a two-dimensional analysis is almost straightforward but involves considerable formulation and computations).

Formulation of the Problem

The equations describing the change in mass, velocity and temperature of the injected particles may be approximated by [1, 2]:

$$\frac{dw_p}{dx} = 0 \tag{1}$$

$$\frac{dV}{dx} = \frac{3}{8} C_D \frac{\rho_g}{D} \cdot \frac{(U-V)|(U-V|}{RV} \quad \text{(Injected particles prior to melting)} \tag{2}$$

$$\frac{dT_p}{dx} = \frac{3}{2} \frac{\mathrm{Nu} C_{pg} \mu^*}{R^2 \mathrm{Pr} D V C_p} (T_g - T_p) \tag{3}$$

$$\frac{dw_p}{dx} = 0 \tag{4}$$

$$\frac{dV}{dx} = \frac{3}{8} C_D \frac{\rho_g}{D} \cdot \frac{(U-V)|U-V|}{RV} \quad \text{(Injected particles during melting)} \tag{5}$$

$$\frac{dT_p}{dx} = 0 \tag{6}$$

$$\frac{dw_p}{dx} = \frac{-3 W_p \mathrm{Nu}^d \mu^* (\chi_{vs} - \chi_{v\infty})}{2R^2 D V \mathrm{Sc}(1-\chi_{vs})} \quad \text{(Injected particles during evaporation)} \tag{7}$$

$$\frac{dV}{dx} = \frac{3}{8} \frac{C_D \rho_g}{D} \cdot \frac{(U-V)|U-V|}{RV} \tag{8}$$

$$W_p C_p \frac{dT_p}{dx} = \frac{3 \mathrm{Nu} C_{pg} W_p \mu^*}{2R^2 \mathrm{Pr} D V} (T_g - T_p) \quad \text{(Injected particles during evaporation)}$$

$$+ [\Delta H^\circ_{\mathrm{vap}} + (C_{pg} - C_{pf})(T_p - T_{pm})] \frac{dW_p}{dx} \tag{9}$$

The normalized (dimensionless) momentum, energy, continuity and state equations for two-phase jet flow may be approximated as [1, 2]:

$$I = (1-\epsilon)(\rho_g + \rho_v) U^2 A + \epsilon D V^2 A + pA \tag{10}$$

$$J = (1-\epsilon)(\rho_g + \rho_v) UH \left(H_g + \frac{1}{2} V^2\right) + \epsilon D V A \left(H_p + \frac{1}{2} V^2\right) \tag{11}$$

$$W_g = (1-\epsilon)\rho_g U A \tag{12}$$

$$W_0 = (1-\epsilon)\rho_v U A + \epsilon D V A + (1-\epsilon)\rho_g U A \tag{13}$$

$$P = \frac{1}{\gamma} \left(\frac{m_0}{m_g} \rho_g + \frac{m_0}{m_v} \rho v\right) T_g \tag{14}$$

where

$$H_g = \frac{1}{\rho_g + \rho_v} [\rho_g C_{pg} (T_g - T_0) + \rho_v (C_{pv} (T_g - T_0) + \Delta H_{\mathrm{vap}}] \tag{15}$$

$$H_p = \begin{cases} C_{ps}(T_p - T_{p0}) & \text{(solid state)} \\ C_{ps}(T_p - T_{p0}) + \Delta H_m + C_{pf}(T_p - T_{pm}) & \text{(liquid state)} \end{cases} \tag{16}$$

To solve this set of (nonlinear) differential equations one needs the proper empirical and/or theoretical expressions for the "heat," Nu^h, and "diffusion," Nu^d, Nusselt numbers as well as for the drag coefficient of the particles in the gas, C_D. Various expressions for these parameters exist in the literature (for review see [2] and [4]. For the purpose of this demonstration we choose the simplest, namely:

$$\mathrm{Nu}^h = 2 + 0.6[\mathrm{Re}]^{1/2}[\mathrm{Pr}]^{1/3} \text{ (heat transfer)} \tag{17}$$

$$\mathrm{Nu}^d = 2 + 0.6[\mathrm{Re}]^{1/2}[\mathrm{Sc}]^{1/3} \text{ (mass transfer)} \tag{18}$$

where the Reynolds number for the injected particles is defined by [2]

$$\mathrm{Re} = 2R(\rho_g + \rho_v)|U-V|/\mu^* \tag{19}$$

One may also use this formulation by resorting to more complicated expressions (as, for instance, derived by this author [2]).

Similarly we employ here a simple correlation for C_D, namely:

$$C_D = 0.48 + 28\,\mathrm{Re}^{-0.85} \tag{20}$$

Equation (20) neglects what we have termed "Diffusion Drag" [2] (which causes C_D to decrease due to the very process of evaporation that produces an additional vectorial thrust force in the direction of the motion of the particles).

In plasma units which employ supersonic nozzles the supersonic

Nomenclature

a_0 = speed of sound at the nozzle exit
$A = W_g/\rho_g U$ = cross-section area of flow
C_D = drag coefficient for the particles in the carrier gas
c_p = specific heat
$C_p = c_p/\gamma\overline{R}$
d = specific density of particle material
$D = d/\rho'_0$, particle to gas mass ratio
h = enthalpy per unit mass
$H = h/a_0^2$, dimensionless enthalpy per unit mass
Δh_{fg} = heat of vaporization per unit mass
$\Delta H_{\mathrm{vap}} = \Delta h_{fg}/a_0^2$
I = total momentum (qv equation (1))
J = total energy (qv equation (2))
m = molecular weight
M_R = relative Mach number (= $|U-V|$)
Nu = Nusselt number for heat transfer (qv equation (17))
Nu^d = Nusselt number for mass transfer (qv equation (18))
p = pressure
$P = p/\rho_0' a_0^2$
p_{v0} = vapor pressure at the interface
Pr = Prandtl number
r = particle radius
R_0 = particle radius $X = 0$, μm
R = gas constant for the specific gas considered
Re = Reynolds number (qv equation (19))
Sc = Schmidt number
T^* = absolute temperature
$T = T^*/T^*_{g0}$ dimensionless temperature
u = gas velocity
$U = u/a_0$ (dimensionless particle velocity)
v = particle velocity
$V = v/a_0$ (dimensionless particle velocity)
w = mass flow rate
$W = w/\rho_0 a_0$
X = length coordinate from nozzle exit along the jet axis
$s = x/r_0$ (dimensionless distance)
γ = gas specific heat ratio
ϵ = volume fraction of particles in the spray-jet
μ = shear viscosity of the gas mixture
$\mu^* = /r_0 a_0 \rho_0'$; nondimensional viscosity
ρ' = gas density
$\rho = \rho'/\rho_0'$
χ = mole fraction

Subscripts

g, G = carrier gas
p = particles
v = particle material in the spray-jet
0 = properties at $X = 0$
s = properties of the solid material at the interface
f = properties of the particles in the liquid state
fg = evaporation
∞ = properties in the gas (far from interface)
m = the melting point

Superscript

$'$ = carrier gas

Downloaded 01 Jun 2010 to 171.66.16.58. Redistribution subject to ASME license or copyright; see http://www.asme.org/terms/Terms_Use.cfm

Table 1 Physical properties of the injected powder

(Molybdenum)

$C_{ps} = 5.19 + 1.658 \times 10^{-3} T^*$	cal/mole °C
$C_{pf} = 10.0$	cal/mole °C
$C_{pv} = 6.17 + 3.2 \dfrac{T^* - 2890}{2890}$	cal/mole °C
$\Delta H_{fusion} = 6650 \ (\equiv \Delta H_m)$	cal/mole °C
$\Delta h_{fg} = 158{,}310(0°K)$; 140,920(50000 K)	cal/mole °C

$\overline{P}_{v0}$(atm) = 8.4×10^{-5}(30,000 K); 2.65×10^{-3}(35,000 K); 3.48×10^{-2}(40,000 K); 0.254(45,000 K); 1.0(49,240 K)
$T^*_{melt} = 2890$ K
$T^*_{vap} = 4924$ K
$\rho = 10.2$ gr/cm^3
$m = 95.95$
R_0 varies from 1 to 25 μm
W_p varies from 1 to 5
T^*_{p0} was taken as equal to 300 K (i.e., $T_{p0} = 300/T^*_{g0}$)

Table 2 Physical Properties of the Carrier Gas

(Argon)

$\mu = 0.02 \times 420 \times T^{1/2} \times (1/273)^{3/2}$	centipoise
$\gamma = 1.66$	
$C_{pg} = 4.97$ cal/mole °C	
$m = 40.0$	

W_f was taken as equal to unity in all runs
T^*_{g0} varies from 18,000 K to 28,000 K; $P = 1$ atm
Initial gas Mach velocity varies from 0.3 to 0.7 M.

relative velocities (i.e., between the injected particles and the jet), may prevail along part of the jet-spray axis. In these cases the relative Mach number M_R must also be taken into account. This specific requirement is shown, for instance, by the following empirical correlations:

$$C_D = 0.97 + 0.3055\left(\frac{1}{M_R} - \frac{1}{2.75}\right) - 0.605\left(\frac{1}{M_R} - \frac{1}{2.75}\right) \quad (21)$$

(for $1.5 < M_R < 4.0$)

$$C_D = 0.814 + 0.761(M_R - 1.0) - 0.206(M_R - 1.0)^2 - 0.918(M_R - 1.0)^3 \quad (22)$$

(for $0.4 < M_R < 1.5$)

The analysis must also be supplemented with correlations for μ^*, χ_{vs}, C_{pv}, C_{ps}, etc. The last depend on the specific materials used. Additional simplifying assumptions are:

1 The gas behaves as an ideal gas with Pr ≈ Sc = 1.

2 The volume fraction occupied by the injected particles in the jet, ϵ, can be neglected.

3 The pressure along the jet-spray axis is constant.

4 The heat of conduction inside the particles is relatively fast so that temperature gradients inside the moving particles can be neglected as a first approximation.

The Case of Plasma Spraying of Molybdenum with Argon as the Carrier Gas

Physical properties and correlations employed in the analysis are given in Tables 1 and 2.

The molybdenum vapor mole fraction at the molybdenum droplet surface is estimated from the Clausius-Clapeyron equation

$$\chi_{vs} = \frac{P_{v0}}{P} \cdot \exp[\gamma \Delta H^\circ_{vap}(1 - T^*_{vap}/T^*_p)] \quad (23)$$

Results and Discussion

The results of the numerical solutions of the set of nonlinear differential and algebraic equations (1–16) are shown in Figs. 1 to 7 as a function of X, the distance from the plasma gun cross-section where the powder is injected into the outflowing jet.

Fig. 1 shows the effect of the gas temperature at the nozzle exit on

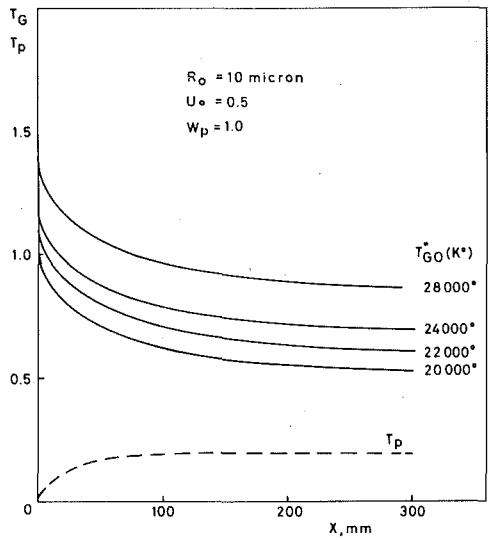


Fig. 1 Effect of plasma temperature on gas and particle temperatures along the jet axis

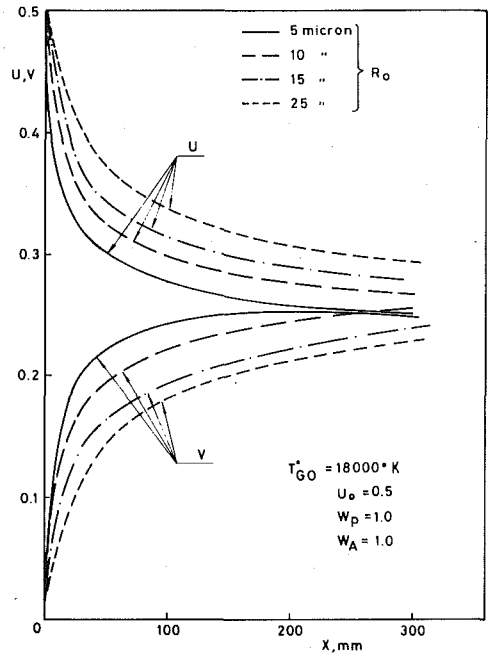


Fig. 2 Effect of particle size on gas and particles velocities along the jet axis. Note that the relaxation distance increases with the particle size

the temperatures of argon and molybdenum particles along the jet axis. These results are for a 10 μm powder and initial gas velocity $U_0 = 0.5$ M. T_p increases with the distance X as the particles are entrained downstream and asymptotically reaches a certain constant temperature which increases with T^*_{G0}. A similar result has been obtained for particles with different sizes (see for instance, Fig. 6). T^*_{G0} also affects V, the particles velocity (Fig. 6), as well as the extent of evaporation of the molybdenum particles (Fig. 7). The particles asymptotic temperature is higher than the melting temperature of molybdenum and may reach T^*_{vap}.

Figs. 1 and 7 indicate that at distances greater than 5 to about 10 cm an increase in the plasma temperature increases the losses of powder material by evaporation.

Fig. 2 shows the relaxation zones of gas and particle velocities. As expected the "relaxation distance" (i.e., where V approaches U) increases with the particle size. A 5 μm powder reaches the maximum impact velocity at about 20 cm downstream of the nozzle, while for a 10 μm powder this distance doubles. The initial acceleration is very

Downloaded 01 Jun 2010 to 171.66.16.58. Redistribution subject to ASME license or copyright; see http://www.asme.org/terms/Terms_Use.cfm

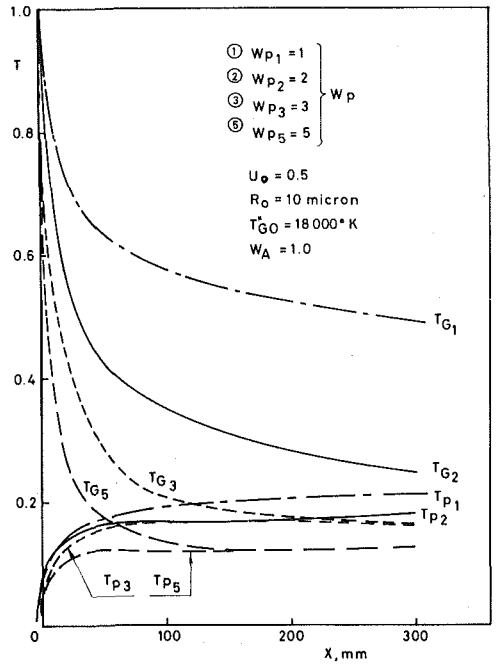


Fig. 3 Effect of particles mass flow rates on gas and particles along the jet axis. Both temperatures decrease with increasing mass flow rates of the injected powder

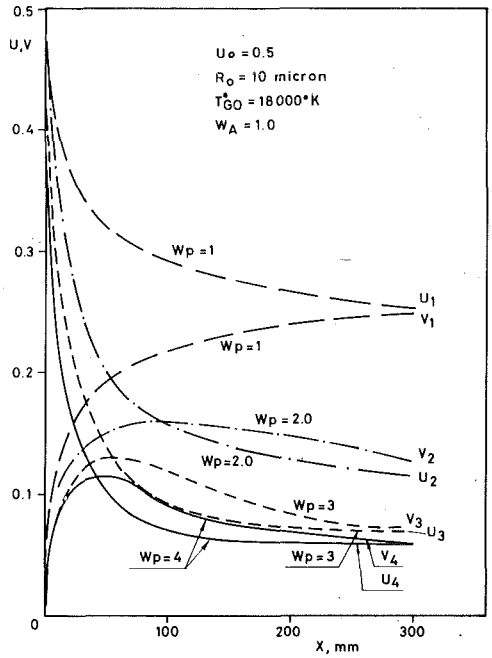


Fig. 4 Effect of particles mass flow rates on gas and particles velocities. Note that the velocities of the particles may exceed the gas velocities

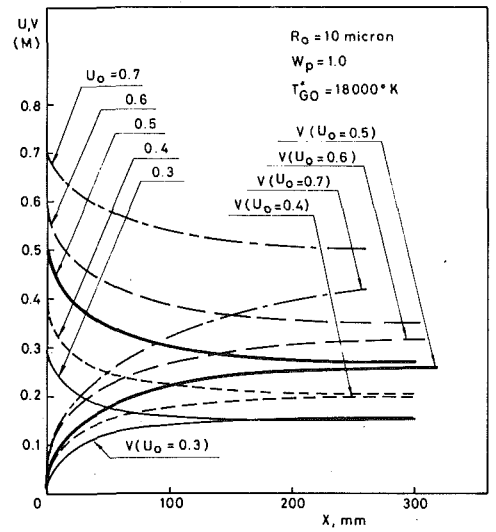


Fig. 5 Effect of initial gas Mach numbers on the particles velocities. Relaxation distance increases with increasing initial gas Mach numbers

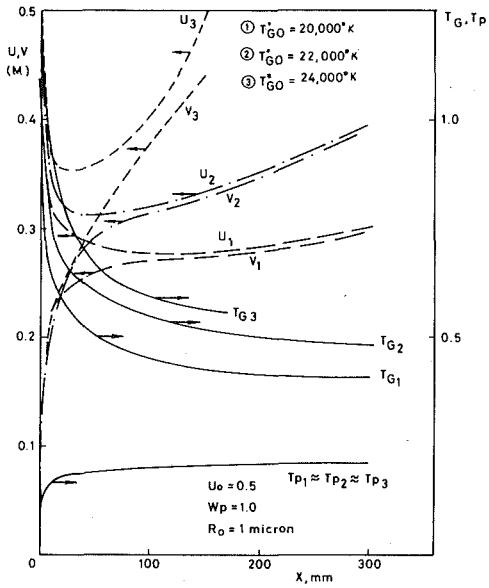


Fig. 6 Effect of initial gas temperature on gas and particles velocities along the jet axis

high in all cases and the particles reach a very high impact velocity (at all sizes) after they have travelled only 5 to 10 cm.

Fig. 3 shows the effect of increased mass flow rates of powder on gas and particles temperatures at different locations along the jet-spray axis. Both gas and particle temperature are decreasing with increasing flow rates of particles. The asymptotic temperature of the particles is shown to be affected by the particle concentration in the spray.

Fig. 4 demonstrates an interesting phenomenon with respect to the (velocity) relaxation distance. Starting from about $W_p = 2.0$ *the particle velocities may exceed the gas velocity*! This effect is due to the high initial acceleration which for large mass flows of particles overcomes a substantial inertia. Further downstream, however, the two velocities approach each other again. At a given U_0, R_0, T_{G0} and W_A we observe that the *lower* the mass flow of the particles the *higher* is their maximum impact velocity. At high mass flow rates of powder the maximum velocity is obtainable quite close to the nozzle exit, at a distance of only about 5 to 9 cm.

Fig. 5 shows the effect of initial gas Mach numbers on the velocities of the particles. As might intuitively be expected, V increases with U_0, while the relaxation distance increases with increasing initial gas Mach numbers.

Fig. 6 demonstrates the effect of T^*_{G0} on U and V for very small particles having radii of 1 μm. The injected particles, by being accelerated, first cause gas deceleration, but later, downstream, accelerate the gas! But contrary to the case with larger particles (i.e., with R_0 = 10 μ, see Fig. 4), V does not reach values higher than those of U. This can be attributed to the smaller inertia of the small particles.

Fig. 7 gives additional results about the rate of powder losses due to the evaporation of molybdenum particles in the hot spray. In general, increasing the Mach number of the outflowing argon gas, decreases losses, while the opposite effect is caused by increasing the plasma temperature.

Downloaded 01 Jun 2010 to 171.66.16.58. Redistribution subject to ASME license or copyright; see http://www.asme.org/terms/Terms_Use.cfm

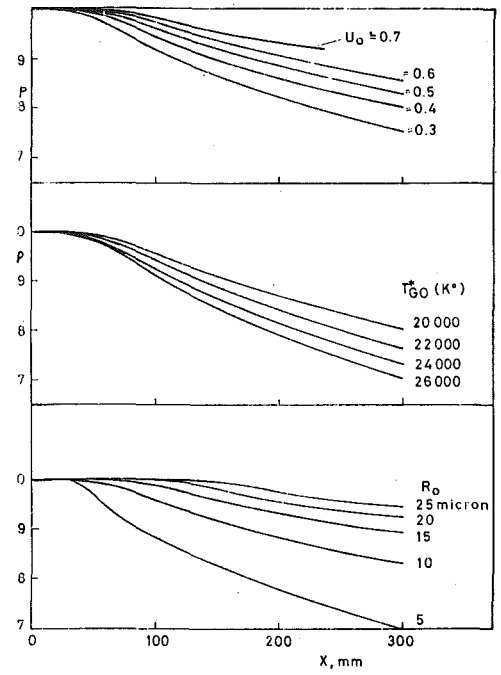


Fig. 7 Effect of initial gas Mach number, initial gas temperature and initial particle size on the degree of evaporation of the injected powder

As the powder particle size is decreased, the rate of losses increases. This effect is a nonlinear one, and more than 30 percent loss of weight may be caused in using powders of particle sizes less than 5 μm.

Unfortunately very few empirical data on the distributions of U, V, T_p, T_G, W_p, etc. along the jet axis are available at present in the literature. Surov and Bobrov [6] give the distribution of velocities along the axes of a single-phase and two-phase high-temperature argon jet as applied to spray coating guns. Their data are, however, not specific enough to allow detailed comparisons between theory and experiment. Nevertheless, their results are qualitatively in agreement with the exponential decay of U as reported in Figs. 1, 2, 4, 5, and 6. They also give empirical data which show that the introduction of powder lowers the gas velocities (in agreement with Fig. 4).

References

1 Narkis, Y., and Gal-Or, B., "Two-Phase Flow through Normal Shock Wave," ASME Spring Annual Meeting, Minn, 1975. ASME Paper 75-FE-25. ASME *Journal of Fluid Engineering.*, March 1975.

2 Gal-Or, B., et al., "Variational Analysis of High Mass Transfer Rates from Spherical Particles," *Int. J Heat and Mass Transfer*, Vol. 15, pp. 2027–2032. "Diffusion Drag on Slowly Evaporating Droplets," *The Phys. of Fluids*, Vol. 16, pp. 1826–1829. "High Reynolds Number Fluid Dynamics and Heat and Mass Transfer in Real Concentrated Particulate Two-Phase Systems," *Int. J Heat and Mass Transfer*, Vol. 16, 1973, pp. 887–895. "Convective Mass or Heat Transfer from Size-Distributed Drops, Bubbles or Solid Particles," ibid. Vol. 14, 1971, p. 727.

3 Surov, N. S., and Bobrov, G. V., "Distribution of Velocities in High-Temperature Spray-Coating Jets," *Avt. Svarka*, No. 2, 1970, pp. 16–19.

4 Rudinger, G., "Relaxation in Gas-Particle Flow," *Non Equilibrium Flows, Part 1*, ed. Marcel Dekker, N.U. 1969. "Some Effects of Finite Particle Volume on the Dynamics of Gas-Particle Mixtures," *AIAA J.* Vol. 3, 1965, p. 1217.

Downloaded 01 Jun 2010 to 171.66.16.58. Redistribution subject to ASME license or copyright; see http://www.asme.org/terms/Terms_Use.cfm

K. Bammert
Professor.

M. Rautenberg
Professor.

Institute for Turbomachinery,
University of Hannover,
Hannover, Germany

W. Wittekindt[1]
Head of Design and Development Department,
Turbocompressors, Klein, Schanzlin
and Becker AG,
Saarbrücken, Germany

Matching of Turbocomponents Described by the Example of Impeller and Diffuser in a Centrifugal Compressor

PART I: Aerothermodynamic Coupling of Impeller and Diffuser

PART II: Optimized Stage Efficiency of a Centrifugal Compressor

An important task in the design of turbo machinery is the determination of the aerothermodynamic parameters necessary to assure optimum matching of the individual compressor components. With centrifugal compressors, the problem is to design impeller and diffuser such that a maximum overall efficiency is achieved for the desired design point. For this purpose, a mathematical model is developed coupling the individual component efficiencies. In the first part of this paper, the aerothermodynamic bases are derived and the coupling equation is illustrated. In the second part, a solution is displayed for the complex problem of matching the impeller and the vaneless diffuser of a centrifugal compressor. The solution is obtained by means of a stochastic-mathematical optimization procedure based on the biological evolution strategy.

Introduction: Part I

Not too long ago it was a common practice in designing turbocompressor stages to optimize each component separately. This method necessarily involved an isolated study of the individual components, although the best efficiency, highest head coefficient, etc., should be achieved for the stages as a whole. A theoretical evaluation of the interaction of coupled components is therefore very complex or not possible at all. Only the experiment reveals the strong interdependence of the individual components. This often results in subsequent redesigning of certain parts of the components.

In the design of axial compressors a more consistent method has been adapted. The calculation of the flow fields of one complete stage or several stages shows their interaction. It allows seaching for optimum combinations. The formerly isolated treatment of rotor and stator blades often resulted in faulty designs, especially with higher specific power requirements.

As early as 1961, Baljé used a method [1] representing a way out of this deadlock. Despite this start, only a few papers have been published dealing with the optimum matching of centrifugal compressor components, such as impeller, diffuser and scroll. An unfortunately not very well known paper by Stiefel [2] shows how much the scroll configuration affects the behavior of the characteristic curves and the efficiency of the entire stage by means of systematic experiments. Furthermore it demonstrates that with careful matching of the scroll, no decrease of the stage efficiency should occur, even if the inlet Mach number of the impeller is considerably increased from the subsonic to the supersonic range. Evidently it must be possible that an optimum coordination of the individual components can be obtained even with the use of a theoretical model.

In this paper we will investigate how the impeller and the vaneless diffuser of a centrifugal compressor can be matched such that mere flow losses are minimized. In the first part, the coupled overall efficiency is determined. In the second part, a proposal for solving the optimization problem is made.

[1] My contribution to this article shall be dedicated to my honorable teacher, Prof. Dr.-Ing. K. Bammert, who will be 70 years old in 1978.

Contributed by the Gas Turbine Division and presented at the 1979 Israel Joint Gas Turbine Congress, July 9–11, 1979, Haifa, Israel of THE AMERICAN SOCIETY OF MECHANICAL ENGINEERS. Manuscript received at ASME Headquarters April 10, 1979. Paper No. 79-GT/Isr-9.

Copyright © 1980 by ASME

Downloaded 01 Jun 2010 to 171.66.16.58. Redistribution subject to ASME license or copyright; see http://www.asme.org/terms/Terms_Use.cfm

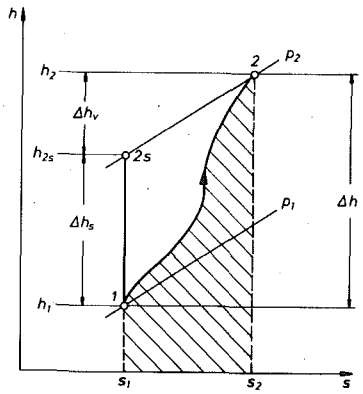


Fig. 1.1 For determination of the static loss efficiency

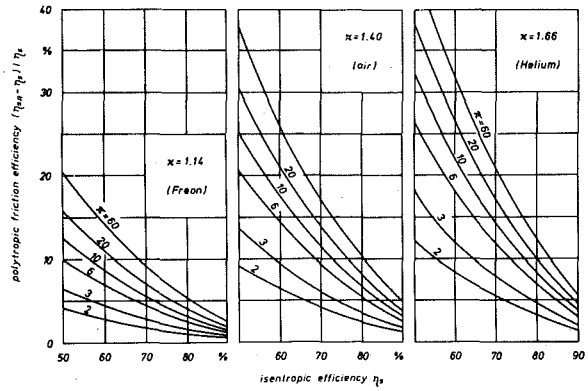


Fig. 1.2 Static loss efficiency and isentropic efficiency

Static Loss Efficiency

If, for an efficiency, the mere flow losses are considered only, the equation for the area beneath the curve from the beginning of the process at 1 to the end of the process at 2 (Fig. 1.1) can be written as follows:

$$\Delta R = \frac{1}{c_p}\int_1^2 h \cdot ds \tag{1}$$

The efficiency thus established, viz.

$$\eta_{sr} = 1 - \frac{\Delta R}{\Delta h} \tag{2}$$

is called "static loss efficiency" according to [3]. The curve between 1 and 2 in Fig. 1.1 can have any shape while the enthalpy losses Δh_v used to express the normal isentropic efficiency

$$\eta_s = 1 - \frac{\Delta h_v}{\Delta h} \tag{3}$$

remain unchanged. Depending on the flow quality, the static loss efficiency η_{SR} can vary a lot, even if the isentropic efficiency η_S remains unchanged. If, for a special compression process according to a polytropic change of state, we write

$$\tau = \pi^{\frac{n-1}{n}} \tag{4}$$

where the polytropic exponent is

$$n = \frac{\ln\pi}{\ln(\pi/\tau)} \tag{5}$$

the linkage between the efficiencies

$$\eta_{SR} = 1 - (1 - \eta_s)\cdot\frac{\Delta R}{\Delta h_v} \tag{6}$$

can be found with the aid of equations (2) and (3) which results in

$$\eta_{SR} = \frac{\ln\pi^{\mu}}{\ln\left(1 + \frac{\pi^{\mu} - 1}{\eta_s}\right)}. \tag{7}$$

This equation is also known as "polytropic efficiency;" its actual importance for the determination of the mere flow losses is, however, rarely appreciated.

Fig. 1.2 illustrates the evaluation of equation (7) for three gases with different isentropic coefficients. The percentage increase of the polytropic friction efficiency $(\eta_{SR} - \eta_S)/\eta_S$ as compared to the isentropic efficiency for various static pressure ratios can clearly be noted. It becomes evident that, even in case of gases with different isentropic exponents at equal frictional losses in the flow, different isentropic efficiencies can be attained. A compression process with helium ($\kappa = 1.66$) and $\eta_s = 70$ percent presents, at a pressure ratio of $\pi = 10$, a 14.5 percent higher loss efficiency. With freon ($\kappa = 1.14$) a nearly 6 percent higher loss efficiency is obtained under the same conditions.

Coupling of Aerothermodynamic Similarity Law Coefficients

Regardless of the turbocompressor component under consideration, the characteristic efficiency curves will hardly be obtainable without employing test results based on the laws of similarity. It is therefore necessary to couple the turbocompressor components with the aid of dimensionless coefficients. It can be demonstrated [3] that 12 physical quantities are acting on a turbo component at its systems limits, as shown in Fig. 1.3. By means of a dimensional analysis according to the Buckingham π-theorem, seven independent dimensionless parameters may then be formed for one component assuming an adiabatic system. Such parameters are:

Nomenclature

b = diffuser width
B = ratio diffuser width/impeller width
c = absolute velocity
c_p = specific heat capacity
D = diameter
h = enthalpy
H = shape factor
k_c = factor
ℓ = length
M = Mach number
$\dot{m}$ = mass flow per second
n = polytropic coefficient
p = pressure
Re = Reynolds number
ΔR = friction loss
R = gas constant
s = entropy
T = temperature
u = circumferential velocity
w = relative velocity
z = number of blades
α = absolute flow angle
β = relative flow angle
δ = gap width
ϵ = ratio jet/wake area
ζ = deceleration ratio or loss coefficient
η = efficiency
ϑ_2/ℓ = related momentum thickness
κ = isentropic exponent
λ_D = diffuser length ratio
μ = exponent = $(\kappa - 1)/\kappa$
ν = viscosity
π = pressure ratio
ρ = density
σ = solidity
τ = temperature ratio
φ = flow coefficient

Subscripts

1 = entrance
2 = exit of impeller
3 = exit of diffuser
a = outer side
c_2 = related to the relative velocity
hydr = hydraulic
M = mixing
max = maximum
opt = optimum
pol = polytropic
s = isentropic
sec = secondary
sp = gap (clearance)
SR = static loss due to friction
st = shock
u = circumferential direction
w = wall

Downloaded 01 Jun 2010 to 171.66.16.58. Redistribution subject to ASME license or copyright; see http://www.asme.org/terms/Terms_Use.cfm

isentropic exponent	κ
static pressure ratio	$\pi = p_2/p_1$
circumferential Mach number	$M_{u2} = u_2/\sqrt{\kappa R T_1}$
Reynolds number	$\mathrm{Re} = u_2 \cdot D_2/\nu_2$
isentropic efficiency	$\eta_s = \Delta h_s/\Delta h$
flow coefficient	$\varphi = \dot{m}/\left(\frac{\pi}{4} \cdot D_2^2 \cdot u_2 \cdot \rho_1\right)$
deceleration ratio	$\zeta = w_2/w_1$

With the aid of the above parameters, all dependent values and a closed calculation model for centrifugal compressor components such as impeller or diffuser, can be derived.

If we now revert to equation (7), we realize that the static loss efficiency to be optimized is written as a function of dimensionless, independent parameters only.

Coupled Overall Efficiency

With the above statements, a system of two individual components may be coupled. For a two component system as shown in Fig. 1.4, 17 independent values are obtained at the system limits. All other quantities, especially the inlet value missing in component 2, which have been independent in the individual component study, can now be determined from the existing basic values. The following are to be added to the above described independent parameters of the individual component: the pressure ratio π_2 of component 2, the inlet Mach number $M_{c2} = c_2/\sqrt{\kappa R T_2}$ at the component limit, the isentropic efficiency $\eta_{s,2}$ of component 2, the deceleration ratio $\zeta_2 = c_2/c_1$ of component 2 and the cooling coefficient of component 2 which is not applicable to the adiabatic system.

With the aid of these parameters, components 1 and 2, representing the impeller and the diffuser in the case of centrifugal compressors, can be coupled. Two simple correlations represent the basis of such coupling, i.e. the overall ratio of the static pressures

$$\pi = \frac{p_3}{p_1} = \frac{p_2}{p_1} \cdot \frac{p_3}{p_2} = \pi_1 \cdot \pi_2 \tag{8}$$

and the overall ratio of the static temperatures

$$\tau = \frac{T_3}{T_1} = \frac{T_2}{T_1} \cdot \frac{T_3}{T_2} = \tau_1 \cdot \tau_2 \tag{9}$$

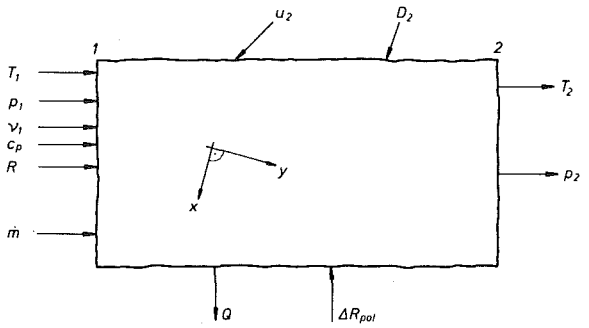


Fig. 1.3 Independent variables of a flow component

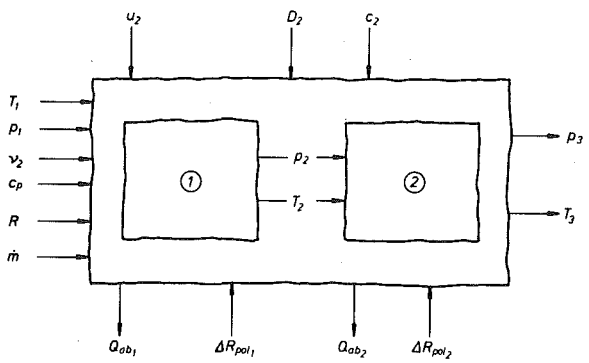


Fig. 1.4 Independent variables of a two-component system

The overall efficiency is defined with

$$\eta_{SR} = 1 - \frac{\Delta R_{\mathrm{pol}}}{\Delta h} = 1 - \frac{\Delta R_{\mathrm{pol},1} + \Delta R_{\mathrm{pol},2}}{\Delta h_1 + \Delta h_2} \tag{10}$$

according to equation (2). Making use of equations (4, 8, 9), and (10) the expression derived for the overall static loss efficiency is

$$\eta_{SR} = 1 - \frac{(1 - \eta_{SR,1})(\pi_1^{\mu/\eta_{SR,1}} - 1) + \pi_1^{\mu/\eta_{SR,1}}(1 - \eta_{SR,2}) \cdot (\pi_2^{\mu/\eta_{SR,2}} - 1)}{\pi^{\mu/\ln\pi(\ln\pi_1/\eta_{SR,1} + \ln\pi_2/\eta_{SR,2})} - 1} \tag{11}$$

This efficiency defines the real frictional losses in the coupled overall system. This efficiency shall now, by way of optimization, become a maximum. If both components have identical static pressure ratios (viz. $\pi_1 = \pi_2$) and identical individual efficiencies ($\eta_{SR,1} = \eta_{SR,2}$) the overall efficiency has the same value as the individual efficiencies.

Correlation between Overall Efficiency and Pressure Ratio

From equation (11), the influence of the individual values on the overall efficiency can not be clearly noted. Hence, an example shall be used to illustrate this correlation. Fig. 1.5 represents η_{SR} for a ficticious stage at an overall pressure ratio of $\pi = 10$. On the abscissa, π_1 and π_2 are plotted; their products exactly amount to $\pi = \pi_1 \cdot \pi_2 = 10$. The plotted curves represent different combinations of individual efficiencies. In one case $\eta_{SR,1} = 70$ percent and $\eta_{SR,2} = 90$ percent and, in the other, $\eta_{SR,1} = 90$ percent and $\eta_{SR,2} = 70$ percent. This is a way to make comparisons at equal pressure ratio combinations and inverse efficiency combinations.

The curves plotted in Fig. 1.5 begin at $\pi_1 = 10$ and $\pi_2 = 1$ with the individual efficiency applicable to component 1. At the same point they also represent the overall efficiency. With combination $\eta_{SR,1} = 90$ percent and $\eta_{SR,2} = 70$ percent, the overall efficiency decreases considerably with slightly rising pressure ratio of component 2. At $\pi_2 = 2.24$, the mean value of $\eta_{SR} = 80$ percent is already reached. If both pressure ratios are identical, i.e., 3.162, the efficiency of 76.7 percent is considerably below the arithmetic mean value. With combination $\pi_1 = 2$ and $\pi_2 = 5$, the overall efficiency is 73.5 percent only. This seems to make clear that component 2 has a stronger influence on the overall efficiency than component one.

To make a comparison, it is recommended to examine the curve with exactly the reverse efficiency combination. In this case the higher efficiency has been attributed to component 2. With rising pressure ratio for component 2, the overall efficiency also rises very quickly. If both components have the same pressure ratio, η_{SR} is 80.7 percent and thus by four points higher than with higher component 1 efficiency. However, if $\pi_1 = 2$ and $\pi_2 = 5$, η_{SR} is 84.5 percent. If $\pi_1 = 5$ and $\pi_2 = 2$, and the efficiencies are exactly inverse to the actual case, the overall efficiency is 81 percent only. The comparison shows the same results, if for one case we assume $\pi_1 = 2$, $\pi_2 = 5$, $\eta_{SR,1} = 0.9$ and $\eta_{SR,2} = 0.7$ and, for the other, $\pi_1 = 5$, $\pi_2 = 2$, $\eta_{SR,1} = 0.7$ and $\eta_{SR,2} = 0.9$. In the first case η_{SR} is 73.5 per cent, the second case η_{SR} is 76.7 percent.

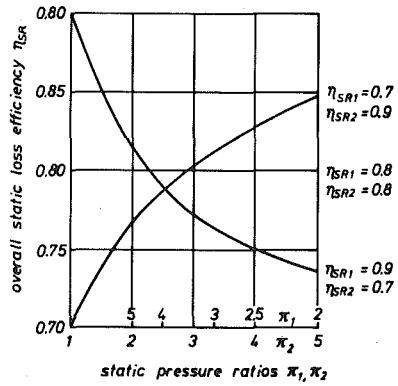


Fig. 1.5 Dependence of the overall efficiency on the static pressure ratio π_1 and π_2 (for $\pi = \pi_1 \cdot \pi_2 = 10$)

Downloaded 01 Jun 2010 to 171.66.16.58. Redistribution subject to ASME license or copyright; see http://www.asme.org/terms/Terms_Use.cfm

The above paragraph clearly shows that it is more advantageous to attribute the higher efficiency to component 2, possibly with higher pressure ratio. Already above $\pi_2 = 2.5$, η_{SR} is better for the entire stage than for the reverse value combination. So, if we succeeded in improving the diffuser of a centrifugal compressor stage, this would result in increased efficiencies of the entire stage. There is a further favourable effect for stages with radial bladed impellers. Due to the low degree of reaction a higher static pressure ratio is reached also in the second component than for stages with backward curved blades. Since the efficiencies of the impeller and also of the diffuser actually depend, to a large extent, on the coefficients used in equation (11), the desired optimization for a centrifugal compressor stage is feasible only when these characteristic values are known. A calculation method for the above will be outlined in Part II.

Introduction: Part II

Equation (11) of Part 1 comprises only dimensionsless main coefficients of the individual components and of the entire system. The individual efficiencies $\eta_{SR,1}$ and $\eta_{SR,2}$ also depend on various coefficients, and their correlations must be known for the purpose of optimization. In the following, a loss model for the impeller and the diffuser is described that can be used to calculate the individual efficiencies. This makes it possible to carry out a coupling calculation such that the optimum efficiency is found.

Loss Portion in the Impeller

In the impeller, the different causes of losses can be determined only hypothetically. It is problematical to measure the efficiency of the impeller, but it is even more difficult to determine the loss portions and their correlations. So we are still dependent on models with which the various dissipation portions may be calculated. The sum of these losses results in the overall loss which can be checked by measurements. In order to select a not too comprehensive but nevertheless physically workable model for the calculation, a procedure relying on (5) is employed, allowing the impeller losses to be subdivided as follows

- shock losses due to incidence at impeller inlet,
- wall frictional losses in the impeller passages,
- leakage losses in the gap between vane and shroud,
- secondary flow losses in the impeller, and
- mixing losses at impeller exit.

The *shock losses due to incidence* are determined according to [6], viz:

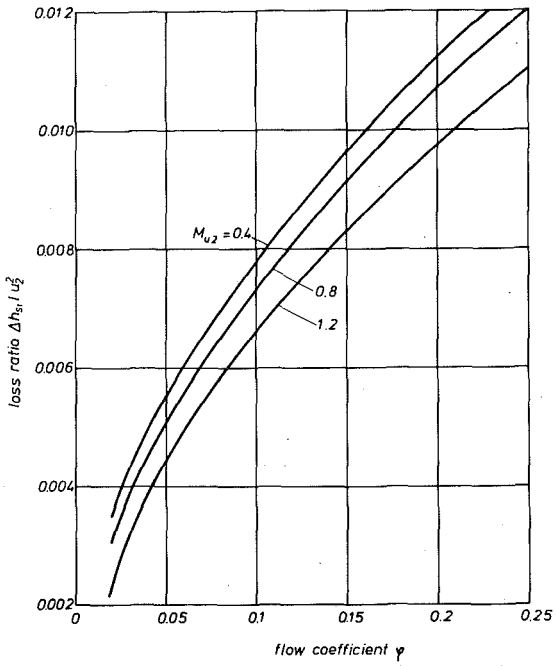


Fig. 2.1 Shock losses due to incidence at centrifugal compressor inlet versus flow coefficient

$$\Delta h_{st} = \frac{1}{2} c_{st}^2 \tag{12}$$

where c_{st} is calculated according to [7], viz:

$$c_{St} = \frac{c_{\max}}{\tan \beta_{1a}} - u_{1a} \tag{13}$$

where the maximum velocity can be calculated with an equation indicating the deviation from the average velocity [4]. Fig. 2.1 shows the result of the evaluation for impellers with different flow coefficients and different circumferential Mach numbers.

The *wall frictional losses* are given by

$$\Delta h_w = \zeta_w \cdot \frac{c_2^2}{2} \tag{14}$$

According to [8] the equation set forth for plate boundary layers with pressure gradients

$$\zeta_w = 2 \cdot \frac{\vartheta_2}{L} \cdot \frac{\sigma}{\sin \beta_2} \cdot \left[1 + \frac{1}{2} \cdot \frac{\vartheta_2}{L} \cdot \frac{\sigma \cdot H^2}{\sin \beta_2}\right] \tag{15}$$

originated from the idea that the boundary layer equation by Truckenbrodt, applicable to flat plates, can be transferred to rotating passages, if only the distribution of the relative velocities on the blade surfaces is known. These have been calculated for various impellers and applied to the above equation in order to determine $\vartheta_2/\mathcal{L}$, see [4]. Fig. 2.2 shows the results of the calculations.

The *leakage losses*

$$\Delta h_{sp} = \zeta_{sp} \cdot (u_2 \cdot c_{2u}) \tag{16}$$

are caused by leakages flowing around and between blades and shroud. The loss coefficient can be computed according to [9] from

$$\zeta_{sp} = 1.2 \cdot \frac{\dot{m}_{sp}}{\dot{m}} \tag{17}$$

and the leakage rate with

$$\dot{m} = z \cdot \int_0^L \delta \cdot \sqrt{2 \cdot \rho(L) \cdot \Delta p(L)} \cdot dL \tag{18}$$

This calls for calculation of the local density and the local pressure difference, resulting from a blade-to-blade calculation. Fig. 2.3 shows the results of the calculations.

The *secondary flow losses* are calculated according to [5] from

$$\Delta h_{\text{sec}} = \zeta_{\text{sec}} \cdot \frac{w_2^2}{2} \tag{19}$$

where the loss coefficient is

$$\zeta_{\text{sec}} = \frac{51}{\left(\frac{w_2 \cdot L}{\nu}\right)^{0.5}} \cdot \left(\frac{u_2}{2 \cdot w_2}\right)^{1,1} \cdot \frac{\mathcal{L}}{d_{\text{hydr.}}} \tag{20}$$

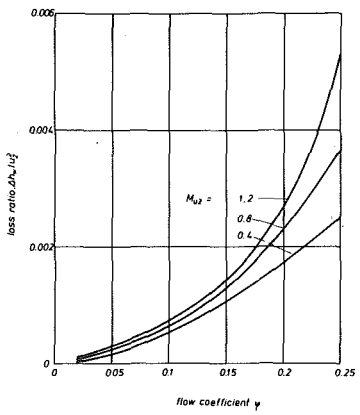


Fig. 2.2 Wall frictional losses within centrifugal compressors versus flow coefficient

Downloaded 01 Jun 2010 to 171.66.16.58. Redistribution subject to ASME license or copyright; see http://www.asme.org/terms/Terms_Use.cfm

The results are shown in Fig. 2.4.

The *mixing losses* downstream of radially bladed impellers are assumed constant according to Johnston and Dean [10]. They can be written as

$$\Delta h_M = \frac{1}{1+\cot^2\alpha_2} \cdot \left(\frac{1-\epsilon-B}{1-\epsilon}\right)^2 \cdot \frac{c_2^2}{2} \tag{21}$$

which results in a value of $\Delta h_M/u^2_2 = 0.0228$. The mixing losses therefore belong to the minor loss portions.

If, based on these loss values, we calculate some radial bladed impellers for various flow coefficients and circumferential Mach numbers M_{u2}, the calculations result in the polytropic efficiency η_{SR} shown in Fig. 2.5. The diagram shows qualitatively the well-known Baljé curve with very steep efficiency rise to approx. $\varphi = 0.1$. Then follows a relatively slight drop to higher flow coefficients. With the above calculation methods, the higher static polytropic efficiencies refer to higher circumferential Mach numbers.

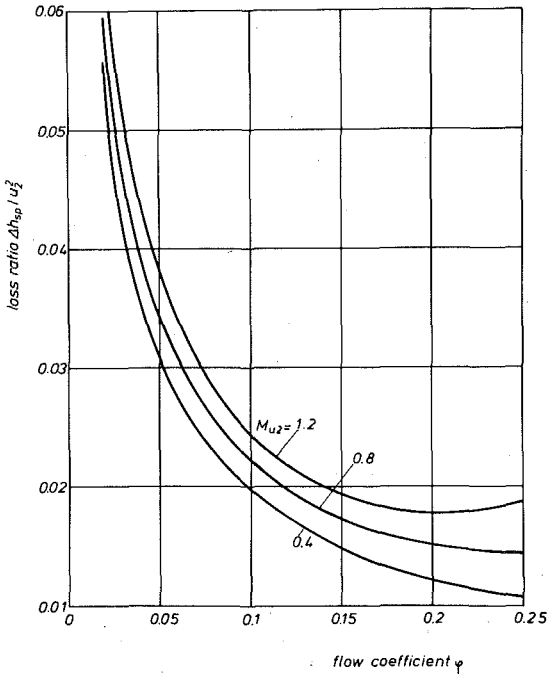


Fig. 2.3 Leakage losses of centrifugal compressor impellers versus flow coefficient

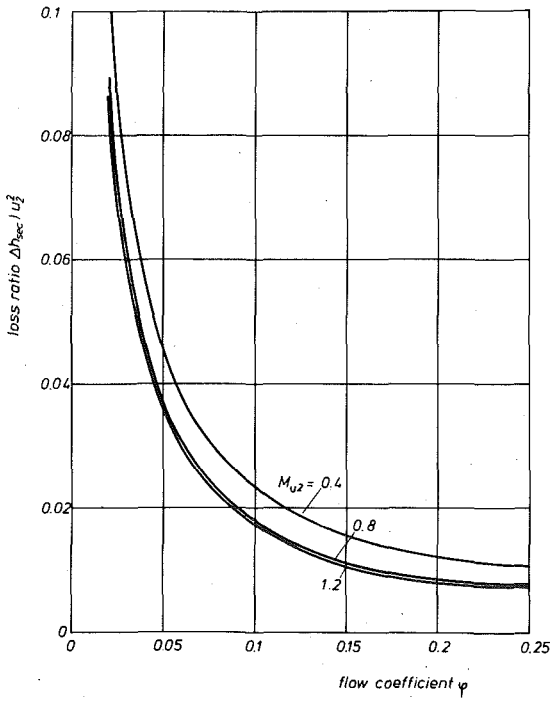


Fig. 2.4 Secondary flow losses of centrifugal compressors versus flow coefficient

Losses through the Diffuser

Based on the experience gained from [4] and [12], the authors could demonstrate in [11] that a relatively simple calculation method permits the precise prediction of the static pressure rise and the total pressure drop, and consequently the losses through the vaneless diffuser, even in case of extreme flow conditions. The assumption that an infinitesimal small ring element is rotating in the diffuser like a solid body and is rubbing only at the walls, leads to the differential equation

$$\frac{d(c_u \cdot r)}{dr} = -c_f \cdot \frac{c_u \cdot r}{b \cdot \cos\alpha} \tag{22}$$

describing the momentum change due to wall friction. When using the equation for the wall friction coefficient for air given by Mager [13]

$$c_f = 2 \cdot k_c \cdot \mathrm{Re}^{-1/5}\left(1 + \frac{\kappa-1}{2}M^2\right)^{-0.45} \tag{23}$$

a dissipation coefficient can be derived from the wall friction coefficient by variation of factor k_c. The dissipation coefficient now permits determination of the diffuser loss.

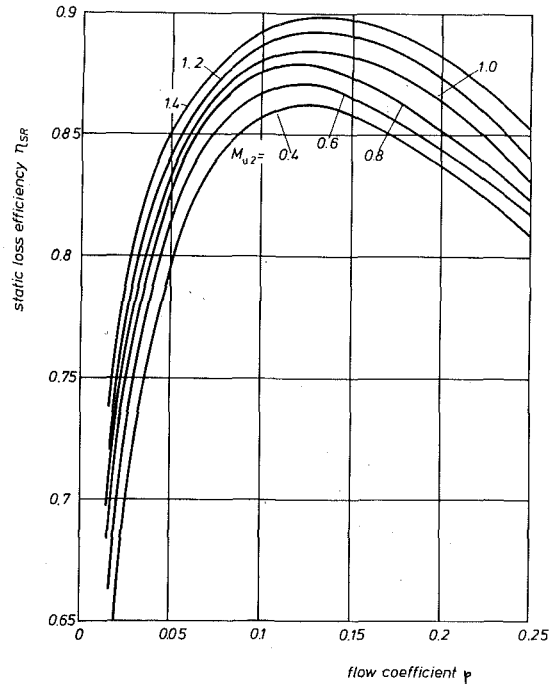


Fig. 2.5 Static loss efficiency of centrifugal compressor impellers versus flow coefficient

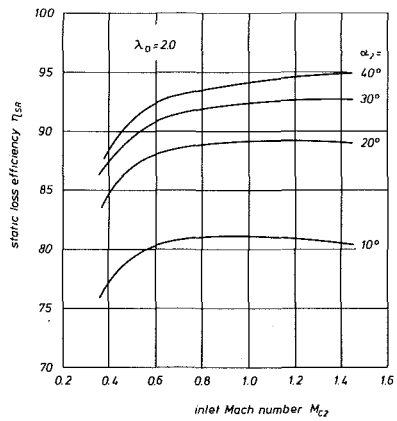


Fig. 2.6 Static loss efficiency of the diffuser versus inlet Mach number

Downloaded 01 Jun 2010 to 171.66.16.58. Redistribution subject to ASME license or copyright; see http://www.asme.org/terms/Terms_Use.cfm

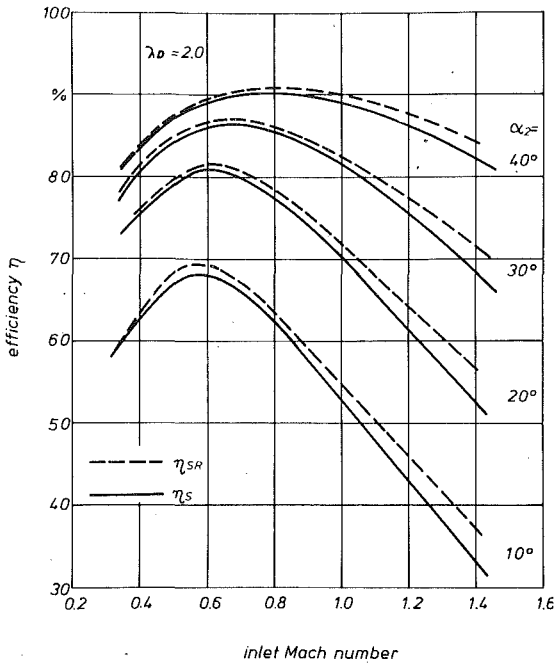


Fig. 2.7 Isentropic and static loss efficiency of the diffuser versus inlet Mach number

With $k_c = 0.0296$, as for a plane wall friction, the values shown in Fig. 2.6 can be determined. The calculation has been carried out for a radius ratio of $\lambda_D = 2.0$, for inlet Mach numbers into the diffuser of $M_{c2} = 0.4$–1.4 and for inlet angles of $\alpha_2 = 10$–40 deg. With the exception of $\alpha_2 = 10$ deg, the static polytropic efficiency in the diffuser rises with increasing inlet Mach number, and the efficiencies are higher than 80 percent. If we now take a value for k_c, applicable to centrifugal compressors, the results are as shown in Fig. 2.7 [4]. In this figure, the static isentropic and the polytropic efficiency are plotted and we note that the polytropic efficiency has somewhat higher values than the isentropic efficiency. The absolute values are considerably lower (η = 60–90 percent) and, for $M_2 > 0.6$–0.8, the efficiencies decrease again for all inlet angles. The stage optimization is based on these values.

Selection of Variables for the Calculation

Fig. 1.4 shows the physical quantities at the system limits of two components used to form dimensionless coefficients. All efficiencies depend on these coefficients, viz. $\eta_{SR,1}$ for the impeller, $\eta_{SR,2}$ for the diffuser and η_{SR} for the entire stage. The results of the individual loss study as indicated above show part of these dependences. It is, however, not possible to perform an isolated study and variation of the coefficients because of the existing interaction. Therefore it is important for the calculation not to vary all possible parameters but to select only a few of them so that the interaction can be analyzed.

Some of the coefficients described in Part I may be omitted from the study. The isentropic exponent certainly also affects the overall efficiency, but in this study air shall be considered only, consequently $\kappa = 1.4 = \text{const}$. According to the studies known up to now, the influence of the Reynolds number can be noticed only when the suction pressure of the air is less than 0.1 bar, so this may be omitted, too. As the dependences for the isentropic efficiencies of the impeller $\eta_{s,1}$ and the diffuser $\eta_{s,2}$ cannot be represented explicitly, they are calculated implicitly with the aid of the mathematic loss models described above. Remain for variation: the stage pressure ratio π, the circumferential Mach number M_{u2} and the deceleration ratio $\zeta = w_2/w_1$ of the impeller. As geometric coefficient, the radius ratio $\lambda_D = r_3/r_2$ of the vaneless diffuser shall be varied.

In order to confine the results for which these methods are applicable, the static pressure ratio of the stage is varied only twice, viz: $\pi = 2$ and $\pi = 3$. The flow coefficient φ should be allowed to take values between 0.1 and 0.25, i.e., it should cover the high specific speed range. If, for the calculation, a certain combination of pairs of variants

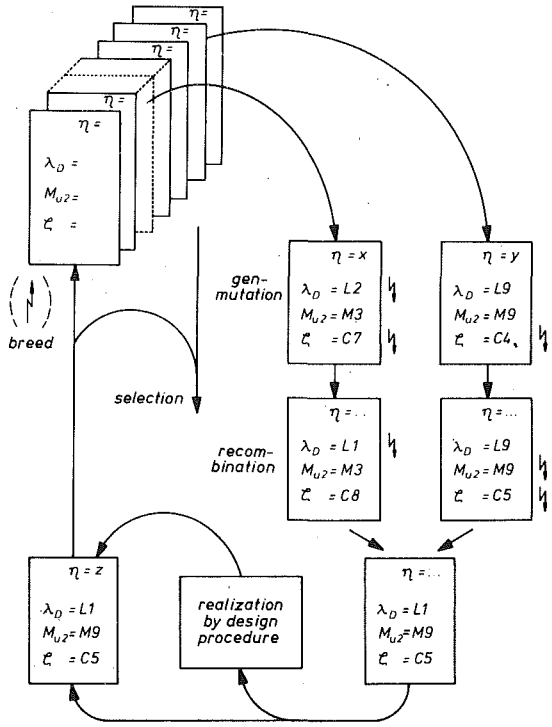


Fig. 2.8 Optimization method according to extended evolution theory

is taken (π, φ), for which the optimum static polytropic efficiency shall be determined, the remaining three coefficients M_{u2}, ζ and λ_D may take any value. The optimization procedure shall then allow $\eta_{opt} = f(M_{u2}, \zeta, \lambda_D)$ to be found.

Solution Method on the Basis of the Evolution Strategy

The described optimization system is too complex to be solved with differential methods with a single objective function. As described above, a great number of interconnected equations will be necessary to calculate the coupled static loss efficiency according to equation (11) for a single parameter combination. For such a problem, Rechenberg [14] has developed a stochastic mathematical optimization method allowing the optimum to be attained rather quickly. This optimization strategy was developed for a model of biological evolution but is used here as mere mathematical means.

Fig. 2.8 shows the steps to be taken in order to solve the problem. A number of start cards comprise the variables λ_D, M_{u2} and $\zeta = w_2/w_1$ in an optional combination which has, however, been selected by way of preliminary examination. With these combinations each individual centrifugal compressor stage is calculated and the losses are determined according to the described models so that the fields for the static loss efficiency are covered too. Now two cards are taken out by means of the Monte Carlo generator. Also by Monte Carlo generator, a selected number of variables on the cards are now mutated, here $L2$ in $L1$ for λ_D and $C7$ in $C8$ for the deceleration ratio ζ on card 1 and on card 2 ζ from $C4$ to $C5$. Rechenberg calls this method Gen-Mutation. Subsequently a random recombination of the 2 times 3 variable values to one single card takes place. In a design procedure, impeller and diffuser are calculated for this variable combination; the losses, and thus the new static loss efficiency $\eta = Z$ are determined according to the described methods. This value is compared with the efficiencies of all start cards. If it is better than any of those the card showing the worst value is sorted out and replaced by the new one. If not, this card is picked out and the procedure is started again. With this principle, the combination results are more and more improved so that, with a certain number of mutations, an optimum may be reached.

One additional difficulty of the set problem is not represented on this illustration. The requirement was to obtain a certain stage pressure ratio. With the random Gen-Mutation we can find out only

Downloaded 01 Jun 2010 to 171.66.16.58. Redistribution subject to ASME license or copyright; see http://www.asme.org/terms/Terms_Use.cfm

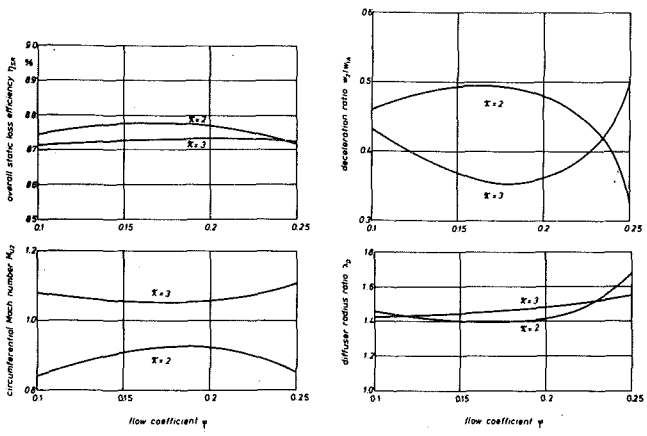


Fig. 2.9 Optimized coefficients of centrifugal compressor stages

during realization of the design procedure, whether π is reached or not. In order to prevent the optimization method according to this strategy becoming too extensive, we start from a multi-member evolution strategy. In the first iteration step a new number of start cards is established still allowing for a 50 percent pressure ratio deviation. Then a limited Gen-Mutation is effected until there are only start cards with a 25 percent pressure ratio deviation. This method is continued until the pressure ratio deviation is 3 percent only. Subsequently a simple mutation selection method is adapted. The card with the best efficiency and with the lowest pressure ratio deviation is mutated e.t.c., and thus the breeding—in other words, optimization—is improved.

Results

As a result of optimization, Fig. 2.9 shows the coefficients for centrifugal compressor stages in the range of $\varphi = 0.1$ up to 0.25 for the static pressure ratios $\pi = 2$ and $\pi = 3$. The static polytropic loss efficiencies are nearly constant over the whole range, contrary to the forecasts, the values for $\pi = 2$ being somewhat higher than for $\pi = 3$. The circumferential Mach numbers are within the expected range. The increasing ratio $\pi = 3$ and the decreasing ratio $\pi = 2$ with high φ values can be explained only in connection with the two other coefficients. For $\pi = 2$, w_2/w_1 decreases considerably above $\phi = 0.2$; λ_D is rising. In order to reach $\pi = 2$ with M_{u2} decreasing, λ_D must rise. The deceleration ratio may decrease, as now the diffuser is dominant for the overall efficiency. Diffuser investigations show that with λ_D the diffuser efficiency increases with decreasing diffuser inlet angle. This is the case with low impeller deceleration ratios like here. With $\pi = 3$ it is just the contrary. Because of the high circumferential Mach number, the polytropic efficiency of the impeller is higher than with $\pi = 2$. The deceleration ratio must increase a little bit.

The examples show that for the average absolute values, the known limits are exceeded. This can especially be noted with deceleration ratios of approx. $w_2/w_1 = 0.45$. In the literature only Stiefel [3] has up to date demonstrated that, even in experiments, a decreasing efficiency is not necessarily stated with these values.

From the results described above, the design engineer may conclude that it is suitable to design high specific mass flow centrifugal compressors with low impeller deceleration ratio and relatively short parallel walled diffusers.

Conclusions

Centrifugal compressor stages consist of interacting components. Their aerothermodynamic behavior should be matched such that the optimum efficiency for the desired application (φ, π) is achieved. To this effect, equation (11) has been developed in Part I for the coupled efficiency and their correlations have been analyzed. In Part II the authors have demonstrated that for the individual efficiencies mathematical models for the losses are suitable on which the calculation may be based. They are used for an optimization method, the mathematical means of which is a model of biological evolution according to Rechenberg [14]. Even with high flow coefficients, good efficiencies may be attained if certain coefficients are changes as compared with the usual limit values. Especially the deceleration ratio of the impeller may be in the range of approximately $w_2/w_1 = 0.45$.

References

1 Baljé, O. E., "A Study on Design Criteria and Matching of Turbomachines: Part B Compressor and Pump Performance and Matching of Turbocomponents," ASME Paper No. 60-WA-231, 1961.

2 Stiefel, W., "Experience in Development of Radial Compressors," VKI Lecture Series on Advanced Compressors, Rhode-St. Genese, 1972.

3 Bammert, K., and Rautenberg, M., "Zur Ähnlichkeitsmechanik von Turboverdichtern," *Wärme*, Vol. 74, No. 1, 1968.

4 Wittekindt, W., "Beitrag zur Entwicklung von Radialverdichtern für hohes Schluckvermögen," Dissertation. Technische Universität Hannover, 1977.

5 Mashimo, T., Watanabe, I., and Ariga I., "Effects of Reynold's Number on Performance Characteristics of a Centrifugal Compressor with Special Reference to Configurations of Impellers," ASME Paper No. 74-GT-59, 1974.

6 Fergueson, T. B., *The Centrifugal Compressor Stage*, Butterworth, London, 1963.

7 Eck, B., *Ventilatoren*, Springer-Verlag, Berlin, Heidelberg, New York, Edition 5, 1972.

8 Baljé, O. E., "Loss and Flow Path Studies on Centrifugal Compressors," Part 1, ASME Paper No. 70-GT-12 a, 1970.

9 Eckert, B., and Schnell, E., *Axial- und Radialkompressoren*, Springer-Verlag, Berlin, Göttingen, Heidelberg, Edition 2, 1961.

10 Johnston, J. P., and Dean, R. C., "Losses in Vaneless Diffusers of Centrifugal Compressors and Pumps," ASME JOURNAL OF ENGINEERING FOR POWER, Vol. 88, No. 1, 1966.

11 Bammert, K., Rautenberg, M., and Wittekindt, W., "Vaneless Diffuser Flow with Extremely Distorted Inlet Profile," ASME Paper No. 78-GT-47, 1978.

12 Haβ, U., "Zum Strömungsverlauf im schaufellosen Diffusor eines hochbelasteten Radialverdichters," Dissertation, Technische Universität Hannover, 1976.

13 Mager, A., "Transformation of the Compressible Turbulent Boundary Layer," *Journal of the Aeronautical Sciences*, 1958, pp. 305–311.

14 Rechenberg, I., *Evolutionsstrategie*, Problemata 15, Frommann-Holzboog, Stuttgart, 1973.

Downloaded 01 Jun 2010 to 171.66.16.58. Redistribution subject to ASME license or copyright; see http://www.asme.org/terms/Terms_Use.cfm

W. O. Afejuku
N. Hay
D. Lampard

Department of Mechanical Engineering,
University of Nottingham,
Nottingham, NG7 2RD U.K.

The Film Cooling Effectiveness of Double Rows of Holes

The film cooling effectiveness provided by two rows of holes separated by a range of distances has been studied experimentally using a mass transfer technique. The blowing rates at the two rows were varied independently. The results are presented in forms suitable for design purposes. Spanwise and area averaged effectivenesses are given for a range of blowing rates. Thus optimum blowing rates for a given row spacing and total coolant flow can be established. Comparisons with a simple superposition theory show that this can be used with safety for design purposes if the holes in the two rows are staggered, but restrictions apply if they are in-line.

1 Introduction

Successive rows of injection holes are commonly used in the film cooling of gas turbine components. The designer may have freedom of choice of blowing rates, injection angles, and row spacings, but there is relatively little published information to guide his decisions. The possible range of parameters is large and it is not practicable to conduct experiments to cover every conceivable combination.

Investigations to date have mostly concentrated on small row spacings, with a limited range of blowing parameters and, usually, the rows of injection holes have been fed from a single plenum chamber so that the blowing rates for all rows have been nominally identical. For example, Jabbari and Goldstein [1] and Hirata [2] reported measurements of effectiveness for a double row of holes at a row spacing to diameter ratio of 2.6 and 6, respectively, with blowing rates identical for the two rows ranging from 0.2 to 1.5 and 0.24 to 1.2, respectively. In both cases, a staggered configuration was adopted for the two rows. This is the most common arrangement, although Kruse [3] has conducted experiments with multiple rows in which both staggered and in-line hole arrangements were used, with row spacings of up to six hole diameters.

In the absence of experimental data, it is usual to calculate the effectiveness resulting from the superposition of two or more films using a simple theory based on the work of Sellers [4]. The basis of this theory is that, at any given station, the effectiveness should be calculated as if the adiabatic film temperature arising from the upstream injection stations were the local mainstream temperature. This hypothesis was originally advanced for the superposition of slot-injected films, but has been validated over a limited range of conditions for discrete hole injection. Mayle and Camarata [5, 6] tested full-coverage film cooling configurations with blowing rates in the range 0.5 to 2.0, while Muska, et al. [7] used two double rows of holes with spacings of 16.7 and 25 diameters between the injection stations and blowing rates of up to 1.3. In both cases it was found that the application of Sellers' hypothesis gave good predictions of effectiveness. While this is encouraging, the range of blowing rate and row spacings currently used extends well outside those studied so far. Further, the rows may be fed from different internal cooling passages and have different blowing rates.

The objectives of the present work were twofold: firstly to provide a wider range of experimental data for preliminary design purposes, and, secondly, to attempt to establish limits within which Sellers' hypothesis can be applied with safety. These objectives imply a range of blowing parameters extending to 3.0 and row spacings from those small enough for interaction of the jets from the two rows to be anticipated, to those around the maximum encountered on turbine blades in practice.

In this paper it is intended to convey the major findings of the investigation in a condensed form suitable for design purposes. A more detailed account of the work and of the results is given by Afejuku [8] and will be the subject of a further publication.

2 The Experiments

In the present work, a mass transfer technique has been employed. A mixture of Freon 12 and air was injected into an airstream through long tubes set in plates forming part of the flat floor of the working section of a wind tunnel. The proportion of Freon in the injectant was such that the density ratio of injectant to mainstream was approximately 2.0, to simulate gas turbine operating conditions. The tunnel wall boundary layer was bled off ahead of the first injecting row, and a trip wire was then used to give a turbulent boundary layer.

A contoured roof provided for acceleration of the mainstream over part of the boundary layer development length to give a boundary layer thickness to hole diameter ratio of the same order as that for turbine blades. The main test parameters are given in Table 1 and the row configurations are shown in Fig. 1.

Samples were drawn through small tappings on the tunnel center line downstream of the second row and the plates in which the injection tubes were set could be traversed laterally past the sampling tappings so that the spanwise distribution of effectiveness could be measured.

Analysis of the samples was carried out by means of a thermal

Contributed by the Gas Turbine Division and presented at the 1979 Israel Joint Gas Turbine Congress, Haifa, Israel, July 9–11, 1979 of THE AMERICAN SOCIETY OF MECHANICAL ENGINEERS. Manuscript received at ASME Headquarters April 13, 1979. Paper No. 79-GT/Isr-10.

Copyright © 1980 by ASME

Downloaded 01 Jun 2010 to 171.66.16.58. Redistribution subject to ASME license or copyright; see http://www.asme.org/terms/Terms_Use.cfm

Table 1 Main test parameters

Hole diameter, D	:	2.27 mm
Spacing to diameter ratio	:	3.0
Number of rows	:	2
Row spacings	:	10D, 20D, 30D, 40D
Injection angles	:	35 deg at both rows or 90 deg at both rows
Row configurations	:	staggered or in-line (see Fig. 1)
Width of tunnel working section	:	381 mm
Injectant : mainstream density ratio, ρ_j/ρ_∞	:	2.0
Mainstream velocity, u_∞	:	25 m/s
Blowing rate, $M(\equiv \rho_j u_j/\rho_\infty u_\infty)$	:	combinations of 0.5, 1, 2, 3 at the two rows
Boundary layer displacement thickness at the first row, $\delta^*/_D$	:	0.16
Pressure gradient	:	zero

conductivity cell to give the concentration of Freon in the sample. The confidence limits on this measurement were to ±2.5 percent. The effectiveness, η, was then calculated from the ratio of the concentration of Freon in the sample, c_w, to that in the injectant, c_i. i.e., $\eta = c_w/c_i$ as described by Ito, et al. [9]. The spanwise averaged effectiveness, $\overline{\eta}$, was calculated by numerical integration of the cross-stream effectiveness distribution.

More detailed information about the rig and experimental techniques are given by Afejuku [8] and by Foster and Lampard [10].

3 Results and Discussion

3.1 Influence of Blowing Rates and Row Spacing on the Effectiveness Distribution Downstream of the Second Row. In Fig. 2 (*a–d*), the streamwise distribution of spanwise averaged effectiveness is shown for small and large row spacings and for low and high blowing rates for staggered rows injecting at an angle of 35 deg in a plane parallel to the mainstream direction. The distribution for a single row is also shown (Fig. 2(*e*)) for comparison with the double row data.

Before looking at these figures in detail it is interesting to do what comparisons are possible with data of other authors. Fig. 2(*f*) compares the data of the authors with that obtained by Pedersen, et al. [11], which is for practically the identical set of parameters including injectant to mainstream density ratio. The agreement is remarkably good at both low and high blowing rates. Further direct comparisons are not possible as the density ratios cannot be matched and it has been shown by Pedersen, et al. [11] and by Foster and Lampard [12] that the effectiveness obtained from discrete hole injection is strongly dependent upon the density ratio.

Referring now to Fig. 2 (*a–d*) for the low downstream blowing rate, the effectiveness distribution downstream of the two rows shows a monotonic decay for both high and low upstream blowing rates and for both the 10D and 40D row spacings, comparable to that for the single row Fig. 2(*e*) at the same low blowing rate of 0.5.

For the high downstream blowing rate, considerable differences are observed in the region immediately downstream of the second row, with variations occurring with both row spacing and upstream blowing rate. The single row behavior at this high blowing rate of 3 is characteristic of that for jet lift-off conditions, with a low effectiveness in the region very close to the injection point and a gradual recovery as the jets mix with the mainstream and spread towards the surface. The initial low level arises from mainstream fluid between the jets being drawn into the region beneath the detached jets.

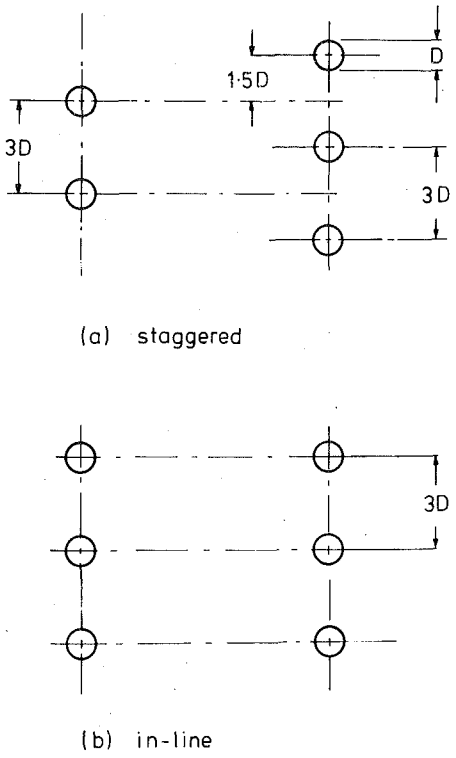


Fig. 1 Row configurations

With two rows injecting it might be anticipated that the level of effectiveness in the region affected by lift-off would be around that resulting from the upstream row alone. However, careful inspection of Fig. 2 shows that this is not so. The positions of the second injection rows relative to the upstream row are indicated in Fig. 2(*e*). It can be seen then that, for the 10D row spacing and 0.5 upstream blowing rate, Fig. 2(*a*), the initial level of effectiveness for $M_{\text{down}} = 3$ is around $\overline{\eta} \simeq 30$ which is the "background" level provided by the upstream row, (see Fig. 2(*e*), $x/D = 10$), but falls below this level further from the injection point at $x/D \simeq 10$. For the wider row spacing, Fig. 2(*b*) $M_{\text{down}} = 3$, the initial level of $\overline{\eta} \simeq 12$ is slightly below that expected from the upstream row alone (Fig. 2(*e*) $x/D = 40$), but recovers quickly to above that level. In both cases, the recovery to a maximum is faster than for a single row injecting at a high blowing rate.

The behavior when both rows are injecting with a high blowing rate depends upon row spacing. At a small row spacing, Fig. 2(*c*), the second row is within the region severely affected by lift-off of the upstream row (see Fig. 2(*e*) $x/D = 10$). A level well above the background level is reached within 4 diameters, and a maximum within 10 diameters. At the large row spacing, Fig. 2(*d*), the recovery distance is increased to around that for a single row. Note that, here, the second row is only slightly ahead of the maximum effectiveness position for the upstream row operating alone (Fig. 2(*e*), $x/D \simeq 50$).

The explanation for these apparently disparate behavior patterns lies in the development of the upstream film. At the low blowing rate, a distance of around 25 diameters is required for the jets from the upstream row to coalesce and achieve a reasonably two-dimensional film. At the high blowing rate however Foster [13] reported that a

Nomenclature

D = injection hole diameter
u = velocity
ρ = density
M = blowing rate $\left(\equiv \dfrac{\rho_j u_j}{\rho_\infty u_\infty}\right)$
x = streamwise coordinate (measured from hole center)
η = film cooling effectiveness (local)
$\overline{\overline{\eta}}$ = spanwise (cross-stream) averaged effectiveness
$\overline{\eta}$ = area averaged effectiveness
L = streamwise distance in area averaged value
δ^* = boundary layer displacement thickness

Subscripts

up = value at upstream row
down = value at downstream row
j = jet (injectant)
∞ = freestream

Downloaded 01 Jun 2010 to 171.66.16.58. Redistribution subject to ASME license or copyright; see http://www.asme.org/terms/Terms_Use.cfm

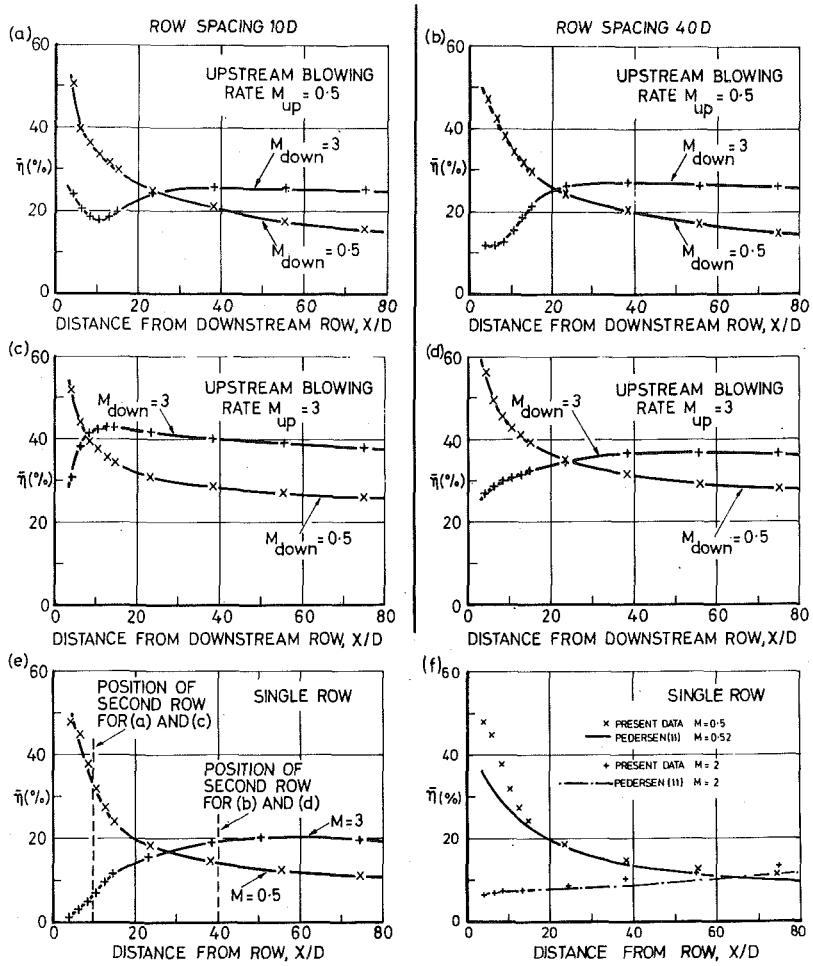


Fig. 2 Variation of spanwise averaged effectiveness with distance from the downstream row showing the effects of row-spacing and blowing rate. (*e*) shows single row data for comparison. (*f*) shows comparisons with Pedersen, *et al.* [11]

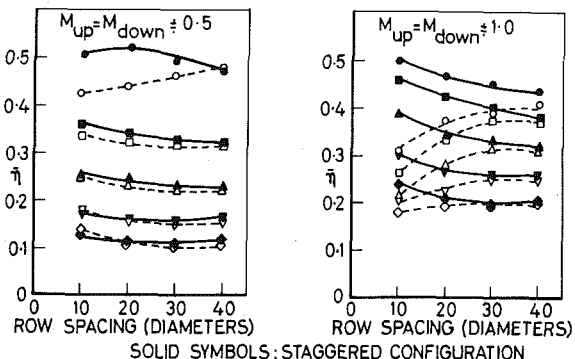
strong jet structure is perceptible over much greater distances. Moreover, whereas the density decreases with distance from the wall (for all but very small downstream distances) when the blowing rate is small and the jet core is attached to the wall, the jet core, and maximum density, lie well above the surface when the jet lifts off.

Thus the fall in effectiveness below the background level observed for high downstream blowing rate and low upstream blowing rate in Fig. 2(*a*) may be caused by fluid being drawn from the dilute regions surrounding the cores of the upstream jets as they pass between the downstream jets. Invoking a similar argument leads to the expectation of the high level seen in Fig. 2(*c*) where both the upstream and downstream blowing rates are high. In this case fluid is drawn from near the core of the upstream jet which is above the surface. The very fast recovery seen in this latter figure may well be due to the strong mixing arising from the high injection rates and small row spacing. It is interesting to note that, for the low downstream blowing rate, the initial fall in effectiveness appears to be rather faster for the small row spacing than for the large, indicating an enhanced mixing rate for small row spacings.

Far from the injection points, the level of effectiveness depends primarily on the total coolant injection.

It is evident from these trends that, in order to avoid regimes of low adiabatic wall effectiveness downstream of the second row, a high downstream blowing rate should not be used unless the upstream blowing rate is also high. Of course, in deciding on the best combinations of blowing rates and row spacings, consideration needs to be given also to the effectiveness distribution in the space between the injecting rows. This will be discussed later.

3.2 Comparison of Staggered and In-Line Configurations.



SYMBOL	DISTANCE FROM DOWNSTREAM ROW
○	4·1 D
□	10·6
△	23·6
▽	55·7
◇	109·6

Fig. 3 Comparison of in-line and staggered configurations

It was found that a staggered injection configuration always gave a cooling effectiveness superior to that of an in-line configuration. In Fig. 3, the spanwise averaged effectiveness for the two configurations are compared at two blowing rates and over a range of row spacings.

The superiority of the staggered configuration decreases with in-

Downloaded 01 Jun 2010 to 171.66.16.58. Redistribution subject to ASME license or copyright; see http://www.asme.org/terms/Terms_Use.cfm

creasing row spacing, and increases as the upstream blowing rate increases. This can again be explained by reference to the state of development of the upstream film. Increasing the row spacing provides for an increased development length for this film and, consequently, it is more fully mixed when the second row is encountered and less dependent upon the row configuration. An increase in the upstream blowing rate results in a longer development length being required to achieve two-dimensional conditions within the upstream film.

Afejuku [8] presents measurements of the lateral distributions of effectiveness. From these results it is apparent that the superiority of the staggered configuration at small row spacings can be ascribed to the better lateral uniformity of the film. The alignment of the upstream jets with the gaps in the downstream row results in improved uniformity, not only at stations close to the second row, but also further downstream. The impingement of the upstream jets on the downstream for the in-line configuration does not appear to provoke greatly enhanced lateral mixing, and, as a result, there are areas of low effectiveness between the holes downstream of the second row.

Detailed studies of 90 deg injection [8] show that use of a 90 deg injection angle results in much faster mixing of the upstream film, with a consequent reduction of the development length required for film uniformity resulting in a large reduction of the differences between staggered and in-line configurations observed for 35 deg injection.

3.3 Contour Plots of Area Averaged Effectiveness. As noted earlier, in order to arrive at an optimum solution, the effectiveness in the space between the injecting rows needs to be considered in addition to that downstream of the second row. In deciding on a final configuration, the designer will need to consider a great many factors including the level of effectiveness required, the avoidance of very low levels of effectiveness which might lead to hot spots and the total coolant flow rate available. Spanwise averaged data are not sufficiently comprehensive for this purpose as they give no indication of the low effectiveness areas which may occur between the holes in the spanwise direction.

For the purpose of initial design assessment and optimization, however, even the spanwise averaged data are too detailed where many parameters are involved, as in the present case. A more immediately comprehensible picture of the gross influence of the various parameters can be gained by looking at the effectiveness averaged over a specified area, measured from the upstream row so that the inter-row region is taken into account. The area-averaged effectiveness is therefore defined as

$$\bar{\bar{\eta}}_L = \frac{1}{L}\int_0^L \bar{\eta}\, dx$$

For the present work, a value of L of 60D has been selected.

In Fig. 4, contours of constant area-averaged effectiveness are plotted for the range of upstream and downstream blowing rates studied. Fig. 4(a) is for 35 deg injection with a 10D row spacing, and Fig. 4(b) for 35 deg injection with 40D row spacing.

Considering first Fig. 4(a), it can be seen that there is a clear peak given by the closed contour where upstream and downstream blowing rates are both of order unity. The maximum recorded value was in fact 38 percent with both blowing rates slightly less than unity.

Two other features are particularly noteworthy. At low downstream blowing rates, $\bar{\bar{\eta}}_{60}$ is virtually independent of the upstream blowing rate, provided that this is in excess of unity. At low upstream blowing rates, however, increasing the downstream blowing rate above unity results in a fall in $\bar{\bar{\eta}}_{60}$. Thus in a situation where cooling air needs to be dumped so that a high blowing rate is unavoidable Fig. 4(a) indicates that it is best to hold the downstream blowing rate at unity, and use the upstream row for the high blowing rate.

The 45 deg chain lines on the figures are lines of constant total coolant flow. Tangency of one of these lines to a particular contour gives the minimum coolant flow required to achieve the average effectiveness represented by the contour and also, from the point at which tangency occurs, the way in which the coolant flow should be divided between the two rows is indicated. It is immediately apparent that cooling of the area considered is best done with two rows rather than one, since moving along any constant flow line from zero downstream blowing rate gives an increase in $\bar{\bar{\eta}}_{60}$.

Comparing Fig. 4(b) with Fig. 4(a), the peak in the effectiveness is still present and is roughly at the same position. The level in this case is considerably lower, however; the maximum recorded was 31.5 percent. A further region of high effectiveness is now apparent with a downstream blowing rate of unity, and an upstream blowing rate approaching 3. Again, if a high blowing rate has to be used, it should be at the upstream row. An important feature to note is the area of low effectiveness which has appeared for an upstream blowing rate of 2 and high downstream blowing rates.

Fig. 4(c) is for 90 deg injection and 10D row spacing. Comparing this with Fig. 4(a), the superiority of 35 deg injection is clear. The maximum level here is the same as for the 40D row spacing with 35 deg injection, but requires much greater coolant flows.

The construction of the contour plots of Fig. 4 required interpolation from data gathered at the four blowing rates given in Table 1, and, consequently, when both blowing rates are high, the position of the contours is subject to a maximum error of around ±0.2 in either blowing rate. This is not sufficient to affect significantly any of the conclusions drawn above.

3.4 Comparison of Measured Results with those Predicted by Superposition Theory. In the film superposition theory referred to earlier, Sellers [3] proposed that the second and subsequent films behaved as if the ambient temperature were the adiabatic wall temperature which would result from the upstream stations. For two rows which, injecting separately, give spanwise averaged effectivenesses of $\bar{\eta}_1$ and $\bar{\eta}_2$ at some point downstream of the second row, the effectiveness with both rows injecting simultaneously is $\bar{\eta} = 1 - (1 - \bar{\eta}_1)(1 - \bar{\eta}_2)$. The simplicity of the method is clearly appealing, but the assumptions underlying its application are that the adiabatic wall temperature is a good indicator of the mean film temperature, and that mixing of the upstream film is complete before the downstream injection station so that the latter is assumed to be injecting into a homogeneous environment. Both assumptions are obviously invalid in the case of discrete hole injection when the row separation is small and the upstream blowing rate is high. They would imply that effectiveness is independent of the relative spanwise positions of the holes in the rows and this has already been seen to be untrue.

The questions remaining to be resolved are the range of blowing rates and row spacings which lead to good predictions of effectiveness, and the ranges over which the method will give a basis for safe design.

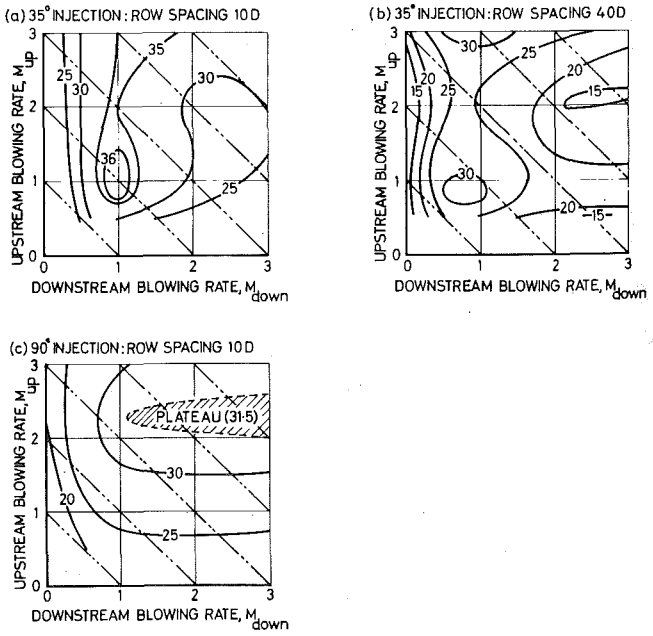


Fig. 4 Contours of area averaged effectiveness (percent) for a region extending 60 diameters from the upstream row (—— - - —— constant total coolant flow)

Downloaded 01 Jun 2010 to 171.66.16.58. Redistribution subject to ASME license or copyright; see http://www.asme.org/terms/Terms_Use.cfm

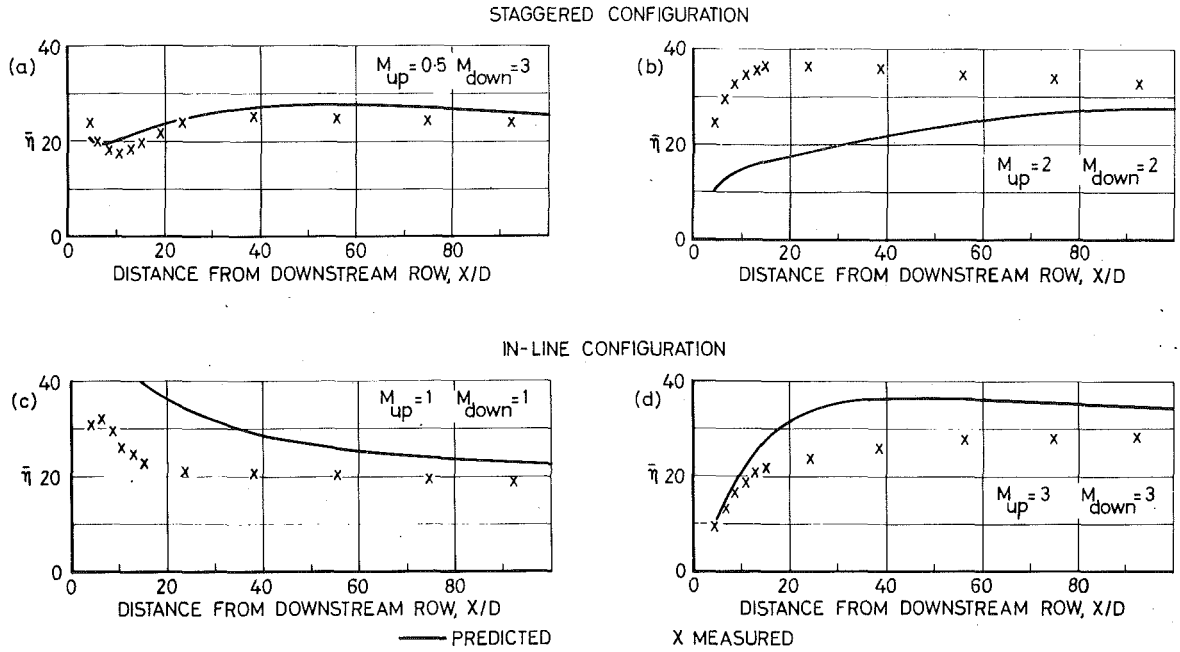


Fig. 5 Comparison of the measured spanwise averaged effectiveness for two rows with that predicted from single row measurements using Sellers' hypothesis (Row spacing 10 diameters; injection angle 35 deg)

Typical results for the staggered configuration for the closest row spacing studied (10 diameters) are shown in Fig. 5(*a*) and (*b*). More detailed results are given by Afejuku [8]. Generally, it was found that for staggered holes good predictions were obtained if the blowing rate was 0.5 at either row (see Fig. 5(*a*) for example). The prediction was especially poor if the upstream blowing rate was 2, and, the downstream 1, 2 or 3 (see Fig. 5(*b*)). Outside these ranges, good agreement was obtained with blowing rates of 3 and 1, or 1 and 3 and fair agreement at all other conditions. However, in all cases where the predicted result differed significantly from that measured, the prediction gave an underestimate and so its use would result in a safe (over-cooled) design. The disagreement was invariably over the initial 20 to 50 diameters. The good predictions found by Muska, et al. [7] referred to earlier are not inconsistent with the present results as they were for much greater distances downstream than 50 diameters.

Increasing the row spacing increases the range of good predictive capability; at a 30D row spacing, only the results at the two highest upstream and downstream blowing rates showed any significant differences between measured and predicted results.

As might be expected from the observed differences between the performance for staggered and in-line configurations (see Section 3.2), predictions for the in-line configurations were much poorer, and serious over-prediction occurred in many cases, as illustrated by Fig. 5(*c*) and (*d*).

Changing the injection angle to 90 deg reduced the discrepancy between experimental and predicted results. In general, then, it appears that the successful application of Sellers' hypothesis for discrete hole film cooling is dependent primarily on the uniformity of the upstream film, although the agreement obtained with a low downstream blowing rate for all upstream blowing rates for the staggered configuration shows that this is not the sole criterion.

4 Conclusions

The preceding sections have shown that, for high adiabatic film cooling effectiveness on a plane surface using two successive rows of discrete holes:

1 A staggered configuration should be used in preference to an in-line configuration.

2 If a high blowing rate has to be used at one row, it should be at the upstream row. This gives the better average effectiveness and avoids areas of low effectiveness downstream of the second row.

3 The use of a 90 deg injection angle at both rows gives a lower cooling effectiveness than a 35 deg injection angle.

4 For maximum area-averaged effectiveness, the blowing rate should be approximately unity at both rows, and the row spacing should be 10 rather than 40 diameters.

5 The use of Sellers' hypothesis to predict the effectiveness downstream of the second row would result in safe design in all the cases studied for staggered row configuration. However, the effectiveness is underpredicted when the blowing rates are high and the row spacing small, and this may in turn lead to an over-prediction of the required coolant flow rate. Under these same conditions, the performance of in-line configurations may be seriously over-predicted. In practice, of course, the effects observed through the adiabatic film cooling effectiveness will be modified by internal cooling and wall conduction, and by changes in the external heat transfer coefficient as reported for example by Goldstein [14]. Nevertheless the conclusions presented here should provide useful initial design guidelines.

Acknowledgments

The research reported here was carried out in the Department of Mechanical Engineering at Nottingham University with a grant from the Science Research Council. The use of the facilities and the financial support are gratefully acknowledged.

References

1 Jabbari, M. Y. and Goldstein, R. J., "Adiabatic Wall Temperature and Heat Transfer Downstream of Injection through Two Rows of Holes," ASME JOURNAL OF ENGINEERING FOR POWER, Vol. 100, 1978, pp. 303–307.

2 Hirata, N., "Measurement of Film Cooling Effectiveness Distributions for Exhausting through a Double Row of Holes," Paper No. 01, JSME/GTST/ASME Joint Gas Turbine Congress, Tokyo, May 1977.

3 Kruse, H., "Investigation on Temperature Distribution Near Film Cooled Aerofoils," Paper No. 8, AGARD CP-229, Feb. 1978.

4 Sellers, J. P., Jr., "Gaseous Film Cooling with Multiple Injection Stations," *AIAA Journal*, Vol. 1, 1963, pp. 2154–2156.

5 Mayle, R. E. and Camarata, F. J., "Heat Transfer Investigation for Multi-Hole Aircraft Turbine Blade Cooling," AFAPL-TR-72-30 Air Force Aero-Propulsion Laboratory, Wright-Patterson Air Force Base, 1973.

6 Mayle, R. E. and Camarata, F. J., "Multi-Hole Cooling Film Effectiveness and Heat Transfer," ASME *Journal of Heat Transfer*, Vol. 97, 1975, pp. 534–538.

7 Muska, J. F., Fish, R. W. and Suo, M., "The Additive Nature of Film Cooling Rows of Holes," ASME JOURNAL OF ENGINEERING FOR POWER, Vol. 98, 1976, pp. 457–464.

Downloaded 01 Jun 2010 to 171.66.16.58. Redistribution subject to ASME license or copyright; see http://www.asme.org/terms/Terms_Use.cfm

8 Afejuku, W. O., "Superposition of Cooling Films," Ph.D. Thesis, University of Nottingham, 1977.

9 Ito, S., Goldstein, R. J. and Eckert, E. R. G., "Film Cooling of a Gas Turbine Blade," Paper No. 03, JSME/GTSJ/ASME, Joint Gas Turbine Congress, Tokyo, May 1977.

10 Foster, N. W. and Lampard, D., "The Flow and Cooling Effectiveness following Injection through a Row of Holes," ASME/Israel Joint Gas Turbine Congress, Haifa, Israel 1979, Paper No. 79-GT/Isr-6.

11 Pedersen, D. R., Eckert, E. R. G. and Goldstein, R. J., "Film Cooling with Large Density Differences Between the Mainstream and the Secondary Fluid Measured by the Heat-Mass Transfer Analogy," ASME *Journal of Heat Transfer*, Vol. 99, Nov. 1977, pp. 620–627.

12 Foster, N. W. and Lampard, D., "Effects of Density and Velocity Ratio on Discrete Hole Film Cooling," *AIAA Journal*, Vol. 13, No. 8, Aug. 1975, pp. 1112–1114.

13 Foster, N. W., "Film Cooling of Gas Turbine Blades," Ph.D. Thesis, University of Nottingham, 1976.

14 Goldstein, R. J. "Some Measurement Techniques in Heat Transfer," Sixth International Heat Transfer Conference, Toronto, 1978, Vol. 6, pp. 495–508.

Downloaded 01 Jun 2010 to 171.66.16.58. Redistribution subject to ASME license or copyright; see http://www.asme.org/terms/Terms_Use.cfm

R. A. Cookson
Head of Applied Mechanics,
School of Mechanical Engineering,
Cranfield Institute of Technology,
Cranfield,
Bedford, England.

P. Bandyopadhyay
Senior Development Engineer,
Bharat Heavy Electricals Ltd.,
Hyperabad
India

A Fiber-Optic Laser-Doppler Probe for Vibration Analysis of Rotating Machines

The problem of obtaining vibratory information from remote, rotating, components within a machine has been overcome by means of a laser-Doppler fiber-optic probe. Laser light is transmitted down the fiber-optic and scattered light is returned for analysis in the same way. The Twyman-Green mode of operation of the laser-Doppler system has been shown to have serious shortcomings for this type of work and a new mode has been produced, and used successfully, in conjunction with Bragg cells for frequency shifting. The use of a single set of Bragg cells to compensate for the average velocity of a rotating system, limits the allowable speed of rotation to about 1000 rpm. However, other techniques for frequency shifting are available. An experimental investigation is reported in which a rotating system, consisting of a disk carrying flat cantilever blades, was rotated at about 1000 rpm while one of the blades was excited at 163 Hz. The measured frequency of the vibrating blade was 162.8 Hz and similar accuracy was obtained for the amplitude measurements.

Introduction

Vibration is a common cause of failure or malfunction of machines, and this is particularly true for modern, high speed rotating machinery. The two most important measurable vibratory parameters are amplitude and frequency. The amplitude of vibration is an indication of the stress level likely to be found in a particular component, while frequency measurements can help to establish the mode of vibration, the source of vibration, and obviously the likelihood of resonance occurring within the running range of the machine.

In machine design, the need to determine the vibration characteristics of machine components so as to avoid resonance which can lead to malfunction and ultimately, through the mechanism of fatigue, to mechanical failure, often arises. A prime example of this requirement in turbomachine design is instanced by the blading of an axial compressor. Compressor blades are, at the same time, amongst the most unpredictable and expensive components which go to make up an axial flow engine and which often cost 30 percent of the total engine price.

The selection of a turbomachine blade as a candidate for vibration analysis, highlights one of the most difficult problems associated with the determination of the vibratory characteristics of machine components, namely the abstraction of vibratory information from a component which is rotating. As a first approximation the appropriate information could be obtained from a static investigation employing say, laser holographic interferometry, in the laboratory. However, the vibratory properties of a rotating blade are somewhat different to those determined under static conditions. For example, the inertia force component effectively increases the stiffness of the blade, which in turn increases the resonance frequencies and alters the mode shape. Other factors which may modify the vibratory properties are the blade fixing and the vibration of the supporting disk. The idealized blade root fixing conditions are rarely achieved in practice, while the effect of the disk on the vibratory properties of the blade are very complex in nature and not completely amenable to analysis. However, in spite of these difficulties in determining the natural frequencies and vibratory modes which can exist in the design speed range, if costly failures are to be avoided these properties must be known, obviously the most reliable approach is to determine them experimentally.

Experimental Techniques. The most popular of the methods employed in abstracting vibratory information from rotating components is that which utilizes strain gauges. When the direction of the axis normal to the nodal lines is known approximately, and they are widely separated compared with the physical dimension of the strain gauge, an array of suitably placed strain gauges can be employed to measure the resonance frequency and modal shape. However, because of the complex geometry of a typical turbomachine blade, the direction of such normals is usually difficult to predict. In fact, one of the main objectives of any experimental technique is to determine the location and position of the nodal lines, and consequently their normals. By the same token, because turbomachine blades are usually quite stiff, the physical separation between lines is often too small to allow for the use of strain gauges in determining the appropriate modal shape. Even in such situations where strain gauges can be used, there is still the problem of transmitting the strain gauge signal from the rotating component to the stationary analyzing equipment. Conventionally, this process is carried out with a slip-ring or a frequency modulated grid system, techniques which introduce high noise level or high cost, respectively.

Holographic interferometry is another technique which is being adapted for situations where vibatory information must be obtained from a rotating component. Pulsed holography is used to stop, or freeze, the vibratory node and fringe pattern, while the more conventional "time-averaged" holographic images can be obtained with the aid of a "de-rotater."

However, in both cases it is obviously difficult to apply these "whole field" techniques to components which are enclosed within a machine.

Contributed by the Gas Turbine Division of THE AMERICAN SOCIETY OF MECHANICAL ENGINEERS and presented at The 1979 Israel Joint Gas Turbine Congress, Haifa, Israel, July 9–11, 1979. Manuscript received at ASME Headquarters April 24, 1979. Paper No. 79-GT/Isr-11.

Copyright © 1980 by ASME

Downloaded 01 Jun 2010 to 171.66.16.58. Redistribution subject to ASME license or copyright; see http://www.asme.org/terms/Terms_Use.cfm

For situations where the component is exposed, as is the case for example with the front fan of a gas turbine, then holographic interferometry is eminently suitable.

Another interesting technique, which can be used in obtaining vibratory information from a moving surface, is the laser-Doppler system. This technique, which utilizes the frequency shift which occurs when a laser light wave-front is scattered from the surface of a vibrating object, is now fairly well established. Application of this technique for vibration measurement of a rotating system has been reported in [1]. Unfortunately, in this simple form the laser-Doppler technique can only obtain measurements from external surfaces since it is essentially a "line-of-sight" process. Also the basic mode of operation of the laser-Doppler process, as employed in [1] cannot be used efficiently for rotating systems.

In this paper a new non-contact technique for obtaining vibratory information from moving surfaces is described. It utilizes the laser-Doppler principle in conjunction with a flexible fiber-optic probe as previously described in [2]. The laser light is transmitted down, and the scattered light back up the fiber-optic. Also, since the usual laser-Doppler modes are not suitable for the determination of vibration amplitudes at all Doppler frequencies, a new mode of laser-Doppler operation, as described in [2] is utilized.

The Laser-Doppler System

It is now well established that a waveform which is scattered by a moving object suffers a change in frequency which is known as the "Doppler frequency." Hence, if the change in frequency of the scattered waveform, brought about by the so-called "Doppler effect", can be measured, then the velocity of the moving object can be determined. There have been many applications of this principle, but since an accurate analysis requires a high degree of uniformity in the frequency of the incident wave, few have been more successful than the optical technique which employs laser light.

The Doppler frequency referred to above can be expressed as follows:

$$\Delta f = f_s - f_i = n\overline{V}(\overline{u}_s - \overline{u}_i)$$
$$= \frac{n\overline{V}}{\lambda} \cdot 2 \cos\frac{\gamma}{2} \cdot \cos\beta \qquad (1)$$

The various laser-Doppler modes are usually separated into two groups, namely, forward-scattering and back-scattering modes. Forward scattering modes are only suitable for fluid flow measurement and are therefore, inappropriate to the present situation. At the same time, a number of the back-scattering modes are only sensible to a particle velocity normal to the direction of the incident light, and are again inappropriate to the present problem. Of the remaining modes, the one most often used for mechanical vibration measurements, is the Twyman-Green mode.

The Twyman-Green mode gives a zero frequency corresponding to the zero velocity of the sinusoidal vibration of the particle and a measurable frequency corresponding to the maximum velocity of the particle. This maximum frequency can be very large, which leads to the practical problem of analyzing a large frequency together with a zero frequency. The limitation lies in the electronic system, since at this time there is no filter available commercially which can filter waves of infinite frequency ratio (maximum frequency/minimum frequency). Hence, when the amplitude is large or the frequency is high, it becomes very difficult to analyse the Doppler frequency pattern, particularly when a frequency tracker and spectrum analyzer is being used. This problem can be overcome by using some frequency shifting device. In this way the reference beam frequency is shifted with an optical, single sideband modulator. As a result the heterodyne signal produced by the photomultiplier is centered at the modulator frequency rather than at zero frequency. Depending upon the Doppler frequency shift, the modulator frequency can be chosen in such a way that the resulting frequency lies in the most efficient part of the selected filter in the frequency tracker, hence reducing the frequency ratio.

When a frequency shifting technique is used, the low frequency noise generated by the laser and the shot noise from the photomultiplier are suppressed when the operating modulator frequency is high. A number of methods of obtaining the required frequency shift have been attempted, for example [3] employed a Kerr cell with the double passage reference beam, [4] utilizing a rotating grating and [5] and [6] used a Bragg cell. Kulczyk, who had attempted the measurement of vibration from a rotating system, describes in [7] a technique which utilizes a moving mirror. Unfortunately, the alignment of the mirror was found to be very critical and this arrangement did not allow steady-state vibration of the mirror to be achieved.

All previous laser-Doppler investigations of mechanically vibrating systems have employed some form of the Twyman-Green mode of operation. In this mode the output from the photomultiplier is fed to a frequency tracker which tracks the Doppler frequency which is in turn a function of the velocity of the vibrating object. Unfortunately, in conditions where the change in velocity between the positive (forward) part of the vibration cycle and the negative (rearward) part is large, the tracker produces ambiguous results. At the same time, the Doppler frequency range is divided into certain select ranges. This is advantageous in that signals outside of these ranges are filtered out, thus reducing the noise level within the range. However, there is, unfortunately, a minimum measurable velocity and maximum detectable vibration frequency associated with each range, and this limitation in turn means that there is a minimum detectable amplitude which can be measured for each frequency range. There is also a maximum measurable amplitude which depends upon the coherence length of the laser.

In all cases where vibratory velocities are superimposed upon a relatively large average velocity, as is discovered for example in measuring the vibratory properties of a rotating bladed disc, a laser-Doppler system which employs the basic Twyman-Green mode will be unable to detect the resulting combined high velocity. This problem can be overcome with the aid of a frequency shifting technique, but such a technique will severely limit the velocity range for which the mode can be used. For example, successive measurements of the vibratory characteristics of stationary components and components which are rotating at realistic speeds, would be impossible.

A further disadvantage of the Twyman-Green mode is the relatively low signal-to-noise ratio which results from the imbalance in the light intensities of the two optical paths.

Nomenclature

A = amplitude of vibration
C = integer constant
δC = fractional constant
f = frequency
n = refractive index of medium in which scattering takes place
N = rotating speed (rpm)
t = time
T = sampling time
u = velocity
U = maximum velocity ($= A\omega$)
$\overline{V}$ = velocity vector of moving object
x = displacement
$\alpha = \omega t_1$ (equation (7))
β = angle between the direction in which the body is moving and the direction of the resultant vector between the scattered light and the incident light
λ = free space wave-length of incident light
ϕ = phase angle
γ = angle between the direction in which the scattered light is collected and the direction of the incident light
ω = circular frequency of vibration

Subscripts

$b1$ = light passing through Bragg cell 1
$b2$ = light passing through Bragg cell 2
i = incident light
s = scattered light

Superscripts

0 = polarization axis
90 = polarization axis
360 = polarization axis

Downloaded 01 Jun 2010 to 171.66.16.58. Redistribution subject to ASME license or copyright; see http://www.asme.org/terms/Terms_Use.cfm

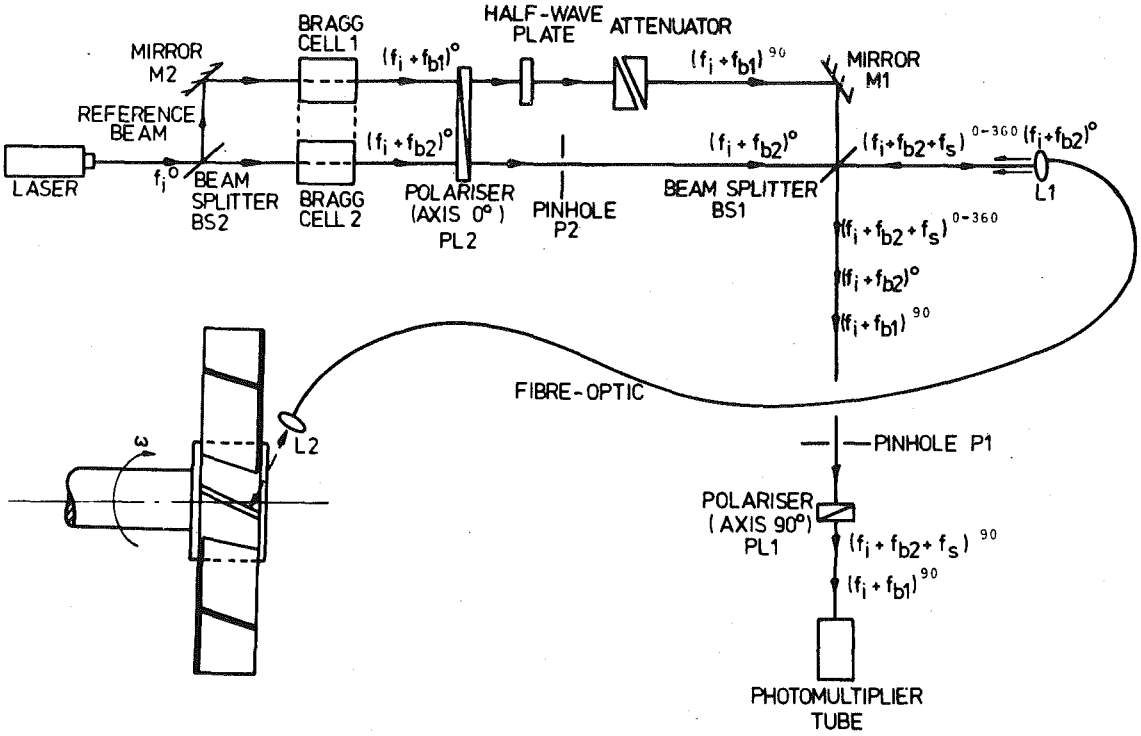


Fig. 1 Fiber-Optic Laser-Doppler Mode for Rotating Machines

Improved Laser-Doppler Mode. Clearly, both the Twyman-Green mode and any existing mode based upon the Twyman-Green mode are unsuitable for the present application. Hence, a new mode of laser-Doppler operation has been devised and is illustrated in Fig. 1. The improved balance between the laser light intensity in the two optical paths of the new mode provides a much improved signal-to-noise ratio and the introduction of Bragg cells into both optical paths overcomes the limitation in measuring large fluctuating velocities. At the same time, the problem associated with extraneous light deflection are overcome by selectively polarizing the appropriate beams and hence filtering out reflected depolarized light.

Experimental

The light from a 5mW He-Ne Spectra Physics model 120 laser operating at 632.8 nm is divided into two beams of equal intensity by the beam-splitter BS2. These two beams (reference and incident) are passed through DISA type 55L02 Bragg cells 1 and 2, thus increasing their frequencies by f_{b1} and f_{b2} respectively. Both beams are then passed through polarizer PL2 which has its polarizing axis set at 0 deg, where the angles quoted are relative to the polarizing axis of the laser. The reference beam is now passed through a half wave ($\lambda/2$) plate, thus changing its polarization axis to 90 deg.

Pinhole $P2$ obstructs the unshifted incident beam from Bragg cell 2, but allows the shifted incident beam to pass to the beam-splitter BS1. Pinhole $P1$ obstructs the unshifted reference beam and allows the shifted reference beam and the parallel light vectors from the fiber-optic to pass. A reduction in the diameter of pinhole $P1$ increases the signal quality but reduces signal strength.

By keeping the axis of the polarizer PL1 at 90 deg, only light in condition $(f_i + f_{b2} + f_s)^{90}$ and $(f_i + f_{b1})^{90}$ is allowed to pass. When these two components are mixed they produce the beat frequencies $(2f_i + f_{b1} + f_{b2} + f_s)^{90}$ and $(f_{b1} - f_{b2} - f_s)^{90}$. The only detectable signal is at the latter frequency since the frequency of the former component is greater than the upper limit of the DISA type 55L10 photomultiplier unit, which utilizes an EM1 9658 B tube which has an upper limit of 25 MHz. By choosing an appropriate value of $(f_{b1} - f_{b2} - f_s)^{90}$ and suitable attenuation of the reference beam, the signal-to-noise ratio can be kept reasonably high. The frequency tracker used in this investigation is a DISA type 55L20 which has seven frequency ranges with the overall maximum frequency being 15 MHz. The Bragg cells can be adjusted to give frequency shifts f_{b1} and f_{b2} such that $f_{b1} - f_{b2}$ is located in the middle of the tracker range. In this way the shifted beams are used most efficiently.

The lens L1 focuses the incident light beam on to the end of the fiber-optic and also collects the light returning down the fiber-optic and returns it to beam splitter BS1. The receiving lens L2 focusses the light, which has been transmitted through the fiber, on to the rotating blades at an optimum depth of focus and spot diameter. Lens L2 also collects a narrow cone of scattered light and transmits it back down the fiber-optic.

The fiber-optic used in this investigation is a Rank Optics Croform 1mm dia monofilament optic.

The bladed-disk analyzed in this investigation is shown in Fig. 2. It is obviously a contrived system in that the eight blades are flat, rectangular plates, but in all other respects the system is realistic. A 5HP variable speed motor, with a range from 400 to 3500 rpm was used to drive the disk. A piezo-electric exciter was attached to one of the blades and driven by means of an oscillator-amplifier arrangement through the slip-ring in Fig. 2.

A sample-and-hold unit was designed specifically for use with the above rotating system. It has a delay system with coarse and fine controls. By adjusting the delay continuous laser-Doppler signals from all of the blades can be sampled at the required analysis point. By varying the delay time, different points of different blades can be analyzed. The sample-and-hold unit is designed to acquire and hold analogue signals of up to 10 Volts with an accuracy of 0.01 percent. The sample time is 5 μs and the minimum hold time is 1ms. The minimum hold time restricts the sampling rate to a maximum of 1000 per second. This is equivalent to 60,000 rpm in a rotating system. The maximum voltage decay at output when in the "hold" mode (known as the droop rate) is 0.5 mV/ms.

The laser-Doppler analogue output from the frequency tracker is fed to the sample-and-hold unit. The output from the recording signal socket of the sample-and-hold unit gives values for the instantaneous velocities (u), and from the time difference between two consecutive signals gives the sample time (T_c).

The output from the recording signal socket of the sample and hold unit was directly connected to an "Interdata 716" mini-computer. The data were analyzed from on-line signals by using built-in software. Those techniques will be described later under the heading of "data-analysis."

Downloaded 01 Jun 2010 to 171.66.16.58. Redistribution subject to ASME license or copyright; see http://www.asme.org/terms/Terms_Use.cfm

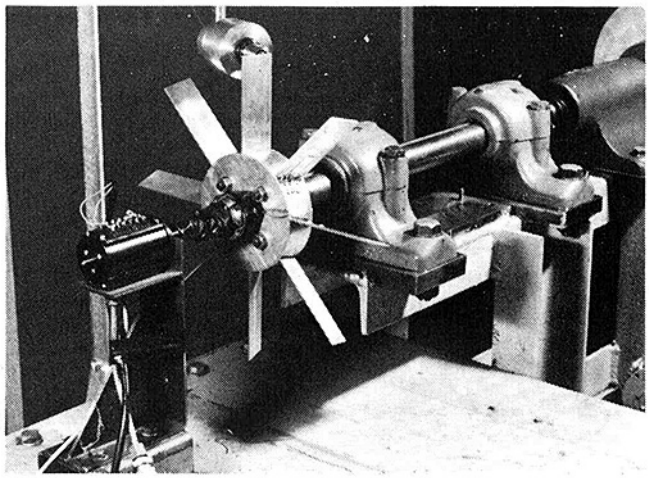


Fig. 2 Signal Collecting Probe and Bladed disk

Analysis of Rotating Blades

The laser-Doppler signal obtained from a rotating blade cannot be continuous and hence it is not possible to see the vibrating velocity pattern on an oscilloscope or similar display system. Therefore, it is necessary to develop an analytical model based upon discrete measurements of the blade velocity.

For simplicity the vibration of a blade in the rotating condition is assumed to be sinusoidal and represented by the following expression.

$$x = A \sin(\omega t + \phi) \tag{2}$$

From this expression, the velocity u at any instant t is given by,

$$u = U \cos(\omega t + \phi) \tag{3}$$

where U is the maximum velocity and is equal to the product $A\omega$.

If three velocities are measured at equal intervals of time t, at say 0, t_1 and $2t_1$, then equation (3) becomes

$$u_1 = U \cos\phi \text{ at } t = 0 \tag{4}$$

$$u_2 = U \cos(\alpha + \phi) \text{ at } t = t \tag{5}$$

and

$$u_3 = U \cos(2\alpha + \phi) \text{ at } t = 2t \tag{6}$$

where

$$\alpha = \omega t_1 < \pi \tag{7}$$

From equations (4–6),

$$u_3/U = \cos 2\alpha \cos\phi - \sin 2\alpha \sin\phi$$

$$= 2(u_2/U)\cos\alpha - u_1/U$$

or

$$\cos\alpha = \frac{u_1 + u_3}{2u_2} \tag{8}$$

Hence, knowing α from equation (8) ω can be calculated from equation (7).

Substracting (4) from (6),

$$u_3 - u_1 = U\cos(2\alpha + \phi) - U\cos\phi$$

$$= -2U \sin(\alpha + \phi)\sin\alpha$$

Squaring this expression and utilizing equation (5), we can express the maximum velocity as,

$$U = \left[\frac{(u_3 - u_1)^2 + 4u_2{}^2 \sin^2\alpha}{4\sin^2\alpha}\right]^{1/2} \tag{9}$$

and hence, the amplitude A which is equal to U/ω is given by,

$$A = \frac{1}{\omega}\left[\frac{(u_3 - u_1)^2 + 4u_2{}^2 \sin^2\alpha}{4\sin^2\alpha}\right]^{1/2} \tag{10}$$

When $t_1 \geq \pi/\omega$ an ambiguous value of α arises from equation (8). There is therefore, a maximum frequency of vibration which can be measured without ambiguity at a single measuring point for any specific rotating speed. The maximum frequency that can be determined by the above analytical treatment, when readings are taken in three consecutive revolutions, can be calculated as follows:-

For a rotating speed of N (rpm)

$$t_1 = \frac{60}{N} \text{ s}$$

and to satisfy equation (7),

$$\frac{60}{N} \leq \pi/\omega$$

or

$$N \geq 60\,\omega/\pi$$

and

$$60\,\omega/\pi = 120f$$

where f is the frequency (Hz) of vibration.

Therefore, at (say) 12,000 rpm the maximum frequency which can be measured without ambiguity is only 100 Hz, which is obviously unrealistically low. This limitation can be overcome for different cases, by different methods. In most practical situations the time of one revolution of the disc T_c is greater than the time for one cycle of vibration of the rotating blade T. If we now consider that we can keep the speed of rotation N constant for three consecutive cycles of rotation and then change it by (say) 1 percent without affecting the vibration frequency, that is T remains constant, then it is possible to determine both the amplitude and the frequency of vibration.

Let

$$T_c = T(C + \delta C) \tag{11}$$

where C is an integer constant and δC is a constant which lies between zero and unity.

From equation (7),

$$\alpha = \omega T_c = 2\pi(C + \delta C) \tag{12}$$

Hence, from equation (8),

$$\cos 2\pi\delta C = \frac{u_1 + u_3}{2u_2} \tag{13}$$

where u_1, u_2 and u_3 are known velocity samples and correspond to consecutive cycles of rotation.

If the speed now changes slightly (say 1 percent) then the sampling time T_c will change to T_c' and the fractional constant δC will change to $\delta C'$, but C and T remain constant.

Therefore, from the second set of data $\delta C'$ can be calculated, and hence knowing T_c, T_c', δC and $\delta C'$, C can be calculated from the expression,

$$C = \frac{T_c'}{T_c' - T_c}(\delta C' - \delta C) - \delta C' \tag{14}$$

which is derived from equation (11) for two sets of data.

Hence, T can be calculated from equation (11) and consequently the frequency f can be determined. The amplitude of vibration can also be calculated from equations (12) and (10), substituting $\omega = 2\pi f$ for any set of values of u_1, u_2 and u_3. From the readings taken, it was found that a 1 percent speed change produced an appreciable change in δC.

Sampling theory indicates that the sampling frequency should be at least twice the vibrating frequency, in order to avoid aliasing errors. But by utilizing a small fluctuation in speed, as previously described,

Downloaded 01 Jun 2010 to 171.66.16.58. Redistribution subject to ASME license or copyright; see http://www.asme.org/terms/Terms_Use.cfm

the frequency of vibration and the associated amplitude can be determined. The limitation in this technique is that the difference in the sampling times at the two different speeds ($T_c' - T_c$) should not be more than, or equal to, the time for one vibration cycle T, that is, $(T_c' - T_c) < T$, otherwise the assumption that C is a constant in equation (11) will not be valid. Hence, for high frequencies the allowable change of speed will be very small and consequently the values of T_c' and T_c must be determined accurately. Even for frequencies as low as 163 Hz, a small error in T_c' or T_c will produce an ambiguous value for T. For that reason, the sample time is averaged over a number of samples and the value of C so determined is approximated to the nearest integer. Similarly, the values of cos $2\pi\delta C$ are determined from a number of equispaced sample regions and averaged to produce a more accurate value. This procedure produces a sufficiently accurate value for T and hence, for the frequency f.

The calculated value of δC can be ambiguous because cos $(2\pi + 2\pi\delta C)$ = cos $(2\pi - 2\pi\delta C)$, thus it would be possible to have two different values of δC for sampling time T_c and another two for sampling time T_c'. From these four values of δC and $\delta C'$, four combinations of $\delta C' - \delta C$, as required in equation (14), would be possible. Since $T_c' > T_c$, $\delta C' > \delta C$ and out of the four combinations of $\delta C'$ and δC, it is possible that one or more combinations can be ignored. Otherwise there would be more than one possible value of the integer C. To discover the exact value of C it is necessary to consider another sampling time, close to the other sampling times, and chosen in such a manner that the difference between the maximum and the minimum sampling times is still less than the time period for the vibration being investigated, that is $(T_{max} - T_{min}) > T$. Hence, from these three different sampling times three different groups of results can be obtained and the value of C present in all of these, results in the value of C being sought.

The value of cos $2\pi\delta C$ closest to the average cos $2\pi\delta C$ is selected from amplitude calculations and corresponding to that value of cos $2\pi\delta C$, the appropriate values of u_1, u_2 and u_3 are employed in determining the maximum velocity of vibration.

Data Analysis. The data transmitted from the sample-to-hold unit are analyzed in the "Interdata 716" computer from on-line signals by means of built-in programs. One of these programs is used to digitize the samples at the rate of 5000 per second and to store them in six different blocks. Each of these blocks can hold 1024 samples at one time. The same program also provides information on the total sampling time for 1024 samples and the maximum and minimum analogue voltage in each block. With the aid of a second program and the range of analogue voltages, a second program plots all of the samples from the six blocks (one block at a time) to the same scale on an X-Y plotter. From the previous analysis it can be seen that results are a function of the difference between two sampling times T_c and T_c'. It is obvious therefore, that accurate measurement of these times is of great importance. Unfortunately, the time axis of the graphical plots is only divided into 85 divisions, each equivalent to (1024/85) (1/5000) seconds, and this degree of accuracy is not sufficient for the present analysis unless the average of several samples is taken.

It was discovered that three samples would give sufficient accuracy for this investigation, but to ensure that the bladed disc was rotating at the same speed for all three samples, they should be consecutive. Hence, the time difference between the first and the second samples will at the same as between the second and third, this being the basic assumption upon which the derived sampling technique is founded.

This procedure is repeated for three speeds of rotation and the derived frequency, common to all three settings, is the appropriate vibration frequency of the blade.

From a knowledge of the maximum analogue voltage the amplitude of vibration is determined.

Table 1 Velocity measurements taken at three different sampling rates

Sampling (Hz)	Rate	Velocity (μm/s) u_1	u_2	u_3	T_c (ms)
16.41	a	0.2	8.0	11.2	60.930
	b	11.2	15.4	18.6	
	c	−19.9	−19.4	−11.8	
16.91	a	15.1	17.4	−10.0	59.123
	b	−10.0	−7.7	19.2	
	c	−7.7	19.2	−15.4	
17.39	a	−0.5	−13.2	17.0	57.516
	b	−14.5	4.8	7.7	
	c	16.2	−8.4	−5.4	

Table 2 Derived values of fractional constants

Sampling (Hz)	Rate	Cos $2\pi\delta C$	Average cos $2\pi\delta C$	δC
16.41	a	0.7125	0.8323	0.0935
	b	0.9675		0.9065
	c	0.8170		
16.91	a	−0.7212	−0.6400	0.3605
	b	−0.5974		0.6394
	c	−0.6015		
17.39	a	−0.6250	−0.6587	0.3644
	b	−0.7083		0.6355
	c	−0.6428		

Results

The bladed disk was rotated at approximately 1000 rpm and the target blade was excited at 163 Hz. The rotation speed was chosen because of the frequency shifting limitation of the Bragg cells and the vibration frequency was chosen because it was found to be the first flexural natural frequency of the rectangular blades. The amplitude of vibration of the target blade was controlled by means of the voltage input to the piezo-electric exciter. Crystal input voltages of 50V, 60V, 70V, 80V and 90V were used in order to obtain amplitude information for comparison with the amplitude calibration. However, when describing frequency measurements in this report only 70V excitation is considered.

The basic data from the sample-and-hold unit was plotted with the aid of an X-Y plotter and from these plots the information given in Table 1 was taken, with the aid of a suitable calibration.

The requirement that T_c should be significantly greater than T, is upheld if the above values for T_c (approximately 60 ms) are compared with T for a vibration frequency of 163 Hz, namely 6.135 ms.

Derived results are given below in Table 2. cos $2\pi\delta C$ from equation (13) leading to two values of δC since cos $(2\pi\delta C)$ = cos $(-2\pi\delta C)$.

By taking combinations of the above sampling rates, we arrive at values for $\delta C'$ and then from equation (14) we can obtain C.

From the various values of C and δC a number of calculated values for the vibration frequency can be obtained.

Table 3 Derived values of integer constants

Sampling Rate Combination	T_c' (ms)	T_c (ms)	$\delta C'$	δC	C	Nearest Integer Value of C
16.41 Hz and 16.91 Hz	60.930	59.123	0.9065	0.3605	17.504	18
				0.6394	8.612	9
16.91 Hz and 17.39 Hz	59.123	57.516	0.6394	0.3644	9.478	9
				0.6355	−0.495	0
16.41 Hz and 17.39 Hz	60.930	57.516	0.9065	0.3644	8.768	9
				0.6355	3.930	4

Table 4 Possible vibration frequencies

Sampling Rate Combination	Calculated Vibration Frequency (Hz).
16.41 Hz & 16.91 Hz	319.79
	158.32
16.91 Hz & 17.39 Hz	162.81
	0.00
16.41 Hz & 17.39 Hz	162.81
	80.59

Downloaded 01 Jun 2010 to 171.66.16.58. Redistribution subject to ASME license or copyright; see http://www.asme.org/terms/Terms_Use.cfm

Table 5 Comparison between calculated and measured amplitudes

Piezo-Electric Oscillator Voltage	Circular Frequency ω (Rad/s)	Velocities u_1	u_2 (μm/s)	u_3	sin α	Calculated Amplitude (μm)	Measured Amplitude (μm)
50	1024.9	−12.7	19.3	−19.2	0.5630	43.64	45.00
60	1022.9	−20.5	−23.9	−25.0	0.3067	54.27	55.00
70	1022.9	16.2	−5.4	15.4	0.7660	63.43	65.00
80	1023.8	21.1	−22.5	−9.0	0.9631	75.99	80.00
90	915.7	−13.8	21.2	−18.2	0.6560	97.58	100.00

Since there is only one vibration frequency which appears twice in the above table, it is obvious that the ambiguity introduced in sampling has been removed and that the measured vibration frequency of the rotating blade is 162.81 Hz.

From equation (10) the amplitude of vibration of the rotating blade is calculated. The values of u_1, u_2, and u_3, and sin α selected for these calculations are those nearest to the average values in each set. These calculated amplitudes are compared with amplitudes measured with the aid of a Wayne-Kerr capacitance bridge at specific piezo-electric exciter voltages. Obviously, these calibrating amplitudes could not be measured on the rotating rig, but instead were taken from a stationary vibrating blade.

Conclusions

The technique of transmitting laser light through a fiber-optic to and from a vibrating surface, which was shown to be feasible in [2], in order that laser-Doppler signals can be obtained, has been employed successfully in this investigation as a noncontact method for obtaining vibratory information from a rotating system.

The measured vibration frequency (162.81 Hz) compares very favorably with the imposed exciting frequency (163 Hz), while the measured amplitudes, given in Table 5, vary by an average of only 3 percent from the static amplitude calibration. Naturally, a static amplitude calibration cannot include the effects of rotation, such as centrifugal stiffening, but at 1000 rpm these effects should not be large.

The Twyman-Green mode of operation of the laser-Doppler system has again been shown to have serious shortcomings for this type of work, and the new mode of operation proposed in [2], has been successfully utilized in this investigation in conjunction with Bragg cells for frequently shifting.

Unfortunately, the use of a single set of Bragg cells to compensate for the average velocity of a rotating system, limits the allowable speed of rotation to about 1000 rpm. Some alternative frequency shifting device will obviously be required for rotating machines with a more realistic speed of rotation.

Although there is no doubt of the effectiveness of this system, there is obviously room for improvement in the analysis of the data obtained. The data analysis procedure described in this report is effective, but time consuming, and an attempt is currently being made to write programs for the Interdata 716, necessary to make the measurement of amplitude and frequency an automatic process.

The novel use of polarization has improved the signal-to-noise ratio of the proposed mode of operation considerably, but further improvements, such as the use of a more powerful laser, are currently being tried.

References

1 Davis, Q. V., and Kulczyk, W. K., "Vibration of Turbine Blades Measured by Means of a Laser," *Nature*, Vol. 222, No. 5192, May 1969, pp. 475–476.

2 Cookson, R. A., and Bandyopadhyay, P., "Mechanical Vibration Measurements using a Fiber-Optic Laser-Doppler Probe," *Optics and Laser Technology*, February 1978, pp. 33–36.

3 Drain, L. E., and Moss, B. C., "The Frequency Shifting of Laser Light by Electro-Optic Techniques," *Opto-Electronics*, Vol. 4, 1972, pp. 429–439.

4 Oldengarm, J., Van Krieken, A. H., and Raternik, H. J., "Laser-Doppler Velocimeter with Optical Frequency Shifting," *Optics and Laser Technology*, Dec. 1973, pp. 249–252.

5 Massey, G. A., "Photomixing with Diffusely Reflected Light," *Applied Optics*, Vol. 4, No. 7, July 1965, pp. 781–784.

6 Buchhave, P., "Laser-Doppler Vibration Measurements using a Variable Frequency Shift," DISA Information 18, Sept. 1975, pp. 15–20.

7 Kulczyk, W. K., "Application of a Laser-Doppler Technique to the Measurement of Vibration of Moving Objects," Ph.D. Thesis, University of Surrey 1971.

Downloaded 01 Jun 2010 to 171.66.16.58. Redistribution subject to ASME license or copyright; see http://www.asme.org/terms/Terms_Use.cfm

A. S. Kesten
Manager,
Energy Research

J. J. Sangiovanni
Senior Research Scientist

United Technologies Research Center,
East Hartford, Conn. 06108

P. Goldberg
Assistant Manager,
Component Engineering/Combustion and Emissions,
Pratt & Whitney Aircraft Group,
Commercial Products Division,
East Hartford, Conn.

Conceptual Examination of Gas Phase Particulate Formation in Gas Turbine Combustors

Recent laboratory studies of droplet combustion indicate the potential for substantial gas phase particulate formation even with single component hydrocarbon fuels. Formation of large particles has been observed in the neighborhood of burning droplet arrays, particularly when the droplets are closely spaced. To provide insight into the potential for particulate formation during the combustion of fuel droplet sprays in gas turbine combustors, a mathematical framework is developed for examining the formation of soot nuclei in droplet combustion. A simplified model of the chemistry of fuel pyrolysis and nuclei formation is used and a series of calculations is made to explore the sensitivity of soot nuclei formation to conditions typical of gas turbine combustion systems.

Introduction

Turbine section erosion resulting from combustor emitted carbon particles has been a recurring problem with gas turbine engines. Large particles emitted from the combustor impact hot turbine section surfaces, remove protective coatings and/or base material and lead to accelerated turbine distress (cf. [1]). Current trends toward the use of fuel with degraded properties, wider distillation ranges and higher carbon to hydrogen ratios, and toward higher operating temperatures in engines can be expected to aggravate this problem in the future.

Analytical studies and experimental measurements indicate that the eroding particles are larger than 50 μm. Smaller particles would, in general, follow the gas path through the turbine without impacting the bounding surfaces of the flow. The larger particles are believed to result principally from carbon that periodically detaches itself from combustor liner walls having been formed as a result of fuel impingement [2]. However, recent laboratory studies indicate the possibility that gas phase reactions may also contribute to large carbon particle formation. Formation of large particles has been observed in the neighborhood of burning droplet arrays, particularly when the droplets are closely spaced.

Some insight into the gas phase soot formation process has been provided using a free droplet combustion experiment in which single or parallel streams of droplets are injected into the post-combustion zone of a flat flame burner. Controlling fuel droplet spacing in monodispersed streams traveling on a precise trajectory in a uniform and stable combustion environment has provided a mechanism for studying effects of droplet interaction on particulate formation. High-speed photomicrographs of the flame structure surrounding burning droplet streams indicate a substantial decrease in burning rate with small droplet spacing and an accompanying increase in gas phase soot formation.

The purpose of this paper is to explore the use of the current state of technology relating to soot formation in diffusion flames to provide insight into gas phase particulate formation during the combustion of fuel droplet sprays typical of gas turbine combustors. To that end the paper will:

1 review the evidence for gas phase particulate formation in droplet diffusion flames,

2 develop a mathematical framework for examining the formation of soot nuclei during the combustion of a single fuel droplet using a simplified model of the chemistry of fuel pyrolysis and nuclei formation, and

3 extend the single droplet model to gain some insight into soot formation during the combustion of droplet arrays under typical gas turbine operating conditions.

Review of Droplet Combustion Results

Changes in flame structure as a result of droplet interaction which causes local oxygen depletion have been shown to have a significant effect on gas phase particulate formation. This effect has been observed in an experimental system developed for investigation of the ignition and combustion characteristics of monodispersed droplet streams of small fuel droplets (100 μm to 300 μm dia) moving on a predictable trajectory in a uniform, stable, and long-path combustion environment. A detailed description of the droplet combustion experiment can be found in [3] and [4]. A schematic of the experimental system is provided in Fig. 1. The hot gas environment for droplet combustion is provided by the post-combustion zone of lean, premixed, laminar, gaseous hydrocarbon/air flames stabilized on a flat flame burner. To generate droplets, a jet of liquid fuel is forced from a capillary orifice at constant pressure while the capillary is vibrated mechanically along the jet axis by an electromagnetic transducer. The periodic disturbance of the jet surface causes it to break up into a continuous monodispersed stream of uniformly sized and spaced droplets with one droplet being produced for each vibration cycle. The number of droplet streams and the spacing between droplets entering the combustion region are regulated by an electrostatic charging and deflection mechanism which periodically selects droplets from the main stream and spreads the selected droplets into parallel streams. The entire droplet combustion experiment is attached to a vertical traversing mechanism to permit flame structure photographs and temperature measurements of the droplet streams throughout the combustion history.

Contributed by the Gas Turbine Division of THE AMERICAN SOCIETY OF MECHANICAL ENGINEERS and presented at The 1979 Israel Joint Gas Turbine Congress, Haifa, Israel, July 9–11, 1979. Manuscript received at ASME Headquarters April 24, 1979. Paper No. 79-GT/Isr-12.

Copyright © 1980 by ASME

Downloaded 01 Jun 2010 to 171.66.16.58. Redistribution subject to ASME license or copyright; see http://www.asme.org/terms/Terms_Use.cfm

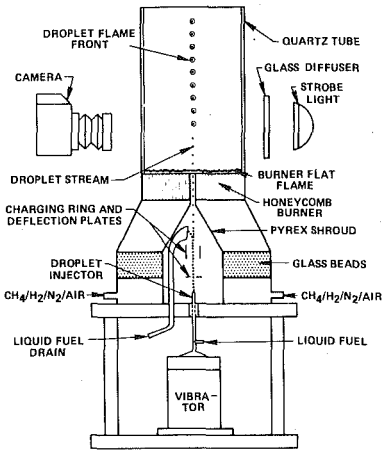


Fig. 1 Schematic of droplet combustion experiment

All of the experimental measurements for this investigation were performed with 200 μm (nominal initial diameter) furfuryl alcohol droplets burning in a high temperature, slightly vitiated air stream so as to simulate the conditions of a practical spray combustion flame for a typical fuel oil. The effect of droplet interaction on flame structure was assessed by varying the droplet spacing from approximately five droplet diameters to nearly one hundred diameters. The potential importance of combustor operating parameters on flame structure was evaluated for variations of ambient temperature (1200 K $\leq T_\infty \leq$ 1450 K), ambient oxygen content ($0.07 \leq (\omega_{02})_\infty \leq 0.155$), and droplet/gas relative velocity (-75 cm/s $\leq V_d - V \leq 50$ cm/s).

Techniques employed for temperature measurements and photographic recording of droplet stream and flame front history throughout the combustion region are described in [5]. Measurements of droplet flame temperature profiles were made by an optical reversal technique known as the Kurlbaum method in which naturally occurring soot particles serve as the reversing medium. Measured line-of-sight reversal temperature profiles along the streamwise axis are shown in Fig. 2 for two successive times during the initial droplet combustion period. These profiles show the same general characteristics about droplet flame structure as the high-speed photographs, which are included as inserts in the figures. Initially the flame structure and temperature profile are symmetric with respect to the droplet as displayed in Fig. 2(a). With increasing burning time, self-induced buoyancy causes the flame around each droplet to move upward forming a wake flame in front of the droplet, as shown in Fig. 2(b). The flame shape and peak temperature do not change significantly after reaching the profile shown in Fig. 2(b) (30 ms after ignition), except for a continual increase in flame length until the flames of adjacent droplets merge, accompanied by a slight shift in the peak temperature away from the droplet.

Effects of droplet spacing on flame structure are illustrated in the sequence of photographs shown in Fig. 3 for the region immediately following droplet ignition. When droplets are closely spaced, individual droplet flames cease to exist and network flames envelop complete chains or groups of droplets shortly after ignition. The apparent effect of local oxygen depletion in the region of closely spaced

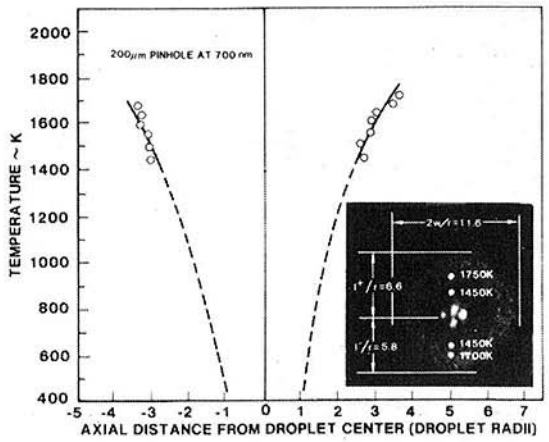


Fig. 2(a) Envelope flame — 13 ms after ignition

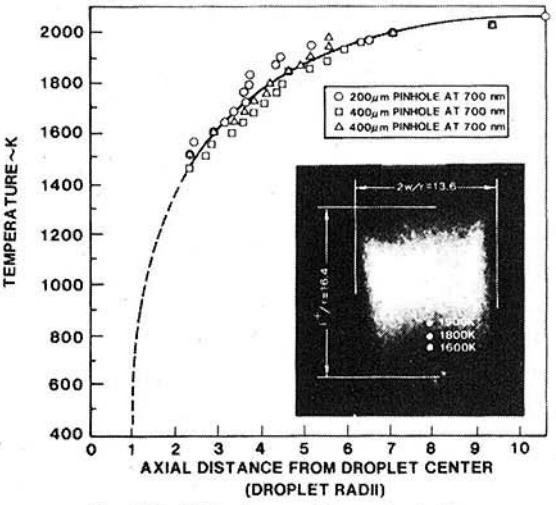


Fig. 2(b) Wake flame — 30 ms after ignition

Fig. 2 Measured temperature profiles along streamwise axis of free droplet flames: ambient air temperature = 1396 K, initial droplet diameter = 245 μm, air velocity = 150 cm/s, initial droplet velocity = 150 cm/s

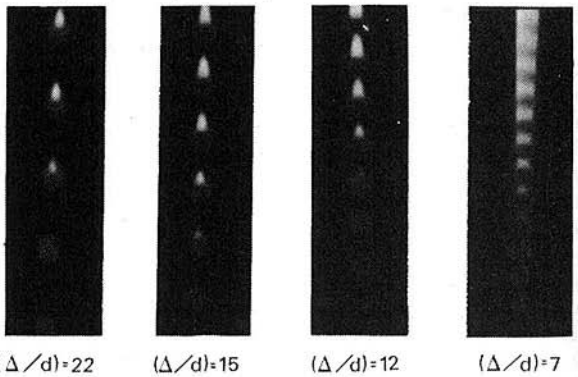


Fig. 3 Effect of droplet spacing on flame structure development

Nomenclature

a = radius of spherical droplet
a_0 = initial droplet radius
b = radial position of the flame front
D_{AB} = diffusion coefficient of soot nuclei in gas mixture
f = linear branching coefficient
g = linear termination coefficient
g_0 = coefficient of linear termination on soot particles
G = Green's function
I = integral of Green's function
L = boundary layer thickness
N = concentration of soot particles
P = pressure
r = radial distance from center of spherical droplet (or droplet radius in Fig. 2)
r_0 = spontaneous origination rate of radical nuclei
r_A = net rate of formation of soot nuclei by chemical reaction
t = time
T = temperature
v = radial convective velocity
w = weight-fraction
x = normalized radial distance ($=r/a$)
β = equals $(\rho_L a/\rho D_{AB})\, da/dt$
ρ = mass density (refers to gas phase unless subscripted)

Subscripts

A = soot nuclei
F = fuel
L = liquid

Downloaded 01 Jun 2010 to 171.66.16.58. Redistribution subject to ASME license or copyright; see http://www.asme.org/terms/Terms_Use.cfm

droplets is to cause the flame zone to move away from the individual droplets. The size of the flames or reaction zone increases to encompass many droplets within a stationary self-supporting envelope flame. For droplet spacings (Δ/d) of approximately ten droplet diameters or less the highly luminous portion of the reaction zone indicates the presence of substantial concentrations of carbon species.

Direct visual evidence of soot nuclei within the combustion region of monodispersed droplet streams is contained in photographs made with diffuse backlighting from a 3μs stroboscopic flash. A typical photograph of a closely spaced droplet stream with relatively large soot particles in the combustion region is shown in Fig. 4. Although alcohols are considered to be clean burning fuels, incipient soot formation has been observed for both butyl alcohol and furfuryl alcohol when the droplet spacing is less than approximately ten droplet diameters. However, a small increase in the droplet spacing was found to decrease the concentration of visible soot particles significantly. Decreasing the ambient oxygen content to less than approximately nine percent also has the effect of eliminating most of the visible soot particles, but the decreased soot formation at reduced levels of ambient oxygen content can be attributed to a substantial lowering of the temperature within the fuel rich combustion region near the droplets; estimates of flame temperature for the experimental conditions encountered indicate an approximate reduction of the maximum flame temperature from 2500 K for an ambient oxygen weight fraction of 0.15 to 1850 K for a weight fraction of 0.05. Lowering flame temperature leads to lower rates of fuel pyrolysis which limits soot formation. This effect is tempered somewhat by the corollary effect of reducing the rate of burnout of any soot formed.

At the location of droplet burnout, coincident with the time for complete droplet vaporization, a small explosive emission of visible light has been observed at the frequency of the monodispersed droplet stream. This unusual phenomenon, shown in a photograph in Fig. 5, was found to be characteristic of a variety of alcohols (ethanol, butanol, heptanol, and furfuryl alcohol) and ambient conditions with droplet spacings ranging from a few droplet diameters to hundreds of diameters. In fact, explosive burnout was observed under all experimental conditions considered. Although this phenomenon is similar in appearance to the explosive burnout of cenospheres reported by Hottel, et al. [6] during the combustion of high molecular weight multicomponent fuels such as residual oils, the formation of carbonaceous residues by liquid phase cracking reactions within the droplets would not be expected with pure fuels having moderate boiling temperatures (of the order of 500 K or less).

In this system, with pure liquid fuels, explosive droplet burnout is believed to be caused by suspension of carbon within the droplets as a result of collisions between fuel droplets and carbon particles within the gas phase combustion region. This mechanism by which carbon particles can become engulfed by fuel droplets is identical to the "scrubbing" process used to remove particulates from a gas stream. Indirect evidence has been produced to suggest that during the combustion process, carbon content within each droplet increases steadily by this scrubbing process until most of the liquid has evaporated and a trace of liquid remains absorbed in the carbon residue which is then heated rapidly. The liquid fuel which is absorbed in the residue boils violently, causing the residue to explode into many smaller particles. As these smaller carbon particles move radially outward, they mix with oxygen which was transported inward behind the collapsing flame surface, and the particles probably ignite and burn. In any case, the temperature of the particles at this time is at least equal to the ambient temperature which is sufficiently high to make the small carbon particles luminous.

Mathematical Framework

Formation of particulates in combustion systems is a complex process involving fuel pyrolysis, polymerization reactions, nucleation, particle growth, and burnout. Representing these processes by using a simplified chemical model is often fraught with the potential for misstating some essential feature of the sooting process. This is particularly true in a diffusion flame where soot radical nuclei born in the vicinity of a flame front can either polymerize, oxidize almost instantly as they diffuse to the oxidizer side of the front or participate in critical branching reactions on the fuel side of the flame front. The potential utility of a simplified chemical model in gaining

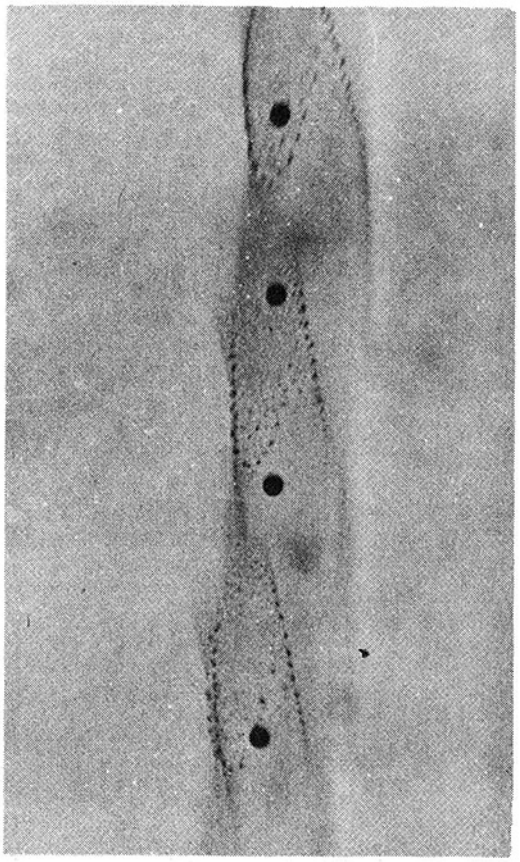


Fig. 4 Gas phase soot formation during droplet combustion

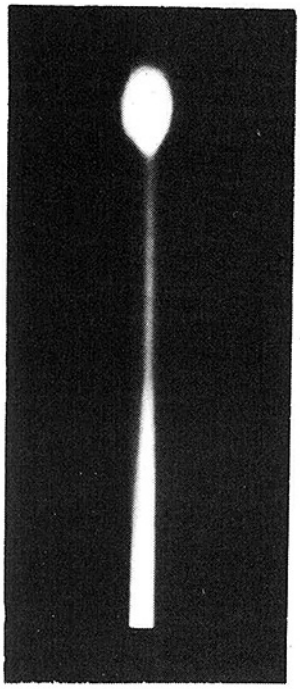


Fig. 5 Explosive burnout of carbon filled fuel droplets

Downloaded 01 Jun 2010 to 171.66.16.58. Redistribution subject to ASME license or copyright; see http://www.asme.org/terms/Terms_Use.cfm

phenomonological insight into the formation of particulates during the combustion of droplets is undeniable. A simple model suggested by Tesner [7] has been shown to represent reasonably well the formation of radical nuclei which represent the building blocks for soot particle formation. By concentrating on the formation, diffusion, and oxidation of these radical nuclei in the diffusion flame around burning fuel droplets, the potential for sooting of different systems can be compared on a qualitative basis at least. This is a reasonable expectation even without evaluating the subsequent growth, transport and burnout of soot particles. The formation of radical nuclei is represented by Tesner as

$$r_A = r_0 + (f - g)w_A\rho - g_0 N w_A \tag{1}$$

in which r_0 = spontaneous origination rate of radical nuclei; f = linear branching coefficient; g = linear termination coefficient; g_o = coefficient of linear termination on soot particles; and N = concentration of soot particles.

The initial stage of the formation process is not complicated by the destruction of active nuclei on the surface of soot particles (i.e., $N \sim 0$). For purposes of comparing the sooting potential of different droplet combustion systems, it is adequate to neglect later stages during the droplet lifetime which involve the actual soot growth process.

The system under consideration is the region outside of a spherical fuel droplet which is entrained in air moving at some velocity relative to the droplet. A boundary layer formed around the burning droplet is taken to be spherically symmetric. The model considers the entire combustion reaction to take place at a flame surface with the rates of transport of fuel and oxidizer to the flame surface occurring in stoichiometric proportions. Reaction of fuel and oxidizer is assumed to occur instantly upon arrival of the reactants at the flame surface. Soot radical nuclei produced by chemical reaction in the high temperature, fuel-rich region outside the burning droplet diffuse radially toward and away from the droplet surface. Any radicals which diffuse radially outward to the flame surface are assumed to oxidize instantly.

Droplet vaporization leads to the convective transport of mass radially outward from the droplet surface. If spatial variations in the product of density and diffusion coefficient, ρD_{AB}, are neglected, the equation describing the formation and dispersion of soot nuclei under transient conditions is

$$\frac{1}{r^2}\frac{\partial}{\partial r}\left(r^2\frac{\partial w_A}{\partial r}\right) - \frac{1}{D_{AB}}\frac{\partial w_A}{\partial t} = \frac{v}{D_{AB}}\frac{\partial w_A}{\partial r} - \frac{r_A}{\rho D_{AB}} \tag{2}$$

where w_A is the weight-fraction of soot nuclei and radial position r is measured from the center of the fuel droplet. The rate of production of soot nuclei by chemical reaction, r_A, is taken as the net rate of formation by reaction (1). The convective velocity, v, due to droplet vaporization may be computed from

$$\rho v r^2 = (\rho_{r=a} - \rho_L)\frac{da}{dt}a^2 \tag{3}$$

Since liquid densities are generally far greater than vapor densities, the velocity can be approximated by

$$v \sim -\frac{\rho_L}{\rho}\frac{a^2}{r^2}\frac{da}{dt} \tag{4}$$

Boundary conditions for equation (2) are

$$w_A(r, t) \to 0 \text{ as } r \to b$$

and

$$\left[-\rho D_{AB}\frac{\partial w_A}{\partial r} + \rho v w_A\right]_{r=a} = 0 \tag{5}$$

The initial condition for the weight fraction for soot nuclei $w_A(r, 0)$, is taken as an arbitrary function of position. Letting $x = r/a(t)$, equation (2) can be written in a normalized coordinate system as

$$\frac{1}{x^2}\frac{\partial}{\partial x}\left(x^2\frac{\partial w_A}{\partial x}\right) - \frac{a^2}{D_{AB}}\frac{\partial w_A}{\partial t} = \frac{a v_x}{D_{AB}}\frac{\partial w_A}{\partial x} - a^2\frac{r_A}{\rho D_{AB}} \tag{6}$$

where the velocity in the x, t system, v, is given by $v = x\,da/dt$ or, using equation (4)

$$v_x = -\frac{da}{dt}\left(\frac{\rho_L}{\rho x^2} + x\right) \tag{7}$$

The boundary condition at the droplet surface is represented by

$$\left[-\frac{\rho D_{AB}}{a}\frac{\partial w_A}{\partial x} + \rho v_x w_A\right]_{x=1} = 0 \tag{8}$$

or

$$\frac{\partial w_A}{\partial x}(1, t) + \beta w_A(1, t) = 0 \quad \beta = \frac{\rho_L a}{\rho D_{AB}}\frac{da}{dt} \tag{9}$$

In addition,

$$w_A(x, t) \to 0 \text{ as } x \to b/a \tag{10}$$

With a knowledge of the reaction kinetics the system is completely defined. Equation (6) must be solved subject to boundary conditions (9) and (10), together with an expression for the net rate of formation of soot nuclei, to determine the soot nuclei weight-fraction distribution as a function of time. Using Green's function techniques [8] this nonhomogeneous diffusion equation can be converted to an implicit integral equation which is far more amenable to numerical solution. Very similar techniques have been employed to analyze NO formation in single droplet combustion [9] and the details are not repeated here. For small intervals of time the weight-fraction of soot radical nuclei can be represented by the implicit integral equation

$$\begin{aligned} w_A(x, t) = \frac{a^2}{4\pi\rho D_{AB}}\Bigg\{\int_1^{b/a}\Bigg[x_0^2 r_A(x_0, 0)I(x, t, x_0) \\ - \frac{w_A(x_0, 0)}{a}\frac{da}{dt}\frac{\partial}{\partial x_0}\left\{(\rho_L + \rho x_0^3)I(x, t, x_0)\right\}\Bigg]dx_0 \\ - \frac{\rho_L}{a}\frac{da}{dt}w_A(1, 0)I(x, t, 1) \\ + \int_1^{b/a}\rho(x_0)x_0^2 w_A(x_0, 0)G(x, t/x_0, 0)dx_0\Bigg\} \end{aligned} \tag{11}$$

where

$$I(x, t, x_0) = \int_0^t G(x, t/x_0, t_0)dt_0 \tag{12}$$

$$G(x, t|x_0, t_0) = \frac{8\pi D_{AB}}{x x_0 a^2}\sum_{n=1}^{\infty} e^{-(D_{AB}/a^2)\alpha_n^2(t-t_0)}R_n(x)R_n(x_0) \tag{13}$$

$$R_n(x) = \frac{(1-\beta)\sin(x-1)\alpha_n + \alpha_n\cos(x-1)\alpha_n}{\left[\left(\frac{b-a}{a}\right)\left(\alpha_n^2 + [1-\beta]^2\right) + (1-\beta)\right]^{1/2}} \tag{14}$$

and the α_n's are defined by

$$(1-\beta)\sin\left(\frac{b-a}{a}\right)\alpha + \alpha\cos\left(\frac{b-a}{a}\right)\alpha = 0 \tag{15}$$

Equation (11) involves only spatial integrals since the time integral in equation (12) can be evaluated independently. These equations can be used to solve for the soot nuclei weight-fraction profiles outside a fuel droplet as functions of time by taking the transient as a series of successive short time intervals. Weight-fractions computed at each value of time become the initial conditions for the computations pertinent to the subsequent time.

From equation (1), the soot nuclei formation rate can be expressed as

$$r_A = \alpha w_F \rho e^{-E/RT} + (f - g)w_A\rho \tag{16}$$

Tesner has found for fuels like toluene that typical values of α, E and $f - g$ are 10^{13} s^{-1}, 140 kcal and 100 s^{-1}, respectively [10].

Calculated Results

To illustrate the transient processes involved in soot nuclei production during droplet combustion, a model of the combustion pro-

Downloaded 01 Jun 2010 to 171.66.16.58. Redistribution subject to ASME license or copyright; see http://www.asme.org/terms/Terms_Use.cfm

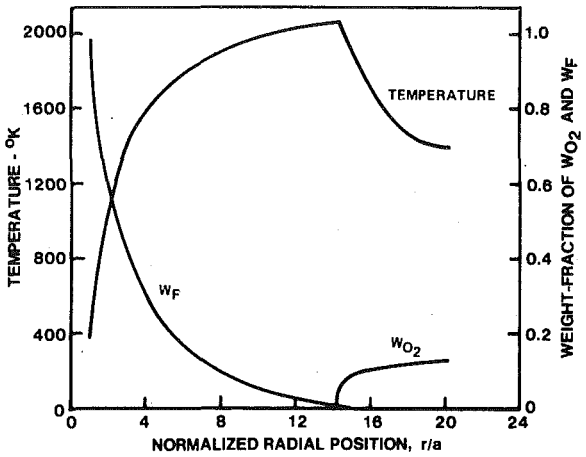


Fig. 6 Toluene droplet combustion temperature and weight fraction profiles: ambient air temperature = 1400 K, pressure = 1 atm

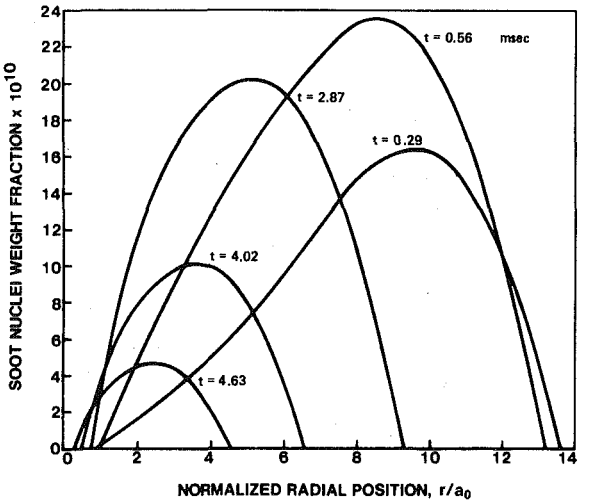


Fig. 7 Toluene droplet combustion variation of soot nuclei weight fraction profiles with time: ambient air temperature = 1400 K, pressure = 1 atm, 40 μm droplet

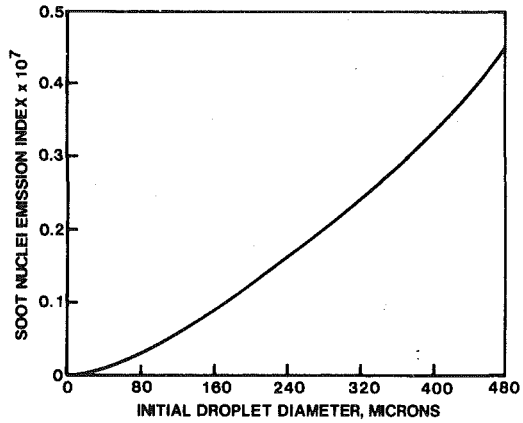


Fig. 8 Toluene droplet combustion effect of droplet size on emission index: flame temperature = 2070 K, pressure = 1 atm

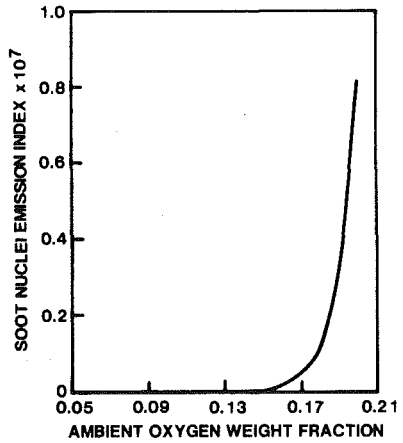


Fig. 9 Toluene droplet combustion effect of ambient oxygen weight fraction on emission index: pressure = 1 atm, 300 μm droplet

cess, described in [11], has been used. The model examines the nonsteady, spherically-symmetric heating, ignition, and combustion of a single component fuel droplet moving relative to an oxidizing ambient. Gas phase heat and mass transfer by either diffusion or convection are regarded as quasi-steady processes and transient conduction is assumed to be the only transport mechanism within the droplet. The nonsteady nature of droplet temperature, flame temperature, burning rate, and flame position as affected by the mode of gas phase heat and mass transfer are examined using a flame surface approximation.

Calculations have been made using a computer program representing the integral equation methods to solve for the extent of soot nuclei formation in toluene droplet combustion. The calculations pertain first to a system at atmospheric pressure with the droplet temperature at a value close to the boiling point. A constant temperature was chosen for simplicity in making calculations of soot nuclei formation; the specific temperature used was chosen by running the full transient droplet combustion case using methods described in [11] and finding the constant value which best represents the flame structure over the droplet lifetime. The temperature and fuel weight-fraction profiles for a toluene droplet burning in a flowing air stream with 25 cm/s velocity relative to the droplet are illustrated in Fig. 6.

The soot nuclei weight fraction profiles are plotted at various times during the combustion of a 40 μm droplet in Fig. 7. At given values of time, the weight-fractions of radical nuclei are plotted as a function of radial position normalized to the initial droplet radius. The effects of diffusion and radial convection of soot nuclei are evident. Soot nuclei are formed from pyrolysis just inside the flame front; radicals diffusing toward the drop can participate in branching reactions while those transported outward by diffusion and radial convection are reacted at the flame front. Since the flame front recedes with time, the formation region diminishes in size. The total mass of soot nuclei formed can be computed by integrating the flux of soot nuclei at the droplet flame front over the droplet lifetime. The mass formed per unit mass of fuel burned is the droplet emission index.

Relevance to Gas Turbine Combustors

The relevance of single droplet models to practical combustion systems is not obvious. When droplets burn in arrays, droplet interaction has a substantial effect on the combustion process. Group combustion is typified by much larger diffusion flames than the envelope flames around single droplets. In fact, as noted in the review of experimental results, these interaction effects play an important role in the soot formation process.

Labowsky and Rosner [12] note that the combustion of groups of closely spaced droplets is analogous in terms of flame structure to the combustion of one large droplet. It may well be revealing then to look at the effect of droplet size on the soot nuclei "emission index" to gain some insight into the effect of the scale of diffusion flame on soot formation. For toluene droplets burning at a given flame temperature, this effect is illustrated in Fig. 8. The large apparent influence on the potential for soot production of size (really of droplet lifetime) results from the rather slow process of fuel pyrolysis even for a pure aromatic fuel. While droplet lifetimes scale approximately with the square of droplet size, the boundary layer thickness divided by the droplet radius decreases with increasing size. The resulting emission index, for a fixed flame temperature, scales approximately with the droplet size

Downloaded 01 Jun 2010 to 171.66.16.58. Redistribution subject to ASME license or copyright; see http://www.asme.org/terms/Terms_Use.cfm

to the 3/2 power. However the effect of flame temperature is very strong. For a fixed ambient air temperature, droplet flame temperature decreases with droplet size. Calculations of emission index for that condition would show a marked decrease with increasing drop size.

Clearly flame temperature has an important effect because of the high activation energy for fuel pyrolysis. Strategies to control flame temperature are often key to controlling particulate formation, like staged combustion with heat extraction between stages. Of course many factors affect flame temperature: the nature of the fuel, oxygen content in the surrounding atmosphere, ambient temperature, and pressure. The effect of ambient oxygen weight-fraction on the droplet emission index is illustrated in Fig. 9.

Increasing pressure can result in raising or lowering of the emission index depending largely on the effect of pressure on the relative velocity between fuel droplets and air. For a fixed relative velocity, raising pressure lowers the boundary layer thickness which results in flame positions closer to the droplet as well as lower flame temperatures. This results in a dramatic decrease in soot nuclei formation with increasing pressure, notwithstanding the increased fuel concentration in the flame zone. If, instead of fixing a relative velocity between fuel droplets and air, the "blowing" rate (i.e., the product of density and relative velocity) were fixed, pressure would have little effect on flame position or temperature. Under these circumstances increasing pressure would result in higher emission indices because of the higher fuel concentrations and the associated rates of fuel pyrolysis.

The effect of the nature of the fuel on the potential for gas phase soot formation is well documented (cf. [13] and [14]). Certainly the aromatic content of gas turbine fuels, for example, is instrumental in the sooting process. As fuel specifications are broadened, it may well be that alternative strategies for control of gas phase particulate formation may be critical. Tailoring of fuel and air injection profiles, staged combustion, different methods of flame stabilization, and catalytic combustion may all warrant increased attention. From the more fundamental side, studies of soot formation in the combustion of droplet streams, together with complementary studies of chemical kinetics in gaseous diffusion flames, may provide useful phenomonological insight to suggest novel control strategies.

Acknowledgments

A special debt of gratitude is owed to Ms. C. J. Hewett for developing the computer program representing the mathematical model.

References

1 Russell, R. J. and Witton, J. J., "An Investigation of Turbine Erosion by Combustor Generated Carbon in a Lightweight Marine Gas Turbine," ASME Paper No. 78-GT-96, presented at the Gas Turbine Conference and Products Show, London, England, Apr. 9–13, 1978.

2 Tomlinson, J. G. and Montgomery, L. N., "Elimination of Turbine Erosion in the T56 Turboprop Engine," presented at the Winter Annual Meeting, Chicago, IL, Nov. 7–11, 1965.

3 Sangiovanni, J. J. and Kesten, A. S., "A Theoretical and Experimental Investigation of the Ignition of Fuel Droplets," *Combustion Science and Technology,* Vol. 16, 1977, pp. 59–70.

4 Sangiovanni, J. J. and Kesten, A. S., "Effects of Droplet Interaction on Ignition in Monodispersed Droplet Streams," *Proceedings of the Sixteenth Symposium (International) on Combustion,* The Combustion Institute, 1977, pp. 577–591.

5 Sangiovanni, J. J. and Dodge, L. G., "Observations of Flame Structure in the Combustion of Monodispersed Droplet Streams," presented at the Seventeenth Symposium (International) on Combustion, The Combustion Institute, 1978.

6 Hottel, H. G., Williams, G. C. and Simpson, H. C., "Combustion of Droplets of Heavy Liquid Fuels," *Proceedings of the Fifth Symposium (International) on Combustion,* The Combustion Institute, 1955, pp. 101–129.

7 Tesner, P. A., Snegiriova, T. D. and Knorre, V. G., "Kinetics of Dispersed Carbon Formation," *Combustion and Flame,* Vol. 17, 1971, pp. 253–260.

8 Morse, P. M. and Feshbach, H., *Methods of Theoretical Physics, Part I,* McGraw-Hill, New York, 1953.

9 Kesten, A. S., "Analysis of NO Formation in Single Droplet Combustion," *Combustion Science and Technology.* Vol. 6, 1972, p. 115.

10 Tesner, P. A., Tsygankova, E. I., Guilazetdinov, L. P., Zuyev, V. P., and Loshakova, G. V., "The Formation of Soot from Aromatic Hydrocarbons in Diffusion Flames of Hydrocarbon-Hydrogen Mixtures," *Combustion and Flame,* Vol. 17, 1971, p. 279.

11 Sangiovanni, J. J., "A Model for the Nonsteady Ignition and Combustion of a Fuel Droplet, Evaporation-Combustion of Fuels," *Advances in Chemistry Series,* Vol. 166, 1978.

12 Labowsky, M. and Rosner, D. E., "Conditions for "Group" Combustion of Droplets in Fuel Clouds, I. Ouasi-Steady Predictions," *Proceedings of the Symposium on Evaporation/Combustion in Fuel Droplets,* American Chemical Society, 1976.

13 Palmer, H. B. and Cullis, C. F., *Chemistry and Physics of Carbon,* Vol. 1, Chapter 5, Dekker, New York, 1965.

14 Glassman, I., *Combustion,* Academic Press, New York, 1977.

Downloaded 01 Jun 2010 to 171.66.16.58. Redistribution subject to ASME license or copyright; see http://www.asme.org/terms/Terms_Use.cfm

C. Bosman

Lecturer,
Mechanical Engineering,
University of Manchester Institute of Science and Technology,
Manchester, England

An Analysis of Three-Dimensional Flow in a Centrifugal Compressor Impeller

This paper presents detailed results of the three-dimensional kinematic flow detail in a centrifugal compressor impeller of common form with inducer and straight radial blade tip sections. The calculation method, which is inviscid and is reported elsewhere, shows the development of a passage vortex in a sense counter to that of blade rotation, initiated in the inducer and disappearing as the flow becomes radial. This vortex unloads the blade shroud sections and combined with slip at the blade tips, produces a jetwake velocity distribution at the blade passage exit. General features of the calculation are at variance with two-dimensional calculations but are in agreement with the experimental results of other workers.

Introduction

A great deal more experimental and theoretical work has been carried out on investigating and developing improved flow in axial flow turbomachine blade rows than in their centrifugal counterparts. Centrifugal impellers and radial inflow turbines present difficult problems of both design and analysis because of the relatively more complex flow which occurs in them. More recently advanced measuring techniques have been applied to centrifugal impellers to reveal an increasing wealth of flow detail and more is becoming available. Contributions in this field have been made by Howard and Lennemann [1] on the effects of secondary flow, McDonald, et al. [2] studying the impeller discharge flow, Howard and Kittmer [3] using shrouded and unshrouded impellers, Mizuki, et al. [4], Fujie [5] using a long radial bladed impeller and more recently Eckardt [6, 7] studying a typical high speed impeller with radial discharge. Fradin [8] has studied impellers with long radial blades and Senoo [9] has contributed a dye injection study of impeller flow with a qualitative explanation of the motions observed. Benson, et al. [10] has made photographic studies of flow through a perspex rotor using water and polystyrene spheres in suspension.

Attempts to calculate flow through centrifugal impellers have been made principally by applying streamsurface calculation techniques of the fixed grid or streamline curvature type applied to hub-shroud streamsurfaces (i.e., S2 streamsurfaces of Wu [11]) or blade-to-blade streamsurfaces (i.e., S1 streamsurfaces [11]). These techniques have been developed by Katsanis [12], Marsh [13], Bosman [14] and others for application to general S2 streamsurfaces and by Katsanis [13], Smith and Forst [14], Hill [15] and others for application to S1 streamsurfaces of revolution. Sturge [16] has attempted to include the effects of suction surface separation on the S1 calculation.

Attempts to include the variation of S1 streamsheet thickness and the departure of the S1 mean streamsurface from the shape of the blade have been made in quasi-three-dimensional methods of Katsanis [17] and Bosman and El-Shaarawi [18]. These calculation improvements offer advantages to flows which do not include a strong passage vortex but in radial turbomachinery which impose large deflections in the meridional plane they prove to be quite inadequate although they have been used consistently in design procedures. Bosman and Highton [19] have shown the total inadequacy of even the quasi three-dimensional techniques in application to a radial inflow turbine. Attempts to calculate the three dimensional flow in ducted flows with particular reference to turbomachinery have been developed by Denton [20] and Highton [21], reported in Bosman and Highton [22]. The work presented here applies the last mentioned method to a centrifugal impeller to determine the details of the three-dimensional flow therein and explains the physical mechanisms which are responsible for the unloading of the impeller shroud blade sections and as inviscid jet-wake efflux pattern.

The Calculation Method

The basic calculation method may be found in [19, 22] with fine detail in [21]. In principle the method employs time marching applied to a three-dimensional grid of control surfaces formed by the computation grid, each cell of which is accurately solved for momentum, continuity and energy as follows:

The time dependent equation of motion is written

$$\frac{\partial}{\partial t}\int_\nu \rho \overline{W}\, d\nu = -\oint_s p\, d\bar{s} - \oint_{s_{\text{upwind}}} \overline{W}(\rho \overline{W}\cdot d\bar{s}) - \int_\nu \rho(2\bar{\omega}x\overline{W} + \bar{\omega}x(\bar{\omega}x\bar{R}))d\nu = (rhs)_1 \quad (1)$$

Since only the steady state is of interest the lhs is approximated

$$\frac{\partial}{\partial t}\int_\nu \rho\overline{W}d\nu = \frac{\partial \overline{W}}{\partial t}\int_n \rho d\nu = \frac{\partial \overline{W}}{\partial t} M \quad (2)$$

where

$$M \equiv \int_\nu \rho d\nu \quad (3)$$

and is the mass contained by the cell.

Contributed by the Gas Turbine Division of THE AMERICAN SOCIETY OF MECHANICAL ENGINEERS and presented at The 1979 Israel Joint Gas Turbine Congress, Haifa, Israel, July 9–11, 1979. Manuscript received at ASME Headquarters April 24, 1979. Paper No. 79-GT/Isr-13.

Copyright © 1980 by ASME

Downloaded 01 Jun 2010 to 171.66.16.58. Redistribution subject to ASME license or copyright; see http://www.asme.org/terms/Terms_Use.cfm

In this approximation the temporal derivative of density is neglected so that the time evolution for compressible flow is not exact even in the limit as the time tends to zero however this does not affect the steady state solution being sought. The equation actually solved for the new time level velocity W_2 is thus

$$2W = 1\ W + \frac{\Delta t}{M}(\text{rhs})_1 \tag{4}$$

The equation of continuity is written

$$\frac{\partial}{\partial t}\int_v \rho dv = -\oint_{s_{\text{upwind}}} \rho(\overline{W}\cdot d\bar{s}) = (\text{rhs})_2 \tag{5}$$

where:

$$\frac{\partial}{\partial t}\int_v \rho dv = \frac{\partial \rho}{\partial t} v \tag{6}$$

so that the equation solved for the new time level density ${}_2\rho$ is

$${}_2\rho = {}_1\rho + \frac{\Delta t}{v}(\text{rhs})_2 \tag{7}$$

This density correction is used to make a corresponding pressure correction on the basis of an isothermal process thus

$${}_2p = {}_1p = ({}_2\rho - {}_1\rho)RT \tag{8}$$

This pressure correction is used immediately to modify the surrounding velocity field using the equation of motion again but since only the pressure term in (1) has changed then:

$${}_3W = {}_2W + \frac{\Delta t}{M}(\text{rhs})_4 \tag{9}$$

where

$$(\text{rhs})_4 = -\oint_s ({}_2p - {}_1p)d\bar{s} \tag{10}$$

The equation of energy conservation is written

$$\frac{\partial}{\partial t}\int_v (\rho u)dv = -\int_v (p\ \text{div}\ \overline{W})dv - \oint_{s_{\text{upwind}}} u(\rho\overline{W}\cdot d\bar{s}) = (\text{rhs})_5 \tag{11}$$

and

$$\frac{\partial}{\partial t}(\rho u)dv = \frac{{}_2(\rho u) - {}_1(\rho u)}{\Delta t} v \tag{12}$$

so that the internal energy u is updated by

$${}_2u = \frac{1}{{}_2\rho}\left\{{}_1(\rho u) + \frac{\Delta t}{v}(\text{rhs})_5\right\} \tag{13}$$

which is used to update temperature and pressure from the equations of state thus

$${}_2T = \frac{{}_2u}{C_v} \tag{14}$$

$${}_3p = {}_3\rho\, R_2T \tag{15}$$

The sequence of calculation for the solution presented was to sweep through the grid cell by cell successively with:

(i) equation (4) thereby updating the velocity field.
(ii) equation (7) thereby updating the density field;
(iii) equation (8) thereby updating the pressure field;
(iv) equation (9) thereby updating the velocity field again.
(v) equations (13) and (14) thereby updating the temperature field;
(vi) equation (15) thereby updating the pressure field again.

Test whether the steady-state criterion

$$\left|\left(\frac{\text{net mass efflux from computational cell}}{\text{gross mass efflux from computation cell}}\right)\right| < \begin{pmatrix}\text{Set convergence}\\ \text{criterion}\end{pmatrix}$$

is satisfied by all computation cells. If this is unsatisfied then return to (i) above or else print out results.

It will be observed that in a single sequence the pressure and velocity field are updated twice and the temperature field once.

As with two-dimensional blade-to-blade calculations, piece-wise periodicity is applied at the blade leading and trailing edges and before and after the blade surfaces. The flow leaving the blade trailing edges is constrained to be tangent to the mean blade camber surface at this station, consequently there is no imposed value of slip, deviation angle or downstream whirl. The natural unloading of the blade at the trailing edge determines this flow feature. The relative velocity distribution and static temperature are imposed at the upstream boundary while the static pressure is imposed at the downstream boundary. The calculation commences by assuming the relative velocity to be zero everywhere except at the upstream boundary and the pressure and temperature distribution to be uniform. The calculation proceeds forward in time steps of one microsecond (in this instance) until the steady state is reached which takes several milliseconds of real time and approximately an hour of computing time to reduce the maximum percentage relative velocity change to 10^{-3} percent (a very fine criterion). Coarser levels of convergence are obtainable in minutes of computing time. The program which is for viscous flow has been used for this application in its inviscid free slip mode which currently takes approximately 0.7 ms per grid point per time step on the CDC 7600 computer. Extended use of the program has shown convergence to be insensitive to grid geometry if a sufficiently small time step is used.

Compressor Configuration

Bosman and Highton [19] report a three-dimensional flow calculation through a small radial inflow turbine, the geometrical details of which may be found in [23]. The blade surfaces of this turbine may be synthesised entirely from radial generator lines which is a geometrical property in common use for blade construction in both radial turbines and centrifugal compressor impellers. Because the geometrical data was already on computer file store for the turbine configuration, it was convenient to use this same basic data applied to the compressor configuration by simply reversing the flow and the direction of rotation.

Nomenclature

$d\bar{s}$ = elemental surface vector of computation cell
m = meridional co-ordinate
p = static pressure
r = radial co-ordinate
t = time
u = internal energy
z = axial co-ordinate
C_v = specific heat at constant volume
M = mass
R = location vector
T = static temperature
U = blade speed
$\overline{W}$ = relative velocity
θ = tangential angular co-ordinate
v = volume
ρ = density
ω = angular velocity of reference frame (i.e., blades)
$b.l.$ = boundary layer
$\oint_s$ = closed surface integral
$\int_v$ = volume integral
$\times$ = vector product
$\cdot$ = scalar product
$\partial/\partial t$ = time derivative at fixed position in reference frame
Δ = finite increment

Subscripts

1,2,3 = (prefixed) successive time levels, distinguishing post-fix
r,θ,z = co-ordinates, direction components
upwind = value of the convected variable (e.g., $\overline{W},\rho,u$) in the integral has been taken from the donor cell position for convection through any face of the computation cell

Downloaded 01 Jun 2010 to 171.66.16.58. Redistribution subject to ASME license or copyright; see http://www.asme.org/terms/Terms_Use.cfm

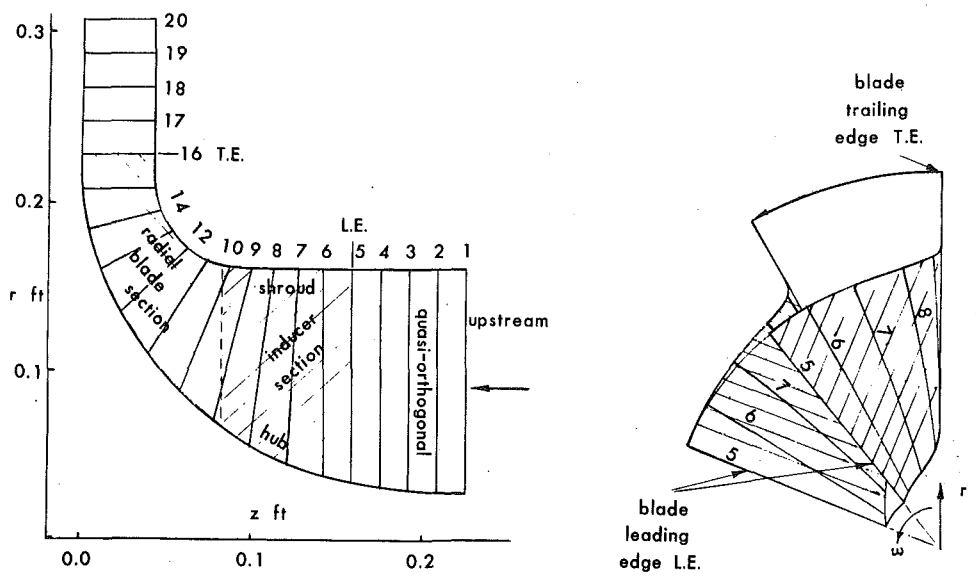


Fig. 1 Compressor configuration and computation grid

The basic layout, including the position and indexing of the quasi-orthogonals (q-o's) used to construct the three-dimensional grid and the blade surface shape seen in end view, are shown in Fig. 1. The impeller has twelve blades having a hub to shroud thickness ratio of 3.6 with sharp leading and trailing edges. The inducer leading edge is at q-o No. 5 and terminates at q-o Nos. 11 and 9 on the shroud and the hub, respectively, after which the blade is radial to the trailing edge at q-o No. 16. The computation grid consists of 20 grid points along the flow, seven points across the flow from hub to shroud and seven points across the flow from blade-to-blade.

The calculations were carried out for a rotational speed of 3500 rad/s giving a T.E. tip speed of 798 ft/s with uniform axial velocity at the inlet of 330 ft/s, this being estimated to give approximately zero incidence on the blade. In fact, slight negative incidence was experienced at the inducer eye tip. The inlet pressure (resulting from the imposed downstream pressure) and imposed inlet temperature were 19 lbf/in^2 and 340 K, giving a pitch mean value of relative Mach number at the inducer eye tip of 0.55 with a local maximum of 0.70 which was also a maximum for the whole flow.

Because the inlet conditions approximate closely to uniformity (remember that the inlet pressure is not imposed) and the flow is inviscid, it will also be approximately irrotational in the absolute sense.

Discussion of Flow Detail

The features of special interest in this investigation were the nature and mechanism of the inviscid three-dimensional effects within a centrifugal compressor impeller blade passage and the flow detail at the passage exit. Bosman and Highton [19] demonstrated wide differences in the meridional velocity distribution at exducer exit, between the three-dimensional and quasi-three-dimensional (i.e., basically, synthesised two-dimensional calculations using hub-to-shroud and blade-to-blade techniques [18]) calculations, where the three-dimensional calculations showed basic agreement with the experimental results.

Passage Vortex Development. In Fig. 2 various streamlines have been constructed from the velocity vectors on the hub, shroud and blade surfaces. These streamline patterns best illustrate the three-dimensionality of the flow, where migration to and from the passage corners shows the departure of the three-dimensional from the two-dimensional flow patterns obtained from conventional streamsurface calculation techniques, the latter necessarily constraining particles to motion along the corners.

Fig. 2(a) shows streamlines on the hub surface where the inducer section terminates at station 9. As from this section all the flow is affected by migration across the passage from blade pressure to blade suction face until station 14 where the effects of slip, consequent upon the unloading of the blade at the trailing edge station 16, initiate the reverse migration across the passage from blade suction to pressure face. The flow migration between stations 9 and 14 acts as to increase the angular momentum of the hub flow and the load on the hub blade sections in a manner consistent with a forward swept blade having the shape of the streamlines.

Fig. 2(b) depicts the streamlines on the shroud surface where the inducer terminates at station 11. Flow at and subsequent to this station experiences migration from the blade suction to blade pressure face, where at station 14 the effects of slip initiate an increase in this migration. This migratory flow is in the reverse direction of that on the hub and acts to unload these shroud blade sections so that they do little or no work.

Fig. 2(c) illustrates the streamlines on the blade suction face where the flow migration downstream from station 10 is from hub to shroud except in the region near the blade trailing edge where the migration reverses quite locally.

In Fig. 2(d) the streamlines on the blade pressure face can be seen with strong migration from shroud to hub over the whole blade face. The more intense migration on the pressure face in the final part of the meridional deflection is due to the migration caused by the centrifuging of the fluid towards the hub surface being reinforced by the passage vortex migration while on the suction face there is some cancellation of these effects. After station 15 when meridional deflection ceases together with the passage vortex, only the centrifugal action remains and the flow as a whole migrates towards the hub. This can be clearly seen in Fig. 3 at the trailing edge station. The departure of streamlines from blade corners merely illustrates the presence of the passage vortex and must not be interpreted as a separation.

It will be observed from these figures that in the radial part of the blade passage after the inducer and until the effects of slip occur at station 14 due to blade unloading at the trailing edge, the relative flow migration on each of the four passage walls is such as to contribute circulation opposite in sense to that produced by blade rotation thereby producing approximately zero absolute circulation as required by the approximate irrotationality of the flow. There exists in this portion of the passage a relative vortex which fills the passage and acts in a sense such that its circulation cancels the circulation due to the blade rotation. Of course the blade rotation only contributes an axial component of circulation so that contours at station 15 and thereafter which have no axial projection, possess no relative circulation. The velocity vectors at the trailing edge station 16 lying in the plane of the trailing edge contour, are shown at Fig. 3, where the lack of circulation is evident. Figs. 2 and 3 together illustrate the growth and decay of an inviscid passage relative vortex as the flow is deflected in the me-

Downloaded 01 Jun 2010 to 171.66.16.58. Redistribution subject to ASME license or copyright; see http://www.asme.org/terms/Terms_Use.cfm

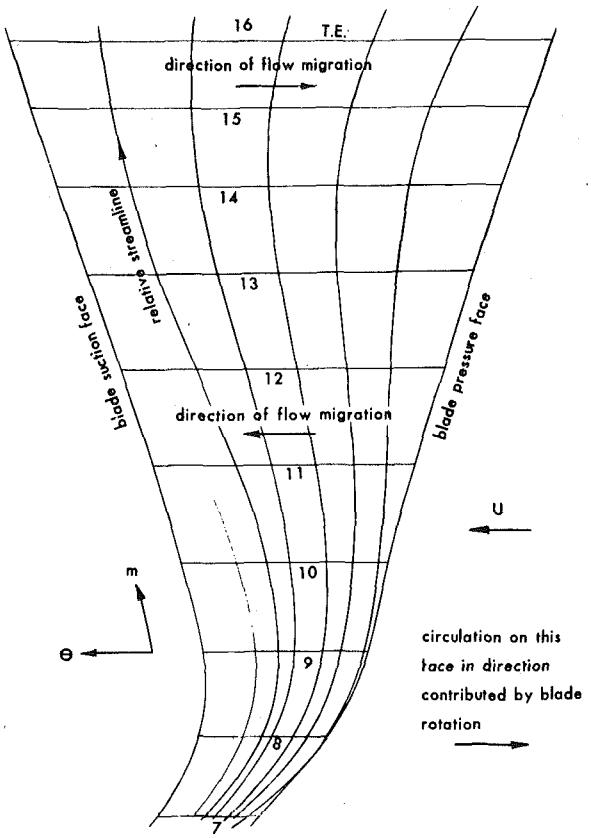


Fig. 2(*a*) Relative flow on the hub surface

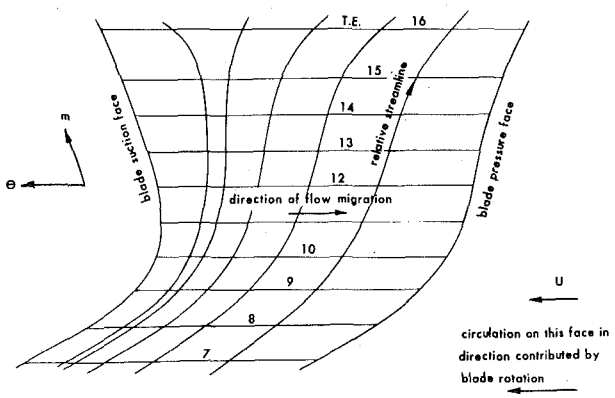


Fig. 2(*b*) Relative flow on the shroud face

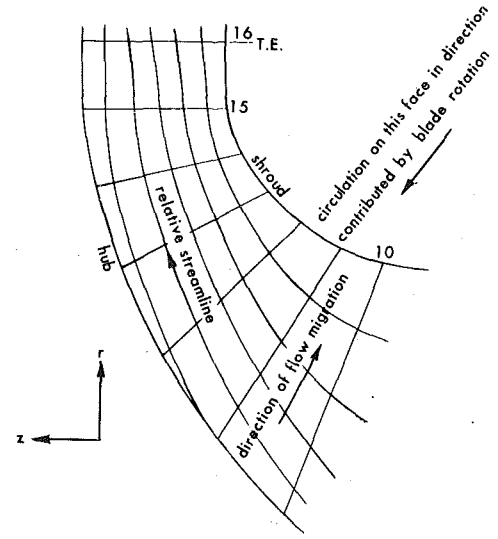


Fig. 2(*c*) Relative flow on the blade suction face

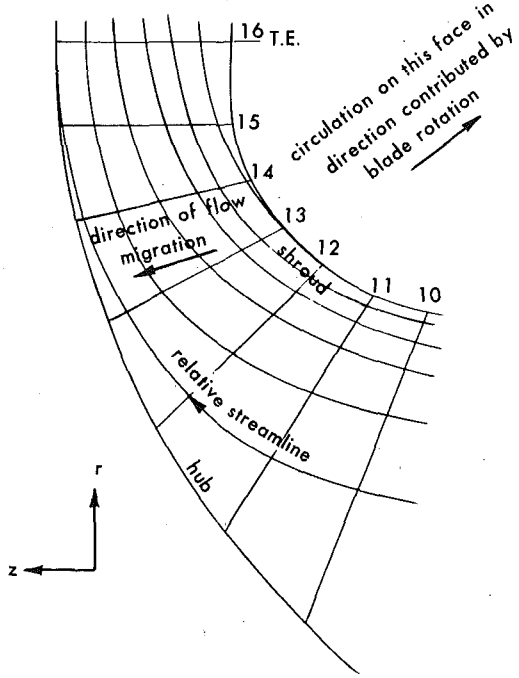


Fig. 2(*d*) Relative flow on the blade pressure face

ridional plane from the axial to the radial direction. The sense of the vortex circulation is counter to the direction of rotation, commencing somewhere in the inducer and terminating when the flow section becomes radial. The effect of the vortex is to increase the load on the blade hub sections and decrease it on the blade shroud sections (in this case to the extent of unloading the latter sections completely). These loadings are evident in Fig. 4. where the velocity distributions along the passage corners are plotted, the shroud sections show no effective loading after station 11 where the inducer terminates.

Passage Efflux. At the blade trailing edge station the negative values of W_θ for the bulk of the flow seen in Fig. 3, represents the slip and integrate to an area mean value of 0.87 which compares with a Stanitz [24] value of 0.835 for the slip factor. This slip has been produced by imposing on the calculation, periodicity of pressure and velocity along the blade trailing edges together with the imposition that the relative velocity vectors at the trailing edge lie tangent to the blade mean camber surface at this station.

Fig. 3 shows that the migration velocity components from shroud to hub at the trailing edge station having a maximum value at mid-blade height. This velocity or streakline plot is however deceptive and does not indicate the spatial rate of approach of particles towards the hub since the meridional velocity is not apparent in this view. Reference to Figs. 2(*c*) and 2(*d*) which show the streamlines on the blade surfaces, clearly demonstrate that at the trailing edge station 16 there is a strong migration in the vicinity of the shroud which experiences low meridional velocities, the migration in the vicinity of the hub being very small on account of the high meridional velocities in that neighborhood. This meridional velocity distribution is of course itself consequence of the shroud to hub flow migration as continuity considerations would suggest.

The mean slip velocity component at the trailing edge is the same at the hub as at the shroud to satisfy irrotationality, as will be seen in Fig. 3 but as above, because the meridional velocities are not apparent in this view, the effect of the slip on the blade-to-blade flow directions is not apparent. Again, because of the high meridional velocities at the hub and low values at the shroud, the slip has a vastly different influence on the flow pattern on these two walls. The flow paths at hub can be seen in Fig. 2(*a*) to produce only small migratory flow from blade suction to pressure face at mid-pitch, thereby increasing the pressure face velocities and reducing the suction face

Downloaded 01 Jun 2010 to 171.66.16.58. Redistribution subject to ASME license or copyright; see http://www.asme.org/terms/Terms_Use.cfm

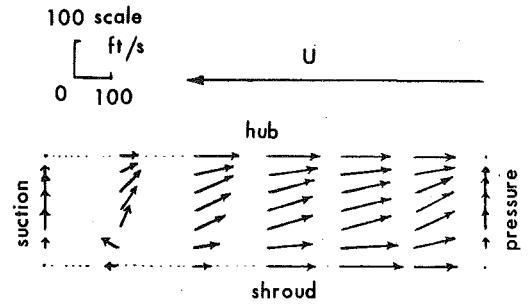


Fig. 3 Velocity vectors in the plane of the trailing edge

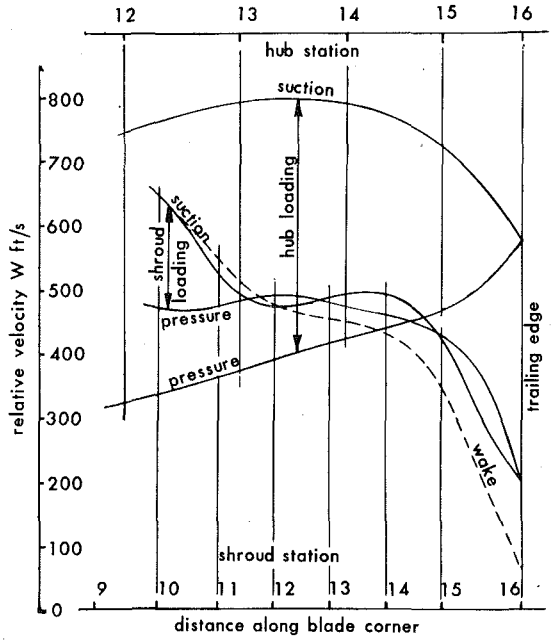


Fig. 4 Hub and shroud loadings and diffusion distributions

velocities so that they equalise at the trailing edge. At the shroud, the blade suction to pressure face migration seen in Fig. 2(*b*) is very large at mid-pitch on account of the low meridional velocity prevailing at this wall. The effect of this is to queeze the bulk of the flow towards the blade pressure face while creating a massive diffusion of the flow in the vicinity of the blade suction face. It must be recalled that the shroud blade sections have been unloaded by the presence of the passage vortex, see Fig. 4, so that the velocities on these blade surfaces are already equalised, consequently the shroud flow migration does not affect the blade surface values but distributes itself to produce greatly increased velocities towards the blade pressure face, peaking at approximately a quarter pitch from this face (see Fig. 5(*c*)). A reversal of this effect occurs towards the blade suction face where a massive diffusion created by the combined migration of the flow away from this shroud-suction corner, both towards the hub and towards the blade pressure face. This produces the low velocity trough in Fig. 5(*c*), having a minimum located at about a quarter of the blade pitch from the suction surface. Figs. 5(*a*) and 5(*b*) illustrate the developing velocity distribution across the passage at stations 14 and 15 respectively, as the trailing edge station (Fig. 5(*c*)) is approached. The almost unloaded shroud blade sections are clearly visible in these views.

The familiar jet-wake velocity distribution made by many observers in the past is in clear evidence in Fig. 5(*c*) which shows a velocity trough in the shroud-suction corner having a minimum particle speed of approximately 50 ft/s while further over towards the blade pressure face on the shroud wall a maximum particle speed of about 350 ft/s is registered. The hub wall velocity distribution if fairly uniform at a level of 600 ft/s. It must be emphasised that this flow is entirely inviscid and originates from an upstream source which is almost uniform so that the whole flow is close to being irrotational in the absolute sense. Both the computed results and the physical mechanism adduced for them, show that the jet-wake efflux from radial centrifugal impellers is possible in the absence of viscous boundary layer effects or the inviscid convection of upstream vorticity. In the inviscid flow the wake region is produced by the action of slip occurring at the passage exit and acting on a shroud flow which has been unloaded by the generation of a passage relative vortex which is caused by the meridional flow deflection. This wake is exacerbated if the trailing edge is located just after the meridional deflection as this induces further diffusion at the shroud.

Viscous Effects. If one considers the above inviscid flow as a core surrounded by viscous boundary layer (*b.l.*) then the *b.l.* growth and migration patterns may be deduced from the inviscid surface velocity and pressure distributions in the usual way.

Examination of Fig. 4 shows that flow approaching the wake experiences a high and prolonged surface diffusion so that the wake intensity and extent are likely to be increased by viscous *b.l.* action. However, the whole of the shroud experiences diffusion of only modestly less degree than the wake itself and one must assume high shroud losses to exist at the impeller tip.

Because the shroud has been unloaded by the passage vortex there is virtually no blade-to-blade pressure gradient so that the shroud *b.l.* is likely to be colateral with the main flow. This is to say that there will be little migration of the *b.l.* relative to the core flow. Note that this is contrary to the conclusions which would be drawn from a two-dimensional inviscid blade-to-blade analysis of the shroud which would show substantial blade loading and would suggest a *b.l.* migration from blade pressure to suction face, relative to the core flow, which would itself have this migratory direction relative to the three-dimensional flow on this wall because of the absence of the passage vortex.

Comparison with Experimental Observations

This particular rotor has not been run experimentally as a compressor impeller, only as a radial inflow turbine. The objective was to calculate and explain the flow behavior in radial impellers of this general type with particular attention to flow after the inducer and at the blade exit. The general features of this calculated and deduced flow may then be correlated with the wide variety of experimental observations made by others cited in the introduction.

This impeller is similar in form to that of Eckhardt [6, 7]. The passage efflux velocity pattern is similar in form to that measured by Eckhardt and shows a strong jet-wake feature which in the calculated results has an inviscid cause. When the radial section of the blades is long and occurs after the meridional deflection the wake effect should be much less pronounced as observed by Fradin [8] and Fujie [5]. Similarly in the absence of an inducer the passage vortex disappears so that no jet-wake pattern would be anticipated as in Kittmer's observations [3], though here his blades were curved but this would not affect the arguments except to alter the slip factor. The impellers studied by Mizuki, et al. [4] generally show a low level of blade shroud section loading with a developing velocity trough in the suction-shroud corner.

Generally the pitch mean meridional velocity at design point operation, at the blade tip, increases from shroud to hub as observed by Eckardt [6, 7], Mizuki, et al. [4] and Fradin [8]. This is in contrast to two-dimensional calculation methods which produce a velocity profile of the opposite slope.

Fradin [8] shows the blade loading distributions for a relatively long bladed impeller with splitter vanes and a gentle rate of meridional deflection. His results show that in the mid-flow design range there is a reversal of loading within the inducer with zero loading at the inducer exit as found in the present study. It should be noted that two-dimensional and quasi-three-dimensional calculations never produce this result.

Conclusions

1 A fully three-dimensional, inviscid calculation is shown to converge successfully for flow through a centrifugal impeller of common geometrical form.

Downloaded 01 Jun 2010 to 171.66.16.58. Redistribution subject to ASME license or copyright; see http://www.asme.org/terms/Terms_Use.cfm

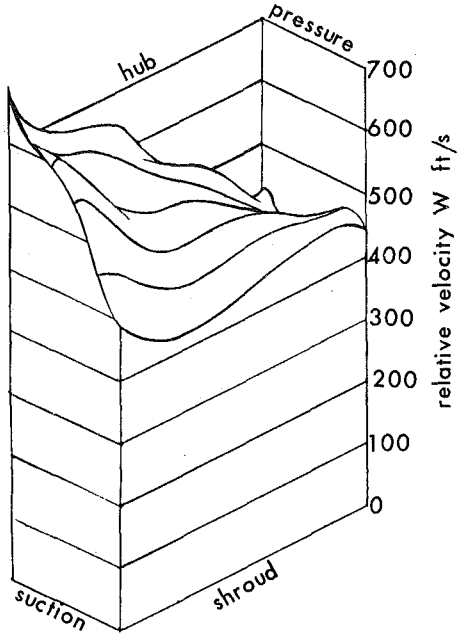


Fig. 5(*a*) Relative velocity distribution at station 14

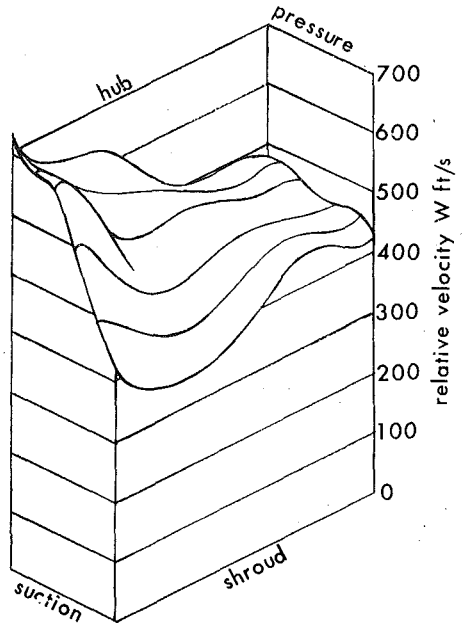


Fig. 5(*b*) Relative velocity distribution at station 15

2 The computed results differ from those of two-dimensional calculations in quite basic flow features.

3 The shroud blade sections prove to be unloaded after the inducer section and during the meridional deflection, due to the development of an inviscid vortex. This result is confirmed by Fradin's [8] observations and cannot be predicted by two-dimensional calculations.

4 The inviscid flow produces the experimentally familiar jet-wake efflux pattern which is caused by the combination of the passage vortex and slip at the blade tips and is exacerbated by a local flow migration towards the hub wall.

5 The slope of the meridional velocity profile at blade tip is the reverse of that predicted by two-dimensional methods and is in agreement with many experimental results. A similar feature was found in application to this rotor when used as a radial turbine [19].

6 Higher velocity-diffusion is found on the shroud wall than would be predicted by two-dimensional calculations, this implies high shroud losses particularly in the shroud-suction corner where diffusion is greatest. This is in general agreement with experimental observations.

7 Because of the virtually unloaded shroud blade sections, the usual assumption of viscous boundary layer migration to the blade suction face will not occur.

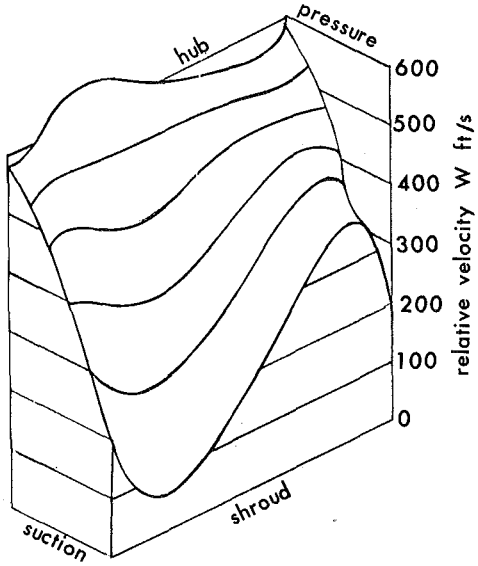


Fig. 5(*c*) Relative velocity distribution at station 16

References

1 Howard, J. H. G., and Lennemann, E., "Measured and Predicted Secondary Flows in Centrifugal Impellers," TRANS ASME, Vol. 93, No. 1, 1971, pp. 126–132.

2 McDonald, G. B., Lennemann, E. and Howard, J. H. G., "Measured and Predicted Flow Near the Exit of a Radial Flow Impeller," TRANS ASME, Vol. 93, No. 4, 1971, pp. 441–446.

3 Howard, J. H. G. and Kittmer, C. W., "Measured Passage Velocities in a Radial Impeller with Shrouded and Unshrouded Configurations," ASME Paper No. 74-GT-66 1974.

4 Mizuki, S., Ariga, I. and Watanabe, I., "Investigations concerning the Blade Loading of Centrifugal Impellers," ASME Paper No. 74-GT-143, 1974.

5 Fujie, K. "Three-dimensional Investigation of Flow in Centrifugal Impellers with Straight Radial Blades," *Bulletin of JSME,* Vol. 1. No. 1, pp. 42–49.

6 Eckardt, D. "Instantaneous Measurements in the Jet-Wake Discharge Flow of a Centrifugal Compressor Impeller," TRANS ASME, Vol. 97, No. 3, 1975, pp. 337–346.

7 Eckardt, D. "Detailed Flow Investigation within a High Speed Centrifugal Compressor Impeller," ASME Paper No. 76-FE-13. 1976.

8 Fradin, C. "Analysis of the Flow Field in a Radial Compressor," ASME Paper No. 78-GT-7, 1978.

9 Senoo, Y. "Shear Flow, Vortices and Secondary Flow," *Memoirs of the Faculty of Engineering,* Kyushi Univ., Vol. 30, No. 3, 1971, pp. 69–86.

10 Benson, R. S., Cartwright, W. and Jackson, D. C. "Flow Studies in a Log Spiral Radial Bladed Impeller", Institution of Mechanical Engineers, Th.Fl.Conf., Paper 15, Glasgow 1970.

11 Wu, C., "A General Theory of Three Dimensional Flow in Subsonic and Supersonic Turbomachines of Axial-Radial-, and Mixed Flow Types," NACA TN2604, 1952.

12 Katsanis, T. "Use of Arbitrary Quasi-Orthogonals for Calculating the Flow Distribution in the Meridional Plane of a Turbomachine," NASA TND 2546, 1964.

13 Katsanis, T. "Use of Arbitrary Quasi-Orthogonals for Calculating Flow Distribution on a Blade-to-Blade Surface in a Turbomachine," NASA TND-2909, 1965.

14 Smith, J. D. L., and Frost, D. H. "Calculations of Flow Past Turbomachine Blades," Institution of Mechanical Engineers, Th.Fl.Conv. Paper 27, Glasgow 1970.

15 Hill, M. "Numerical Solutions for Mixed Flow Turbomachines," Ph.D.

Downloaded 01 Jun 2010 to 171.66.16.58. Redistribution subject to ASME license or copyright; see http://www.asme.org/terms/Terms_Use.cfm

Thesis, UMIST, Manchester, England 1974.
16 Sturge, D. P. "Compressible Flow in a Centrifugal Impeller with Separation: A Two-Dimensional Calculation Method," SUED/A-Turbo/TR.82. Dept. of Mech. Eng., Cambridge Univ., England, 1976.
17 Katsanis, T. "Quasi-Three-Dimensional Calculation of Velocities in Turbomachine Blade Rows," ASME Paper No. 72-WA/GT-7. 1972.
18 Bosman, C. and El-Shaarawi, M. A. I., "Quasi-Three-Dimensional Numerical Solution of Flow in Tubomachines," ASME Paper No. 76-FE-23, 1976.
19 Bosman, C. and Highton, J., "A Calculation Procedure for Three-Dimensional, Time-Dependent, Compressible Flow through Turbomachine Blades of any Geometry," Institution of Mechanical Engineers, JMES Feb. 1979.
20 Denton, J. "Extension of the Finite Area Time Marching Method to Three Dimensions," von Karman Institute for Fluid Mechanics, Lecture Series 84, Feb. 2–6, 1976.
21 Highton, J. "The Computation of Three-Dimensional Viscous Flow with Generalised Geometry," Ph.D. Thesis, UMIST, Manchester, England, 1976.
22 Bosman, C. and Highton, J. "The Computation of Three Dimensional Viscous, Compressible Flow," International Conference on Numerical Methods in Laminar and Turbulent Flow. Univ. Coll. of Swansea, Wales, U.K. March 1978.
23 Hiett, G. F. and Johnson, I. H., "Experiments Concerning the Aerodynamic Performance of Inward Flow RadialTurbines," *Proceedings of the Institute of Mechanical Engineers,* Vol. 178, Pt. 31 1964c.
24 Stanitz, J. D. "Some Theoretical Aerodynamic Investigation of Impellers in Radial and Mixed Flow Centrifugal Impellers," TRANS ASME, Vol. 74, 1952, p. 473.

Downloaded 01 Jun 2010 to 171.66.16.58. Redistribution subject to ASME license or copyright; see http://www.asme.org/terms/Terms_Use.cfm

E. Tjonneland
Senior Group Supervisor.

S. F. Birch
Specialist Engineer.

Boeing Military Airplane Development,
Seattle, Wash.

Application of Viscous Analyses to the Design of Jet Exhaust Powered Lift Installations

The application of available numerical methods to the design of powered lift installations is reviewed. For this application, where strong coupling exists between the jet exhaust and the external flow, a three-dimensional viscous analysis tool is needed. The task of selecting a suitable analysis procedure is first outlined, with particular emphasis on the need for careful coordination of the various elements of the task. Problems and progress in the development of turbulence models are then discussed, and some selected three-dimensional calculations are presented to illustrate recent progress. Finally, a numerical procedure, currently under development for a particular powered lift application, is briefly described.

Introduction

VTOL and STOL aircraft currently in development or in design are employing powered lift for enhanced take-off and landing performance, and for improved maneuvering capability in various other flight regimes. The direct coupling of the engine exhaust flow with the wing flow causes significant changes in the circulation around the wing and in the coupling with the airplane flight control system. These aircraft also differ from CTOL aircraft in that their inlets and nozzles are required to operate effectively over a much broader flight envelope.

A number of powered lift aircraft, like the YC-14 [1, 2] or the YC-15 military STOL transport prototypes, and the NASA QSRA [3] aircraft utilized for research in the low speed flight regime of STOL aircraft, have recently been developed. Other military aircraft like the NAVY XFV-12A [4] are in various stages of preliminary design or prototype development.

In spite of the increasing use of numerical methods in aircraft design over the last 10 years, the engine installation designs of current V/STOL aircraft were based on parametric wind tunnel test results. The flight control systems for these aircraft were also designed using test derived aerodynamic force coefficients in the stability and controls simulations [5]. Two major problems necessitated the use of a test based design approach. First, because of limitations in computer speed and storage capacity, the flows characteristic of these installations were too complex for the available numerical methods. The second problem was the lack of suitable turbulence models. These models are used to substitute for information lost when the flow equations are time averaged, which is required since solutions of the full time-dependent Navier-Stokes equations are impractical with computers currently available or in development. Turbulence models, empirical models, for the Reynolds Stresses are important where flow gradients are high, such as in the critical viscous regions of exhaust and wing flow interactions. Although the propulsion installation is unique to each powered lift aircraft design, the flow in the region of the nozzle in all cases is dominated by viscous effects. This means that an accurate simulation of the flow requires a turbulence model which can accurately model the turbulent mixing in the complex three-dimensional flow just downstream of the nozzle, and such models simply did not exist.

Welliver [6] suggested recently that the increasing availability of large computers, the recent and projected development of powerful fluid flow analyses, and the rapidly rising cost of wind tunnel testing make an analysis based design process look increasingly more attractive. An analysis based design process, as envisioned here, is similar to a test based process except that parametric analysis replaces parametric testing. Model and full scale testing are still required for analysis validation and configuration optimization. The amount of wind tunnel testing is, however, greatly reduced and this can result in a large reduction in the development cost to design a given installation. A second advantage of the analysis based design approach is that it leads to a much better understanding of the flow, and this should result in most cases in a better final design. A third advantage of this design approach is that it is not constrained by the available test data base in the configuring of new aircraft.

The use of fluid flow analyses for the detailed design of a propulsion installation requires that the available analysis tools accurately and efficiently predict the flow phenomena characteristic of the device being designed. These flows can range from very simple to very complex. One strategy currently in use to guide the development of these analyses is to make available to the designer a set of computer codes suitable for a range of flows. For a given problem, the designer would select from the available codes the simplest and most efficient codes applicable to his design problem. A second strategy is to identify as early as possible the potential problems which may hinder the development of a particular analysis and to coordinate the research on these problems.

Welliver [6] discusses the importance of this early identification of problem areas and a careful coordination of research in each to efficiently achieve an analysis based design procedure. The five analysis elements which must be coordinated were identified as:

Contributed by the Gas Turbine Division of THE AMERICAN SOCIETY OF MECHANICAL ENGINEERS and presented at The 1979 Israel Joint Gas Turbine Congress, Haifa, Israel, July 9–11, 1979. Manuscript received at ASME Headquarters May 7, 1979. Paper No. 79-GT/Isr-15.

Copyright © 1980 by ASME

Downloaded 01 Jun 2010 to 171.66.16.58. Redistribution subject to ASME license or copyright; see http://www.asme.org/terms/Terms_Use.cfm

- Numerics and computational mesh generation for solution of the flow equations
- Turbulence modeling—Reynolds stress terms to close the time averaged Navier-Stokes equations
- Computing capacity present and future—dictates the extent of the solution details and the need for zonal analyses
- Data handling and display—computer flow quantities must be manipulated and interpreted
- Analysis validation—through comparisons with test data

The selection and development of suitable turbulence models, the selection of a strategy for the numerical analysis and the coordination of the numerics development with the turbulence modeling have proven to be particularly difficult elements of the problem of developing flow analyses useful for design.

This paper discusses briefly the problem of selecting an optimum numerical strategy, the current status and problems with turbulence modeling, and presents progress toward the development of an analysis based design procedure for powered lift installations in the context of one particular installation of current interest.

Numerical Algorithm Requirements

A direct solution of even the time averaged 3-D Navier-Stokes equations is still beyond our present capability for problems of practical interest on commonly available computer systems. One particularly useful strategy which has been used to achieve the desired solutions with available computers is that of zonal modeling. Zonal modeling takes advantage of differences between flow regions to simplify the numerical problem. A second strategy is to minimize the number of mesh points required and the number of arithmetic operations for each mesh point, in order to minimize computer storage and run time requirements.

In implementing the zonal modeling strategy, potential flow or linearized potential flow analysis could be used to predict a subsonic or transonic inviscid flow region. Boundary layer analysis could be used to predict the three-dimensional boundary layers developing over various installation surfaces. The internal nozzle mixing flows and the external jet flows can be predicted with available parabolic or partially parabolic marching procedures.

Fig. 1 illustrates how in practice the zonal modeling strategy is applied to a powered lift installation. The flow about this installation is divided into viscous and inviscid regions. The boundaries of the viscous and inviscid regions overlap and the solutions in each region can be iterated until the properties along a common "matching" surface are consistent. The location of this surface need not change during the iteration process.

In this example, the outer inviscid flow surrounding the jet would be solved with a linearized potential or a full potential solution procedure with the plume "edge" simulated as a surface with specified boundary conditions which are allowed to change in succeeding solutions to achieve convergence. To simplify the definition of this simulated plume in the inviscid analysis, any conveniently shaped surface, whose geometry does not change, but is contained within the larger viscous box, may be specified. The jet, if subsonic, would be solved with a parabolic or partially parabolic marching procedure inside the viscous box whose boundary properties are determined by the outer, but overlapping inviscid solution. These boundary properties are also determined in part by the location and the local entrainment of the jet as specified for the inviscid solution from the previous iteration of the viscous jet calculation. The jet, if supersonic, would be solved with a hyperbolic marching procedure. The subsonic, internal nozzle flow would be solved with a parabolic or partially parabolic marching procedure similar to that used for the jet. Turbulence models would be selected which could predict the turbulent flow phenomena known to be present in the viscous internal mixing and external jet flows.

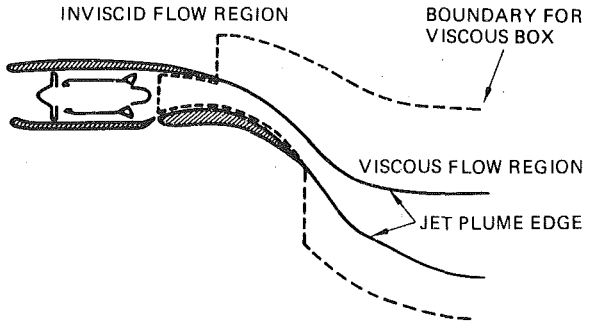


Fig. 1 Coupling of inviscid and viscous algorithms

The use of zonal modeling is facilitated by a common modular program structure for each of the component analyses. With this structure, each component shares common input and output formats, mesh generators, handling of boundary conditions, turbulence models, etc., and hence interface problems between the component analyses are minimized. Also with shared elements, an improvement to one element of one analysis is an improvement to all of the analyses which share this common feature.

To implement the strategy of minimizing computer run time and storage requirements, various tactics are listed below. These tactics can be applied to each analysis used in the zonal modeling approach.

1 *Discontinuity Fitting* [7, 8]. By aligning the computational mesh with steep gradient regions such as shock or shear layers, computational noise and the amount of mesh which is required for desired levels of accuracy can be minimized.

2 *Body Fitted Mesh* [9, 10]. A numerically generated body fitted mesh can be employed to eliminate severely distorted mesh in the computational plane, match constraints of body shape and fitted discontinuities, and for control of the mesh distribution. The elimination of irregular cells facilitates the use of higher order numerics. The ability to concentrate the mesh into steep gradient regions minimizes the number of points necessary to compute a flow to a given level of accuracy.

3 *Filtering Techniques* [11, 12]. The use of second or higher order numerical schemes may lead to numerical noise which, if not controlled, can destroy the solution. A filter must be used to eliminate this noise. One that searches the solution and suppresses noise only when and where it is identified is essential to achieve the potential that higher order schemes offer.

4 *Convergence Rate Acceleration Tactics* [13–15]. Relaxation schemes which are necessary for solving elliptic flow regions are known to have poor solution convergence properties. Multi-grid and solution extrapolation schemes can be used to reduce the number of iterations required to achieve a given level of accuracy by orders-of-magnitude.

Nomenclature

d_0 = height of rectangular nozzle
$\mathcal{D}$ = rate of dissipation of turbulence energy
l = turbulence length scale
L = local length scale
q = turbulence kinetic energy
t = time
U = velocity component in main flow direction
ΔU = velocity difference across shear layer
U_i = velocity component in main flow direction
V_{total} = total velocity
V_{jet} = total velocity at nozzle exit
X = main flow direction
X_i = Cartesian coordinate
$Y_{1/2}$ = jet half width in the Y direction
$Z_{1/2}$ = jet half width in the Z direction
ϵ = turbulent kinematic viscosity
μ_t = turbulent viscosity
ρ = density
σ_q = effective turbulent Prandtl number for q
$\sigma_{\mathcal{D}}$ = effective turbulent Prandtl number for $\mathcal{D}$

Downloaded 01 Jun 2010 to 171.66.16.58. Redistribution subject to ASME license or copyright; see http://www.asme.org/terms/Terms_Use.cfm

5 *High Order Numerics* [*11, 16, 17*]. High order finite difference formulations coupled with discrete filtering and a body fitted mesh can be used to minimize the mesh required to compute a given flow.

Turbulence Model Requirements

The task of developing a turbulence model or models which would be appropriate for an installation such as that shown in Fig. 1 should not be underestimated. A general classification system for turbulent flows, which is required if one is to consider complex three-dimensional flows, is outlined below, followed with a discussion of the status and problems with current turbulence models.

The success of many powered lift designs is directly dependent on transferring part of the energy of a high velocity engine exhaust jet to a larger mass of slower moving air. The development of numerical design tools for powered lift applications thus requires the careful modeling of the turbulent mixing associated with the jet exhaust. Most turbulence models presently available were developed for relatively simple two-dimensional flows and the literature contains very limited advice for the user interested in predicting complex three-dimensional flows.

In discussing the extrapolation of turbulence models from two-dimensional to three-dimensional flows, it is important to note that three-dimensionality in itself is not a major problem. Turbulent flows are always three-dimensional even if the mean flow is two-dimensional. There are some turbulence modeling problems which are inherently three-dimensional, but the major difficulty in three dimensions is the great number of different flows which may be encountered. For example, if we consider two dimensional jet flows, there are only three possibilities: the jet can be planar, it can be axisymmetric, or it can be radial. In three dimensions the possibilities are infinite. In two dimensions each jet flow can be studied separately and the performances of various turbulence models can be evaluated directly by comparing their predictions with experimental data. In three dimensions such as approach is obviously impossible.

A basic prerequisite for the discussion of the use of turbulence models for three-dimensional flows is thus a practical classification system which can be used to determine whether or not a given turbulence model can be used for the prediction of a particular flow. A classification system of some sort is implicit in most work on turbulence models, but Bradshaw [18] has developed the idea more systematically and more completely than most other workers. Bradshaw observes that the effects of turbulent stress gradients on the overall mean flow are generally restricted to thin or fairly thin shear layers, since the turbulent stresses themselves are quite small. Therefore, even in general three-dimensional flows, the turbulence problem effectively reduces to a consideration of the interactions or perturbations of a number of shear layers. The principle advantage of such a classification system, based on flow phenomenon rather than flow geometry, is that the number of different interactions possible between shear layers, or the number of ways in which they can be perturbed, is limited. A second important advantage of such a classification scheme is that it is generally possible to study the different flow phenomena separately, often using relatively simple flow geometries. The importance of experimental work in the development of turbulence models cannot be over emphasized and the above remarks on the necessity of developing a usable classification system for turbulent flows applies not only to the development of turbulence models, but also to the design of experiments.

Modeling Considerations. To illustrate the use of such a classification system in practice and as a basis for the discussion of turbulence modeling problems associated with powered lift, we will return to the powered lift application introduced earlier. For simplicity, the present discussion will be limited to the region of the jet downstream of the nozzle exit. A schematic diagram of this flow field is shown in Fig. 2 with the principle problem areas identified. Although the relative importance of the various turbulence phenomena can differ for different flows, these major modeling problems are common to most powered lift installations.

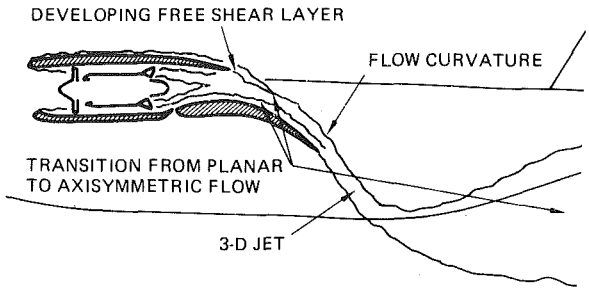


Fig. 2 Fluid flow problems of propulsion powered lift installations

There are four basic problems inherent in the flow structure shown in Fig. 2. The first is the failure of current turbulence models to accurately predict axisymmetric jets with the same constants used for planar flows. The problem is not so much the inconvenience of having to change constants as the flow changes, but the absence of a clear understanding of why the change is necessary and how it can be generalized for three-dimensional flows. The second problem concerns the developing region of a free shear layer as it relaxes from a wall boundary layer. This problem is encountered in the near field of jets and just downstream of separation. Our inability to accurately predict this region of the flow is a major source of error in most two-dimensional jet predictions and in many three-dimensional jet predictions. The third problem relates to turbulence interactions which are inherently three-dimensional and which are not predicted by the simpler turbulence models. The objective is to find a way of extending turbulence models, initially developed for two-dimensional flows, to account for these effects without greatly increasing their complexity. The fourth problem is the effect of streamline curvature on the turbulence. An excellent and very comprehensive review of the importance of streamline curvature has recently been published by Bradshaw [19] and the problem need not be discussed in more detail here. Progress on the three remaining problems, however, will be briefly outlined.

The Planar to Axisymmetric Jet Transition Problem. Although a number of methods have been developed to automatically adjust the turbulence model constants for axisymmetric jets, as the flow geometry changes, it is generally recognized that these procedures are unsatisfactory in that they lack generality. Three attempts have been made recently to develop generally applicable methods which overcome these objections. The discussion here will focus briefly on the physical hypotheses of these methods.

The first proposal is due to Vollmers and Rotta [20]. From a consideration of an exact equation for the quantity ql, where q is the turbulence kinetic energy and l is a turbulence length scale, they show that the production term can be expressed in terms of two point correlation functions. The usual procedure is to expand this expression in a Taylor series and to retain only the first term. Vollmers and Rotta argue that the higher order terms are not necessarily negligible and show that their inclusion can lead to correct predictions for both the planar and axisymmetric jets.

Pope [21] argues that, since the large turbulent eddies tend to be aligned with the mean vorticity, a stretching of the flow in the direction of the mean vorticity will distort the large turbulent eddies and therefore lead to a change in the mixing rate of a jet. He therefore proposes adding, to a differential equation describing the turbulence dissipation, an additional production term to account for this effect. Since this type of stretching occurs in an axisymmetric jet but not in a planar jet, this additional term can be adjusted to lead to correct predictions for the spreading rate of both flows.

The proposal by Hanjalic and Launder [22] resembles that by Pope in that it also suggests the need for an additional term in the dissipation equation, but the two proposals differ in detail. Hanjalic and Launder argue that the available experimental data suggest that irrotational strains lead to higher rates of dissipation than rotational strains. They attempt to account for this effect by the addition of a term which models the contribution of normal strains to the dissipation rate.

Downloaded 01 Jun 2010 to 171.66.16.58. Redistribution subject to ASME license or copyright; see http://www.asme.org/terms/Terms_Use.cfm

All three proposals lead to turbulence models which give improved prediction for planar and axisymmetric jets, using the same set of constants. On balance the proposal due to Vollmers and Rotta appears to be the most promising, and this is the approach which we are currently pursuing. None of these proposals, however, have been extensively tested, and, in view of the limited data base at present available, the relative merits of the three proposals will not be discussed in detail here.

Developing Free Shear Layers. There is growing evidence that strongly perturbed flows, or flows responding to sudden changes in boundary conditions, are not well predicted by current turbulence models. This appears to be due to the need to account for changes in the shape of the turbulence energy spectrum. This need has been recognized for some years [23] but the development of such a model has been attempted only recently [24]. In [25] Launder and Morse point out that a basic problem with current turbulence models is the use of a single turbulence velocity scale and a single turbulence length scale. This implies a universal turbulence energy spectrum shape which cannot in general be valid (see also [26]). The need for such a model is perhaps most obvious for flows involving a transition from laminar to turbulent flow, but significant changes in spectrum shape occur in all strongly perturbed flows. In the present context the discussion will be limited primarily to the relaxation region of a mixing layer as it develops from a turbulent wall boundary layer.

The problem with using a two-equation turbulence model to predict this flow can be illustrated by noting that since

$$\frac{1}{K}\frac{D\epsilon}{Dt} = \frac{m-2n}{2m}\frac{1}{q^{1/2}}\frac{Dq}{Dt} + q^{(1/2-m)}\frac{1^{(1-m)}}{m}\frac{D(q^n 1^m)}{Dt} \tag{1}$$

where the turbulence viscosity $\epsilon = Kq^{1/2}1$ and n and m are constants, it is possible in principle to contract a two equation model for the turbulence energy and a length scale containing quantity, $q^n 1^m$, to a single equation model for ϵ. For simple free shear flows, a one-dimensional version of such a model retains most of the characteristics of a more complex two-equation model. Consider for example the one-dimensional model given below.

$$\overline{U}\frac{d\epsilon}{dx} = A\epsilon\frac{\Delta U}{L} - B\frac{\epsilon 2}{L^2} \tag{2}$$

Convection Production Destruction

Here A and B are constants, $\overline{U}$ is the average velocity in the shear layer, L is the width of the layer, and ΔU is the velocity difference across the layer. As was demonstrated in [27], this model was found to give predictions comparable with more complex multi-equation models for a range of free shear flows. If one defines ϵ^* to be the value of ϵ when $d\epsilon/dx = 0$, then

$$\epsilon^* = \frac{A}{B}L\Delta U \tag{3}$$

which when substituted in equation (2) gives

$$\frac{L}{\epsilon}\frac{d\epsilon}{dx} = \frac{B}{UL}(\epsilon^* - \epsilon) \tag{4}$$

The significance of equation (4), in the present context, is that it is a first order differential equation. A model of this form requires that, if the turbulent viscosity is initially perturbed from its equilibrium value, it must return to equilibrium monotonically. This does not appear to be in agreement with the available experimental data. For example, some experimental results for a plane shear layer developing from a turbulent wall boundary layer are shown in Fig. 3 (see also [28]). Downstream of the separation point the spreading rate, and presumably also the shear stress, starts to increase slowly, overshoots its equilibrium value and then returns to equilibrium farther downstream. Although detailed turbulence measurements are not available over the whole developing region for this flow, some preliminary results were found to give improved predictions for this flow, using a simplified multi-scale model. The results in [24] also show improved performance, obtained with a multi-scale model, for the prediction of the variation of grid-generated turbulence through a 4:1 contraction. Additional development work is still required before any of these models can be used to replace models presently in use, but the progress obtained to-date appears to be very promising.

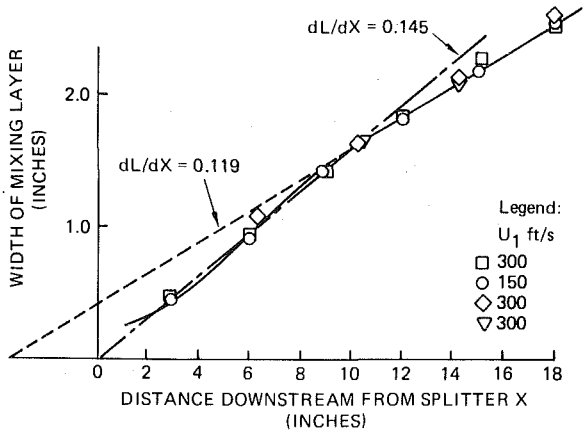


Fig. 3 Spreading rate for mean velocity profile

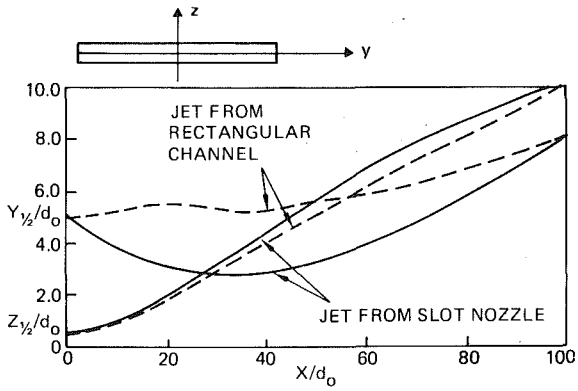


Fig. 4 Downstream development of two rectangular jets

Three-Dimensional Jets. The third problem to be considered here is different from the two previous problems in that it is directly associated with the three-dimensionality of the flow. Some three-dimensional jet flows have been predicted with reasonable accuracy using a two-equation turbulence model and some examples of these calculations will be discussed later in this paper, but this approach can lead to substantial errors for certain flow geometries.

This is probably best illustrated using the available experimental [29–33] results for large aspect ratio jets. The results by Sfeir [29] shown in Fig. 4 are for two different and rather extreme nozzle geometries. One nozzle is a sharp edged slot nozzle and the other is a rectangular channel which is fifty nozzle heights long. Both nozzles have an aspect ratio of ten. The dimensions $Y_{1/2}$ and $Z_{1/2}$ are the two half widths of the jet and d_0 is the nozzle height.

The most notable feature of the flow downstream of both nozzles is the secondary flow which causes the jet to first become circular and then to become elliptical again with the major and minor axes interchanged.

For the slot nozzle the flow contracts along the width of the nozzle and expands along the height of the nozzle as the flow develops downstream of the slot and the jet becomes circular in about 25 nozzle heights. For the channel nozzle the effect is much weaker and the jet in this case does not become circular until about 60 nozzle heights downstream of the nozzle exit plane.

At present it appears that there may be at least two different effects involved here. Some preliminary numerical results obtained recently by the second author suggest that the flow from the channel nozzle may be due primarily to turbulence driven secondary flows generated downstream of the nozzle exit. A calculation using an algebraic Reynolds stress model, similar to that used by Tatchell [34], and Gosman and Rapley [35], and assuming axial flow at the nozzle exit, is compared with Sfeir's results from the channel nozzle in Fig. 5. In

Downloaded 01 Jun 2010 to 171.66.16.58. Redistribution subject to ASME license or copyright; see http://www.asme.org/terms/Terms_Use.cfm

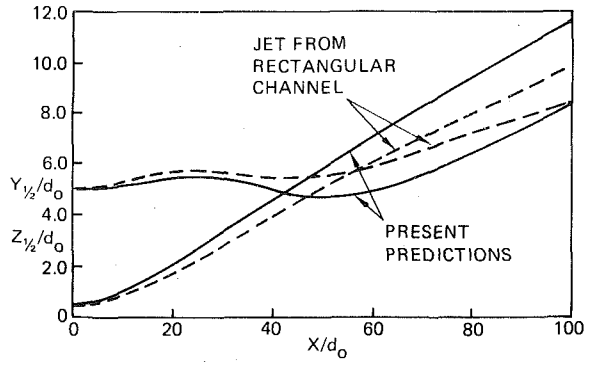


Fig. 5 Experimental data and predictions for rectangular jet

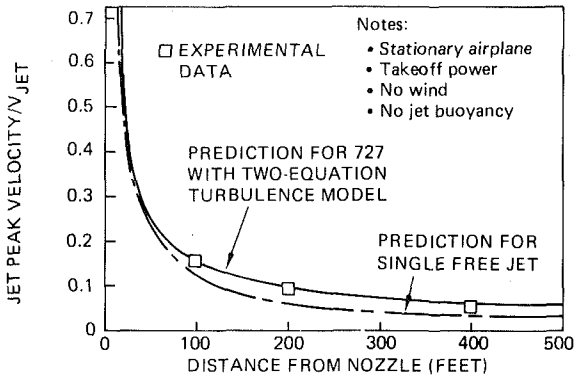


Fig. 6 Jet velocity decay for 727 jet engine exhaust installation

view of the fact that no attempt was made to exactly match the experimental initial conditions, the agreement is quite good.

For the jet from the slot nozzle, however, the initial contraction is much larger. McGuirk and Rodi [36] have shown that an accurate prediction for this flow requires a strong secondary flow at the nozzle exit. Whether or not this secondary flow is pressure driven and generated within the nozzle remains to be determined.

As with the other problems discussed here, additional work is still required before all outstanding questions are satisfactorily answered. Based on the results at present available, however, it does appear that the accuracy of three-dimensional jet calculations can be significantly improved over those obtained using a standard two-equation turbulence model, with only a very modest increase in complexity.

Recent Complex Jet Flow Calculations

The paper so far has dealt with the general requirements for a powered lift calculation procedure, and it would be misleading to end without some mention of progress, because over the last ten years there has been a significant improvement in our ability to predict turbulent flows of practical importance. The examples presented here, selected from recent work by the authors and their colleagues, illustrate some recent predictions of complex three-dimensional flows of the type required for powered lift applications.

The first example is the predicted jet wake decay behind a commercial tri-jet. The difficulty here is the interaction, first between the jets themselves, and then between the jets and the ground, which makes the problem three-dimensional. Both of these interactions tend to reduce the jet decay rate and, as is shown in Fig. 6, result in higher jet velocities downstream of the nozzle than would be predicted from an axisymmetric calculation. The data shown on this figure were obtained from a full scale test conducted after the calculations were performed. These calculations were performed using a three-dimensional parabolic marching procedure based on the work of Patankar and Spalding [37]. The use of a marching procedure made them relatively inexpensive in spite of the fact that they were run to 400 ft downstream of the nozzle exit.

The second example, using the same computer program, is a previously unpublished calculation for the jet development downstream of a model scale multi-element nozzle. This flow is different from that described in [38] in that a 12 lobed mixer, which was fitted upstream

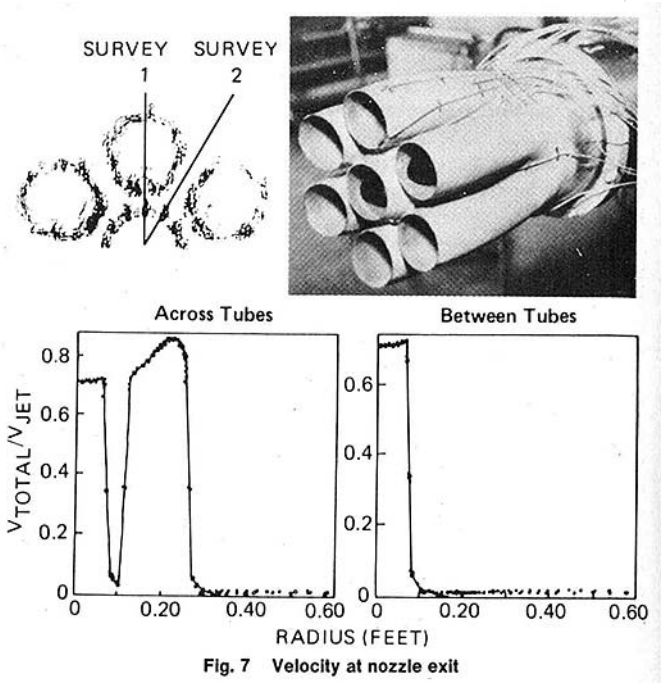


Fig. 7 Velocity at nozzle exit

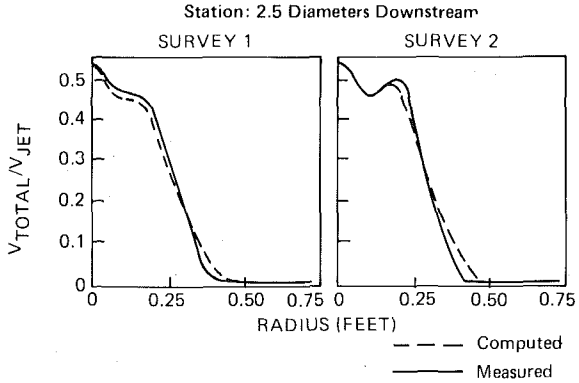


Fig. 8 Comparison of measured and computed velocity profiles

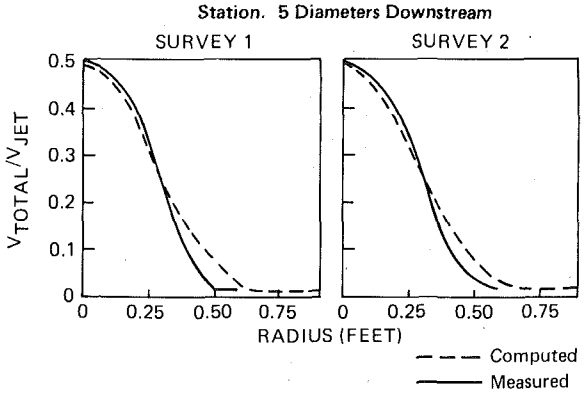


Fig. 9 Comparison of measured and computed velocity profiles

of the nozzle exit, partially mixed the hot primary stream and the cooler secondary stream of this model scale simulation of a turbofan engine. The experimentally measured flow at the nozzle exit, shown in Fig. 7, was used to start the calculations. A comparison between the predicted and measured velocities, at the two circumferential positions indicated in Fig. 7 and at different axial distances, is shown in Figs. 8 and 9.

In both of these examples the turbulence stresses were calculated using the following two equation turbulence model.

$$\rho \frac{Dq}{Dt} = \frac{\partial}{\partial x_k}\left[\frac{\mu_t}{\sigma_q}\frac{\partial q}{\partial x_k}\right] + \mu_t\left(\frac{\partial U_i}{\partial x_k} + \frac{\partial U_k}{\partial x_i}\right)\frac{\partial U_i}{\partial x_k} - \mathcal{D} \qquad (5)$$

Downloaded 01 Jun 2010 to 171.66.16.58. Redistribution subject to ASME license or copyright; see http://www.asme.org/terms/Terms_Use.cfm

$$\rho \frac{D\mathcal{D}}{Dt} = \frac{\partial}{\partial x_k}\left[\frac{\mu_t}{\sigma_{\mathcal{D}}}\frac{\partial \mathcal{D}}{\partial x_k}\right] + 1.4\frac{\mu_t \mathcal{D}}{q} \cdots \quad (6)$$
$$\cdots\left(\frac{\partial U_i}{\partial x_k} + \frac{\partial U_k}{\partial x_i}\right)\frac{\partial U_i}{\partial x_k} - 1.92\frac{\mathcal{D}^2}{q}$$

Since the flows were assumed to be parabolic, derivatives with respect to the main flow direction were ignored for the terms on the right hand side of these equations. In this model one equation is solved for the turbulence energy q, and a second equation is solved for the turbulence energy dissipation rate $\mathcal{D}$. The shear stresses were then calculated in terms of these quantities using an effective turbulence viscosity μ_t defined as

$$\mu_t = 0.09\,\rho\frac{q^2}{\mathcal{D}} \quad (7)$$

The agreement between predictions and measurements is not always as good as these results might indicate, but the results do illustrate the accuracy which is possible with modern numerical prediction methods. As was described previously, the problem in calculations of this type is due primarily to uncertainties in the prediction of the initial developing region. At present it is possible to partially compensate for this in the specification of the initial conditions; but to do this consistently on a prediction rather than a postdiction basis, requires considerable experience and perhaps also a little luck. With the development of an improved model for the intial developing region, this uncertainty could be greatly reduced.

Concluding Remarks

Although a number of problems still remain to be resolved, many of the basic elements required for the development of useful design tools for powered lift applications already exist. For example, we have recently started assembling a numerical procedure[1] which we believe can be used as an aid in the design of aircraft using upper surface *blowing*. In essence, the approach is to couple a three-dimensional parabolic program, which will be used to calculate the viscous portion of the flow, with a linearized potential flow [39] solution, which will be used to calculate the inviscid portion of the flow. Because of the complex geometry involved in these calculations, the parabolic program is written in a general curvilinear co-ordinate system and uses a machine generated body-fitted mesh. A detailed description of this program is given in [10]. The initial phase of the work will concentrate on solving the numerical problems associated with the coupling procedure. The concurrent work on the development of improved turbulence models is intended to mesh with a second phase of this development program. This second phase will concentrate primarily on improving the individual analysis components.

References

1 Wimpress, J. K., "Upper Surface Blowing Technology as Applied to the YC-14 Airplane," presented at SAE Aerospace Engineering and Manufacturing Meeting, Paper No. 730916, Oct. 1973.

2 Skavdahl, H., Wang, T., and Hirt, W. J., "Nozzle Development for the Upper Surface-Blown Jet Flap on the YC-14 Airplane," SAE Air Transport Meeting, Paper No. 740469, Apr. 1974.

3 *QSRA Configuration Definition,* Boeing Document D642487, Nov. 1976, The Boeing Company, Seattle, Wash.

4 Murphy, R., "Thrust-Augmenting-Wing Prototype Aircraft," *Proceedings of the Workshop on Thrust Augmenting Ejectors,* NASA Ames, June 1978 (to be published).

5 Glover, J. H., and Gotlieb, P., "V/STOL Lift Fan Commercial Short Haul Transports—An Automatic Flight Control System Capable of Compensating for Propulsion System Failure," NASA CR-137612, 1975.

6 Welliver, A. D., "Propulsion Research Requirements for Powered Lift Aircraft," *Proceedings of the Workshop on Engine-Airframe Integration,* Project SQUID, 1977, pp. 199–242.

7 Forester, C. K., "Numerical Simulation of the Interaction of Jet and Freestream Flows in Engine Exhaust Systems," AIAA Paper No. 78-144, Jan. 1978.

8 Schiff, L. B., "The Axisymmetric Jet Counterflow Problem," AIAA Paper No. 76-325, 1976.

9 Peery, K. M., and Forester, C. K., "Numerical Simulation of Multi-Stream Nozzle Flows," AIAA Paper No. 79-1549, July 1979.

[1] Supported in part by NASA contract NAS2-10100.

10 Roberts, D. W., and Forester, C. K., "A Parabolic Procedure for Ducts with Arbitrary Cross-Sections," *AIAA Journal,* Vol. 17, No. 1, 1979, pp. 33–40.

11 Forester, C. K., "Higher Order Monotonic Convective Difference Schemes," *Journal of Computational Physics,* Vol. 23, No. 1, 1977, pp. 1–22.

12 Zalesak, S. T., "Fully Multi-Dimensional Flux-Corrected Transport," Memorandum Report 3716, May 1978, Naval Research Lab.

13 Caughey, D. A., Jameson, A., "Accelerated Iteractive Calculation of Transonic Nacelle Flowfields," *AIAA Journal,* Vol. 15, No. 10, Oct. 1977, pp. 1474–1480.

14 Brandt, A., Dendi, Jr., J. E., and Ruppel, H., "The Multi-Grid Method for Semi-Implicit Hydrodynamic Codes," LA-UR 78-3066, Feb. 1979, Los Alamos Scientific Lab., Los Alamos, NM.

15 Brandt, A., Multi-Level Adaptive Techniques (MLAT) for Partial Differential Equations: Ideas and Software," *Proceedings of the Mathematical Software Symposium No. 39,* Mathematical Software iii, (Math, Res. Center: No. 39) Academic Press, 1977, pp. 277–318.

16 Kreiss, H. O., and Oliger, J., "Comparison of Accurate Methods for the Integration of Hyperbolic Equations," *Tellus,* XXIV3, 1972, pp. 199–215.

17 Rubin, S. G., and Khosla, P. K., "An Integral Spline Method for Boundary Layer Equations," Poly M/AE Report No. 77-12, July 1977, Polytechnic Institute of New York, N. Y.

18 Bradshaw, P., "Review-Complex Turbulent Flows," ASME *Journal of Fluids Engineering,* June 1975, pp. 146–154.

19 Bradshaw, P., "Effects of Streamline Curvature on Turbulent Flow," AGARD-AG-169, Aug. 1973.

20 Vollmers, H., and Rotta, J. C., "Similar Solutions of the Mean velocity, Turbulent Energy and Length Scale Equation," *AIAA Journal,* Vol. 15, No. 5, May 1977, pp. 714–720.

21 Pope, S. B., "An Explanation of the Turbulent Round-Jet/Plane-Jet Anomaly," *AIAA Journal,* Vol. 16, No. 3, Mar. 1978, pp. 279–281.

22 Hanjalic, K., and Launder, B. E., "Preferential Spectral Transport by Irrotational Straining," ASME Symposium on Turbulent Boundary Layers, June 1979, (to be published).

23 Launder, B. E., and Spalding, D. B., *Mathematical Models of Turbulence,* Academic Press, London and New York, 1972.

24 Hanjalic, K., and Launder, B. E., "Turbulent Transport Modeling of Separating and Reattaching Shear Flows," TRF/78/8, 1978, University of California, Davis, CA.

25 Launder, B. E., and Morse, A., "Numerical Prediction of Axisymmetric Free Shear Flows with a Second-order Reynolds Stress Closure," *Proceedings of the Symposium on Turbulent Shear Flows,* The Pennsylvania State University, Apr. 1977, pp. 4.21–4.30.

26 Birch, S. F., "Turbulence Models from the Point of View of an Industrial User, "*Proceedings of the Workshop on Future Computer Requirements for Computational Aerodynamics,* NASA Ames, NASA Conference Publication 2032, Feb. 1978, pp. 248–259.

27 Birch, S. F., "A Critical Reynolds Number Hypothesis and Its Relation to Phenomenological Turbulence Models," *Proceedings of the 1976 Heat Transfer and Fluid Mechanics Institute,* June 1976, p. 152–164.

28 Birch, S. F., "On the Developing Region of a Plane Mixing Layer," *Proceedings of the Project SQUID Workshop on Turbulence in Internal Flows,* June 1976, pp. 89–100.

29 Sfeir, A. A., "The Velocity and Temperature Fields of Rectangular Jets," *International Journal of Heat and Mass Transfer,* Vol. 19, 1976, pp. 1289–1297.

30 Kamatsu, Y., "Fluid Dynamics of Jets," *Nihon University, Research Institute of Science and Technology, Journal,* Sept. 1970, pp. 1–75, (In Japanese, with abstract in English).

31 Sforza, P. M., Steiger, M. H., and Trentacosta, N., "Studies on Three-Dimensional Viscous Jets," *AIAA Journal,* Vol. 4, No. 5, May 1966, pp. 800–806.

32 Trentacosta, N., and Sforza, P. M. "Further Experimental Results for Three-Dimensional Free Jets," *AIAA Journal,* Vol. 5, No. 5, May 1967, pp. 885–891.

33 Sfeir, A., "Investigation of Three Dimensional Rectangular Jets," AIAA Paper No. 78-1185, July 1978.

34 Tatchell, D. G., "Convection Processes in Confined, Three-Dimensional Boundary Layers," Ph.D. Thesis, University of London, July 1975.

35 Gosman, A. D., and Rapley, C. W., "A Prediction Method for Fully-Developed Flow Through Non-Circular Passages," *Proceedings of the First International Conference on Numerical Methods in Laminar and Turbulent Flow,* University College Swansea, Swansea, U. K., July 1978, 271–285.

36 McGuirk, J. J., and Rodi, W., "The Calculation of Three-Dimensional Turbulent Free Jets," *Proceedings of the Symposium on Turbulent Shear Flows,* The Pennsylvania State University, April 1977, pp. 1.29–1.36.

37 Patankar, S. V., and Spalding, D. B., "A Calculation Procedure for Heat, Mass and Momentum Transfer in Three-Dimensional Parabolic Flows," *International Journal of Heat and Mass Transfer,* Vol. 15, 1972, pp. 1787–1806.

38 Barton, J. M., Birch, S. F., Paynter, G. C., and Crouch, R. W., "An Experimental and Numerical Study of Three-Dimensional Turbulent Jets," AIAA Paper No. 78-994, July 1978.

39 Johnson, F. T., and Rubbert, P. E., "Advanced Panel-Type Influence Coefficient Methods Applied to Subsonic Flows," AIAA Paper No. 75-50, January 1975

Downloaded 01 Jun 2010 to 171.66.16.58. Redistribution subject to ASME license or copyright; see http://www.asme.org/terms/Terms_Use.cfm

A. Goulas
Research Fellow,
Cranfield Institute of Technology,
Cranfield, Bedford, U.K.

A Blade-to-Blade Solution of the Flow in a Centrifugal Compressor Impeller with Splitters

The matrix through flow analysis is used to predict the blade-to-blade flow in a centrifugal compressor impeller which contains splitters (half vanes). The presence of solid boundaries in the flow field and the stagnation points associated with it are treated by assuming that the flow around the stagnation point is isentropic. This removes the instability which the matrix through flow method suffers when stagnation points are encountered within the flow field. The splitters in the present work have the same profile with the full blades. Three different geometries are tested. In the first, the leading edge is 3 mm from the eye, the next is 6 mm, and the third has the leading edge at the exit of the inducer. The calculations show that the differences shown between the three cases are linked with different circumferential components of velocity. The geometry, therefore, of the leading edge is of basic importance in the development of the velocity profiles inside the different channels of the impeller. It is also shown that the distance between the eye of the impeller and the leading edge of the splitter does not affect the flow greatly as long as the leading edge is within the axial part of the impeller. The presence of splitters in general is shown to reduce the width of the suction side boundary layer.

1 Introduction

The present day centrifugal compressor impellers contain a significant number of splitters (half vanes) in order to improve the flow through the impeller. The calculation, therefore, of the flow field in such an impeller is of importance to centrifugal compressor designers.

Two-dimensional calculations of the flow on a blade-to-blade stream surface have been performed by Stanitz [1], Krimerman and Adler [2] and several other researchers. They assumed that the flow is inviscid. Goulas [3] reported a procedure to solve for viscous and turbulent flow on a blade-to-blade stream surface of a centrifugal compressor impeller. This work is the starting point for the present paper.

The matrix through flow method in its original form as presented by Bosman and Marsh [4] cannot deal with stagnation points inside the flow field as the right hand side of the equation for the stream function becomes infinite.

In this work, the matrix through flow method as modified by Goulas [3] is used to predict the flow field on a blade-to-blade stream surface of a centrifugal compressor impeller containing splitters.

2 The Equations Governing the Flow

The complete theoretical analysis can be found in [3] and [5]. Here only the basic equations will be given.

For a curvilinear orthogonal system of coordinates with axes S along and N across the streamline on the stream surface and a third axis n normal to the surface, the equations governing the flow on a stream surface are:

(i) Continuity.

$$\nabla \cdot (\rho r W) = 0$$

(ii) Equation of motion for the N-direction:

$$\overline{N} \cdot \overline{W} \times (\nabla \times \overline{V}) = \overline{N} \cdot (\nabla I - T \nabla s) \tag{1}$$

(iii) Equation of motion for the S-direction:

$$T \frac{Ds}{Dt} = -\overline{W} \cdot \overline{D} \tag{2}$$

(iv) A geometrical condition necessary for the flow to follow the stream surface:

$$\overline{W} \cdot \overline{F} = 0 \tag{3}$$

(v) The energy equation for steady flow:

$$\frac{DI}{Dt} = 0 \tag{4}$$

(vi) and the equation of state:

$$p = \rho R T$$

The equation of motion in the n-direction has been replaced by the geometrical condition and can be used if required to calculate the body force $\overline{F}$ which must be applied for the flow to follow the stream surface.

As is explained in [3], because of the shape of the stream surface—part of it is axial and part of it is radial—two different sets of co-ordinates must be used. In the axial part, the co-ordinates must be $z - \theta$ and in the radial part, $r - \theta$.

The introduction of Wu's special derivatives in the form:

Contributed by the Gas Turbine Division of THE AMERICAN SOCIETY OF MECHANICAL ENGINEERS and presented at The 1979 Israel Joint Gas Turbine Congress, Haifa, Israel, July 9–11, 1979. Manuscript received at ASME Headquarters May 8, 1979. Paper No. 79-GT/Isr-17.

Copyright © 1980 by ASME
Downloaded 01 Jun 2010 to 171.66.16.58. Redistribution subject to ASME license or copyright; see http://www.asme.org/terms/Terms_Use.cfm

$$\frac{\bar{\delta}}{\partial x_i} = \frac{\partial}{\partial x_i} - \frac{n_i}{n_r}\frac{\partial}{\partial r} \tag{5}$$

for the $z - \theta$ system of co-ordinates and a stream function ψ, which satisfies the continuity equation, defined as

$$\frac{\bar{\delta}\psi}{\partial z} = -B\rho W_u \tag{6a}$$

$$\frac{1}{r}\frac{\bar{\delta}\psi}{\partial \theta} = B\rho W_z \tag{6b}$$

into the N-equation of motion will yield the following equation for the stream function:

$$\frac{1}{r^2}\frac{\bar{\delta}^2\psi}{\partial\theta^2} + \frac{\bar{\delta}^2\psi}{\partial z^2} = \frac{W_z}{r}\frac{\bar{\delta}}{\partial\theta}(B\rho) + (\rho B)^2\frac{dI}{d\psi} - W_u\frac{\bar{\delta}}{\partial z}(B\rho)$$
$$- \frac{TB\rho}{W^2}\left(\frac{1}{r}\frac{\bar{\delta}s}{\partial\theta}(W_z - W_r\tan\lambda) - \frac{\bar{\delta}s}{\partial z}(W_u - W_r\tan\mu)\right)$$
$$+ B\rho\left(\frac{1}{r}\frac{\bar{\delta}W_r}{\partial\theta}\tan\lambda - \frac{\bar{\delta}W_r}{\partial z}\tan\mu - \left(\frac{W_u}{r} + 2\omega\right)\tan\lambda\right) \tag{7}$$

For the $r - \theta$ set of co-ordinates, Wu's special derivatives are

$$\frac{\bar{\delta}}{\partial x_i} = \frac{\partial}{\partial x_i} - \frac{n_i}{n_z}\frac{\partial}{\partial_z} \tag{8}$$

A stream function ψ can then be defined as:

$$\frac{\bar{\delta}\psi}{\partial r} = -B\rho W_u \tag{9a}$$

$$\frac{1}{r}\frac{\bar{\delta}\psi}{\partial\theta} = B\rho W_r \tag{9b}$$

The N-equation of motion, therefore, will become

$$\frac{\bar{\delta}^2\psi}{\partial r^2} + \frac{1}{r^2}\frac{\bar{\delta}^2\psi}{\partial\theta^2} = \frac{W_r}{r}\frac{\bar{\delta}}{\partial\theta}(B\rho) - W_u\frac{\bar{\delta}}{\partial r}(B\rho) + (B\rho)^2\frac{dI}{d\psi}$$
$$+ \frac{TB\rho}{W^2}\left(\frac{\bar{\delta}s}{\partial r}(W_u - W_z\tan\mu) - \frac{1}{r}\frac{\bar{\delta}s}{\partial\theta}(W_r - W_z\tan\lambda)\right)$$
$$+ B\rho\left(\tan\lambda\frac{1}{r}\frac{\bar{\delta}W_z}{\partial\theta} - \tan\mu\frac{\bar{\delta}W_z}{\partial r} + \frac{W_u}{r} + 2\omega\right) \tag{10}$$

Equations (7) and (10) have to be solved iteratively to obtain a solution of the flow on a blade-to-blade stream surface of a centrifugal compressor.

The dissipation force is given in [3] by the expression:

$$\bar{D} = \frac{1}{\rho}(\nabla\cdot\tau) \tag{11}$$

The stress tensor is given as

$$\tau_{ij} = \mu\left(\frac{\partial W_i}{\partial x_j} + \frac{\partial W_j}{\partial x_i}\right) \tag{12}$$

where μ is the viscosity of the air. Near the boundaries the shear stress is obtained using the logarithmic law of the wall in order to take into account the effects of turbulence in the boundary layers.

3 The Numerical Solution

The flow field on a blade-to-blade stream surface can be obtained by solving simultaneously equations (2) and (7–10) at distinct points within the flow field. Those points are the intersections of two sets of grid lines. One set consists of lines which follow approximately the mean flow (called x-lines) and the other set consists of lines which are approximately normal to the x-lines (called the y-lines).

3.1 The Finite Differences. Each partial derivative has been substituted with a finite difference expression of the form

$$\frac{\bar{\delta}q}{\partial x_\kappa} = \sum_{i=1}^{n} a_{i\kappa}q_i - q_0\sum_{i=1}^{n} a_{i\kappa} \tag{13}$$

and

$$\frac{\bar{\delta}^2\psi}{\partial r^2} + \frac{\bar{\delta}^2\psi}{\partial z^2} = \sum_{i=1}^{n} a_i\psi_i - \psi_0\sum a_i \tag{14}$$

The coefficients $a_{i\kappa}$ and a_j are calculated using Taylor's series for a lattice which has ten grid points ($n = 9$) extended over four grid lines in each direction.

3.2 The Solution Procedure. The first step for the solution is to assume a distribution of the stream function ψ. The corresponding two components of the velocity vector are then calculated from equation (6) or (9) depending upon the position of the point. The third component of velocity can be calculated from the geometry of the stream surface, i.e., $\bar{W}\cdot\bar{n} = 0$.

The second step is to calculate the resulting stresses from equation (12) and, finally, the dissipation force from equation (11).

The third step is to integrate equation (2) along a stream line assuming that the expression $(\bar{W}\cdot\bar{D})/(TW)$ is constant along a stream line between two consecutive y-lines. This integration yields an entropy field in accordance with the velocity field assumed. The exact position of the point of intersection between stream line passing through the point under consideration and the upstream y-line is found by fitting a cubic-spline polynomial to the stream function distribution along the y-line.

Finally, with velocity, entropy and density known, the right hand side of equation (7) or (10) can be calculated and a banded matrix set up to solve either of them.

The resulting distribution of ψ has to be compared with the initial one and the whole procedure repeated until a convergence criterion defined as

$$\left|\frac{\psi_{\text{new}} - \psi_{\text{old}}}{\psi_{\text{old}}}\right| < 0.001 \tag{15}$$

is satisfied at each point.

4 The Boundary Conditions

The distribution of the stream function ψ at the inlet can be obtained by integrating equation (6b) across the inlet for a given uniform axial velocity profile and is given as:

$$\psi = \rho W_{z_e} r(\theta - \theta_p) \tag{16}$$

with the integration factor being taken equal to one. The distribution of entropy at the inlet is uniform.

Nomenclature

B = integration factor
D = dissipation force per unit mass
F = body force
h_0 = stagnation enthalpy
h = enthalpy
I = rothalpy ($I = h_0 - \omega r V_u$)
N = normal to the stream line
n = normal to the stream surface
p = pressure
r = radius
R = gas constant
S = streamwise direction
s = entropy
T = temperature
V = absolute velocity
W = relative velocity
x_i = Cartesian space co-ordinates (S, N, n)
z = axial direction
λ, μ = angles of stream surface
θ = angle
ρ = density
τ = stress tensor
ψ = stream function
ω = angular velocity

Subscripts

r = radial direction
u = circumferential direction
z = axial direction
p = pressure side
e = eye

Downloaded 01 Jun 2010 to 171.66.16.58. Redistribution subject to ASME license or copyright; see http://www.asme.org/terms/Terms_Use.cfm

Along solid boundaries the stream function ψ is constant and the relative velocity is taken equal to zero.

At the exit of the flow field, the distribution of the stream function is not necessary, as an upstream finite difference scheme is employed in this particular region. In mathematical terms, this is equivalent to: third order derivatives of the stream function ψ being negligible, i.e.,

$$\left|\frac{\partial^3\psi}{\partial r^3}\right| \ll 0$$

The above boundary condition is applied to all points at the exit except to the one nearest to the pressure side of the blade where ψ is taken as

$$\psi = 0.5 W_{z_e} \rho r_e (\theta - \theta_r) \tag{17}$$

This is chosen to ensure that the velocity of the air near the pressure side is high and in line with experimental results.

This boundary condition is considered appropriate for a blade-to-blade solution without splitters by Goulas [3].

The stresses at the boundaries are calculated using the logarithmic law of the wall as is given by Launder and Spalding [4].

5 The Treatment of the Splitters

The presence of a splitter in the flow field introduces two new problems in the matrix through flow analysis. The first is the solid boundary with zero velocity on the surface; the second is the formation under certain circumstances of a small recirculation zone containing a stagnation point.

The first problem can be handled by the matrix through flow analysis as the boundary is a streamline. Therefore $\psi = \psi_c$ = constant along the surface of the splitter. The value of ψ_c, though, is unknown and must be calculated by integrating either equation (6*b*) or (9*b*), depending on the co-ordinates used, near the splitter wall assuming

1 a linear velocity profile for the isentropic flow, or

2 a logarithmic velocity profile for the turbulent flow.

The point where the integration takes place is usually far downstream of the leading edge so the flow is reattached and the choice of the above profiles is realistic.

The second point is more difficult to handle because as Bosman and Marsh [5] have pointed out, the matrix through flow method cannot deal with flows which contain stagnation points because part of the right hand side of equation (7) or (10) will become infinite and the whole solution will become unstable. A way round the problem is to assume that in the region of the stagnation point, gradients of entropy are zero; i.e., the flow is isentropic. Then the equations for the stream function at the stagnation point will become

$$\frac{\bar{\delta}^2\psi}{r^2\partial\theta^2} + \frac{\bar{\delta}^2\psi}{\partial z^2} = B\rho\left(\tan\lambda\frac{1}{r}\frac{\bar{\delta}W_r}{\partial\theta} - \tan\mu\frac{\bar{\delta}W_r}{\partial z} - 2\omega\tan\lambda\right) \tag{18a}$$

$$\frac{\bar{\delta}^2\psi}{\partial r^2} + \frac{1}{r^2}\frac{\bar{\delta}^2\psi}{\partial\theta^2} = B\rho\left(\tan\lambda\frac{1}{r}\frac{\bar{\delta}W_z}{\partial\theta} - \tan\mu\frac{\bar{\delta}W_z}{\partial r} + 2\omega\right) \tag{18b}$$

depending upon the co-ordinates of the stagnation point. These two equations will replace equations (7) and (10) at the stagnation point. The right hand side of equation (12) is finite so the solution will be stable.

The assumption of zero entropy gradient of the stagnation point can be justified as follows.

For a closed streamline as is the case in recirculating flows and for steady flow the gradient of entropy along the streamline must be zero otherwise the entropy within the recirculating area will keep increasing as a function of time which is against the assumption of steady flow. As the closed streamlines now are lines of constant entropy at the stagnation point, the function $s = f(N)$ must have a local maximum because the expression $\partial s/\partial N$ changes sign at the stagnation point. Therefore:

$$\left.\frac{\partial s}{\partial x_i}\right)_{\text{stagnation}} = 0$$

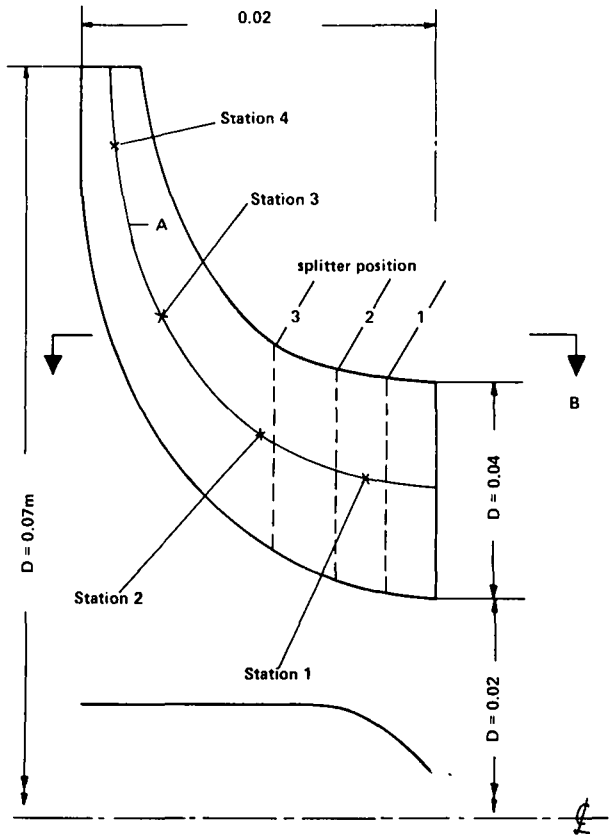


Fig. 1 Meridional profile of the centrifugal compressor

6 The Geometry of the Stream Surface

Fig. 1 gives the meridional plane of the impeller which has 16 blades. The blade-to-blade stream surface under consideration is an axisymmetric surface produced by rotating the line A of Fig. 1. The thickness of the stream sheet B is obtained by solving for a hub-to-shroud stream surface.

The splitter which is situated at the centre of the channel has the same geometry as the blade at the same axial and radial position. Three different positions for the leading edge are tested:

No. 1 with the leading edge 3 mm from the eye

No. 2 with the leading edge 6 mm from the eye

No. 3 with the leading edge at the exit of the inducer

It is considered that these are representative of the current engineering practice.

The rotational speed is taken as 60,000 rpm and the velocity profile at the inlet as uniform and equal to:

$$W_{z_e} = 96.5 \text{ m/s}$$

which is equivalent to a mass flow of 0.143 kg/s.

7 Discussion of the Results

Fig. 2 shows the streamlines for isentropic flow and the prediction obtained using the simple model for turbulence for the No. 2 splitter.[1]

Figs. 3–8 give the velocity profiles at various stations along the stream surface for isentropic flow. At station 1 near the inlet, Fig. 3, the axial velocity profiles are the same with or without splitters.

This result is expected for the No. 2 and 3 splitter configurations as the leading edge for both cases is downstream of point 1. The No.

[1] The absissa of the graph is the circumferential distance from the pressure side of the blade. The ordinate is the meridional distance of the stream surface. Points with the same r or z have the same ordinate.

Downloaded 01 Jun 2010 to 171.66.16.58. Redistribution subject to ASME license or copyright; see http://www.asme.org/terms/Terms_Use.cfm

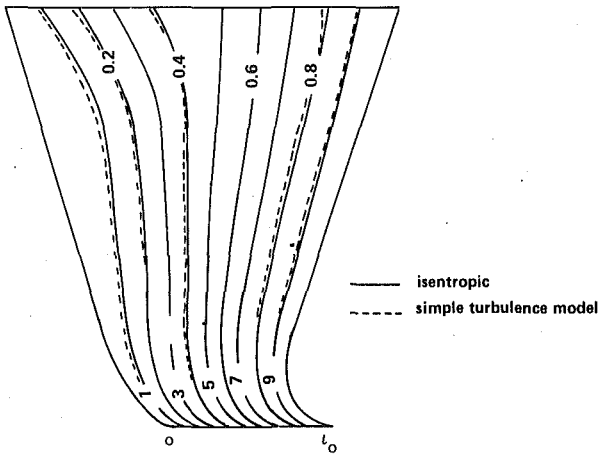


Fig. 2 Streamline patterns for isentropic flow and prediction using the simple turbulence model-splitter configuration No. 2

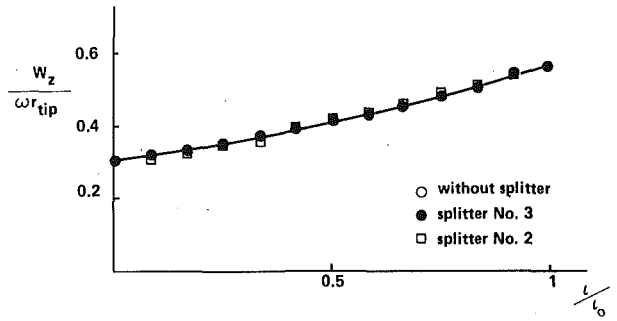


Fig. 3 Axial velocity profile at station 1—isentropic flow

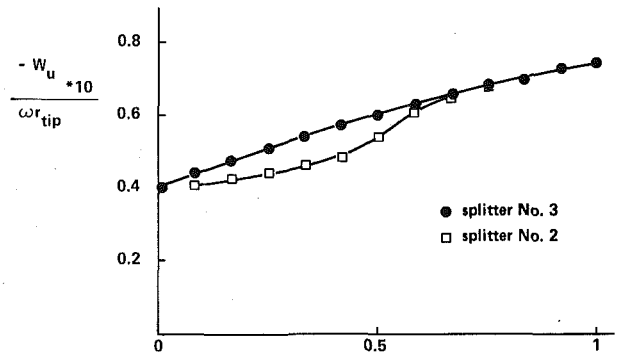


Fig. 4 Circumferential velocity profiles at station 1 just upstream of the No. 2 splitter leading edge—isentropic flow

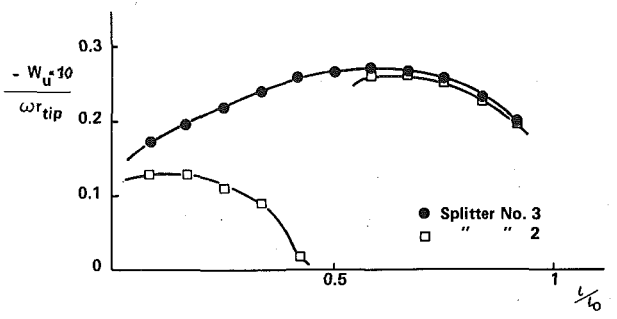


Fig. 5 Circumferential velocity profiles just downstream of the No. 2 leading edge—isentropic flow

1 splitter has the same velocity profiles because of the high solidity of the impeller at the inducer and the relatively small thickness of the leading edge. As a result, the flow is guided quite well in this region and the flow follows the blades. Furthermore, the flow near the eye of the impeller is dominated by the inlet boundary conditions which will overshadow any changes produced by the presence of the splitters.

Fig. 4 gives the circumferential velocity profiles for splitters No. 2 and 3 at station 1 which is near to the leading edge for the No. 2 splitter. The presence of the leading edge changes the velocity profile at the blade-splitter channel leaving the circumferential component at the other one unaffected. This is expected as the flow is towards the pressure side of the blade.

Fig. 5 gives the circumferential velocity profile just downstream of the leading edge where the effect of the leading edge on the circumferential component of velocity is more evident.

The effect of the splitter on the main flow, axial or radial component of velocity, starts becoming more evident at station 2, Fig. 6. At stations 3 and 4, the circumferential component of velocity has become zero. The radial velocity profiles at the same stations, Figs. 7 and 8, show that the isentropic velocity profiles become almost similar for the blade-splitter and splitter-blade channel for the No. 3 splitter position, i.e., the leading edge at the exit of the inducer.

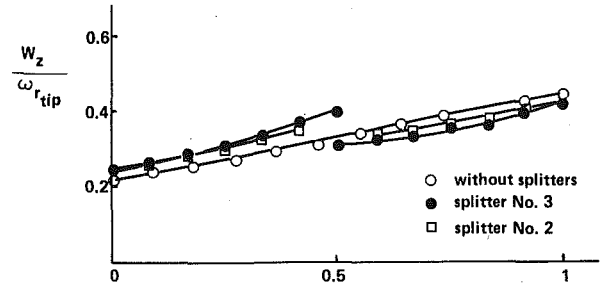


Fig. 6 Axial velocity profile at station 2—isentropic flow

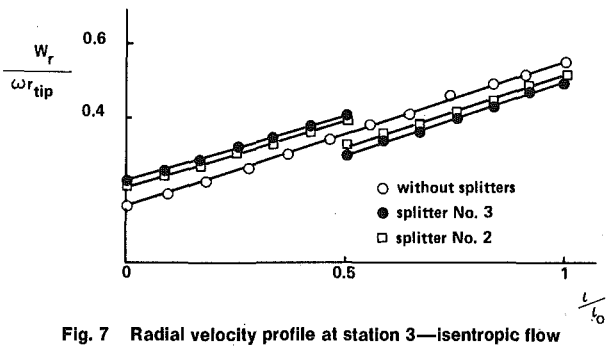


Fig. 7 Radial velocity profile at station 3—isentropic flow

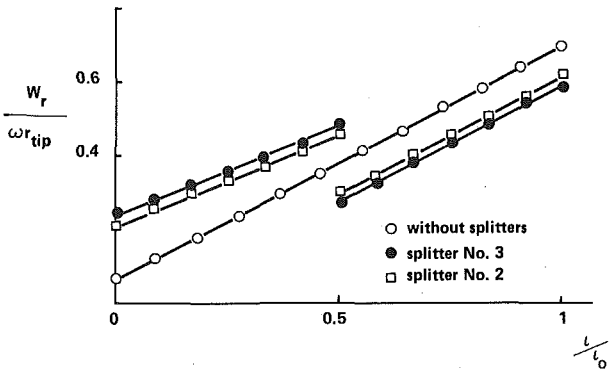


Fig. 8 Radial velocity profile at station 4—isentropic flow

Downloaded 01 Jun 2010 to 171.66.16.58. Redistribution subject to ASME license or copyright; see http://www.asme.org/terms/Terms_Use.cfm

Fig. 9 gives the axial velocity profile at station 1 for the simple turbulence model. The profiles are the same for the channel without splitters and for all splitter geometries. The reasons for this have already been discussed for the isentropic case.

Fig. 10 gives the circumferential component of velocity at station 2. The presence of the splitter just downstream of the station is causing an increase of velocity near the leading edge where the isentropic solution predicts the opposite. This is due to the fact that the isentropic flow is attached to the splitter where the non-isentropic solution predicts a small area of recirculating flow behind the leading edge. This region acts as blockage and forces the streamlines to deviate towards the pressure side of the blade, thus producing higher circumferential components of the relative velocity near the leading edge at station 1 and for the No. 2 splitter geometry.

The axial velocity profiles at station 2, Fig. 11, indicate that the width of the blade suction side boundary layer has been reduced and the profile is more uniform for both types of splitters. The same applies for stations 3 and 4, Figs. 12 and 13, respectively. The differences for the two splitter geometries are concentrated near the boundaries of the splitters as the boundary layer growth is a function of the splitter length.

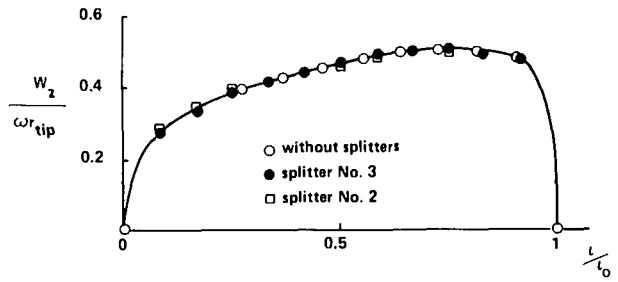


Fig. 9 Axial velocity profile at station 1—simple turbulence model

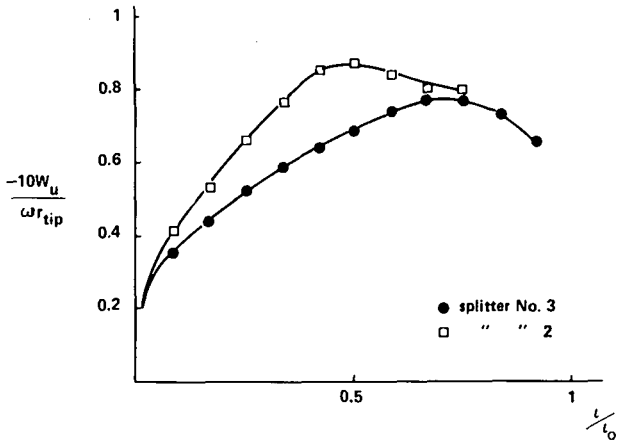


Fig. 10 Circumferential velocity profiles just upstream of No. 2 splitter leading edge—simple turbulence model

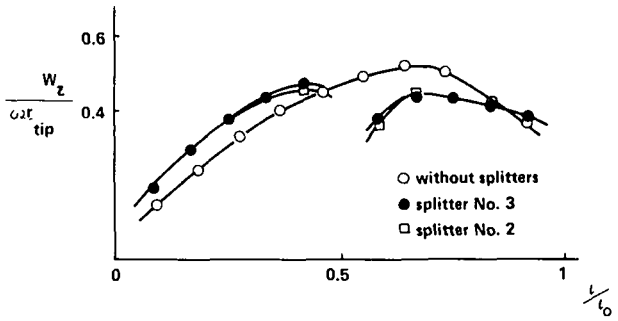


Fig. 11 Axial velocity profile at station 2—simple turbulence model

The above method is not very accurate though in predicting the wake growth because, as Eckardt [6] has shown, at the suction side of the blade high entropy fluid is accumulated. This fluid is transported at the suction side by the secondary flow which results from the interaction of rotation with the boundary layers. In the present approach, this mechanism is not included as it is the result of the three-dimensionality of the flow field but a similar accumulation of entropy can be obtained by using the turbulence model introduced in Section 2. The large circumferential gradients of μ_t can reproduce the large entropy gradients responsible for the growth of the wake.

8 Conclusions

The matrix through flow analysis has been extended to cover flows with stagnation points to the flow field as in the case of blade-to-blade calculations of the flow in a centrifugal compressor impeller. This is achieved by showing that entropy gradients at the stagnation point are zero thus removing the instability inherent in the matrix through flow analysis.

Using the above method then, the flow on a blade-to-blade stream surface of a centrifugal compressor impeller is predicted for isentropic flow and by using a simple turbulence model. The splitter has the same geometry as the full blade. The distance between the leading edge of the splitter and the eye of the impeller has been changed, and the flow for three different distances has been obtained.

It has been shown that the development of the flow within each channel is mainly affected by the circumferential component of velocity near the leading edge of the splitter. This, therefore, suggests that changes in geometry around the leading edge will produce changes in the flow inside the impeller.

It has also been shown that the distance between the eye and the leading edge of the splitter does not greatly affect the flow in the impeller studied as long as the leading edge is within the axial part of the impeller. This is basically due to the high solidity of the impeller at the inducer and may not apply to every impeller.

The presence of splitters in the flow has been shown to decrease the width of the suction side boundary layer. This, of course, may not be the case when the secondary flow effects are introduced into the flow, although the basic result of the secondary flow, which is the accumulation of high entropy fluid into the suction side, is reproduced by the turbulence model used.

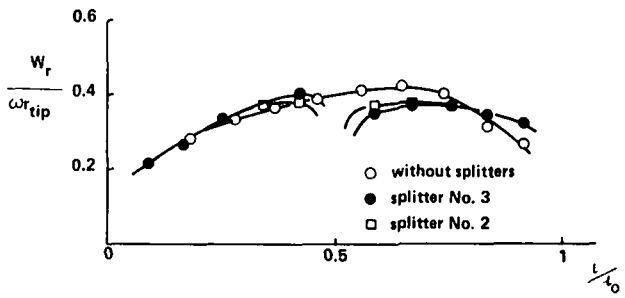


Fig. 12 Radial velocity profile at station 3—simple turbulence model

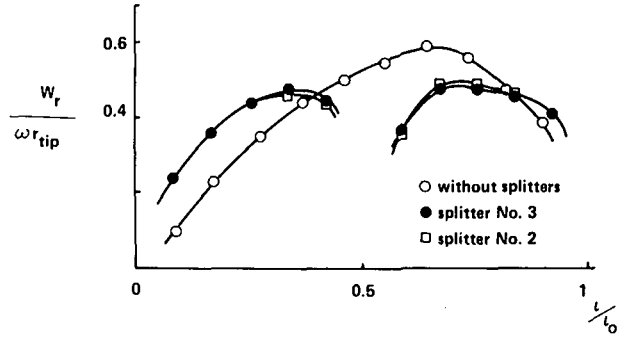


Fig. 13 Radial velocity profile at station 4—simple turbulence model

Downloaded 01 Jun 2010 to 171.66.16.58. Redistribution subject to ASME license or copyright; see http://www.asme.org/terms/Terms_Use.cfm

9 Acknowledgments

This work was carried out under contract with the Ministry of Defence. I particularly wish to thank Professor R. C. Baker of Cranfield Institute of Technology and Mr. P. M. Came of the National Gas Turbine Establishment for their interest, advice and encouragement.

References

1 Stanitz, J. D., "Some Theoretical Aerodynamic Investigations of Impellers in Radial and Mixed Flow Centrifugal Compressor Impellers," *Trans. ASME,* 74, 1972, p. 473.

2 Krimerman, Y. and Adler, D., "The Complete Three-Dimensional Calculation of the Compressible Flow Field in Turbo Impellers," *Journal of Mechanical Engineering Science,* 20, 1978, p. 149.

3 Goulas, A., "On the Internal Flow in Centrifugal Compressor Impellers," London University, Ph.D. Thesis, 1977.

4 Launder, B. and Spalding, D. B., "The Numerical Computation of Turbulent Flows," *Computer Methods in Applied Mechanics and Engineering, 3,* 1974, p. 269.

5 Bosman, C. and Marsh, H., "An Improved Method for Calculating the Flow in Turbomachinery Using a Consistent Loss Model," *Journal of Mechanical Engineering Science,* 16, 1974, p. 25.

6 Eckardt, D., "Detailed Flow Investigation Within a High Speed Centrifugal Compressor Impeller," ASME *Journal of Fluid Engineering,* 98, 1976, p. 390.

Downloaded 01 Jun 2010 to 171.66.16.58. Redistribution subject to ASME license or copyright; see http://www.asme.org/terms/Terms_Use.cfm

Z. Kovats

Senior Scientist,
Mechanics Department,
Westinghouse Electric Corporation,
Research and Development Center,
Pittsburgh, PA 15235

Interferometrically Measured Aerodynamic Forces on a Vibrating Turbine Blade Group

The instantaneous aerodynamic force and force center during a vibration cycle were determined from interferometrically measured pressure distributions around the leading blade of a low pressure turbine blade group vibrating in the tangential, axial or twist modes. The corresponding reduced frequencies were 0.0796, 0.1088 and 0.1312, and the inlet flow Mach number was 0.59 in all tests. The energy exchange per vibration cycle between the air flow and the leading blade of a group, and the lift and drag dynamic loops were determined for each of the three vibration modes. The periodic aerodynamic force coefficients were nearly sinusoidal for the axial and torsional modes but not for the tangential mode. At large negative flow incidence, the four-blade group tested is strongly unstable in the twist mode, weakly unstable in the axial mode, and strongly stable in the tangential mode. The experimental results can be used to investigate the validity of analytical predictions of the aerodynamic forces on a vibrating low pressure blade group.

1 Introduction

The instantaneous aerodynamic forces on the leading blade in a low pressure turbine blade group vibrating in the tangential, axial or twist mode were determined interferometrically during the vibration cycle. Records of the instantaneous gas density distribution around the blade were made with a Mach Zehnder interferometer at 24 equally-spaced instants during a vibration cycle. Evaluation of these records (interferograms) yielded the time histories of the distributed pressure around the blade and therefore the aerodynamic forces acting on the blade.

The purpose of these tests was to obtain experimental data on the instantaneous aerodynamic forces on the leading blade of a vibrating blade group so that analytical methods for predicting instantaneous blade forces during stall flutter or normal operation can be verified and improved.

The computer program used for evaluating the aerodynamic forces and the energy exchange between air flow and blade is discussed together with the experimental results for the three test conditions.

The inlet flow conditions for the tests were selected so that the blade group was deep inside the twist-mode and axial-mode unstable regions determined earlier by the average power flow method [1]. The inlet flow Mach number was 0.59 and the exit flow Mach number ranged between 0.55 and 0.60 in the reported tests. The inlet flow Mach number was varied between 0.2 and 0.9 in other tests with negative flow incidence in the range of 0 and −47.5 deg, and the exit Mach number was varied between 0.6 and 2 in tests with unstalled flow. The inlet flow angles were 160, 175 and 170 deg and the reduced frequencies were 0.0796, 0.1088 and 0.1312 for the tangential, axial and twist modes of vibration, respectively. The side blade groups were clamped to prevent them from vibrating.

Contributed by the Gas Turbine Division and presented at the Winter Annual Meeting, New York, NY, December 2–7, 1979 of THE AMERICAN SOCIETY OF MECHANICAL ENGINEERS. Manuscript received at ASME Headquarters July 25, 1979. Paper No. 79-WA/GT-1.

The interferometrically obtained energy exchange between the air flow and the leading blade in the group is −0.14255, 0.09578 or 0.5952 joules/m, and this energy contribution is 23, 34, or 46 percent of the total energy exchange between air flow and blade group measured by the power flow method, respectively, for the tangential, axial or twist mode of vibration.

The blade group consisted of four rigid uniform cross section, model low pressure blades vibrating in various modes in a two-dimensional steady and uniform air flow. A detailed description of the dynamic cascade and blowdown wind tunnel test facility is given in [1].

The work presented here is part of the experimental study initiated in 1970 which found the effects of flow, blading and vibration parameters on blade group instability and aerodynamic damping. It is the first time that the aerodynamic damping or energy per vibration cycle has been measured interferometrically on a blade group vibrating with high frequency and large amplitude at a stalling flow condition.

2 Test Setup

A rigid model blade group was flexibly mounted in a blowdown wind tunnel simulating the tangential, axial or twist modes of vibration of low pressure turbine blade groups. The blowdown wind tunnel is described in [1]. The vibration frequencies were 142.6, 195.0 and 235.1 Hz; the vibration amplitudes were 0.1524 cm S.P., 0.1524 cm S.P. and 0.075 radians S.P.; and the reduced frequencies $\pi fc/(aM_1) = 0.0796$, 0.1088 and 0.1312 for the first, second, and twist modes, respectively.

The rigid uniform cross section airfoils having the profile shown in Fig. 1 were held together by side bars to form a rigid group as shown in Fig. 2. The cascade parameters were: stagger angle $\theta_s = 42$ deg, camber angle $\theta_c = 32$ deg, and pitch/chord ratio $s/c = 0.87$. The side blade groups were clamped to prevent them from vibrating.

During the air blowdown the constant vibration amplitude of the middle blade group was maintained by an electromagnetic shaker and

Copyright © 1980 by ASME

Downloaded 01 Jun 2010 to 171.66.16.58. Redistribution subject to ASME license or copyright; see http://www.asme.org/terms/Terms_Use.cfm

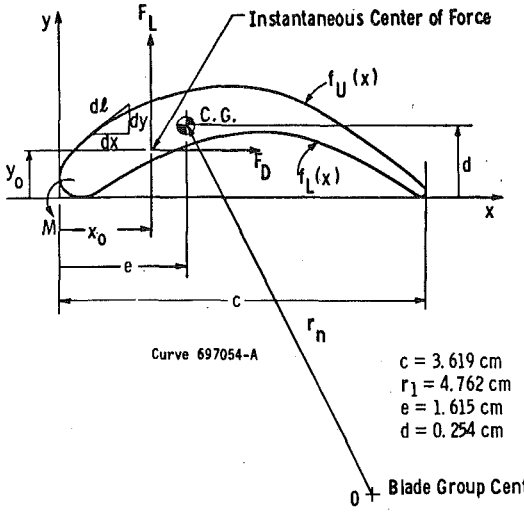


Fig. 1 Blade profile and the location of total instantaneous aerodynamic lift and drag forces and of blade section center of gravity

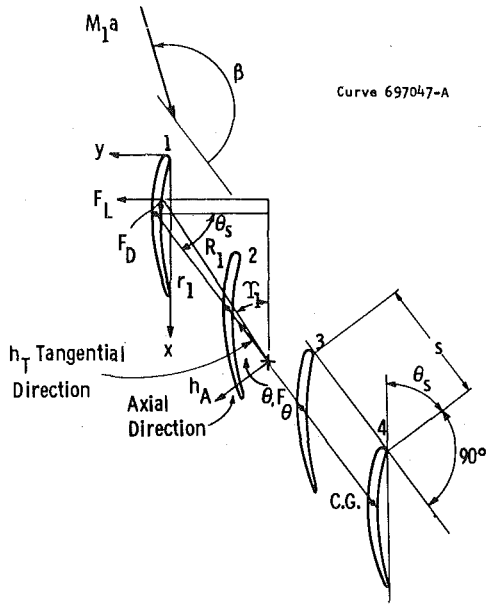


Fig. 2 Blade group geometry, forces and motions (see Fig. 1)

automatic gain control system. The inlet flow Mach number was calculated from pressures obtained from a pitot-static tube located 18 cm upstream from the center of the middle blade group. It was assumed that the inlet flow pressure and temperature in the upper part of the view field are the same as they are at the pitot-static tube and thermocouple locations. The inlet flow total temperature was 295 ± 3 K in all of the tests; the inlet flow pressure was 102.73 kPa, 108.94 kPa and 107.56 kPa; and the inlet flow angle was β = 160, 175 and 170 deg in the tangential, axial and twist mode tests, respectively.

3 Interferometric Data

At each predetermined instant in the vibration cycle, six interferograms were taken at the same inlet flow Mach number, inlet flow angle and vibration amplitude. Of these six interferograms, five were taken with the infinite-fringe setting and one was taken with a finite-fringe setting. Infinite-fringe interferograms show the magnitude of the gas density variation with good resolution, but do not show whether the pressure is increasing or decreasing. Finite-fringe interferograms give the absolute value of density change with less accuracy than the infinite-fringe interferograms, but they give additional information about the direction of the density gradient. The two types of interferograms complement each other. Both types were used for finding the pressure distribution around the blades. A typical infinite-fringe interferogram is shown in Fig. 3. Interferograms were taken of the flow field around the leading blade of the group only because the view of that blade is blocked the least by the blade support bars.

The coordinates of the fringe and blade intersection points were measured with an optical-electromechanical instrument. From this information and inlet flow data, the pressure at various specified fringe order points on the blade surface was computed. The pressures at intermediate points were then obtained by linear interpolation. This was done for 101 points along the chord length. These calculated

Nomenclature

a = sonic velocity

C_D = drag coefficient of a blade, $C_D = \dfrac{F_D}{\frac{1}{2}\rho_1 M_1^2 a^2 Lc}$

C_L = lift coefficient of a blade, $C_L = \dfrac{F_L}{\frac{1}{2}\rho_1 M_1^2 a^2 Lc}$

C_θ = moment coefficient of blade group

c = chord length of blade

d = height of blade CG above chord line

e = chordwise distance of blade CG from blade leading edge

E_D = energy input by the drag force per unit span

E_L = energy input by the lift force per unit span

E_t = total energy input to the blade group by the lift and drag forces

E_{max} = total vibration energy stored in the vibrating blade group

F_D = blade drag force per unit span parallel to chord line x

F_L = blade lift force per unit span perpendicular to chord line x

F_M = aerodynamic moment per unit span on blade

F_θ = aerodynamic moment per unit span on blade group about blade group center

f_{nT} = tangential mode natural frequency of blade group, Hz

$f_L(x)$ = function that describes lower (concave) blade surface

$f_U(x)$ = function that describes upper (convex) blade surface

$f_L'(x)$ and $f_U'(x)$ = derivatives of $f_L(x)$ and $f_U(x)$ functions with respect to x, respectively

h_A = single-peak amplitude of vibration in axial direction

h_T = single-peak amplitude of vibration in tangential direction

k_T = stiffness of blade group in tangential direction

k_θ = rotational stiffness of blade group

L = blade span

M = aerodynamic moment on blade about the origin of the coordinate axes (see Fig. 1)

M_1 = Mach number of inlet flow

n = sample size and blade number in the group, as shown in Fig. 2

p_L = pressure on the lower (concave) surface of blade

p_U = pressure on the upper (convex) surface of blade

R_n = distance between the blade group center and the force center of blade n, (see Fig. 2)

r_n = distance between blade group center and center of gravity of blade section

V_1 = inlet flow velocity

x = coordinate axis in chord direction

x_0 = location of center of force in x direction

y = coordinate axis in lift direction

y_0 = location of center of force in y direction

β = inlet flow angle

β_i = instantaneous inlet flow angle

δ = aerodynamic damping of vibrating blade group, equivalent log decrement $\delta = \pi F_\theta/k_\theta\theta_0$ or $\delta = \pi F_T/k_T h_T$

θ_0 = single-peak amplitude of torsional vibration

θ_s = blade stagger angle

θ_c = camber angle

ρ_1 = inlet flow density

γ_n = angle between chord line and the line R_n connecting the blade group center and the center of force on an airfoil

ϕ = vibration phase angle

ω = circular vibration frequency, rad/s

Downloaded 01 Jun 2010 to 171.66.16.58. Redistribution subject to ASME license or copyright; see http://www.asme.org/terms/Terms_Use.cfm



Fig. 3 Typical inferogram taken at phase angle $\phi = 255$ deg of the tangential mode of vibration

pressures were averaged for similar test runs. It is believed that these averaged values accurately represent the actual pressure distribution on the blade surface. Typical average pressure distributions on both the convex and concave surfaces are given in Fig. 4. The computer program also calculated the standard deviation of pressure that ranged between 0.689 kPa (0.1 psi) and 4.14 kPa (0.6 psi) for the five pressure values obtained at each selected vibration phase angle.

4 Aerodynamic Coefficients Evaluated from Interferometric Data

The output of the computer program discussed in the appendix is discussed for the interferometric data of the first, second, and twist modes of vibration in this section.

The pressure distribution along the surface of blade 1 was found from interferograms taken at successive points in the vibration cycle, as discussed previously. From the set of interferograms taken under the same conditions, the average value of instantaneous pressure at each point on the blade surface was calculated by the computer. A typical pressure distribution curve is shown in Fig. 4. The resulting average pressure distribution curves are further used to calculate the instantaneous dimensionless per-unit-span aerodynamic blade forces C_L, C_D and moment C_M. These force coefficients per blade versus time or blade vibration phase angle are shown in Fig. 5 for the tangential mode of vibration. The total aerodynamic tangential force coefficient for the blade group is approximately four times larger than the values shown in the case of a four blade per group configuration. The average magnitude of the lift coefficient is about seven times larger than the drag coefficient. The lift and drag coefficients change periodically with the blade vibration; however, the test points of the lift and drag coefficients do not form a smooth curve. At the present time, it is not known whether the curves, as shown in Fig. 5, are the true form of these periodic functions. Since some scatter is present, even though the individual points are averages of five interferograms, the curves should probably be smoothed. The location of the instantaneous force center versus blade vibration phase angle is shown in Fig. 6.

The total aerodynamic energy exchange between the leading blade of the group and air flow versus vibration phase angle ϕ is shown in

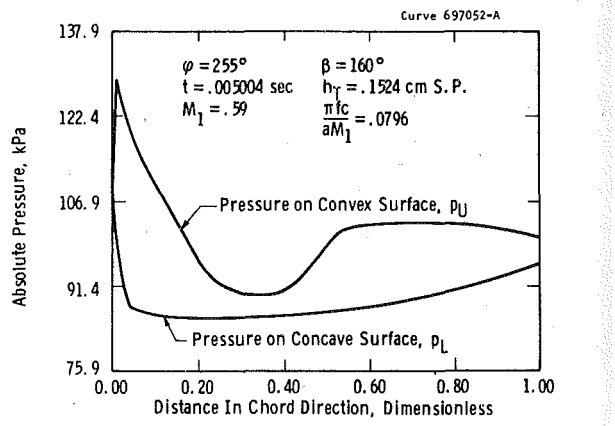


Fig. 4 Instantaneous pressure distribution on the concave and convex sides of the first blade in a model turbine blade group vibrating in first mode

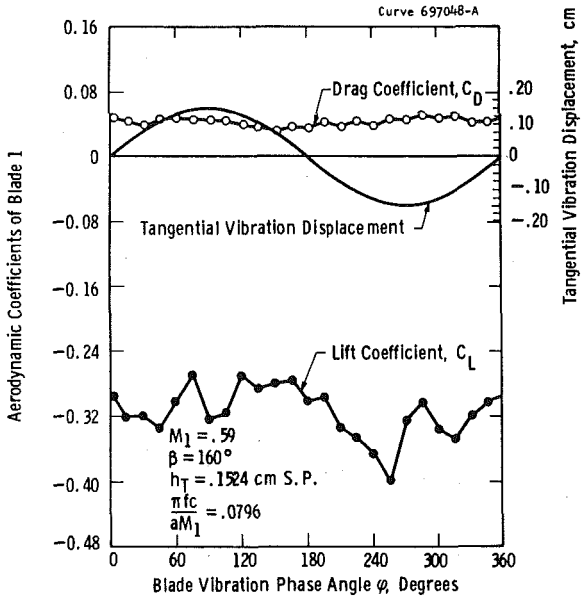


Fig. 5 Instantaneous aerodynamic lift and drag coefficients versus time during a tangential vibration cycle. The instantaneous location of the force center is shown in Fig. 6

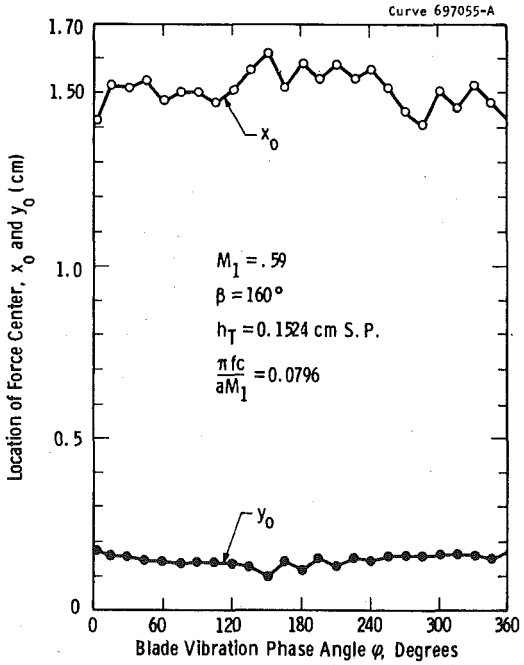


Fig. 6 Instantaneous location of force center during a tangential vibration cycle

Downloaded 01 Jun 2010 to 171.66.16.58. Redistribution subject to ASME license or copyright; see http://www.asme.org/terms/Terms_Use.cfm

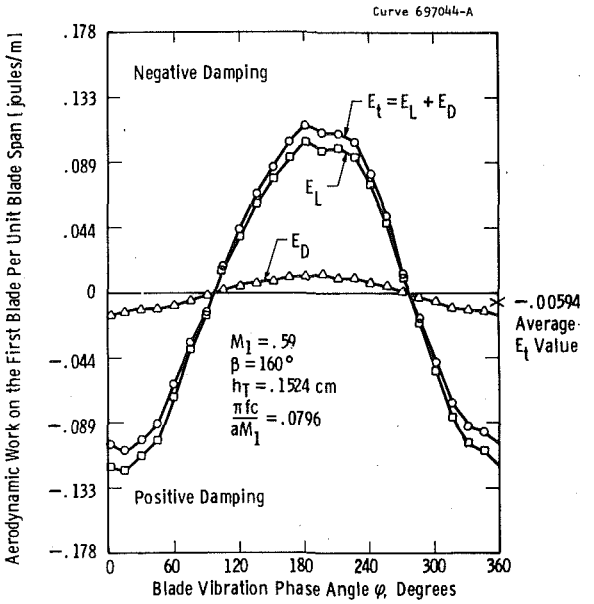


Fig. 7 Lift and drag force contributions to the aerodynamic work on the first blade of the model blade group during each 1/24 of the tangential-mode vibration cycle. Total work per cycle = −0.14255 joules/m

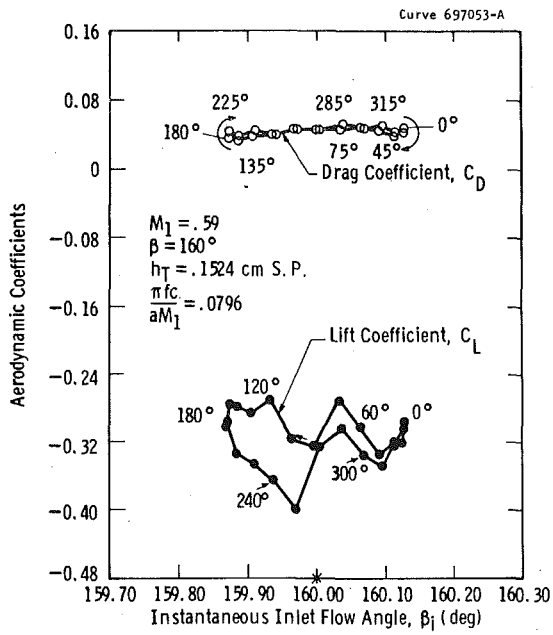


Fig. 8 Instantaneous lift and drag coefficients versus instantaneous inlet flow angle for the first blade of the model blade group vibrating in the tangential mode

Fig. 7. The individual components of the energy exchange caused by the lift and drag forces are also shown in Fig. 7. The contribution of drag force to the total instantaneous energy exchange between air flow and blade is about one-eighth of the lift force contribution. The energy exchange per vibration cycle is:

$$\sum_{0}^{\phi=360\ \text{deg}} E_{L1} = -0.11346\ \text{joules/m}\ (-0.0255\ \text{lb in/in})$$

$$\sum_{0}^{\phi=360\ \text{deg}} E_{D1} = -0.02909\ \text{joules/m}\ (-0.00654\ \text{lb in/in}) \quad (1)$$

by the lift and drag force, respectively. Note that the negative sign indicates that energy flows from the blade to the air flow (positive damping). This results from the sign convention adopted here for the positive force and displacement directions.

The total energy exchange between blade group and air flow is calculated from the aerodynamic damping $\delta = 0.0176$ measured by the power flow method:

$$\sum_{n=1}^{4}\sum_{\phi=0}^{360\ \text{deg}} (E_{Ln} + E_{Dn}) = -\frac{2E_{\max}\delta_{\text{aero}}}{L}$$

$$= -\frac{2(1.362\ \text{joules})(0.0176)}{(0.0762\ \text{m})} = -0.6292\ \text{joules/m} \quad (2)$$

where $E_{\max}$ is the maximum vibration strain energy stored in the vibrating blade group, which is equal to:

$$E_{\max} = \frac{k_T h_T^2}{2} = \frac{\left(1173097\ \frac{\text{newton}}{\text{m}}\right)(0.001524\ \text{m})^2}{2}$$

$$= 1.362\ \text{joules}\ (12.06\ \text{lb in}) \quad (3)$$

Therefore, the first-blade contribution to the total energy input per vibration cycle is:

$$\frac{\sum_{0}^{\phi=360\ \text{deg}} (E_{L1} + E_{D1})}{\sum_{n=1}^{4}\sum_{\phi=0}^{360\ \text{deg}} (E_{Ln} + E_{Dn})} = \frac{-0.14255}{-0.6292} = 0.23 \quad (4)$$

Interferometric results show that a sizable aerodynamic moment acts on the blade; however, no work is done by this moment when the blade vibrates in a pure tangential mode.

The periodically varying aerodynamic force coefficients C_L and C_D can be plotted against β_i, the instantaneous inlet flow angle relative to a vibrating blade (the inlet flow angle as seen by an observer located on the CG of the vibrating leading blade). The dynamic loops for the aerodynamic coefficients C_L and C_D are shown in Fig. 8. Fig. 8 shows that the drag dynamic loop has a much smaller area than the lift dynamic loop. It should be emphasized that the aerodynamic loop area is not proportional to the energy exchange per cycle in the case of tangential or axial mode vibration. (Aerodynamic loop area is approximately proportional to the energy exchange per cycle in the case of twist mode vibration if the incremental inlet flow angle is proportional to blade group rotation angle alone, with only negligible contribution from blade group angular velocity.) The area enclosed by a plot of force versus vibration displacement in the direction of the force would be proportional to the energy exchange. For tangential and axial mode vibration, the incremental instantaneous inlet flow angle is proportional to the vibration velocity.

Similar sets of curves are shown for the axial and twist modes of vibration in the following pages.

The aerodynamic coefficients for the axial mode vibration versus time or blade vibration phase angle are shown in Fig. 9. The lift and drag coefficients show a large first harmonic sinusoidal component. The location of the instantaneous force center versus blade vibration phase angle is shown in Fig. 10. The total aerodynamic energy exchange between the first blade and air flow versus vibration phase angle ϕ is shown in Fig. 11, and the axial mode dynamic loop is shown in Fig. 12.

The total energy exchange between the blade group and air flow measured by the power flow method for the axial mode is 0.27970 joules/m (0.06288 lb-in/in) which corresponds to aerodynamic damping $\delta_{\text{aero}} = -0.0045$ log decrement. The interferometrically-obtained energy exchange by the leading blade in the group is 0.09578 joules/m (0.012153 lb-in/in). Therefore, the first blade contribution to the total aerodynamic energy exchange is 34 percent in the axial mode.

The aerodynamic coefficients for the twist-mode of vibration versus time or vibration phase angle are shown in Fig. 13. For the twist mode, the aerodynamic coefficients also show a large first harmonic sinusoidal component. The instantaneous location of the force center during a vibration cycle is shown in Fig. 14. The force center does not vary sinusoidally for the twist mode of vibration. The aerodynamic energy exchange between blade and air flow versus vibration phase angle is shown in Fig. 15, and the twist mode dynamic loop is shown in Fig. 16.

The total energy exchange per cycle between the air flow and the torsionally-vibrating blade group measured by the power flow method

Downloaded 01 Jun 2010 to 171.66.16.58. Redistribution subject to ASME license or copyright; see http://www.asme.org/terms/Terms_Use.cfm

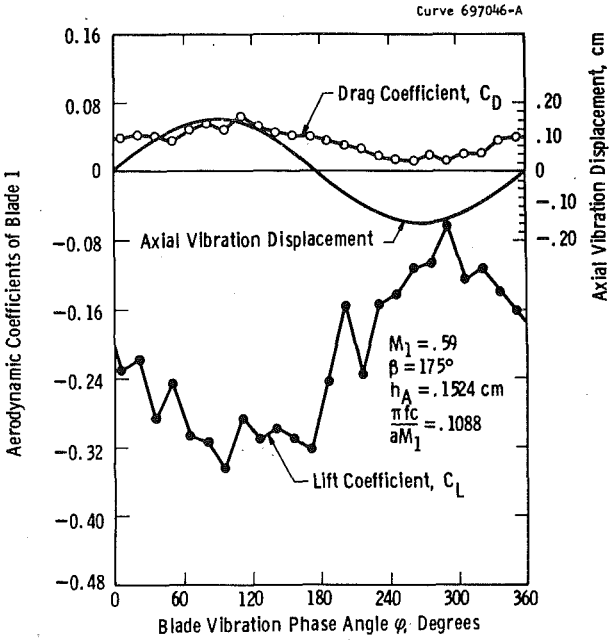


Fig. 9 Instantaneous aerodynamic lift and drag coefficients versus time during an axial vibration cycle. The instantaneous location of force center is given in Fig. 10

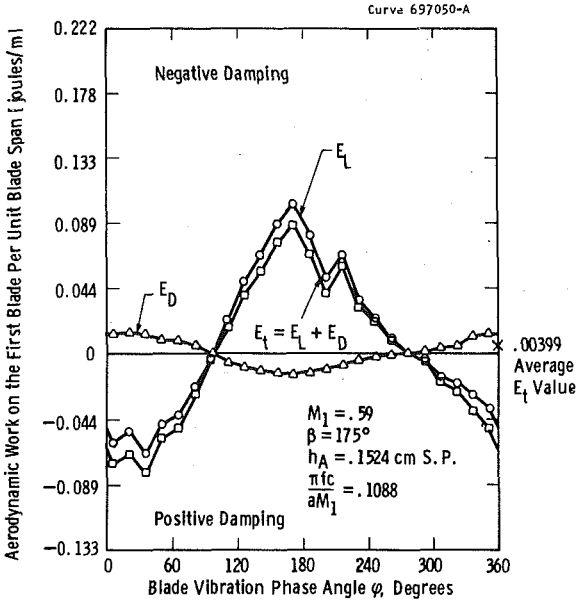


Fig. 11 Lift and drag force contributions to the aerodynamic work on the first blade of the model blade group during each 1/24 of the axial vibration cycle. Total work per cycle = 0.09578 joules/m

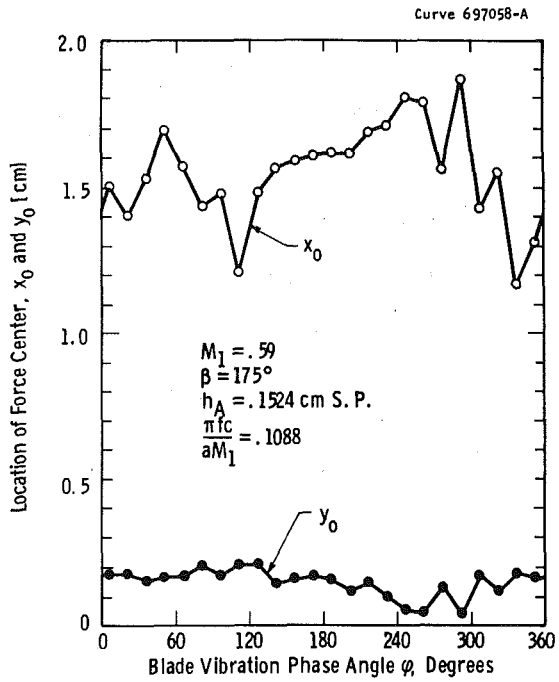


Fig. 10 Instantaneous location of force center during an axial vibration cycle

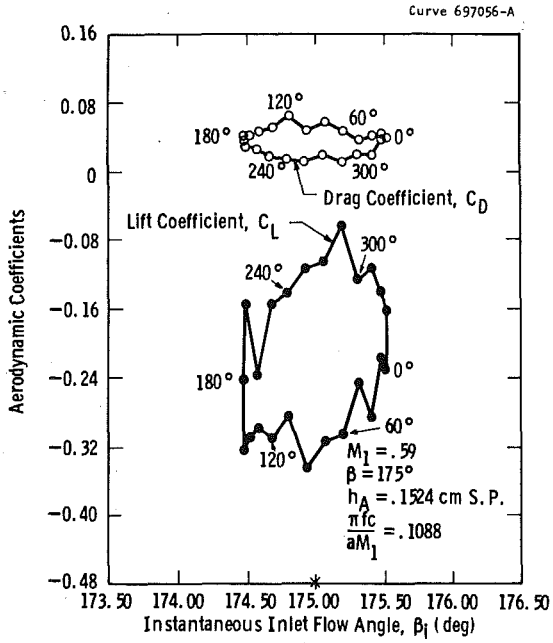


Fig. 12 Instantaneous lift and drag coefficients versus instantaneous inlet flow angle for the first blade of the model blade group vibrating in the axial mode

is 1.2777 joules/m (0.2872 lb-in/in) which corresponds to aerodynamic damping $\delta_{aero} = -0.015$ log decrement, and the interferometrically obtained aerodynamic energy exchange per cycle for the leading blade is 0.5952 joules/m (0.13382 lb-in/in). Therefore, the first blade contribution to the total aerodynamic energy exchange is 46 percent in the twist mode.

5 Conclusions

1 Time histories of the aerodynamic forces on a vibrating model turbine blade can be determined interferometrically.

2 At large negative flow incidence, the four-blade group tested is strongly unstable in the twist mode, weakly unstable in the axial mode, and strongly stable in the tangential mode.

3 The contribution of the leading blade to the total aerodynamic energy exchange per vibration cycle of a blade group vibrating in the tangential, axial, or twist mode is 23, 34 or 46 percent, respectively, when the inlet flow Mach number $M_1 = 0.59$ at large negative incidence.

4 The peak aerodynamic power flow during the vibration cycle is much larger than the average power flow per cycle. See Figs. 7, 11, and 15.

5 The twist-mode and axial-mode aerodynamic forces are nearly sinusoidal and close to 180 deg out-of-phase with the vibration displacement. The fundamental component of the tangential-mode aerodynamic force is small compared to the average value.

6 In stalled flow, the average position of the instantaneous force center is about 42 percent of the chord length from the leading edge, but it varies in position substantially at some vibration phase angles.

Downloaded 01 Jun 2010 to 171.66.16.58. Redistribution subject to ASME license or copyright; see http://www.asme.org/terms/Terms_Use.cfm

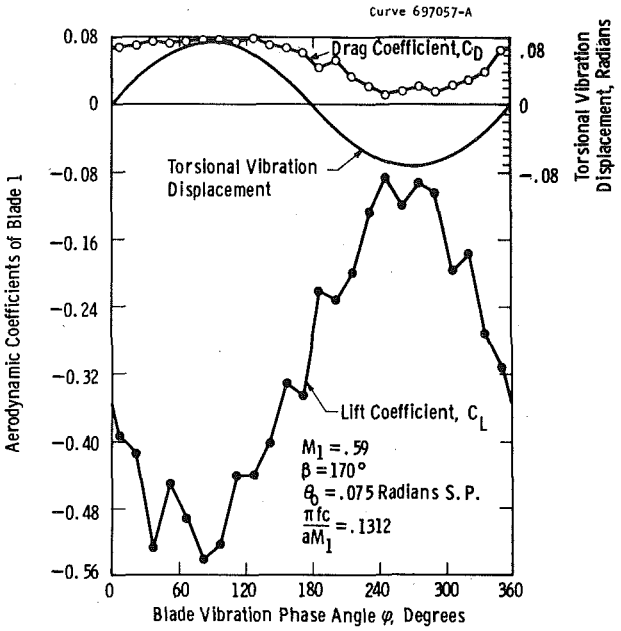


Fig. 13 Instantaneous aerodynamic lift and drag coefficients versus time during a torsional vibration cycle. The instantaneous location of force center is given in Fig. 14

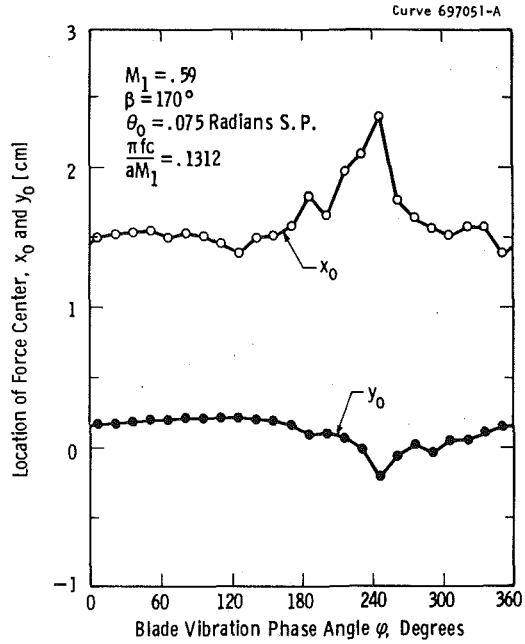


Fig. 14 Instantaneous location of force center during a torsional vibration cycle

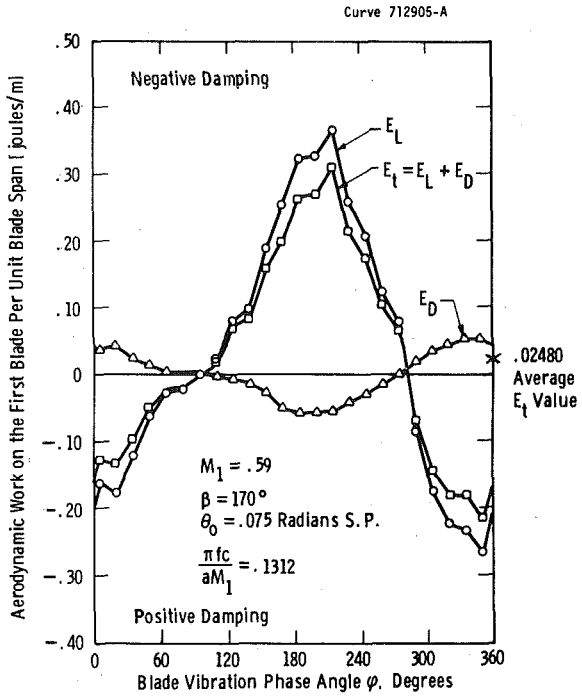


Fig. 15 Lift and drag force contributions to the aerodynamic work on the first blade of the model blade group during each 1/24 of the torsional vibration cycle. Total work per cycle = 0.5952 joules/m

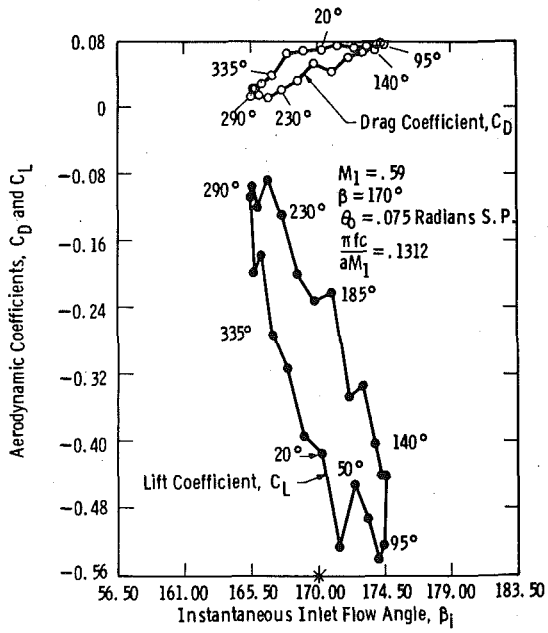


Fig. 16 Instantaneous lift and drag coefficients versus instantaneous inlet flow angle for the first blade of the model blade group vibrating in the torsional mode

Reference

1 Kovats, Z., "Dynamic Cascade Facility and Methods for Investigating Flow-Excited Vibration and Aerodynamic Damping of Model Low Pressure Blade Groups," ASME Paper No. 79-WA/GT-6.

APPENDIX

The computer program discussed in the following paragraphs calculates the aerodynamic blade force, the aerodynamic moment and the energy exchange between air flow and each blade of the group from the interferometrically obtained instantaneous pressure distribution on the blade surfaces. In this section, the discussion includes the aerodynamic forces and moments on both a single blade and a group of blades, but experimental results are presented for one blade only.

The aerodynamic blade forces, moments and their direction relative to the blade section are shown in Figs. 1 and 2. In these figures, the following are also shown: the center of forces, the center of gravity of the blade sections, the positive directions of the vibration displacements and the rotational center of the blade group.

The interferometrically-determined blade forces and moments about the origin of the coordinate axes, both per inch of blade length, can be determined from the air pressure distribution on the blade surfaces of each blade using the following formulas (see Fig. 1):

$$F_L = \int_0^c p_L(x)dx - \int_0^c p_u(x)dx \qquad \text{(A1)}$$

$$F_D = \int_0^c p_u(x)f_u'(x)dx - \int_0^c p_L(x)f_L'(x)dx \qquad \text{(A2)}$$

Downloaded 01 Jun 2010 to 171.66.16.58. Redistribution subject to ASME license or copyright; see http://www.asme.org/terms/Terms_Use.cfm

$$M = \int_0^c p_L(x)x\,dx + \int_0^c f_L(x)f_L'(x)p_L(x)\,dx - \int_0^c p_u(x)x\,dx - \int_0^c f_u(x)f_u'(x)p_u(x)\,dx \quad \text{(A3)}$$

The coordinates x_0 and y_0 are calculated as follows:

$$x_0 = \frac{\int_0^c p_L(x)x\,dx - \int_0^c p_u(x)x\,dx}{F_L} \quad \text{(A4)}$$

$$y_0 = \frac{-\int_0^c p_L(x)f_L(x)f_L'(x)\,dx + \int_0^c p_u(x)f_u(x)f_u'(x)\,dx}{F_D} \quad \text{(A5)}$$

The total aerodynamic forces and moment for the blade group are calculated differently for the various modes of vibration. The best way to find the total aerodynamic force on the blade group is by summing up the actual forces for each blade in the group. The aerodynamic flow around each blade is different because the adjacent blade motions are different for each blade. For example, in the first vibration mode, all of the blades of the middle blade group move together, but the side blade groups are clamped. Therefore, the actual aerodynamic force on the first blade is somewhat different from the forces on the second, third and fourth blades. In the twist vibration mode, each blade in the vibrating group has a different vibration amplitude and, therefore, a different relative flow incidence. Extensive experimental evidence shows that the unsteady aerodynamic force depends strongly on the relative flow incidence (Fig. 16), and that this force varies nearly linearly with the vibration amplitude. The twist mode aerodynamic moment for the blade group is calculated as follows:

$$F_\theta = -\sum_{n=1}^{n_t} \{F_{Dn}[r_n \cos(\theta_s) - d + y_0] + F_{Ln}[r_n \sin(\theta_s) + e - x_0]\} \quad \text{(A6)}$$

where F_{Dn} and F_{Ln} are determined as functions of time from interferograms for each blade while the blade group is vibrating in the twist mode.

The instantaneous force center is assumed to be stationary with respect to the blade during a small time increment $t_2 - t_1$, but the blade CG is not stationary relative to a stationary observer when the blades are vibrating. The incremental displacements of the instantaneous force center in the directions of forces F_D and F_L (in the x and y directions, respectively) in a time interval $(t_2 - t_1)$ are calculated as:

$$\Delta x_n = [-R_n\theta_0 \sin(\gamma_n) + h_A \cos(\theta_s) - h_T \sin(\theta_s)] \times [\sin \omega t_2 - \sin \omega t_1] \quad \text{(A7)}$$

$$\Delta y_n = [-R_n\theta_0 \cos(\gamma_n) + h_A \sin(\theta_s) + h_T \cos(\theta_s)] \times [\sin \omega t_2 - \sin \omega t_1] \quad \text{(A8)}$$

$$R_n = \frac{r_n}{|r_n|}\sqrt{[r_n \cos(\theta_s) - d + y_0]^2 + [r_n \sin(\theta_s) + e - x_0]^2} \quad \text{(A9)}$$

$$\gamma_n = \tan^{-1}\left(\frac{r_n \cos(\theta_s) - d + y_0}{r_n \sin(\theta_s) + e - x_0}\right) \quad \text{(A10)}$$

The energy input for each blade during a time increment $(t_{i+1} - t_i)$ by F_{Dn} and F_{Ln} forces is calculated. The energy input to a blade by the lift and drag forces are:

$$E_{Ln} = F_{Ln}\Delta y \qquad E_{Dn} = F_{Dn}\Delta x \quad \text{(A11)}$$

where F_{Ln} and F_{Dn} are functions of ωt.

The computer program also calculates the instantaneous drag, lift and moment coefficients per unit span for a blade and the moment coefficient per unit span for the blade group. Each force coefficient per unit length is defined in terms of the dynamic pressure $\rho v_1^2/2$ such that $C = 2F/\rho V_1^2 c$. By using the relation $a^2 = \gamma p/\rho$ and $\gamma = 1.40$, the various force and moment coefficients of the blade become:

$$C_L = \frac{F_L}{0.70\, p_0 M_1^2 c} \qquad C_D = \frac{F_D}{0.70\, p_0 M_1^2 c} \qquad C_M = \frac{F_M}{0.70\, p_0 M_1^2 c^2} \quad \text{(A12)}$$

The moment coefficient of a blade group is:

$$C_\theta = \frac{F_\theta}{0.70\, p_0 M_1^2 c^2} \quad \text{(A13)}$$

The instantaneous inlet flow angle β_1 relative to the blade CG is calculated for each blade in the group from:

$$\beta_i = \frac{180}{\pi}\left\{\pi + \theta_0 \sin\phi - \tan^{-1}\left[\frac{M_1 a \sin\frac{\pi}{180}(180 - \beta) - h_A\,\omega\cos\phi + r_n\theta_0\omega\cos\phi}{M_1 a \cos\frac{\pi}{180}(180 - \beta) + h_T\,\omega\cos\phi}\right]\right\} \quad \text{(A14)}$$

Downloaded 01 Jun 2010 to 171.66.16.58. Redistribution subject to ASME license or copyright; see http://www.asme.org/terms/Terms_Use.cfm

$$M = \int_0^c p_L(x)x\,dx + \int_0^c f_L(x)f_L'(x)p_L(x)\,dx - \int_0^c p_u(x)x\,dx - \int_0^c f_u(x)f_u'(x)p_u(x)\,dx \quad \text{(A3)}$$

The coordinates x_0 and y_0 are calculated as follows:

$$x_0 = \frac{\int_0^c p_L(x)x\,dx - \int_0^c p_u(x)x\,dx}{F_L} \quad \text{(A4)}$$

$$y_0 = \frac{-\int_0^c p_L(x)f_L(x)f_L'(x)\,dx + \int_0^c p_u(x)f_u(x)f_u'(x)\,dx}{F_D} \quad \text{(A5)}$$

The total aerodynamic forces and moment for the blade group are calculated differently for the various modes of vibration. The best way to find the total aerodynamic force on the blade group is by summing up the actual forces for each blade in the group. The aerodynamic flow around each blade is different because the adjacent blade motions are different for each blade. For example, in the first vibration mode, all of the blades of the middle blade group move together, but the side blade groups are clamped. Therefore, the actual aerodynamic force on the first blade is somewhat different from the forces on the second, third and fourth blades. In the twist vibration mode, each blade in the vibrating group has a different vibration amplitude and, therefore, a different relative flow incidence. Extensive experimental evidence shows that the unsteady aerodynamic force depends strongly on the relative flow incidence (Fig. 16), and that this force varies nearly linearly with the vibration amplitude. The twist mode aerodynamic moment for the blade group is calculated as follows:

$$F_\theta = -\sum_{n=1}^{n_t} \{F_{Dn}[r_n \cos(\theta_s) - d + y_0] + F_{Ln}[r_n \sin(\theta_s) + e - x_0]\} \quad \text{(A6)}$$

where F_{Dn} and F_{Ln} are determined as functions of time from interferograms for each blade while the blade group is vibrating in the twist mode.

The instantaneous force center is assumed to be stationary with respect to the blade during a small time increment $t_2 - t_1$, but the blade CG is not stationary relative to a stationary observer when the blades are vibrating. The incremental displacements of the instantaneous force center in the directions of forces F_D and F_L (in the x and y directions, respectively) in a time interval $(t_2 - t_1)$ are calculated as:

$$\Delta x_n = [-R_n\theta_0 \sin(\gamma_n) + h_A \cos(\theta_s) - h_T \sin(\theta_s)] \times [\sin \omega t_2 - \sin \omega t_1] \quad \text{(A7)}$$

$$\Delta y_n = [-R_n\theta_0 \cos(\gamma_n) + h_A \sin(\theta_s) + h_T \cos(\theta_s)] \times [\sin \omega t_2 - \sin \omega t_1] \quad \text{(A8)}$$

$$R_n = \frac{r_n}{|r_n|}\sqrt{[r_n \cos(\theta_s) - d + y_0]^2 + [r_n \sin(\theta_s) + e - x_0]^2} \quad \text{(A9)}$$

$$\gamma_n = \tan^{-1}\left(\frac{r_n \cos(\theta_s) - d + y_0}{r_n \sin(\theta_s) + e - x_0}\right) \quad \text{(A10)}$$

The energy input for each blade during a time increment $(t_{i+1} - t_i)$ by F_{Dn} and F_{Ln} forces is calculated. The energy input to a blade by the lift and drag forces are:

$$E_{Ln} = F_{Ln}\Delta y \qquad E_{Dn} = F_{Dn}\Delta x \quad \text{(A11)}$$

where F_{Ln} and F_{Dn} are functions of ωt.

The computer program also calculates the instantaneous drag, lift and moment coefficients per unit span for a blade and the moment coefficient per unit span for the blade group. Each force coefficient per unit length is defined in terms of the dynamic pressure $\rho v_1^2/2$ such that $C = 2F/\rho V_1^2 c$. By using the relation $a^2 = \gamma p/\rho$ and $\gamma = 1.40$, the various force and moment coefficients of the blade become:

$$C_L = \frac{F_L}{0.70\, p_0 M_1^2 c} \qquad C_D = \frac{F_D}{0.70\, p_0 M_1^2 c} \qquad C_M = \frac{F_M}{0.70\, p_0 M_1^2 c^2} \quad \text{(A12)}$$

The moment coefficient of a blade group is:

$$C_\theta = \frac{F_\theta}{0.70\, p_0 M_1^2 c^2} \quad \text{(A13)}$$

The instantaneous inlet flow angle β_1 relative to the blade CG is calculated for each blade in the group from:

$$\beta_i = \frac{180}{\pi}\left\{\pi + \theta_0 \sin\phi - \tan^{-1}\left[\frac{M_1 a \sin\frac{\pi}{180}(180 - \beta) - h_A\,\omega\cos\phi + r_n\theta_0\omega\cos\phi}{M_1 a \cos\frac{\pi}{180}(180 - \beta) + h_T\,\omega\cos\phi}\right]\right\} \quad \text{(A14)}$$

DISCUSSION

F. Sisto[1]

This paper, and its companion paper describing the experimental apparatus (79-WA/GT-6 "Dynamic Cascade Facility and Methods for Investigating Flow-Excited Vibration and Aerodynamic Damping of Model Low Pressure Blade Groups" by Z. Kovats) are an interesting and informative introduction to the engineering community of an intriguing new program for the acquisition of unsteady cascade flow data. A similar program was initiated years ago at the Gas Turbine Laboratory at M.I.T. using a single moving airfoil in a cascade of fixed neighbors. The present program is much more ambitious and results of practical interest, i.e., with moving half-group neighbors, are anticipated with interest.

Stemming from the uncertainty of cycle-to-cycle repeatability of the nonsteady components, whether due to physical flow variability or unavoidable random measurement errors, additional information on this question might be available from presenting the range of values of, say, the lift coefficient, in addition to the average obtained from 5 determinations. Presenting only the averaged data does not give all the information that is available.

As a middle ground towards obtaining more data with the present apparatus, short of oscillating the two end half-groups of blades one wonders whether the cascade blading could be reversed, or the interferometric window moved to the other side of the tunnel, so that data could be obtained for blade #4 in the lashed packet (assuming the data already obtained is for the blade labelled #1).

All in all, however, one has to recognize that the data received to date are very preliminary. Presuming the reliability to be good, one can look forward to the experimental results from parametric variations of the governing variables as useful and eagerly awaited information from this program.

[1] Department of Mechanical Engineering, Stevens Institute of Technology, Castle Point Station, Hoboken, NJ, 07030

Copyright © 1980 by ASME

Downloaded 01 Jun 2010 to 171.66.16.58. Redistribution subject to ASME license or copyright; see http://www.asme.org/terms/Terms_Use.cfm

Author's Closure

I wish to thank Dr. Sisto for his discussion and welcome the opportunity to provide further clarification.

To find the cycle-to-cycle repeatability of the nonsteady components, the standard deviation of pressure was calculated at each point on the blade surface from the following equation

$$\sigma = \left[\frac{\sum_{i=1}^{n} (p_i - \bar{p})^2}{n-1} \right]^{1/2}$$

where $\bar{p}$ is the average of n sample values. The standard deviation ranged between 0.7 and 3kPa for the five pressure values obtained at each vibration position. Typical values for $\bar{p}$ along the blade surfaces are shown in Fig. 4 of the paper.

Interferometric data for Blade 4 have not yet been obtained, but will be in the future. The test apparatus is built so that the observation windows can be moved to the proper position for measuring the gas density field around Blade 4, as shown in Fig. 2 of companion paper 79-WA/GT-6.

Downloaded 01 Jun 2010 to 171.66.16.58. Redistribution subject to ASME license or copyright; see http://www.asme.org/terms/Terms_Use.cfm

H. C. Simmons
Director of Engineering,
Gas Turbine Fuel Systems Division,
Parker Hannifin Corporation,
Cleveland, OH
Mem. ASME

The Prediction of Sauter Mean Diameter for Gas Turbine Fuel Nozzles of Different Types

Reviewing the more important published equations for predicting SMD for various types of fuel nozzles it is pointed out that there is no universal or common approach to cover different nozzle designs. In particular there is no effort to bridge the gap between pressure-atomizers and air-atomizers, especially the air-assisted simplex nozzle. Furthermore many of the equations provide no basis for estimating the effect of dimensions which is essential in modeling. An equation is presented, based on both new and published data, which satisfies these objections, and is shown to be related to previous methods. Suggestions are made with regard to the choice of constants in the prediction equation so as to represent fairly the present state of the art.

Introduction

For certain aspects of modeling the combustion process in a gas turbine a knowledge of the behavior and characteristics of the fuel spray produced by a fuel nozzle is important. Of the many ways of characterizing sprays that are possible, the statistical parameter which is most widely accepted and used is the Sauter Mean Diameter (SMD), partly because of its physical significance (as an inverse function of surface/volume ratio) and also because it can be readily calculated from observed drop-size data. For many years the only data available on the SMD's of fuel sprays were obtained under normal atmospheric discharge conditions and even now the amount of data published for other conditions more representative of engine operation is very limited. For the present purpose, therefore, we are confining our study to what can be described as the "nominal" performance of fuel nozzles as determined by measurement of SMD under laboratory conditions.

With a given fuel nozzle SMD varies with the operating conditions and the fuel properties and it has become customary to present the relationships in the form of empirical equations which "predict" the SMD. The mathematical form of these equations varies considerably depending on the type of fuel nozzle investigated but in general published equations do not easily relate to the physical dimensions of fuel nozzles and there has been no real effort to produce a common equation which would be suitable for both pressure-atomizing and air-atomizing nozzles. The need for such an equation is made evident for example when using an air-assisted simplex nozzle which can be operated with or without air-assistance.

In this paper a number of the more important prediction equations is examined and compared and a new equation is presented which satisfies the previous requirement. The paper is not intended as a review of spray analysis methods and their accuracy, nor as a study of the relative merits of different fuel nozzle types.

Contributed by the Gas Turbine Division and presented at the Winter Annual Meeting, December 2–7, 1979, New York, New York, of THE AMERICAN SOCIETY OF MECHANICAL ENGINEERS. Manuscript received at ASME Headquarters August 13, 1979. Paper No. 79-WA/GT-5.

The three different basic types of fuel nozzle considered here are:

1 Fuel-pressure-atomizing (simplex) nozzles discharging into a static atmosphere

2 Air-blast nozzles, relying almost entirely on atomization by high-velocity (combustion) air passing through the nozzle

3 Air-assisted simplex nozzles, utilizing both fuel-pressure and externally-supplied high pressure-air, discharging into a static atmosphere

The Effects of Fuel Properties on SMD

Part of the difficulty of reconciling the various published equations on SMD prediction is due to the apparent preoccupation of investigators with the effects of the physical properties of the fuels or other liquids employed. In particular, viscosity, which can vary over wide limits, had a significant effect on the atomizing capability of many early designs of nozzles and therefore it was regarded as essential to include viscosity terms in the equations. The same tendency occurred, but to a less extent, with surface tension which is of course much higher for water and alcohols as compared with most hydrocarbons.

When considering gas turbine fuel nozzles however, for the purpose of this paper, the comparison of equations can be very much simplified by initially ignoring viscosity and surface tension as variables since the majority of engines use fuels very close in properties to kerosene and similar liquids have been widely used as standards for laboratory testing. The effects of these variables are, however, discussed later in the paper.

The Variables Affecting SMD

The atomization of fuels for our purposes can be considered to be a result of the interaction of a liquid sheet or jet with the surrounding air due to relative motion. It might be expected therefore that fluid velocity would be the most important variable though frequently disguised as a pressure or pressure-drop. The quantity of liquid (per unit time) being atomized might also be important. It could be considered also that the quantity of air with which the liquid is interacting

Copyright © 1980 by ASME

Downloaded 01 Jun 2010 to 171.66.16.58. Redistribution subject to ASME license or copyright; see http://www.asme.org/terms/Terms_Use.cfm

would be significant but it is evident that there are considerable difficulties involved in defining the air quantity *a priori* (even ignoring air density as a variable). The physical dimensions of the liquid sheet or jet have not been regarded by many investigators as even worthy of mention and in some noteworthy cases there has been no indication at all of the dimensions of the fuel nozzles under study.

In the case of the simplex nozzle the flow number has been widely used in equations since it is a prime design variable which can be related readily to physical dimensions; in some cases also the nominal "spray angle" is introduced as a design variable having a minor effect.

The Form of SMD Prediction Equations

The measurement of SMD (and drop sizes in general) is extremely difficult and the analysis and presentation of results is complicated by the large number of potential and actual variables involved. Disentangling the separate effects of each variable is not always possible with a single piece of test hardware and the correlation of data is often done using mathematical forms which are not directly representative of conceivable physical processes.

The simplest form of equation makes the SMD proportional to powers of each variable. For example, for a simplex nozzle

$$\text{SMD} \propto \dot{W}_F{}^a \cdot \Delta P_F{}^{-b} \tag{1}$$

where $a = 0.20$ and $b = 0.35$ are typical observed values. This equation can be rewritten as

$$\text{SMD} \propto F_N{}^a \cdot \Delta P_F{}^{-(b-a/2)} \tag{2}$$

since $F_N = \dot{W}_F/\Delta P_F{}^{1/2}$ by definition, or typically

$$\text{SMD} = F_N{}^{0.20} \cdot \Delta P_F{}^{-0.25} \tag{2a}$$

Now F_N is equivalent to a (flow) area which can be stated as $\propto D_F{}^2$ where D_F is some characteristic dimension, and $\Delta P_F \propto V_F{}^2$ where V_F is the velocity of the liquid interacting with "static" air, so we can write

$$\text{SMD} \propto D_F{}^{2a} \cdot V_F{}^{-(2b-a)} \tag{3}$$

as possibly the most basic relationship for the simplex fuel-pressure-atomizer where we can totally ignore the air behavior and properties.

For the so-called "twin-fluid atomizer," in which a high-velocity air stream interacts with a generally slower-moving liquid sheet or jet, the prediction equations introduce the concepts of V_A the air velocity (sometimes *relative* to the fuel) and the ratio of air/liquid flow rates (sometimes as volume flow rates but more often as mass flow rates) and a typical form [1] is

$$\text{SMD} \propto V_A{}^{-c} \cdot (1 + \dot{W}_F/\dot{W}_A)^d \tag{4}$$

where $c = 1$ approximately, and d varies from $\frac{1}{2}$ to $1\frac{1}{2}$. A feature introduced by Nukiyama and Tanasawa [2] was the use of two terms with the second dominated by liquid viscosity, thus

$$\text{SMD} = A \cdot V_A{}^{-1} + B \cdot \eta_F{}^{.45} \cdot (\dot{W}_F/\dot{W}_A)^{1.5} \tag{5}$$

where A and B are constants for a given liquid and air density.

A similar equation was used by Rizkalla and Lefebvre [3] and can be written as

$$\text{SMD} = A'(\rho_A V_A)^{-1} \cdot (1 + \dot{W}_F/\dot{W}_A) D_F{}^{0.5} + B' \cdot \eta_F{}^{0.85}(1 + \dot{W}_F/\dot{W}_A)^2 \cdot D_F{}^{0.575} \tag{5a}$$

where A' and B' are constants for a given liquid and air density, and D_F is a "characteristic dimension" of the nozzle.

There are several objections to the use of these equations: first, the concept of two separate contributions to the SMD, each having the dimensions of a length (or portion of a drop diameter) does not represent any imaginable physical process; secondly, the effect of design and operating variables can not be deduced by inspection. It will be noted also that equation (5) has no term referring to a size or dimension, and although equation (5*a*) includes the term D_F, all the data of [3] were obtained with a single fuel nozzle of a fixed size so there is no direct evidence supporting this aspect.

The present paper later discusses a method of introducing nozzle size into an equation similar to (4), but even when this is done there is still the fundamental objection to any of these equations that they become meaningless for $\dot{W}_A = 0$ since this makes SMD = ∞. It is the purpose of this paper to present an equation which reconciles all these difficulties.

The Important Dimensions of Fuel Atomizers

To characterize the size of a fuel nozzle for most modeling purposes we need only consider those dimensions normal to the axis of the nozzle and combustor and for the Simplex pressure atomizer the diameter of the discharge orifice (Fig. 1) is basic. Following the well-known design procedures of [4], for example, if the spray cone angle and required flow number are defined the discharge coefficient (C_d) and the orifice diameter (D_0) are directly determined, while the other dimensions of the swirl chamber of the nozzle can be adjusted to equate with the nondimensional parameter K. Thus for a given spray cone angle

$$D_0{}^2 = \text{const.} \times F_N \tag{6}$$

From a more fundamental viewpoint it has always been considered that spray drop sizes must be closely related to the thickness of the initial fuel film or sheet just as the drops produced by the classic Rayleigh instability of jets are related to the jet diameter. In the Simplex nozzle case the design basis implies that the thickness of the fuel sheet (t) at the discharge orifice is proportional to the orifice diameter for a given spray cone angle, therefore, from equation (6)

$$t^2 \propto F_N \tag{7}$$

and equation (2) becomes

$$\text{SMD} \propto t^{2a} \cdot \Delta P_F{}^{-(b-a/2)} \tag{8}$$

Nomenclature

SMD = Sauter Mean Diameter, microns (μm), micrometers (μm)†

ρ_F = fuel density*, g/cm^3 (specific gravity), Kg/m^3, 10^{-3} g/cm^3

σ_F = fuel surface tension*, dynes/cm, N/m, 10^3 dynes/cm

η_F = fuel absolute viscosity*, centipoise, mPa·s, 1 centipoise

K_{FR} = combined factor for fuel properties, (nondimensional)

$\dot{W}_F/\dot{W}_A$ = fuel, air, mass flow rates*, lb/hr, Kg/hr, 2.205 lb/hr

V_F = fuel velocity equivalent to ΔP_F, ft/s, m/s, 3.281 ft/s

ΔP_F = fuel pressure drop through nozzle*, psi, KPa, 0.145 psi

F_N = flow number (= $\dot{W}_F/\sqrt{\Delta P_F}$), lb/($\sqrt{\text{psi}}$ · hr), Kg/$\sqrt{\text{KPa}}$ · hr), 5.79 lb/($\sqrt{\text{psi}}$ · hr)

D_0 = Orifice dia of simplex nozzle, in., cm, 0.394 in.

D_p = fuel film lip dia, in., cm, 0.394 in.

t_F* = hypothetical film thickness, μm, μm,

ρ_A = air density*, lb/ft^3, Kg/m^3, 0.0624 lb/ft^3

V_A = air velocity (for atomization) equivalent to ΔP_A, ft/s, m/s, 3.281 ft/s

ΔP_A = air pressure drop through nozzle*, psi, KPa, 0.145 psi

K_7, K_8, K_9 = "constants" in prediction equations. (Values depend on units used. See Table 2.)

C = coefficient = effective fraction of atomizing air. (nondimensional)

a, b, c, d, m, x = exponents

Subscripts

A = air

AR = value of variable relative to sea-level, room temperature air conditions

F = fuel

FR = value of variable relative to properties of standard calibrating fluid (Mil-F-704II) at room temperature

† Units indicated are conventional units, SI units and the conversion factor for 1 SI unit, respectively.

* These units are not required for the prediction equations given in this paper.

Downloaded 01 Jun 2010 to 171.66.16.58. Redistribution subject to ASME license or copyright; see http://www.asme.org/terms/Terms_Use.cfm

Table 1 Comparative dimensions of air-blast fuel nozzles given in conventional units

	Symbol	Units	Lefebvre	P-H Type J	P-H Type S
Overall Diameter	—	in.	2.75	1.75	2.0
Frontal Area	—	$in.^2$	5.9	1.4	1.1
Airflow Area		$in.^2$	1.70	0.262	0.272
Fuel Film Lip Dia.	D_p	in.	1.5	1.00	1.015
Fuel Flow Number	F_N	$\frac{pph}{\sqrt{psi}}$	33	137	93
F_N/D_p	—	F_N/in.	22	137	92
Fuel Film Thickness	t_F*	microns	11	67	45

Table 2 Range of values of constant K_8 in SF7 SMD-prediction equations for units given in the Nomenclature

Nozzle Type	*Conventional Units*	*SI Units*
Simplex Nozzles		
With or Without	200	104
Air-Assist	300	156
Air-Blast Nozzles		
"Zero Length" Prefilmers	650	338
"Long" Prefilmers	1300	676

A considerable amount of published data has established the value of the exponent "a" as close to 0.20; thus

$$\text{SMD} \propto t^{0.4} \text{ approximately, for Simplex nozzles.}$$

It was considered that there would be an advantage in replacing "t" by the thickness t_F* of a hypothetical film equivalent to a given volume of fuel flowing at a known axial velocity on the inside of the cylindrical surface of the discharge orifice. We assume that the entire fuel pressure drop across the swirl chamber is converted into axial velocity and then the flow area is given by

$$\pi D_0 \cdot t_F^* \text{ (for } t_F^* \ll D_0)$$

thus

$$t_F^* = \left(\frac{\text{volume flow rate}}{\text{velocity}}\right) \times \frac{1}{\pi D_0} \tag{9}$$

The term in brackets is of course equivalent to F_N for a given fuel density and equation (9) becomes (for a Simplex nozzle)

$$t_F^* = \text{const.} \times F_N/D_0 \tag{10}$$

and equation (8) becomes

$$\text{SMD} \propto (F_N/D_0)^{2a} \cdot \Delta P_F^{-(b-a/2)} \tag{11}$$

The best known type of air-blast nozzle is shown diagrammatically in Fig. 2. The fuel is spread into a thin sheet on the "prefilming" cylindrical surface and leaves the surface at an edge of diameter D_p where it is atomized by high-velocity air on both sides of the sheet. Most designs spread the fuel by injecting it through tangential slots or holes into the rudimentary swirl chamber which of course can be characterized by a flow number just as a Simplex nozzle; it is therefore possible to define a hypothetical film thickness for a prefilming air-blast nozzle in the same way as equation (10),

$$t_F^* = \text{const.} \times F_N/D_p \tag{12}$$

where the constants are identical for both equations for similar units. (See Appendix 1.)

In an air-blast nozzle of this type there need be no particular relationship between F_N and D_p; this is illustrated by comparing three different designs of prefilming air-blast nozzles. The first is the laboratory model air-blast nozzle used by Lefebvre and his co-workers in [3], the others (type J and S) are designs by Parker-Hannifin for experimental gas turbine combustors. Values of F_N, D_p and t_F* are tabulated in Table 1 for these designs, using conventional units.

To compare the results of these nozzles equation (13) was constructed, using data from [3] and as obtained by the author with the Parker Spray Analyzer [5].

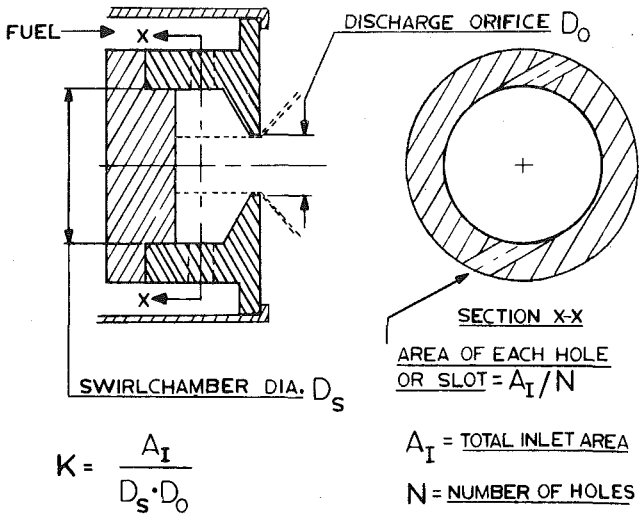


Fig. 1 Principal dimensions of a Simplex fuel nozzle

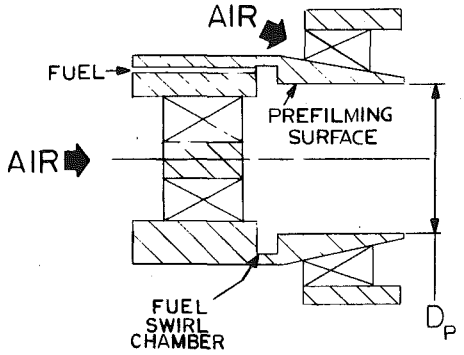


Fig. 2 Principal dimensions of an Air-blast fuel nozzle

$$\text{SMD} \propto \Delta P_A^{-0.5} \cdot \rho_{AR}^{-0.375} \cdot (1 + \dot{W}_F/\dot{W}_A) \tag{13}$$

The data for the three nozzles are plotted in Fig. 3; the right-hand side of equation (13) has been inverted. It will be seen that there is a wide variation in the level of performance between the nozzles. When the dimensional term $t_F^{*0.375}$ is introduced however, as in Fig. 4, the results agree satisfactorily thus justifying the use of SMD $\propto t_F^{*0.375}$ or SMD $\propto (F_N/D_p)^{0.375}$ for prefilming air-blast nozzles of similar general design.

This last conclusion has recently been confirmed in a striking manner by Rizk and Lefebvre [6] who designed an air-atomizer in which the film thickness could be varied and directly measured; their results clearly indicate SMD $\propto t_F^{*0.38}$.

The agreement of these values for the exponent on t_F* with the value of 0.4 approximately found earlier for simplex nozzles is very gratifying. It is obvious therefore that similar values can be expected for air-assisted simplex nozzles.

The other important dimensions of both air-blast and air-assisted nozzles are obviously concerned with the size and shape of the air passages which are determined by the air-flow rates and velocities required to obtain a given degree of atomization. This is discussed in the next section.

Atomizing Air Requirements

Fuel atomization can be described as a system of interaction of two immiscible fluids which results in one fluid (liquid) being broken up into disconnected regions, and it is obvious that momentum transfer is the basic mechanism involved. This is confirmed by the experimental evidence of fluid velocity being the most important variable in determining SMD at a given air density. There is no record however, of any attempt to construct an SMD correlation equation using momentum terms as such, possibly because it is difficult to decide

Downloaded 01 Jun 2010 to 171.66.16.58. Redistribution subject to ASME license or copyright; see http://www.asme.org/terms/Terms_Use.cfm

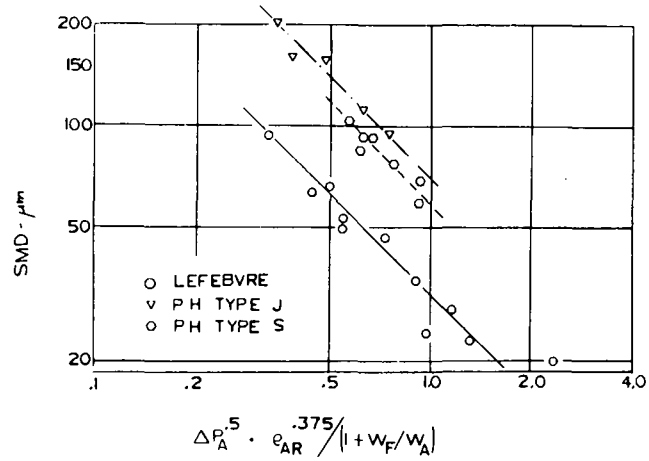


Fig. 3 Comparison of three different Air-blast nozzles using equation (13)

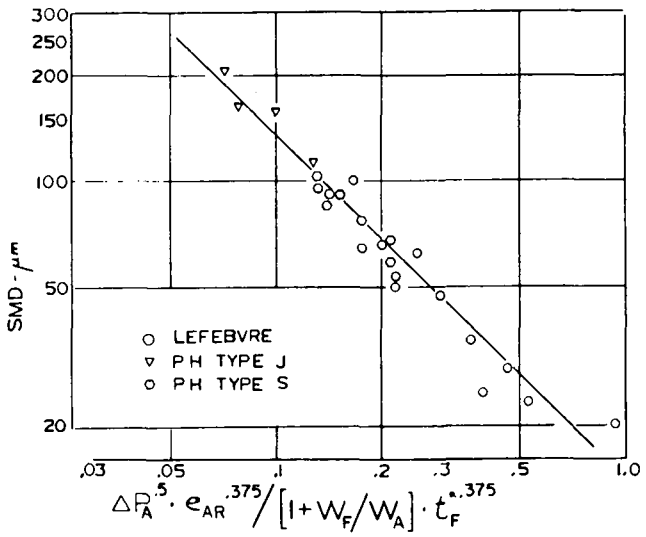


Fig. 4 Correlation of results from the nozzles of Fig. 3 by the use of a film-thickness term

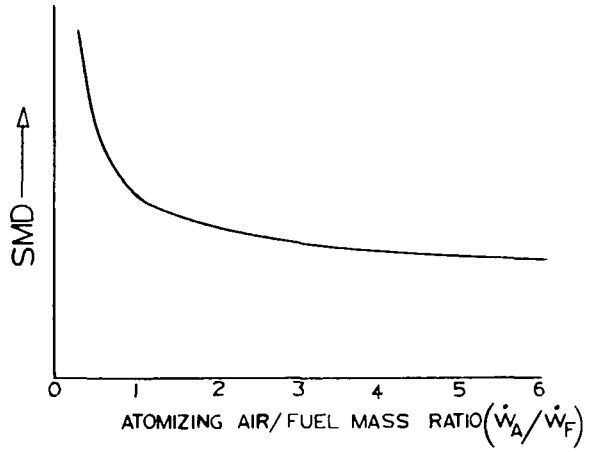


Fig. 5 Effect of air/fuel ratio on SMD for typical air-atomizing nozzles

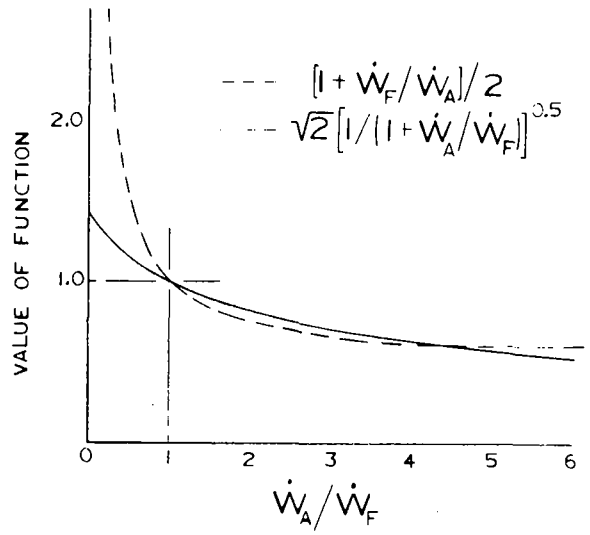


Fig. 6 Comparison of functions of $\dot{W}_A/\dot{W}_F$

what quantity of air is involved in the process with pressure-atomizers. Even with air-atomizers there is the same difficulty as part of the air supplied may be superfluous. If air/fuel (mass flow) ratio is used as a test or design variable with a given fuel nozzle the SMD will vary generally as shown in Fig. 5, i.e., below $\dot{W}_A/\dot{W}_F = 1$ approximately the atomization rapidly becomes very poor, while above $\dot{W}_A/\dot{W}_F = 5$ approximately there is little further improvement. In fitting curves to correlate test data it was found by several investigators that the term $(1 + \dot{W}_F/\dot{W}_A)$ of equation (4) was convenient and the fact that it becomes $= \infty$ at zero air flow was unimportant in an atomizing device not intended to operate without air. A similar curve-fitting procedure led Nukiyama and Tanasawa to use the simple ratio Q_F/Q_A in equation (5) with the same limitation.

The case of the air-assisted simplex nozzle (or even some types of air-blast nozzle) where there is a design requirement to operate without air presented a special problem in reconciling equations such as (3) or (4) since a single equation having a continuous function was preferred. The first step was to use the term

$$[1/(1 + \dot{W}_A/\dot{W}_F)]^m \text{ instead of } (1 + \dot{W}_F/\dot{W}_A)^n$$

since this term = 1 for $\dot{W}_A = 0$. These terms give similar values over a range of $\dot{W}_A/\dot{W}_F$ from 0.5 to 4 when adjusted to be equal at $\dot{W}_A/\dot{W}_F = 1$ as shown by Fig. 6.

Rewriting,

$$1/(1 + \dot{W}_A/\dot{W}_F) = \dot{W}_F/(\dot{W}_F + \dot{W}_A) \quad (14)$$

and since this expression is intended to represent an aspect of exchange of momentum between air and fuel in the atomizing process it is appropriate to bring the fuel and air velocities of equations (3) and (4), which are normally represented by ΔP terms in the prediction equations, inside the brackets of the denominator, thus:

$$\text{SMD} \propto [\dot{W}_F/(\dot{W}_F \cdot V_F + \dot{W}_A \cdot V_A)]^m \quad (15)$$

It will be noted that accepted values for $(2b - a)$ in equation (3) range from 0.7 to 0.9 while values for c in equation (4) are usually close to 1, justifying the similar treatment of fuel and air velocities.

Fig. 7 shows the good fit of this expression to typical data from air-assisted simplex and air-blast nozzles when $m = 0.55$. These nozzles all had large flow-numbers (58–93), low fuel velocities ($V_F <$ 21 ft/s), air velocities V_A up to 500 ft/s and $\dot{W}_A/\dot{W}_F$ ranging from 0 to 10. Equation (15) was therefore used as a basis for the SMD prediction equation discussed below, which has been given the computer-program name of SF7 for ease of reference.

The Effects of Air Properties

Before setting down the SF7 equation in its entirety it is necessary to consider the effects of air and fuel properties which were ignored previously to simplify comparison of equations. Air pressure (absolute) and temperature are usually regarded only as components of air density which is however a powerful variable in controlling atomization by air. The Rizkalla-Lefebvre data [3] is the most significant source of information in this respect and shows clearly that SMD $\propto \rho_A^{-0.875}$ approximately in the prefilming air-blast nozzle.

The behavior of large flow number simplex nozzles spraying into a static atmosphere at high pressure has been reported in [7], which shows that the spray cone angle can be reduced to low values, ac-

Downloaded 01 Jun 2010 to 171.66.16.58. Redistribution subject to ASME license or copyright; see http://www.asme.org/terms/Terms_Use.cfm

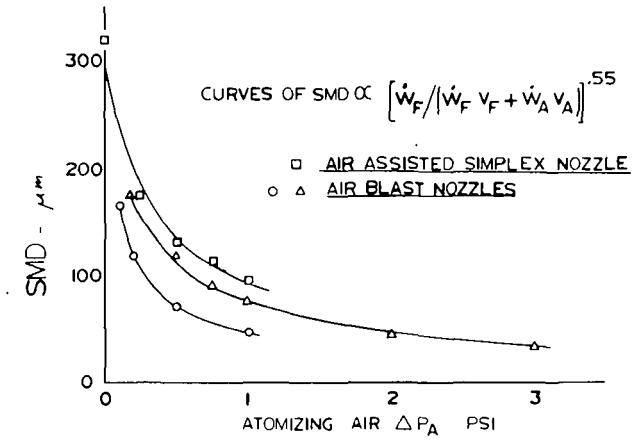


Fig. 7 Correlation of data using equation (15), for three different fuel nozzles—effect of air velocity

companied by large increases in SMD. Although in actual combustors there have been indirect indications of a reduction in spray angle, such as increasing smoke, there is no evidence of complete collapse of the spray, probably because most nozzles are surrounded by an air shroud or swirler through which air is flowing under engine operating conditions. More recent work by Ballal and Lefebvre [8] on a typical small-flow-number simplex nozzle showed SMD $\propto P_A^{-0.1}$ i.e., decreasing slightly with atmospheric density. The behavior of a simplex nozzle with static air is, however, a matter of almost academic interest; the air-assisted simplex nozzle appears to behave in essentially the same way as an air-blast nozzle and thus must react similarly to changes in air density.

The Effects of Fuel Properties

With regard to fuel properties, as stated earlier there are only minor differences in fuel density and surface tension for most gas turbine fuels so these present little problem in correlating data, and we can safely use the well-established data such as [3]. Viscosity, however, can vary by almost two orders of magnitude in many applications so it is important for modeling purposes that an SMD prediction equation shall give proper weight to this factor. Most of the published and widely used equations for simplex nozzles add a viscosity (η_F) term to equation (1) thus,

$$\text{SMD} \propto \dot{W}_F{}^a \cdot \Delta P_F{}^{-b} \cdot \eta_F{}^x \tag{16}$$

where $x = 0.2$ approximately.

This method is not entirely satisfactory since it appears to be a mean correlation which does not reflect either the extreme sensitivity of small simplex nozzles to viscosity or the decreasing sensitivity of large simplex nozzles. It is beyond the scope of this paper to discuss the question in detail, but it is known that the actual observed flow number F_{N_0} of small simplex nozzles increases by as much as a factor of 2 with high fuel viscosities, depending mainly on the Reynolds Number in the swirl chamber; therefore, by equation (10), $t_F{}^*$ can also increase proportionately. In using such an equation as (16) it is usual to keep the fuel flow $\dot{W}_F$ constant; the ΔP_F term will then vary as $1/F_{N_0}{}^2$ so combining these two effects equation (16) becomes

$$\text{SMD} \propto F_{N_0}{}^{(2a+2b)} \cdot \eta_F{}^x \tag{17}$$

The exponent $2a + 2b = 1$ approximately so that if F_{N_0} doubles due to fuel viscosity (Reynolds Number) then SMD will also be doubled.

On the other hand, the evidence of tests with large simplex nozzles (or dual orifice nozzles) operated at high fuel pressures (giving high Reynolds Numbers in the swirl chamber) is that x may be reduced to values as low as 0.05.

This is demonstrated clearly by the results of Fig. 8 from a series of tests on a typical duel-orifice nozzle having a small-flow-number primary and a much larger secondary. Taking data from the smoothed curves the value of x in equation (16) changes from 0.35 for the primary only case to about 0.06 at the highest flow (at which point the secondary flow is 16 times the primary flow). The graph also illustrates the difficulties and risks of limited parametric investigations. It is evident that modeling the effects of fuel viscosity on atomization requires considerable caution.

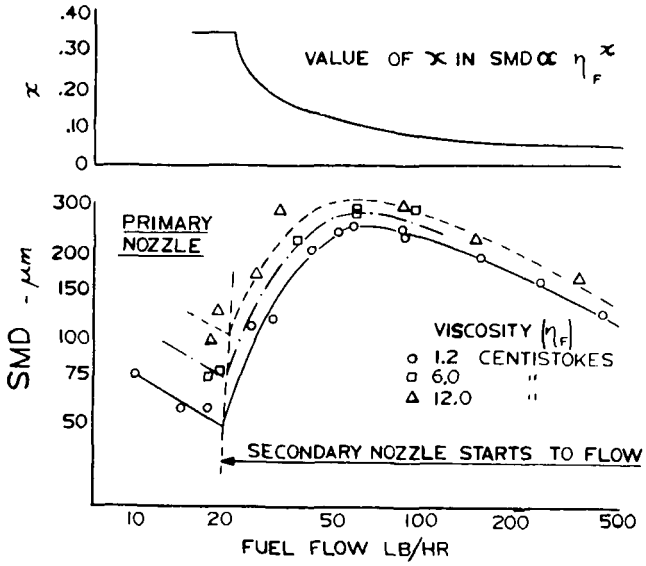


Fig. 8 Effect of the fuel viscosity on SMD using a typical dual-orifice fuel nozzle

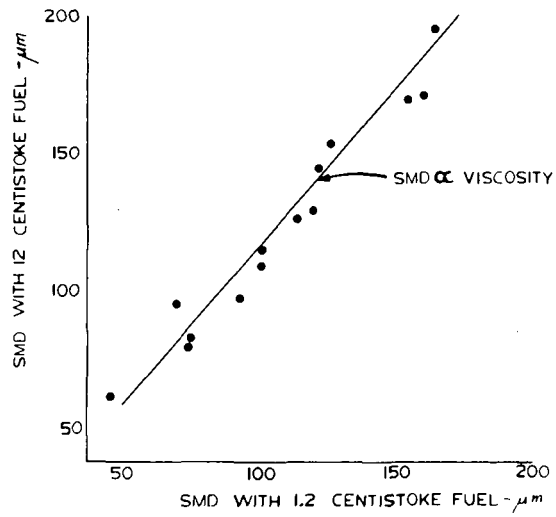


Fig. 9 Effect of fuel viscosity on SMD for prefilming air-blast fuel nozzles

With air-blast nozzles there is ample evidence that the effect of viscosity is very small with most designs. For typical engine-size prefilming air-blast nozzles, such as types J and S of Fig. 3, $x = 0.06$ as shown in Fig. 9. This value is confirmed by the recent work of Jasuja [9] for the Lefebvre-type air-blast nozzle which, when analyzed in the same manner, gives $x = 0.08$ approximately for normal values of $\dot{W}_A/\dot{W}_F$ and ΔP_A, comparing heated residual fuel oil at 41 times the absolute viscosity of kerosene.

Air-assisted simplex nozzles are theoretically subject to the same Reynolds Number effects on film thickness as non-air-assisted simplex nozzles, but in practice appear to behave similarly to air-blast nozzles.

It was decided, therefore, to combine all the terms representing the effects of fuel properties into one coefficient K_{FR}, thus:

$$K_{FR} = \rho_{FR}{}^{0.25} \cdot \eta_{FR}{}^{0.06} \cdot \sigma_{FR}{}^{0.375} \tag{18}$$

which appears to give satisfactory correlation with air-atomizing types of nozzle and can be used for non-air-assisted simplex nozzles if the effect of viscosity on the observed flow number is known. Note that

Downloaded 01 Jun 2010 to 171.66.16.58. Redistribution subject to ASME license or copyright; see http://www.asme.org/terms/Terms_Use.cfm

the problem of different systems of units is avoided by making all the terms relative to the values of the properties of the commonly-used reference fuel of kerosene-type, i.e. for this fuel at room-temperature $K_{FR} = 1$.

The SF7 SMD-Prediction Equation

Combining all the preceding considerations, and using equation (15) as a basis the general form of the SF7 equation was finally established as

$$\text{SMD} = K_7 \cdot \rho_{AR}{}^{-0.325}[\dot{W}_F/(\dot{W}_F V_F + C \cdot \dot{W}_A V_A)]^{.55} \cdot K_{FR} \quad (19)$$

where

$$K_7 = K_8 \cdot t_F{}^{*0.375} \quad (19a)$$

and C is a coefficient introduced to represent the proportion of air flow usefully employed in atomizing the fuel. $C = 1$ for all the cases in this paper.

The correlation of observed data by use of equation (19) is shown in Figs. 10 and 11, but before discussing these it is useful to compare SF7 with previously published equations.

Agreement of SF7 with Previous Equations

Since $\dot{W}_A \propto \rho_A \cdot V_A$ for a given nozzle the air term in the denominator of equation (19) can be written as

$$K_9 \cdot \rho_{AR} \cdot V_A{}^2$$

where K_9 is a constant. If we consider a given air-blast nozzle where $V_F \ll V_A$ we can eliminate the $\dot{W}_F \cdot V_F$ term and write for given values of V_A and $\dot{W}_F$,

$$\text{SMD} \propto \rho_{AR}{}^{-0.325}(1/\rho_{AR})^{0.55}$$

i.e.,

$$\text{SMD} \propto \rho_{AR}{}^{-0.875} \quad (20)$$

The exponent $^{-0.325}$ was chosen to satisfy this relationship and also equation (13) which can be written as

$$\text{SMD} \propto (\rho_{AR} V_A{}^2)^{-0.5} \rho_{AR}{}^{-0.375}(1 + \dot{W}_F/\dot{W}_A)$$

Similarly we have for given values of ρ_{AR} and $\dot{W}_F$

$$\text{SMD} \propto V_A{}^{-1.1} \quad (21)$$

which is also in good agreement with [3].

For the simplex nozzle with "static" air $\dot{W}_A = 0$, and equation (19) becomes

$$\text{SMD} \propto V_F{}^{-0.55}$$

or, for a given fuel and nozzle,

$$\text{SMD} \propto F_{NS}{}^{0.1875} \cdot \Delta P_F{}^{-0.275} \quad (22)$$

in general agreement with equation (2a).

It is evident, therefore, that the SF7 equation will give results compatible with other methods.

Correlation of Test Data Using SF7

It will have been noted that up to this point the units used have not been important since we were primarily concerned with proportionate effects of the variables; however, the system of units used will affect the numerical values of the constants K_7 and K_8. To avoid confusion, therefore, in the ensuing discussion we will employ only the numbers resulting from the "conventional" system of units given in the Nomenclature. (Corresponding values for the SI system units are given in Table 2; it should be noted that there is at present no accepted SI equivalent to the U. S. flow number).

Most of the fuel nozzle testing with which the author is associated is primarily concerned with performance of various nozzles at specified conditions rather than extensive parametric investigations of a single design. The data presented here therefore exhibits not only the scatter due to the experimental techniques but also the variations due to differences in design. Fig. 10, for example, gives data for five different air-assisted simplex nozzles and seven different simplex-nozzles

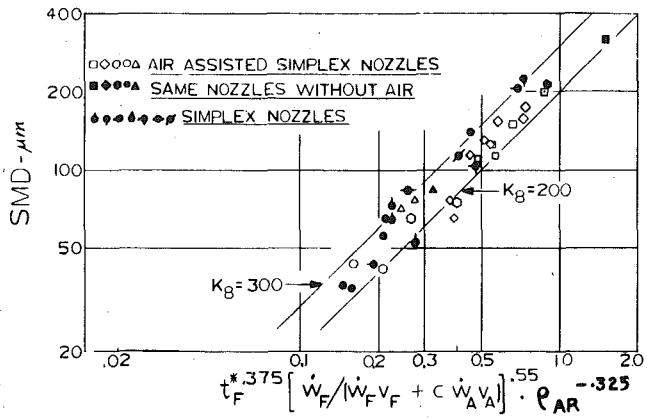


Fig. 10 Correlation of results from Air-assisted and non-air-assisted Simplex nozzles using the SF7 equation (19)

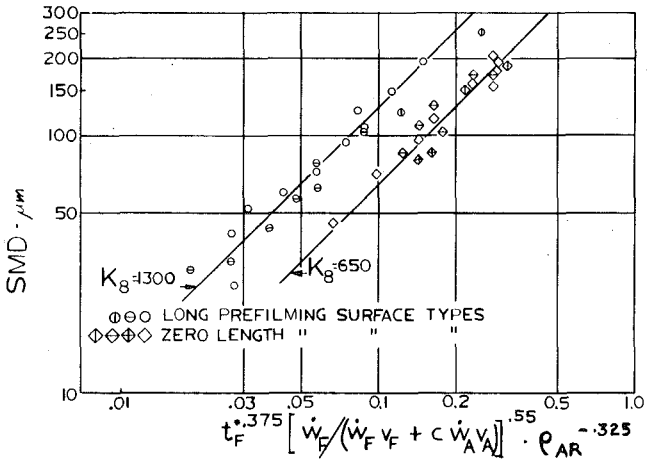


Fig. 11 Correlation of results from Air-blast nozzles of two different types, using the SF7 equation (19)

not designed for air-assist, the range of flow number being from 1 to 93. It can be seen that the individual designs generally follow the proportionality of equation (19) reasonably well, but that the "constant" K_8 can vary from 200 to 300. This should not cause any surprise; it has been known for years that differences of this order of magnitude are shown by published data and equations obtained by different methods. It is noteworthy, however, that all the data here was obtained by a single method [5] so the major differences in results can only be attributed to differences in design and manufacture. It is evident that for accurate modeling purposes it is advantageous to have some factual data from which to compute K_8 in each case.

The variation in the values of K_8 shown by Fig. 10 does not appear to correlate with any particular design feature in the nozzle. However, when a similar plot is made for air-blast nozzles, as in Fig. 11, the results fall into two distinguishable categories, the upper "family" consisting of "long prefilmers" of the Lefebvre type while the lower "family" consists of "zero-length" prefilmers of the type described in [10]. In each family the general agreement with the proportionality of equation (19) is good but the variation in K_8 again points out the need for basic data on particular fuel nozzle designs when doing modeling studies.

The range of values for K_8 is tabulated in Table 2.

Conclusion

In spite of the variation in K_8 values between the different types of nozzle it is concluded that the use of the t_F* film thickness concept provides a satisfactory means of allowing for the major dimensional factors in both Simplex and air-atomizing nozzles since t_F* is directly calculable from known or measurable data (F_N and D_p).

There will always be some doubt as to the true value of V_A, the air velocity at the point of atomization of the liquid film for a given air pressure drop ΔP_A, due to differences in design resulting in different

Downloaded 01 Jun 2010 to 171.66.16.58. Redistribution subject to ASME license or copyright; see http://www.asme.org/terms/Terms_Use.cfm

exit velocity profiles. Similarly the constant C in equation (19) may be <1 in an over-designed air-atomizing nozzle. Nevertheless the SF7 prediction equation has the capability of handling the awkward transition from no-air to air-atomizing conditions which has not been possible with previously published equations.

The form of the equation allows identification of the effects of major design and operating variables virtually by inspection, and it is believed that the use of recognizable momentum terms will be of value in interpreting the behavior of each nozzle design.

Acknowledgments

The author wishes to thank the Parker Hannifin Corporation and in particular Mr. Richard F. Ferrel, General Manager of the Gas Turbine Fuel Systems Division, for permission to publish this paper.

References

1 Wigg, L. D., "Drop Size Prediction for Twin-Fluid Atomizers," NGTE Memo M343, National Gas Turbine Establishment, England, 1960.

2 Nukiyama, S., and Tanasawa, Y., "Experiments on the Atomization of Liquids in an Air Stream," *Trans. Soc. Mech. Engrs.,* Japan, Vols. 4–6, 1938–1940.

3 Rizkalla, A. A., and Lefebvre, A. H., "The Influence of Air and Liquid Properties on Airblast Atomization," ASME *Journal of Fluids Engineering,* Vol. 97, Sept. 1975.

4 Giffen, E., and Murasjew, A., *The Atomization of Liquid Fuels,* John Wiley and Sons, New York, 1953.

5 Simmons, H. C., "The Correlation of Drop-Size Distributions in Fuel Nozzle Sprays," ASME, JOURNAL OF ENGINEERING FOR POWER, Vol. 99, July 1977.

6 Rizk, N. K., and Lefebvre, A. H., "The Influence of Liquid Film Thickness on Airblast-Atomization," paper presented at ASME Meeting, Atlanta, GA., Dec., 1977.

7 De Corso, S. M., "Spray Distribution and Droplet Size from Swirl Atomizers," ASME Paper No. 61-WA-300, 1962.

8 Ballal, D. R., and Lefebvre, A. H., "Ignition of Liquid Fuel Sprays at Subatmospheric Pressures," *Combustion and Flame,* 31, 1978, pp. 115–126.

9 Jusuja, A. K., "Atomization of Crude and Residual Fuel Oils," ASME 78-GT-83, 1978.

10 Simmons, H. C., et al., U. S. Patent 3,980,233.

APPENDIX

Calculation of Hypothetical Film Thickness t_F*. Since t_F* is calculated from volume flow rates and velocities it is necessary to include fuel density in equations using Flow Number on a mass-flow basis. With appropriate conversion factors equation (12) becomes

$$t_F^* = 0.48(F_N/\sqrt{\rho_{FR}})/D_p \tag{12a}$$

in conventional units used here

$$= 7.06(F_N/\sqrt{\rho_{FR}})/D_p \tag{12b}$$

in the SI units used here.

The equations for Simplex nozzles are identical when D_0 is substituted for D_p. For typical Simplex nozzles having a spray angle about 90 deg

$$t_F^* = 27.3\sqrt{F_N/\rho_{FR}} \tag{10a}$$

in conventional units

$$= 65.6\sqrt{F_N/\rho_{FR}} \tag{10b}$$

in SI units.

Downloaded 01 Jun 2010 to 171.66.16.58. Redistribution subject to ASME license or copyright; see http://www.asme.org/terms/Terms_Use.cfm

Effects of Nonuniform Passages on Compact Heat Exchanger Performance

R. K. Shah

Technical Director of Research,
Harrison Radiator Division,
General Motors Corporation,
Lockport, NY 14094.
Mem. ASME

A. L. London

Professor,
Department of Mechanical Engineering,
Stanford University,
Stanford, CA 94305
Fellow ASME

Neighboring passages in a compact heat exchanger such as a rotary regenerator are never geometrically identical due to manufacturing tolerances. This passage-to-passage nonuniformity can result in a significant penalty on heat transfer performance with only a small compensating effect of reduced pressure drop. Continuous cylindrical passage geometries, operating with laminar flow, are particularly sensitive to these effects. In this paper, a procedure is outlined to establish the effective friction factors and Nusselt numbers for one fluid side of an exchanger having n different cylindrical passage geometries. Two special cases of longitudinal wall temperature variation are considered corresponding to conditions of C_{min}/C_{max} of zero and unity. The analysis is presented for both fully developed and developing laminar flow.

Introduction

Interest in compact surface geometries, having high ratio of heat transfer area to core volume, is increasing because the use of such surfaces for clean fluids results in smaller, lighter-weight and lower cost heat exchangers. Passage geometries of these heat exchangers are never uniform and identical. If interrupted surfaces (such as strip and louvered fins) are employed, the passage-to-passage nonuniformity results in a negligible influence on the surface heat transfer and flow friction characteristics. However, for laminar flow in continuous cylindrical passage geometries, such as those employed in disk-type rotary regenerators, cross section nonuniformities have a significant effect on both heat transfer and flow friction performance.

An analytical method to determine the influence of passage-to-passage nonuniformity on the *laminar regime* surface characteristics was proposed by London [1]. In this treatment, the heat exchanger core was specified as consisting of two different passage cross section geometries of the same flow length. Fluid properties ρ, μ, k and c_p were treated as constant, the flow was specified as laminar and fully developed. Entrance and exit flow losses in the exchanger were neglected. With the same pressure drop in both sets of passages, the flow distribution for the two passage sizes was deduced. As a larger portion of the fluid passes through passages having the lower flow resistance, the core pressure drop is lower for the two-size passage model relative to a uniform core. With the flow distribution known, the decrease in core N_{tu}, and hence in Nu, is evaluated for a heat exchanger with $C^* = 1$ (this corresponds to the (H1) or (H2) boundary condition [2]).

Mondt [3] characterized the passage-to-passage variations for a deepfold surface by two parameters: a fin spacing channel deviation parameter and a "bulginess" channel deviation parameter. He then combined these parameters to form a total channel deviation parameter, and applied the two-size passage model to predict the reduction in both N_{tu} and Δp. These predictions agreed qualitatively with his experimental results and also analytical values deduced by Shah [4] for a trapezoidal cross-section passage.

In this paper, to eliminate the constraints imposed by the two-size passage model, the influence of passage-to-passage nonuniformity for an n-size passage model is developed for several different cylindrical cross sections.[1] For the heat transfer performance, two special cases, $C^* = 0$ and 1, are considered for the exchanger. Only the $C^* = 1$ case, as typified by the gas turbine regenerator application, was considered previously. Empirical treatment of the results of several computer runs supports the view that a single channel deviation parameter can be used to characterize an n-size passage core behavior.

Analysis

An approximate method is presented to calculate the effective fRe and Nu for a core[2] consisting of m-passage in parallel characterized by n different size-or-shape passages ($n \leq m$).

Specifying the number of the i-th shaped passages as N_i yields

$$N_1 + N_2 + \ldots + N_i + \ldots + N_n = m. \tag{1}$$

With $\chi_i = N_i/m$ describing the fractional distribution,

$$\sum_{i=1}^{n} \chi_i = 1. \tag{2}$$

Fully Developed Flows. All of the idealizations described earlier for the London two-size model are invoked here. In particular, the entrance and exit pressure losses in the heat exchanger are deemed to be relatively small. Hence, the flow distribution within the heat exchanger core is dependent only upon the nonuniform passage distribution. The procedures to determine the effective average magnitudes for $(f\text{Re})_e$ and $\text{Nu}_{bc,e}$ are described next.

Contributed by the Gas Turbine Division and presented at the Winter Annual Meeting December 2–7, 1979 New York, NY, of THE AMERICAN SOCIETY OF MECHANICAL ENGINEERS. Manuscript received at ASME Headquarters August 20, 1979. Paper No. 79-WA/GT-9.

[1] Theoretical solutions for laminar flow are available in [2] for 40 passage geometries.

[2] For a two-fluid heat exchanger, only one side having passage-to-passage nonuniformity is considered.

Copyright © 1980 by ASME

Downloaded 01 Jun 2010 to 171.66.16.58. Redistribution subject to ASME license or copyright; see http://www.asme.org/terms/Terms_Use.cfm

Flow Distribution, Pressure Drop and $(fRe)_e$. The pressure drop for flow through one of the i-th shaped passages is given by

$$\Delta p = f_i \frac{4L}{D_{h,i}} \frac{\rho u_{m,i}^2}{2g_c} = \left(\frac{2\mu L}{g_c \rho}\right)\left(\frac{(f\mathrm{Re})_i}{A_{c,i} D_{h,i}^2}\right) W_i \tag{3}$$

If $(f\mathrm{Re})_e$ represents the effective value for the m-passage core, the pressure drop is also given by

$$\Delta p = \left(\frac{2\mu L}{g_c \rho}\right)\left(\frac{(f\mathrm{Re})_e}{A_c D_h^2}\right) W \tag{4}$$

where

$$A_c = \sum_{i=1}^{n} N_i A_{c,i} = \sum_{i=1}^{n} m\chi_i A_{c,i} \tag{5}$$

The hydraulic diameter D_h is defined in terms of the passage perimeter P and flow cross section A_c as follows.

$$P = \sum_{i=1}^{n} N_i P_i = \sum_{i=1}^{n} m\chi_i P_i, \tag{6}$$

$$D_h = \frac{4A_c}{P}. \tag{7}$$

From the continuity equation,

$$W = \sum_{i=1}^{n} N_i W_i = \sum_{i=1}^{n} m\chi_i W_i \tag{8}$$

Substituting W and W_i from equations (3) and (4) into equation (8) and rearranging yields

$$\frac{1}{(f\mathrm{Re})_e} = \sum_{i=1}^{n} \frac{1}{(f\mathrm{Re})_i}\left(\frac{D_{h,i}}{D_h}\right)^2\left(\frac{N_i A_{c,i}}{A_c}\right) \tag{9}$$

Again, as Δp is common to all the passages, the flow distribution is obtained by equating equations (3) and (4).

$$\frac{W_i}{W} = \left[\frac{(f\mathrm{Re})_e}{(f\mathrm{Re})_i}\right]\left[\frac{D_{h,i}}{D_h}\right]^2\left[\frac{A_{c,i}}{A_c}\right] \tag{10}$$

The flow rate through N_i passages, all of the i-th shape, is then given by

$$\left.\begin{matrix}\text{fraction flow rate through}\\ N_i\ i\text{-th shaped passages}\end{matrix}\right\} = \frac{N_i W_i}{W} \tag{11}$$

Thus, if the distribution $m\chi_i$ $(= N_i)$ of the flow passages is given, and if $(f\mathrm{Re})_i$ for these passages is known, one can determine the effective $f\mathrm{Re}$ factor from equation (9), the flow distributions from equations (10) and (11), and the pressure drop through the heat exchanger from either equation (3) or (4).

Passage-to-passage cross-sectional nonuniformity results in a greater proportion of flow going through the larger passages relative to the smaller passages. Hence the actual pressure drop in a core with nonuniform passages is lower than the nominal or reference value for a core with uniform passages. This advantageous reduction in pressure drop is expressed as

$$\Delta p^*_{\text{gain}} = 1 - \frac{\Delta p_{\text{actual}}}{\Delta p_{\text{nominal}}} \tag{12}$$

Heat Transfer and $Nu_{bc,e}$. The following relation stems from the definition of the Nusselt number $\mathrm{Nu}_{bc,i}$ for the i-th passage, and $D_{h,i} = 4A_{c,i}L/A_i$.

$$\left(\frac{hA}{Wc_p}\right)_i = \left(\frac{kL}{c_p}\right)\left(\frac{4A_{c,i}}{D_{h,i}^2}\right)\left(\frac{1}{W_i}\right)\mathrm{Nu}_{bc,i} \tag{13a}$$

This equation can be rearranged to

$$\left(\frac{hA}{Wc_p}\right)_i = \frac{\mathrm{Nu}_{bc,i}}{\mathrm{PrRe}_i}\frac{4L}{D_{h,i}} \tag{13b}$$

This can readily be recognized as leading to the identity

$$\mathrm{Nu} = \mathrm{St\ Re\ Pr} = \mathrm{St\ Pe} \tag{14}$$

As heat transfer rates differ through the different shaped passages and result in different temperature differences from the hot-to-cold fluids, a simple mass flow weighting of conductances h_1, h_2, etc. will

Nomenclature

A = heat transfer or flow friction area, m^2
A_c = flow cross section area, m^2
b, c = rectangular passage dimensions, m
C = flow stream capacity rate = Wc_p, W/°C
C^* = heat capacity rate ratio for a heat exchanger = $C_{\min}/C_{\max}$, dimensionless
c_p = specific heat of the fluid at constant pressure, J/kg °C
D_h = passage hydraulic diameter = $4A_c/P$, m
f = "Fanning" or "small" friction factor = $\tau/(\rho u_m^2/2)$, dimensionless
f_{app} = apparent Fanning friction factor for developing flow; it accounts for the skin friction and the change in momentum rate, dimensionless
g_c = proportionality constant in Newton's second law of motion, unity and dimensionless in SI units
(H1) = thermal boundary condition referring to constant axial wall heat flux with constant peripheral wall temperature
(H2) = thermal boundary condition referring to constant wall heat flux both axially and peripherally
h = convective heat transfer coefficient, W/m^2 °C
k = fluid thermal conductivity, W/m °C
L = length of the heat exchanger flow passages, m
L_{hy} = hydrodynamic entrance length [2], m
L_{th} = thermal entrance length [2], m
m = a total number of passages on one side of the exchanger
N_i = number of i-th shaped passages
N_{tu} = number of heat transfer units on one fluid side of the exchanger, hA/Wc_p
$N^*_{tu,\text{cost}}$ = heat transfer penalty, defined by equation (24), dimensionless
Nu_{bc} = Nusselt number = hD_h/k; subscript bc designates the thermal boundary condition such as (H1) or (T), dimensionless
$\mathrm{Nu}_{m,bc}$ = mean Nusselt number for the thermal entrance region, dimensionless
n = number of different passage geometries on one side of the exchanger
P = passage wetted perimeter, m
Pe = Péclet number = RePr = $u_m D_h \rho c_p/k$, dimensionless
Δp = fluid static pressure drop on one side of the exchange, Pa
Δp^* = pressure drop reduction, defined by equation (12), dimensionless
Re = Reynolds number = $\rho u_m D_h/\mu$, dimensionless
(T) = thermal boundary condition referring to constant wall temperature
t = temperature of the fluid to a specified arbitrary datum, °C
t^* = normalized temperature difference = $(t - t_{\text{in}})/(t_{w,\max} - t_{\text{in}})$, dimensionless
t_w = perimeter average wall temperature, °C
U = overall heat transfer coefficient in a two-fluid heat exchanger, W/m^2 °C
u_m = fluid mean axial velocity, m/s
W = fluid mass flow rate = $\rho u_m A_c$, on one side of the exchanger if no subscript, kg/s
x = axial coordinate along the fluid flow passage, m
α^* = aspect ratio of rectangular passages, ratio of width to height of the rectangles, $\alpha^* \le 1$, dimensionless
δ_c = channel deviation parameter, defined by equation (32) or (37), dimensionless
ϵ = heat exchanger effectiveness, dimensionless
μ = fluid dynamic viscosity coefficient, Pa • s
ρ = fluid density, kg/m^3
χ_i = fractional distribution of the i-th shaped passages, dimensionless

Subscripts

ave = average
bc = thermal boundary condition
e = effective
i = referring to the i-th passage
m = mean
max = maximum
min = minimum
r = reference value for a nominal size or average size passage
w = wall

Downloaded 01 Jun 2010 to 171.66.16.58. Redistribution subject to ASME license or copyright; see http://www.asme.org/terms/Terms_Use.cfm

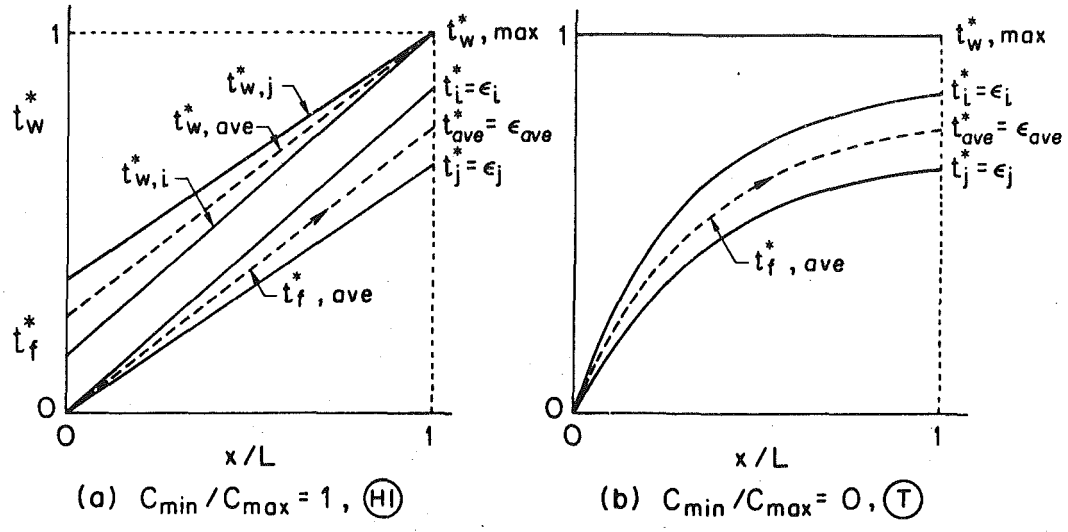


Fig. 1 Idealized wall and fluid temperature variations for the $N_{tu,e}$ evaluation

not yield an effective Nusselt number. A heat exchanger model is required and the model selected will influence the magnitude of $\mathrm{Nu}_{bc,e}$. Fig. 1 describes the temperature conditions in two such models selected for this presentation.

Fig. 1(a) describes the temperature conditions that would be obtained in a counterflow heat exchanger with $C^* = 1$ providing the controlling thermal resistance is on one fluid side so that the wall temperature is essentially that of the other fluid. Fig. 1(b) describes a $C^* = 0$ exchanger having any flow arrangement, but again with one fluid (the $C_{\min}$ fluid) providing the controlling resistance. Except for the idealization of a controlling resistance on one fluid side (the cold-side is illustrated), the model Fig. 1(a) would be descriptive of a vehicular gas turbine regenerator; and Fig. 1(b) would be for a condenser, an evaporator or a liquid-to-gas heat exchanger with the liquid capacity rate being $C_{\max}$ and $C_{\max} \gg C_{\min}$. These two extreme cases should provide the range of $\mathrm{Nu}_{bc,e}$ for multipassage geometry heat exchanger. It will be explained later how the following procedure may be extended for other heat exchanger flow arrangements.

The idealization of a controlling resistance is required in order to achieve a reasonably simple analysis. It does focus attention on the effective thermal conductance on one fluid side. The left-hand side of equations (13a) and (13b) will be defined as the number of heat transfer units for the i-th passage

$$\mathrm{N}_{tu,i} \triangleq \left(\frac{hA}{Wc_p}\right)_i = \mathrm{St}_i \frac{4L}{D_{h,i}} \tag{15}$$

Normalizing the i-th passage magnitude relative to that of the nominal or reference passage and with $D_h = 4A_cL/A$,

$$\frac{N_{tu,i}}{N_{tu,r}} = \left(\frac{D_{h,r}}{D_{h,i}}\right)^2 \left(\frac{A_{c,i}}{A_{c,r}}\right) \left(\frac{W_r}{W_i}\right) \left(\frac{\mathrm{Nu}_{bc,i}}{\mathrm{Nu}_{bc,r}}\right) \tag{16}$$

1 A Counterflow Heat Exchanger with $C^* = 1$. The relationship between exchanger effectiveness and N_{tu} for this case is [5]

$$\epsilon = \frac{N_{tu}}{1 + N_{tu}} \tag{17}$$

For each passage, the wall temperature variation parallels the fluid temperature as shown in Fig. 1(a). Consequently, it can be shown for the i-th passage that t_i^* of Fig. 1(a) is related to $N_{tu,i}$ by[3]

$$t_i^* = \frac{N_{tu,i}}{1 + N_{tu,i}} \tag{18}$$

Note that the fluid inlet temperature, Fig. 1(a), is used as the datum and that t_i^* is the outlet fluid temperature normalized with respect to the fixed wall temperature $t_{w,\max}$ at the outlet section.

The bulk average outlet temperature of the fluid is given by an energy balance as

$$Wc_p t^*_{\mathrm{ave}} = c_p \sum_{i=1}^{n} N_i W_i t_i^* \tag{19}$$

or, alternatively,

$$t^*_{\mathrm{ave}} = \sum_{i=1}^{n} \frac{N_i W_i}{W} t_i^*. \tag{20}$$

This bulk average exit fluid temperature establishes the effective N_{tu} as

$$N_{tu,e} = \frac{t^*_{\mathrm{ave}}}{1 - t^*_{\mathrm{ave}}}, \tag{21}$$

The effective Nusselt number is

$$\mathrm{Nu}_{bc,e} = \left(\frac{c_p}{kL}\right)\left(\frac{WD_h^2 N_{tu,e}}{4A_c}\right), \tag{22}$$

where A_c and D_h for the m-passage exchanger are expressed by equations (5) and (7). As the corresponding quantities are known for a reference (nominal) core designated with a subscript, r, $\mathrm{Nu}_{bc,e}$ is calculated from

$$\mathrm{Nu}_{bc,e} = \mathrm{Nu}_{bc,r} \left(\frac{N_{tu,e}}{N_{tu,r}}\right)\left(\frac{D_h}{D_{h,r}}\right)^2 \left(\frac{A_{c,r}}{A_c}\right) \tag{23}$$

Passage-to-passage nonuniformity results in a decrease in $N_{tu,e}$, $\mathrm{Nu}_{bc,e}$ and heat transfer. The decrease in heat exchanger performance may be expressed in terms of reduction in N_{tu} as

$$N^*_{tu,\mathrm{cost}} = 1 - \frac{N_{tu,e}}{N_{tu,r}} \tag{24}$$

2 A Heat Exchanger with $C^* = 0$. In this case, the relationship of effectiveness and N_{tu} for a heat exchanger of any flow arrangement reduces to the following expression [5].

$$\epsilon = 1 - \exp(-N_{tu}). \tag{25}$$

Hence, from Fig. 1(b), the effectiveness of the i-th passage will be

$$t_i^* = 1 - \exp(-N_{tu,i}). \tag{26}$$

Thus, paralleling the development of equations (20) and (21), the exchanger core average effectiveness and the effective N_{tu} are given by

$$t^*_{\mathrm{ave}} = \sum_{i=1}^{n} \frac{N_i W_i}{W} t_i^*, \tag{27}$$

[3] The t_i^* and t^*_{ave} of Fig. 1(a) may be considered as the heat exchanger effectiveness for the individual passages and the core, respectively [5]. Equation (18) is exact providing $C^* = 1$ is also obtained for the individual passages.

Downloaded 01 Jun 2010 to 171.66.16.58. Redistribution subject to ASME license or copyright; see http://www.asme.org/terms/Terms_Use.cfm

$$N_{tu,e} = \ln\left(\frac{1}{1 - t^*_{ave}}\right) \tag{28}$$

The effective Nusselt number is again expressed by equation (22) or (23), and the fractional reduction in exchanger performance by equation (24).

The thermal boundary conditions for the two heat exchanger models of Figs. 1(*a*) and 1(*b*), are, respectively, axially constant heat flux [(H1) or (H2)] and constant wall temperature (T). These qualifications are required to establish $Nu_{bc,r}$ and $Nu_{bc,i}$ in equation (16).

3 Heat Exchangers with Other Flow Arrangements. In the foregoing two special cases, it was idealized that $t_{w,max}$ was the same for all passages of different shapes at $x = L$ in Fig. 1. As a result, t_i^* magnitudes were based on the same initial temperature difference $(t_{w,max} - t_{in})$. This in turn provided a method to calculate t^*_{ave} from equation (20) or (27), and subsequently determined $N_{tu,e}$. However, for flow arrangements other than pictured in Fig. 1, the $(t_{w,max} - t_{in})$ difference for each of the multi-geometry passages will not be the same. As a consequence, one cannot arrive at t^*_{ave} and hence $N_{tu,e}$.

To alleviate the problem, an approximate method is to determine the effective heat transfer coefficient h_e and hence $Nu_{bc,e}$ first, and then determine $N_{tu,e}$ for a specific flow arrangement as follows. For a heat exchanger having a specified passage-to-passage nonuniformity, consider (1) counterflow with $C^* = 1$, and (2) an exchanger with $C^* = 0$. For both cases, determine $N_{tu,e}$ from equations (21) and (28), respectively, and subsequently evaluate $Nu_{bc,e}$ for each case using equation (22). The thermal boundary condition for a counterflow heat exchanger with $C^* = 1$ is the axially constant heat flux (H1) or (H2); while for $C^* = 0$, the boundary condition is uniform wall temperature (T). Thus $Nu_{bc,e}$ derived for the two cases represent effective Nusselt numbers for (H1) or (H2) and (T) boundary conditions, respectively. As these boundary conditions are limiting cases of the actual boundary conditions in most heat exchangers [2], a judicial choice is made for a value of effective Nusselt number. Subsequently, effective h and N_{tu} are calculated. And a proper expression for $\epsilon - N_{tu}$ relationship is employed for heat exchanger analysis to determine ϵ for the case of nonuniform passages.

Developing Flows. If the velocity and/or temperature profiles are developing, as is the case for short tube $L/D_h < 100$ heat exchanger surfaces,[4] the foregoing development is valid if $(fRe)_i$ and $Nu_{bc,i}$ are replaced by $(f_{app}Re)_i$ and $(Nu_{m,bc})_i$. However, these latter quantities are not constant as in fully developed flow. They are dependent upon L_i^+ $(= L_{hy}/D_h Re)$ and L_i^* $(= L_{th}/D_h Pe)$ which are dependent upon the i-th passage L/D_h and Re for a given Pr. Once L_i^+ are known, $(f_{app}Re)_i$ and $(Nu_{m,bc})_i$ are determined from the respective entry length solutions. However, the flow distribution must be known to determine L_i^+ and L_i^*. Hence, the calculation procedure becomes an iterative one as follows.

1 Start with a uniform flow distribution. Determine Re_i, L_i^+, and $(f_{app}Re)_i$ for the i-th shaped passages. Subsequently, calculate $(f_{app}Re)_e$ using equation (9) and the flow distribution from equation (10). With this flow distribution, calculate new values of Re_i, L_i^+, and $(f_{app}Re)_i$. Repeat the above procedure until the solution converges to the desired degree of accuracy.[5]

2 Employing the converged solution for the flow distribution and the known thermal entry length solution will provide $(Nu_{m,bc})_e$, in a straightforward manner (no iterations), for the two special cases of heat exchangers described by Fig. 1.

Illustrative Results (Fully Developed Laminar Flow)

The analysis presented in the preceding section has been applied to rectangular and triangular passages for three types of nonuniformities characterized by two passage sizes. Thermally and hydrodynamically fully developed flow is postulated. The results obtained are presented only for the (H1) and (T) boundary conditions. No results are presented for developing flows.

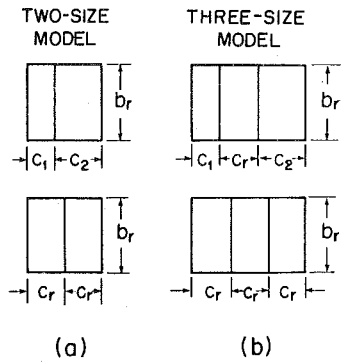


Fig. 2 Two-passage and three-passage fin-spacing type nonuniformity models for rectangular passages

Rectangular Passages.

Two-Passage Fin-Spacing Type Nonuniformity. A large and a small passage and the corresponding two nominal size rectangular passages are shown in Fig. 2(*a*). London [1] provided the results for this nonuniformity for two aspect ratios, $\alpha_r^* = 0.125$ and 1, for the (H1) boundary condition for $N_{tu,r} = 20$.[6] These are extended for both the (H1) and (T) boundary conditions for $\alpha_r^* = 0.125, 0.25, 0.50, 1$, and $N_{tu,r} = 1, 5, 10, 20, 50$. The core is considered to have 50 percent large and 50 percent small passages. The following theoretical values of friction factors and Nusselt numbers have been used for fully developed laminar flow through rectangular passages [2].

$$fRe = 24\,[1 - 1.3553\alpha^* + 1.9467\alpha^{*2} - 1.7012\alpha^{*3} + 0.9564\alpha^{*4} - 0.2537\alpha^{*5}] \tag{29}$$

$$Nu_{H1} = 8.235\,[1 - 2.0421\alpha^* + 3.0853\alpha^{*2} - 2.4765\alpha^{*3} + 1.0578\alpha^{*4} - 0.1861\alpha^{*5}] \tag{30}$$

$$Nu_T = 7.541\,[1 - 2.610\alpha^* + 4.970\alpha^{*2} - 5.119\alpha^{*3} + 2.702\alpha^{*4} - 0.548\alpha^{*5}] \tag{31}$$

Typical results for two-passage nonuniformity are presented in Figs. 3, 4, and 5 with $(fRe)_e$ and $Nu_{bc,e}$ graphed as functions of the channel deviation δ_c, the nominal or reference aspect ratio α_r^*, and $N_{tu,r}$. The Nusselt numbers for the (H1) boundary condition are presented in Figs. 4 and 5 as an illustration. Fig. 6 provides a comparison of the results for the (T) and (H1) boundary conditions described in Figs. 1(*a*) and 1(*b*).

It is evident from Figs. 4 and 5 that the $N_{tu,r} = 5$ curve is representative of the higher $N_{tu,r}$ range and is therefore typical of high effectiveness heat exchangers. In contrasting Figs. 4 and 5, it is clear that the penalties in heat transfer are greater for the smaller aspect ratio passages.

Three-Passage Nonuniformity. A three-passage model considered consists of a small, a nominal and a large rectangular passage as shown in Fig. 2(*b*). Two variables of nonuniformity are analyzed: the passage size such that $c_r - c_1 = c_2 - c_r$, and the number of passages for each size such that $\chi_1 = \chi_2$, and $\chi_3 (= \chi_r) = 1 - (\chi_1 + \chi_2)$. Thus passage distribution is selected as symmetric so that the total surface and flow areas of the three-size passages are the same as that for the reference geometry. $(fRe)_e$, and $Nu_{bc,e}$, are evaluated for the following ranges: $(1 - c_1/c_r) = 0.05, 0.10, 0.15, 0.20$, and 0.25; $\chi_1 = \chi_2 = 0.10, 0.20, 0.30, 0.333, 0.40$, and 0.50. Note that when $\chi_1 = \chi_2 = 0.50$, the number of nominal passages is zero, and the three-passage model reduces to the previously considered two-passage model.

For a three-passage model, the passage-to-passage nonuniformity is influenced by two variables associated with this nonuniformity: $(1 - c_1/c_r)$ and $\chi_1 (= \chi_2)$. Several combinations of these variables were

[4] For highly interrupted heat exchanger surfaces, flow uniformity tends to be assured so that the passage-to-passage nonuniformity is not of a great importance.

[5] Since the $(f_{app}Re)_e$ versus x^+ (a dimensionless axial variable x/D_h Re) curve is smooth and monotonic, the Newton-Raphson or a similar method should converge easily, although we have not made any calculations.

[6] Numerical errors found in the $\alpha^* = 1$ results of [1] produced the negative sign for Δp^*_{gain} in Table 1 of [1].

Downloaded 01 Jun 2010 to 171.66.16.58. Redistribution subject to ASME license or copyright; see http://www.asme.org/terms/Terms_Use.cfm

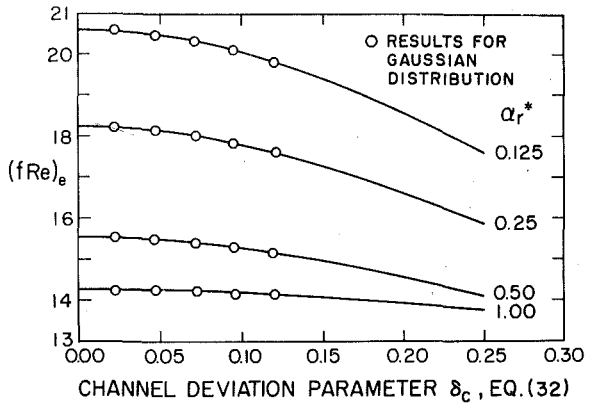


Fig. 3 Two-passage nonuniformity in rectangular passages; $(fRe)_e$ as a function of the channel deviation and aspect ratio. Data points are for the eleven-passage Gaussian distribution

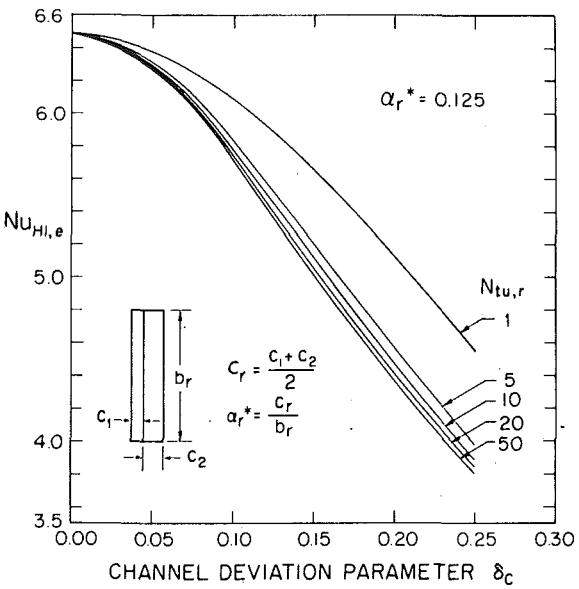


Fig. 4 Two-passage nonuniformity in rectangular passages of nominal aspect ratio of 0.125; $Nu_{H1,e}$ as a function of channel deviation and reference N_{tu} (for nominal passages)

investigated and the following channel "standard" deviation parameter δ_c was found to correlate very well the results to be discussed.

$$\delta_c = \sum_{i=1}^{n} \left[\chi_i \left(1 - \frac{c_i}{c_r} \right)^2 \right]^{1/2} \tag{32}$$

For a two-passage model ($n = 2$) with $\chi_1 = \chi_2 = 0.50$, the standard deviation parameter of equation (32) reduces to

$$\delta_c = 1 - c_1/c_r \tag{33}$$

as used previously in Figs. 3–6. Fig. 7 illustrates the adequacy of δ_c of equation (32) as a correlating parameter. The solid line curves are for the two-size model with the results for the three-size model superimposed as data points. The correlation appears to be quite adequate for both heat transfer and flow friction behavior.

Gaussian Distribution Passage-to-Passage Nonuniformity. There is probably a considerable spectrum in passage-to-passage variation in heat exchanger matrix. To investigate this point, a Gaussian passage size distribution was approximated by treating it as an equivalent eleven-passage model as illustrated in Table 1.

Results were established for Gaussian passage-to-passage nonuniformities with nominal passages of $\alpha_r^* = 0.125, 0.25, 0.5$ and 1 and with channel width extremes $(1 - c_1/c_r)$ of 0.05, 0.10, 0.15, 0.20, and 0.25. The channel standard deviation parameter δ_c of equation (32) was evaluated as indicated in Table 2.[7] $Nu_{bc,e}$ and $(fRe)_e$ results for the Gaussian passage-to-passage nonuniformity are superimposed in Figs. 6 and 3 as data points. Again, it can be seen that the standard deviation δ_c correlates very well the results for the Gaussian passage distribution.

[7] It should be noted that the value of δ_c is significantly lower for 11-passage Gaussian distribution compared to that for a two-passage nonuniformity for a specified value of $(1 - c_1/c_r)$.

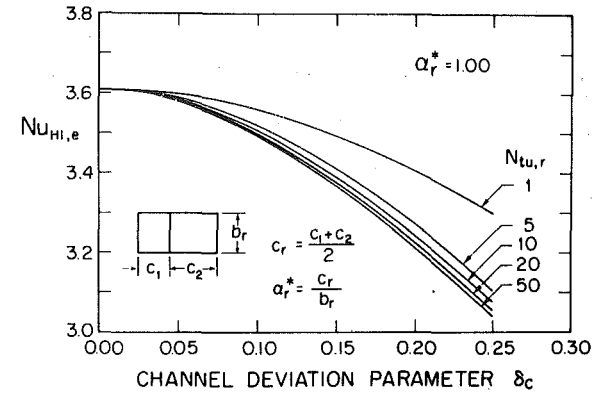


Fig. 5 Two-passage nonuniformity in rectangular passages of nominal aspect ratio of 1; $Nu_{H1,e}$ as a function of channel deviation and reference N_{tu}

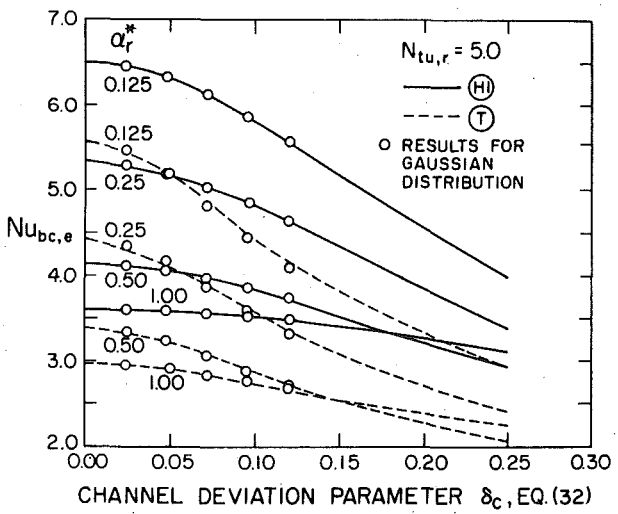


Fig. 6 Two-passage nonuniformity in rectangular passages; a comparison of $Nu_{H1,e}$ and $Nu_{T,e}$. Data points are for the eleven-passage Gaussian distribution

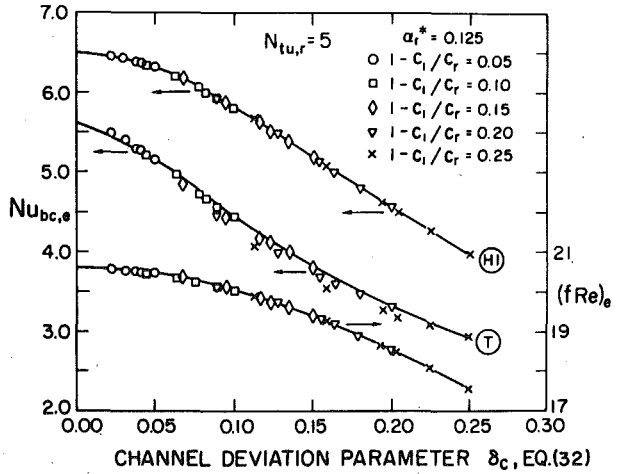


Fig. 7 Three-passage nonuniformity in rectangular passages; $Nu_{H1,e}$, $Nu_{T,e}$, and $(fRe)_e$ for $\alpha_r^* = 0.125$ plotted as data points. The solid lines are for the two-passage model of Figs. 3 and 6 for $\alpha_r^* = 0.125$

Downloaded 01 Jun 2010 to 171.66.16.58. Redistribution subject to ASME license or copyright; see http://www.asme.org/terms/Terms_Use.cfm

Table 1 Approximate Gaussian passage distribution for eleven rectangular passages model, $\alpha_r^* = 0.125$, $(1 - c_1/c_r) = 0.05$ and $\delta_c = 0.0240$

i	α_i^*	χ_i
1	0.1193	0.0436
2	0.1204	0.0649
3	0.1216	0.0884
4	0.1227	0.1107
5	0.1239	0.1262
6	0.1250	0.1324
7	0.1261	0.1262
8	0.1273	0.1107
9	0.1284	0.0884
10	0.1295	0.0649
11	0.1307	0.0436
		$\Sigma = 1.000$

Table 2 Standard deviation for the approximate Gaussian distribution investigated for $\alpha_r^* = 0.125$

$(1 - c_1/c_r)$	δ_c from equation (32)	$\delta_c/(1 - c_1/c_r)$
0.05	0.0240	0.48
0.10	0.0481	0.48
0.15	0.0721	0.48
0.20	0.0961	0.48
0.25	0.1201	0.48

Triangular Passages.

Two-Passage Plate-Spacing Type Nonuniformity. A two-size model of this type is shown in Fig. 8(*a*). London [1] provided the results for this nonuniformity for the (H1) boundary condition for $N_{tu,r} = 20$. These results are extended for both the (H1) and (T) boundary conditions for $N_{tu,r} = 1, 5, 10$ and 20. In the two-passage model, the number of large and small passages is the same. The following theoretical values of friction factors and Nusselt numbers have been used for fully developed laminar flow through equilateral triangular passages [2].

$$fRe = 13.333 \tag{34}$$

$$Nu_{H1} = 3.111 \tag{35}$$

$$Nu_T = 2.47 \tag{36}$$

The results for the two-passage model are presented in Figs. 9 and 10. The standard deviation parameter δ_c is defined in equation (37) in a manner similar to that for the rectangular passages. The ratio of base lengths is identical to the ratio of hydraulic radii. Hence for triangular passages,

$$\delta_c = \sum_{i=1}^{n} \left[\chi_i \left(1 - \frac{r_{h,i}}{r_{h,r}} \right)^2 \right]^{1/2} \tag{37}$$

which simplifies to the following for the two-size model under consideration

$$\delta_c = 1 - r_{h,1}/r_{h,r} = 1 - c_1/c_r \tag{38}$$

To maintain the total flow area of the nonuniform passages the same as the reference passages, the hydraulic radii are related by

$$r_{h,1}^2 + r_{h,2}^2 = 2r_{h,r}^2 \tag{39}$$

or

$$\frac{r_{h,2}}{r_{h,r}} = \left[2 - \left(\frac{r_{h,1}}{r_{h,r}} \right)^2 \right]^{1/2} \tag{40}$$

The results are presented in Fig. 9 for both the (H1) and (T) boundary conditions.

Three-Passage Plate-Spacing Type Nonuniformity. A three-passage model of this type is shown in Fig. 8(*b*). Paralleling the rectangular passage investigation, two variables of nonuniformity are studied: $(1 - r_{h,1}/r_{h,r})$ and χ_1. The passage distribution is selected symmetric so that $\chi_1 = \chi_2$ and $\chi_3 = 1 - (\chi_1 + \chi_2)$. For $\chi_1 = \chi_2 = 0.50$, the three-passage model reduces to the two-passage model.

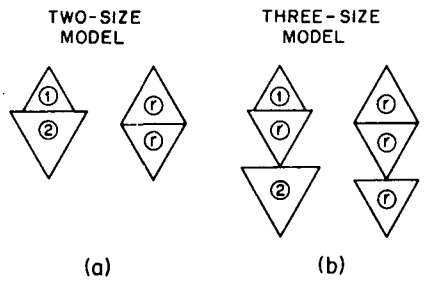


Fig. 8 Two and three passage nonuniformity models for equilateral triangular passages

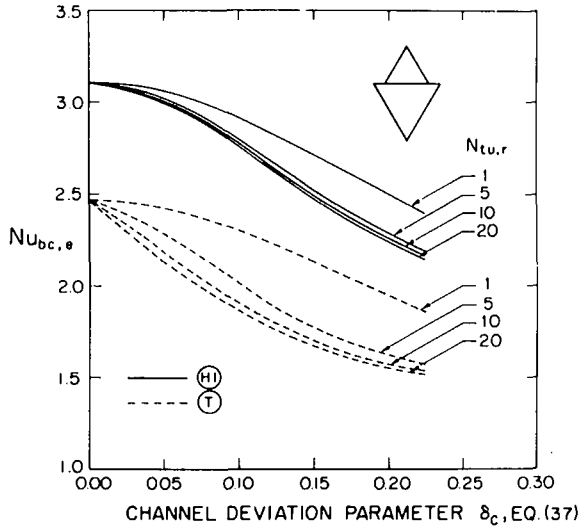


Fig. 9 Two-passage nonuniformity in triangular passages: $Nu_{H1,e}$, $Nu_{T,e}$ and $(fRe)_e$ as functions of δ_c and $N_{tu,r}$

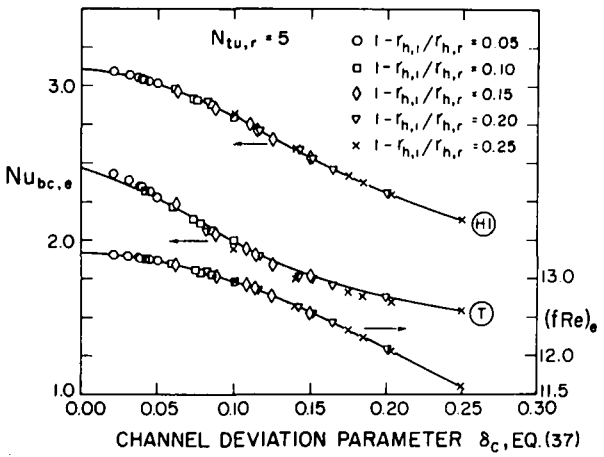


Fig. 10 Three-passage nonuniformity in triangular passages: $Nu_{H1,e}$, $Nu_{T,e}$ and $(fRe)_e$ plotted as data points. The solid lines are for the two-passage model results from Fig. 9

The results for the three-passage model are shown in Fig. 10 as a function of the channel standard deviation parameter of equation (37). The solid lines are for the two-passage model. As for the rectangular passages, Fig. 7, it is apparent that the channel standard deviation parameter provides a very good correlation.

Gaussian Distribution Plate-Spacing Type Nonuniformity. Based on the experience with the rectangular passage geometries, Figs. 3 and 6 relative to 7, it is expected that the channel standard deviation factor of equation (37) should provide a good correlation with the two-size and three-size models for plate-spacing type nonuniformities having a Gaussian distribution.

Downloaded 01 Jun 2010 to 171.66.16.58. Redistribution subject to ASME license or copyright; see http://www.asme.org/terms/Terms_Use.cfm

Discussion and Conclusions

An analytical procedure is presented to establish the effective friction factors and Nusselt numbers for a heat exchanger core consisting of cylindrical passage channels having different cross sections. The illustrative numerical results demonstrate the validity of using a standard deviation parameter δ_c, defined by equations (32) and (37), to characterize the nonuniformities in channel cross sections for the geometries described in Figs. 2 and 8. Moreover, Mondt's experimental results [3] suggest that a bulginess standard deviation parameter may be combined with fin spacing standard deviation factor into a single total deviation factor[8] for deepfold surfaces.

A comparison of the results in Figs. 3, 6 and 7 clearly show that the deterioration in performance[9] is less severe for a given channel deviation $(1 - c_1/c_r)$, if the nonuniformity is considered as having n passages ($n > 2$) instead of two passages. For example, $(1 - c_1/c_r)$ of 0.25 for a two-passage model results in $\delta_c = 0.25$. For the same lowest and highest aspect ratios, an eleven-passage model with Gaussian distribution results in $\delta_c = 0.12$. Thus the two-passage model will provide the greatest deterioration in performance if the passage-to-passage nonuniformity is considered to be symmetrical around the nominal passages.

Figs. 7 and 10 illustrate that a channel standard deviation as small as 5 percent result in heat transfer penalties of the order of 10 percent for the (T) boundary condition and a smaller amount for the (H1) boundary condition. The corresponding gain of reduced pressure drop is negligible. It is recommended, therefore, that manufacturing tolerance goals should be set for $\delta_c \leq 5$ percent.

The foregoing comments apply to passage nonuniformities that are distributed in a symmetrical manner about the nominal or reference passage dimension. A computer test of some skewed distributions demonstrated that δ_c as defined by equations (32) and (37) is inadequate as a correlating parameter.

For approximately symmetrical distribution of nonuniformities, with 95 percent of the passages contained within the bounds

$$0.90 < (c/c_r \text{ or } D_h/D_{h,r}) < 1.10$$

the standard deviation parameter may be approximated by

$$\delta_c = \frac{1}{2}\left(1 - \frac{c_1}{c_r}\right) \quad \text{or} \quad \frac{1}{2}\left(1 - \frac{D_{h,1}}{D_{h,r}}\right) \tag{41}$$

where the subscript 1 represents the lower bound. This conclusion assumes that the distribution is approximately Gaussian and stems from the computer results plotted as data points in Figs. 3 and 6 corresponding to the δ_c's of Table 2. Thus, the previous recommendation for a manufacturing tolerance goal of $\delta_c \leq 5$ percent corresponds to the ±10 percent range indicated above.

More experiments of the type described by Mondt [3] are needed for actual core passage size and geometry distributions, together with heat transfer and flow friction performance. This information would be of value in substantiating or modifying the manufacturing tolerance goals proposed here.

Acknowledgments

The authors appreciate the assistance provided by E. Sanderson and R. Johnson for calculating the numerical results for the illustrative examples.

References

1 London, A. L., "Laminar Flow Gas Turbine Regenerators—The Influence of Manufacturing Tolerances," ASME JOURNAL OF ENGINEERING FOR POWER, Vol. 92, 1970, pp. 46–56.

2 Shah, R. K., and London, A. L., *Laminar Flow Forced Convection in Ducts*, Supplement 1 to *Advances in Heat Transfer*, Academic Press, New York, 1978.

3 Mondt, J. R., "Effects of Nonuniform Passages on Deepfold Heat Exchanger Performance," ASME JOURNAL OF ENGINEERING FOR POWER, Vol. 99, 1977, pp. 657–663; discussion by A. L. London, ASME JOURNAL OF ENGINEERING FOR POWER, Vol. 102, No. 2, Apr. 1980.

4 Shah, R. K., "Laminar Flow Friction and Forced Convection Heat Transfer in Ducts of Arbitrary Geometry," *International Journal of Heat and Mass Transfer*, Vol. 18, 1975, pp. 849–862.

5 Kays, W. M., and London, A. L., *Compact Heat Exchangers*, Second Edition, McGraw-Hill Book Co., New York, 1964.

[8] See discussion of [3] where a square root of the sum of the squares total factor is proposed.

[9] Meaning the reduction in heat transfer ($Nu_{bc,e}$ or $N^*_{tu,cost}$).

Downloaded 01 Jun 2010 to 171.66.16.58. Redistribution subject to ASME license or copyright; see http://www.asme.org/terms/Terms_Use.cfm

Discussion and Conclusions

An analytical procedure is presented to establish the effective friction factors and Nusselt numbers for a heat exchanger core consisting of cylindrical passage channels having different cross sections. The illustrative numerical results demonstrate the validity of using a standard deviation parameter δ_c, defined by equations (32) and (37), to characterize the nonuniformities in channel cross sections for the geometries described in Figs. 2 and 8. Moreover, Mondt's experimental results [3] suggest that a bulginess standard deviation parameter may be combined with fin spacing standard deviation factor into a single total deviation factor[8] for deepfold surfaces.

A comparison of the results in Figs. 3, 6 and 7 clearly show that the deterioration in performance[9] is less severe for a given channel deviation $(1 - c_1/c_r)$, if the nonuniformity is considered as having n passages ($n > 2$) instead of two passages. For example, $(1 - c_1/c_r)$ of 0.25 for a two-passage model results in $\delta_c = 0.25$. For the same lowest and highest aspect ratios, an eleven-passage model with Gaussian distribution results in $\delta_c = 0.12$. Thus the two-passage model will provide the greatest deterioration in performance if the passage-to-passage nonuniformity is considered to be symmetrical around the nominal passages.

Figs. 7 and 10 illustrate that a channel standard deviation as small as 5 percent result in heat transfer penalties of the order of 10 percent for the (T) boundary condition and a smaller amount for the (H1) boundary condition. The corresponding gain of reduced pressure drop is negligible. It is recommended, therefore, that manufacturing tolerance goals should be set for $\delta_c \leq 5$ percent.

The foregoing comments apply to passage nonuniformities that are distributed in a symmetrical manner about the nominal or reference passage dimension. A computer test of some skewed distributions demonstrated that δ_c as defined by equations (32) and (37) is inadequate as a correlating parameter.

For approximately symmetrical distribution of nonuniformities, with 95 percent of the passages contained within the bounds

$$0.90 < (c/c_r \text{ or } D_h/D_{h,r}) < 1.10$$

the standard deviation parameter may be approximated by

$$\delta_c = \frac{1}{2}\left(1 - \frac{c_1}{c_r}\right) \quad \text{or} \quad \frac{1}{2}\left(1 - \frac{D_{h,1}}{D_{h,r}}\right) \tag{41}$$

where the subscript 1 represents the lower bound. This conclusion assumes that the distribution is approximately Gaussian and stems from the computer results plotted as data points in Figs. 3 and 6 corresponding to the δ_c's of Table 2. Thus, the previous recommendation for a manufacturing tolerance goal of $\delta_c \leq 5$ percent corresponds to the ±10 percent range indicated above.

More experiments of the type described by Mondt [3] are needed for actual core passage size and geometry distributions, together with heat transfer and flow friction performance. This information would be of value in substantiating or modifying the manufacturing tolerance goals proposed here.

Acknowledgments

The authors appreciate the assistance provided by E. Sanderson and R. Johnson for calculating the numerical results for the illustrative examples.

References

1 London, A. L., "Laminar Flow Gas Turbine Regenerators—The Influence of Manufacturing Tolerances," ASME JOURNAL OF ENGINEERING FOR POWER, Vol. 92, 1970, pp. 46–56.

2 Shah, R. K., and London, A. L., *Laminar Flow Forced Convection in Ducts*, Supplement 1 to *Advances in Heat Transfer*, Academic Press, New York, 1978.

3 Mondt, J. R., "Effects of Nonuniform Passages on Deepfold Heat Exchanger Performance," ASME JOURNAL OF ENGINEERING FOR POWER, Vol. 99, 1977, pp. 657–663; discussion by A. L. London, ASME JOURNAL OF ENGINEERING FOR POWER, Vol. 102, No. 2, Apr. 1980.

4 Shah, R. K., "Laminar Flow Friction and Forced Convection Heat Transfer in Ducts of Arbitrary Geometry," *International Journal of Heat and Mass Transfer*, Vol. 18, 1975, pp. 849–862.

5 Kays, W. M., and London, A. L., *Compact Heat Exchangers*, Second Edition, McGraw-Hill Book Co., New York, 1964.

[8] See discussion of [3] where a square root of the sum of the squares total factor is proposed.

[9] Meaning the reduction in heat transfer ($Nu_{bc,e}$ or $N^*_{tu,cost}$).

DISCUSSION

J. R. Mondt.[1] The authors of this paper deserve congratulations for a valuable contribution to the technical literature on nonuniform passages in heat exchangers. Using the correlations in this paper, the designer of a compact heat exchanger can assess the impact of passage-to-passage nonuniformities on performance. With the effects of nonuniformities known, the designer can enlarge the heat exchanger to compensate for the performance loss, or the designer can specify better control of manufacturing tolerances.

It is encouraging that the root-sum-square or standard deviation parameter correlates the performance decrement for the three-passage models and Gaussian-passage distribution. This standard deviation parameter is an extension of the correlation used to combine deepfold nonuniformities, channel deviation and bulginess [3].

The authors present correlations for the 8 to 1 and 1 to 1 rectangle passage as well as the equilateral triangle, thereby giving the designer information for the most popular flow passages. Performance loss is correlated for a channel deviation up to 0.25. To substantiate these correlations, additional experiments are needed.

[1] Engine Research Department, General Motors Research Laboratories, Warren, Mich. 48090.

Authors' Closure

We appreciate Mr. Mondt's discussion and fully agree with the need for further experimental work to either substantiate or modify the reported theoretical results. These are difficult experiments to model successfully because of the requirement of high precision for the statistical-geometrical measurements and the heat transfer and flow friction measurements.

Copyright © 1980 by ASME

Downloaded 01 Jun 2010 to 171.66.16.58. Redistribution subject to ASME license or copyright; see http://www.asme.org/terms/Terms_Use.cfm

S. M. Cho

Manager,
Thermal/Hydraulic and Systems Engineering,
Nuclear and Advanced Technology Operations,
Foster Wheeler Energy Corporation,
Livingston, NJ 07039
Mem. ASME

R. S. Kane

Assistant Professor,
Mechanical Engineering Department,
Manhattan College,
Riverdale, NY 10471
Mem. ASME

Techniques for the Thermal/ Hydraulic Analysis of LMFBR Check Valves

A thermal/hydraulic analysis of the check valves in liquid sodium service for LMFBR plants is required to provide temperature data for thermal stress analysis of the valves for specified transient conditions. Because of the complex three-dimensional flow pattern within the valve, the heat transfer analysis techniques for less complicated shapes could not be used. This paper discusses the thermal analysis techniques used to assure that the valve stress analysis is conservative. These techniques include a method for evaluating the recirculating flow patterns and for selecting appropriately conservative heat transfer correlations in various regions of the valve.

Introduction

The Clinch River Breeder Reaction Plant (CRBRP) will be the first major U. S. demonstration plant of a large size, liquid metal fast breeder reactor (LMFBR) power plant. Multiple and redundant safeguards against overheating of the reactor are an integral feature of the plant design [1]. The reactor is cooled by liquid sodium in three loops. Each of these three loops in turn transfers the heat removed from the reactor to intermediate loops also carrying liquid sodium. The intermediate sodium loops then transfer this heat to steam/water loops which eventually use the energy obtained, to drive a steam turbine and generate electrical power. The sodium coolant passing through the reactor is driven by the action of three primary sodium pumps. Although the three loops are essentially independent, the three coolant streams affect each other in the reactor core itself. In the event of a trip of one of the primary pumps and a loss of flow in that loop, the remaining two operational pumps would tend to reverse the flow of coolant from the idle loop and attempt to drive the tripped pump like a turbine. This cannot be permitted. In order to prevent this from occurring, the system design includes a tilting disc check valve in the cold leg of each of the three primary cooling loops. A failure of the pump in that loop and the resultant inception of reverse flow would cause the check valve disk to move toward a closed position. Previous work [2] describes the behavior and operation of this type of valve under both forward and reverse flow conditions. This paper describes the heat transfer and related analysis performed to aid the thermal stress analysis of these valves and thereby assure the structural integrity of the valve under a variety of specified transient events.

Contributed by the Nuclear Engineering Division and presented at the Winter Annual Meeting, December 2–7, 1979, New York, New York, of THE AMERICAN SOCIETY OF MECHANICAL ENGINEERS. Manuscript received at ASME Headquarters August 1, 1979. Paper No. 79-WA/NE-4.

Valve Description and Thermal Stress Analysis Approach

Fig. 1 is a schematic of the CRBRP check valve. Each of the three valves is constructed of type 304 stainless steel and is buttwelded into the 0.610m (24 in.) return piping between the intermediate heat exchanger and the reactor. The valve features a tilting disc which during normal forward flow operation is limited to a maximum open angle of 36 deg from the vertical. At the lowest normal forward flow, natural circulation in the primary loop, the disk will be located near its free hang angle of 13.4 deg. Flows lower than the natural circulation flow will occur only if a pump has failed and a flow coastdown toward impending reverse flow is in progress. As the disk approaches its seat, the disc closure from an angle of 6 deg down to zero is slowed by an orifice-controlled dashpot (the dashpot is not shown in Fig. 1). The dashpot is designed to prevent excessively rapid closures and therefore to prevent excessively high fluid hammer transient pressures.

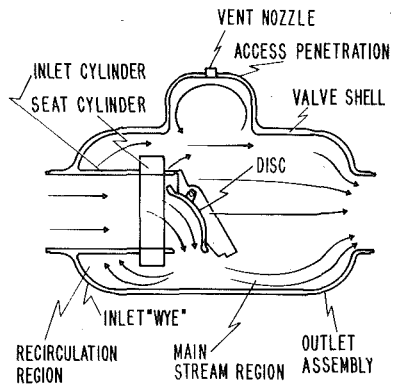


Fig. 1 Primary loop, cold leg check valve

Copyright © 1980 by ASME

Downloaded 01 Jun 2010 to 171.66.16.58. Redistribution subject to ASME license or copyright; see http://www.asme.org/terms/Terms_Use.cfm

The shape of the valve body, the presence of the disc, the location of the dashpot and a large welded access opening with a vent nozzle complicate the flow patterns even during normal forward flow conditions as shown in Fig. 1. The flow is straight-through from the inlet piping through the inlet passage leading to the disk. As the flow nears the disk, some of the flow will be deflected by the disk and form a symmetrical recirculating flow that passes under and then circumferentially around the inlet passage. This flow passes over the top of the disc to rejoin the main flow stream beyond the disk then leaves the valve and enters the downstream piping. The access opening and vent nozzle are welded in place except when removed for repairs and maintenance during shutdown periods. The flow in these areas will be characterized by large, for the access opening, and small, for the vent nozzle, recirculation zones.

The thermal stress analysis of the valve required calculation of heat transfer coefficients and specification of sodium temperatures during certain transient events. Because of the complicated flow patterns in the valve, the thermal analysis of the valve structure was subdivided into smaller regions, each characterized or dominated by one particular type of convective heat transfer mechanism. In those regions where alternative heat transfer mechanisms could be postulated, the most conservative one was used. In general (with the outside surface of the inlet pipe as a notable exception) the most conservative mechanism was the one that gave the highest heat transfer coefficients and therefore most rapidly transmitted sharp changes in fluid temperature to the valve structure. The task of the structural analysis was then to verify the ability of the valve to withstand a specified number of certain types of thermal cycles. The configuration of the valve suggested that the computerized thermal stress analysis of the valve be performed by subdividing the valve into four major sections. Each section was then considered to be influenced over limited regions, as shown in Figs. 2–5, by one type of convective heat transfer mechanism. For specified transients, the convective heat transfer coefficients were supplied for each region.

Linearization of Transient Flow and Fluid Temperature Data

Prior to the actual analysis, a histogram giving frequency versus severity of transients (as determined by the rate and duration of the most severe temperature change during the event) was developed from the design specification. Similar events in terms of their most severe temperature changes were conservatively placed within a single group that was as severe as the most severe event included in the group. This technique provided a method for evaluating the adequacy of the structure for all specified transients within the framework of an increased frequency but smaller number of separate events. Typically these groups could be characterized as the most severe upshock (rapid increase in temperature), the most severe downshock (rapid decrease in temperature), and the most severe combination of both upshock and downshock.

In order to provide a tractable amount of data for the structural analysis, the curves of sodium temperature and flow rate through the valve as functions of time for specified transient conditions were linearized. The curves were approximated by limited numbers of discrete temperature and flow rate points that if connected by straight lines gave a close description of the actual curve. Portions of the curves characterized by sharp and fluctuating changes in slope within small time spans required closely spaced points. However, many lengthy portions existed where slope changes were infrequent and therefore easily described by widely spaced points. Most of the sharp temperature changes usually occurred within the first 1200 seconds of an event. A typical case required about 20 points for an accurate description.

One characteristic of the transient descriptions was that the points needed to linearize the temperature curve did not generally coincide with the points needed to linearize the flow curve. To simplify the calculation of heat transfer coefficients, the flow curve points alone were used to establish the points for linearized curves of heat transfer coefficient versus time. The temperature variations were considered to have only a secondary effect, through variation of fluid properties, on the value of the local heat transfer coefficients. However the temperature points were considered to be of equal, if not primary importance, in the input to the structural analysis work. Therefore both linearized sets of data, heat transfer coefficients versus time based on the linearized flow curves, and the fluid temperature versus time were supplied. The preponderant effect of flow on heat transfer coefficient as compared to that of temperature permitted the structural analysis to safely interpolate linearly in the heat transfer coefficient data to obtain coefficients corresponding to the linearized temperature data points.

Heat Transfer Correlations

Table 1 lists the heat transfer correlations used for the regions shown in Figs. 2–5. (Most of the correlations cited in the table were taken from [3] which provides an excellent collection of liquid metal heat transfer information.) Correlation (1) is obtained from a solution for fully developed turbulent flow in a pipe. This situation does not occur anywhere within the valve where a pipe flow correlation is most appropriate. The flow into the valve is disturbed by the presence of an elbow only about 6 diameters upstream of the valve inlet. Consequently, the heat transfer coefficients based on correlation (1) were modified using correlation (2) which accounts for the effects of developing flow.

The region around the outside of the inlet passage is subject to both a reverse axial flow and a circumferential flow (the analysis used to determine the velocity distribution in this region is described later). A conservative stress analysis in this region results from the use of the heat transfer correlation that gives the lowest reasonable heat transfer coefficient. The combination of a high heat transfer coefficient on the inside of the inlet passage and a lower heat transfer coefficient on the

Nomenclature

A_{pfp} = area of a flat plate projected on a cavity, m^2
A_w = total area of cavity walls, m^2
D = inside diameter of a pipe, m
D_i = inner diameter of an annulus, m
D_o = outer diameter of an annulus, m
f = multiplicative factor in equation (12)
g_i = body force per unit mass, $m \cdot s^{-2}$
h = heat transfer coefficient, $W \cdot m^{-2} \cdot °C^{-1}$
h_{pfp} = heat transfer coefficient for a flat plate projected onto a cavity, $W \cdot m^{-2} \cdot °C^{-1}$
h_w = heat transfer coefficient on a cavity wall, $W \cdot m^{-2} \cdot °C^{-1}$
K_i = distributed resistance coefficient, m^{-1}
L = length of entrance region, m
Nu = Nusselt number, dimensionless
Nu_{local} = entrance region Nusselt number, dimensionless
Nu_∞ = fully developed flow Nusselt number, dimensionless
p = pressure, Pa
Pe = Peclet number, dimensionless
Pr = Prandtl number, dimensionless
q = specific turbulence energy, $m^2 \cdot s^{-2}$
r_i = distributed resistance, $m \cdot s^{-2}$
R_{ij} = Reynolds stress, Pa
u_i, u_j = velocity components, $m \cdot s^{-1}$
x_i, x_j = linear spatial dimension, m
α = factor in correlation (3), dimensionless
α_1 = dissipation coefficient, turbulent parameter in equation (15), dimensionless
β = factor in correlation (3), dimensionless
γ = factor in correlation (3), dimensionless
γ_1, γ_2 = relative diffusivity coefficients, turbulent parameters in equation (16), dimensionless
δ_{ij} = Kronecker delta, dimensionless
ϵ_M = eddy momentum diffusivity, $m^2 \cdot s^{-1}$
ν = molecular momentum diffusivity, $m^2 \cdot s^{-1}$
ϕ = ratio of heat transfer on a projected flat plate to heat transfer on a cavity wall, dimensionless
$\bar{\psi}$ = average value of the ratio of thermal eddy diffusivity to momentum eddy diffusivity, dimensionless
σ = turbulent kinematic viscosity, $m^2 \cdot s^{-1}$

Downloaded 01 Jun 2010 to 171.66.16.58. Redistribution subject to ASME license or copyright; see http://www.asme.org/terms/Terms_Use.cfm

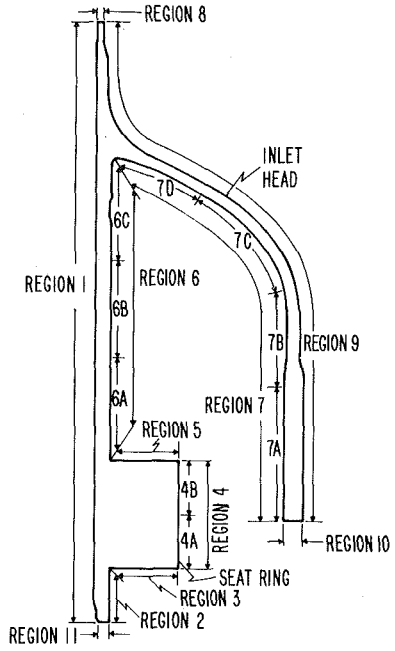


Fig. 2 Inlet and seat assembly, heat transfer regions

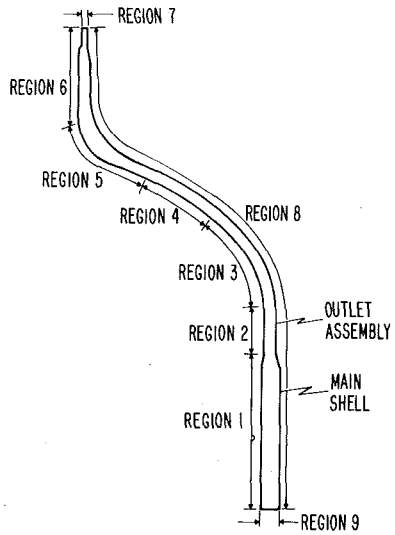


Fig. 3 Outlet Assembly, heat transfer regions

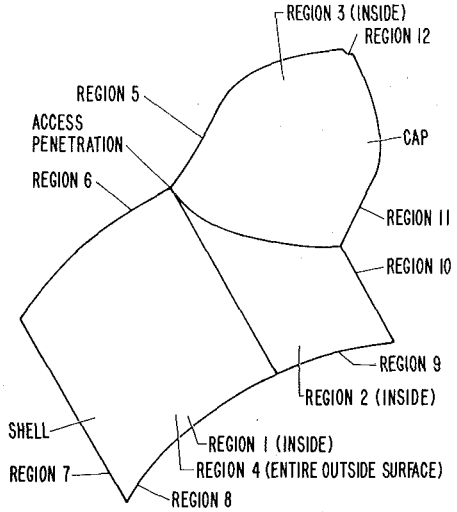


Fig. 4 Access penetration assembly, heat transfer regions

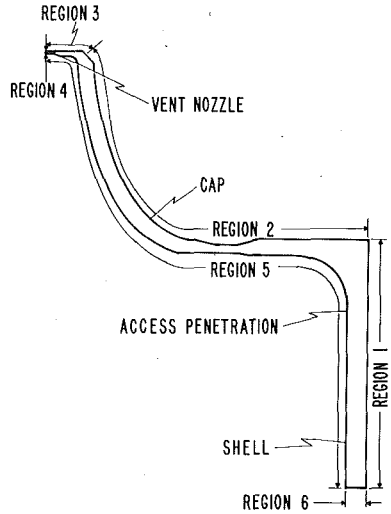


Fig. 5 Vent nozzle assembly, heat transfer region

outside of the inlet passage increases the transient thermal stresses across the wall during periods of rapidly varying fluid temperatures. The correlation that was used for the outside of the inlet passage, correlation (3), satisfies the criteria for the conservative stress analysis. Correlation (3) is appropriate for annular flow, using the reverse axial velocities, and gives lower heat transfer coefficients than any reasonable correlation that might have been used for the somewhat higher circumferential velocities in this region. In correlation (3), the hydraulic diameter of an annulus was used as the characteristic dimension in the Nusselt and Peclet numbers. The momentum diffusivity ratio (ϵ_M/ν) appearing in this correlation is a function of Reynolds number and geometry. Curves suitable for design calculations appear in [3]. The theoretical background and derivation of relationships for the momentum diffusivity ratio are given in [9]. If the thermal-to-momentum diffusivity ratio, $\bar{\psi}$, became negative, the ratio was set equal to zero. For some very low flow rates, the Nusselt number from correlation (3) was calculated to be lower than would exist by molecular conduction alone. In those cases correlation (4), which was derived from the basic heat transfer equations for molecular conduction only, was used.

Correlation (5) was used to evaluate the heat transfer coefficients in regions where the flow was better described as flow over a flat plate rather than flow in a pipe. This was the case near regions of a recirculating flow where circumferential flow was expected. The Nusselt and Peclet numbers were then based on an estimate of the average path length of a circumferential flow along the valve wall. This technique gave conservatively high values for the heat transfer coefficient.

Correlation (6) was used to evaluate the heat transfer coefficients over the sides of the seat ring surface. Because of the flow recirculation in this region, a conservative estimate for the coefficient is obtained by assuming that reverse axial flow here behaves similarly to flow over a sphere. On these surfaces, as indicated earlier for the outer surface of the inlet passage itself, a conservative stress analysis results if the lowest reasonable value of heat transfer coefficient is chosen. The combination of rapid response on the inner pipe surface and a slower response on the outer pipe surface provides a more severe loading condition for the thermal stress analysis. The characteristic length for correlation (6) was taken as the outer diameter of the seat ring.

Correlation (7) was used to evaluate heat transfer coefficients where stationary recirculation regions were expected as in the access opening and in the vent nozzle. The flat plate coefficients needed in correlation (7) were obtained from correlation (5). The area ratio, as suggested in [5], was considered a reasonable approximation for a mixing length ratio required for the correlation. The heat transfer ratio, ϕ, required in correlation (7) was obtained from a curve of the heat transfer ratio

Downloaded 01 Jun 2010 to 171.66.16.58. Redistribution subject to ASME license or copyright; see http://www.asme.org/terms/Terms_Use.cfm

Table 1 Heat transfer correlations

	Correlation	Applicable Region Fig. No.	Region No.	Reference
(1)	$Nu_\infty = 5.0 + 0.025Pe^{0.8}$	2 3	(1) (3, 4, 5, 6)	[3]
(2)	$Nu_{local} = 1.72\left(\frac{D}{L}\right)^{0.16} \cdot Nu_\infty$	2 3	(1) (3, 4, 5, 6)	[4]
(3)	$Nu = \alpha + \beta(\bar{\psi}Pe)^\gamma$ where $\alpha = 4.82 + 0.697\left(\frac{D_0}{D_i}\right)$ $\beta = 0.0222$ $\gamma = 0.758\left(\frac{D_0}{D_i}\right)^{0.053}$ $\bar{\psi} = 1 - \frac{1.82}{Pr(\epsilon_M/\nu)^{1.4}_{max}}$	2	(2, 4, 6)	[3]
(4)	$Nu = 4.98 + 0.662\left(\frac{D_0}{D_i}\right)$	2	(2, 4, 6)	[3]
(5)	$Nu = 0.42Pe^{0.65}$	2 3 4 5	(7) (1, 2) (1, 2) (1)	[4]
(6)	$Nu = 1.13Pe^{0.5}$	2	(3, 5)	[3]
(7)	$h_w = h_{pfp}\frac{1}{\phi}\frac{A_{pfp}}{A_w}$	4 5	(3) (2, 3)	[5]
(8)	$Nu = 5.0$	5	(3)	[3]
(9)	$h = 0$	2 3 4 5	(8, 9, 10) (7, 8, 9) (4, 5, 6, 7, 8, 9, 10, 11, 12) (4, 5, 6)	—
(10)	$Nu = a + fb(\bar{\psi}Pe)^c$	2	(11)	—

versus mixing length ratio given in [5]. For the smaller vent nozzle opening, there existed the possibility that molecular conduction alone would give a higher coefficient than the convective correlation. Correlation (8) was used to check this possibility. The heat transfer regions listed in Table 1 for correlation (9) represented the outer, insulated surface of the valve or arbitrary breaks between valve model subdivisions. In these regions, the heat transfer coefficient was set equal to zero (adiabatic boundary condition). Correlation (10) was used for the edge of the inlet passage. As discussed below, the coefficient in this region was evaluated by treating it as a rearward facing step in the entrance region of a pipe. In application to this heat transfer region, correlation (10) became identical to correlation (1) as modified by correlation (2) when $f = 1$ and $\bar{\psi} = 1$.

Because of the complex geometry that might be seen in future valve designs, a more general approach may be used to develop liquid metal correlations from more common liquid (non-metal) heat transfer correlations. It is noted that liquid metal correlations are typically of the form:

$$Nu = a + b(\bar{\psi}Pe)^c \tag{11}$$

The first term on the right hand side of this equation represents a molecular conduction contribution for a liquid metal that is not normally seen in a non-metallic liquid correlation. The second term represents the turbulent eddy contribution which is normally seen in a non-metallic liquid correlation. One may reason that the enhancement or reduction seen in the heat transfer of a non-metallic liquid from flow disturbances should also be seen in similar proportion in a liquid metal if only the hydrodynamic part of the liquid metal correlation is considered. Although the liquid metal has vastly different conduction properties, its hydrodynamic behavior in turbulent flow and the effect of flow disturbances is not greatly different from that seen with more typical liquids. One can therefore modify equation (11) to appear as:

$$Nu = a + fb(\bar{\psi}Pe)^c \tag{12}$$

The multiplicative factor f can be used to modify known liquid metal correlations, if the effect of a flow disturbance on the basic flow pattern, for example a pipe bend in a generally straight pipe, is known from ordinary liquid studies.

The technique of using multiplicative factors to develop correlations from a basic flow pattern for a disturbed flow pattern has been successfully used before. Ito [6] uses this procedure to give the factor f for a curved pipe in terms of the radius of curvature, pipe radius, and Reynolds Number. Although the example cited [6] provides a multiplicative factor for friction, this can be extended to that part of the liquid metal Nusselt number correlation that depends on hydrodynamics alone. Similar multiplication factors for cavities and forward and rearward facing steps may be found in [10–12]. The same concept can also be used for a surface with protuberances. It should be noted that the factor $\bar{\psi}$ in equation (12) accounts for the effect of differing thermal and momentum eddy diffusivities for liquid metals and has been retained in equation (12). The factor f would account for flow pattern disturbances which in ordinary liquid correlations have similar effects on both heat transfer and friction. Therefore either friction or heat transfer data for disturbed flows of ordinary liquids could be used to evaluate the factor f. A frequently encountered example of this technique is in the evaluation of heat transfer in a cavity or near steps where f typically is of the order of 0.5. In the analyses described previously for the access opening and for the vent nozzle an available closed form correlation was used, except for the edge of the inlet passage (Region 11 of Fig. 2) where f was taken to be 1.0 in order to give a conservatively high heat transfer coefficient due to additional turbulence created by the presence of the disk assembly.

Sodium Flow Distribution

A modified version of a computer program, known as VARR-II [7] capable of handling turbulent flows was used to evaluate the portion of the flow that recirculates around and over the inlet flow passage after striking the disk. The computer program uses a numerical method to calculate multi-dimensional, axisymmetric, time-dependent, turbulent flows with small density variations. The solution technique is based on the simplified marker-and-cell (SMAC) method. It allows for a variety of initial and boundary conditions as well as

Downloaded 01 Jun 2010 to 171.66.16.58. Redistribution subject to ASME license or copyright; see http://www.asme.org/terms/Terms_Use.cfm

arbitrarily placed internal obstacles. The program has been used previously to evaluate velocity distributions in the CRBRP-IHX [8].

VARR-II provides a solution to the finite difference formulation of the governing equations for an incompressible turbulent flow. The governing equations, in differential form, are:

$$\frac{\partial}{\partial x_j} u_j = 0 \tag{13}$$

$$\frac{\partial u_i}{\partial t} + \frac{\partial}{\partial x_j}(u_i u_j) = -\frac{1}{\rho}\frac{\partial p}{\partial x_i} + g_i - \frac{1}{\rho}\frac{\partial}{\partial x_j}(R_{ij}) \tag{14}$$

$$\frac{\partial q}{\partial t} + \frac{\partial}{\partial x_j}(u_j q) = \frac{1}{2}\sigma\left(\frac{\partial u_i}{\partial x_j} + \frac{\partial u_j}{\partial x_i}\right)^2 + \frac{\partial}{\partial x_j}\left(\gamma_1 \sigma \frac{\partial q}{\partial x_j}\right) - \alpha_1 \frac{(2q)^2}{\sigma} \tag{15}$$

$$\frac{\partial \sigma}{\partial t} + \frac{\partial}{\partial x_j}(u_j \sigma) = \frac{\sigma^2}{4q}\left(\frac{\partial u_i}{\partial x_j} + \frac{\partial u_j}{\partial x_i}\right)^2 + \frac{\sigma}{q}\frac{\partial}{\partial x_j}\left(\gamma_1 \sigma \frac{\partial q}{\partial x_j}\right) - \frac{\sigma^3}{q^2}\frac{\partial}{\partial x_j}\left[\gamma_2 q \frac{\partial}{\partial x_j}\left(\frac{q}{\sigma}\right)\right] - \alpha_1 q \tag{16}$$

$$R_{ij} = \frac{2}{3}\rho q \delta_{ij} - \rho\sigma\left(\frac{\partial u_i}{\partial x_j} + \frac{\partial u_j}{\partial x_i}\right) \tag{17}$$

The double subscript tensor notation has been used in equations (13–17) where a repeated j indicates summation over all three values of j. Although shown in cartesian form, the program will handle a cylindrical coordinate system by internally modifying the equations to the appropriate form.

Equation (13) is the continuity equation for an incompressible fluid. Equation (14) is the unsteady momentum equation. In the finite difference formulation of equation (14), an additional distributed resistance term, r_i defined as:

$$r_i = K_i \frac{{u_i}^2}{2} \tag{18}$$

is included. This term is necessitated by the cellular description of the flow field and the possible presence of solid obstacles within individual flow cells. This term would not be present if infinitesimally small cell sizes could be used around any solid obstacles. In that extreme case, the equations would reduce to the original differential form and solid obstacles would become boundary conditions. In the finite difference formulation, only the overall boundaries of the cellular grid system are treated as boundary conditions. Local obstacles are included within the flow field.

Equations (15) and (16) provide a two-equation, three-parameter model of the turbulence. Equation (15) describes the distribution of turbulent kinetic energy while equation (16) describes the variation of the turbulent kinematic viscosity. Equation (17) defines the Reynolds stress terms of equation (14).

The VARR-II analysis of the check valve was done in two parts. The flow field in the recirculation region around the inlet flow passage was calculated first. The velocities calculated from this model were used as input to a second model for the flow field downstream of the inlet passage. The disc in this model was treated as a local obstacle. In the recirculation region analysis, it was assumed, as would be expected, that the major velocity components are circumferential and axial. In the downstream model, the major velocity components were assumed to be radial and axial.

Fig. 6 shows averages of calculated circumferential and axial velocities for the recirculation region model. These velocities give a recirculation of about 35 percent of the total flow into the valve. A less sophisticated approach based simply on the equivalence of pressure losses for the recirculating and straight-through flow path to the exit of the valve gave a recirculation of about 30 percent. In this second approach, each right angle turn in a postulated flow path was assumed to have the same loss coefficient regardless of whether the flow path was in the main or recirculating flow stream. The slightly higher recirculation of the computer program was used to evaluate the heat transfer coefficients.

In the recirculation region, the average circumferential velocities are larger than the axial velocities. This tendency weakens as the recirculation region ends beyond the seat ring. As explained previously in evaluating the most conservative heat transfer coefficients, these results were considered in generally choosing annular correlations based on axial velocities in the recirculation region for the outside surface of the inlet pipe and flat plate correlations further downstream for the inside surface of the valve body. The velocities in Fig. 6 are based on full design flow into the valve. The highly turbulent nature of the flow suggested that a Reynolds number invariance was a reasonable description as Reynolds numbers greater than 1,000,000 in the inlet pipe were typical, even at low flows. It was therefore assumed that the flow distribution was similar for lower inlet flows and that local velocities decreased linearly with decreases in the inlet velocity. Provided that Reynolds numbers are very large, Reynolds number invariance can also be used for other valve geometries to realistically justify use of a known flow distribution to evaluate local and average velocities at flow rates other than the one used to develop the known distribution.

At full flow, heat transfer coefficients ranged from as high as 29,200 $W \cdot m^{-2} \cdot °C^{-1}$ (5136 BTU/hr-ft^2-°F) in Region 1 of the inlet assembly to as low as 1870 $W \cdot m^{-2} \cdot °C^{-1}$ (330 BTU/hr-ft^2-°F) in Region 6C of the inlet assembly (Fig. 2). Regions with high coefficients, such as Region 1, had values decrease by as much as 80 percent because of large decreases in flow rate during some of the transients considered. Regions with initially low coefficients, such as Region 6C mentioned above, could not undergo such large variations since molecular conduction provided a uniform lower bound on the size of the coefficient.

Summary

An approach to the problem of evaluating heat transfer coefficients in the complex geometry of an LMFBR check valve has been presented. The correlations used to calculate the coefficients were based on a realistic assessment of the flow patterns within the valve. Where choices between correlations were considered, the correlation that yielded results giving a more conservative thermal stress analysis was chosen.

Acknowledgment

This paper is based partly on work supported by the U. S. Department of Energy under Westinghouse-Advanced Reactors Division

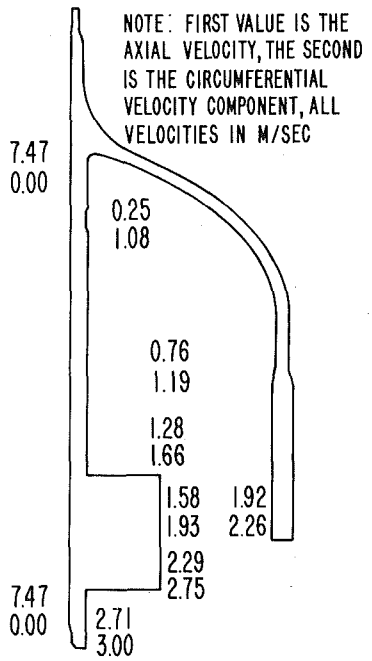


Fig. 6 Recirculation zone, average velocities at full design flow

Downloaded 01 Jun 2010 to 171.66.16.58. Redistribution subject to ASME license or copyright; see http://www.asme.org/terms/Terms_Use.cfm

Contract No. 54-7CCY-199282 and Foster Wheeler Energy Corporation Contract No. 8-33-2752. The authors thank the members of the valve project team at Foster Wheeler Energy Corporation for their contribution to this work.

References

1 Anon, "Clinch River Breeder Reactor Plant Project, Design Description," Breeder Reactor Corporation, CRBRP-PMC-77-06, Oak Ridge, Tenn 37830.

2 Kane, R. S., and Cho, S. M., "Hydraulic Characteristics of Tilting-Disc Check Valves," *Journal of the Hydraulic Division,* ASCE Vol. 102, No. HYI, January 1976, pp. 57–72.

3 Dwyer, O. E., *Liquid Metal Heat Transfer,* Brookhaven National Laboratroy, BNL 11936R, Jan. 1969.

4 Kutateladze, S. S., et al., *Liquid Metal Heat Transfer Media,* Supplement No. 2 of the *Soviet Journal of Atomic Energy,* Translated by Consultants Bureau, Inc. of N. Y., Chapman and Hall, Ltd. London, 1959.

5 Fenton, L., and White , R. A., "Heat Transfer in Resonant Cavities Spanned by Low Speed, Turbulent Shear Layers," ASME *Journal of Basic Engineering,* Vol. 93, Sept. 1971, pp. 455–457.

6 Ito, H., "Friction Factors for Turbulent Flow in Curved Pipes," ASME *Journal of Basic Engineering,* June 1959, pp. 123–134.

7 Cook, J. L., and Nakayama, P. I., "VARR-II, A Computer Program for Calculating Time Dependent Turbulent Fluid Flows with Slight Density Variation," Westinghouse Electric Corporation, Advanced Reactors Division, Report No. CRBRP-ARD-0106 (availability USDOE Technical Information Center).

8 Aburomia, M. M., Chan, B. C., and Cho, S. M., "Flow Distribution Analysis in Nuclear Heat Exchangers with Application to CRBRP-IHX," *Proceedings of the 1976 Heat Transfer and Fluid Mechanics Institute,* Stanford University Press, 1976.

9. Dwyer, O. E., "Eddy Transport in Liquid-Metal Heat Transfer," *AIChE Journal,* Vol. 9, No. 2, March 1963, pp. 261–268.

10 Charwat, A. F., Dewey, C. F., Ross, J. N., and Hitz, J. A., "An Investigation of Separated Flows—Part II: Flow in the Cavity and Heat Transfer," *Journal of the Aerospace Sciences,* Vol. 28, No. 7, July 1961, pp. 513–527.

11 Saki, N., Fukusako, S., and Hirata, T., "Laminar Heat Transfer Downstream of a Sudden Enlargement of a Duct," *Bulletin of the JSME,* Vol. 21, No. 152, Feb. 1978, pp. 254–257.

12 Chilcott, R. E., "A Review of Separated and Reattaching Flows with Heat Transfer," *Int. J. of Heat and Mass Transfer,* Vol. 10, 1967, pp. 783–797.

Downloaded 01 Jun 2010 to 171.66.16.58. Redistribution subject to ASME license or copyright; see http://www.asme.org/terms/Terms_Use.cfm

E. C. Winegartner
C. J. Lin

EXXON Research and Engineering,
Synthetic Fuels Research Laboratory,
P.O. Box 4255,
Baytown, TX 77520

Laboratory Combustibility Testing of Solid Fuel

A laboratory furnace having a controlled wall temperature is used to measure the combustibility of coal and other solid fuels. Operation at wall temperatures of 1260–1370°C (2300°–2500°F) permits determination of percent carbon burnout as a function of residence time and excess oxygen under furnace conditions representative of those encountered in large boilers. Operation at decreasing wall temperatures provides information on flame stability under conditions approaching those encountered under low load conditions in operating boilers. Firing rates are generally in the range of 11.7–29.3 KW_t (40–100k BTU/hr) permitting testing of 100–150 kg (200–300 lb.) samples which can reasonably be obtained by core drilling or from small pilot units.

Introduction

The writers are frequently called upon to evaluate coals from completely new fields in areas of the world where coal has not been mined in the past. We are also asked to evaluate the suitability of various byproducts from synthetic fuel processes as fuels. The value assigned to these by-products may control the economics of the synthetic fuels process and reasonable estimates of the burning qualities of such fuels must be made from very limited size samples.

Many factors are involved in assessing the quality of solid fuels including how rapidly and completely the fuel burns, how the ash behaves in the furnace, how easy it is to collect the fly ash, and what happens to sulfur and trace elements in the coal during and following combustion. The test furnace described in this paper has been very useful in each of these fields of investigation. Cooled probes are used to assess slagging problems in the combustor and fouling problems in the convection section. In situ resistivity tests have shown that fly ash from the test furnace has electrical properties similar to fly ash from a commercial furnace. SO_2 measurements have shown that fly ash from the test furnace picks up the same amount of sulfur from the flue gas as occurs in commercial furnaces. The furnace is also used to determine how trace elements in the coal end up in the environment and is currently being used to produce fly ash for EPA leaching studies.

The present paper deals only with our work on developing a test to measure the combustibility of solid fuels. Occasional reports of problems occurring in the field [1, 2] indicate the desirability of some type of furnace combustion test during the evaluation of a new fuel. Most furnace combustion tests require large size samples. Some useful information may be obtained with samples as small as 1 ton by burning in furnaces firing 100–250 kg (250–500 lbs.) per hour; however, meaningful results generally require a sample of at least 45 tonnes (50 tons), and preferably 9000 tonnes (10,000 tons). Even 0.9 tonnes (1 ton) samples are generally not available if a mine is not open or a large size pilot plant in operation. We were thus faced with the problem of developing a meaningful combustion test which could be applied to core hole size samples.

Combustibility

Combustibility of solid fuels is generally described by three rather poorly defined terms; ignitability, combustion efficiency, and flame stability. The boiler operator is interested in how easily the coal catches fire, how much of the available calorific value of the fuel is released in the fire box, and whether or not the flame in the furnace will go out under low load or upset conditions.

Over 40 years ago, ASTM Committee D-5 adopted a definition of ignitability: however, there is still no ASTM test for determining it. The crossing point method [3, 4] came close to becoming a standard test procedure until Orning [5] showed that the T_{15} temperature obtained in this test could be calculated quite accurately from simply knowing the volatiles content of the fuel. Finney and Spicer at Penn State [6] used a "drop tube" furnace to study the ignitability of coal particles by blowing a small sample of the coal through a preheated furnace at various temperatures to determine what furnace temperature was required to ignite the particles. Results obtained with this type of test indicate that the range of ignition temperatures obtained from a wide variety of coals was quite narrow: about 100°C (180°F) and thus the test does not show small differences between similar fuels. More recently, efforts have been made to use thermogravimetric analysis as the basis for determining the burning properties of solid fuels. This "combustion profile" [7, 8] provides a "fingerprint" of the combustion properties. Information from such a test is useful, and provides a correct measurement of the rate of burning of coal particles versus temperature; however, the temperatures employed and burning rates obtained are much lower than those encountered in actual furnace practice.

Combustion efficiency is generally determined by measuring the carbon remaining in the ash after combustion, and expressing this as the percentage of the carbon fed to the furnace. Results are highly dependent on furnace conditions; however, reasonable estimates can be made by comparing the results of firing a test fuel and a fuel with known burning qualities in the same furnace. Such tests generally require burning of relatively large size samples in test furnaces rated

Contributed by the Fuels Division and presented at the Winter Annual Meeting, December 2–7, 1979, New York, New York, of THE AMERICAN SOCIETY OF MECHANICAL ENGINEERS. Manuscript received at ASME Headquarters August 2, 1979. Paper No. 79-WA/Fu-1.

Copyright © 1980 by ASME

Downloaded 01 Jun 2010 to 171.66.16.58. Redistribution subject to ASME license or copyright; see http://www.asme.org/terms/Terms_Use.cfm

at 100 kg/hr (250 lbs/hr) of fuel and up in order to obtain reliable results. In addition, there are generally the "what if" questions remaining from such tests: What if I had used a different air preheat temperature, a different degree of swirl in the burner, a different heat release rate in the furnace. Careful work by the investigator, however, can answer many of these what if questions and produce useful results. An example of such test work is given in a paper by C. R. McCann [9].

Flame stability is much more difficult to assess even in large test furnaces. The question of what is a stable flame is hard to define and is very subject to the opinion and experience of the test operator. Generally, such tests are carried out in larger laboratory furnaces and results reported in terms of the amount of supplementary fuel required to obtain a stable flame, or in terms of adjustments needed to burner swirl or air preheat to obtain what the investigator believes to be stable flames. As with combustion efficiency, large samples are required, and the results leave some of the what if questions still unanswered since no fundamental properties are measured.

A much more thorough review of test methods for determining the combustion properties of coal is given in Finney's paper [6] mentioned earlier. In general, today, when only small samples are available, combustibility is judged primarily on the basis of volatiles content, the heat content of the volatile matter, and occasional use of the crossing point method, drop tube furnace, or variations of the combustion profile techniques discussed above. None of these techniques involves actually burning the coal under conditions similar to those encountered in large furnaces. Improved techniques are necessary and are currently being developed in our laboratory facilities at Baytown. This paper presents the preliminary results of this development program, which is continuing. It is hoped that additional improvements will be made, both in the facilities and in interpretation of data obtained.

Description of Equipment

The Solid Fuel Evaluation Unit (SFEU) used in these studies was patterned after the LAF furnace of B & W described by Attig and Barnhart in their paper at the Marchwood Conference [10] and is shown in Fig. 1. The test fuel is burned inside of a silicon carbide tube, 0.23m (9 in.) ID by 1.22m (4 ft) tall, which is physically located inside of a gas-fired furnace which serves to control the wall temperature of the combustion tube. Pre-pulverized test fuel is stored in a hopper and fed at the rate of 1.8 to 4.5 kg/hr (4 to 10 lbs/hr) into a circulating loop, in which it is mixed with the primary air. The primary air and coal feed joins preheated secondary air directly above the test combustor. At a feed rate of 3.64 kg/hr (8 lbs/hr), and combustor temperature of 1288°C (2350°F) the residence time in this combustor is approximately one second. Hot gases exit the furnace through a refractory lined spool which serves to simulate the superheater and reheater section of a utility furnace. During the 1/2 second residence time in this section, furnace gas temperature is reduced approximately 550°C (1000°F). From the refractory lined spool, the gases are further cooled to 150°C (300°F) in a pressurized water jacketed heat exchanger. Fly ash is separated from the combustion products in a cyclone, the gases are analyzed, and the remaining gas discarded through a bag house to a stack. A second set of analytical instruments is connected to the unit at the combustor outlet.

With this type of test facility, we attempt to create conditions similar to those existing inside of a large combustion chamber by operating with a wall temperature of approximately 1260–1370°C (2300 to 2500°F). Heat release rate in the combustor is in the range of 300 to 400 kW/m^3 (30–40 kBtu's/hr per cubic foot), which is in a range similar to that encountered in large furnaces. The heat release rate per unit area of plan, however, is much lower in order to avoid an excessively tall furnace. The temperature of the silicon carbide combustion tube is measured and controlled by a radiation pyrometer, operating at a wave length of 5.1 μm, so that it can look through the surrounding gas flame and determine the temperature of the silicon carbide itself. A second radiation pyrometer, not shown in Fig. 1, is positioned to look in the top sight port. The wave length for this pyrometer is also selected to avoid radiation from CO_2 and H_2O so that it can determine the temperature of the coal particles themselves. There is still some uncertainty regarding particle temperature, since the emissivity of the particles is not well known.

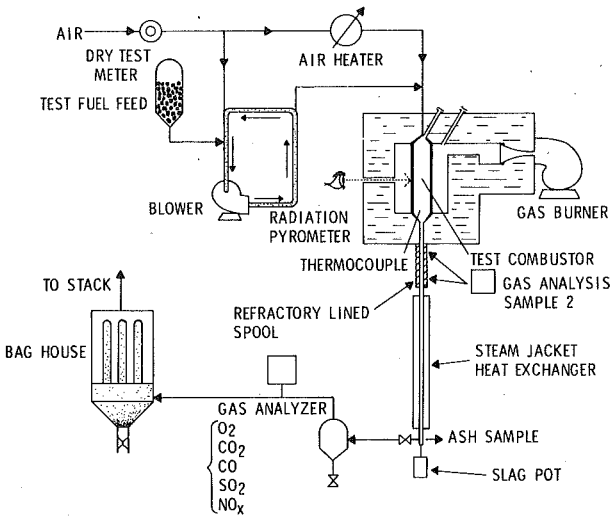


Fig. 1 Solid fuel evaluation unit

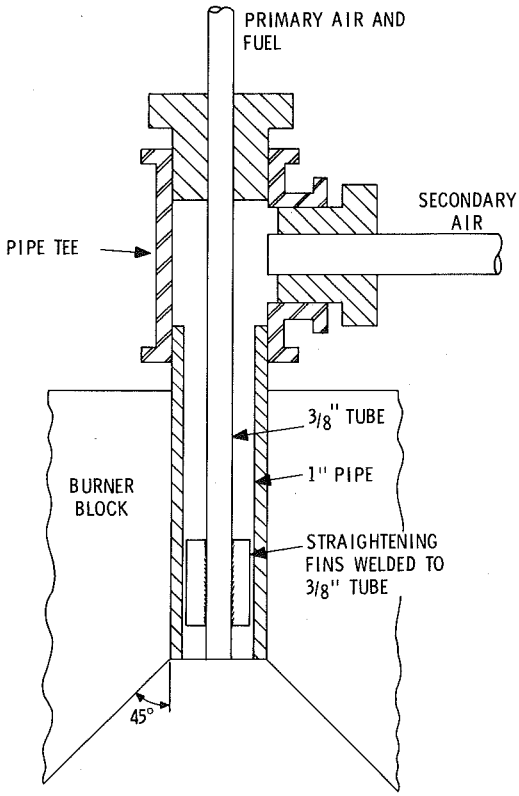


Fig. 2 SFEU burner

All instruments on the SFEU read out through an on-line computer. The coal feed rate is calculated by the computer from the air rate measured by a dry test meter and from the oxygen content of the combustion gases. Residence time of the particles in the combustion chamber is calculated from the air rate, the volume of the silicon carbide reactor, and the measured wall temperature. In the combustibility work reported in this paper, the firing rate is adjusted for a constant residence time, usually one second, resulting in different firing rates at different wall temperatures.

In designing the burner, we recognized that the degree of mixing produced by the burner arrangement would have an important bearing on rate of combustion and flame stability. The final design

Downloaded 01 Jun 2010 to 171.66.16.58. Redistribution subject to ASME license or copyright; see http://www.asme.org/terms/Terms_Use.cfm

was selected because we were most interested in the effect of fuel properties on combustibility, not on the effects of degree of mixing. The burner arrangement, shown in Fig. 2, is designed for no turbulence at the point of entry to eliminate, insofar as possible, mixing as a variable in the experiments.

The percent carbon burnout of the test fuel is calculated at the outlet of the combustor tube from a material balance, as shown in Fig. 3. The O_2 and CO_2 concentrations in the two gas samples are monitored continuously during each run. A fly ash sample is collected at the bottom of the jacketed heat exchanger section after the combustion gases have been cooled to 150°C (300°F), and prior to entering the cyclone. The percent carbon and hydrogen on the ash is determined in the laboratory. The percent carbon on fly ash particles leaving the combustor tube is then calculated from this value, using the change in O_2 content of the gas between the two sampling points. This procedure eliminates uncertainties due to the changes in residence time and cooling rate, which may occur in the backend of the unit as firing conditions vary. By knowing the coal feed rate, air flow rate, flue gas oxygen content, and carbon on ash, the CO_2 concentration can be calculated from the material balance on carbon. The calculated CO_2 value can be checked with the measured value. Generally good agreement was found on the two CO_2 values, which validated this experimental technique.

Test Results

In preliminary test work samples of coal from various seams in the U.S. representing various coal ranks were tested under a series of conditions, including variations in residence time and tube temperature. Analysis of all of the fuels discussed in this paper are given in Table 1. It will be noted that samples of anthracite and Pocahontas seam coal are higher than normal in ash content since they had not been cleaned prior to testing. The moisture contents in Table 1 are the percent moisture in the coal as burned. Samples are partially air dried prior to burning to facilitate feeding and to more closely represent the moisture content of coal fired after partial drying in the pulverizer.

Typical test results for a sample of anthracite from Pennsylvania, a low volatile bituminous coal from the Pocahontas No. 3 seam in West Virginia, a high volatile bituminous coal from the Lower Winifrede seam in West Virginia, and a sample of lignite from a test pit in the Gulf Coast region are shown in Fig. 4. In all cases, the test fuels were prepulverized to approximately 70 percent through 75 μm (200 mesh) prior to firing. It will be observed from Fig. 4 that at 1288 to 1370°C (2350 to 2500°F), 85 percent of the carbon in the anthracite was burned in one second. Increasing residence time or pulverization increased the carbon burnout; however, the particle size and residence time used were selected to obtain a reasonable spread of data and to provide a means of evaluating the different fuels. As furnace wall temperature is decreased, we find a rapid dropoff in carbon burnout for the anthracite below a temperature of about 1200°C (2200°F). Note that the temperatures given are the tube temperature. At the higher temperatures the temperature of the combustion products in the furnace is believed to be within 15 to 30°C (25–50°F) of the tube wall temperature. As tube wall temperature drops, however, the combustion temperature deviates further and further from the tube temperature. Efforts to accurately measure this temperature are still underway. At a tube wall temperature of 815°C (1500°F) it is believed that the combustion temperature is approximately 160°C (300°F) higher, or 975°C (1800°F). With the low volatile bituminous coal (Pocahontas No. 3) percent carbon burnout at the higher temperatures increases to approximately 90 percent, and the curves do not tend to break over until the tube wall temperature has reached ap-

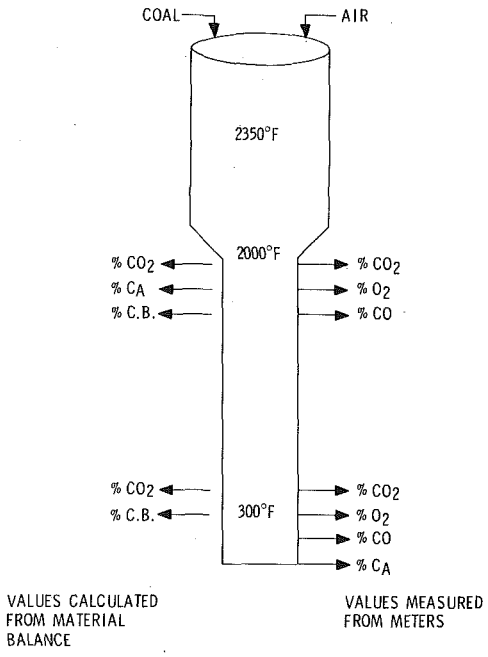


Fig. 3 Carbon balance scheme

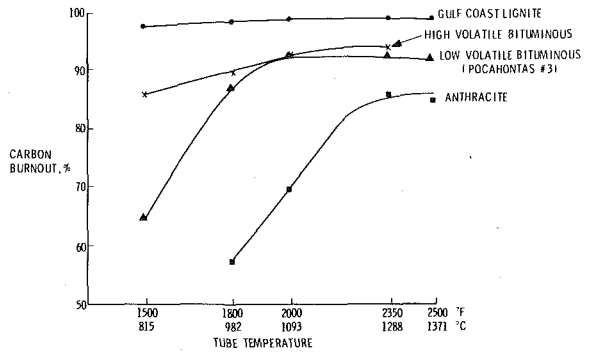


Fig. 4 Laboratory furnace combustion test

Table 1 Analysis of coals used in this paper (analysis as burned)

Coal	Anthracite[1]	Low Volatile[2] Bituminous	High Volatile[3] Bituminous	Bituminous[4] No. 1	Bituminous[4] No. 2	Bituminous[4] No. 3	Bituminous[4] No. 4	Lignite[5]	Char[6]
Moisture	4.25	1.00	2.10	7.21	12.78	10.90	9.32	12.32	0.72
Ash	8.83	17.69	6.65	6.83	4.00	7.34	6.35	18.00	
Volatiles	2.97	14.34	34.91	34.05	34.33	32.43	33.97	44.90	5.86
Fixed C	83.95	66.96	56.34	51.91	48.89	49.33	50.46	24.78	
BTU/lb	12,669	12,548	13,840	12,488	11,755	11,576	12,069	9,254	
C	81.64	73.24	77.72	70.34	66.27	65.94	68.00	51.39	
H	1.62	3.65	5.08	4.67	4.47	4.48	4.63	4.23	
S	0.54	0.55	0.79	0.71	0.50	0.43	0.54	0.71	
N	0.86	0.93	1.39	1.24	1.19	1.13	1.23	0.81	
O	2.26	2.94	6.27	9.00	10.79	9.78	10.03	12.54	

Source of samples: (1) Pennsylvania (2) Pocahontas #3 Seam (3) Lower Winifrede Seam (4) Cerrejon, Colombia, S.A. (5) Test Pit, Gulf Coast (6) Pyrolysis Char from Gulf Coast Lignite

Downloaded 01 Jun 2010 to 171.66.16.58. Redistribution subject to ASME license or copyright; see http://www.asme.org/terms/Terms_Use.cfm

proximately 980°C (1800°F). The high volatile bituminous showed 94 percent burnout at 1288°C (2350°F) and dropped off slightly to 86 percent burnout at 815°C (1500°F). With a very easily burned material, such as the Gulf Coast lignite, almost 100 percent carbon burnout is obtained at higher temperatures, and there is very little dropoff, even at 815°C (1500°F).

The curves in Fig. 4 tell us what we all know: lignite burns much easier than anthracite. Experiments can readily be carried out to determine the degree of increased grinding or increased residence time required to obtain good carbon burnout. We believe the break in the curves shown for anthracite and low volatile bituminous coal is related to the flame stability, and this will be discussed in more detail in a subsequent section on interpretation of results.

In connection with exploration work conducted in Colombia, S.A., we tested the burning characteristics of four composites of core hole samples. Composite 1 represented the oldest seams in the Cerrejon deposit and would be rated as a High Volatile B Bituminous coal. Composite 2 represented the youngest seams and would be rated as a High Volatile C bituminous. Sample 3 was in between samples 1 and 2, and Sample 4 was a composite of Samples 1, 2 and 3. The combustibility curves of the four coal samples are shown in Fig. 5. Only two points were taken for each coal, due to the limited sample available from a core drilling program. The curve for Composite 1, the least reactive coal, is similar to the curve for a similar high volatile bituminous coal obtained from the Lower Winifrede seam in West Virginia. Composite 2 was identical to the lignite in this combustion test and curves 3 and 4 fell between them as expected.

In a separate test program we examined the burning properties of a low temperature char produced by pyrolysis of a Gulf Coast lignite. The char used in these tests contained approximately 6 percent volatile matter. The results of these tests are shown in Fig. 6, together with the previously given curves for anthracite, Pocahontas and the parent lignite. It will be noted that the char does not burn quite as well as the parent lignite, but is approximately equivalent to the high volatile bituminous coal shown in Fig. 4. This curve raises some interesting questions since the reactivity of the char is apparently very adequate and there is no dropoff in reactivity at lower temperatures. Most people knowledgeable in combustion of coal would assume that, with a volatiles content of less than 20 percent, auxiliary firing would be required to obtain stable combustion. The results of this test indicate that this is not true when dealing with low temperature chars where the reactivity may be a function of surface area. It should be pointed out that not all chars and cokes behave in this manner. The parent coal and the heat treatment which it has received greatly effect the reactivity of the carbonaceous material. It will be interesting to see how this material behaves in a larger furnace once sufficient quantities are available for testing.

Interpretation of Results

The combustion properties being measured in the SFEU, as well as those measured with more conventional ignition tests, may be understood based on the combustion model outlined by Field, et al. in "Combustion of Pulverized Coal" [11]. The rate of heat generation when burning a fuel sample ($-\Delta Q$) in practical circumstances may be expected to take the form shown by the "S" shaped curve A shown in Fig. 7. This is a plot of the rate at which heat would be generated in a combustion chamber if the suspension were to be maintained at a temperature T for fixed values of such quantities as fuel type, particle size, throughput, and fuel/air ratio. The vertical axis represents the percent of the fuel present which is burned per unit of time; i.e., per second. The reason for this shape is that at low temperature the rate of reaction of the fuel is very low. As the temperature is increased, the reaction rate rises very steeply. However, the rate of heat generation in the chamber cannot exceed the rate of supply in the form of fuel and therefore, the curve must flatten off. There may be other reasons why the curve should flatten off, such as the onset of diffusion control in the reaction, but in practical systems, the residence time in the chamber will be chosen in such a way that the rate of heat generation approaches 100 percent at the firing temperature. If this were not done, then the combustion would be inefficient.

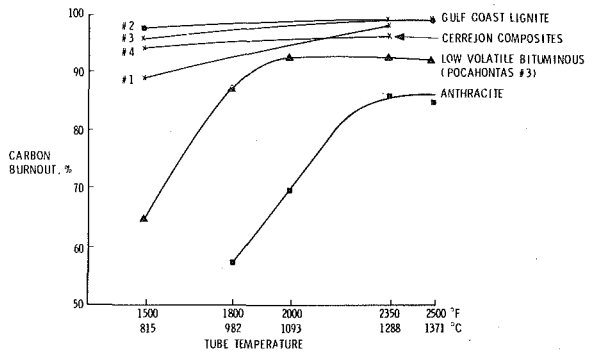


Fig. 5 Laboratory furnace combustion test—one second residence time

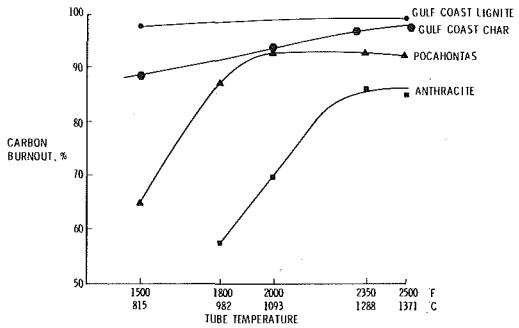


Fig. 6 Laboratory furnace combustion test—one second residence time

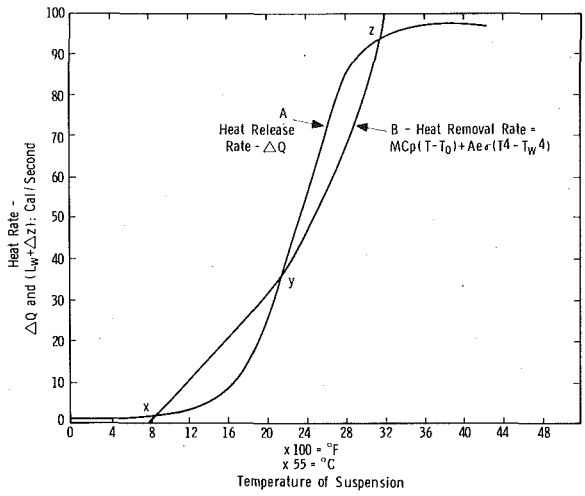


Fig. 7 Idealized combustion

The states of thermal equilibrium in the combustor can be found by superimposing the curve for the rate of heat removal and the rate of heat generation for a given set of input conditions. The rate of heat removal in Fig. 7 is given by Curve B, which is shown to be composed of the heat removed by the high temperature combustion products plus the heat removed by radiation to the wall. The intersection points represent states of thermal equilibrium. Points X, Y and Z all represent equilibrium conditions which satisfy the energy balance. The temperatures at the intersections, therefore, all represent thermal equilibrium temperatures.

An examination of the nature of the states of equilibrium will show that only intersections X and Z correspond to stable equilibrium states. The intersection Y represents an unstable equilibrium, and therefore, cannot be obtained physically. This can be seen from the way in which the curves cross. Where the curves cross as at "X" or "Z", when the temperature of the suspension is displaced slightly in either direction, it tends to return to the equilibrium point; but where

Downloaded 01 Jun 2010 to 171.66.16.58. Redistribution subject to ASME license or copyright; see http://www.asme.org/terms/Terms_Use.cfm

they cross as at "Y", the temperature of the suspension tends to move away in whichever direction the displacement occurs.

Thus, there are two stable equilibrium states: X and Z on the diagram, both corresponding to the same input conditions to the combustion chamber. The equilibrium state X is a state where the amount of combustion is negligible, and the temperature is close to the inlet temperature. The equilibrium state Z is a state where the degree of combustion is approaching completion in the chamber. If point Z were to move to the left into the steep portion of the curve, the flame would tend to be unstable since small changes in temperature or heat input would make rapid changes in the rate of combustion. If one considers the limiting case where curve B is just tangent to curve A, then any further slight decrease in heat generation or increase in heat removal rate would immediately cause a very rapid drop in reaction rate; i.e., the flame would go out.

If one now compares the theoretical curves in Fig. 7 with those obtained in the SFEU combustibility test, the significance of the SFEU test is immediately apparent. In the SFEU test we force point Z to move along the heat release rate curve. We set the temperature for point Z by changing the wall temperature and thus determine the shape of the heat release rate curve in the temperature range of interest. The break in the SFEU combustibility curves represents the point at which the reaction rate of the solid fuel begins to rapidly decrease. Once we are in this region the flame in a large furnace would become unstable. In the SFEU, however, it is possible to operate under these unstable conditions because heat is being continuously supplied from the wall. In a more normal test furnace this point is found when flame tends to go out, however, the point is characteristic of the heat removal rate for the specific furnace being used, and no information is obtained on the shape of the reactivity curve.

Let us now look at what happens in a large utility boiler when load is reduced. When we reduce load, by definition, we reduce the rate of heat release or ΔQ. Let us examine what happens to the rate of heat removal. The furnace must be operating at an equilibrium point defined by point Z in Fig. 7. Point Z may be defined mathematically as follows:

$$-\Delta Q = MC_p(T - T_0) + Ae\sigma(T^4 - T_w{}^4)$$

where

$-\Delta Q$ = rate of heat release
M = mass of combustion gases
C_p = specific heat of gases
T = temperature of the suspension
T_0 = standard reference temperature
A = area of heat receiving surface
e = emissivity
σ = Stefan-Boltzmann constant
T_2 = temperature of furnace wall

In this equation, $-\Delta Q$ is the rate of heat released in the furnace. On the righthand side of the equation the first term represents the heat capacity of the products of combustion, and the second term represents the heat removed by radiation to the furnace wall. Since the righthand side of the equation must get smaller when the lefthand side is reduced, let us examine what happens to the terms on the righthand side of the equation under reduced firing conditions. Looking first at the second term, which is the radiation loss, we see that it is composed of the area of the heat receiving surface, the emissivity of the flame, and the Stefan-Boltzmann constant. Area can be varied somewhat by turning off rows of burners or by changing burner tilt, but emissivity and Stefan-Boltzman constant do not change. The balance of the term is composed of the difference between the suspension temperature to the fourth power minus the wall temperature to the fourth power. Wall temperature again remains essentially constant since it is controlled by the boiling point of water at the operating pressure. The suspension temperature T is thus forced to vary to balance the equation.

In the first term, we see that as firing rate is reduced M, which is the mass of the combustion gases, decreases linearly. The specific heat of the gases also decreases slightly; however, most of the change must occur in T, which is the temperature of the burning suspension. Thus, as firing rate is reduced, the temperature of the suspension must also decrease and may enter a region of flame instability. The operator, knowing this, has several alternatives. Increasing the air preheat would increase ΔQ, and therefore, increase the suspension temperature; but this is not generally under operator control. He can also increase the ΔQ or rate of heat release by increasing the quantity of excess air, thus increasing the partial pressure of oxygen in the furnace. This, however, is only partially effective since this also increases M, or the mass of combustion gases in the righthand side of the equation. In addition we can also decrease the effective heat receiving area, as discussed above, by changing burner tilt or turning off rows of burners.

We thus see that the operator has some control on flame stability and combustion efficiency; however, he is limited in what he can do by the reactivity of the fuel, which is the prime component of the rate of heat release. Eventually the point is reached where the rate of heat removal exceeds the rate of heat release, and the flame goes out. If the boiler designer knows the temperature at which reactivity drops off rapidly, he may be able to utilize this information in determining the optimum furnace configuration.

Let us now look briefly at what is measured in other combustibility tests. With the crossing point method of measuring ignition temperature the test is run under adiabatic conditions; in other words, we shift curve B, the rate of heat removal, far to the right so that heat removal does not effect the rate of heat release. Results are generally obtained in the temperature range of 200–540°C (400 to 1000°F). We thus determine the temperature at which curve A in Fig. 7 first starts to rise at an appreciable rate under a fixed set of standard conditions.

In the combustion profile test a small sample of fuel is continuously weighed while suspended within a furnace, the temperature of which is continuously increased. Results generally are plotted in the range of 200–1100°C (400 to 2000°F). With this type of measurement we are determining where the heat release curve first starts to rise, and in addition, how rapidly it rises. Again we are looking at the heat release rate curve in the region between points X and Y and determining the shape of curve A in Fig. 7 in the lower regions.

The flammability index test involves dropping a small sample of coal through a heated furnace and determining at what temperature the coal catches fire. This is somewhat different in that the heat removal rate also plays a role since the burning coal particles are hotter than the tube wall. With this test we are trying to determine the point Y in Fig. 7. With such a test one would expect that the diameter of the tube, which influences A in the heat removal rate equation, might have a significant influence on the result.

It would appear that all three of the standard ignition measuring tests provide useful information which can be interpreted from the type of plot given in Fig. 7. All of this information, however, is collected in the region where the heat release rate curve is at or below the metastable equilibrium point Y. The SFEU combustibility test, on the other hand, provides information on the combustibility of solid fuels in the temperature range above this metastable equilibrium point, which is the region in which any commercial furnace must operate.

Conclusions

We have found the SFEU to be a very useful tool in evaluating the combustion properties of solid fuels. The basic heated wall design allows us to simulate operating conditions in a large furnace over the temperature range of interest to boiler operators. The furnace is used for studying ash properties including fouling, slagging, leachability, sulfur absorption, and electrical resistivity as well as for the combustibility studies reported here.

The SFEU combustibility test provides information on the reactivity (rate of burning) of solid fuels as a function of temperature. This information can be interpreted in terms of completeness of combustion and provides a quantitative measure of flame stability. To the

Downloaded 01 Jun 2010 to 171.66.16.58. Redistribution subject to ASME license or copyright; see http://www.asme.org/terms/Terms_Use.cfm

best of our knowledge, this is the only quantitative test for flame stability which has been reported in the literature.

Specific conclusions for the tests reported here may be summarized as follows:

1 The SFEU produces information on the combustion efficiency and flame stability of solid fuels under conditions similar to those existing in commercial pulverized fuel fired furnaces.

2 The SFEU combustibility test correctly predicts the behavior of low volatile bituminous (Pocahontas No. 3) and anthracite coals in commercial furnaces.

3 The SFEU combustibility test predicts that a 66 percent volatiles, low temperature char produced from a Gulf Coast lignite would behave similarly to a high volatile bituminous coal in a commercial furnace.

4 The SFEU permits meaningful determination of combustion properties on small samples of solid fuels, thus permitting test work on core samples and on materials produced in small pilot units.

5 Combustibility data obtained in the SFEU as well as the more conventional ignitability tests can be interpreted in terms of the heat release and heat absorption model presented by Field, et al. [11]. Only the SFEU produces data under conditions similar to operating furnaces, however.

Acknowledgments

The authors wish to thank Art Ubbens, who helped design the furnace and the tests used in this program. We also wish to thank Lee Robertson, Sr., Tony Gobert, and Bill Traywick, who were instrumental in learning to run the furnace and whose careful work permitted development of the tests described here. We would also like to thank the Carter Oil Company, whose financial support made the whole program possible, for permission to publish the data.

References

1 Nandi, B. N., Brown, T. D., and Lee, G. K., "Inert Coal Materials in Combustion," *Fuel*, Vol. 56, No. 2, April, 1977, pp. 125–130.

2 Borio, R. W., "A Laboratory Study of Anthracites Burned At A Spanish Generating Station," AMSE paper No. 74-WA/FU-2, 1974.

3 Sebastian, J. J. S. and Mayers, M. A., "Coke Reactivity Determination by a Modified Ignition Point Method," *Industrial and Engineering Chemistry*, Vol. 29, 1937, pp. 1118–1124.

4 Sherman, Ralph A., Pilcher, J. M., and Ostborg, H. N. "A Laboratory Test for the Ignitability of Coal," *ASTM Bulletin*, Oct. 1941, pp. 23–24.

5 Orning, A. A. "Reactivity of Solid Fuels," *Industrial and Engineering. Chemistry*, Vol. 36, No. 9, Sept. 1944, pp. 813–816.

6 Finney, C. S. and Spicer, T. S., "The Influence of Particle Size and Volatile Content on the Ignitability of Pulverized Bituminous Coal," *Pyrodynamics*, Vol. 1, 1964, pp. 231–249. Also ASME Paper No. 62-WA-195.

7 Wagoner, C. L. and Duzy, A. F., "Burning Profiles for Solid Fuels," presented at ASME Annual Meeting, Pittsburgh, PA, Nov. 12–16, 1967.

8 Wagoner, C. L. and Winegartner, E. C., "Further Development of the Burning Profile," ASME JOURNAL OF ENGINEERING FOR POWER, Vol. 95, No. 2, April 1973, pp. 119–123.

9 McCann, C. R., Demeter, J. J., Orning, A. A. and Bienstock, D., "Combustion of Pulverized Char," paper presented to 162nd ACS National Meeting, Washington, DC, Sept. 12–17, 1971, ACS Fuels Division.

10 Attig, R. C. and Barnhart, D. H., "A Laboratory Method of Evaluating Factors Affecting Tube Bank Fouling in Coal-Fired Boilers," *Proceedings of the Marchwood Conference on "The Mechanism of Corrosion by Fuel Impurities,"* H. R. Johnson and D. J. Littler, Editors, Butterworths, London, 1963, pp. 173–191.

11 Field, M. A., Gill, D. W., Morgan, B. B. and Hawsley, P. G. W., "Combustion of Pulverized Coal," published by the British Coal Utilization Research Association, Leatherhead, England, 1967.

Downloaded 01 Jun 2010 to 171.66.16.58. Redistribution subject to ASME license or copyright; see http://www.asme.org/terms/Terms_Use.cfm

W. Downs
Research Specialist.

S. J. Vecci
Senior Research Chemist.
The Babcock & Wilcox Company,
Research and Development Division,
Alliance, OH

J. A. Barsin
Manager, Combustion Systems,
The Babcock & Wilcox Company,
Fossil Power Generation Division,
Barberton, OH

W. C. Rovesti
Project Manager,
The Electric Power Research Institute,
Palo Alto, CA

Characterization and Combustion of SRC II Fuel Oil

This paper deals with an experimental evaluation of the combustion properties of solvent refined coal II fuel oil. The purpose was to identify problems, if any, associated with handling, storing, pumping, and burning SRC fuel oil. Detailed fuels characterizations were performed and compared to petroleum distillate products. Laboratory fuel analyses and combustion tests were performed with SRC fuel oil, No. 2 fuel oil, and No. 5 fuel oil. Four B&W atomizers were tested and two B&W oil burners were utilized. The laboratory fuel analyses indicated that in most respects this SRC fuel oil sample behaved similarly to No. 2 fuel oil. The combustion tests confirmed that expectation. The one identified problem was relatively high concentrations of fuel-bound nitrogen and, consequently NO_X emissions were relatively high. It was concluded that SRC fuel oil may require the application of NO_X combustion control techniques.

Introduction

The commercialization of coal liquefaction technology to satisfy the future energy requirements of the electric utility industry is one option currently being pursued by that industry, by government, and by the energy industry in general. The motivation for this accelerating interest in coal liquefaction includes both environmental considerations and the prospect of dwindling petroleum supplies in the not-too-distant future.

The reawakening of interest in this technology in the United States began in the early 1960's and was directed principally towards providing an alternative to flue gas treatment. To desulfurize and deash coal before it is burned rather than to clean the flue gas after combustion has many intrinsic advantages not the least of which is a simplification of the power cycle. The capability of coal liquefaction products to meet existing and future emission limits for sulfur dioxide, particulates, and nitrogen oxides will require an ongoing development effort of both liquefaction and combustion technologies.

Aside from conservation measures the national effort to reduce dependency on imported oil has focused on the electric utility industry. This results from the Industry's significant use of oil for power generation (about 10 percent of national consumption) and also from the Utility Industry's susceptibility to regulation and control. The President's edict to reduce or eliminate the use of oil in power generation wherever possible is thwarted by the realization that only a fraction of boilers fueled by oil are directly convertible to coal. The application of coal liquefaction products for use in this sector of the electric utility market has been receiving rapidly increasing attention and is utlimately responsible for the research described in this paper. Specifically, the results of tests performed on about 400 barrels of distillate SRC II fuel oil are described. This fuel was produced at the Fort Lewis, Washington, Solvent Refined Coal (SRC) Pilot Plant. Both laboratory characterization tests and combustion tests were performed at Babcock & Wilcox Company's (B&W) Alliance Research Center. Combustion tests were performed on a modified industrial boiler.

The overall objective of this research program was to provide information on the handling, combustion, and emission characteristics of SRC II fuel oil in advance of a field demonstration at the 74th Street Station of the Consolidated Edison Company of New York. In that field demonstration 4500 barrels of SRC II fuel oil were consumed [1].

Solvent Refined Coal Process. Of the coal liquefaction processes currently under development it is widely held that the Solvent Refined Coal (SRC) Process is the most advanced coal liquefaction process from the standpoint of scaleup of technology. The SRC process was originally developed by the Spencer Chemical Company in the early 1960's. Spencer Chemical Company was subsequently acquired by Gulf Oil Company where the process development has continued. Two major pilot facilities were built; one at Wilsonville, Alabama, and another at Fort Lewis near Tacoma, Washington. The Wilsonville facility is managed by Southern Company Services under joint DOE/EPRI sponsorship while the Fort Lewis facility is operated by a Gulf subsidiary for DOE.

The SRC process has undergone substantial change during the past decade and in particular during the past 5 years to the point where two distinctive versions have emerged. These are known as the SRC I process and the SRC II process. The SRC I process produces small quantities of gaseous and liquid products but the principal product is a low ash, low sulfur solid fuel referred to simply as SRC. This process has been described extensively [2, 3]. The SRC II process differs from the SRC I process in many ways which are beyond the scope of this paper. Descriptions of the SRC II Process are available elsewhere [4]. The principal manifestation of these process differences is a product mix from the SRC II Process consisting mostly of liquid fuels.

The main product of the SRC II process is a distillate fuel referred to as SRC II fuel oil. The SRC II fuel oil (hereafter referred to simply

Contributed by the Fuels Division and presented at the Winter Annual Meeting, December 2-7, 1979, New York, New York of THE AMERICAN SOCIETY OF MECHANICAL ENGINEERS. Manuscript received at ASME Headquarters August 8, 1979. Paper No. 79-WA/Fu-2.

Copyright © 1980 by ASME
Downloaded 01 Jun 2010 to 171.66.16.58. Redistribution subject to ASME license or copyright; see http://www.asme.org/terms/Terms_Use.cfm

as SRC fuel oil) is a mixture of two distillation cuts known as middle distillate and heavy distillate. The boiling point range of the middle distillate is approximately 175 to 290°C and the heavy distillate boiling point range is approximately 290 to 455°C. The composition and combustion properties of this synthetic fuel oil might be expected to depend upon the relative quantities of middle and heavy distillate used to produce the SRC fuel oil. The SRC fuel oil utilized for this test program was 5.75 parts middle distillate to one part heavy distillate. This is the same blending ratio as the SRC fuel oil utilized by Consolidated Edison for the full-scale demonstration test. However, due to the range of compositions of SRC fuel oil evaluated by others in the past [5] and the composition variations likely to be produced in future commercial enterprises, some caution should be applied when drawing conclusions based upon these tests.

Fuel Characterization

Numerous special and routine laboratory procedures are used to characterize fuel oils to permit prediction of performance in utility boilers and other combustion equipment. The results of these analyses provide information on how liquid fuels behave with respect to storage, handling, combustion and ash deposition.

Discussion of the fuel analyses performed on SRC II fuel oil is divided into two categories: analyses describing physical properties related to storage and handling, and analyses providing information on combustion characteristics including ash deposition.

The SRC fuel oil sample used in this detailed fuels characterization was a representative sample drawn from the supply used for subsequent combustion tests. To provide reference fuel characteristics with which to compare SRC fuel oil and guide initial boiler settings for the combustion tests, many of the analytical procedures were also applied to No. 2 and No. 5 fuel oil samples taken from the B&W Alliance Research Center storage facilities.

Fuel analysis data were determined using ASTM standards, special Babcock & Wilcox methods, and standard practices based on instrument manufacturers' recommendations.

Physical Properties of SRC Fuel Oil. *Viscosity* of SRC fuel oil was determined by the ASTM D 88 Procedure (Saybolt Viscosity) and a method based on the Haake Rotovisco viscometer. The former method provides no information about Newtonian behavior of the fluid tested. For new fuels such as SRC fuel oil, viscosity in Saybolt Seconds Universal alone is inadequate to determine atomization and pumping characteristics. The Rotovisco method, however, could provide an indication of non-Newtonian behavior of the SRC fuel oil to show whether its viscosity characteristics under the shear stress associated with pumping and atomization differed from those measured with the Saybolt method. The results of experiments performed on this fuel to determine degree of Newtonian behavior indicated that the SRC fuel oil and No. 2 fuel oil are both approximately Newtonian at ambient and elevated temperatures, but that the No. 5 fuel oil sample is not. Thus, the utilization of Saybolt viscosity data for SRC fuel oil as applied to various facets of fluid mechanics should be unambiguous. The agreement between the results of the Saybolt procedure and those using the Rotovisco system was excellent as is illustrated in Fig. 1. The Saybolt data in SSU units were converted to centipoise to permit comparison with the Rotovisco results.

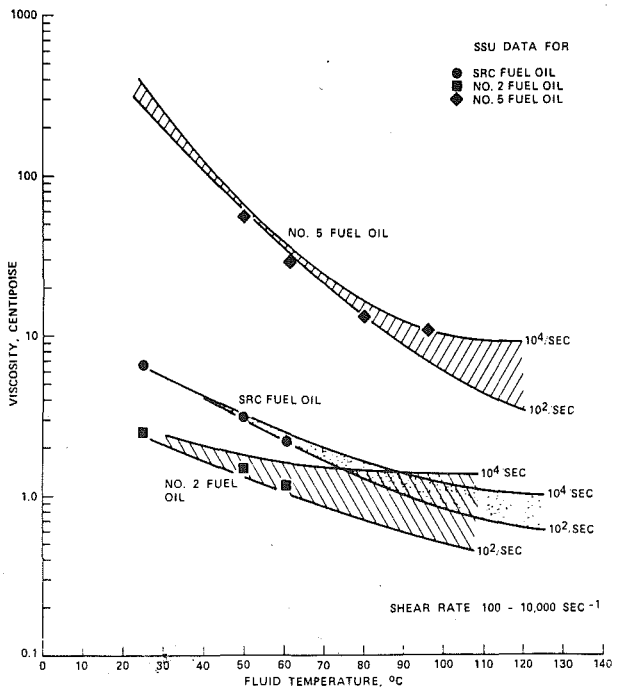


Fig. 1 Viscosities by Saybolt and Rotovisco methods

Some of the other properties relating to the physical handling characteristics of liquid fuels were measured for the SRC fuel oil and the reference fuels (No. 2 and No. 5 fuel oils). The results of these measurements are summarized in Table 1.

- *Density* and *viscosity* data reflect the difference between SRC fuel oil and petroleum distillates. For petroleum distillates, a strong correlation normally exists between specific gravity and viscosity. The term "heavy oil" would generally refer to dense oil of high viscosity. By contrast, SRC fuel oil has a high specific gravity similar to No. 5 fuel oil and a low viscosity similar to No. 2 fuel oil.
- *Pour point* (ASTM D 97-66) provides an indication of handling problems which could occur under conditions of outside storage of liquid fuel at low temperature. The SRC fuel oil pour point is below −37°C and would not normally exhibit low temperature fluidity problems nor require heated storage tanks (except under extremely severe weather conditions).
- *Sediment* was measured by two methods, Sediment by Toluene Extraction (ASTM D 473-69) and Sediment and Water (ASTM D 96-73). Of significance for SRC fuel oil is the use of these methods as indicators of entrained particulate matter and consequential handling problems. In this regard SRC fuel oil compares favorably with No. 5 fuel oil.
- *Surface Tension* affects the atomization properties of liquid fuels but does not vary widely among petroleum distillates when compared to the wide variability of viscosity (an equally important fluid property affecting atomization). Surface tension, therefore, is normally of less concern than viscosity. SRC fuel oil is similar in surface tension to No. 2 and No. 5 fuel oils. Atomization differences

Table 1 Physical handling properties of SRC fuel oil versus petroleum distillates

	SRC Fuel Oil	No. 2 Fuel Oil	No. 5 Fuel Oil
Density			
API at 25°C	12.4	40.3	16.0
API at 16°C	11.5	39.0	15.1
API at 19°C	0.9895	0.8299	0.9652
Pour Point, °C	Below −37	−29	−18
Sediment by Toluene Extraction, percent	0.05	None	0.10
Sediment and Water (ASTM D96-73)	1.0	None	1.9
Miscibility (one to one)			
SRC in	- - - -	Totally Miscible	Totally Miscible
No. 2 in	- - - -	- - - -	Totally Miscible
No. 2 and No. 5 Mixture in	Totally Miscible	- - - -	- - - -
Copper Corrosion (ASTM D130-75)	Moderate, 2b-Color: Lavender	Slight, 1b-Color: Dark Orange	Moderate, 2c-Color: Multi-colored
Surface Tension, dynes/cm at 22°C	34.1	29.9	34.5
Oxidation Stability, mg/100 ml (ASTM D2274)	4.0	10.7	- - - -

Downloaded 01 Jun 2010 to 171.66.16.58. Redistribution subject to ASME license or copyright; see http://www.asme.org/terms/Terms_Use.cfm

among these three fuels should be more greatly influenced by viscosity variations with temperature than by surface tension differences.

• *Copper Strip Corrosion Test* (ASTM D 13-75) is a semi-quantitative measure of corrosive forms of sulfur such as sulfides, polysulfides and mercaptans in petroleum fuels. The test results indicate that the corrosive sulfur content of SRC fuel oil is intermediate between the No. 2 and No. 5 fuel oils.

Combustion-Related Properties of SRC Fuel Oil. *Ultimate Analysis* (ASTM D 271-70) and *Heating Value* (ASTM D 2015-66) determined for SRC fuel oil and No. 2 and No. 5 fuel oils, are shown in Table 2. Of particular significance are the molar ratios of hydrogen to carbon in the fuels. The ratio for SRC fuel oil is 0.62, compared to No. 2 fuel oil at 0.92 and No. 5 fuel oil at 0.73. Consistent with this ratio, is the fact that the SRC fuel oil has a lower heating value than either of these two petroleum fuel oils. However, other properties of traditional petroleum distillates such as boiling point, viscosity, flash and fire points generally increase with decreasing hydrogen/carbon ratios. SRC fuel oil shows seemingly anomalous behavior which can be rationalized by the differences in molecular structure of the organic species constituting SRC fuel oil and normal petroleum distillates.

The nitrogen content of SRC fuel oil is relatively high compared to petroleum fuels causing concern that NO_x control might be a problem during combustion. This concern was borne out by the performance of SRC fuel oil in the combustion tests discussed later.

Burning profiles determined using a thermogravimetric procedure developed by B&W provide a "fingerprint" of the combustion of liquid and solid fuels and permit comparisons of unknown fuels with those which have known full-scale combustion characteristics [6]. Fuels with similar burning profiles would be expected to behave similarly when burned in full-scale equipment. The burning profile technique employs a thermogravimetric test procedure in which a known quantity of sample is heated at a fixed rate in a flowing air atmosphere during which time the rate of weight loss is measured. The plot of rate of weight loss versus furnace temperature is the "burning profile." For liquid fuel the lower temperature portion of the profile (below ~300°C) describes the distillation of the more volatile components of the fuel. At higher temperatures the curve describes the rate of oxidation of the heavy ends of the fuel. Fuels in which most of the weight loss occurs at low temperature would be expected to ignite and burn out more rapidly than those showing comparatively greater portions of the weight loss occurring at high temperatures. Fig. 2 compares the burning profiles of SRC fuel oil, and No. 2 and No. 5 fuel oils. According to these profiles, SRC fuel oil is remarkably similar to No. 2 fuel oil, volatilizing in about the same low temperature range as the latter. Its ignition and burnout characteristics would be expected to be similar to No. 2 fuel oil. Compared to No. 5 fuel oil, SRC fuel oil would be substantially easier to burn.

Atmospheric Distillation (ASTM D 86) curves for each of the three samples are shown in Fig. 3. As with virtually all other combustion characterization parameters implemented in this study, SRC fuel oil and No. 2 fuel oil appear to be very similar. These data reinforce the expectation that SRC fuel oil should behave similarly to No. 2 fuel oil from an ignition and combustion standpoint.

Other combustion related properties are shown in Table 3 and include *flash and fire points* (Cleveland Open Cup Method ASTM D 92-66), and *Conradson Carbon Residue* (ASTM D 189-76). Since the flash temperature of SRC fuel oil (93 C) is higher than 60°C special safely precautions would not be required during storage. In addition, SRC fuel oil should be only slightly more difficult to ignite by high energy electric spark than to No. 2 fuel oil, which is routinely ignited in this manner. Fire points in excess of 200°C usually indicate that carbon burnout problems can be expected. SRC fuel oil has a low fire point, (104°C) well below that of No. 5 fuel oil (168°C), and on this basis carbon burnout should not be a problem.

Table 2 Ultimate analyses, percentage (ASTM D 271-70)

	SRC Fuel Oil	No. 2 Fuel Oil	No. 5 Fuel Oil
Carbon	85.6	86.3	87.2
Hydrogen	8.8	13.3	10.6
Nitrogen	0.8	0.03	0.2
Sulfur	0.26	0.23	1.5
Ash	0.014	Trace	0.025
Oxygen (Diff)	4.526	0.14	0.475
Heating Value Btu/lb (ASTM D 2015-66)	17070	19600	18440

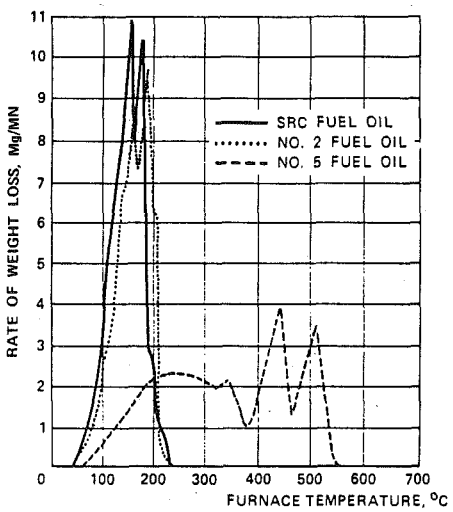


Fig. 2 Comparison of burning profiles

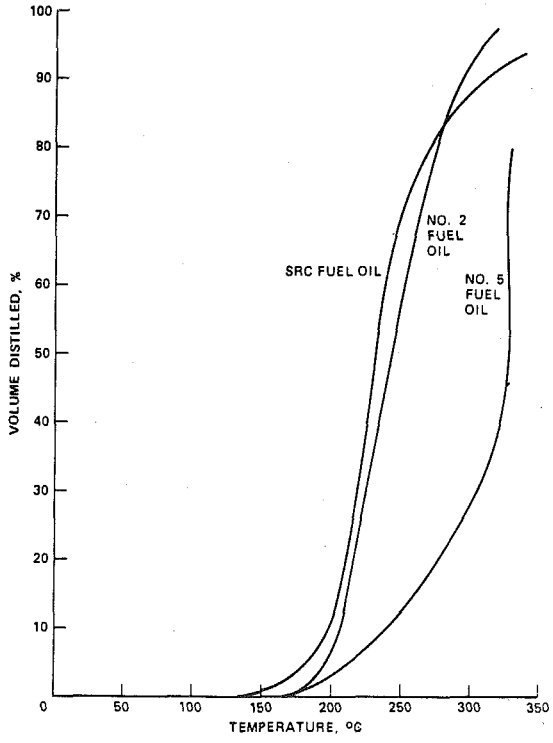
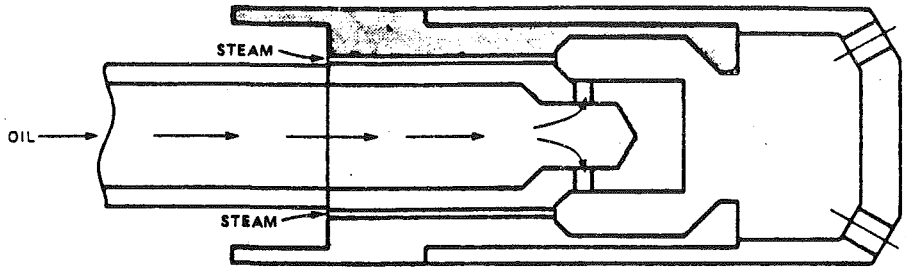


Fig. 3 Atmospheric distillation curves (ASTM D 86)

Table 3 Some combustion properties of fuels

	SRC Fuel Oil	No. 2 Fuel Oil	No. 5 Fuel Oil
Flash Point by Cleveland Open Cup Method, °C	93	82	113
Fire Point by Cleveland Open Cup Method, °C	104	85	168
Carbon Residue, Conradson percent	0.3	<0.1	7.8

Downloaded 01 Jun 2010 to 171.66.16.58. Redistribution subject to ASME license or copyright; see http://www.asme.org/terms/Terms_Use.cfm



T-Jet Atomizer

Fig. 4(a)

Conradson Carbon Residue permits assessing the coking or pyrolytic carbonizing tendency of fuels and the consequent extent of fouling of the fuel atomizer, burner parts, and boiler surfaces in the vicinity of the burner. The Conradson carbon of SRC fuel oil indicates that coking should not be a problem and in fact the coking tendency of this fuel is substantially less than other coal-derived fuels tested to date by B&W.

Ash Characteristics. The ash constituents of SRC fuel oil were determined using emission spectrographic and flame photometric procedures. For SRC fuel oil, the ash analysis was found to be similar to that of an eastern bituminous coal. Slagging and fouling indexes calculated from ash constituents have been correlated with deposition in full scale boilers through years of observation of coal burning units [7]. Processed fuel, in which the natural form and distribution of ash constituents may have been altered, however, may not always be unambiguously evaluated using slagging and fouling indexes established for coals. Keeping this limitation in mind, application of standard calculations for slagging and fouling of eastern coals to SRC fuel oil indicates that it should have a low slagging potential and a high fouling potential. The high fusion temperatures measured for SRC fuel oil ash further supports the low slagging potential assessment. The high fouling potential of SRC fuel oil may be mitigated by its significantly lower ash content (0.014 percent compared to ~10 percent for eastern bituminous coal). However, the low ash content does not in itself preclude the concern for including soot blowing provisions as are often required on boilers firing heavy fuel oil.

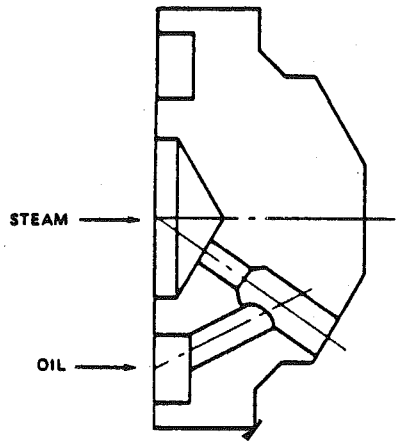
Combustion Facilities

Combustion tests were performed on a Babcock & Wilcox package boiler. The combustion gases pass horizontally through both the furnace and steam generator. This bottom supported boiler (Model FM 1070) was designed to produce 50,000 lb/hr (22.7 Mg/hr) steam at multiple pressure ranges from 150 psig (10.3 BAR gauge) to 1050 psig (72.4 BAR gauge). The support facilities included a separately fired air heater, air flow meter, fans, pumps, controls, and fuel storage facilities. Approximately 17,000 gallons of SRC fuel oil were stored in a rail tank car.

Two different burners were utilized for this combustion study. Initially, a circular burner was studied and later replaced with a dual register burner. The circular burner which consists of a circular register, fuel atomizer assembly, and various startup and control components is the most frequently used burner for fuel oil combustion on wall-mounted boiler designs. The circular register consists of a series of tangentially disposed doors which provide the turbulence necessary to mix the fuel and air during combustion.

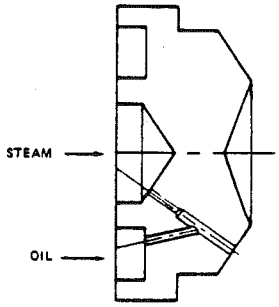
Upon completion of about 180 tests with the circular burner, it was replaced by a dual register oil burner. The purpose was to determine whether this dual register burner with its potential flame shaping capabilities could reduce NO_x emissions.

Four fuel atomizer designs were utilized during this test program. B&W's designation for these atomizers are T-jet, Y-jet, Racer, and return flow mechanical atomizer. These atomizers are displayed in Fig. 4. The first three employ pneumatic atomization of the oil while the latter one accomplishes the desired degree of atomization by op-



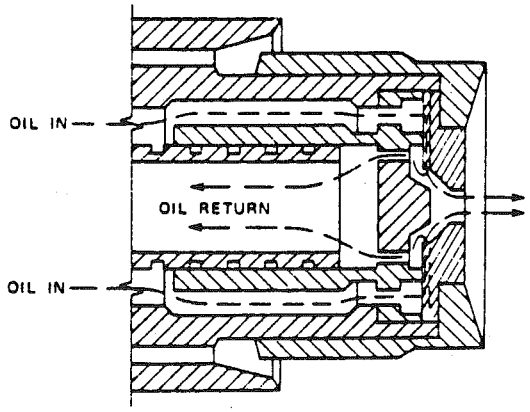
Y-Jet Atomizer

Fig. 4(b)



Racer Atomizer

Fig. 4(c)



Return Flow Mechanical Atomizer

Fig. 4(d)

Fig. 4 B & W fuel atomizers

Downloaded 01 Jun 2010 to 171.66.16.58. Redistribution subject to ASME license or copyright; see http://www.asme.org/terms/Terms_Use.cfm

erating at high pressure (40 to 70 BAR). All four of these atomizer designs have wide commercial use.

Handling and Pumping SRC Fuel Oil. Several special preparations and precautions were taken to handle SRC fuel oil. For instance, SRC fuel oil was believed to severely attack commonly used elastomers. Two elastomers which are thought to perform satisfactorily on SRC fuel oil are Viton and Teflon. Wherever possible gaskets, seals, and pipe joints were refitted with Teflon or Viton. One notable exception was the hose used to connect the SRC rail car to the plant piping. Here Type 82-A gasoline tank hose was used. This hose was selected because it was approved for intermittent service with creosote (a coal pyrolysis product).

Precautions were directed towards personnel exposure to SRC fuel oil. Since this fuel is highly phenolic, absorption into the skin with subsequent inflammation was a recognized problem. Each individual who was likely to be involved with this project was given specific instructions to avoid contact with SRC fuel oil and to follow certain hygiene procedures in case of contact.

Pumping of SRC fuel oil was another area where special precautions were taken. Similarities between SRC fuel and No. 2 fuel oil indicated that their lubricity would also be similar. Positive displacement pumps used for burner applications usually rely upon the lubrication qualities of the pumping fluid to protect wear parts. It is recognized that pumps designed for heavy oils are often not suitable for use with No. 2 fuel oil because of its relatively lower lubricity. Possible damage to the facility's existing fuel pumps was avoided by purchasing and installing new gear pumps. Two pumps were purchased for 10 BAR service and one pump was purchased for 40 BAR service. These pumps were constructed of iron and steel and were designed for normal-service duty on self-lubricating fluids. The two low pressure pumps were equipped with standard stuffing boxes and the high pressure pump was equipped with a labyrinth type mechanical seal.

During the rather modest length of time these pumps were in use no loss of pressure or capacity was observed. However, none of the pump seals were adequate to prevent excessive leakage. Pump seal leakage from fuel oil pumps is a commonly tolerated situation. SRC fuel oil leakage, because of its pungent odor and handling properties, probably will not be tolerated commercially. This point must be addressed when specifying new pumps for SRC fuel oil. It is anticipated that pumps suitable for No. 2 fuel oil service supplied with seals to minimize leakage can probably be recommended for SRC fuel oil.

Combustion Tests

The combustion program consisted of a parameter study for which the control variables were register setting, excess air, and firing rate. The equipment parameters included the burner design (two burners), fuel atomizer (four atomizer designs), and fuel oil type (No. 2, No. 5, and SRC fuel oil). For each of these test conditions, the principal measurements included NO concentration, CO concentration, and stack opacity. Over 275 tests were performed during this program.

An objective of this combustion study was to determine whether SRC fuel oil possesses any unique properties which might influence its substitution for conventional petroleum fuels in existing electric utility equipment. Limited supplies of this coal derived liquid necessitated small boiler testing prior to a planned fuel test in a utility boiler. Potentially excessive NO_X emissions and/or excessive particulate emissions were the two principal concerns. These emission parameters can be (and were) measured quantatively and the results will be presented subsequently. Conversely, combustion performance as it relates to flame appearance, burner stability, furnace rumble, etc. is somewhat subjective. Regardless, it plays an important role in assessing the suitability of a potentially new fuel such as SRC fuel oil for use with conventional combustion equipment. Although flame appearance varied widely from test to test, variations were not attributable to fuel type per se. Rather, register settings, atomizer type, and excess air had the predominating influence upon combustion appearance.

A consistent relationship existed amongst flame appearance, minimum allowable excess air, and NO_X formation. If the flame was luminescent and clear, NO_X was generally high. No significant differences in flame appearance were discernible between SRC fuel oil and the petroleum fuel oils.

Influence of Fuel-Bound Nitrogen. The combustion of SRC fuel oil resulted in significantly higher NO_x emissions than did either No. 5 or No. 2 fuel oil. The SRC fuel oil contained about 0.8 percent fuel-bound nitrogen compared to 0.2 percent for No. 5 fuel oil and 0.03 percent for No. 2 fuel oil. A plot of the predicted[1] and observed NO_X emissions for this small industrial boiler design as a function of fuel-bound nitrogen is presented in Fig. 5. The expected "thermal NO_X" component of the total observed NO_X emission for this boiler operating at full load and 15 percent excess air is about 100 ppm ±10 ppm when the air is preheated to 400°F (205°C). If the thermal NO_X component does not deviate substantially from this 100 ppm estimate, then the oxidation of fuel nitrogen in SRC fuel oil is apparently the predominant mechanism for NO_X formation. In fact, while NO_X emissions from the combustion of No. 5 and No. 2 fuel oils agreed closely with expectations, SRC fuel oil combustion produced higher NO_X emissions than predicted. The implication is that the fuel-bound nitrogen in SRC fuel oil may be more readily oxidized than fuel-bound nitrogen in other high nitrogen/liquid fuels (within B&W's experience on small industrial type boilers).

Influences of Fuel Atomizer Design. Fuel atomizer design had a predominating effect upon both NO_X emissions and combustion performance when burning SRC fuel oil. For the circular burner at full load, NO_x emissions avaveraged about 125 ppm higher utilizing the Y-jet when compared to the T-jet and about 175 ppm higher than the return flow mechanical atomizer. This data is presented in Fig. 6. The dual register burner also exhibited this strong sensitivity to atomizer design.

The atomizer design influences both the atomization quality (Sauter Mean Diameter) and the spray pattern. For B&W's atomizers, the atomization quality can be listed in the following approximate rank starting with the highest quality atomization: (1) T-jet, (2) Y-jet, (3) Racer, (4) High Pressure Mechanical (Return Flow).

As a first order effect, one would expect NO_x emissions to increase with increasing atomization quality. However, on the circular burner, the Y-jet was found to yield higher NO emission than a T-jet atomizer. Likewise, the mechanical return flow atomizer produced higher NO emission on the dual register burner than did the Y-jet atomizer with its apparent superior atomization quality.

As a consequence of these observations, it is concluded that atomizer spray patterns and subsequent mixing in the combustion zone of the furnace apparently play significant roles in the NO formation mechanisms. In support of this generalization was the observation that a correlation existed between NO_x emissions and combustion appearance. Without exception, for a given fuel and burner setup, NO_x emissions increased as the brightness and clarity of the fire increased.

Other Effects upon NO_X Formation and Combustion Quality. The capability of the dual register burner to control NO_X formation from SRC fuel oil combustion was disappointing. This burner differs from the circular burner principally in its capability for directing a portion of combustion air devoid of swirl along the central axis of the flame. The intent is to control the shape of the flame. Due to a scale-down design problem and because of a compressed project schedule which did not permit design or testing iterations, the flame shaping capabilities of this small industrial sized dual register burner were inadequate. The result was an inability to control NO_X without a corresponding reduction in combustion quality.

Burner register adjustments had little influence upon NO_X formation. Register adjustments are intended to control the swirl intensity of the combustion air. This lack of NO_X control via register adjustments coupled with the strong influence of atomizer design

[1] The predicted curve is based upon tests performed by B&W on many industrial boilers burning a myriad of nitrogen-containing fuels. None of these fuels previously tested were coal derived liquids.

Downloaded 01 Jun 2010 to 171.66.16.58. Redistribution subject to ASME license or copyright; see http://www.asme.org/terms/Terms_Use.cfm

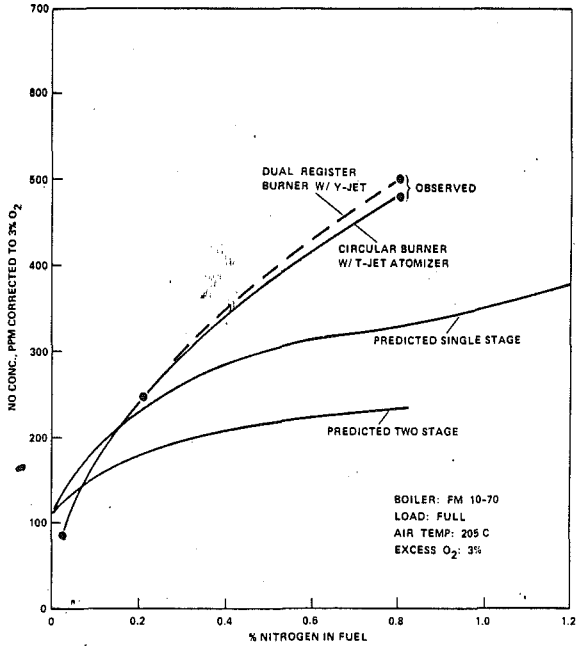


Fig. 5 Comparison of observed and predicted NO_x emissions

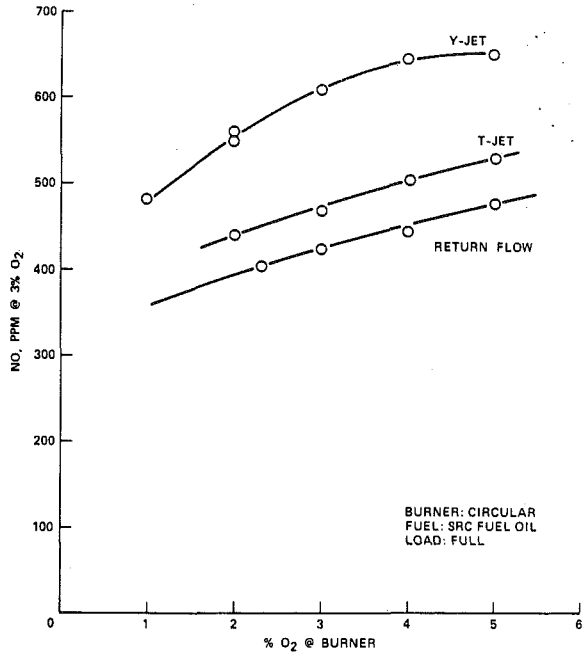


Fig. 6 Influence of fuel atomizer design on NO_x emissions

suggests that mixing is actually controlled much more by the oil spray pattern than by air swirl intensity.

The influence of boiler load on NO_X also reflected the strong dependence upon atomizer design. NO_X increased sharply with increasing load when the Y-jet atomizer was utilized. Conversely, NO_X actually diminished with increasing load when utilizing the mechanical return flow atomizer.

Particulate Emissions. A total of 22 dust loadings were measured. Ten of these were taken during No. 5 fuel oil combustion tests and eleven were taken while burning SRC fuel oil. The remaining test was performed on No. 2 fuel oil. On a carbon-free basis, the No. 5 fuel oil tests averaged 0.050 pound of ash per million Btu with a standard deviation of 0.0024 pound per million Btu (~5 percent). This dust loading is about 3.5 times higher than the dust loading which would be expected from the available ash in the No. 5 fuel oil. The SRC fuel oil averaged 0.0198 pound per million Btu on a carbon-free basis and had a standard deviation of 0.0014 pound per million Btu (6.9 percent). This average dust loading is about 2.5 times higher than that which would be expected from the laboratory ash analysis of SRC fuel oil.

The variance between actual and expected dust loadings for both No. 5 fuel oil and SRC fuel oil could result from either or both of the following factors:

1 These oils may contain volatile ash constituents which are not recoverable by ASTM D 271-70.
2 Tramp material such as rust, sediment, pipe scale, and residual ash in the boiler may contribute significant quantities of ash.

The second factor seems more likely and is supported by the fact that for SRC fuel oil the carbon-free dust loadings diminished generally with each successive test. Further, the strainers in the SRC fuel oil lines showed a small accumulation of rust and scale.

Commercial Implications

Storage and Handling. A utility boiler equipped to fire No. 6 fuel oil could shift relatively easily to SRC II fuel oil. The flash point of about 200°F (93°C) is sufficiently high and the pour point is sufficiently low to allow the use of existing storage facilities. The unusual aspects of SRC fuel oil which should be addressed are:

1 Plant personnel must be educated about the distinctions between petroleum oils and SRC fuel oil. For example, the use of barrier creams, and daily change of clothing, if contact is high, may be required.
2 Pumps should be selected on the basis that SRC fuel oil is similar to No. 2 fuel oil from a lubrication standpoint. Therefore, existing standard practice for most No. 2 fuel oil installation should be suitable for SRC fuel oil. Mechanical seals will probably be required.

Combustion. The burning of SRC fuel oil appears to pose no major technological roadblocks to its use as a fuel for electric power generation. Standard oil atomizers, burners, and furnaces appear to be suitable.

NO_X generation is typically controlled on boilers with wall mounted burners by applying known NO_X control techniques such as low NO_x burner design, classic two stage combustion, (i.e., fuel rich combustion at the burners with additional air injected through NO_X ports located above the burner zone) or *Burners Out of Service* (BOOS). In spite of the relative ineffectiveness, during these tests, of the dual register oil burner, due to scale-down problems (from 200×10^6 Btu/hr to 50×10^6 Btu/hr), this double air zone burner design may still be applicable for NO_x control with SRC II fuel oil. The dual register burner has been successfully utilized at Southern California Edison's Mandalay Steam Plant and several units within the Florida Power and Light system. A similar dual register burner design for pulverized coal has received much wider application for NO_x control because the majority of new units are fired directly with coal. The Burners Out of Service approach would require increasing fuel inputs to active burners to compensate for the loss of burners dedicated to BOOS. BOOS has been utilized extensively on conventional oil fired boilers and is an acceptable NO_X control technique for that fuel without sacrificing "Maximum Continuous Rating" capability or total excess air levels. When SRC fuel oil is applied to specific furnace designs it might be necessary to vary the secondary air preheat or the percentage of SRC fuel oil blended with low fuel nitrogen oils to stay within NO_X emission limits. However, these operational variations are now well understood and can be managed.

Future Applications. Even with current world oil pricing trends, it would appear that products from the first coal liquefaction demonstration or pioneer plants may not be cost competitive with petroleum fuels prior to about 1985. However, given the rapidly escalating cost of foreign oil, these coal liquids may in fact become cost competitive for power generation in equipment dedicated to peaking and intermediate service in the period after 1985 [8].[2]

[2] The specific date at which coal liquefaction will become competitive with petroleum fuels is, of course, uncertain. A detailed discussion of this projected timetable is beyond the scope of this paper.

Downloaded 01 Jun 2010 to 171.66.16.58. Redistribution subject to ASME license or copyright; see http://www.asme.org/terms/Terms_Use.cfm

Specifically addressing the substitution of coal derived liquids for oil or natural gas in utility boilers, these fuels could become important for utilization in existing units that will still have a long service life remaining. This substitution might be dictated by either gas and oil availability or by government regulation of the use of these fossil fuels. Replacement of these oil and gas fired units with new direct coal fired or nuclear units would impose a severe cost burden on utilities. The installation of coal handling or emission control equipment to allow conversion to solid fuels on those few units where direct coal firing is physically possible would also be very costly. Thus, despite a potentially higher cost, the use of coal liquids in certain segments of electric utility industry may be economically viable within a relatively few years.

Summary and Conclusions

In order to assess the technical implications of using SRC II fuel oil as a substitute fuel in oil fired electric utility boilers several laboratory fuel characterization and commercial scale combustion tests were performed. The fuels analysis showed that the sulfur and ash content are low enough to meet Federal New Source Performance Standards (assuming complete combustion). Most laboratory tests revealed SRC fuel oil to have a marked similarity to No. 2 fuel oil. The principal concern as a result of these laboratory analyses was with SRC fuel oil's relatively high fuel-bound nitrogen content.

The combustion tests demonstrated that the high fuel nitrogen content resulted in relatively high NO_X emissions. From a combustion appearance standpoint SRC fuel oil was indistinguishable from the petroleum fuel oils.

The principal conclusions which can be drawn from this preliminary study are summarized as follows:

Tank Storage and Pumping

- From a safety standpoint SRC fuel oil should be storable in tankage designed for No. 6 fuel oil.
- For short term storage, sedimentation should be no problem. Long term storage effects were not studied although an accelerated oxidation stability test revealed no problem.
- Positive displacement pumps designed specifically for low viscosity liquids will be required for SRC fuel oil.

Combustion

- The ignitability, atomization, coking, and combustion of SRC fuel oil should be similar to No. 2 fuel oil.
- Sulfur and particulate emissions should be below the New Source Performance Standards. SRC fuel oil should exhibit no significant smoking tendency.
- Although the capability to burn SRC fuel oil in such a way as to limit NO_X emissions to less than EPA's New Source Performance Standard of 0.5 pound NO_x/million Btu was not demonstrated, it appears that this new limit could be met on the typical wall-fired utility boiler by the use of two-stage combustion or possibly by the proper matching of burner and atomizer designs.

Acknowledgment

This work reported herein was sponsored by and performed for the Electric Power Research Institute (EPRI) as part of their ongoing research efforts to evaluate the use of synthetic fuels by the United States electric utility industry. The work was supported by EPRI Research Projects 1235 and 1412. A detailed report of this work is available from EPRI [9].

References

1 Piper, B. F., Hersh, S., and Nazimowitz, W., "Combustion Demonstration of SRC II Fuel Oil in a Tangentially Fired Boiler," EPRI FP-1029, May 1979.

2 Brant, V. L. and Schmid, B. K., "Pilot Plant for Deashed Coal Production," *Chemical Engineering Progress*, Vol. 65, No. 12, 1969, pp. 55–60.

3 Jimeson, R. M. and Maddox, R. R., "Solvent Refined Coal Processing in the United States," GVC/AIChE Joint Meeting, Müchen, Vol. II, Sept. 17–20, 1974, B 6-3.

4 Schmid, B. K. and Jackson, D. M., "The SRC II Process," paper presented at the Second Pacific Chemical Engineering Congress, Pachee 1977.

5 Arand, J. K. and Muzio, L. J., "Combustion and Emissions Evaluation of SRC Fuel Oil, A Synthetic Liquid Fuel from Coal," KVB Report 19900-773, Dec. 1977.

6 Wagoner, C. L. and Duzy, A. F., "Burning Profiles for Solid Fuels," ASME Paper No. 67-WA/FU-4, Pittsburgh, PA, Nov. 12–17, 1967.

7 Vecci, S. J., Wagoner, C. L., Olson, G. B., "Fuel and Ash Characterization and Its Effect on the Design of Industrial Boilers," American Power Conference, Chicago, Ill., April 24–26, 1978.

8 Wolk, R. H. and Albert, S. B., "Coal Liquifaction and the Electric Utility Industry," Presented at the ACS Symposium: Coal Dilemma II, Colorado Springs, CO, Feb. 1979.

9 Downs, W. and Kubasco, A. J., "Characterization and Combustion of SRC II Fuel Oil," EPRI Report FP-1028, June 1979.

Downloaded 01 Jun 2010 to 171.66.16.58. Redistribution subject to ASME license or copyright; see http://www.asme.org/terms/Terms_Use.cfm

A. K. Moza
Graduate Student,
Fuels Science

L. G. Austin
Professor of Fuels and Mineral Engineering

R. E. Tressler
Associate Professor of Ceramic Science

Department of Material Sciences,
The Pennsylvania State University,
University Park, PA 16802

Some Results of the Wetting and Adherence of Synthetic Coal Ash Droplets on Steel

As part of a study of slagging in boiler furnaces the sticking temperature, strength of adhesion and contact angle of molten mineral glass drops on various oxidized steel substrates have been investigated. The freezing of the interface between the drop and the metal substrate occurs in milliseconds and in this time a bond is formed between the glass and the oxide coating on the steel. Mineral compositions of low melting point which have reduced liquidus temperatures when iron is dissolved from the surface appear to give the lowest sticking temperatures. Stainless steels which were not heavily oxidized gave low strengths of adhesion. Pyrrhotite formed from melting of pyrite wetted the oxidized surfaces well and gave low sticking temperatures.

Introduction

When a pulverized coal particle is burned the mineral matter associated with the particle melts to form droplets of molten glass. The large water tube boilers used for steam raising for power generation are commonly fired with pulverized coal, and the adherence of the droplets can form slag coatings in the hotter parts of the boiler furnace. Of particular concern is adherence in the upper region of the furnace at the screen tubes, since the accumulation of a large mass of fused slag which then breaks away and falls can seriously damage the bottom tubes. As part of a project concerned with various aspects of this problem, a laboratory test has been developed [1, 2] which is an indication of the ability of a molten droplet to adhere to a cooler substrate. This paper is a further report on results obtained with this test.

Experimental Techniques

The apparatus has been described previously [2]. The test consists of forming a small pellet (about 0.1 g) from ash, or a mixture of pulverized minerals, on the end of a platinum wire. The pellet is heated at the center of two small opposed methane-oxygen (oxygen-rich) flames to temperatures up to 1700°C. After melting the viscosity decreases until the molten droplet falls off; it falls 50 mm through a hole onto a horizontal substrate maintained at a controlled temperature by an auxiliary electric furnace. The droplet freezes on the substrate and adheres or does not adhere, depending on the composition of the droplet, the material, and temperature of the substrate. If it adheres, the droplet is sheared off the substrate (still at the controlled temperature) by a ram moving parallel to the surface, and the shearing force required is measured. An apparent contact angle α is calculated from the equation

$$\tan(\alpha/2) = 2h/b \quad (1)$$

where h is the height of the drop and b the diameter of the contact area.

Contributed by the Fuels Division and presented at the Winter Annual Meeting, December 2–7, 1979, New York, New York, of THE AMERICAN SOCIETY OF MECHANICAL ENGINEERS. Manuscript received at ASME Headquarters August 8, 1979. Paper No. 79-WA/Fu-3.

In the tests discussed here, the metal substrates were washed in acetone, polished to smoothness with 400 grit Carbimet paper in water, washed again with acetone, dried with tissue paper and oxidized in air in a furnace at 400°C for about 20 hr.

Most tests were performed on a synthetic coal mineral mixture containing 37 weight percent CaO, 20.4 percent SiO_2, 18.9 percent Al_2O_3 and 23.7 percent Fe_2O_3 ground together with a mortar and pestle. It had already been demonstrated that the degree of grinding did not affect the result, nor did the absence or presence of carbon. The liquidus temperature of this composition is 1480°C [3]. The mild steel substrate had the composition, 0.20 weight percent C, 0.50 percent Mn, 0.04 percent P, 0.05 percent S, remainder Fe.

Tests were also conducted with (1) synthetic ash mixtures of CaO and Fe_2O_3 (with and without SiO_2) (2) pure minerals such as pyrite, hematite, clays and quartz, (3) high C and high Mn mild steel and (4) stainless steels (SS 316 and SS304).

Results

A pellet was heated to 1400°C, below the liquidus temperature, in a platinum crucible and tipped into the mild steel substrate held at 700°C. There was no adherence, showing that melting and droplet formation is necessary for sticking. Pellets were melted, dropped in air to cool, and collected. These were used in a series of tests where a pellet was reheated to 650°C and dropped onto a substrate which had been coated with molten K_2SO_4. The substrate temperature was varied from 400 to 900°C, so that the K_2SO_4 varied from the solidified condition to the molten condition. No adherence occurred in the test time of five min, showing that frozen droplets do not adhere to a layer of K_2SO_4. Of course, an initially non-adherent deposit left on an alkali layer might develop adherence with time.

High-speed photography at 1000 frames per second gave the following picture of solidification and adherence under normal test conditions (see Fig. 1). The droplet is molten when it strikes the surface and it flattens somewhat on impact then reverts within 3 ms to a shape nearer that of a sphere, flattens somewhat again, etc. The contact area solidifies within 2 to 3 ms and a zone of solidification moves up through the drop, giving complete solidification in 30 to 40 ms. The rate of chilling of the interface is, therefore, roughly 10,000°C

Copyright © 1980 by ASME
Downloaded 01 Jun 2010 to 171.66.16.58. Redistribution subject to ASME license or copyright; see http://www.asme.org/terms/Terms_Use.cfm

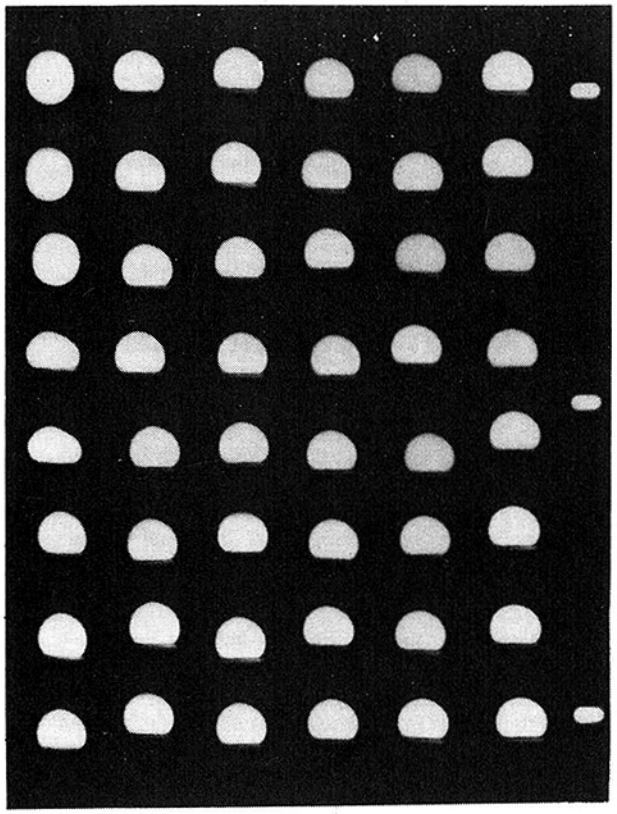


Fig. 1 Collision of droplet with oxidized mild steel substrate held at 480°C (above sticking temperature): frames at 1000 per second from top left hand corner down

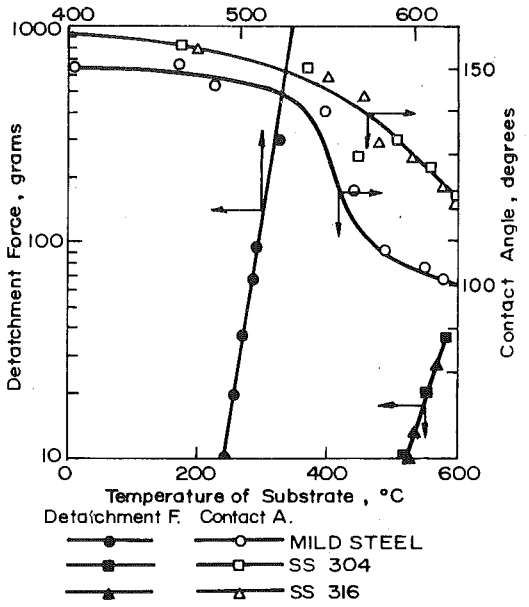


Fig. 2 Slag droplet adhesion force and contact angle as a function of substrate temperature for three different substrates

s^{-1}, so that it is unlikely that equilibrium can be reached at the interface. It is also expected that the interface will be a glass with little crystallinity (see discussion below).

Synthetic Ash on Mild Steel. Fig. 2 shows the force of adherence and the apparent contact angle for the droplet formed from the synthetic mixture dropped onto the oxidized mild steel substrate. Adhesion is sufficient to prevent the solidified drop from falling off the substrate when it is tipped vertically when the temperature is about 460°C, which is defined as the sticking temperature T_s. Over the relatively small range of substrate temperature shown in the figure the adhesion strength based on a contact area of 0.28 cm^2 is given approximately by

$$s = \exp\left[(T - T_s + 0.5)/2\right] \text{ g/cm}^2 \qquad (2)$$

where T is substrate temperature in °C. The degree of wetting of the surface achieved in the few ms solidification is shown by the apparent contact angle. The contact angle decreases and wetting increases as the substrate temperature increases.

After the droplet was sheared off it was polished in a vertical plane and viewed in a scanning electron microscope and with an electron microprobe. Fig. 3 shows the result; the dark area on the left is the epoxy mounting medium. It is clear that the region in the drop next to the substrate drop interface is clear glass, and crystallinity develops about 500 μm away from the interface, Fig. 3(a). The irregular dark areas in the crystallization on the right correspond to crystallization of an iron-deficient phase. The rounded dark areas are bubbles in the glass. At higher magnification, Fig. 3(b), a layer of iron oxide sticking on the drop at the interface is clearly visible. This layer has been broken off the substrate, but it does not appear to adhere smoothly and perfectly to the glass, or to cover the whole surface. It is approximately 8 μm in thickness.

Fig. 4 shows the results of perpendicular viewing of the interface, for substrate temperature of 400, 450 and 500°C. The white patches were shown to be iron oxide. The smooth patches are areas where the glass apparently did not wet the metal, since they do not show the

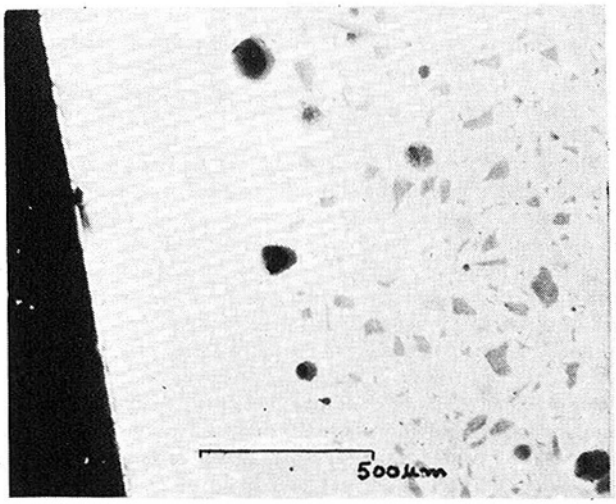


Fig. 3(a)

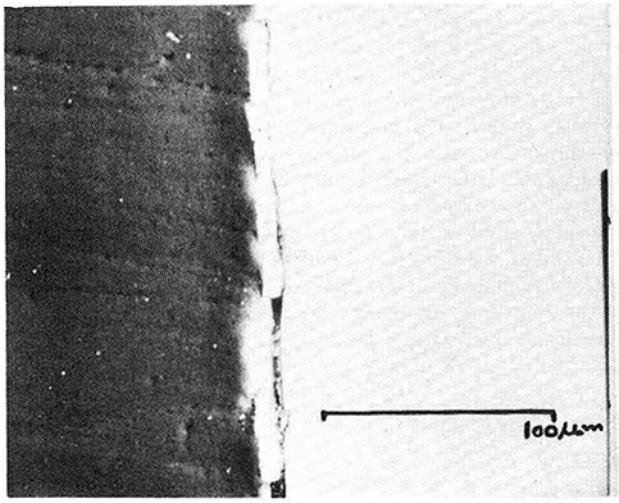


Fig. 3 (b)

Fig. 3 Electron backscatter image of a vertical section of the droplet at different magnifications

Downloaded 01 Jun 2010 to 171.66.16.58. Redistribution subject to ASME license or copyright; see http://www.asme.org/terms/Terms_Use.cfm

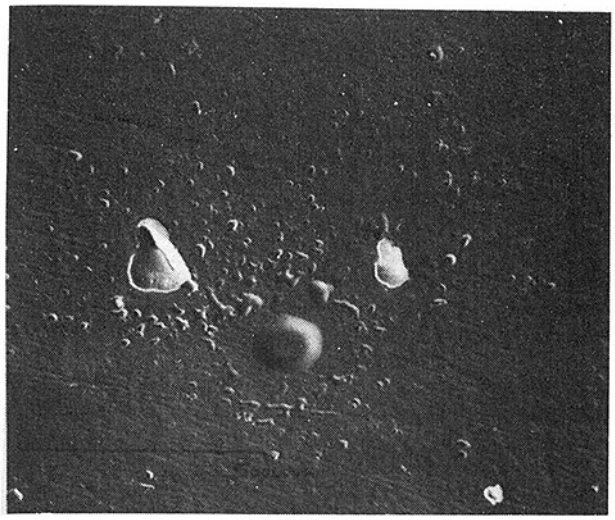


Fig. 4(*a*) 400°C

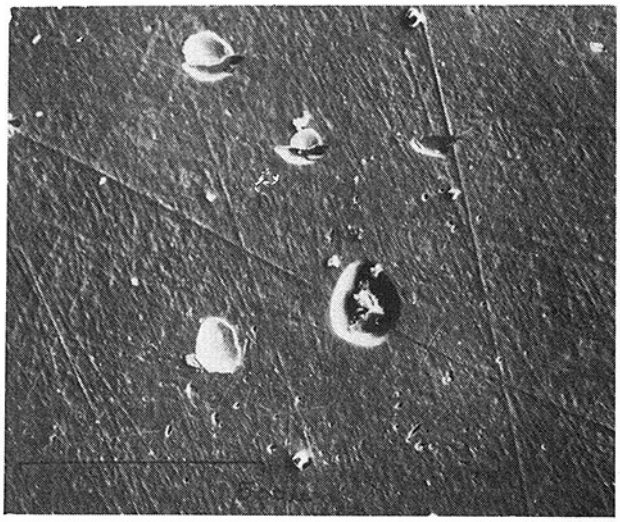


Fig. 4(*b*) 450°C

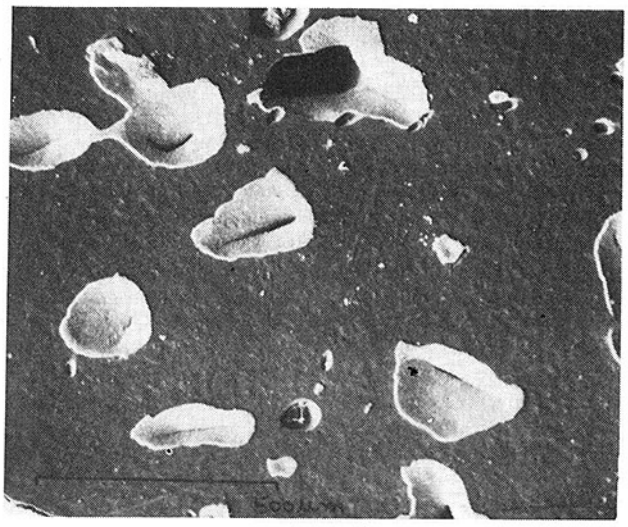


Fig. 4(*c*) 500°C

Fig. 4 Secondary electron image of perpendicular view of the interface for substrate temperature of (*a*) 400°C, (*b*) 450°C, (*c*) 500°C

polishing striations on the substrate. Some holes caused by bubbles are also present. It is concluded that the adhesion strength is due to a very rapid interaction of the glass with the oxide layer on the mild steel, but that this interaction is stronger at certain patches, and is not uniform over the whole surface. When the droplet is sheared off, the strongly reacted patches of oxide film break off the metal, while glass breaks off the oxide at the weak areas. As the substrate temperature increases, the patches of strong interaction are more numerous and larger in area. At 500°C, the patches represented about 25 percent of the contact area and with a shearing force of 89 g this represents a shear strength of the oxide film of about 3000 g/cm^2.

Synthetic Ash on Stainless Steel Substrates. Substrates of two stainless steels (S.S. 304 and S.S. 316) were also polished and heat-treated in air as described above. The results of sticking tests with the synthetic mixture are also shown in Fig. 2. The droplets do not wet stainless steel below 600°C and the adhesion force is small.

Effect of Sodium Chloride Coating on Substrate. Substrates of mild steel were coated with 10 percent NaCl-H_2O solution, covered with a glass slide to squeeze out the liquid, and the sandwich freeze-dried. After removal of the slide, the increase in weight corresponded to a layer of NaCl on the metal of about 50 μm thick. The procedure was repeated for S.S. 304. Sticking tests on these substrates gave the results shown in Fig. 5. On mild steel the droplets stick at all substrate temperatures and develop a shear strength at 400°C comparable to that on uncoated mild steel at 500°C. Droplets also stick on the coated stainless steel substrate, giving the same strength of adhesion as on uncoated mild steel at 525°C. Obviously, the NaCl melts when the droplet strikes and, hence, fluxes the glass to give increased adhesion. More work is needed to determine the mechanism of adherence under these conditions.

Effect of Pyrite Addition to Pellet. The synthetic mixture was modified by the addition of 12 percent weight of FeS_2. The result is shown in Fig. 6. The presence of pyrite in the droplet caused the sticking temperature to fall to about 200°C, with increased wetting of the surface. A given adhesion strength was reached at about 70°C lower temperature than for the synthetic mixture. The droplet was further analyzed chemically and found to contain about 3 percent sulfur indicating that the sulfur did not burn off completely during melting. The phase relations for this system indicate [3] that the liquidus temperature is lowered by the addition of more iron.

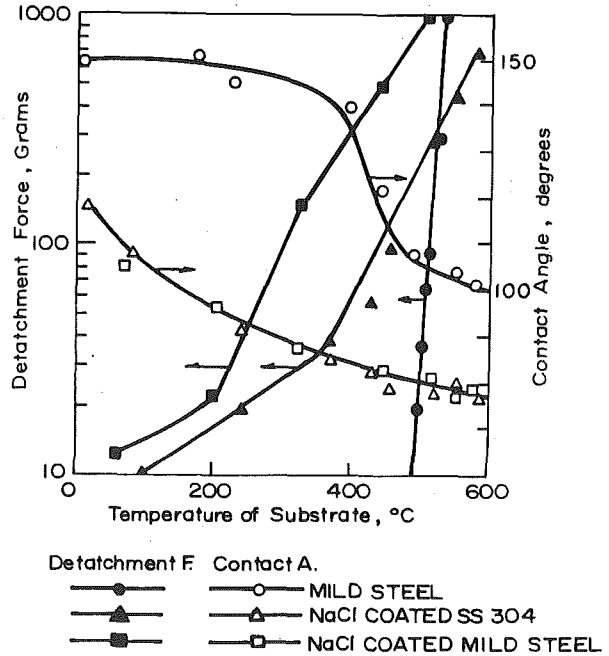


Fig. 5 Slag droplet adhesion force and contact angle as a function of substrate temperature for substrates coated with sodium chloride. Curve for uncoated mild steel is shown for comparison

Downloaded 01 Jun 2010 to 171.66.16.58. Redistribution subject to ASME license or copyright; see http://www.asme.org/terms/Terms_Use.cfm

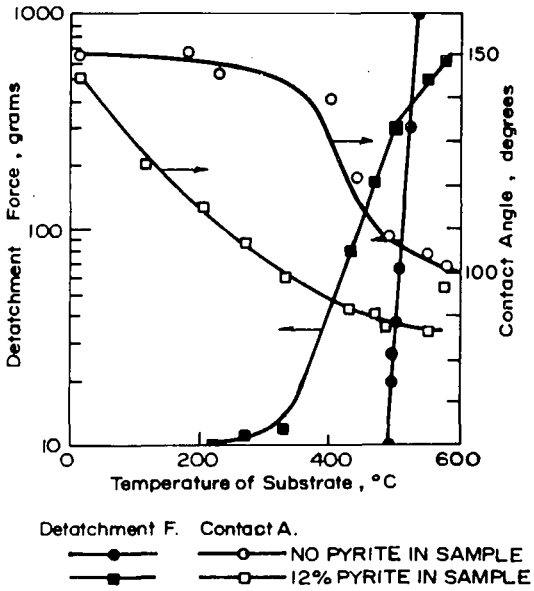


Fig. 6 Effect of pyrite addition to the slag droplet on adhesion force and contact angle

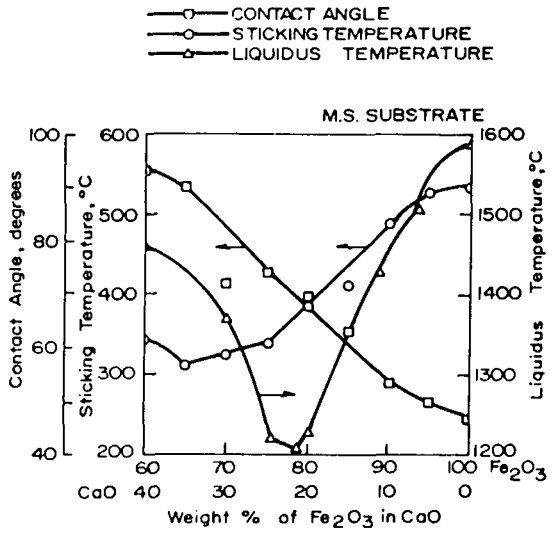


Fig. 7 Slag droplet sticking temperature and contact angle as a function of liquidus temperature of the droplet

Effect of Variation of Liquidus Temperature of Pellet. In order to study the effect of liquidus temperature the simple system CaO-Fe_2O_3 was chosen for the following reasons: (1) the oxidized layer on the substrate was primarily Fe_2O_3 (2) the liquidus temperatures of this system in the composition range studied are below 1600°C and (3) the liquidus temperatures of the system are accurately known [4]. Pellets made from mixtures of powdered CaO-Fe_2O_3 were tested on a high carbon steel substrate (C = 0.44, Mn = 0.8, P and S less than 0.04 percent). This was oxidized at 400°C for 20 hr, followed by further oxidation for two hours at 590°C to develop a predominantly Fe_2O_3 layer [5]. All the pellets were melted under identical flame and temperature conditions, so that the temperatures of the droplets at the time of fall were identical. The results are shown in Fig. 7. The apparent contact angle at the sticking temperature decreased as the iron content increased, indicating improved wetting. The sticking temperature passed through a minimum at a pellet composition of 65 percent Fe_2O_3 and 35 percent CaO. The liquidus temperature of the composition chosen is also plotted. The curves indicate that sticking temperature followed a similar trend to that of liquidus temperature, except that the sticking temperatures had shifted somewhat to the left, that is, to lower Fe_2O_3 content. It will be remembered that previous results indicated a chemical bonding between the substrate oxide layer and the droplet, which suggests that the region of the droplet at the interface had adsorbed Fe_2O_3, thus giving higher Fe_2O_3 percentage than the pellet composition. Sticking occurred better at a lower liquidus temperature, because the time for the interface to solidify is then extended, thus increasing the reaction time of molten slag in contact with the oxide layer.

To study the effect on the sticking temperature of pick-up of Fe_2O_3 from the iron substrate, two compositions of the SiO_2-CaO-Fe_2O_3 system were tested. The results are shown in Table 1. The results showed that sticking temperature is lower for the case in which further addition of Fe_2O_3 would reduce the liquidus temperature, in spite of the fact that both initial compositions have the same liquidus temperature. Thus, if the composition of the flyash drop is such that it can be fluxed by the oxide on the boiler tube surface, better sticking of the ash particle would result. In this case the interface between droplet and metal would remain molten for a longer time as compared to a non-fluxing case.

Sticking Behavior of Pure Minerals. Tests were also conducted with pure minerals that are commonly found in coal. The results are shown in Table 2. The results with clays and quartz are somewhat deceptive because these were melted at temperatures in excess of 1800°C, higher than that usually employed in the test. It is unlikely that clays or quartz would melt in a normal coal flame.

Table 1 Effect of Fe_2O_3 pick-up from the substrate on the sticking temperature

Composition, Weight percent			Liquidus Temperature °C	Sticking Temperature °C	Effect of added Fe_2O_3 on liquidus temperature [6]
SiO_2	CaO	Fe_2O_3			
33	28	39	368	1300	Increase
33.3	33.3	33.3	327	1305	Decrease

Table 2 Comparative sticking temperature of pure minerals

Mineral	Sticking Temperature
Pyrite (chemical grade	280
Hematite (chemical grade)	538
Montmorillonite (Belle Forche, South Dakota)	490
Illite (Fithian, Illinois)	470
Kaolinite (Georgia)	465
Quartz (chemical grade)	480

Pyrite droplets showed excellent wetting of the substrate, the contact angle at the sticking temperature being 76 deg. X-ray diffraction studies on these droplets indicated that they contained predominantly pyrrhotite ($Fe_{0.995}S$), small amounts of magnetite and no wustite, pyrite or hematite. The chemical analysis of the droplet confirmed it contained approximately 86.6 percent pyrrhotite and 13.4 percent of Fe_3O_4. In these experiments, the time taken to melt the pyrite was 10–15 s, which is much longer than the time the pyrite particle would remain in the flame region in a boiler, although the drop is of course much larger than a fly ash particle. It is possible that during combustion pyrite particles might stick to metal surfaces as pyrrhotite and then subsequently become oxidized to iron oxides. It is also possible that the metal surface may have alkali metal salts condensed on it, and, as a result, reactions leading to the formation of alkali metal trisulfates, iron sulfates, sodium sulfate, iron trisulfates might take place.

Discussion

For the ash droplet to adhere strongly to a relatively cold metal surface, it is necessary that there should be a continuous interfacial region between the two. This region should extend on both sides into

Downloaded 01 Jun 2010 to 171.66.16.58. Redistribution subject to ASME license or copyright; see http://www.asme.org/terms/Terms_Use.cfm

the structure of metal and ash particle. Upon contact, both the metal surface and the ash particle have to contribute to the formation of this continuous interfacial region. In view of the nonadherence between solid droplets and substrate observed in this study, it appears that this contribution was not possible in the solid state. Since the interface formation would involve considerable mass transport of reacting species between the ash droplet and metal surface, which is possible only in the liquid state, it is reasonable to conclude that in its initial stages of formation, the interfacial region was liquid. Once the interfacial region was solidified, its growth rate would be considerably reduced and by the time it had reached the temperature of the metal (below 650°C) the growth would have stopped for all practical purposes. As indicated by high speed photography, the time of formation of this interfacial region would be in the milliseconds range at metal temperatures below 600°C.

In the lower portions of the boiler where metal temperatures are low enough to prevent sintering of the deposit with metal, sticking would occur only if one of the following conditions were met:

1 the ash particle is molten,

2 the metal surface has a coating of molten salt (alkali metal sulfates),

3 the metal surface is coated with a material that would melt on contact with a hot solid ash particle, such as alkalis.

The first condition, that the slag droplet be molten, would depend on the composition of the ash particle. Compositions with low melting points would therefore have some chance of adhering to an oxidized metal surface. In addition, it seems reasonable that the interface must remain liquid for some period of time to enable a strong enough bond to develop to give sticking. This is enhanced by compositions which give lower liquidus temperatures on interchange of species across the interface, since this keeps the interface liquid for longer periods of time.

In addition to the above factors, the growth of the interfacial region is also influenced by the chemical compatability of the metal surface and the droplet. In the current study, stainless steels were found to tive higher sticking temperature and effective contact angles as compared to mild steel (Fig. 2). The high contact angle indicates poor wetting of the substrate by the droplet. The extent of this wetting depends on the chemical nature of the droplet and the surface. It is well known in the enamelling industry that for an enamelling liquid to wet the metal, it is essential that the metal surface should be oxidized. The stainless steels were not oxidized under our experimental conditions and as a result droplets were not able to wet the surface. Since the droplets are mainly oxides, their surfaces would be electronegative because of the dominance by large oxygen anions (the anion to cation radius ratio being greater than unity in most of these oxides). Such oxides would be repelled by the negative electron cloud of the metal, leading to non-wetting [7]. On the other hand, the mild steel surface consisted of an oxidized layer and as a result better wetting and sticking was observed.

Acknowledgments

This work was carried out on DOE contract No. EF-76-S-01-2316.

References

1 Moza, A. K., and Austin, L. G., "Note: A New Test for Characterizing the Slag Deposition Properties of a Coal Ash: the Sticking Temperature," *Journal of Institute of Energy,* Vol. 52, March 1979, pp. 15–16.

2 Moza, A. K., Shoji, K., and Austin, L. G., "The Sticking Temperature and Adhesion Force of Slag Droplets from Four Coals on Mild Steel," ASME Paper No. 78-WA/CD-1.

3 Levin, E. M., Robbin, C. R., and McMurdie, H. F., *Phase Diagrams for Ceramists,* 3rd ed., American Ceramic Society, 1964, Fig. 943-946, pp. 305–307.

4 Ibid, Fig. 43, pp. 49.

5 Partridge, J. H., *Glass to Metal Seals,* The Society of Glass technology, Sheffield, 1949, pp. 201–206.

6 Levin, E. M., Robbins, C. R., and McMurdie, H. F., ed., *Phase Diagrams for Ceramists,* 3rd ed., American Ceramic Society, 1964, Fig. 656, pp. 228.

7 Livey, D. T., and Murray, P., "The wetting properties of solid oxides and carbides by liquid metals," *Plansee Proceedings,* Pergamon, Oxford, 1955, pp. 375–404.

Downloaded 01 Jun 2010 to 171.66.16.58. Redistribution subject to ASME license or copyright; see http://www.asme.org/terms/Terms_Use.cfm

Further Development of an Advanced Low-NO_x Combustion System and its Potential Application to Coal-Fired Utility Boilers

T. M. Sommer
Development Engineer,
Fossil Power Generation Division,
Babcock and Wilcox Company,
Barberton, OH
Assoc. Mem. ASME

S. A. Johnson
Senior Research Engineer

G. D. Lindstrom
Group Supervisor,
Research and Development Division,
Babcock and Wilcox Company,
Alliance, OH
Assoc. Mem. ASME

The Babcock & Wilcox Company (B&W), under contract with the Electric Power Research Institute (EPRI), has designed and tested an advanced staged combustion system on a four million Btu/hr (4.2-million kJ/hr) scale. Results of these tests showed the potential to limit the emission of nitrogen oxides from coal-fired boilers to 100–150 ppm and identified a new kinetic mechanism for NO destruction. Subsequently, the correlations and initial design parameters derived from the small-scale tests were applied to a conceptual commercial system to ensure that this concept was indeed commercially feasible. These design considerations and the favored preliminary arrangement of a low-NO_x combustion system will be discussed herein. Before commercializing this concept, however, further research is necessary. Testing on a nominal 50-million Btu/hr (53-million kJ/hr) prototype system is now in progress. Initial results indicate that NO_x emission correlations and design parameters will need only slight revisions before the concept is ready for a field demonstration.

Introduction

One of the most important factors impacting the design of today's genre of coal-fired utility boilers is the emission of nitrogen oxides (NO_x). Uncontrolled, these gases could comprise over 0.1 percent of the flue gas, but by modifying the combustion process (e.g., delayed fuel/air mixing, staged combustion, increased furnace cooling surface), NO_x emissions can be significantly reduced. Boiler manufacturers have been designing utility steam generators to emit less than 0.7 lb $NO_2/10^6$ Btu (301 ng/J) to comply with emission standards set forth by the U.S. Environmental Protection Agency (EPA) in 1971 [1].

Just recently, however, the EPA promulgated stricter NO_x limitations for coal-fired boilers [2]. New boilers sold for firing bituminous coal, or certain lignites will not be allowed to exceed NO_x levels of 0.6 lb/10^6 Btu (260 ng/J), and those firing sub-bituminous coal must meet 0.5 lb/10^6 Btu (210 ng/J). Lignite mined in North Dakota, South Dakota, or Montana and fired in a wet bottom (slagtap) unit shall be limited to no more than 0.8 lb/10^6 Btu (340 ng/J) of NO_x. Compliance to these new rules can be achieved by refinements to the combustion modification techniques mentioned above.

The magnitude of the problem comes into focus, however, when one realizes that the EPA is considering still further reductions to the NO_x emission standards. The professed EPA research goals of demonstrating 200 ppm of NO_x by 1980 and 100 ppm by 1985 [3] could decrease current NO_x limits by a factor of 2 to 4!

Achievement of very low NO_x emissions by relatively minor equipment design changes or boiler operating procedures seems very unlikely. The alternatives are drastic combustion "process" modifications or "tailend" NO_x removal. This paper describes technical progress toward the commercialization of an advanced combustion process and outlines its advantages over expensive and potentially unreliable flue gas NO_x removal processes.

Low NO_X Combustion System (LNCS)

In response to the EPA emission goals, the Babcock and Wilcox Company (B&W) and the Electric Power Research Institute (EPRI) entered into a contract in late 1976 to define and develop a commercially viable low-NO_x combustion system. KVB, Inc. was subcontracted to perform bench-scale tests and to provide insight into the fuel nitrogen conversion mechanisms. Fig. 1 shows how the various tasks of the program were organized. It is a marriage of a theoretical understanding of fuel nitrogen reactions [4] with the practical considerations of commercial boiler design which was consummated with the successful development of the Primary Combustion Furnace (PCF) concept on a four million Btu/hr scale.

Though the small scale test results were reported previously [5, 6], a brief description of the Primary Combustion Furnace concept is warranted here. Previous work at B&W [7] indicated that the full potential of staged combustion could be achieved by increased physical separation between stages. Utilizing this idea, a combustion system was conceptualized, and subsequently developed, in which the fuel-rich, first stage flame was isolated within a separate and distinct water-cooled combustion chamber. This concept, as applied to a conventional utility boiler, is shown in Fig. 2. A number of Primary Furnaces are to be attached around the periphery of the boiler. Each Primary Furnace is fired by a modified commercial burner to

Contributed by the Fuels Division and presented at the Winter Annual Meeting, December 2–7, 1979, New York, New York, of THE AMERICAN SOCIETY OF MECHANICAL ENGINEERS. Manuscript received at ASME Headquarters August 20, 1979. Paper No. 79-WA/Fu-4.

Copyright © 1980 by ASME
Downloaded 01 Jun 2010 to 171.66.16.58. Redistribution subject to ASME license or copyright; see http://www.asme.org/terms/Terms_Use.cfm

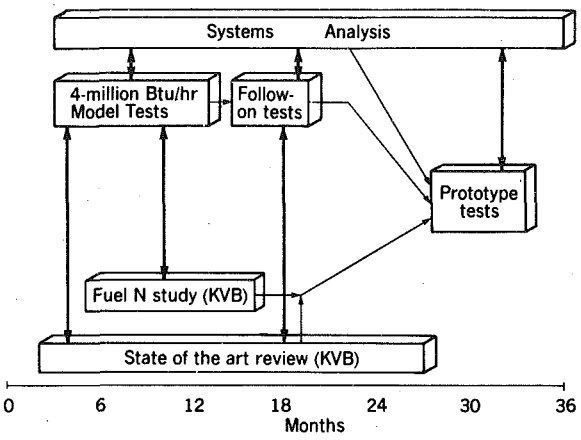


Fig. 1 B&W/EPRI research program

produce a stable, fuel-rich flame. The waterwall construction provides the surface for cooling the first-stage gases. This helps to prevent the formation of molten ash deposits and to control second-stage temperatures within a range that is conducive to low NO_x emissions. Products of partial combustion then pass into the main furnace where the air necessary to complete combustion is added through slots surrounding the first-stage exit. The velocity and direction of both the first stage effluent and the second stage air streams are designed to provide a gradual mixing of the two streams. This results in a long, diffusion-type flame in the second stage, which is a key to the success of the concept.

Physically separating the stages in this manner was expected to have several advantages:

1 It provides ample residence time under reducing conditions to allow much of the initial NO_x formed in the oxidizing zones near the burner to be reduced to harmless N_2.

2 It provides adequate surface area to cool the first-stage gases so that low flame front temperatures are achieved in the second stage. Our results have shown that the second-stage flame temperature has a profound effect on the final system NO_x emission.

3 It confines any potential corrosion caused by the reducing conditions (50–90 percent of theoretical air) to a relatively small area. The main furnace will always remain in an oxidizing atmosphere. The primary furnaces could be designed to require a minimum of downtime to replace or repair if necessary.

The development of the Primary Combustion Furnace is taking place on two size scales. Initial development tests were performed on a 4-million Btu/hr test furnace (see Fig. 3) located at B&W's Alliance (Ohio) Research Center. The purpose of this initial work was to evaluate the process and design variables in order to provide a basis for larger scale prototype tests. The prototype device was sized for a nominal 50 million Btu/hr. It has been operational since March of 1979. Results from both test programs will be presented in the sections that follow, with special emphasis on the impact of these results on potential commercial designs.

Summary of Four Million Btu/hr Scale Results

The model Low NO_x Combustion System (LNCS) consisted of a Primary Furnace, fabricated in separate, water-cooled sections to provide a range of first-stage residence times, mounted on a refractory-lined test tunnel which represented the main boiler cavity. Further description of this apparatus can be found elsewhere in the literature [5, 6].

The development of the four million Btu/hr Primary Combustion furnace took place in four phases over a 16 month period. Though slightly overlapping, these phases can be described as shown below:

1 *Shakedown Phase.* This was an investigation of the effect of burner/furnace combinations on system operability and NO_x emissions. Burner velocities and swirl, and furnace residence time and heat absorption were investigated.

2 *Optimization Phase.* Once the basic equipment configuration

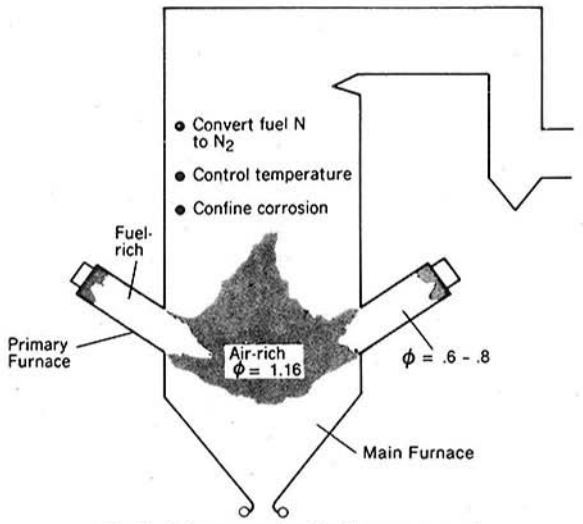


Fig. 2 Primary combustion furnace concept

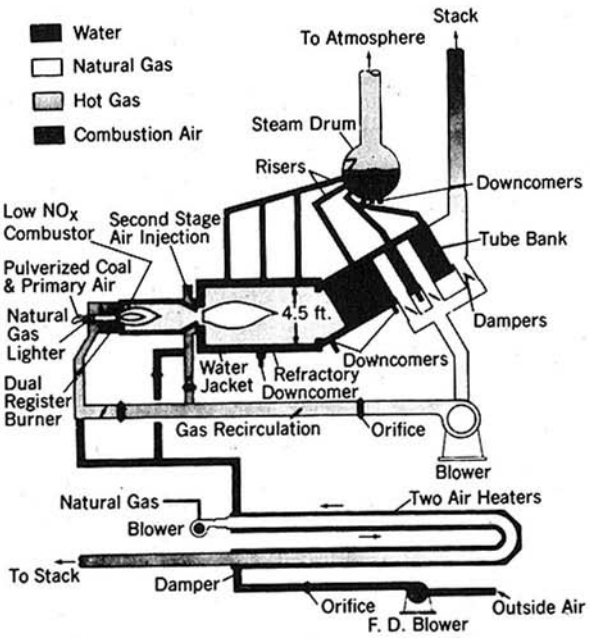


Fig. 3 Four million Btu/hr primary combustion furnace

was chosen, a detailed study of the operating variables was undertaken. These variables included first-stage stoichiometry, flue gas recirculation to either windbox, secondary air preheat temperature, coal fineness, coal flow, and overall excess air.

3 *Development Phase.* After the range of operating conditions was characterized, a representative set of conditions was chosen for detailed investigation. During these tests, both furnaces were traversed radially and axially for NO, O_2, CO, HCN, NH_3, char, and temperature. Four types of coal were fired during this phase: Pittsburgh seam No. 8 bituminous, Illinois seam No. 6 bituminous, Montana sub-bituminous (Decker seam), and North Dakota lignite. A typical analysis of each of these fuels is given in Table 1.

4 *Follow-on Phase.* The dual purpose of this work was to optimize the system operation when firing western coals, and to further investigate the dependence of NO emissions on second-stage temperature noted during previous tests.

The most significant result of the small-scale testing was the dominant influence of second stage flame front temperature on the final NO emission from the system. This measured temperature could be influenced by first stage stoichiometry, system heat input, and the amount of flue gas recirculated to either windbox.

A plot of NO_x emissions as a function of the characteristic second stage flame temperature for a number of different coals is presented

Downloaded 01 Jun 2010 to 171.66.16.58. Redistribution subject to ASME license or copyright; see http://www.asme.org/terms/Terms_Use.cfm

Table 1 Typical coal analyses

COAL TYPE	PITTSBURGH SEAM #8 BITUMINOUS	MONTANA SUBBITUM-INOUS	ILLINOIS SEAM #6 BITUMINOUS	NORTH DAKOTA LIGNITE
MOISTURE (TOTAL), %	4.7	24.9	17.6	33.3
PROXIMATE ANALYSIS, %				
VOLATILE MATTER	44.3	41.4	44.2	43.6
FIXED CARBON	48.6	52.6	45.0	45.3
ASH	7.1	6.0	10.8	11.1
ULTIMATE ANALYSIS, %				
CARBON	74.1	71.4	69.0	63.3
HYDROGEN	5.2	4.9	4.9	4.5
NITROGEN	1.3	1.0	1.0	1.0
SULFUR	3.6	0.4	4.3	1.1
ASH	7.1	6.0	10.8	11.1
OXYGEN (BY DIFF.)	8.7	16.3	10.0	19.0
HIGHER HEATING VALUE, BTU/LB (DRY)	13,420	12,260	12,500	10,630
ASH ANALYSIS, %				
SiO_2	43.0	34.2	41.7	29.8
Al_2O_3	23.5	16.0	20.0	10.0
Fe_2O_3	25.0	9.0	19.0	9.0
TiO_2	0.7	0.7	0.8	0.4
CaO	2.5	16.0	8.0	19.0
MgO	0.6	3.0	0.8	5.0
Na_2O	0.7	6.7	1.6	5.8
K_2O	1.5	0.5	1.6	0.5
SO_3	1.5	15.4	4.4	20.8

in Fig. 4. The data encompass the following range of test conditions:

First stage stoichiometry	50–75 percent
Heat input	2.6–5.0 million Btu/hr
Flue gas recirculation	0–32 percent

The optimum first stage stoichiometry was found to be approximately 70 percent, though first stage NO concentrations decreased with lower stoichiometries. This stoichiometry produced adequate gas phase reducing conditions in the first stage, while allowing a substantial fraction of the heat input (30 percent) to be absorbed in the first stage. Therefore, low temperatures and further NO reductions could be achieved in the second stage. At very low temperatures, more than 50 percent of the first stage NO was destroyed within the second stage flame.

The NO reduction in the second stage, upon addition of the air necessary to complete combustion, was a surprising but not unprecedented phenomenon [8–10]. Its coincidence, however, with the theoretical equilibrium curve for NO in the presence of 3 percent oxygen (actual stack gas O_2 concentration) is new. It can be seen that the agreement of the data with the equilibrium curve was very close, but more importantly, the change in NO concentration across the flame front (i.e., between the first stage exit and the stack) was always in the direction of equilibrium. Since such behavior generally indicates fast gas phase kinetics, we have eliminated the absorption of NO on char particles as noted by Beer [11] and De Soete [12] as a potential mechanism for this important reaction.

The other important result of these tests was the influence of second stage mixing of fuel and air on NO_x emissions. The second stage air admission slots (see Fig. 5) were designed to pivot so that air could be injected at any angle from 0 deg (parallel to the first stage exit gas stream) to 40 deg toward the furnace center. By varying the air injection angle, the initial rate of mixing of air with the products of partial combustion could be controlled.

The effect of second stage air admission angle on NO_x emissions is shown in Fig. 6. It can be seen that with a 40 deg slot angle, the NO_x emission averaged about 180 ppm. The corresponding flame was observed to be 4–6 ft long and confined to the center of the furnace. As the slot angle was decreased, however, the NO emission steadily decreased as the flame began to billow and lengthen. At an angle of 10–20 deg the CO emission became unsteady and increased, indicating that combustion was no longer being completed within the furnace. The corresponding NO emission at this angle was about 135 ppm. Further straightening of the slot angle resulted in lower NO emissions at the expense of high CO emissions and combustibles losses. The implication of this result is that both second stage air admission angle and

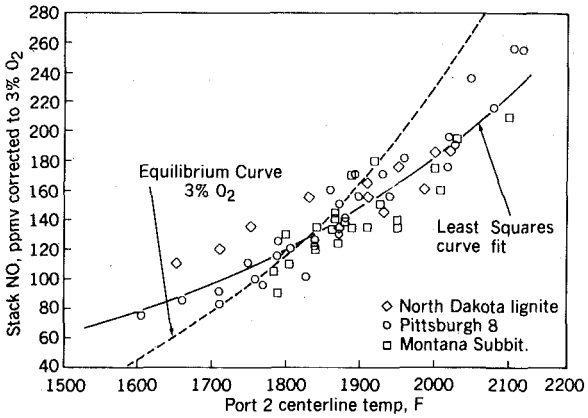


Fig. 4 NO emissions as a function of measured second stage flame temperature

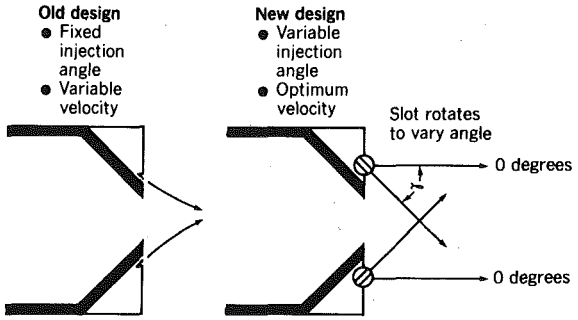


Fig. 5 Second stage air injection slot design

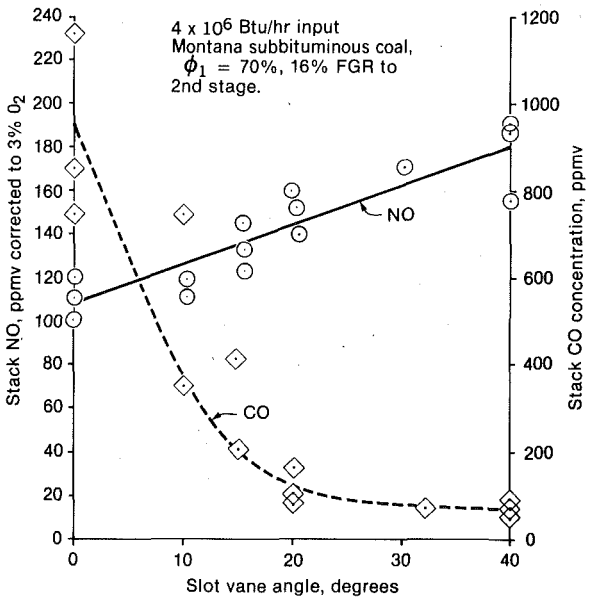


Fig. 6 Effect of second stage air injection angle on NO emissions

velocity must be carefully controlled when designing the large-scale system for both low NO_x emissions and complete combustion.

We have formulated a kinetic mechanism that helps explain the second stage NO_x chemistry observed during these tests. It is well-known that a fraction of the fuel nitrogen intermediates can be oxidized to NO. Our measurements indicate that these species (NH_3, HCN)enter the second stage in significant quantities. Therefore, if NO is to be destroyed, a competing reaction must be taking place. Tyson, et al. [13] have hypothesized the following reaction scheme for NO destruction:

$$NO + \cdot OH \rightleftharpoons HNO\cdot + O\cdot \text{ and/or} \quad (1)$$

$$NO + \cdot H + M \rightleftharpoons HNO\cdot + M \quad (1a)$$

$$HNO\cdot + CO \rightleftharpoons HN\cdot + CO_2 \quad (2)$$

Downloaded 01 Jun 2010 to 171.66.16.58. Redistribution subject to ASME license or copyright; see http://www.asme.org/terms/Terms_Use.cfm

$$N\cdot \rightleftharpoons NH\cdot \rightleftharpoons \cdot HN_2 \rightleftharpoons \cdot NH_3 \quad (3)$$

$$\cdot NH_2 + NO \rightleftharpoons N_2 + H_2O \text{ and/or} \quad (4)$$

$$N\cdot + NO \rightleftharpoons N_2 + O\cdot \quad (4a)$$

Reaction 1 requires the presence of free radicals which are rapidly produced when air is added to the flame. It is possible that other fuel nitrogen species would interact with the free radicals in a similar manner. Reaction 2 requires the presence of large quantities of CO, on the order of several percent, to proceed at a rapid rate. We have measured CO concentrations of 1–5 percent at the exit of the first stage furnace. Once the imidogen radical (NH) is formed, it quickly equilibrates with all the other possible ammonia species as shown in reaction 3. One of these species, amidogen (NH_2) is known [14] to react rapidly with NO to form N_2. This reaction sequence is very temperature sensitive, proceeding most rapidly at temperatures above 1650°F where free radicals are available for initiation.

The competing ammonia oxidation reaction depends on the availability of oxygen atoms to proceed at a rapid rate. The formation and distribution of oxygen atoms is greatly enhanced by turbulent mixing within the flame zone. If on the other hand, the flame provided a reaction envelope, separating fuel-rich gases on one side and air-rich gases on the other, the rate of nitrogen oxidation would depend on the relatively slow transport of reactants to the flame front by eddy diffusion. Under such slow mixing conditions, the NO destruction reactions would dominate. At higher temperatures, the NO destruction reaction will still occur at high rates, but now the final NO value is limited by equilibrium and very low emissions are not possible.

Preliminary Commercial Evaluation

As work progressed on the laboratory model, it became apparent that some preliminary study by B&W's Fossil Power Generation Division (FPGD) would be very beneficial in directing the development program. Hence, a preliminary "systems analysis" of the low NO_x combustion system concept was initiated by the FPGD boiler engineering staff. Due to the small scale of the model LNCS, results of any analysis must be viewed with some degree of apprehension because the extrapolations necessary to scale data collected on the four million Btu/hr primary furnace to a commercially acceptable size (approximately 250 million Btu/hr) are not straightforward.

Commercial Primary Furnace Design. Test data from the four million Btu/hr model primary furnace identified a correlation of NO_x emissions to a measured second-stage temperature. Fig. 4 illustrates that correlation. Assuming that the correlation can be applied directly to a full-scale system, the first stage furnace size must be determined by the heat absorption necessary to give the desired second-stage temperature.

When designing utility boilers, B&W uses calculated adiabatic temperatures for predicting heat absorptions, since actual flame temperatures are difficult and expensive to measure in the field. By using an emissivity correction factor, the measured heat absorptions from operating boilers have been found to agree very well with predicted values using the adiabatic design temperatures. The same calculation procedure was also used to predict first stage heat absorption. The second-stage theoretical temperatures were calculated from the four million Btu/hr model data and correlated with their respective NO_x emissions. Fig. 7 illustrates that correlation. A theoretical temperature of 2600°F was selected as a practical initial value for the initial sizing study. This temperature corresponds to a predicted NO_x emission range of 100–170 ppm, depending on furnace heat input.

A very critical aspect of second-stage temperature prediction is the calculation of first stage furnace heat absorption. The internal gas composition data collected from the four million Btu/hr model were analyzed to determine the theoretical gas emissivities. The actual emissivities were back-calculated from measured heat absorption. A linear regression analysis was then applied to determine a correction factor which, when applied to the theoretical emissivity, could be used to predict measured absorptions. The correction factor is a function of load, flue gas recirculation, and PCF stoichiometry.

The same correction factor was applied to the theoretical gas emissivities calculated for the 250 million Btu/hr furnace and related to heat absorption. To achieve a second-stage temperature of approximately 2600°F, this procedure determined that a first stage furnace, in the shape of a right circular cylinder 10 ft in diameter, would have to be 35 ft long.

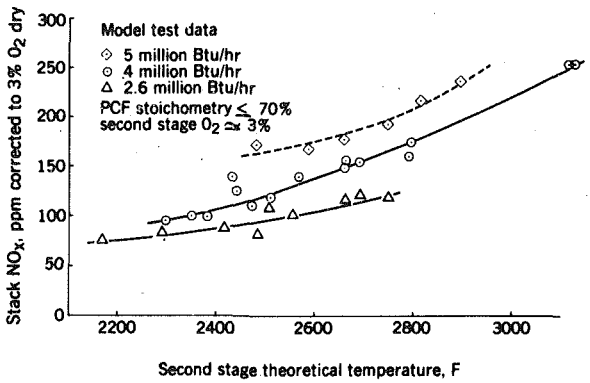


Fig. 7 Correlation of NO emissions with theoretical second stage temperature

The 10 ft dia was selected due to transportation constraints. For the purpose of this initial study, it was assumed that standard fabrication practices, low cost and readily available materials, and ordinary shipping practices would be utilized.

600-MWe Conceptual Boiler Design. Once the first stage furnace size and second-stage adiabatic temperatures were determined, the remainder of the boiler design was addressed. A production furnace heat transfer program was utilized to predict absorption in the secondary or main furnace.

Main Furnace Design. The main furnace was sized after assuming a conventional convection pass cross-section and gas velocity. As a first iteration, the furnace plan area was sized to minimize unusual tube configurations at the furnace/convection pass transition. In addition, limits for heat input per square foot of furnace plan area were not exceeded. Mechanical considerations determined the minimum amount of furnace length necessary above, below, and between primary furnace levels. These considerations include clearances for ducts, piping, and work space, and minimum tube bend to workpoint distances.

Several other design criteria were assumed to allow the preliminary study to proceed without performing extensive design "optimization" studies. These criteria included:

1 Maintaining furnace exit gas temperature greater than or equal to 2100°F to maintain an economical convection pass heat transfer surface arrangement.

2 Requiring the first stage furnace to be fired toward an imaginary circle in the center of the boiler to promote mixing and carbon burnout.

3 Attaching primary furnaces to the main furnace, tilted downward at a 30 deg angle to horizontal, to facilitate ash removal.

4 Supplying air and flue gas recirculation to each individual first stage furnace to control temperature and stoichiometry.

Keeping the above criteria in mind, furnace layouts were made for square, rectangular, round, and polygonal shaped main furnaces. With the square furnace, an obvious physical arrangement problem occurs at each corner. The limited amount of space does not allow for the necessary ductwork to the second stage windbox. When this arrangement is applied to a 1300 MWe boiler, the physical limitations become even more extreme. The problem is even worse for a rectangular arrangement in which primary furnaces fire at two imaginary circles.

A round or polygonal furnace, would allow equal spacing of primary furnaces and identical mounting configurations for every first stage/second stage wall connection. A polygonal concept would also allow the use of conventional flat, membrane wall, tube panels to form each side of the polygon.

Downloaded 01 Jun 2010 to 171.66.16.58. Redistribution subject to ASME license or copyright; see http://www.asme.org/terms/Terms_Use.cfm

The heat absorption of a 600 MWe polygonal main furnace was estimated assuming the 2600°F adiabatic temperature at the main furnace entrance. Fig. 8 shows the predicted furnace temperature profile and the effect of a 20 percent change in first stage heat absorption. In either case, the furnace exit gas temperature is acceptable for a natural circulation boiler. This temperature will result in an end temperature differential of approximately 115°F. That is the temperature differential between the gas temperature leaving the last superheater or reheater bank less the entering steam temperature of the bank. To maintain a reasonable amount of heat transfer surface in the convective pass, this differential should be maintained above 100°F.

Convection Pass Design. The review of each furnace configuration also included an evaluation of two different convection pass arrangements. Fig. 9 illustrates the "Carolina" and the "Tower" convection pass designs. The Carolina design utilizes horizontal and downward flue gas flow over the convective heat transfer surface, while the Tower design utilizes only upward flow. The Tower design is uncommon for domestic coal-fired boilers; however, for European brown coal-fired units, B&W's standard offering is the Tower design. This design lends itself to lower furnace exit gas temperature applications which require increased radiant heat transfer to the superheater from the firebox below.

The more common Carolina design was judged inferior for economic reasons. Due to the length of the primary combustion furnace, the horizontal section of the pass must become quite long to avoid interference of the first stage furnaces with the downflow convective section. The boiler cost would increase drastically and ash removal would become a problem if the convective pass had a long, flat floor.

A conceptual design for a duct arrangement which permits separate, controlled air and flue gas recirculation flows to every first stage windbox is shown as part of Fig. 10. The Tower boiler design appears to be a beneficial arrangement from a duct location standpoint. No serious interferences are apparent with piping, steelwork, or removal space requirements.

The conclusion of the furnace/convective pass arrangement review was that the polygonal furnace and the "Tower" convection pass design was the best combination for the low NO_x combustion application. We do not foresee any insurmountable problems with fabrication or erection of a boiler of this design. The conceptual 600 MWe design is illustrated in Fig. 10.

Additional Considerations. *Circulation.* Some forced circulation appears to be necessary due to the waterside pressure drop across the first stage furnace. A small amount of pumping capacity is being considered as an alternative to first stage furnace circuitry changes and numerous furnace riser tubes.

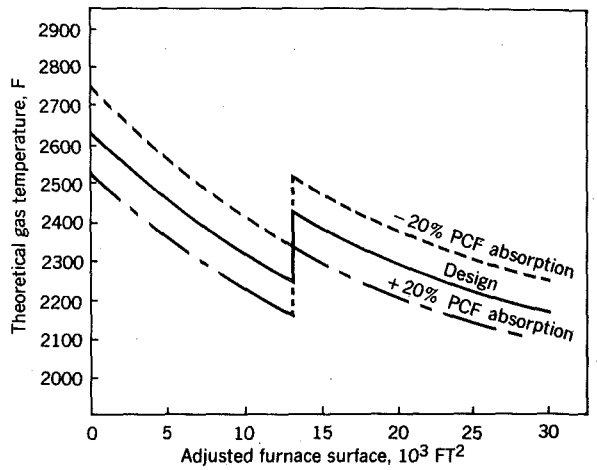


Fig. 8 Predicted 600 MWe furnace temperature profile

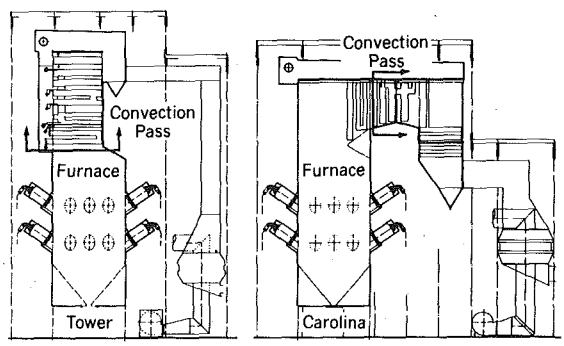


Fig. 9 Convection pass designs

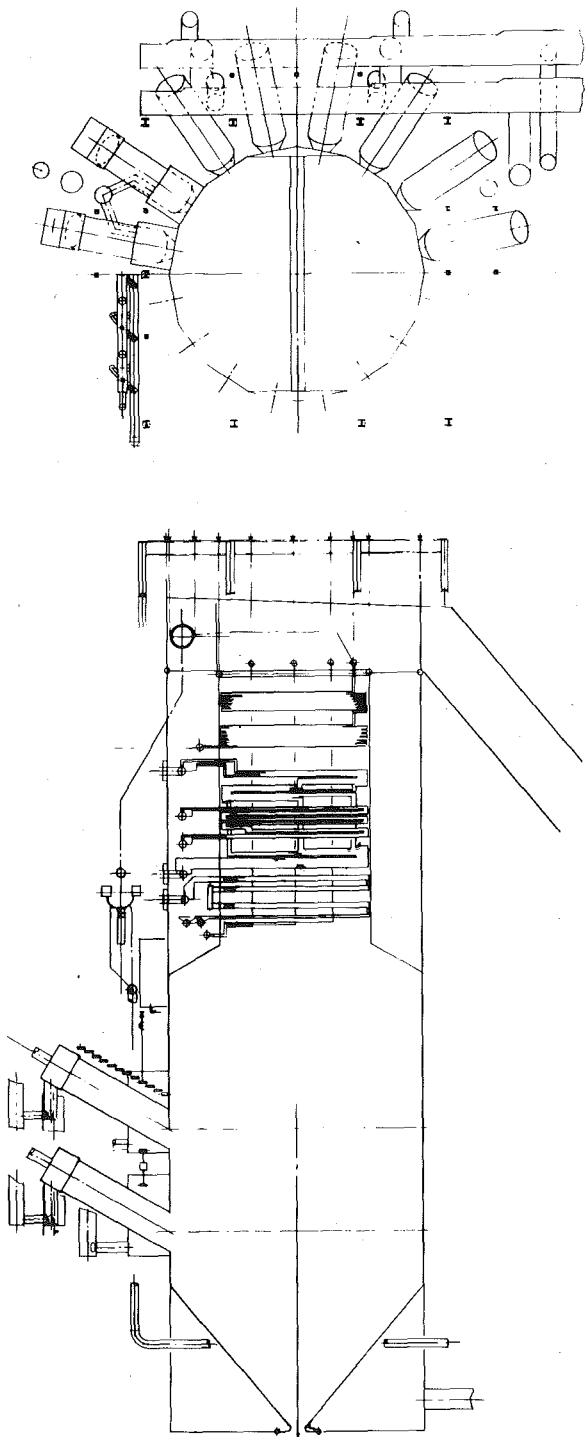


Fig. 10 Conceptual 600 MWe LNC/tower boiler design

Downloaded 01 Jun 2010 to 171.66.16.58. Redistribution subject to ASME license or copyright; see http://www.asme.org/terms/Terms_Use.cfm

Corrosion. No definitive information is available concerning the corrosion rates which may be expected in the Primary Combustion Furnace. The low NO_x combustion system was first conceived with the thought that the primary furnace rather than the entire boiler furnace would be subject to a reducing atmosphere. The first stage furnaces could then be replaced as necessary without affecting the integrity of the main furnace. Small scale corrosion tests and/or field tests will be required to define the first stage corrosion rate. In the meantime, initial deisgns will include coated tubes, corrosion resistant metals or minimum furnace wall temperatures.

Several alternative two-stage combustion system designs are also being evaluated. Each alternate design subjects some portion of the main furnace to a reducing atmosphere. System performance, economic considerations, market conditions, and customer acceptability will eventually determine which concept becomes a commercial product.

Slagging. Slagging is not expected to be a problem with the LNCS boiler design. The primary furnaces will be operated slag-free, utilizing flue gas recirculation and heat absorption by the walls to cool the particles. The dry deposits which collect can then be removed using conventional soot blowing equipment. The secondary furnace exit gas temperature will be below 2200°F, which is low enough to prevent severe upper furnace slagging and fouling in the convective passes with most coals. The LNCS design will incorporate an adequate amount of initial sootblowers and future sootblower locations. A certain amount of secondary furnace slagging is anticipated and will be handled in the normal fashion.

Control. The LNCS design will require some combustion control changes. These changes should be relatively minor once the operating conditions for low NO_x emissions are firmly defined. An ideal control situation would be to have a signal fed back from each primary furnace to determine secondary air and flue gas recirculation flow to each windbox. This signal could conceivably come from some, as yet undertermined, optical analyzer, gas analyzer, temperature probe, etc. which would be indicative of the NO_x emission. If this is impractical, a totally feed-forward system can be designed utilizing the measured fuel flow and the measured gas flows to each windbox. In either case, the system components will be conventional equipment used in present systems.

Cost. It is estimated that the LNCS steam generator will cost approximately 30 percent more than a conventional boiler. This estimate is based on the comparison of the conceptual 600 MW LNCS/Tower design to a 600 MW, wall-fired Carolina design. The cost would include the normal scope of supply of the boiler manufacturer. That scope includes the boiler and all auxiliary equipment between the coal feeder outlet and the air heater outlet. The increased cost represents the investment necessary to lower the NO_x emission from 0.7 lb/10^6 Btu (conventional design) to 0.2 lb/10^6 Btu (LNC design) and is primarily due to the primary furnaces themselves, circulation pumps, a flue gas recirculation system, and increased ductwork.

An exact estimate is far beyond the scope of this preliminary study. As more data become available, the confidence in the preliminary design and its estimated cost, will increase. However, when compared to catalytic flue gas treatment systems for NO_x reduction, which are currently being quoted at costs equal to the cost of the boiler, the expected cost increase of 30 percent for low NO_x combustors is still attractive.

Future Commercialization Studies

The next step in the development of the LNCS is the collection of data from the nominal 50 million Btu/hr input prototype system. Confirmation of the NO_x versus temperature correlations and the emissivity correction factor calculation are necessary to increase confidence in the first 250 million Btu/hr demonstration system design. A final systems analysis study will be completed and a more refined estimate of the cost of the LNCS boiler will be made as part of the present EPRI contract. This second study will result in more detailed arrangement drawings of the boiler, first stage furnace, and convective section. The convective heat transfer surface will be sized and materials selected. Further studies of the unit circulation, operation, control, and reliability will be performed.

In addition, a discussion of design changes which may result due to fuel type will be completed. The basis for this discussion will be data collected from both the 4 million and the 50 million Btu/hr tests while firing a western sub-bituminous coal.

The final step in the commercialization process will be to retrofit the primary furnace(s) to an existing boiler and demonstrate the performance of a full-scale system. A host site for the demonstration program is being sought at this time.

Prototype Primary Combustion Furnace Facility

A second and larger size primary combustion furnace was required to fill the gap between the small four million Btu/hr test apparatus and the expected commercial size of 200 to 300 million Btu/hr (each). A size was chosen that would accommodate a nominal 30 to 50 million Btu/hr coal firing rate with a high degree of flexibility. The unit that was built and is now operational has a five foot square internal cross section, and measures approximately 13 ft long. In the approach to the second stage the furnace width reduces to 19.5 in. Fig. 11 shows a view from the burner throat looking toward the first stage exit throat. The unit is constructed of membrane wall panels.

Many of the characteristics of this test unit are typical of commercial practice. The burner is a 40 percent scale version of a modified B&W Dual Register Burner, and is fired directly from a commercial ball and race pulverizer. The PCF is attached to an existing 4-drum Stirling boiler at B&W's Alliance, Ohio Research Center. The unit has the necessary ducting and controls (see Fig. 12) to supply and individually measure, secondary air and recirculated flue gas to both the main burner and the second stage air injection point. The secondary air is separately heated and can be controlled to accommodate firing conditions from 50–130 percent stoichiometry in the first stage, while supplying the required second stage air to achieve 3–6 percent excess O_2 levels for good burnout. The total system was designed to fire a variety of coals ranging from Pittsburgh seam bituminous to North Dakota lignite.

The circulating cooling water in the membrane wall of the primary furnace is maintained in a subcooled state to allow a total heat absorption measurement, while spot heat flux measurements are made via 24 chordal thermocouple sections within the circuitry.

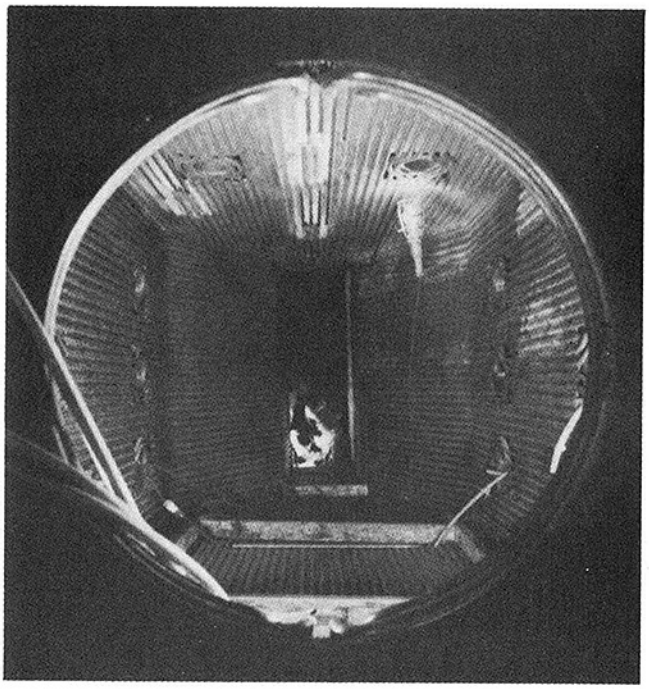


Fig. 11 Internal view of prototype primary furnace

Downloaded 01 Jun 2010 to 171.66.16.58. Redistribution subject to ASME license or copyright; see http://www.asme.org/terms/Terms_Use.cfm

The total data collection system was purposely kept simple. Extensive use is made of simple but reliable manometers for measurement of pressure drops across various flow orifices. The more sensitive pressure measurements, along with all of the thermocouple readings, are recorded by a digital data logger. An on-site computer terminal is utilized to provide a rapid and accurate readout of operating conditions and pertinent results. The final data reduction is done off line *via a computer to provide consistent data handling at the most reasonable cost.*

A large number of probe ports have been included to allow detailed characterization of gas and particulate concentrations throughout the system.

Preliminary Prototype Results

As of this writing, the prototype low NO_x combustion system has been operating for about five weeks. During this time, test conditions were varied over the same range as they were on the model scale, and emissions and temperature data were collected. Although analysis of these data are still progressing, the following generalizations can be made from the preliminary results.

Effect of First Stage Stoichiometry. Fig. 13 shows the NO_x emissions as a function of first stage stoichiometry for a number of tests at 35–40 million Btu/hr load. These plots appear to show the same characteristic "U"-shaped curves noted previously on the four million Btu/hr scale. The optimum stoichiometry seems to shift toward slightly lower stoichiometries, and NO_x values at the lower stoichiometries are generally lower than they were on the smaller scale. Note that an incremental NO_x reduction was achieved when flue gas recirculation was increased or when load was reduced.

Effect of Second-Stage Temperature. Fig. 14 presents the *correlation between NO_x emissions and calculated second stage flame* temperature developed during the model tests. Superimposed on these curves are data from the prototype device. It can be seen that very low NO_x emissions have also been achieved on the prototype scale. Further, our correlations and basis for commercial designs also seem to hold true for both model and prototype.

This figure also shows the effect of load on NO_x emissions on the prototype system. The points shown correspond to three loads: 37-million Btu/hr, 28-million Btu/hr and 20-million Btu/hr. Note that

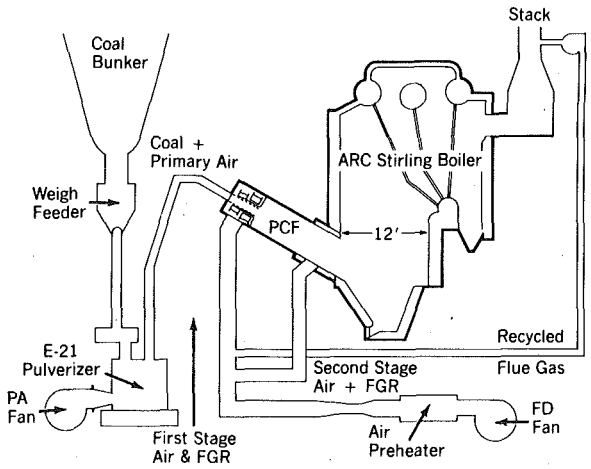


Fig. 12 Prototype low-NO_x combustion system

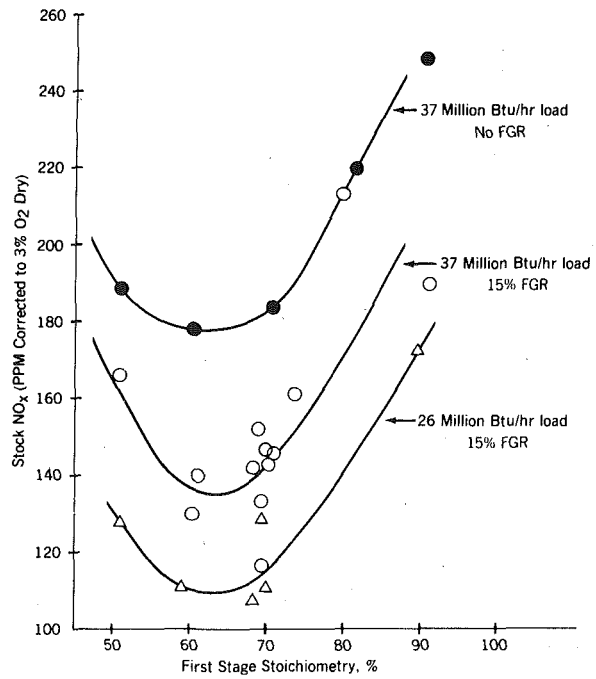


Fig. 13 Variation of NO emissions with first stage stoichiometry

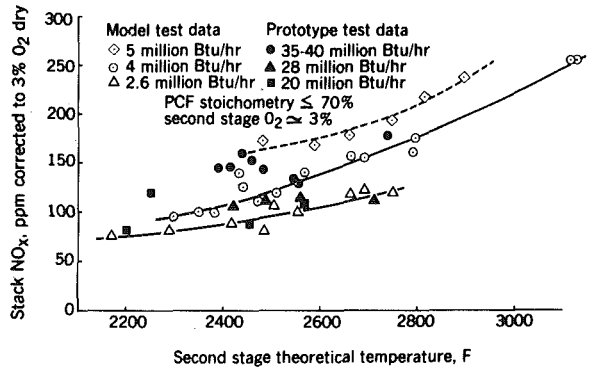


Fig. 14 Effect of second stage temperature on NO emissions

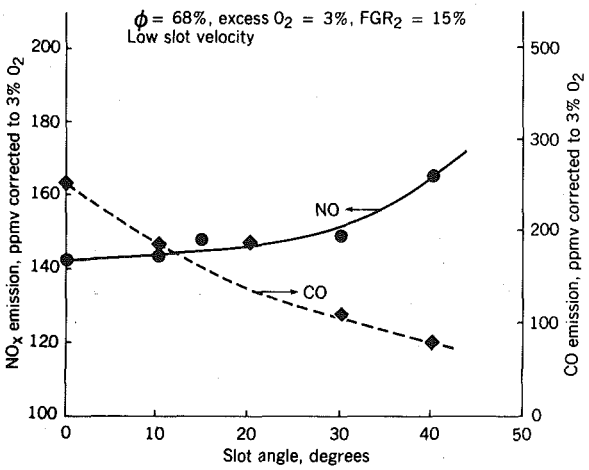


Fig. 15 Effect of second stage air injection angle on NO emissions

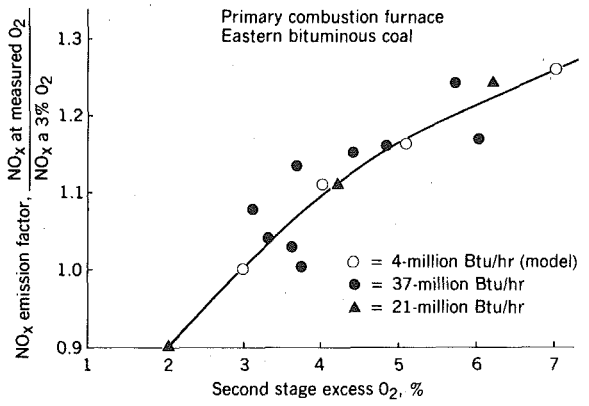


Fig. 16 NO emissions as a function of flue gas oxygen concentration

Downloaded 01 Jun 2010 to 171.66.16.58. Redistribution subject to ASME license or copyright; see http://www.asme.org/terms/Terms_Use.cfm

reducing load caused a significant reduction in NO_x emissions. Reducing load has two effects on the process. First, it reduces first stage temperatures (although changes in first stage heat absorption resulted in equivalent calculated second stage temperatures). It also reduces the level of turbulence in both furnaces. Since our earlier observation was that second stage temperatures determined the final NO_x emission, we interpret the curves to indicate the effect of second stage mixing.

Effect of Second Stage Mixing. To further amplify the effect of second stage mixing on NO_x, we offer Fig. 15, which is similar to Fig. 6 shown previously for the model data. Again, NO_x and CO emissions are plotted as a function of second stage air injection angle. The slopes of these curves are not as great as they were for the four million Btu/hr tests, but the same trend of higher NO_x with increasing injection angle, and higher CO with decreasing injection angle are apparent.

Effect of Excess Air. An important part of any NO_x emission study is the documentation of the effect of excess air on those emissions. This relationship is shown on Fig. 16 for both the model and prototype systems. Here a normalized NO_x emission factor is plotted against flue gas oxygen concentration. Though there is some data scatter caused by minor variations in test conditions, the agreement with previous results is quite consistent.

Closing Remarks

Assuming that small scale test results can be applied to a commercial sized unit, a feasible low NO_x combustion system can be conceived. Initial data from an intermediate-size prototype device agree well with the small scale results, thus giving us added confidence that our initial design criteria are indeed valid.

However, there are several concerns that must be addressed before this concept can be judged commercially acceptable. These include the following items:

1 Primary furnace corrosion rate.
2 Reliability of combustion controls.
3 Long-term integrity of geometrical deviations from current furnace design.
4 Necessity for flue gas recirculation.
5 Complexity of air and coal supply systems.

Many of these concerns are being considered during the prototype test program and subsequent systems analysis task. New conservative designs and arrangements for implementing the basis concept are the goals of this work.

The next step, then, will be the application of these designs to a full-scale utility boiler. Only after several years of operation at carefully defined low NO_x conditions can the low NO_x combustion system benefit the utility industry. It is this final step that transforms a process from a "laboratory curiosity" to operating hardware.

Acknowledgments

The authors acknowledge the interest and support for this work provided by M. W. McElroy, EPRI project manager.

Significant contributions were also made by Dr. R. J. Yang, Senior Research Engineer, Babcock and Wilcox Co., toward the analysis and understanding of the data presented herein.

References

1 Ruckelshaus, W. D., *Federal Register*, Vol. 36 Number 247, Thursday, Dec. 23, 1971.

2 Hawkins, D. G., *Federal Register*, Vol. 43, Number 182, Tuesday, Sept. 19, 1978.

3 Mason, H. B. and Waterland, L. R., "Environmental Assessment of Stationary Source NO_x Combustion Modification Technologies," *Proceedings of the Second Stationary Source Combustion Symposium*, Vol. 1, EPA-600/7-77-073 a, July, 1977.

4 Muzio, L. J., Maloney, K. L., and Shiomoto, G. H., "NO Formation Mechanisms in a Jet Stirred Reactor," *Proceedings of the Conference on Coal Combustion Technology and Emissions Control*, Pasadena, Calif. Feb., 1979.

5 Johnson, S. A., Cioffi, P. L., and McElroy, M. W., "Development of an Advanced Combustion System to Minimize NO_x Emissions from Coal-Fired Boilers," presented to the 1978 ASME/IEEE Joint Power Generation Conference, Dallas, Texas, Sept. 11, 1978.

6 Johnson, S. A., Cioffi, P. L., Sommer, T. M. and McElroy, M. W., "The Primary Combustion Furnace System—An Advanced Low NO_x Concept for Pulverized Coal Combustion," presented at the Second EPRI NO_x Control Technology Seminar, Denver, Col., Nov. 9, 1978.

7 Armento, W. J., "Effect of Design and Operating Variables on NO_x from Coal-Fired Furnaces, Phase II," EPA Final Report 650/2-74-002b, 1975.

8 Wendt, J. O. L., Pershing, D. W., Lee, J. W., and Glass, J. W., "Pulverized Coal Combustion NO_x Formation Mechanisms under Fuel-Rich and Staged Combustion Conditions," 17th Symposium (International) on Combustion, The Combustion Institute, Aug. 1978.

9 Bienstock, D., Bergman, P. D., Henry, J. M., Demski, R. J., Demeter, J. J., and Plants, K. D., "Air Pollution Aspects of MHD Power Generation," presented to the Intersociety Energy Conversion Engineering Conference, Bureau of Mines, 1973.

10 Johnson, S. A., and Rawdon, A. H., "NO_x Control by Furnace and Burner Design," *Handbook of Energy Technology*, edited by D. M. Considine, McGraw-Hill, New York, New York, 1977.

11 Beer, J. M., Sarofim, A. F., Chan, L. K., and Sprouse, A. M., "NO Reduction by Char in Fluidized Combustion," presented at the Fifth International Fluidized Bed Combustion Conference, Washington, D.C., Dec., 1977.

12 De Soete, G. G., and Fargard, J., "Reduction of Nitrogen Oxides by Soot in Combustion Processes," Proceedings of Fifth Members Conference, International Flame Research Foundation, Ijmuidan, Holland, 1978.

13 Tyson, T. J., Heap, M. P., Kau, C. J., Corley, T. L., "Transport Processes and Numerical Model Development—FCR Program Elements," *Proceedings of the Third Stationary Source Combustion Symposium*, Vol. IV, EPA-600/7-79-050 d, U.S. Environmental Protection Agency, Feb. 1979.

14 Lyon, R. K., et al, "Applications of the Exxon Thermal DeNO$_x$ Process," *Proceedings of the Second NO_x Control Technology Seminar*, EPRI report FP-1109-SR, Denver, Colo. July, 1979.

Downloaded 01 Jun 2010 to 171.66.16.58. Redistribution subject to ASME license or copyright; see http://www.asme.org/terms/Terms_Use.cfm

R. R. Fessler
Section Manager.

A. J. Skidmore
Principal Specialist.

H. R. Hazard
Senior Research Scientist,
Fellow ASME

Battelle
Columbus Laboratories
Columbus, OH 43201

J. P. Dimmer
Project Manager,
Electric Power Research Institute,
Palo Alto, CA
Fellow, ASME

Composition and Microstructure of a Furnace Ash Deposit from a Coal-Fired Utility Boiler[1]

An exploratory study of the structure and composition of furnace-ash deposits was carried out using optical metallography, electron microprobe analysis, scanning electron microscopy, and energy-dispersive X-ray analysis. The results of these analyses were supplemented by studies of particulate melting temperatures using hot-stage microscopy to measure melting temperatures, and energy-dispersive X-ray analyses to measure composition of melted particles. It was found that the general structure of the ash deposit was a matrix of glassy, spherical particles having a wide range of compositions in which unfused particles containing iron oxide and calcium oxide were dispersed. At the imprint of the tube surface a considerable concentration of calcium, sulfur, and iron was found. Near the fused outer surface of the deposit, the glassy materials had melted into a porous, glassy slag containing spherical globules of iron oxide combined with other materials. There were no systematic compositional gradients from the tube surface to the fused outer layer except for the sulfur layer found only at the tube surface. However, there were significant differences in composition from particle to particle, and these differences were similar to those found in the coal mineral matter as isolated by low-temperature ashing. Single particles of low-temperature ash were found having low fusion temperatures, in the range of fusion temperatures for particles in furnace ash. Thus, the glassy spheres found in furnace deposits could originate from single coal particles, without the need for interactions among coal particles or ash particles.

Introduction

The exploratory study of the structure and composition of a furnace ash deposit reported in this paper was carried out as part of a project for the Electric Power Research Institute on the effects of coal mineral matter on boiler slagging and fouling. Six utility boilers having different slagging characteristics and fired with different coals have been tested, and extensive analyses of coal and ash samples from these tests have been carried out and discussed in previous publications [1, 2]. In the current study, the microstructure and composition of furnace deposits from six boilers were examined in detail using optical metallography, electron microprobe analysis, scanning electron microscopy, hot-stage microscopy, and energy-dispersive X-ray analysis. One pair of these samples, from the front wall at the bottom of the superheater pendants of Labadie Boiler 1, proved to have a complete range of structure, from lightly sintered ash bearing the imprint of the furnace-wall tube, to a fused mass on the furnace side. These samples provided considerable insight into the nature of the ash deposit, its structure, the source of material of low melting temperature, and the transitions that took place within the deposit after deposition. Most of the data in this paper refer to the samples from Labadie Boiler 1.

Description of the Sample of Furnace Deposit

Two samples of furnace deposit were obtained from the Labadie 1 boiler, a 600 MW unit which had exhibited a severe slagging problem. One of the samples appeared to be a sintered collection of particles and it contained the imprint of the furnace-tube surface. The other sample was more glassy, and it probably existed farther from the furnace-wall tube than did the former.

Descriptions of the ash in the coal and the mineral content of the low-temperature ash are listed in Tables 1–3. A more complete description of the furnace and the ash has been presented elsewhere [1, 2].

Analytical Techniques

The analytical techniques used in this study were relatively standard and straightforward. Optical metallography provided a convenient way for studying the physical characteristics of the deposits and also provided suitable samples for study in the electron microprobe analyzer and scanning electron microscope. Samples prepared for chemical analysis by those techniques were ground only with diamond grinding material in order to avoid contamination by alumina or sil-

[1] Legal Notice—This paper was prepared by Battelle Columbus Laboratories as an account of work sponsored by the Electric Power Research Institute, Inc. (EPRI). Neither EPRI, members of EPRI, Battelle, nor any person acting on behalf of either: (a) makes any warranty or representation, express or implied, with respect to the accuracy, completeness, or usefulness of the information contained in this paper, or that the use of any information, apparatus, method, or process disclosed in this paper may not infringe privately owned rights; or (b) assumes any liabilities with respect to the use of, or for damages resulting from the use of, any information, apparatus, method, or process disclosed in this paper.

Contributed by the Corrosion and Deposits Committee and presented at the Winter Annual Meeting, December 2–7, 1979, New York, New York, of THE AMERICAN SOCIETY OF MECHANICAL ENGINEERS. Manuscript received at ASME Headquarters August 3, 1979. Paper No. 79-WA/CD-1.

Copyright © 1980 by ASME

Downloaded 01 Jun 2010 to 171.66.16.58. Redistribution subject to ASME license or copyright; see http://www.asme.org/terms/Terms_Use.cfm

Table 1 Description of the ash and low-temperature ash

Compounds in Ash		Minerals in Low-Temperature Ash	
Compound	Content, percent	Mineral	Content, percent
SiO_2	53.5	Quartz (SiO_2)	25
Al_2O_3	19.7	Pyrite (FeS_2)	20
Fe_2O_3	17.0	Calcite ($CaCO_3$)	5
TiO_2	1.01	Gypsum ($CaSO_4 \cdot 2H_2O$)	1–5
MgO	1.07	Kaolinite ($Al_2O_3 \cdot 2SiO_2 \cdot 2H_2O$)	20
CaO	4.70	Illite + MLC	25
Na_2O	0.51	($K_2O \cdot 3Al_2O_3 \cdot 6SiO_2 \cdot 2H_2O$)	
K_2O	2.38	$FeSO_4$	1–5
P_2O_5	0.16		

Table 3 Ash fusion temperatures, °F, Labadie 1

Oxidizing atmosphere	
Initial deformation	2320
Softening	2400
Hemisphere	2480
Fluid	2500
Reducing atmosphere	
Initial deformation	1700
Softening	2120
Hemisphere	2180
Fluid	2320

Table 2 Ash analyses of coal density fractions, Labadie 4[a]

Sp Gr: Float	1.30	1.40	1.50	1.60	—	1.60	2.00	2.80	—	Total
Sink	0	1.30	1.40	1.50	1.60	0	1.60	2.00	2.80	coal
Percent ash	1.9	4.0	10.6	17.2	52.0	8.27	21.7	64.6	60.1	11.8
Percent of coal	26.5	34.2	22.9	5.26	11.2	90.4	5.06	3.19	1.39	100
SiO_2	49.9	55.3	59.5	58.0	47.2	58.0	53.2	45.3	6.98	51.8
Al_2O_3	25.2	24.4	22.9	22.0	15.7	22.1	19.8	13.5	2.91	19.2
TiO_2	3.23	2.26	1.20	0.80	0.47	1.30	0.69	0.38	0.32	1.00
Fe_2O_3	11.9	11.1	11.6	14.0	27.0	12.1	20.5	22.2	87.2	19.8
MgO	1.55	1.30	1.19	1.13	0.45	1.25	1.15	0.75	0.05	1.04
CaO	3.70	1.51	0.83	0.74	6.93	1.75	1.66	15.8	1.78	4.08
Na_2O	1.43	0.98	0.57	0.44	0.37	0.65	0.42	0.34	0.31	0.53
K_2O	2.99	3.12	3.06	2.83	1.83	2.76	2.36	1.47	0.06	2.30
P_2O_5	0.11	0.08	0.08	0.07	0.08	0.13	0.14	0.25	0.38	0.12
Tcv	2320	2410	2590	2580	2720	2590	2500	3200	2600	2500
Slag Viscosity										
2600°F	340	790	990	640	28	730	160	15	1	130
2300°F	5000	20000	29000	14000	140	17000	1600	70	3	1000

[a] Analyses of density fractions were not carried out for Boiler 1 coal, but the overall analysis was closely similar to that for the Boiler 4 coal.

icon carbide that could come from other types of grinding materials. The electron microprobe analyzer can be used to obtain quantitative analyses of spots or general areas within the sample. However, to do so requires comparatively long times, and that technique was soon abandoned because it was found that there were great variations in composition from particle to particle and the exact composition of any individual particle did not appear to be significant. Qualitative analysis by EDS (energy dispersive X-ray system) associated with the scanning electron microscope was found to be much more useful and more convenient. Although it did not provide exact analyses of individual particles, it provided information on the relative amounts of various elements at various locations so much more quickly that it was used as the primary analytical tool in this study.

The relationship between the EDS data and the chemical composition of the samples is summarized in Table 4. EDS analyses were conducted for several samples for which the composition was well known, and the amounts of the various compounds in the samples were compared with the percentage of the EDS counts attributable to the metallic element from each compound. In most cases, the ratio of the percentage of the sample represented by a certain oxide to the percent of the EDS counts associated with the metal from that oxide was between ½ and 2. Thus, as a first approximation, the percentage of EDS counts associated with a certain metal such as silicon, for example, can be taken to be comparable to the percentage of the oxide in the sample, SiO_2 in this case. It should be recalled however that that rule of thumb is only good within about a factor of 2 because, for an EDS analysis, the relationship depends on the nature and quantities of other materials in the sample. Most of the information from the EDS comes from an area probably no more than 2 μm in diameter surrounding the aim point of the beam, or an area 2 mm in diameter at 1000×.

Nature of the Furnace Deposits

Deposit in Contact with the Furnace Tube. The surface of the deposit that had been in direct contact with the furnace tube consisted of small spherical particles embedded in a somewhat featureless matrix. The overall composition of the deposit at the furnace tube surface is indicated in Table 5. It agrees quite well with the overall composition of the deposit except that the sulfur content was much higher than that found in the bulk of the material. A high magnification view of a portion of the deposit in contact with the furnace tube is shown in Fig. 1. Using the EDS analysis, compositional variations from spot to spot at several such locations were studied, and the nature of those variations is summarized in Table 6. It can be seen that the spherical particles consisted primarily of silica and alumina, with small amounts of the oxides of the other elements in the deposit. At the point where two spherical particles were joined together, there was a somewhat higher concentration of iron, sulfur, and calcium. In addition, the matrix material contained much higher quantities of iron and sulfur than did the spherical particles.

Deposit Near the Furnace Tube. A section perpendicular to the furnace tube through the deposit was prepared for an examination to detect any variations with distance from the tube wall. As is shown in Fig. 2, the bulk composition of the deposit showed virtually no significant variations from the tube surface to a position 48 mm from the tube except for the high sulfur content immediately adjacent to the tube. However, as is shown in Fig. 3, when the composition was measured on smaller areas, some significant variations in composition did occur from area to area but, again, there was no consistent trend from the tube surface to positions far away from it. Several interesting observations can be made from Fig. 3. It is clear that there was a correlation among the silicon, aluminum, and potassium contents. This correlation probably was related to the fact that illite, which contains oxides of those three metals, was one of the main constituents of the furnace ash. It also is apparent from Fig. 3 that there was a negative correlation between the iron content and the silicon content but, in general, the iron content was not related to the sulfur content. These relationships suggest that the particles of pyrite, which also were major constituents of the original material, had been oxidized to iron oxide in the flame and those particles retained their identity.

Downloaded 01 Jun 2010 to 171.66.16.58. Redistribution subject to ASME license or copyright; see http://www.asme.org/terms/Terms_Use.cfm

Table 4 Relationship between composition of a furnace-deposit or ash sample and the data obtained by energy dispersive X-ray analysis[a]

Compound/Element	Range of Ratio of percent Compound to percent EDS Counts
SiO_2/Si	0.8–1.4
Al_2O_3/Al	0.7–1.8
Fe_2O_3/Fe	0.6–2.0
S	0–1.0
CaO/Ca	0.6–0.8
K_2O/K	1.0–1.3
TiO_2/Ti	0.9–1.0
P_2O_5/P	0–0.5
MgO/Mg	ND[(b)]
Na_2O/Na	ND

[a] Based upon data obtained from two standard mixtures prepared at Battelle, an illite standard, and the furnace deposit from the boiler.
[b] ND = Not detected by EDS.

Furthermore, it is clear that there was a correlation between the calcium and sulfur contents, but those elements did not correlate with either the iron or the silicon. Apparently, much of the sulfur became associated with the calcium in the form of calcium sulfide or calcium sulfate, some of which was found in the original coal.

A typical example of one of the areas that was relatively high in silicon is shown in Fig. 4, and the compositions of several representative particles are indicated in Table 7. It can be seen that many of the particles were hollow, but some appear to be solid. The optical photomicrograph shows that there was a considerable difference in reflectivity among the particles. Comparing the reflectivity with the data in Table 7 shows that the particles with higher reflectivity contained higher amounts of iron. Thus, it can be seen that most of the spherical particles near the furnace tube were rich in silica and alumina, but a few of the particles were relatively high in iron. The matrix in which the particles were embedded is rather high in iron and sulfur. The relatively high calcium content of the entire area compared with the individual particles suggests that there must have been some particles that were not analyzed individually that consisted of calcium sulfate or calcium oxide.

A typical region that contained relatively high amounts of iron and calcium is shown in Fig. 5 and the analyses of selected particles are given in Table 8. The area on the right side of Fig. 5 is a high-magnification view of a small portion of the area shown in the upper left corner of the left portion. It can be seen that the small spheres consisted primarily of silica and alumina, whereas the large light colored areas were primarily iron oxide, and the large, dark areas contained large amounts of calcium oxide. It is interesting to note that the boundary between the iron oxide and calcium oxide particles (particles 10 and 12, respectively) indicated by Points 11 and 13 contained a relatively large amount of sulfur, which was not found in either of the two particles.

No measurable composition gradients were detected within any of the individual particles. Fig. 6 and the data in Table 9 illustrate that observation. Note that the composition at all four spots within the spherical particles was virtually constant.

At many interfaces between two bound particles, no unusually high concentration of any element was detected. An example of this is illustrated in Fig. 7. Fig. 7(*a*) shows an optical micrograph of two particles that are bound together; the lighter of the two contained several holes. The particles were embedded in a mounting material that was not part of the furnace deposit. The X-ray maps for the various elements show that the composition within each particle was relatively uniform and that there was relatively little diffusion of material from one particle to another across the interface. Also no unusually high concentration of any of the components was present at the interface. The X-ray maps shown in Fig. 7 were made with an electron-microprobe analyzer. Virtually identical maps could have been produced in the scanning electron microscope with the energy dispersive system.

Deposits Farther from the Furnace Wall-Tube Surface. The temperature of the furnace deposit can be expected to increase sig-

Table 5 Range of compositions observed on the imprint of the furnace tube on the sample from the boiler[a]

EDS Analysis, percentage of total counts						
Si	Al	Fe	S	Ca	K	Ti
22–34	8–19	22–32	16–28	4–6	3–5	0.5–1.0

[a] Analyses were obtained for 5.2 square millimeter areas.

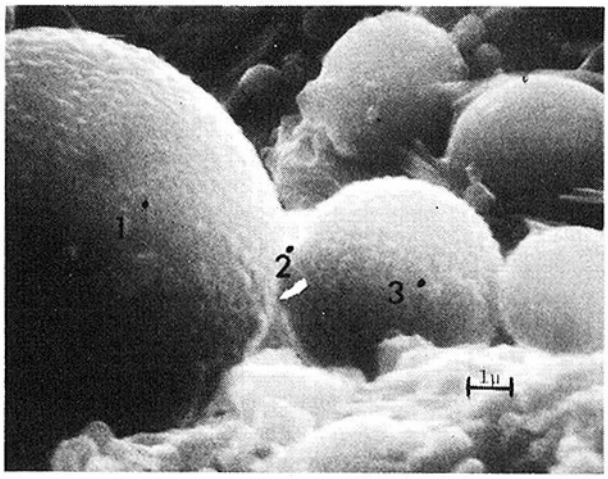


Fig. 1 Scanning electron micrograph showing spherical particles in an area in contact with the furnace tube, 7500×

Table 6 Compositions of particles and bonding material at the furnace tube

Particle or Area	EDS Analysis, percentage of total counts							
	Si	Al	Fe	S	Ca	K	Ti	Mg
Particle 1[a]	68	18	7	1	2	3	0.5	0
Particle 3[a]	51	28	6	3	1	5	3	3
Interface 1/3[a]	46	16	11	16	5	4	2	0
Particle 5[b]	58	26	5	3	2	5	1	0
Particle 6[b]	77	15	2	0.5	0.5	4	0.5	0
Interface 5/6[b]	48	19	15	5	5	5	2	0
Matrix material[a]	16	5	46	20	3	8	0.5	0

[a] Shown in Fig. 1.
[b] Particles not shown in Fig. 1.

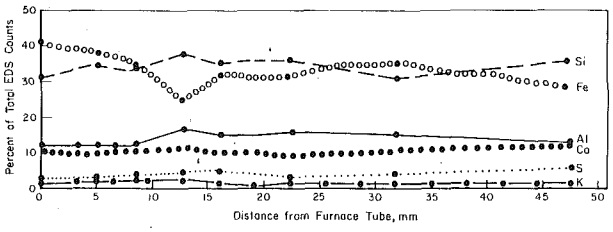


Fig. 2 Variation in composition of furnace deposit in Labadie boiler as measured on 5.2 square mm areas

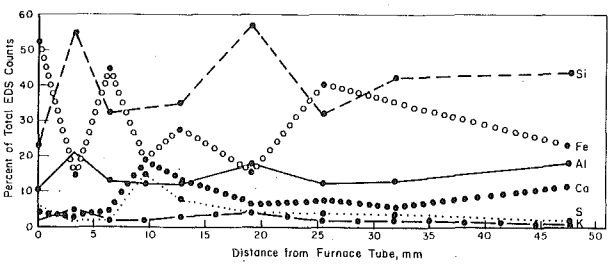


Fig. 3 Variation in composition of furnace deposit in Labadie boiler as measured on 0.21 square mm areas

Downloaded 01 Jun 2010 to 171.66.16.58. Redistribution subject to ASME license or copyright; see http://www.asme.org/terms/Terms_Use.cfm

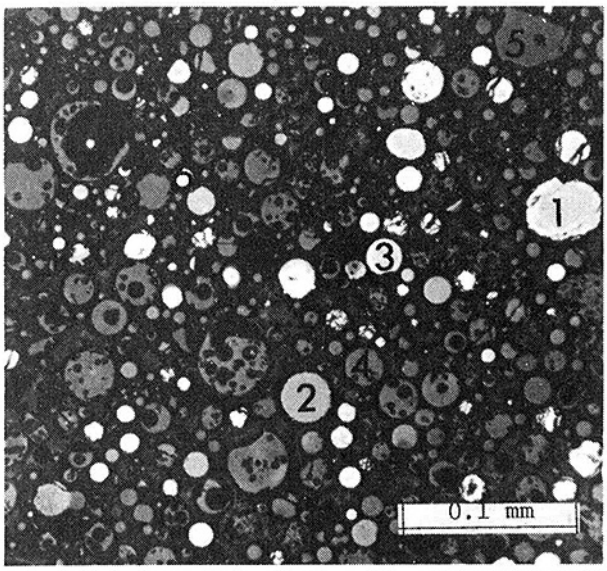


Fig. 4 Optical micrograph of section through furnace deposit 19 mm from the furnace tube showing a typical area of relatively high silicon content, 250×

Table 7 Compositions of small spherical particles in the furnace deposit near the furnace tube

Particle[a]	EDS Analysis, percentage of total counts						
	Si	Al	Fe	S	Ca	K	Ti
1	10	3	87	0	0	0	0
2	42	19	33	0	1	3	2
3	14	9	75	0	1	0	0.5
4	56	32	4	0	1	4	3
5	99	0	0.5	0	0	0	0
6	0.5	1	98	0	0	0	0
Matrix	23	10	40	13	2	2	6
Entire Area	36	15	32	4	10	1	1

[a] Numbers refer to particles shown in Fig. 4.

nificantly with increasing distance from the wall-tube surface. Because of this temperature gradient, the physical nature of the furnace deposits changes while the average chemical composition is relatively unaffected. An example of a furnace deposit from a relatively long distance from the tube surface is shown in Fig. 8. As is indicated by the data in Table 10, the deposit consists of roughly spherical regions that contained relatively large amounts of iron embedded in a glassy matrix that consisted primarily of silica and contained many holes. Apparently, because of the higher temperatures, the material that consisted of spherical particles of silica very near the furnace tubes had fused to form the glassy matrix, and the irregularly shaped particles containing iron had become spherical and possible molten within the silica matrix. Clearly, there is no direct relationship between the structure shown and the original particles that joined to form the furnace deposit. As a result, little significant information on the original deposit structure before fusion can be obtained from a study of glassy samples.

Characteristics of the Low-Temperature Ash

Samples of low-temperature ash were studied in a hot-stage optical microscope to identify particles with low melting points. Many of the particles contained more than one phase. Melting points in the range of 870 to 1070°C were observed, which is essentially the same range as that observed for particles of ground furnace ash. Thus, it appears that interaction of particles in the flame, though possible, is not required to explain the compositions and melting points observed in the furnace deposit.

Formation of Low-Melting-Temperature Materials in the Furnace

The bonding of ash particles to furnace-wall tubes and to existing ash deposits would be aided by the presence of ash constituents having

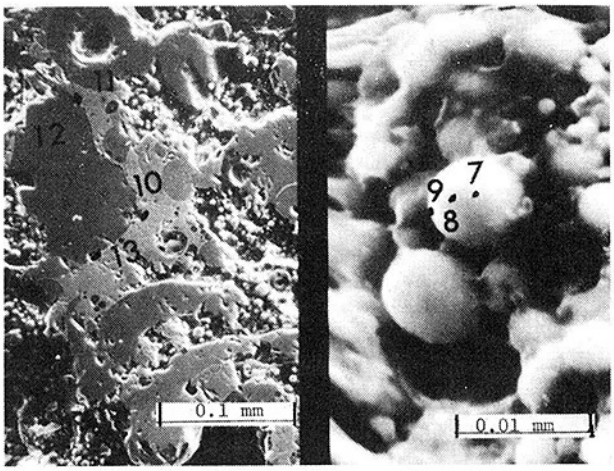


Fig. 5 Scanning electron micrograph of a section through the furnace deposit 3 mm from the furnace tube, 250×

Table 8 Composition of various constituents in the portion of the furnace deposit shown in Fig. 5

Particle or Area	EDS Analysis, percent of total counts							
	Si	Al	Fe	S	Ca	K	Ti	Mg
7	47	31	7	0	10	5	0	0
8	58	29	8	0	0	3	2	0
9	49	27	7	0	2	5	3	7
10	2	0	96	0	2	0	0	0
11	5	2	63	6	25	0	0	0
12	15	5	17	0	60	0	0	3
13	7	2	47	8	37	0	0	0

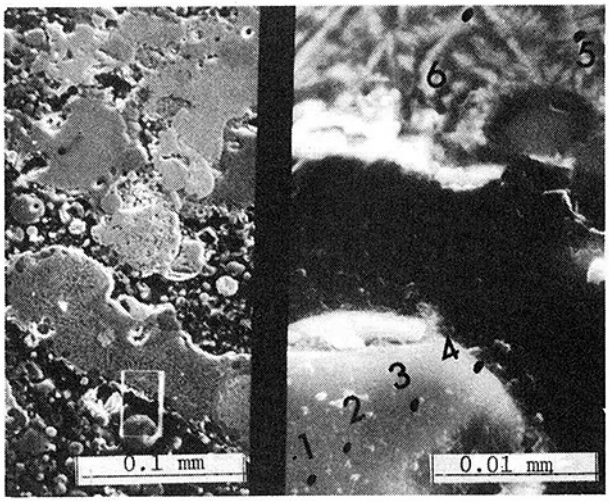


Fig. 6 Scanning electron micrograph of a section through the furnace deposit 32 mm from the furnace tube, 250×

Table 9 Composition of various areas in the portion of the furnace deposit shown in Fig. 6

Spot	EDS Analysis, percent of total counts							
	Si	Al	Fe	S	Ca	K	Ti	Mg
1	65	23	0	0	0	12	0	0
2	69	20	0	0	0	11	0	0
3	68	20	0	0	0	12	0	0
4	67	21	2	0	0	9	0	0
5	22	18	56	2	0	0	0	2
6	27	14	54	2	2	2	0	0

Downloaded 01 Jun 2010 to 171.66.16.58. Redistribution subject to ASME license or copyright; see http://www.asme.org/terms/Terms_Use.cfm

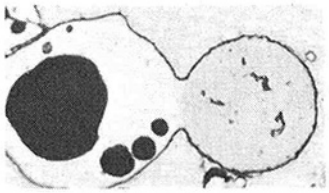


Fig. 7(*a*) Optical micrograph

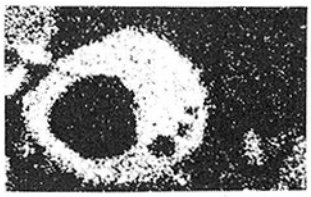


Fig. 7(*b*) X-ray map for silicon

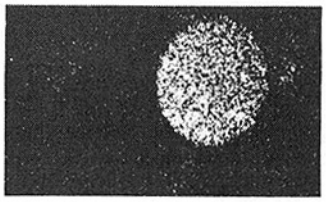


Fig. 7(*c*) X-ray map for iron

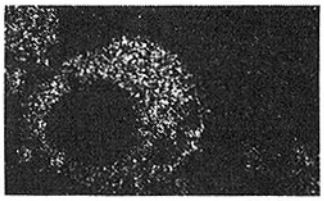


Fig. 7(*d*) X-ray map for aluminum

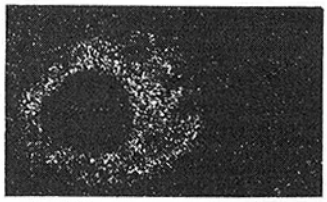


Fig. 7(*e*) X-ray map for calcium



Fig. 7(*f*) X-ray map for sulfur

Fig. 7 Elemental distribution in two bonded particles as revealed on X-ray maps produced with the electron-microprobe analyzer, 500×

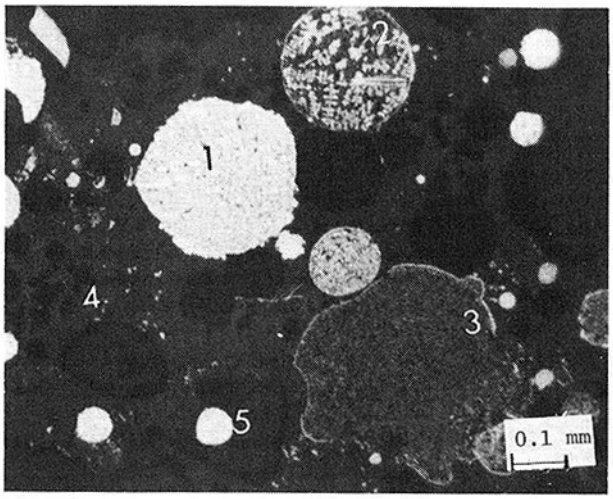


Fig. 8 Optical micrograph of a section through a portion of the furnace deposit at a relatively long distance from the furnace wall, 500×

a liquid phase at deposition temperature. A study of the relevant phase diagrams for mixtures of the components of the furnace ash shows that mixing the constituents can cause significant decreases in the melting temperature. For example, the FeO–SiO_2–Al_2O_3 phase diagram [3] shows that a proper mixture of FeO and SiO_2 can produce Fayalite, which has a melting point almost 200°C below that of the iron oxide and 550°C below that of SiO_2. Adding an appropriate amount of Al_2O_3 can depress the melting point further by almost 100°C.

Particles having low melting temperatures will be fused in the flame, where temperatures above 1370°C occur, and will approach the wall as molten spheres. As they approach the wall, they radiate heat to the cold wall tubes and may freeze before impact. However,

Table 10 Composition of various constituents of the furnace deposit as shown in Fig. 8

	EDS Analysis, percentage of total counts							
Spot	Si	Al	Fe	S	Ca	K	Ti	Mg
1	12	5	82	0	0.7	0	0.3	0
2	41	14	38	0	3	3	1	0
3	51	23	18	0	1	3	0.7	2
4	95	0	2.3	0	2	0.7	0	0
5	10	4	84	0	2	0	0	0

if they are still molten on impact, they may bond mechanically or electrostatically to the tube surface. The tube surface is oxidized and quite rough, so that mechanical bonding may be sufficient for initial sticking of the particle to the wall. As the ash layer becomes thicker, the temperature gradient through the ash, which is a good insulator, will result in progressively higher surface temperatures, making interparticle bonding easier. At some thickness, the ash surface will be molten and will capture unmelted particles impinging on it. If the temperature is high enough, these may dissolve in the molten slag.

There appears to be some possibility that reactions may take place between molten particles and the iron oxide of the tube surface, or between particles of unlike composition. The reaction zone, if it exists, must be very thin, as diffusion of constituents from one particle to another appeared small or non-existent in scanning-electron-microscope studies. For example, a clay particle containing silica and alumina might react with iron oxide to form a thin film of low-melting-temperature material that would bond them together.

A different mechanism may explain the concentration of calcium and sulfur near the tube surface. There appears to be a possibility that sulfur compounds diffuse into the ash deposit because of the temperature gradient and concentrate near the tube surface where the temperature is low. They may not have been there when deposition first occurred.

Downloaded 01 Jun 2010 to 171.66.16.58. Redistribution subject to ASME license or copyright; see http://www.asme.org/terms/Terms_Use.cfm

The chemistry of ash deposition appears complex, and it appears necessary to examine more samples, covering a broader range of ash compositions, furnace conditions, and deposit age to fully understand how the furnace deposits form.

Conclusions

It has been demonstrated that a number of analytical procedures can provide useful information for characterizing the constituents of furnace deposits including the material that bonds the particulate matter together. These analytical procedures include scanning electron microscopy, energy dispersive X-ray analysis, electron microprobe analysis, and optical metallography.

The following significant features were observed on the sample that was available for a detailed study:

- The ash deposit contained a high concentration of glassy spheres, varying widely in composition and size.
- At the furnace-tube surface, there was a high concentration of sulfur, which seemed to be associated with a matrix material. The matrix material contained iron, sulfur, and some silica and alumina, with minor amounts of calcium oxide and potassium oxide.
- With the exception of the high sulfur content at the tube surface, there were no gross composition gradients in the deposits, but localized gradients did exist. Certain areas were rich in silica, alumina, and potassium, all of which seemed to be found together. These were also found together in the original coal mineral matter, as isolated by low-temperature ashing. Particles of high iron content had relatively low silica content, probably because the iron-rich particles and the silica-rich particles did not react significantly with each other before they struck the furnace wall. Except for the portion of the deposit in direct contact with the tube surface, the sulfur seemed to be associated primarily with regions of high calcium content.
- No measurable composition gradients were detected within individual particles.
- The resolution of the methods used was probably 0.1 to 1 particle diameter, depending on the particle size. A unique bonding material to bond ash particles together was not found. Bonding between particles seemed to be related primarily to the compositions of the specific particles that were attached to each other.
- In most of the deposits, the matrix material appeared to be a glassy mixture of silica, alumina, and iron oxide along with some calcium oxide and potassium oxide. At some locations, relatively high sulfur contents were detected in the matrix material.

Acknowledgments

The research described in this paper was sponsored by the Electric Power Research Institute, to which the authors are grateful. The authors also acknowledge the helpful discussions and suggestions from Don Anson and the assistance in the scanning-electron-microscope studies by Ronald Pratt of the Battelle Columbus Laboratories.

References

1 Hazard, H. R., Barrett, R. E., and Dimmer, J. P., "Coal Mineral Matter and Furnace Slagging," presented at the American Power Conference, Chicago, April 23–25, 1979.

2 Hazard, H. R., Barrett, R. E., and Dimmer, J. P., "Field Studies of Slagging in Tangentially Fired Boiler Furnaces—Part 1, Labadie Field Trial," ASME Paper No. 78-WA/FU-10, presented at 1978 ASME Winter Annual Meeting.

3 Levin, E. M., Robbins, C. R., and McMurdie, H. F., *Phase Diagrams for Ceramists*, The American Ceramic Society, 1964.

Downloaded 01 Jun 2010 to 171.66.16.58. Redistribution subject to ASME license or copyright; see http://www.asme.org/terms/Terms_Use.cfm

H. H. Krause
P. W. Cover
W. E. Berry
Columbus Laboratories
Battelle Memorial Institute
Columbus, OH 43201

R. A. Olexsey
Industrial Environmental Research Laboratory
U. S. Environmental Protection Agency
Cincinnati, OH
Mem. ASME

Corrosion and Deposits from Combustion of Solid Waste

Part VII: Coincineration of Refuse and Sewage Sludge

Corrosion probe exposures were conducted in the Harrisburg, Pennsylvania, incinerator to determine the effects of burning low-chloride sewage sludge with municipal refuse. Probes having controlled temperature gradients were used to measure corrosion rates for exposure times up to 816 hours. The effects of exposure time, metal temperature, and gas temperature were studied. The results demonstrated that the addition of the sludge reduced the initial corrosion rates of carbon and low-alloy steels to about half that from refuse alone. Little effect was observed on the rates for Types 310 and 347 stainless steels. An aluminized coating on steel resisted corrosion effectively and offers promise as a cost-effective substitute for expensive alloys. In the range 500–900°F the corrosion rates of carbon steel and T22 increased with temperature while those for the stainless steels decreased. Reducing the flue gas temperature from 1500°F to 1100°F reduced corrosion rates significantly and made them less dependent on metal temperature. The addition of low-chloride sludge to refuse is recommended as a corrosion prevention measure and a waste disposal technique.

Introduction

The objective of this research program was to determine the effect of the addition of low chloride sewage sludge to municipal refuse on the wastage rates of boiler tube metals. The work was carried out at the Harrisburg, Pennsylvania, incinerator, where during initial operation, tube failures occurred every three to five months when only bulk solid waste was burned. However, for the past several years no tube failures have occurred, but during this period municipal sewage sludge has been burned along with the refuse. In addition, soot blowing was reduced in frequency and some of the carbon steel tubes were replaced with a low-chromium alloy. Consequently, the reason for the reduced metal wastage at the Harrisburg incinerator was uncertain and corrosion studies were needed to evaluate the effect of adding the sewage sludge to the refuse combustion environment.

Previous papers in this series discussed the general nature of the deposits and the corrosion that results from the burning of refuse [1], the effects of chlorine [2], and of sulfur [3] in the refuse. Data on the initial corrosion rates from the co-firing of refuse and coal [4, 5] as well as longer term corrosion rates [6] also were presented. The current program supplemented the past work by obtaining additional data on the burning of bulk refuse and comparing it with that obtained when sewage sludge was mixed with the refuse.

Background

The Harrisburg, Pennsylvania, incinerator began operation in October, 1972. This facility has two identical boilers, each with a nominal capacity of 360 T/day (327 megagrams (Mg) per day) of refuse. At this rate of 15 tons (13.6 Mg) of refuse per hour, the normal steam production is 92,500 lb/hr (42.0 Mg/hr). The steam pressure at the superheater outlet is 250 psig (18.6 kg/cm^2) at a temperature of 456°F (236°C). These multidrum boilers with welded water walls are fed from a single refuse pit and are exhausted through individual electrostatic precipitators before discharge into a single stack as shown in Fig. 1.

This figure shows the location of the superheaters where the early tube failures occurred and where the corrosion probes were inserted for this work. Although Boiler Number 1 started in operation before Unit Number 2, the first superheater tube failure occurred in Unit 2 after about 3000 hours. It failed with a ductile split several inches long while the wall thickness of adjacent tubes was reduced to 0.020 in. (0.051 cm) from the original 0.165 in. (0.42 cm) wall. Wall thickness of tubes remote from the soot blower was reduced to about 0.150 in. (0.38 cm). By March, 1974 the entire bank of carbon steel superheater tubes had been replaced with T22 alloy. Fortunately by this time the effect of soot blowing on metal wastage was recognized and the blowers were used sparingly. Then in June, 1975, the burning of sewage sludge with the refuse was begun, and this mode of operation has continued to the present.

Prior to delivery to the incinerator, the sludge is processed conventionally. Wastes from the entire city and some adjacent regions are treated first by grinding, grit removal, and preliminary settling. Subsequently, anaerobic digestors are used with a polymer treatment to thicken the supernatant liquid. The coagulant used in the sludge treatment process is an organic-based filter aid, employed at the rate of 27 pounds (12.3 kg) per 10,000 pounds (4,545 kg) of dry solids. As this organic polymer is probably a combination of amines and acrylates, it is much more suitable for use in sludge which is to be incin-

Contributed by the Corrosions and Deposits Committee and presented at the Winter Annual Meeting, December 2–7, 1979, New York, New York, of THE AMERICAN SOCIETY OF MECHANICAL ENGINEERS. Manuscript received at ASME Headquarters August 10, 1979. Paper No. 79-WA/CD-2.

Copyright © 1980 by ASME
Downloaded 01 Jun 2010 to 171.66.16.58. Redistribution subject to ASME license or copyright; see http://www.asme.org/terms/Terms_Use.cfm

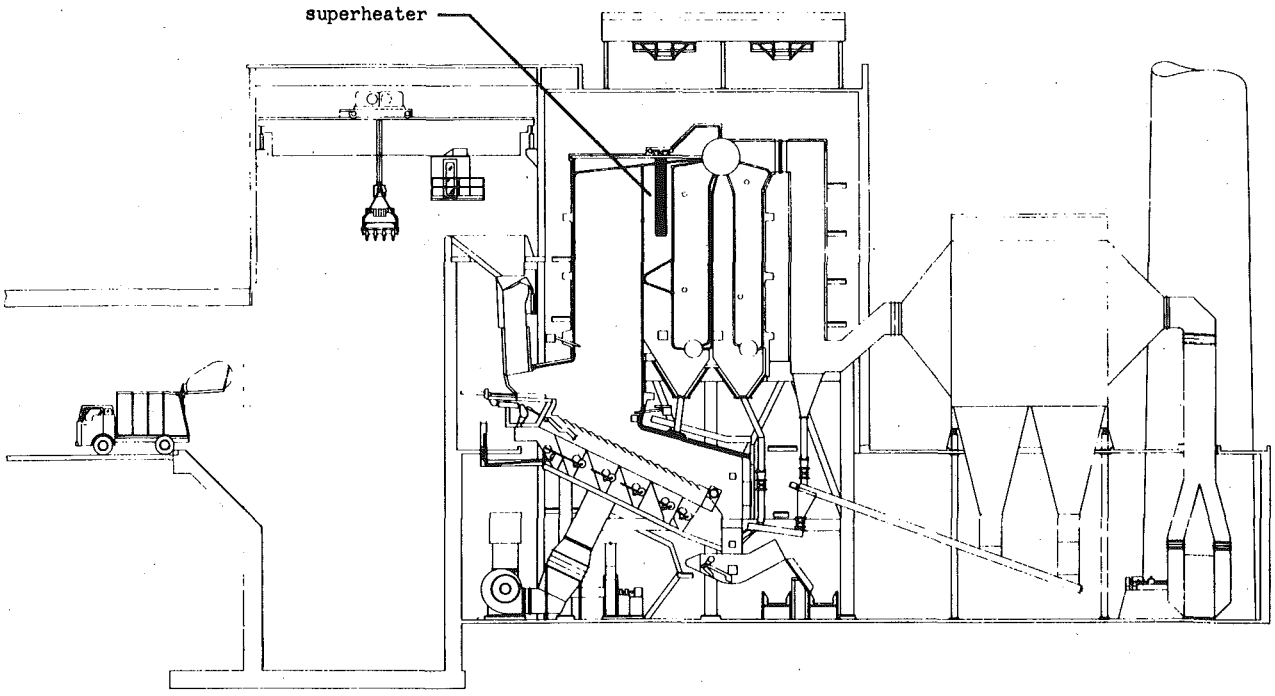


Fig. 1 Harrisburg, Pennsylvania, refuse burning facility

erated than would be ferric chloride, which was used previously. About 15 to 20 tons (13.6 to 18.3 Mg) of partially dried sewage sludge are delivered by truck to the incinerator every 24 hours, and the sludge is dumped onto the refuse in the pit. This material contains 20 to 22 percent solids, so the incinerator handles the equivalent of about 5 to 6 tons (4.5–5.5 Mg) per day of dry solids. During the course of these corrosion studies, the partially dried sludge was delivered at an average rate of 16.5 tons (15 Mg) per working day. During the 8-hour and 80-hour probe exposures, the weight ratio of sludge to solid waste was about 1:10 on an as-received basis, but during the long-term run the ratio dropped to about 1:20.

As currently practiced, the dewatered sludge filter cake containing about 22 percent solids is mixed with the municipal refuse in the receiving pit. Considerable mixing occurs in the pit before the sludge and refuse are fed into the furnace charging chute. It seemed likely that sulfur and silica were present in the sludge in sufficient quantity and were burned effectively to reduce the corrosive effects of chlorine in the refuse.

Experimental Program

Six corrosion probe exposures were made during this program, with three exposure times, two fuels, and two gas temperatures. The conditions for these different corrosion probe runs are shown in Table 1. During the 816 hour exposure, an explosion and fire in the incinerator pit interrupted plant operations for about four weeks, during which time the probe was removed and covered to protect it from damage. This interruption occurred about 100 hours into the exposure period, and the loss of protective deposits from several specimens resulted in slightly higher corrosion rates on these specimens.

In general, the sewage sludge was delivered to the incinerator at irregular intervals in a 24 hour period. However, this timing was not critical because the crane operators were able to extend the sludge distribution over the intervals between loads of sludge. In addition, the earlier reactions that occur on a clean metal surface are more important than the subsequent reaction of the deposit-encrusted tube. Thus, short periods of operation on refuse alone after a protective oxide layer has built up on the tubes have less effect on the total corrosion than they would have early in the exposure.

Fuel Evaluation. No analyses of the refuse were made during this program because extensive data of this type were collected during the early days of operation of the Harrisburg incinerator. No new sources of refuse of any importance have developed since that time, and visual inspection of the refuse pit showed that typical municipal waste was being burned. The composition of the Harrisburg refuse as determined at the startup period is shown in Table 2. The distribution of materials is typical of municipal refuse in the U. S. The results of similar refuse classification at the Miami County Incinerator, Troy, Ohio, are also presented in Table 2, because corrosion probe data from the location are compared with the Harrisburg results. The refuse compositions for the two sites are sufficiently similar so that comparison of results is meaningful.

Samples of the wet sewage sludge as received at the Harrisburg incinerator were taken on four different days during which probes were exposed. Samples were dried and analyzed for total sulfur and chlorine, heavy metals, and ash content. Moderate drying conditions were used in order to avoid oxidation of the sludge. It was dried at a temperature of 120°F (50°C) for a month and then overnight at 230°F (110°C). The solids content of the sludge averaged about 20 percent, as shown in Table 3. The heat of combustion of the sludge also was determined and was found to have an average value of about 3000 Btu/lb (6960 J/g). Gross heating values for the normal refuse measured at the beginning of the operation of the incinerator ranged from 4000 to 5100 Btu/lb (9280 to 11,830 J/g).

Analyses for total sulfur and for chloride made on the dried sludge gave an average value for sulfur of 3.4 percent, while the chloride averaged 0.09 percent. The amount of sludge being burned with the refuse would add only about 0.04 percent sulfur to the total fuel supply. Sulfur added to the system in this quantity would not be sufficient to counteract the corrosion due to chlorine in the refuse. However, analyses of the sewage sludge and its ash by optical emission spectroscopy and X-ray diffraction showed that there is a high concentration of silica in both. The combustion train yielded an average ash content of 68.1 percent with the major ingredient of the ash identified as silica (SiO_2). The SiO_2 content of the sludge is definitely higher than that of the municipal refuse. This material can function in the same manner as sulfur to inhibit corrosion by chlorine. In addition, the silica in the wet sludge is carried into the combustion zone, whereas in the case of bulk refuse the drier material allows the silica to sift out and drop through the grates rather than be carried into the hot combustion zone. As shown in Table 3, the other metals which were present in significant amounts were aluminum, calcium, iron, potassium, magnesium, and sodium.

Experimental Apparatus and Procedure. The details of the corrosion probe design used in this work have been published previ-

Downloaded 01 Jun 2010 to 171.66.16.58. Redistribution subject to ASME license or copyright; see http://www.asme.org/terms/Terms_Use.cfm

ously [5]. The specimens were machined from 1 in., schedule 40 pipe or equivalent tubing and were nested together end-to-end on the probe. Internal cooling of the specimens by high velocity air that flowed over a tapered center body provided a temperature gradient along the probe. The alloys used in the corrosion probe exposures ranged from ordinary carbon steel to high chromium steel and high chromium nickel alloys as shown in Table 4. An aluminum coating (Alonized) which showed promise in previous work also was included in these exposures. The probes were exposed in two zones of the superheater. The higher temperature location was in front of the first row of superheater tubes where the gas temperature was about 1500°F (816°C). The cooler location with an average gas temperature of 1150°F (621°C) was at the rear of the superheater section.

Table 1 Corrosion probe experiments at the Harrisburg incinerator

Probe No.	Exposure time, hours	Fuel	Location	Gas temperature C	Gas temperature F
41	8	Refuse	Superheater inlet	816	1500
42	8	Refuse	Superheater rear	621	1150
43	80	Refuse + sludge	Superheater inlet	816	1500
44	8	Refuse + sludge	Superheater rear	621	1150
45	8	Refuse + sludge	Superheater inlet	816	1500
46	816	Refuse + sludge	Superheater inlet	816	1500

Table 2 Refuse compositions

	Components, weight percent	
	Harrisburg, Pennsylvania(a)	Troy, Ohio(b)
Paper:		
Mixed	23.6	35.6
News	9.0	6.5
Corrugated	8.5	6.5
Magazines/books	2.3	3.2
Wood	2.6	3.6
Grass/garden waste	8.9	7.4
Cloth	3.3	2.1
Garbage, bones	5.1	10.3
Plastics:	–	4.0
Flexible	2.7	–
Rigid	1.0	–
Rubber	0.3	–
Miscellaneous fines	12.1	5.8
Dirt	9.8	–
Glass/ceramics	1.9	6.8
Metal:	–	8.2
Magnetic	7.6	–
Nonmagnetic	1.3	–

(a) Average of eight days in May 1972.
(b) Average of four days in 1972.

On completion of a probe exposure, the surface of the specimens was covered with a thin layer of corrosion product scale plus a thick fly ash deposit. The deposit reached a maximum thickness of about 2 in. (5 cm) in 80 hours and did not increase much with longer exposure. The deposits were removed from the probes in three sections, each covering about one-third of the specimen zone. Analyses of these deposit sections provided data on variations in composition as a function of metal temperature.

Corrosion Results

Corrosion rates were determined by weight loss measurements after removal of the scale layer by cathodic stripping. The corrosion rate in mils/hour was calculated from the weight loss, assuming uniform attack around the specimen surface. Corrosion rates were plotted as

Table 3 Elemental analyses of dry sewage sludge and sludge ash

Element	Composition, weight percent Sludge	Sludge ash
Si	10–20	20–40
Al	3–5	5–7
Ca	3–5	5–7
Fe	2–4	3–5
S(a)	3.35	4.9
K	0.8–2	1–4
Mg	0.5	0.8
Na	0.3	0.5
Ti	0.2	0.4
Cl(a)	0.09	0.13
Cu	0.08	0.2
Pb	0.08	0.1
Ba	0.05	0.1
Cr	0.06	0.1
Mn	0.05	0.08
Zr	0.01	0.03
Ni	0.01	0.02
Sn	0.01	0.02
V	<0.01	0.01
Co	<0.01	<0.01
Ag	<0.01	<0.01
B	<0.01	<0.01
Bi	<0.01	<0.01

(a) By wet chemistry; others by optical emission spectroscopy.

Table 4 Certified compositions of corrosion probe alloys

Alloy	Elements, weight percent Cr	Ni	Mn	Mo	Si	P	S	C	Fe	Others
A106	–	–	0.72	–	0.29	0.026	0.014	0.26	Bal	–
P/T22(a)	2.28	–	0.37	0.98	0.31	0.018	0.011	0.12	Bal	–
310SS	24.6	21.7	1.69	0.24	0.36	0.030	0.010	0.043	Bal	0.20 Cu
347SS	18.0	12.5	1.74	–	0.55	0.025	0.018	0.05	Bal	0.8 Nb; 0.02 Ta
Incoloy 825	21.5	41.5	0.37	2.95	0.16	–	0.004	0.01	Bal	1.8 Cu; 0.07 Al; 0.98 Ti

(a) P22 and T22 have the same elemental composition. T22 designates tubing, characterized by exact OD size, while P22 indicates pipe, sized by ID. Both are under ASME pressure vessel codes duplicated by a corresponding ASTM number: for P22, ASME SA 335 and ASTM A 335; for T22, ASME SA 213 and ASTM A 213. In this program P22 specimens were used, while the Harrisburg superheater tubes are T22.

Downloaded 01 Jun 2010 to 171.66.16.58. Redistribution subject to ASME license or copyright; see http://www.asme.org/terms/Terms_Use.cfm

functions of time and temperature and each point designated in the plots represents a single corrosion specimen.

Effect of Exposure Time. The corrosion rates for the carbon steel specimens are shown as a function of time in Fig. 2. These results are compared with the corrosion data obtained previously at the Miami County Incinerator at Troy, Ohio, where bulk refuse alone was burned [7]. The data were interpolated from several specimen temperatures to a common temperature of 500°F (260°C). This temperature was selected to be similar to that of the Harrisburg incinerator superheater tubes which operate at a steam temperature of 450°F (232°C). The data point for the eight hour exposure time at Harrisburg when refuse alone was burned compared favorably with that from the Troy Incinerator for which longer exposure times up to 828 hours also were obtained. The corrosion rate was slightly higher at Troy because the probe there was exposed to some flame radiation. The data of Fig. 2 emphasized the fact that eight hour exposure results can not be applied to longer term exposure except for cases such as the early operation at Harrisburg, when it was the practice to use the soot blowers on the superheaters quite frequently. At that time the soot blowing was conducted as often as once each shift during the five day-a-week operation. This frequent soot blowing resulted in a high tube wastage rate as shown in Fig. 2, which led to a superheater failure after approximately 3000 hours of operation [8]. Sections of the failed tube which were not subjected to the soot blower blast showed relatively minor tube wastage. In the same time interval, the soot blown section lost 145 mils (3.62 mm) while the wastage on the unblown sections amounted to only 15 mils (0.38 mm). Hence the high wastage rate of the cleaned areas was equivalent to that measured on clean specimens exposed for about 200 hours on the corrosion probe. Similarly, the uncleaned portions of the tubes gave a low wastage rate consistent with an extrapolation of that data for probe specimens exposed longer than the 820 hour test.

The addition of sewage sludge to the refuse reduced the initial corrosion rate of the carbon steel by about a factor of 2. However, as the exposure time increased, the corrosion rates for operation with and without sludge converged. Thus at the 800 hour point, the rate experienced for the small amounts of sludge burned at Harrisburg was only slightly less than that for refuse alone at the Troy Incinerator. Nevertheless, if the difference in the two curves at the 1000 hour point were to be maintained indefinitely, the result would be a 35 to 40 percent increase in boiler tube life for the system with the sludge added.

The corrosion rates for the other alloys used in the probe exposures at Harrisburg are given as a function of time in Table 5 for three temperatures covering the exposure range. The P22 alloy had metal wastage rates essentially the same as those for the carbon steel. Significantly lower rates were observed for the Type 310 and 347 stainless steels and the Incoloy 825.

As expected, the wastage rates of the ferritic alloys (A106 and P22) were reduced substantially in the 80 hour exposure, with less reduction in the 816 hour period. At the longer times of 80 and 816 hours, the effects of temperature were reduced to the extent that the loss rates were nearly identical at a value of 0.009 mils/hr (0.23 μm/hour) over the entire temperature range studied. The extrapolation of the corrosion rates to longer times suggest wastage rates that gradually would decrease to values well below those measured. The observed rates would indicate boiler tube life of only two to three years, but there has been no further evidence of deterioration of tubes at Harrisburg since the corrective measures were taken. Consequently, the corrosion rates will most likely decrease further with time by a factor of 5 to 10.

Predictable trends were observed in the wastage of the austenitic steel specimens. As a rule, the stainless steels 310, 347 and Incoloy 825 showed wastages equivalent to a fifth or less of that for the ferritic steels. The most durable appeared to be the 310 stainless steel and the Incoloy 825, both of which were only slightly better than the 347 stainless steel in corrosion resistance. All three of these alloys showed anomalous increase in wastage rate during the longest exposure time of 816 hours. This fact suggests that furnace operating conditions were different during the longer exposure period. Examination of the incinerator log showed that less sludge than usual was burned in the month after the incinerator resumed operation following the pit fire. The corrosion data obtained at the Troy incinerator showed that the high alloy steels responded more dramatically to corrosion inhibitors than ferritic steels. The reverse effect may have occurred at Harrisburg when less sludge was burned than during the shorter term runs.

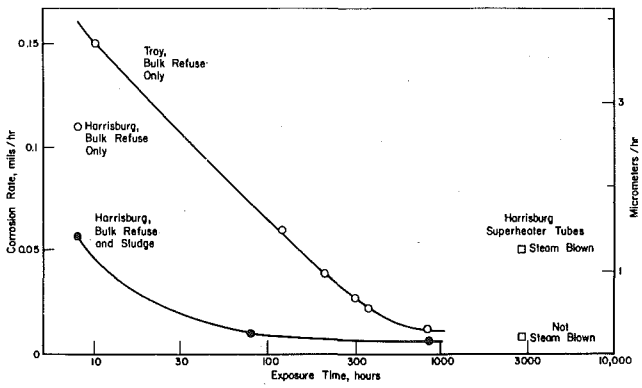


Fig. 2 Corrosion rates of carbon steel at a metal temperature of 500°F (260°C) versus exposure time

Table 5 Corrosion rates for 8, 80 and 816 hour exposures to burning refuse with sludge (interpolated to fixed temperature values)

Alloy	Metal temperature F	Metal temperature C	Wastage rate, mils/hr, for time indicated 8 hours	80 hours	816 hours
A106	500	260	0.051	0.0093	0.0082
	700	371	0.100	0.0093	0.0086
	900	482	0.132	0.0105	0.0087
T/P 22	500	260	0.059	0.0098	0.0083
	700	371	0.080	0.0096	0.0085
	900	482	0.140	0.0102	0.0090
310SS	500	260	0.024	<0.0001	0.0011
	700	371	0.022	0.0002	0.0011
	900	482	0.007	0.0009	0.0017[a]
347SS	500	260	0.038	0.0003	0.0025
	700	371	0.023	0.0011	0.0020
	900	482	0.009	0.0022	0.0020
Incoloy 825	500	260	<0.005	<0.0001	0.0011
	700	371	0.015	0.0005	0.0012
	900	482	0.014	0.0009	0.0020

(a) Similar wastage rate of .00153 mils per hour was observed for this same alloy during a 1318 hour exposure with metal temperatures averaging 890 F (±60) in the Norfolk, Virginia, Incinerator (Ref. 3).

Effect of Metal Temperature. A plot of wastage rates for A106 carbon steel over the temperature range 300 to 800°F for the eight hours exposure to the burning refuse with and without sludge additions is shown in Fig. 3. The line drawn on this figure from the studies conducted at the Troy, Ohio, incinerator is based upon ten or more A106 specimens exposed at a gas temperature of 1500°F (816°C) which is comparable to that of the Harrisburg probe in the superheater inlet. The increase in corrosion rate starting at 800°F (427°C) is typical of that found for carbon steel and low alloy steels in our past experience with the burning of bulk refuse at high gas temperatures. The three data points obtained for the carbon steel exposed to comparable conditions in the Harrisburg incinerator fall close to the curve established for the Troy incinerator. The corrosivity of the environment was significantly reduced when the sewage sludge was burned with the refuse. As shown in Fig. 3, the eight hour corrosion rates with sludge present in the fuel are 2 to 2.5 times lower than those with refuse alone.

Downloaded 01 Jun 2010 to 171.66.16.58. Redistribution subject to ASME license or copyright; see http://www.asme.org/terms/Terms_Use.cfm

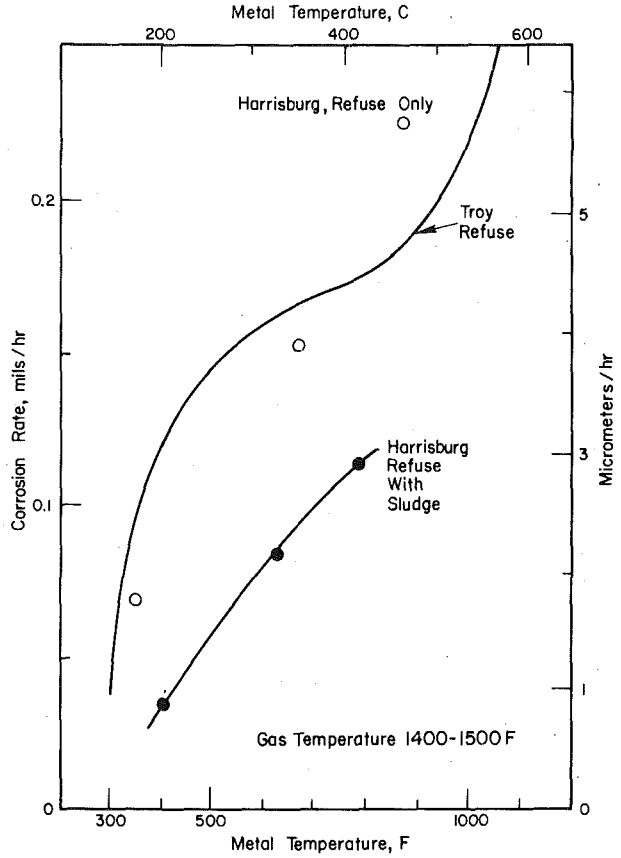


Fig. 3 Corrosion rates of carbon steel (A106) exposed for eight hours to burning refuse alone and with sludge

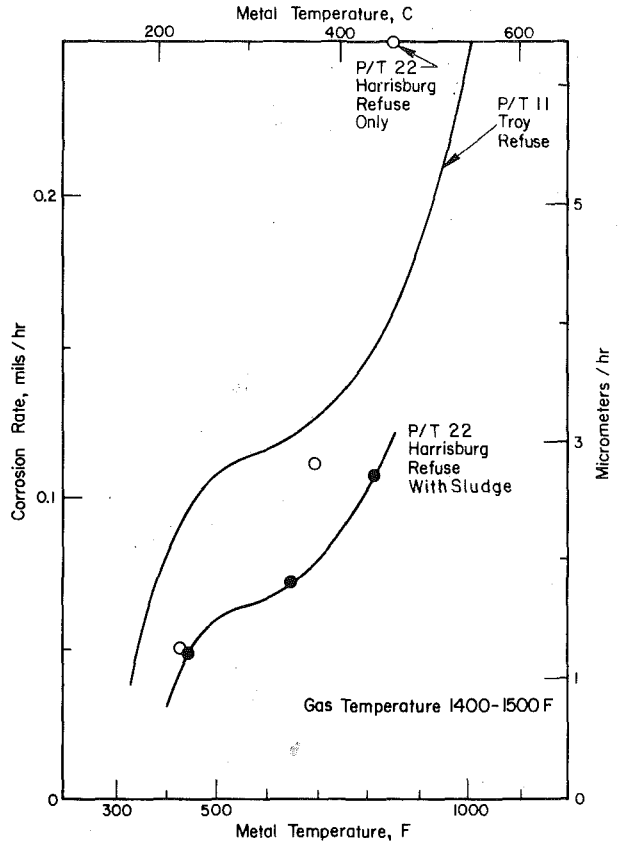


Fig. 4 Corrosion rates of low chromium alloys exposed for eight hours to burning refuse alone and with sludge

Similar conditions and results are shown in Fig. 4 for the low chromium alloy, T22 now being used for the superheater tubes in the Harrisburg incinerator. The difference in corrosivity of the two fuels becomes more pronounced for both alloys as the metal temperature increases. Here again the line drawn in the figure was obtained at Troy for a similar low chromium alloy, T11. In comparing the performance of carbon steel and T22 when sewage sludge was burned with the refuse, little difference was observed in the corrosion rates, as noted in Figs. 3 and 4. When refuse alone was burned the corrosion rate for T22 alloy was slightly lower than that of A106 at temperatures up to 700°F (370°C). However, at about 800°F (427°C) there was little difference in the corrosion rate of the two materials. These results indicate that the reduction in tube failures at the Harrisburg incinerator in recent years was not the result of replacing carbon steel tubes with the T22 alloy.

Both Type 310 and 347 stainless steel as well as Incoloy 825 showed very low wastage rates in the aggressive incinerator environment, as summarized in Fig. 5. In comparable eight hour exposures the corrosion rates of these alloys at temperatures between 500°F (260°C) and 900°F (482°C) were only about one-fifth as great as those for the carbon steel and the low-alloy steel. These high chromium-nickel alloys afforded more protection as the temperature increased, probably due to more rapid diffusion of the chromium and nickel into the oxide layer with the formation of a thicker protective scale. The addition of sludge to the refuse had practically no effect on the corrosion rates of Type 310 and 347 stainless steel. The sludge did, however, slightly reduce the attack on Incoloy 825, particularly at lower temperatures.

Effect of Gas Temperature. The experience with boiler operation at Harrisburg demonstrated the typical increased attack of boiler tubes at higher temperatures in that first, the upstream superheater tubes failed, and then the more remote banks failed. Although convective and radiant heat transfer ratios fluctuate rapidly with dynamic changes in the combustion process and flame temperature, tube metal wastage rates are in general lower in sites at which the gas temperature is lower. For this program two different locations for probe exposure were selected on the basis of their respective gas temperatures. The higher temperature location was in front of the first superheater bank and 6 feet below the location of the plant thermocouple for furnace temperature measurement. Gas temperatures in this zone are monitored and maintained near 1500°F (815 °C). At this point the gas flow reversed from the upward flow in the combustion chamber to a somewhat downward flow through the superheater. Flakes of burning refuse carried in the flue gas stream resulted in relatively high temperature and a blizzard of impinging particles.

Two of the eight hour probe runs were made in a relatively cool location which was about 15 ft downstream of the hotter location. At this point the tubes were practically black and the gas temperature as monitored by the probe thermocouple was in the range 1100–1200°F (593–650°C). The corrosion rates of the carbon steel and the P-22 alloy (Fig. 6) exposed at low gas temperature showed only a slight variation with metal temperature as compared to Figs. 3 and 4 where the corrosion rates increased rapidly with metal temperature when exposed to high gas temperature. The corrosion data demonstrated that the same reduced temperature dependence existed at low gas temperature when the sludge was burned with the refuse. Under these low-temperature conditions, there was no apparent difference in the corrosion rates between the carbon steel and the P-22 alloy.

It should be noted that a reduction in gas temperature is more effective in reducing the corrosivity of the environment over the entire metal temperature range than is the addition of sludge to the fuel. Thus, although additives to the refuse may improve the life of boiler tubes the design of the boiler to reduce the temperature in the steam generator section would also provide a significant improvement in boiler tube life.

Effects of "Alonizing". Another corrosion-resistant material employed on this program was an Alonized coating. This coating consisted of an aluminum-rich layer about 15 mils (381 micrometers) thick applied to the A106 carbon steel by a pack-aluminizing process. This process forms layers of hard intermetallic aluminum-iron com-

Downloaded 01 Jun 2010 to 171.66.16.58. Redistribution subject to ASME license or copyright; see http://www.asme.org/terms/Terms_Use.cfm

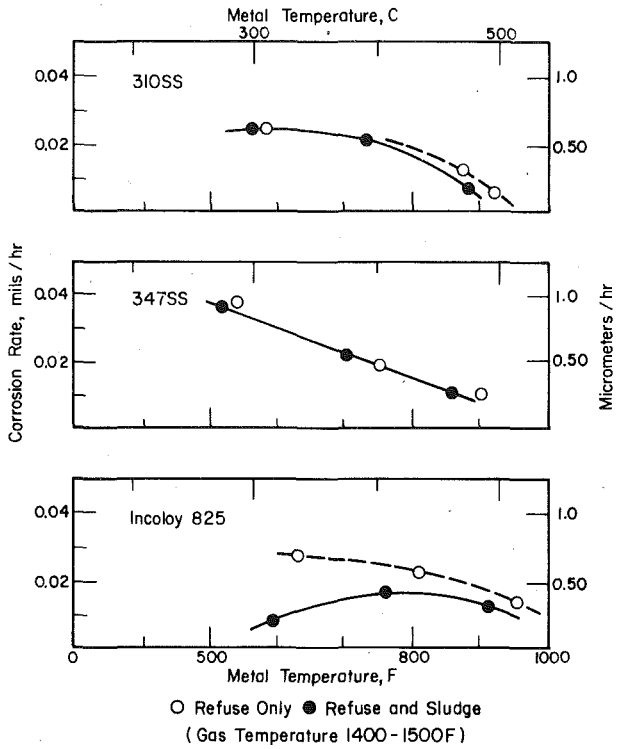


Fig. 5 Corrosion rates of stainless steels and Incoloy 825 as a function of metal temperature (eight hours exposure)

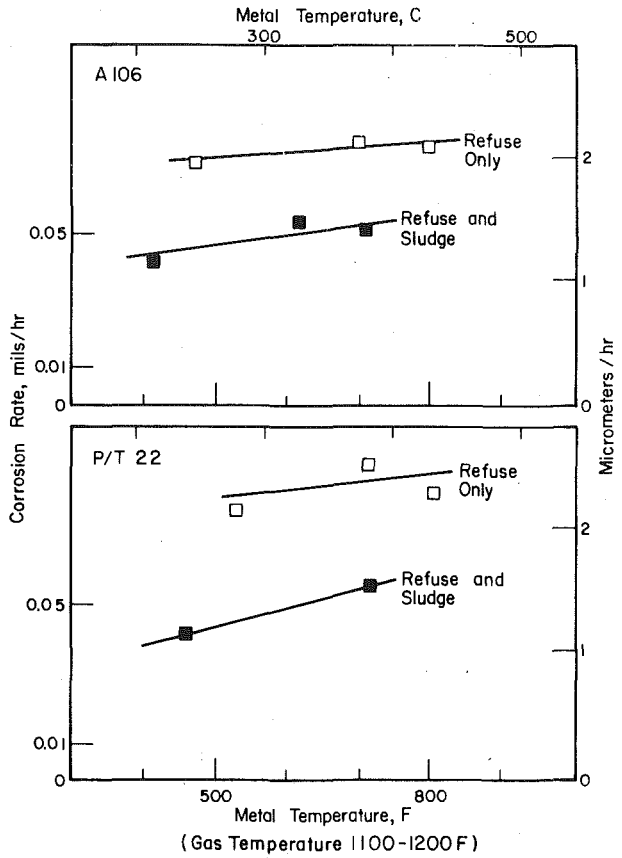


Fig. 6 Corrosion rates of carbon and low alloy steel at reduced gas temperature (eight hour exposure)

pounds with the capability of forming a corrosion-resistant aluminum oxide on the outer surface.

Due to the nature of the coating process, the durability of the Alonized specimens could not be measured quantitatively. Both the thickness and the reaction depth of the coating varied from sample to sample and were measured only after sectioning for metallography following the exposure. As applied to the A 106 steel the coating thicknesses ranged from 9 to 18 mils. The variation of thickness in different locations on single samples varied only 1 to 6 mils after exposure. In all cases a protective iron-rich intermetallic compound remained intact on the parent metal. This innermost layer (probably Fe_3Al) was at least 3 mils thick. The outermost layer, possibly $FeAl_3$, showed occasional fissures as deep as 9 mils but usually only 3 to 4 mils. Thus the Alonizing demonstrated complete protection during exposures of 8, 80, and 816 hours, for average metal temperatures between 400 and 830°F (204 and 443°C).

Flue Gas Analyses. The composition of the furnace gases in the location of the higher temperature probe was determined for refuse burning with and without sewage sludge. Standard EPA sampling techniques were used for measurement of sulfur oxides, nitrogen oxides, and furnace particulate collection. HCl concentrations were determined by measuring the chloride content of the impingers in the sulfur oxides train. Oxygen and CO_2 were measured by Orsat analysis of a bag sample of the gases accumulated during a run. The CO and organic compounds were determined by mass spectrometer analysis of grab samples taken in evacuated bulbs. The results of the measurements are summarized in Table 6.

The data show that more SO_2 was present in the flue gases when sewage sludge was burned than when refuse was burned alone. This result is indicative of the additional sulfur contributed by the sludge, which would inhibit chloride corrosion, as demonstrated in our earlier work [3]. There also was less HCl in the combustion gases when sludge was burned, indicating some dilution of the refuse by the low chloride sludge. The other gas components that were measured did not show much difference in concentration for the two fuel compositions. An increase in moisture was observed when the sludge was burned, reflecting the high moisture content (78 percent) of that material. The completeness of combustion is indicated by the low concentrations of carbon monoxide and methane. The gas samples were examined

Table 6 Composition of flue gases at Harrisburg incinerator

	Flue gas composition for fuel indicated	
	Refuse	Refuse & sewage sludge
SO_2, ppm	135	240
SO_3, ppm	4	3
HCl, ppm	485	345
NO_x, ppm	106	84
O_2, %	9.0	8.5
CO_2, %	7.5	9.5
CO, %	0.03	0
H_2O, %	8.8	9.8
CH_4, ppm	10	17

for other hydrocarbons in addition to methane, but their concentrations all proved to be below the detection limit of 0.1 ppm.

Deposit and Corrosion Product Analyses. Since the corrosion probe and boiler tubes were not soot blown during any of the experiments, all specimens collected particulate deposits and sometimes an appreciable layer of iron oxides and corrosion product "scale" which was originally the outer surface of the metallic specimens. Susceptible metals produced porous scales up to about 0.05 in. (1.3 mm) thick. Over the scale of metallic oxides were thicker layers of deposited particles. These ranged from about 0.06 to 0.5 in. (1.6 to 12.7 mm) in thickness after the 8-hour exposures and about twice that for the 80 and 816 hour runs. These loose deposits were brushed from the probe and identified by their location on the probe in three groups: i.e., Specimens 1–6 for low metal temperatures, Specimens 7–12 for moderate, and Specimens 13–18 for highest metal temperatures.

Deposits were individually analyzed by wet chemistry for total

Downloaded 01 Jun 2010 to 171.66.16.58. Redistribution subject to ASME license or copyright; see http://www.asme.org/terms/Terms_Use.cfm

sulfur and chlorides. As in prior studies, chlorine levels were higher for lower metal temperatures and briefer exposure times. All values are tabulated along with the optical emission analyses for metals in Table 7. High chloride levels are associated with the rapid early attack of exposed metal. However, ferric chloride decomposes at temperatures above 600°F (315°C) leaving little trace of chloride but leaving a porous iron structure susceptible to oxidation. The eventual oxidation products may be influenced by the nature and composition of the ensuing deposits. The previous Battelle work demonstrated the function of a sulfur-bearing fuel in converting chlorides to sulfates prior to deposition. The sulfates accumulate in the slag and deposits rather than chlorides, thus preventing corrosion by HCl and chlorine.

As a long term result, the tube life is extended while the sulfur accumulates and the chloride remains in the gaseous phase. Thus the amount of sulfur remains near 8 to 10 weight percent for deposits collected over 8, 80, or 816 hours for all regions of the corrosion probe. However, the concentration of chlorides falls from 3 to 5 percent for deposits on cool tubes exposed 8 hours, down to practically zero chloride in deposits collected during the 816-hour exposure (Probe 46). During this same range of exposure times, the amounts of heavy metals associated with the sulfates remained relatively constant. These elements are calcium, potassium, sodium, lead, magnesium and zinc.

Chlorides were easily identified only in the short-term deposits on the specimens where metal temperatures were below 600°F (315°C). However, weak X-ray diffraction patterns for sodium chloride were identified on two of the three scale samples examined. Even stronger evidence for the earlier presence of iron chloride was the strong X-ray diffraction pattern for β-FeOOH. This compound is the product of hydrolyzing the iron chloride. Other compounds identified by X-ray diffraction in the metallic scale include iron sulfide and iron oxides (magnetite, hematite, and wustite).

In the loose deposits, the major compounds identified were silica or quartz, calcium sulfate, and iron oxides. Many of these particles were spheroids and had probably melted in the combustion zone. Selected deposits were analyzed by energy dispersion of their X-rays (EDAX) to confirm and to localize the elemental analyses from optical emission spectroscopy.

The EDAX technique also was able to detect a reasonable level of chloride in the oxide scales removed from two carbon steel specimens on the 80-hour probe and also in the edge of a surface pit in a T22 specimen from that probe. Typical X-ray intensities of the chlorides averaged about a tenth that of iron as the parent metal basis. In the intact shells of oxide peeled from the carbon steel specimens, the chloride intensity was 0.12 and 0.02 of the iron intensity, respectively. Hence chlorides were positively identified at the bottom of pits and at the interface between sound metal and scaling oxides, demonstrating participation by chlorine in the corrosion reactions. Conversely, chlorides were difficult or impossible to detect in the outer layers of deposited particles.

Conclusions

Corrosion probe exposures conducted at the Harrisburg, Pennsylvania, incinerator demonstrated that the addition of low-chloride sewage sludge to municipal refuse reduced the corrosion of susceptible metals caused by chlorine in the refuse. Specific conclusions from this research program were:

1 The corrosiveness of the refuse combustion environment to carbon steel as indicated by 8-hour exposures was only ½ as great with sewage sludge present. Less reduction occurred with T22 steel, very little with Incoloy 825 and essentially none with Types 310 and 347 stainless steel.

2 The corrosion resistance of alloys to the refuse-sludge combination in decreasing order was Incoloy 825, 310 stainless steel, 347 stainless steel, T22 low chromium alloy, and A106 carbon

Table 7 Elemental analyses of deposits on corrosion probes

Probe No.	Composition, weight percent																	
	41			42			43			44			45			46		
Temperature zone[a]	L	M	H	L	M	H	L	M	H	L	M	H	L	M	H	L	M	H
Element																		
Si	7	7	7	6	6	6	6	6	6	6	6	6	10	8	10	8	8	8
Al	7	7	7	7	7	7	4	4	4	4	5	4	4	3	4	5	6	8
Ca	11	11	14	6	6	6	10	10	10	10	10	10	8	10	10	10	10	10
Fe	3	2	2	3	3	3	2	2	2	2	2	2	3	4	3	8	3	8
S[b]	8.0	9.5	8.2	8.1	8.8	9.3	10.4	11.5	10.5	8.5	9.6	9.5	7.7	10.6	10.7	11.3	9.7	10.2
Pb	4	4	2	6	11	11	5	3	3	4	10	10	5	.5	4	4	4	4
K	7	14	14	6	7	11	6	6	6	2	3	3	3	5	6	6	4	6
Mg	0.8	0.8	0.8	0.8	0.8	0.8	1	1	1	1	1	1	1	1	2	1	1	1
Zn	4	4	4	5	5	5	5	5	5	5	8	8	4	3	6	3	3	3
Na	6	6	6	6	6	6	6	4	5	2	3	3	5	5	6	3	3	3
Cl[b]	5.6	1.5	0.4	3.3	2.2	1.8	0.5	0.1	0.04	2.9	1.8	1.8	4.6	0.3	1.4	0.01	0.01	00
Ti	0.8	0.8	0.8	0.8	0.8	0.8	0.5	0.5	0.5	0.5	0.5	0.5	0.5	0.5	0.5	0.5	0.5	0.5
Cu	0.05	0.05	0.05	0.05	0.05	0.05	0.1	0.1	0.1	0.1	0.1	0.1	0.3	0.1	0.2	0.1	0.1	0.1
Cd	0.1	0.1	0.05	0.05	0.05	0.05	0.1	0.08	0.08	0.08	0.2	0.1	0.1	ND	0.1	0.1	0.08	0.1
Ba	0.1	0.1	0.1	0.06	0.06	0.06	0.05	0.05	0.06	0.06	0.06	0.04	0.08	0.08	0.08	0.06	0.06	0.06
Cr	0.2	0.2	0.2	0.5	0.5	0.5	0.05	0.05	0.05	0.08	0.08	0.05	0.1	0.8	0.1	0.5	0.08	0.4
Sb	0.08	0.08	0.05	0.1	0.1	0.1	0.1	0.1	0.1	0.1	0.1	0.1	0.5	0.3	0.5	0.1	0.08	0.08
Mn	0.2	0.2	0.1	0.1	0.08	0.08	0.01	0.01	0.01	0.02	0.02	0.02	0.2	0.2	0.2	0.05	0.01	0.04
Zr	0.01	0.01	0.02	0.01	0.01	0.01	0.02	0.01	0.03	0.02	00	00	0.02	0.02	0.02	0.02	0.05	0.04
Ni	0.6	0.06	0.06	0.2	0.1	0.1	0.03	0.03	0.05	0.05	0.02	0.02	0.03	0.2	0.1	0.2	0.1	0.5
Sn	0.6	0.6	0.4	0.8	0.8	0.8	0.2	0.1	0.1	0.2	0.4	0.5	0.2	0.2	0.3	0.5	0.1	0.4
V	0.02	0.02	0.02	0.01	0.01	0.01	0.02	0.02	0.02	0.02	0.02	0.02	0.01	0.01	0.01	0.02	0.02	0.02
Mo	0.01	0.01	0.01	0.02	0.02	0.01	0.01	0.01	0.01	0.02	0.02	0.01	00	0.02	00	0.05	0.01	0.04
Ag	0.01	0.01	0.01	0.01	0.01	0.01	00	00	00	00	00	00	00	00	00	00	0.01	0.01
B	0.02	0.02	0.03	0.03	0.02	0.02	0.02	0.01	0.02	0.02	0.02	0.02	0.02	0.02	0.02	00	0.01	0.01
Bi	0.01	0.01	0.01	0.01	0.01	0.01	00	00	00	00	00	00	00	00	00	0.01	00	0.01
Co	00	00	00	00	00	00	00	00	00	00	00	00	00	00	00	0.01	0.02	0.02

(a) Specimens from each probe were subdivided into groups from three metal temperature regions: L for low (300 to 600 F), M for medium (500 to 800 F), and H for high (700 to 1000 F).

(b) Wet chemistry techniques were used for sulfur and chlorine only. Others were semiquantitative, optical emission spectroscopy.

Note: 00 = barely detectable.

Downloaded 01 Jun 2010 to 171.66.16.58. Redistribution subject to ASME license or copyright; see http://www.asme.org/terms/Terms_Use.cfm

steel. An aluminized coating on steel remained intact during the exposures and could be a cost-effective alternative.

3 The corrosion rates decreased with exposure time in the presence of sewage sludge and appeared to level off at about 1000 hours.

4 For carbon and low alloy steels the corrosion rates increased with metal temperature in the range 500–900°F (260–482°C), while those for stainless steels decreased.

5 The short-term corrosion rates at gas temperatures of 1100–1200°F (593–649°C) were only 1/5 as great as at 1500°F (815°C) and showed less increase with metal temperature.

6 The increased superheater tube life at the Harrisburg incinerator is the result of the addition of sewage sludge and reduced frequency of soot blowing rather than the use of T22 alloy for the tubing.

The cofiring of sewage sludge with municipal refuse is a practical means of reducing corrosion of heat recovery surfaces and at the same time providing sludge disposal. However, it should be pointed out that the sewage should not have been treated with ferric chloride, because chloride residue in the sludge would promote corrosion.

Acknowledgments

This project has been financed in part with Federal funds from the Environmental Protection Agency under Grant No. R-804008-02-2 from the Industrial Environmental Research Laboratory, Cincinnati, Ohio. The contents do not necessarily reflect the views and policies of the Environmental Protection Agency, nor does mention of trade names or commercial products constitute endorsement or recommendation for use.

The cooperation of the Bureau of Incineration, Harrisburg, Pennsylvania, particularly Mr. Jack R. Karper, Deputy Director of Public Works, and Mr. James E. Wilt, Bureau Chief, Bureau of Incineration, is gratefully acknowledged. Also the recommendations and assistance of the Project Officer, Mr. Robert A. Olexsey of the Industrial Environmental Research Laboratory is acknowledged. Battelle personnel contributing special assistance to the program were Mr. J. S. McNulty, Mr. L. A. Salmons, and Mr. R. R. White.

References

1 Krause, H. H., Vaughan, D. A., Miller, P. D., "Corrosion and Deposits From Combustion of Solid Waste," ASME JOURNAL OF ENGINEERING FOR POWER, Vol 95, No. 1, Jan. 1973, pp 45–52.

2 Krause, H. H., Vaughan, D. A., Miller, P. D., "Corrosion and Deposits From Combustion of Solid Waste, Part 2—Chloride Effects on Boiler Tube and Scrubber Metals," ASME JOURNAL OF ENGINEERING FOR POWER, Vol 96, No. 3, July, 1974, pp 216–222.

3 Krause, H. H., Vaughan, D. A., Boyd, W. K., "Corrosion and Deposits From Combustion of Solid Waste, Part 3—Effects of Sulfur on Boiler Tube Metals," ASME JOURNAL OF ENGINEERING FOR POWER, Vol 97, No. 3, July, 1975, pp 448–452.

4 Krause, H. H., Vaughan, D. A., and Boyd, W. K., "Corrosion and Deposits From Combustion of Solid Waste, Part 4—Combined Firing of Refuse and Coal," ASME JOURNAL OF ENGINEERING FOR POWER, Vol 98, No. 3, July, 1976, pp 369–374.

5 Krause, H. H., Vaughan, D. A., Cover, P. W., Boyd, W. K., Oberacker, D. A., "Corrosion and Deposits From Combustion of Solid Waste, Part 5—Firing of Refuse With High-Sulfur Coal," ASME JOURNAL OF ENGINEERING FOR POWER, Vol 99, No. 3, July, 1977, pp 449–459.

6 Krause, H. H., Vaughan, D. A., Cover, P. W., Boyd, W. K., Olexsey, R. A., "Corrosion and Deposits From Combustion of Solid Wastes, Part 6—Processed Refuse as a Supplementary Fuel in a Stoker-Fired Boiler," Paper No. 78-WA/FU-4, ASME Winter Annual Meeting, Dec. 1978.

7 Miller, P. D. and Krause, H. H., "Corrosion Studies in Municipal Incinerators," U.S. Environmental Protection Agency Report SW-72-3-3, 1972.

8 Letter Report to Gannett, Fleming, Corddry, and Carpenter, Inc., Harrisburg, Pa. from Battelle's Columbus Laboratories, Sept. 14, 1973.

Downloaded 01 Jun 2010 to 171.66.16.58. Redistribution subject to ASME license or copyright; see http://www.asme.org/terms/Terms_Use.cfm

N. K. Rizk
Lecturer.
Faculty of Engineering, Mechanical Department,
Cairo University,
Giza, Egypt

A. H. Lefebvre
Professor and Head,
School of Mechanical Engineering,
Purdue University,
West Lafayette, Ind.

The Influence of Liquid Film Thickness on Airblast Atomization

The influence of initial liquid film thickness on mean drop size and drop-size distribution was examined using two specially designed airblast atomizers. Both were constructed to produce a flat liquid sheet across the centerline of a two-dimensional air duct with the liquid sheet exposed on both sides to high velocity air. In one case a thin film of uniform thickness was produced by injecting the liquid through a porous plate located just upstream of the atomizing edge. The film thickness, t, was then measured by a needle contact device. In the second design the fuel entered the air stream through a thin slot whose height could be adjusted accurately to vary and control the initial film thickness. Drop sizes were measured by the well-established light-scattering technique. From analysis of the processes involved, and from correlation of the experimental data, it was found that high values of liquid viscosity and liquid flow rate result in thicker films. It was also observed that thinner liquid films produce better atomization, according to the relationship, $SMD \propto t^{0.38}$.

Introduction

Many airblast atomizers of the type employed in gas turbine combustors are based on a simple concept whereby the liquid fuel is first spread into a thin continuous sheet or film before being exposed to the atomizing action of high velocity air. A typical example is illustrated in Fig. 1. In this design the liquid flows through a number of equispaced slots into a weir from which it flows over a "prefilming" surface before being discharged at the tip of "edge" of the atomizer. Usually, the slots are cut tangentially in order to impart a swirling motion to the liquid as it flows downstream, which helps to promote a uniform film thickness. Another contributing factor to uniformity of film thickness is the drag exerted on the liquid surface by the air flowing through the atomizer. Thus, in a well designed airblast atomizer, the combined effect of initial fuel swirl and the drag forces created at the liquid/air interface is to produce a liquid sheet of fairly uniform thickness at the atomizing edge.

As airblast atomizers have become more widely used in both aircraft and industrial applications, much interest has been aroused in the contribution made by this prefilming of the fuel to its subsequent atomization. Of special concern is the minimum thickness attained by the liquid sheet because, if this thickness is related to the mean drop size of the spray, then clearly it should be an important consideration in airblast atomizer design.

In order to shed more light on the role of the prefilming process in airblast atomization, it was decided to initiate an experimental program and to conduct the investigation in two separate parts. One part comprised a series of experiments on the factors governing the thickness of the liquid film at the atomizing edge. The second part was designed to clarify the relationship between liquid film thickness and the mean drop size of the spray.

Experimental

In order to produce a liquid film that would be flat and consequently easier to measure, control and photograph, the conventional type of airblast atomizer of circular cross-section, was discarded in favor of a two-dimensional design, as illustrated in Figs. 2 and 3. The air passages were made clean and smooth to avoid any disturbance to the flow, with minimum area at the atomizing edge to attain maximum velocity in the plane of the initial disintegration of the liquid sheet. The two separate air streams which enclosed the liquid sheet

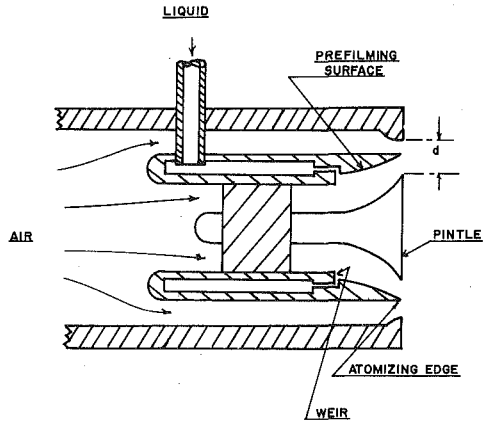


Fig. 1 Typical prefilming type of airblast atomizer

Contributed by the Gas Turbine Division for publication in the JOURNAL OF ENGINEERING FOR POWER. Manuscript received at ASME Headquarters March 16, 1978.

Copyright © 1980 by ASME
Downloaded 01 Jun 2010 to 171.66.16.58. Redistribution subject to ASME license or copyright; see http://www.asme.org/terms/Terms_Use.cfm

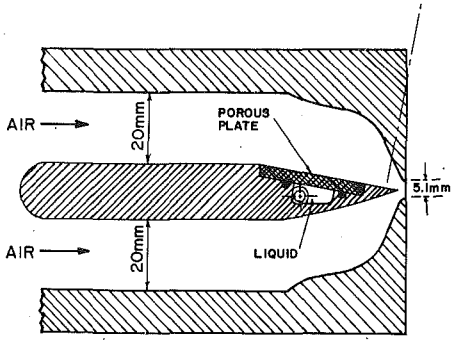


Fig. 2 Cross-sectional view of atomizer A

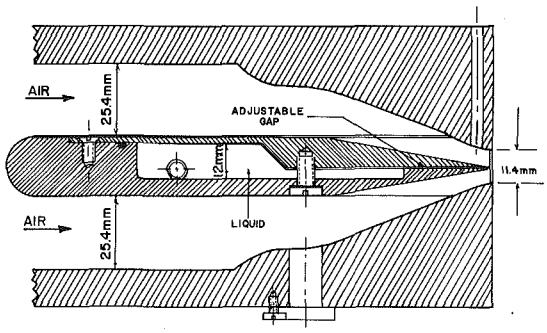


Fig. 3 Cross-sectional view of atomizer B

issued from the atomizer in a direction parallel to the sheet in order to achieve the best possible atomization.

Two different types of atomizer were used in the tests. In one, atomizer A, the two side walls were made of plexiglass to facilitate observation of the formation of the liquid film. The liquid was supplied to the central body of the atomizer through holes in the side walls, an arrangement which helped to maintain the air passages aerodynamically clean. The liquid emerged into the upper air stream through a plate of sintered metal which was located flush with the prefilmer at a short distance from the atomization edge. Along the centerline of the atomizer a hole was drilled in the upper nozzle, as illustrated in Fig. 2, through which a micrometer spindle could move in a direction at right angles to the prefilmer surface. This micrometer was used to measure liquid film thickness at a point just upstream of the atomizing edge.

A drawback to atomizer A was that no control could be exercised over the liquid film thickness which was governed solely by the physical properties of the liquid and by the relative flow rates of liquid and air. This deficiency was eliminated in atomizer B, for which a main design objective was to have the capability of varying and controlling the liquid film thickness in order to establish its influence on atomization quality. The mechanism employed to accomplish this is illustrated in Fig. 3. It featured a variable-width slot through which the liquid was injected along the axis of the atomizer into the intersection of two parallel air streams. The width of the slot was varied by turning a screw which had a special thread to allow the gap width to be controlled to fine limits. The gap width was read from a dial indicator which was calibrated in 2.5 μm intervals. It was also frequently checked using accurate feeler gauges. The two plexiglass walls used with design A were replaced with metal counterparts, and the width of the atomizer was made smaller (5 cm) to control the gap width more accurately. However, the system of feeding the liquid through the side walls was retained.

As the air flow rates required for these tests were fairly low, a small rotary fan proved quite adequate. The total air supply was divided into two separate paths leading to the atomizer. The two air streams were regulated by valves and also by bleeding off air at the outlet of the fan. Air mass flow rates were measured using standard orifice plates fitted with D and $D/2$ pressure tappings according to BS1042. Air temperature was monitored by means of thermocouples, while the air velocity of both streams was measured on centrally located rakes of four pitot tubes in each air duct. All tests were conducted at normal atmospheric conditions of pressure and temperature.

The liquids employed were: water ($\mu = 0.001$, $\sigma = 0.0735$ and $\rho = 1000$) and kerosine ($\mu = 0.00129$, $\sigma = 0.02767$, and $\rho = 784$). The water was delivered directly from the test house supply while kerosine was fed to the atomizer from a nitrogen-pressurized drum. Liquid flow rates were measured on calibrated Fisher and Porter flowmeters.

Measurement of Liquid Film Thickness. Various methods of measuring liquid film thickness were considered for atomizer A, and several tested, the most satisfactory being a needle contact device. The needle was mounted on the tip of a micrometer spindle, and the whole unit was made part of an electrical circuit so that a lamp was caused to light at the first contact between the liquid and the needle. By this means the liquid thickness could be measured to an accuracy of 2.5 μm. The point of contact was also observed visually by means of light reflected on the liquid surface and magnified by a lens on the other side. For kerosine, which is not electrically conductive, the point of contact was always detected in this manner.

The effects of air velocity and liquid flow rate on water film thickness are illustrated in Fig. 4. The observed decrease in film thickness with increase in velocity is perhaps to be expected, due to the higher shear stress exerted by the air on the water surface. Raising the liquid flow rate might also be anticipated to produce a thicker film, and this is confirmed by the data plotted in Fig. 4.

The results for kerosine show similar trends in regard to the effects of air velocity and liquid flow rate on film thickness, as illustrated in Fig. 5. Comparison of Figs. 4 and 5 indicates that under comparable flow conditions, the film thickness for kerosine is always greater than that of water.

Measurement of Mean Drop Size. Drop sizes were measured using the light-scattering technique first proposed by Dobbins, Crocco and Glassman [1]. The method is based on the forward scattering of a parallel beam of light due to its passage through the spray. The optical system employed and its modus operandi are fully described in [2, 3]. Its main advantage is that it provides an accurate measurement of spray SMD (Sauter Mean Diameter), and it does not affect secondary atomization as occurs with certain physico-chemical techniques, e.g., droplet freezing.

The method employed for atomizer B was to set the liquid discharge slot to some predetermined width and then to examine the effects of air velocity, liquid flow rate and air/liquid ratio (ALR) on SMD. In all tests the SMD was measured with the light path at right angles to

Nomenclature

SMD = Sauter mean diameter = $\Sigma nd^3/\Sigma nd^2$, μm
n = number of drops, the diameter of which is d μm
W = mass flow rate, kg/s
U = flow velocity, m/s
t = liquid film thickness, m
A = cross-sectional area of airflow passage in plane of maximum air velocity, m^2
d_h = annulus height measured in same plane as A, m
f = friction factor
Re = Reynolds number
μ = viscosity, kg/ms
ρ = density, kg/m^3
σ = surface tension, N/m
τ = shear stress, N/m^2

Subscripts

A = air
L = liquid
i = interface (liquid/air)

Downloaded 01 Jun 2010 to 171.66.16.58. Redistribution subject to ASME license or copyright; see http://www.asme.org/terms/Terms_Use.cfm

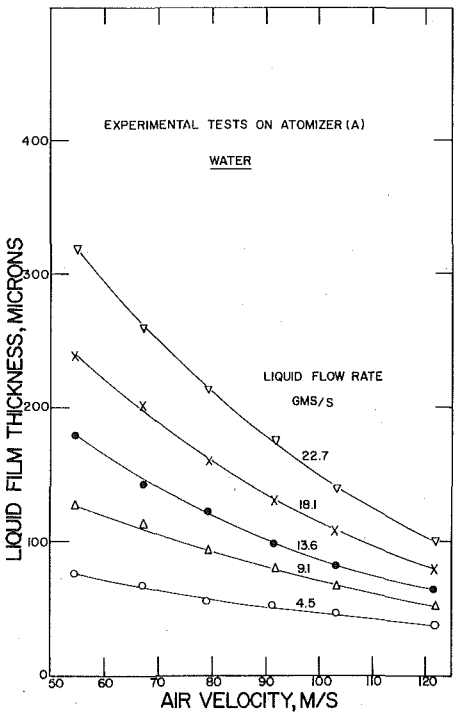


Fig. 4 Variation of water film thickness with air velocity for different water flow rates

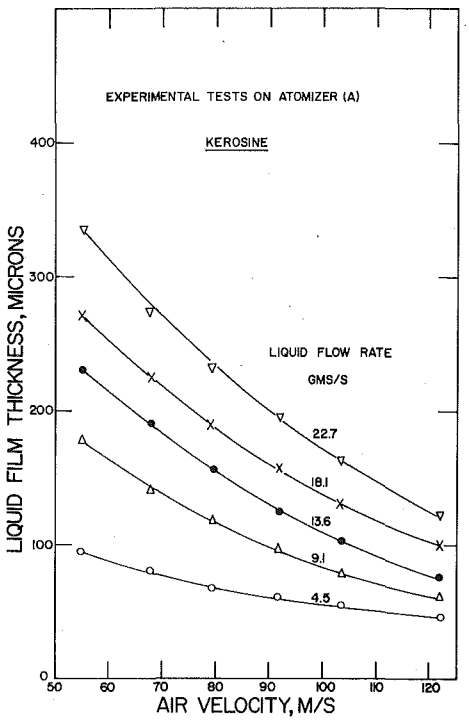


Fig. 5 Variation of kerosine film thickness with air velocity for different kerosine flow rates

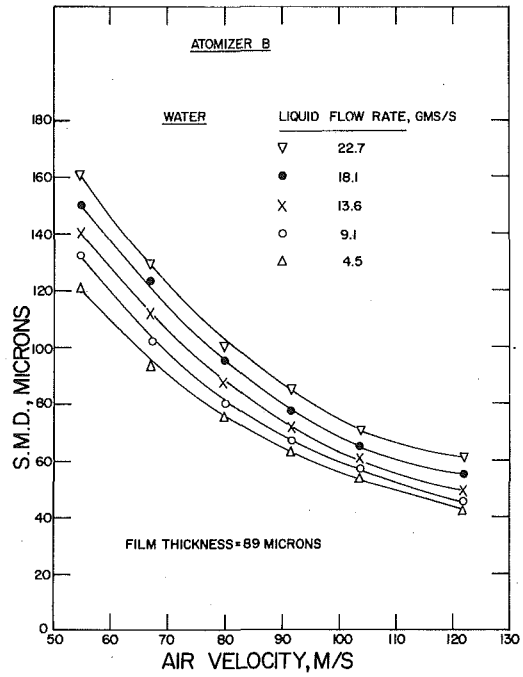


Fig. 6 Influence of air velocity on SMD for various liquid flow rates

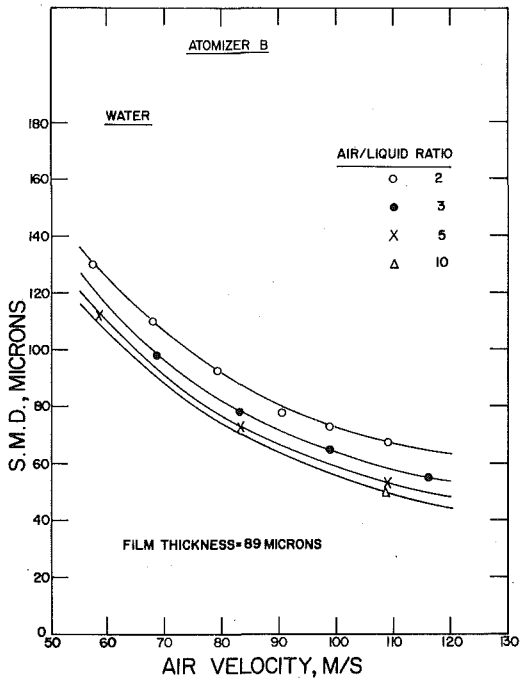


Fig. 7 Influence of air velocity on SMD for various air/liquid ratios

the liquid sheet. Only the central section of the sheet was examined, in order to avoid the large drops that are produced at the extremities of the atomizing edge. The results obtained with water for a slot width (assumed equal to initial liquid film thickness) of 89 μm are shown in Fig. 6 and 7. Fig. 6 illustrates the effects of air velocity and liquid flow rate on SMD, while Fig. 7 demonstrates the influence of air/liquid ratio. It is of interest to note in this figure that the highest measured values of SMD correspond roughly to twice the initial liquid film thickness.

By repeating these tests for different slot widths, the curves shown in Fig. 8, 9 and 10 could be plotted. Corresponding curves were also obtained for kerosine. All the figures show that a reduction in the initial liquid film thickness produces a finer spray. In fact, by plotting the data on logarithmic paper, it was found that, for both water and kerosine SMD $\propto t^{0.38}$. Thus, in the design of airblast atomizers, every effort should be made to insure the thinnest possible liquid sheet at the atomizing edge. In the following section the factors which govern the liquid film thickness in prefilming types of airblast atomizer are considered in more detail.

Downloaded 01 Jun 2010 to 171.66.16.58. Redistribution subject to ASME license or copyright; see http://www.asme.org/terms/Terms_Use.cfm

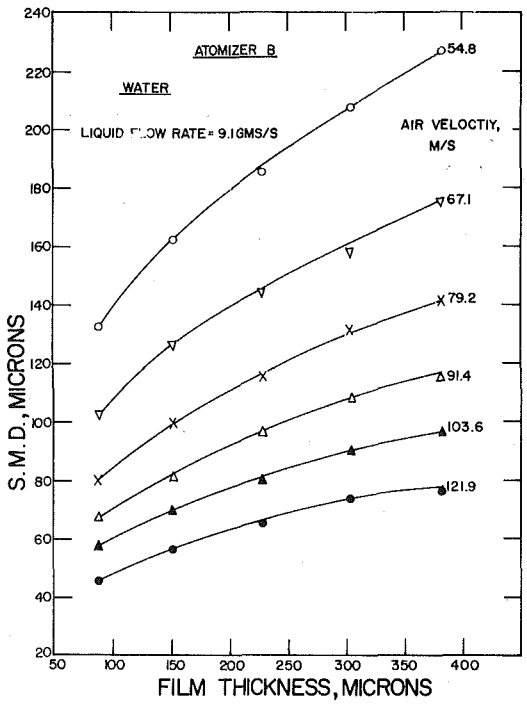


Fig. 8 Effect of film thickness on SMD for various air velocities

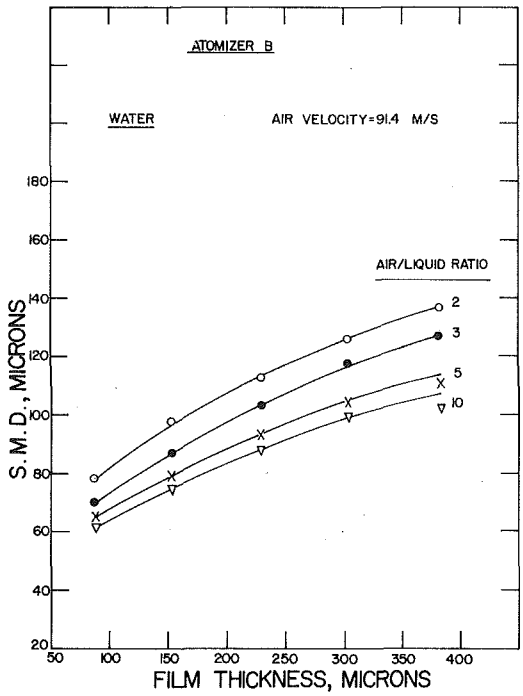


Fig. 10 Effect of film thickness on SMD for various air/liquid ratios

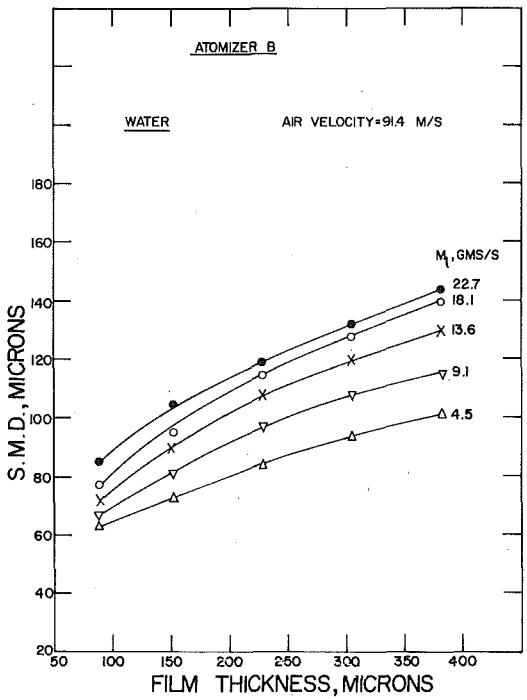


Fig. 9 Effect of film thickness on SMD for various liquid flow rates

Analysis of Experimental Data on Liquid Film Thickness. It is desirable to derive an expression for liquid film thickness in terms of all the relevant physical properties and flow parameters. To facilitate this, the shear stress in the thin liquid film will be assumed constant and equal to the wall shear stress, i.e.,

$$\tau = \mu_L U_i/t = 2\mu_L U_L/t \tag{1}$$

where

U_i = interfacial liquid velocity

U_L = mean velocity of liquid film

t = liquid film thickness

For the simplest case of a thin liquid film flowing along the inner wall of a circular pipe which also contains air flowing in the same direction, we have:

$$\tau = 2\mu_L W_L/t\rho_L A_L = 2\mu_L W_L/t^2\rho_L \pi d \tag{2}$$

where

d = equivalent diameter of pipe

A_L = cross-sectional area of liquid film

The interfacial friction factor is given by:

$$f_i = \tau/0.5\rho_A U_A{}^2 \tag{3}$$

Substituting τ from (2) into (3) gives:

$$f_i = 4\mu_L W_L/\pi\rho_A\rho_L d\, t^2 U_A{}^2 \tag{4}$$

According to Hewitt and Hill-Taylor [4], the interfacial friction factor is given by:

$$f_i = f_A(1 + 300t/d)$$

where f_A is the friction factor for air flowing along a smooth-walled tube in the absence of a liquid film.

For turbulent flow f_A is given by the Blasius equation:

$$f_A = 0.79(\mathrm{Re}_A)^{-0.25}$$

hence

$$f_i = 0.79(1 + 300t/d)(\mathrm{Re}_A)^{-0.25} \tag{5}$$

equating (4) and (5) leads to the following equation for liquid film thickness, t:

$$t^2(1 + 300t/d) = 16\mu_L W_L(W_A d/A\mu_A)^{0.25}/\rho_L\rho_A d\, U_A{}^2 \tag{6}$$

Values of t obtained from the above equation by a process of iteration were found to be appreciably higher than those observed experimentally. However, this equation did prove more successful in regard to its ability to predict general trends, which tended to suggest that it contained most if not all of the key parameters affecting liquid film thickness. On this assumption it was decided to seek an expres-

Downloaded 01 Jun 2010 to 171.66.16.58. Redistribution subject to ASME license or copyright; see http://www.asme.org/terms/Terms_Use.cfm

sion for t by dimensional analysis based on the main parameters contained in equation (6), i.e.,

$$t = f[\mu_L, \rho_L, \rho_A, U_A, (W_L/W_A), d]$$

This approach, combined with analysis of the experimental data, led to the following dimensionless expression for liquid film thickness:

$$(t/d_h) = 132(\mu_L/\rho_L d_h U_A)^{0.4}(W_L/W_A)^{0.8} \quad (7)$$

or

$$(t/d_h) = 132(\mathrm{Re}_L)^{-0.4}(W_L/W_A)^{0.8} \quad (8)$$

where Re_L is the Reynolds number of the liquid film, based on the air velocity, U_A, and the discharge annulus height, d_h.

The level of agreement between the predictions of t based on equation (8) and the corresponding experimental values obtained for water and kerosine, as shown plotted in Figs. 4 and 5, is illustrated in Fig. 11.

The main conclusion to be drawn from equation (8) is that, for any given prefilming type of airblast atomizer, the thickness of the liquid film produced at the atomizing edge is governed mainly by the liquid viscosity, the air velocity and the relative mass flow rates of liquid and air.

Conclusions

From a series of experiments carried out on two specially designed prefilming types of airblast atomizer, it was concluded that thicker liquid films lead to coarser sprays. Measurements of mean drop size obtained over wide ranges of air velocity, air/liquid ratio and initial film thickness, t, indicated that for water and kerosine, SMD $\propto t^{0.38}$.

It was also found that the thickness of the liquid film at the atomizing edge is described quite accurately by the following dimensionless equation:

$$t/d_h = 132(\mathrm{Re}_L)^{-0.4}(W_L/W_A)^{0.8}$$

Thus, high values of liquid viscosity and liquid flow rate result in thicker films, while high air velocity and high air density are conducive to thinner films and hence to better atomization. A thinner liquid film may also be obtained by reducing the annulus height of the air discharge nozzle. In practice, for any specified values of air velocity and liquid and water flow rates, this implies an increase in the diameter of the atomizing edge.

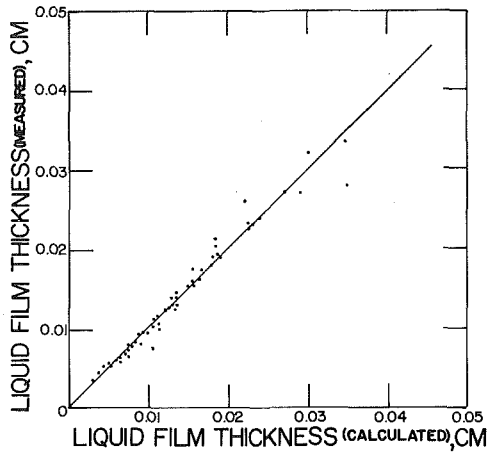


Fig. 11 Comparison between calculated and measured values of liquid film thickness

References

1 Dobbins, R. A., Crocco, L. and Glassman, J., "Measurements of Mean Particle Sizes of Sprays from Diffractively Scattered Light," *Journal of the American Institute of Aeronautics and Astronautics*, Vol. 1, No. 8, Aug. 1963, pp. 1882–1886.

2 Godfrey, C., "An Assessment of a Light-Scattering Technique for Drop Size Measurement," M.Sc. Thesis, Cranfield, 1969.

3 Rizk, N. K., "Studies on Liquid Sheet Disintegration in Air-Blast Atomizers," Ph.D. Thesis, Cranfield, 1977.

4 Hewitt, G. F. and Hill-Taylor, N. S., *Annular Two-Phase Flow*, Pergamon Press, 1970.

Downloaded 01 Jun 2010 to 171.66.16.58. Redistribution subject to ASME license or copyright; see http://www.asme.org/terms/Terms_Use.cfm

C. H. Sieverding
M. Stanislas
J. Snoeck

Von Karman Institute for Fluid Dynamics,
Chaussee De Waterloo,
72 B—1640 Rhode Saint Genese,
Belgium

The Base Pressure Problem in Transonic Turbine Cascades

Introduction

This paper summarizes the results of base pressure studies on transonic turbine cascades carried out at VKI in the past years.

The knowledge of the base pressure is of primary importance for the calculation of the trailing edge losses and the mass flow rate of cooling air in the case of trailing edge ejection as well as for the determination of the trailing edge shock system in supersonic outlet flow. The difficulty of the prediction of the base pressure is due to the predominant effect of viscous shear stresses in the trailing edge region. In fact the weakness of all potential flow methods lies in their incapacity to come up with that unique solution which is postulated by the presence of viscous forces.

The information on base pressure measurements in cascades is extremely scarce in the literature. Base pressure data were therefore systematically collected at VKI on a great number of cascades. An attempt is made to correlate these data by relating the base pressure to important cascade and flow parameters.

The term base pressure refers in general implicitly to a constant pressure zone at the base of the trailing edge. Base pressure measurements on blades in cascade assemblies are in general, however, limited to one single pressure tapping in the trailing edge because of the small trailing edge thickness. These measurements can therefore not give any information on the actual pressure distribution around the trailing edge. In view of these shortcomings resulting from tests on complete cascade configurations an additional test program was undertaken with the aim of obtaining more detailed information on the flow around the trailing edge. These tests were performed on a model representing the overhang section of converging turbine blade passages.

The particular objectives of these tests were:

- determination of the strength of the trailing edge separation shocks in the case of rounded trailing edges.
- comparison of the base pressure for rounded and rectangular trailing edges.
- control of the validity of the assumption of an isobaric mixing zone at the trailing edge.

Because of the more fundamental character of these tests compared to the cascade tests we shall start with the description of the model tests.

The experimental results of both the model and cascade tests will be compared to base pressure theories.

Contributed by the Gas Turbine Division of THE AMERICAN SOCIETY OF MECHANICAL ENGINEERS and presented at the Gas Turbine Conference and Exhibit and Solar Energy Conference, San Diego, Calif., March 12–15, 1979. Manuscript received at ASME Headquarters March 22, 1979. Paper No. 78-GT-120.

Model

The model shown in Fig. 1 is basically the same as the one described by Sieverding, et al. in [1], the main difference consisting in (1) an increased range of gauging angles defined as $\beta_2^* = \arcsin 0/g$ (2) a further improved pressure tapping distribution around the trailing edge.

The main bulk of the tests were carried out at limit loading conditions characterized by the shock configuration indicated in Fig 1 (the tail board shock S_1' passes behind reattachment point R). The angle β_2^* was varied from 90 to 19.4 deg with corresponding trailing edge suction side Mach numbers $M_{s,t} = 1.0$ to 2.3. The pressure side Mach number at the trailing edge was $M_{p,t} = 1.02$ and remained constant for all tests.

With respect to the simulation of limit loading conditions in cascades the above tests are only useful in the β_2^*-range of 19.4 to 45 deg. The justification of testing over a much wider range of β_2^*-values lies in the fact that the primary aim of these tests is the variation of $M_{s,t}$ rather than of β_2^* because the evaluation of the base pressure, through the base pressure theories, requires apart from the assumption of a fully developed turbulent boundary layer, only the knowledge of the suction side and pressure side Mach numbers at the trailing edge and the momentum thickness of the corresponding boundary layers.

A second test series was concerned with the variation of the downstream flow conditions at constant β_2^*. These tests were characterized by an interference of the tailboard shock S_1' with the suction side boundary layer of the main plate, the position of the interference point depending on the inclination of the tailboard.

The model length was chosen such that the ratios of the boundary layer momentum thickness at the trailing edge to the trailing edge thickness were in the range of typical cascade values:

$$\frac{\theta_s + \theta_p}{te} \simeq 0.05 \rightarrow 0.10$$

The plate was instrumented with very closely spaced pressure tappings. Special care was given to the trailing edge which was equipped with 19 pressure tappings (trailing edge thickness $te = 5$ mm). Compared to the model described in reference 1 the number of tappings of the present model was twice as high in the region of high pressure gradients. The pressure hole diameter was reduced to 0.2 mm.

Test Conditions

Total temperature T_0	280 K
Total upstream pressure (for all tests) P_0	2.3 bar
Reynolds number Re (based on inlet flow conditions and blade length)	10^7
Turbulence level	1 per cent
Blade surface	polished
State of boundary layer at trailing edge	turbulent

Copyright © 1980 by ASME

Downloaded 01 Jun 2010 to 171.66.16.58. Redistribution subject to ASME license or copyright; see http://www.asme.org/terms/Terms_Use.cfm

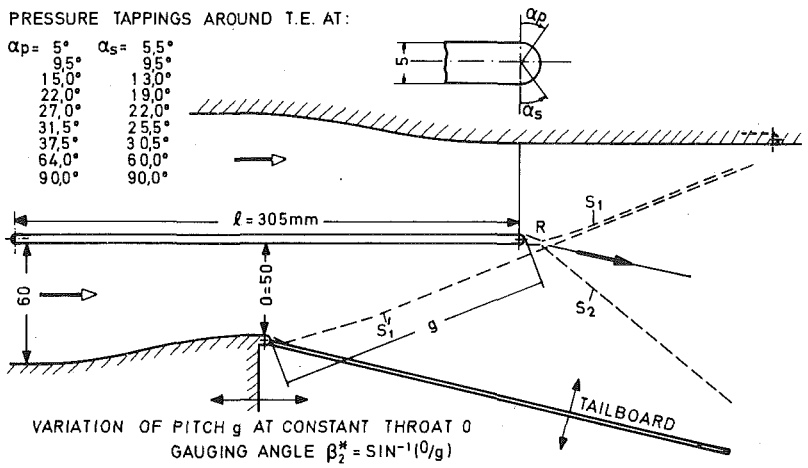


Fig. 1 Model

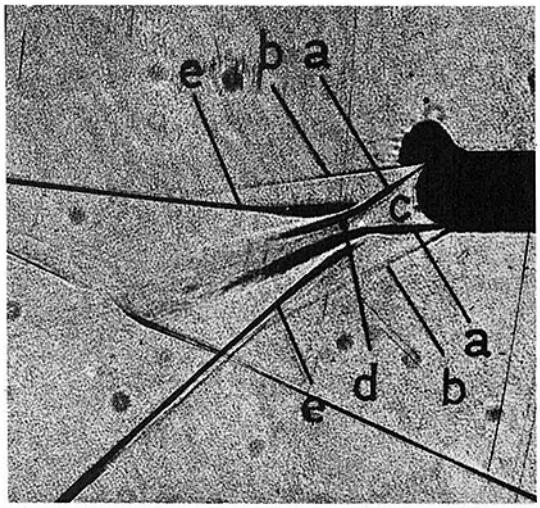


Fig. 2 Schlieren photograph of model at limit loading condition

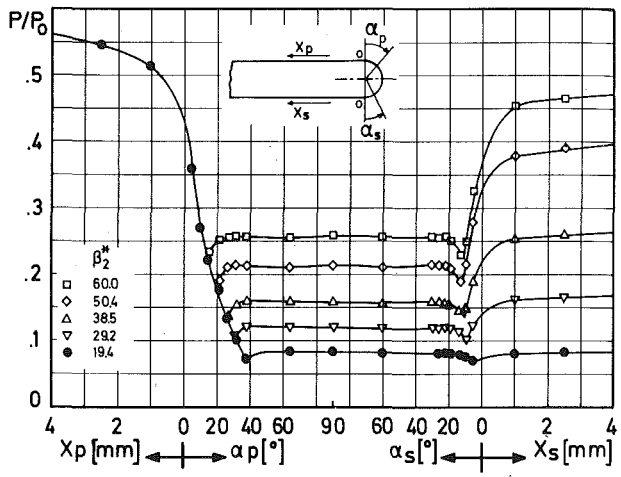


Fig. 3 Trailing edge pressure distribution for limit loading conditions (model)

Model Test Results

Limit Loading Condition. The Schlieren photograph in Fig. 2 shows all details of the trailing edge flow patterns for a rounded trailing edge at limit loading conditions: (a) free shear layers, (b) separation shocks, (c) dead water region, (d) reattachment region, (e) wake shocks, which are in general referred to as trailing edge shocks. The picture is taken for the model configuration $\beta_2^* = 20.8$ deg; the corresponding pressure side and suction side Mach numbers at the trailing edge are: $M_{p,t} = 1.02$ and $M_{s,t} = 2.25$.

The pressure distributions taken around the trailing edge allow us to define with sufficient accuracy the strength of the separation shocks. Fig. 3 presents only a few examples of the pressure distributions of all tested model configurations. The separation shock strength data of all configurations are replotted in Fig 4. However, only those

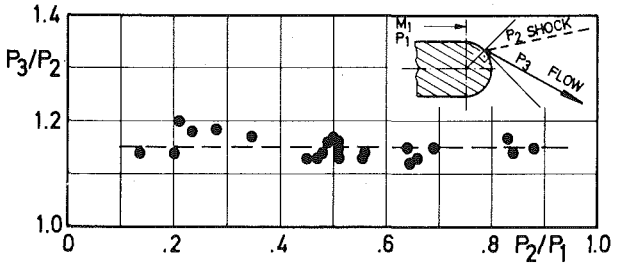


Fig. 4 Trailing edge separation shock strength

Nomenclature

A = area
A^* = throat area
c = chord
g = pitch
M = Mach number
M_b = base Mach number, $M_b = f(P_b/P_{01})$ (= velocity in free stream adjacent to trailing edge dead water region)
0 = throat height
p = pressure
te = trailing edge thickness
u = velocity
X = coordinate
α = angular position of pressure tappings around trailing edge
β_1 = inlet angle
β_2^* = gauging angle, $\beta_2^* = \arcsin 0/g$
δ = boundary layer thickness or trailing edge wedge angle
δ^* = boundary layer displacement thickness
θ = boundary layer momentum thickness
ϵ = angle between tangents to blade suction side in the throat and at the trailing edge, also called "suction side curvature"
exp. = experimental
S.S. curv. = rear suction curvature

Subscripts

b = base
C = correlation
e = free stream
p = pressure side
s = suction side or static
t = trailing edge
0 = total
1 = upstream
(except if noted otherwise in the text)
2 = downstream
3 = defined in Fig. 4

Downloaded 01 Jun 2010 to 171.66.16.58. Redistribution subject to ASME license or copyright; see http://www.asme.org/terms/Terms_Use.cfm

data which allowed a clear definition of the shock strength are used here. Differing from the notation generally used for the flow around the trailing edge, we shall use for the definition of the separation shock strength the following subscripts indicated in Fig. 4 i.e., (1) at the beginning of the trailing edge circle, (2) just ahead of the separation shock, (3) just downstream of the separation shock (base region). All data are within a bandwidth of $P_3/P_2 = 1.1 \rightarrow 1.2$. We propose as a separation criterion the mean value, $P_3/P_2 = 1.15$.

This result is in fact very close to the results of pressure measurements obtained earlier on a model with a much less refined pressure tapping distribution around the trailing edge (1). The very small scatter of the shock intensity data based on pressure measurements is in strong contrast to the wide scatter of shock strength data derived from measurements of shock and expansion angles from corresponding Schlieren photographs. It should be noted that the above separation criterion is furthermore confirmed by trailing edge pressure distributions taken at part load conditions. In conclusion it can be said that the local overexpansion at the trailing edge and the subsequent recompression through the separation shock are a local flow phenomenon without any significant effect on the evaluation of the base pressure and the trailing edge losses.

For comparison reasons the test program was extended to blades with rectangular trailing edges. It has been shown in [2] that as for the rounded trailing edge an overexpansion takes place at the trailing edge corner such that the separation point is situated slightly below this corner. Although Schlieren photographs taken on the blade with the rectangular trailing edge confirmed the existence of these shocks it was not possible to pick up this effect by pressure measurements across the trailing edge. The first pressure tapping was however only at a distance of 0.3 mm below the corner (trailing edge thickness te = 5 mm). In any event, any deviation within this distance with respect to the otherwise constant pressure distribution across the trailing edge should have only a minor effect on the integrated base pressure and therewith on the trailing edge losses.

Fig. 5 shows the evolution of the base Mach number, M_b (velocity in the free stream adjacent to the base region), as a function of the suction side Mach number at the trailing edge, $M_{s,t}$, for both the rounded and rectangular trailing edge. (The pressure side Mach number remains constant, $M_{p,t} = 1.02$). The difference between the two trailing edge geometries is insignificant except in the low supersonic range in which strong trailing edge flow instabilities were observed.

The experimental data in Fig. 5 were compared with results from base pressure theories for turbulent flows. For the present study the angular reattachment criterion of Carrière [3] was used. The application of this method requires in principle:

- uniform flow conditions at the trailing edge
- a fully developed turbulent boundary layer at the point of separation
- a boundary layer thickness which is small compared to the trailing edge thickness.
- an isobaric mixing zone

The first condition was partially removed by Carrière himself by introducing a correction term taking into account the effect of an interference of external expansion waves with the wake region, a case which is typical for a cascade working at limit loading conditions.

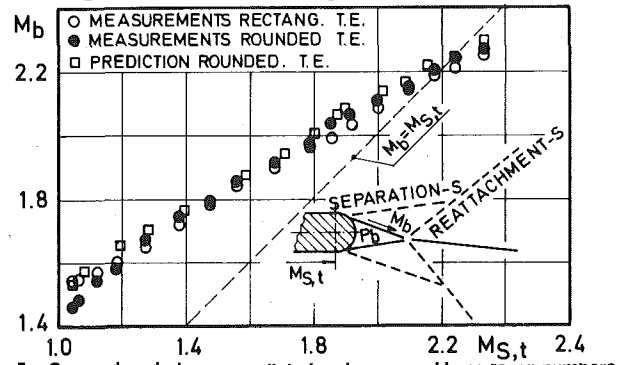


Fig. 5 Comparison between predicted and measured base Mach numbers at limit loading conditions for rounded and rectangular trailing edge (model)

With respect to the second and third condition it should be noted that the boundary layer was indeed turbulent on both sides of the trailing edge but that the boundary layer cannot be considered at all as being small compared to the trailing edge thickness. In fact δ/te was typically of the order of 0.5.

With respect to the last condition, i.e., isobaric mixing zone, we can refer to Fig. 6 reproduced from [1], which shows a typical static pressure distribution on the wake center line taken at $\beta_2^* = 46$ deg at limit loading condition. The figure shows that the isobaric mixing zone is in fact small compared to the recompression zone.

In spite of the differences between the required and actual flow conditions, the agreement between experimental and theoretical results is remarkable (Fig. 5), which indicates that the domain of practical application of Carrière's angular reattachment criterion is greater as assumed originally.

Part Load Conditions. The term part load conditions is used here in contrast to limit load conditions and refers to flow conditions characterized by a suction side shock boundary layer interaction. The shock positions were varied through the inclination of the tailboard. Tests were performed for the model configurations $\beta_2^* = 29.2$, 24.0 and 19.4 deg with the blade having the rounded trailing edge. Fig. 7 shows as an example the blade velocity distributions for $\beta_2^* = 29.2$

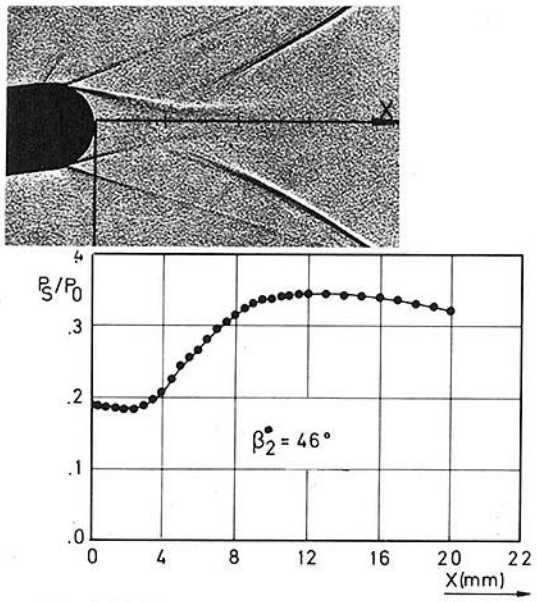


Fig. 6 Static pressure evolution on wake center line

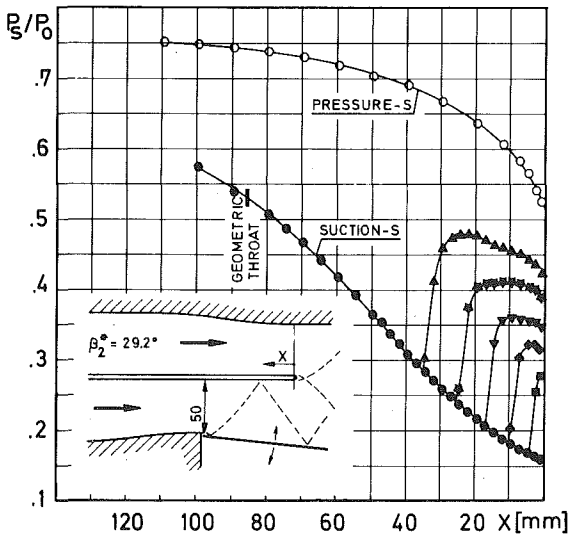


Fig. 7 Blade pressure distributions at part load conditions

Downloaded 01 Jun 2010 to 171.66.16.58. Redistribution subject to ASME license or copyright; see http://www.asme.org/terms/Terms_Use.cfm

deg. The characteristic parameter for the various flow conditions is the distance with respect to the trailing edge at which the tailboard shock interferes with the blade suction side. The curve representing the fully expanded suction side flow implies not necessarily limit loading conditions but rather the fact that the shock has left the suction surface and interferes with the base region or the blade wake. The range over which the shock impingement point on the blade suction side can be moved upstream is limited by the condition that the shock after being reflected back to the tailboard, might not interfere a second time with the blade flow.

Fig. 8 shows the comparison of measured and predicted base Mach numbers for the model configurations $\beta_2^* = 29.2$ and 19.4 deg (the curves for $\beta_2^* = 24.0$ deg are not presented in order not to overload the figure; they confirm, however, in all aspects, the results for the two other configurations). As before, the base Mach number M_b is plotted against the suction side Mach number at the trailing edge $M_{s,t}$ the corresponding pressure side Mach number remaining constant, $M_{p,t} = 1.02$. In cases in which the measured suction side velocity distribution near the trailing edge was visibly affected by the trailing edge expansion, the trailing edge Mach number $M_{s,t}$ was corrected on the basis of the velocity distribution recorded further upstream. In order to facilitate the interpretation of the curves in Fig. 8, a sketch showing the most significant shock positions for $\beta_2^* = 29.2$ deg was added on the same figure. Point A presents the last shock impingement before the trailing edge, for which the pressure recovery through the shock has been completed when arriving at the trailing edge. Point B is situated just downstream of the beginning of the trailing edge circle (i.e., downstream of the point at which we define the trailing edge Mach number, $M_{s,t}$). The shock position C presents limit loading conditions. The range between A and C obviously cannot be covered with simple base pressure theories. In fact for these flow conditions a complete solution of the entire flow field is needed. For shock conditions upstream of point A the base pressure prediction can be qualified as very satisfactory for both model configurations. The calculation procedure takes into account the difference in total pressure on both blade sides caused by the shock interaction on the suction side as well as the effect of a re-accelerating suction side flow after the shock impingement. The boundary layer momentum thickness was calculated following [4] but using an improved treatment of the shock boundary layer interaction resulting in errors of the calculated momentum thickness of less than 15 percent compared to the measured momentum thickness. The suction side shock strength expressed through the Mach number ratio M_2/M_1 (M_1 before the shock, M_2 behind the shock) was for both model configurations comparable to values of equivalent cascades: for $\beta_2 = 29.2$ deg the ratio M_2/M_1 varied from 0.75 to 0.83 with increasing outlet Mach number and for $\beta_2 = 19.4$ deg from 0.81 to 0.91.

In [1] it was suggested that a shock interaction near the trailing edge was likely to produce a boundary layer profile at the trailing edge which would differ significantly from the undisturbed boundary layer profile assumed in the base pressure prediction method of [3]. Boundary layer traverses showed that in the present cases, i.e., shock boundary layer interactions in a highly accelerating flow field, with a shock strength as indicated above, the boundary layer recovers very rapidly a "normal" profile. This is demonstrated at the example of the blade velocity distribution for the shock position at about 8 mm distance from the trailing edge shown in Fig 7. The boundary layer traverses taken at 4 mm before the beginning of the deceleration and 2 mm behind the end of the deceleration are presented in Fig. 9.

The corresponding boundary layer displacement thickness, momentum thickness and shape factor are:

	before shock	*behind shock*
M	1.72	1.37
δ^*	0.29 mm	0.44mm
θ	0.12 mm	0.20 mm
$H_{1,2}$	2.42	2.2

For comparison, the shape factor for a boundary layer developing shock free to a Mach number of M = 1.37 at the trailing edge would be approximately $H_{1,2} = 1.9$.

In conclusion it can be said that, as far as the model tests are concerned, Carrière's angular reattachment criterion satisfactorily predicts the base pressure (or base Mach number) as long as the deceleration process through the shock can be accomplished before the trailing edge (i.e., before the beginning of the trailing edge curvature) thus allowing clear definition of the flow conditions before the trailing edge expansion.

Cascade Tests

From the point of view of the base pressure prediction, the cascade tests can roughly be divided into two categories:

1 blades with a very dense blade surface instrumentation allowing the same approach as in the model tests, i.e., the study of the base pressure or base Mach number as a function of the flow conditions before the trailing edge.

2 blades instrumented with a base pressure tapping but without provision for a sufficiently detailed blade surface pressure distribution. In this case the base pressure can only be related to the downstream pressure and it depends on the number of available cascade test results whether important geometric influence parameters can be defined.

Experimental results of ten cascades of the first category were available at VKI to define more clearly the possibilities and limitations of supersonic base pressure theories. A few typical examples are shown in Fig. 10. The main cascade characteristics are given in Table 1. For comparison we have added the most significant model configurations to the table.

The tests covered a large range of outlet Mach numbers. The use of a cascade facility of the blow down type did not allow an independent variation of the Reynolds numbers. Within the limits indicated below the Reynolds number-Mach number relation can be approximated by a linear variation of RE with M_2.

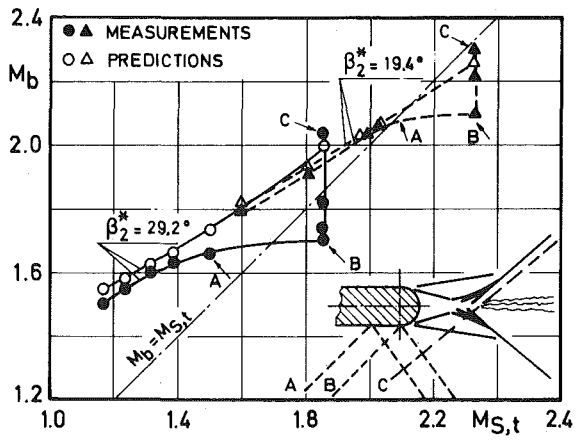


Fig. 8 Comparison of predicted and measured base Mach numbers at part load (model tests)

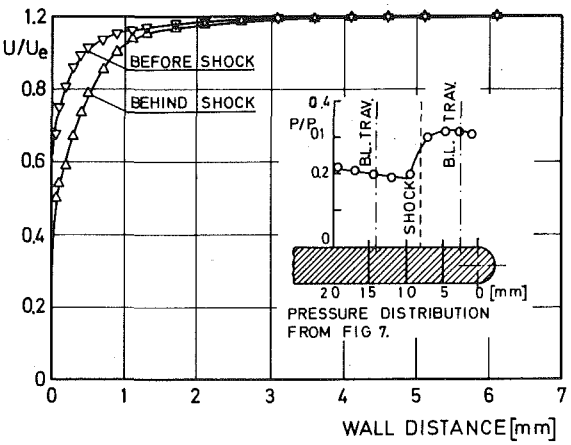


Fig. 9 Boundary layer traverses across shock boundary layer interaction (model)

Downloaded 01 Jun 2010 to 171.66.16.58. Redistribution subject to ASME license or copyright; see http://www.asme.org/terms/Terms_Use.cfm

Blade	$M_{2,is}$	RE $\times 10^{-6}$
1*a*	0.6 – 1.8	0.60 – 1.80
1*b*	0.6 – 1.45	0.55 – 1.10
2	0.7 – 1.7	0.30 – 0.60
3	0.6 – 1.2	0.20 – 0.50
4	0.6 – 1.8	0.60 – 1.50
5	0.7 – 1.75	0.60 – 1.60

The downstream Mach number M_2 is derived from side wall static pressure tappings positioned at an axial distance from the trailing edge plane equal to 40 → 60 percent of the blade chord and the total upstream pressure. The above Reynolds numbers are based on inlet flow conditions and chord length.

In spite of the very careful instrumentation of the blades (distance between pressure tappings of 5 to 2.5 percent of the chord length for chord lengths of 36 to 66 mm) the pressure distribution was not as detailed as in the case of the model. In particular, it was difficult and in most cases impossible to define the exact pressure at the end of the deceleration process for shock positions between $X/C = 0.9$ and 1.0. Hence the gap between limit loading conditions and the last well defined shock boundary layer interaction on the blade suction side was greater than for the model. The gap is closed (dotted line in Fig. 11) by evaluating approximately the relation $M_b = f(M_{s,t})$ in this domain on the basis of experimental evidence from the model tests in Fig. 8.

Apart from the difficulty in properly defining the flow conditions behind the shock for shock interference near the trailing edge, a second problem was encountered in the low supersonic outlet Mach number domain due to the fact that the minimum suction side Mach number at the trailing edge for which a theoretical solution for the base Mach number was found, increased with increasing trailing edge wedge angle δ. This is demonstrated in the example of blade 3 for flow conditions characterized by a suction side Mach number $M_{s,t} = 1.28$ ($M_{p,t} = 1.0$). For zero wedge angle δ, a base $M_b = 1.64$ is predicted.

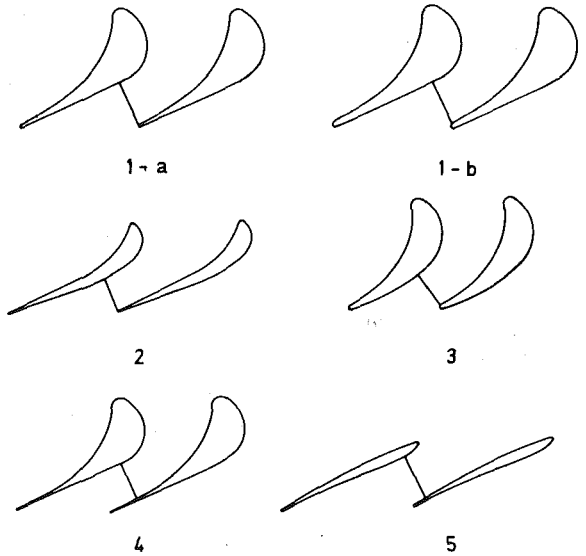


Fig. 10 Cascade configurations corresponding to base Mach number predictions in Fig. 11

With increasing δ, M_b drops until $M_b = 1.47$ at $\delta = 7$ deg. No solution is obtained for $\delta > 7$ deg while the real blade wedge angle amounts to $\delta = 11.5$ deg.

The relation between the trailing edge wedge angle δ and the corresponding reduction in base Mach number is linear and can be expressed for all blades investigated at VKI by

$$\Delta M_b = 0.023\,\delta$$

This relation was used to obtain approximate solutions also for those cases in which the prediction method failed as for instance in the above mentioned example of blade 3 with $M_{s,t} = 1.28$. For this particular case the base Mach number is evaluated as $M_b = 1.37$ for $\delta = 11.5$ deg. Taking blade 1*a* as a reference blade because of its intermediate position between convergent-divergent blades on one side and convergent blades with a convex suction surface downstream of the throat on the other side the base Mach number can be described by several characteristic phases (see Fig. 11(*a*)):

1 In the subsonic outlet Mach number range M_b is slightly higher than $M_{s,t}$. The curve $M_b = f(M_{s,t})$ runs almost parallel to the straight line $M_b = M_{s,t}$.

2 In the transonic range the base Mach number starts to deviate rapidly from the line $M_b = M_{s,t}$ due to the formation of the trailing edge shock system.

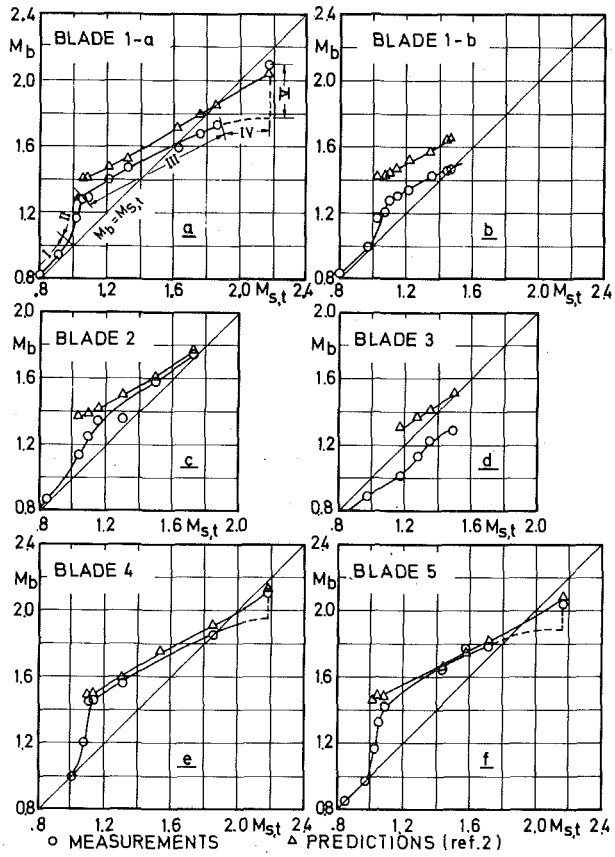


Fig. 11 Comparison of measured and predicted base Mach numbers in cascades

Table 1 Blade characteristics corresponding to blading in Fig. 10

BLADE	β_1	$\sin^{-1}0/g$	g/C	$te/0$	*SS*-curv. ϵ	δ	channel type
1*a*	60	22	0.75	0.075	0	3.9	conv.
1*b*	60	21	0.75	0.145	0	4.2	conv.
2	66	18	0.70	0.06	5	4.5	conv.
3	60	22.2	0.71	0.18	20	11.5	conv.
4	60	21.3	0.64	0.055	—	3.0	con-div.
5	156	19.6	0.86	0.06	—	2.0	con-div.
MODEL		29.2; 24 19.4	—	0.10	0	0	conv.

Note: All angles are indicated in degrees.

Downloaded 01 Jun 2010 to 171.66.16.58. Redistribution subject to ASME license or copyright; see http://www.asme.org/terms/Terms_Use.cfm

3 The suction side shock boundary layer interference point shifts gradually towards the trailing edge. The rate at which the suction side flow expands into the base region is gradually reduced and is finally replaced by a recompression, i.e., $M_b < M_{s,t}$.

4 In the final approach of the shock boundary layer interference point to the trailing edge, the base Mach number remains nearly constant.

5 This phase represents the shock wake interaction until limit loading conditions are reached. $M_{s,t}$ remains constant while M_b changes rapidly until $M_b = M_{b,max}$.

Phases 3 to 5 were already observed in the model tests. The theoretical prediction is practically limited to phase 3 and of course the limit loading point. The above described characteristic evolution—in particular the strong increase of M_b in the transonic range (phase 2)—becomes even more pronounced for convergent-divergent blades; but it vanishes gradually with increasing suction side curvature and trailing edge wedge angle.

The blades, the overhang sections of which are simulated best in the model tests (in particular model configuration $\beta_2^* = 19.4$ deg at part load), are those designated as number 1*a*, 1*b* and 2 in Table 1. The base Mach number predictions are satisfactory for blades 1*a* and 2 (Fig. 11(*a*) and 11(*c*)), the predicted value does not exceed 5 to 10 percent of the experimental value. For blade 1*b*, (Fig. 11(*b*)) which is derived from blade 1*a* by adding a uniform thickness to the pressure side, the prediction is much poorer, the predicted and measured base Mach numbers differing by as much as 10 to 20 percent. The main difference between the aerodynamics of the blades 1*a* and 1*b* is the suction side shock strength. The Mach number ratio across the shock amounts to $M_2/M_1 = 0.69$ to 0.73 for blade 1*b* with the thick trailing edge compared to $M_2/M_1 = 0.75$ to 0.86 for blade 1a at equivalent values of M_1. The shock strengths of blade 2 and of the above mentioned model configuration are similar to those of blade 1*a*. The small size of the cascade blades unfortunately did not allow one to make boundary layer traverses to determine whether, contrary to the model tests, the greater shock strength of blade 1*b* would have a lasting effect on the suction side boundary layer profile and thereby on the base pressure. The base Mach number prediction for blade 3 is absolutely unsatisfactory (Fig. 11(*d*)). With respect to blade 1*a* the present blade differs by a particular thick trailing edge, a high trailing edge wedge angle and a strong convex suction side downstream of the throat. Contrary to blade 1*b* the thick trailing edge does not entail a particular strong shock boundary layer interaction on the suction side because of the shock impinging on a convex blade surface. The resulting shock strength is in fact comparable to that of blade 1*a*. Considering that the wedge angle effect is taken into account by the prediction method, the failure seems to be linked to the strong suction side curvature.

For both convergent-divergent blades the base Mach number is well predicted with the restriction of course that the comparison is again limited to phase 3 and limit loading condition (Fig. 11(*e*) and 11(*f*)).

Base Pressure Correlation. So far the flow conditions existing at the base of the trailing edge have been looked at by an observer at the trailing edge which is the only physically sound approach to the problem. Nevertheless, in view of the strong limitations of presently available base pressure prediction methods and due to the fact that it is advantageous in many cases to know the base pressure-downstream pressure relation without knowing details about the blade velocity distributions, it seems worth-while to attempt to establish a simple experimental base pressure correlation.

A typical evolution of $P_b/P_{01} = f(P_{s2}/P_{01})$ is described in Fig 12 at the example of blade 1*a* (see Fig. 10). For this blade the base pressure is always lower than the downstream pressure, the strongest deviation occurring during the early phase of the establishment of the trailing edge shock system.

The evolution of the base pressure for other blades having approximately the same gauging angle, can be described with respect to the reference curve in Fig. 12. Basically the difference between P_b and P_{s2} will decrease with increasing suction side curvature, the characteristic features of the reference curve will gradually vanish and eventually P_b will become greater than P_{s2}. On the other side the difference between base pressure and downstream pressure will increase when going to convergent-divergent bladings and the characteristic features of the base pressure evolution as demonstrated by the reference curve will become more pronounced.

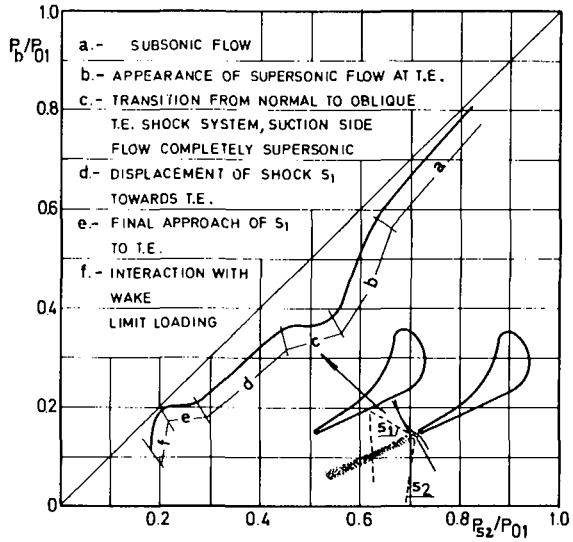


Fig. 12 Evolution of base pressure in function of downstream pressure for reference blade (blade 1*a* Fig. 10)

A great problem consists in relating correctly the passage flow conditions, in particular the base pressure, to the downstream flow conditions. In fact the periodicity of the outlet flow field of turbine cascades operated at transonic and supersonic downstream flow conditions suffers considerably from strong wave reflections generated at the cascade extremities and this independently whether the cascade extremity is a free shear layer or a tailboard. Care was taken that only those tests were selected for the correlation in which there was no direct interference of external shock waves (i.e., shock waves generated at the cascade extremities) with the cascade flow between the blades used for the base pressure measurements and for which the non-periodicity of the downstream flow (measuring plane at $X/C_{ax} = 0.4$ to 0.6) for the three central passages expressed as

$$\Delta M = \frac{\overline{M}_{2,1 \text{ pitch}} - \overline{M}_{2,3 \text{ pitches}}}{\overline{M}_{2,3 \text{ pitches}}}$$

did not exceed the value $\Delta M = 0.03$ (exceptionally 0.04).

Base pressure data on some 20 cascades were available for the correlation. The test data covered both convergent and convergent-divergent bladings. Cascades characterized by no overlapping between two successive blades are not included.

The parameters which might influence the base pressure are: (1) incidence angle, i, (2) shape of blade channel upstream of the throat, (3) trailing edge thickness, te, (4) gauging angle $\beta_2^* = \arcsin(0/g)$, (5) trailing edge wedge angle, δ, (6) blade suction side curvature downstream of the throat expressed by the angle ϵ between the tangents to the suction surface in the throat and at the trailing edge, (7) area ratio A/A^* of the supersonic part of the blade channel in case of convergent-divergent bladings (A^* – throat area, A – channel area at trailing edge).

From the limited amount of data it seems that neither a variation of the incidence angle (within the normal operating range of the blade) nor the shape of the blade channel upstream of the throat have any significant influence on the base pressure, in other words, the effect of a variation of the boundary layer thickness is very limited. The role of the trailing edge thickness is less clear. Basically the trailing edge thickness may affect the base pressure in two ways: (1) through the ratio of the boundary layer thickness to trailing edge thickness and (2) through its influence on the rear suction side velocity distribution. Both effects can have an opposite influence on the base pressure and the end effect seems to be Mach number dependent. At present we are unable to include the trailing edge thickness in a simple way in our base pressure correlation.

Downloaded 01 Jun 2010 to 171.66.16.58. Redistribution subject to ASME license or copyright; see http://www.asme.org/terms/Terms_Use.cfm

Table 2 Bladings providing data body for base pressure correlation

blade	β_1	β_2*	g/C	$te/0$	δ	ϵ	channel type	A/A*	symb	remarks
1	90	22	0.72	0.12	16.5	18	conv.	—	○	
2	60	22.2	0.70	0.18	11.5	20	conv.	—	☆	3
3	46	22.5	0.7	0.16	8.5	10	conv.	—	○	
4	90	21	0.66	0.04	2.0	concav suct.-s.	conv.	—	⬭	
5	60	22	0.75	0.075	3.9	0	conv.	—	△	1*a*
6	60	21	0.75	0.145	4.2	0	conv.	—	△	1*b*
7	60	21.3	0.75	0.075	3	concav. suct.-s.	conv.		◊	
8	90	25.8	0.72	0.10	16.5	16.5	conv.	—	△	
9	90	25.8	0.72	0.10	4.5	13	conv.	—	▽	
10	45	26.2	0.49	0.13	10	10	conv.	—	□	
11	48	26.8	0.65	0.09	5.3	5.8	conv.	—	⏢	
12	45	30.7	0.32	0.16	6	5.5	conv.	—	▷	
13	60	31.8	0.75	0.19	11	14	conv.	—	◇	
14	60	34	0.84	0.12	8	14	conv.	—	▱	
15	60	21.3	0.64	0.055	3	—	conv.-div.	1.02		4
16	156	19.6	0.86	0.06	2	—	conv.-div.	1.05		5

Note: a) numbers in last column correspond to blades in Table 1.
b) symbols as used in Fig. 14.
c) all angles are indicated in degrees.

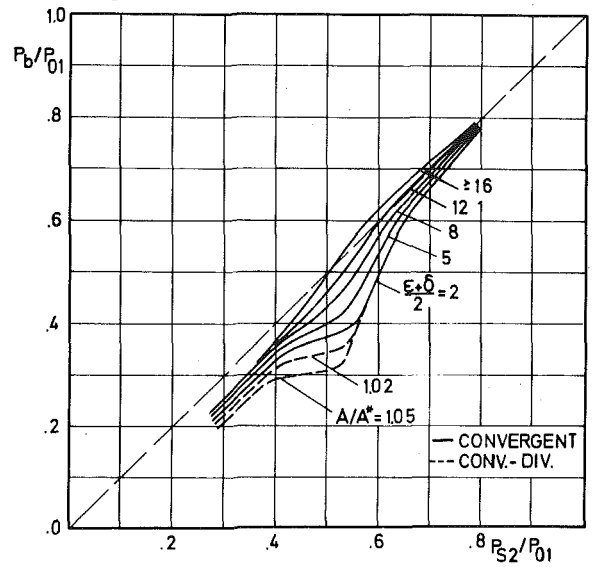


Fig. 13 Base pressure correlation

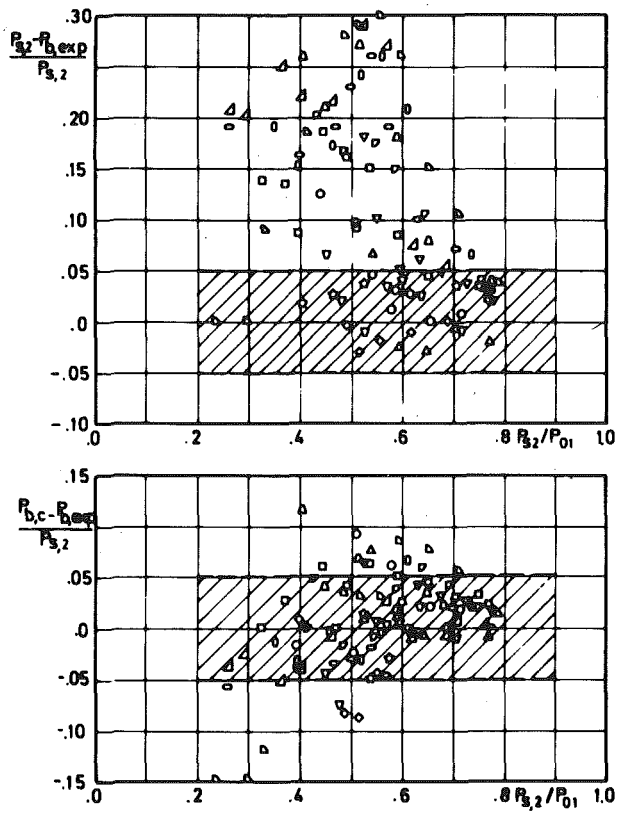


Fig. 14 Prediction capability of base pressure correlation

The influence of the gauging angle β_2* on the base pressure for flow conditions approaching limit loading conditions (i.e., phase *e* and *f* in Fig. 12) is so strong that it can hardly be handled by an experimental correlation without incurring great errors. Hence, the correlation was limited to the flow regimes *a* to *d* in Fig. 12. Within this domain an influence of β_2* was still observed but the test data were insufficient to separate clearly this effect. However, within the gauging angle range β_2* = 20 to 30 deg the gauging angle effect can be neglected to a first approximation in comparison with the two following parameters: the trailing edge angle δ and the suction side curvature downstream of the throat, ϵ. For two thirds of all convergent blades with convex rear suction surface tested, the angles δ and ϵ were of the same order of magnitude, the difference $\epsilon - \delta$ being smaller than 2 deg. For the other blades ϵ was always bigger than δ, the maximum difference amounting to 8.5 deg. In view of lack of experimental data on blades with an independent variation of δ and ϵ it was decided to use the mean value $\epsilon + \delta/2$ as parameter.

Tests on several convergent-divergent cascades demonstrated the extreme sensitivity of the base pressure to the parameter A/A* (internal area increase in supersonic part of blade channel). Within the above mentioned gauging angle range β_2* = 20 − 30 deg the convergent-divergent cascades investigated were characterized by a small A/A* ratio and a small trailing edge angle δ of 2 to 3 deg. The effect of A/A* is tentatively indicated in Fig. 13 by dotted lines for A/A* = 1.02 and 1.05. The base pressure continues to drop with a further increase of A/A* but the available data do not allow one to make a more precise statement.

Table 2 lists all cascades which form the basis of the base pressure correlation. The table contains only that information which may be of importance with respect to the base pressure evaluation. The Reynolds numbers for all cascades are within the range of $0.2 \times 10^6 < RE < 1.6 \times 10^6$ (see Table 2).

The correlation is presented in graphical form in Fig. 13. In order to evaluate the benefit of the correlation Fig. 14 shows the experimental base pressure (1) with respect to the downstream pressure under the form $(P_{s,2} - P_{b,exp})/P_{s,2} = f(P_{s,2}/P_{01})$ and (2) with respect to the curves representing the base pressure correlation under the form $(P_{b,correl.} - P_{b,exp})/P_{s,2} = f(P_{s,2}/P_{01})$. The comparison is restricted to convergent bladings. In the case of the correlation 80 percent of all data points fall within a bandwidth of ±5 percent, while only 40 percent of all experimental data differ by less than 5 percent from the downstream pressure.

Conclusions

The result of the present study is three-fold:

1 a better understanding of the trailing edge flow of transonic

Downloaded 01 Jun 2010 to 171.66.16.58. Redistribution subject to ASME license or copyright; see http://www.asme.org/terms/Terms_Use.cfm

turbine cascades, in particular the finding of a nearly constant separation shock strength for rounded trailing edges (Fig. 4),

2 an evaluation of the potentials and restrictions of supersonic base pressure theories for their application to the prediction of flow through turbines cascades (Fig. 11),

3 a simple base pressure correlation covering a wide range of outlet Mach numbers for cascades with gauging angles β_2^* between 20 and 30 deg (Fig. 13).

References

1 Sieverding, C., et al., "Model Tests for the Detailed Investigations of the Trailing Edge Flow in Convergent Transonic Turbine Blades," ASME 76-GT-30.

2 Hama, F. R., "Experimental Studies on the Lip Shock," *AIAA Journal*, Vol. 6, 1968.

3 Carrière, P. and Sirieix, M, "Facteurs d'Influence du Recollement d'un Ëcoulement Supersonique," X° Congrès International de Mécanique Appliquée, STRESA, 1960.

4 Stratford, B. S., Beavers, G. S., "The Calculation of the Compressible Turbulent Boundary Layer in an Arbitrary Pressure Gradient," ARC M 3207, 1959.

Downloaded 01 Jun 2010 to 171.66.16.58. Redistribution subject to ASME license or copyright; see http://www.asme.org/terms/Terms_Use.cfm

Ali Montakhab[1]
Mechanical Engineering Department,
Stanford University,
Stanford, CA
Mem. ASME

Waste Heat Disposal to Air with Mechanical and Natural Draft—Some Analytical Design Considerations

There is a growing acceptance of the future necessity of dry and wet/dry cooling tower systems for large power stations in spite of their economic penalty compared with once-through cooling, cooling ponds, and evaporative cooling towers. If technological improvements succeed in reducing the current costs of dry cooling towers, their future applications will be accelerated. The main objective of this work is to quantify the factors that reduce the overall size and cost of the tower and the associated heat transfer system and to provide a basis for establishing the conditions that result in dry cooling tower cost reductions. As a first-step, the design equations for forced- and natural-draft dry cooling towers are derived in close form to give explicit relations for salient design variables. Subsequently, these equations are used to establish a set of influence coefficients for quantifying the effects of various key design variables on the design of forced- and natural-draft cooling towers.

Introduction

The use of dry and wet/dry cooling towers for thermal electric power stations has been stimulated by a growing demand for electrical energy [1], a shortage of water at potential sites of large power stations [2, 3], and stringent environmental legislations limiting the use of rivers, lakes, or ocean water for waste heat rejection [4]. Dry and wet/dry cooling towers, however, are associated with economic penalties compared with once-through cooling, cooling ponds, and evaporative cooling towers [5, 7]. Most studies have shown that if dry and wet/dry cooling are used, the cost of electric power generation will be 10 to 20 percent higher than that for wet cooling towers. The cost of dry cooling is higher because of the higher plant capital costs and poorer thermal efficiency of the dry-cooled power stations. The high plant capital costs derive from the requirement for an extensive finned-tube heat transfer area associated with the dry cooling tower, and the poor thermal efficiency is the result of higher turbine exhaust pressure. Because turbine exhaust pressure is dependent on condenser coolant temperature, which in turn is dependent on ambient dry-bulb temperature, high turbine exhaust pressure can be expected during summer operation. Consequently, dry cooling plants are substantially penalized in terms of kilowatt output capacity and thermal efficiency compared with plants employing once-through cooling, cooling ponds, or evaporative cooling towers.

The main objective of this paper is to quantify the factors that affect the overall size and cost of the tower and the associated heat transfer system, and to provide a basis for establishing the conditions that result in dry cooling tower cost reductions. As a first step, the fundamental design equations for forced- and natural-draft cooling towers are derived in closed form to give explicit relations for salient design variables. Subsequently, these equations are used to establish a set of influence coefficients for the design, performance evaluation, and optimization of dry cooling towers and for quantifying the effects of various key design variables on the design of forced- and natural-draft dry cooling towers.

The final results are applicable to the direct or indirect dry cooling systems with mechanical or natural draft. In the case of the indirect system, the coupling fluid can be water or other working fluids such as ammonia or hydrocarbons.

Fundamental Equations

Definitions and Assumptions. One-dimensional steady flow conditions are assumed within the tower for the derivation of the governing equations. The air outside the tower is considered stagnant, and the ambient pressure is assumed to change hydrostatically.

For the idealized induced-draft tower, the ambient air is accelerated smoothly from the ambient condition to the heat exchanger zone beginning Section 1 (Fig. 1(*a*)). The air leaves the heat exchanger at Section 2 and proceeds to the fan at Section A. The air leaves the fan at Section B, flows through the outlet duct, and exits from the tower at Section 3. In a forced-draft tower (Fig. 1(*b*)), the ambient air enters the fan at Section A after acceleration through the inlet section of the tower. The air leaves the fan at Section B, proceeds to the heat exchanger inlet at Section 1, and exits from the heat exchanger at Section 2. It then flows through the outlet duct and leaves the tower at Section 3. The small pressure drops caused by changes in the potential energy of the air across the fan and the heat exchanger are neglected relative to the total pressure change across these components. The pressure of the air at the outlet section of the tower is assumed to be equal to that of the ambient atmosphere at level of 3 (Fig. 1). The entire kinetic energy of the air leaving the tower is dissipated in the mixing process outside the tower exit.

[1] Present address: Teheran University of Technology, P.O. Box 3406, Teheran, Iran.

Contributed by the Power Division for publication in the JOURNAL OF ENGINEERING FOR POWER. Manuscript received at ASME Headquarters May 17, 1979.

Copyright © 1980 by ASME
Downloaded 01 Jun 2010 to 171.66.16.58. Redistribution subject to ASME license or copyright; see http://www.asme.org/terms/Terms_Use.cfm

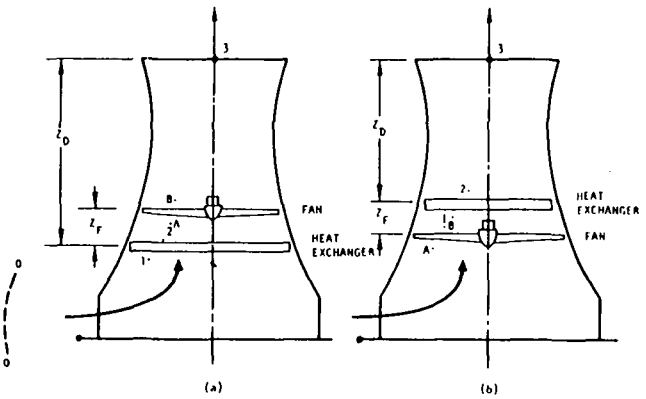


Fig. 1 Generalized schematic arrangement of dry-cooling tower: (*a*) induced draft, (*b*) forced draft

Draft Equation. The general draft equation for the induced-draft tower can be derived assuming the conditions stated above; the draft equation for the forced-draft tower can be derived in a similar manner. Either equations can be reduced in a form suitable for the natural-draft tower.

The derivation of the draft equation for the induced-draft tower, Fig. 1(*a*), is based on the one-dimensional laws of gas dynamics. Between Sections 0 and 1, the air accelerates from stagnation ambient conditions to the conditions at the inlet of the heat exchanger, and undergoes a pressure drop caused by aerodynamic losses and changes of elevation and air velocity. The density of the air between Sections 0 and 1 is treated as constant. As the air passes through the heat exchanger, it experiences a pressure drop ΔP_E caused by viscous friction, form drag, and flow acceleration. The air undergoes a change of elevation as it travels from Section 2 to A, and there is a possibility of flow acceleration or deceleration. The density of the air flow through the heat exchanger zone varies, but between Section 2 and A it is treated as a constant. When the air goes through the fan, it experiences a pressure rise ΔP_F. The changes in flow area and elevation in the fan zone are treated as negligible but the air density change in the fan zone is taken into consideration. After the air leaves the fan, it flows through the outlet duct to Section 3. The air density between Sections B and 3 is treated as a constant.[1]

The equations governing the processes described above are given in Appendix 1. These equations are combined to give the draft equation for the induced-draft tower. First, all intermediate pressures are eliminated by algebraic manipulation. Intermediate velocities are removed by introducing appropriate continuity relations. The pressure difference $p_0 - p_3$ is written in terms of the effective height Z_D assuming that the variation of ambient pressure with elevation is hydrostatic. This results in the draft equation for induced-draft tower:

$$\frac{\Delta P_F - \Delta P_E - \Delta P_T}{\rho_1 V_1^2/2g_c} + \left[(\rho_E^* - 1) - \rho_E^* \left(\frac{A_1}{A_3}\right)^2\right] + \frac{Z_D}{V_1^2/2g}\left(1 - \frac{\rho_F^*}{\rho_E^*}\right) = (\rho_F^* - 1)\left\{\frac{\rho_E^*}{\rho_F^*}\left(\frac{A_1}{A_3}\right)^2\left[\left(\frac{A_3}{A_A}\right)^2 - 1\right] - \frac{1}{\rho_F^*}\frac{Z_F}{V_1^2/2g}\right\}, \quad (1)$$

where ρ_1 and V_1 are density and velocity, respectively, of the air at the heat exchanger inlet section, and ρ_E^* and ρ_F^* are the density ratios across the heat exchanger and fan, respectively; i.e.,

[1] The effect of neglecting the variations of ambient density with elevation outside the tower tends to somewhat cancel the effect of neglecting the variation of air density inside the tower shell.

Nomenclature

A = cross-sectional area
A_c = free-flow area, air-side free-flow area
$A_s = \equiv \pi D_s H$
A_1 = heat exchanger frontal area
A_3 = tower exit area
$\bar{A}$ = heat transfer surface area
C = capacity rate
c_P = specific heat at constant pressure, air side
c_w = specific heat of water
d = heat exchanger depth
D_h = hydraulic diameter, air side hydraulic diameter
D_i = tube inside diameter
D_s = skirt diameter of the tower
F = correction factor for log mean rate equation
f = friction factor, air-side friction factor
g = acceleration due to gravity
g_c = proportionality constant in Newton's Second Law
H = heat exchanger height
h = convective heat transfer coefficient, air-side convective coefficient
h_d = heat transfer coefficient for scale deposits, air-side heat transfer coefficients for deposits
I = initial temperature difference $(T_{w1} - T_1)$
k = thermal conductivity, air-side thermal conductivity
k_ℓ = defined by equation (40)
K_c = inlet loss coefficient
K_e = exit loss coefficient
ℓ_p = longitudinal tube spacing
n = number of passes
n_r = number of tube rows
N_{tu} = number of heat transfer units
$P^* \equiv (T_{w2} - T_1)/(T_{w1} - T_1)$, approach (see Fig. 2)
p = pressure
$\dot{q}$ = heat transfer rate
$R^* \equiv (T_{w1} - T_{w2})/(T_{w1} - T_1)$, range (see Fig. 2)
St = Stanton number, air-side Stanton number
T = temperature, absolute scale (Absolute temperature scale is used throughout this paper to avoid ambiguity. The reader, however, can use a relative temperature scale wherever appropriate.)
T_F = temperature at fan inlet
U = overall heat transfer coefficient
V = velocity, air velocity
V_w = water velocity in heat exchanger tube passages
V_1 = air velocity at the heat exchanger inlet
w = flow rate, air flow rate
$\dot{W}k$ = shaft power
Z = effective draft height, defined by equation (8)
Z_A = draft height due to flow acceleration outside heat exchanger
Z_D = defined by Fig. 1 and/or Fig. 3
Z_E = draft height due to heat exchanger drag
Z_F = defined by Fig. 1
Z_{K_c} = draft height due to entrance effect
Z_{K_e} = draft height due to exit effect
Z_θ = draft height due to heat exchanger flow acceleration
α = surface area density (transfer area per total volume), air-side surface area density
$\alpha_1^* = (T_2 - T_1)/(T_{w1} - T_1)$, see Fig. 2
Δ = difference
$\Delta t_{\ell m}$ = log mean temperature difference
$\delta = T_{w1}/T_1 - 1$
δ_{wall} = tube wall thickness
ϵ = heat transfer effectiveness
η = efficiency
η_0 = surface effectiveness
$\theta = T_2/T_1$
$\theta_m = (\theta + 1)/2$
$\lambda = h/U$, (see equation (13))
ρ = density
$\rho_E^* = \rho_1/\rho_2$
$\rho_F^* = \rho_B/\rho_A$
σ = ratio of free-flow area/frontal area, ratio of air-side free-flow area/frontal area

Subscripts

a = air
E = heat exchanger
F = fan
max = maximum value
min = minimum value
P = pump
T = tower
w = water
w_1, w_2 = water inlet and outlet condition
0, 1, 2, 3, A, B = positions in the tower (Fig. 1)

Downloaded 01 Jun 2010 to 171.66.16.58. Redistribution subject to ASME license or copyright; see http://www.asme.org/terms/Terms_Use.cfm

$$\rho_E^* \equiv \frac{\rho_1}{\rho_2} (\geq 1)$$

$$\rho_F^* \equiv \frac{\rho_B}{\rho_A} (\geq 1)$$

Locations 1, 3, and A and heights Z_D and Z_F are defined in Fig. 1.

A similar procedure is used to derive the draft equation for the forced-draft tower:

$$\frac{\Delta p_F - \Delta p_E - \Delta p_T}{\rho_1 V_1^2/2g_c} + \left[(\rho_E^* - 1) - \rho_E^* \left(\frac{A_1}{A_3}\right)^2\right] + \frac{Z_D}{V_1^2/2g} \frac{1}{\rho_F^*} \left(1 - \frac{\rho_F^*}{\rho_E^*}\right) = (\rho_F^* - 1)\left[\frac{1}{\rho_F^*} \frac{Z_F}{V_1^2/2g} + \left(\frac{A_1}{A_A}\right)^2\right] \quad (2)$$

The righ-hand side of equations (1) and (2) account for the buoyancy and flow acceleration effects associated with the fan. In most cases, these effects are small because $\rho_F^* - 1 \sim 0$, in which case the right-hand side can be treated as zero.

Equations (1) and (2) reduce to an identical form under pure natural-draft conditions ($\Delta p_F = 0$, $\rho_F^* = 1$), and the right-hand sides of both equation vanish, resulting in a dynamic balance between natural draft, flow acceleration, and pressure drop in the heat exchanger core:

$$\underbrace{\left(1 - \frac{1}{\rho_E^*}\right) \frac{Z_D}{V_1^2/2g}}_{\text{natural draft effect}} = \underbrace{\frac{\Delta p_E + \Delta p_T}{\rho_1 \left(\frac{V_1^2}{2g_c}\right)}}_{\text{heat exchanger and tower } \Delta p} + \underbrace{\rho_E^* \left(\frac{A_1}{A_3}\right)^2 - (\rho_E^* - 1).}_{\text{flow acceleration effects}} \quad (3)$$

In this case, the flow acceleration effect is due to heating and flow area change, and the draft is caused by the buoyancy of the hot air above the heat exchanger zone. In the case of natural-draft towers, the idealization of one-dimensional flow requires the tower to be slender enough so that the flow property differences across the flow section are unimportant. A tower which is low and wide may fail to meet this idealization, and the desired draft requirements cannot be satisfied. When the natural-draft effect and the quantities on the right side of equations (1) and (2) are negligible compared with the mechanical draft effect, both equations reduce to the following form:

$$\underbrace{\frac{\Delta p_F}{\rho_1 \left(\frac{V_1^2}{2g_c}\right)}}_{\text{mech. draft effect}} = \underbrace{\frac{\Delta p_E + \Delta p_T}{\rho_1 \left(\frac{V_1^2}{2g_c}\right)}}_{\text{heat exch. and tower } \Delta p} + \underbrace{\rho_E^* \left(\frac{A_1}{A_3}\right)^2 - (\rho_E^* - 1).}_{\text{flow acceleration effects}} \quad (4)$$

Heat Exchanger Pressure Drop. The equation for heat exchanger pressure drop is [8]

$$\frac{\Delta p_E}{\rho_1 \left(\frac{V_1^2}{2g_c}\right)} = \underbrace{\frac{f}{\sigma^2} \bar{\rho}_E^* \frac{\overline{A}}{A_c}}_{\text{heat exch. drag}} + \underbrace{\left(1 + \frac{1}{\sigma^2}\right)(\rho_E^* - 1)}_{\text{heat exch. flow acceler. effect}} + \underbrace{\frac{K_c' + K_e' \rho_E^*}{\sigma^2}}_{\text{inlet/exit effects}} \quad (5)$$

where $\bar{\rho}_E^* \sim (1 + \rho_E^*)/2$, f is the friction factor, and σ is the ratio of free-flow area to the frontal area of the heat exchanger core. The coefficients K_c' and K_e' are the heat exchanger inlet and exit loss coefficients, respectively.

The first term on the right-hand side of equation (5) is due to viscous friction and form drag within the heat exchanger core, the second term represents flow acceleration caused by a change of density due to heat transfer, and the last term accounts for the heat exchanger entrance and exit effects, which are caused by a sudden contraction at the inlet section of the core followed by a sudden expansion at the core exit. For flow over banks of either bare or finned tubes, each tube rows consists of a contraction and an expansion. Therefore, the friction behavior of the first and last tube rows in the core is not substantially different from that of the interior tube rows. Thus, the inlet and exit behavior are already taken into consideration in the friction factor, and the entrance and exit loss coefficients are treated as zero.

Terms similar to the heat exchanger inlet and exit effects in equation (5) can be used to describe the aerodynamic losses within the tower shell before and after the heat exchanger. The representative velocity head for defining these loss coefficients is of course arbitrary but it is convenient to use the velocity head corresponding to the heat exchanger minimum free-flow area. If this is done, the aerodynamic losses within the tower shell can be described by expressions identical to the heat exchanger inlet and exit losses in equation (5). Thus,

$$\frac{\Delta p_T}{\rho_1 \left(\frac{V_1^2}{2g_c}\right)} = \frac{K_c'' + K_e'' \rho_E^*}{\sigma^2}, \quad (6)$$

where K_c'' and K_e'' are tower pressure loss coefficients before and after the heat exchanger, respectively.

Effective Draft Height. Equations (3) and (4) can be written as a single equation by introducing the concept of effective draft height. To do this, θ is substituted for ρ_E^*, since $\rho_E^* \sim \theta$. Next, Δp_E (from equation (5)) and Δp_T (from equation (6)) are introduced, and the following equation is obtained:

$$\frac{Z}{V_1^2/2g} = \underbrace{\frac{\theta \theta_m}{\theta - 1} \frac{f\overline{A}}{\sigma^2 A_c}}_{\text{heat exchanger drag}} + \underbrace{\frac{\theta^2}{\theta - 1}\left(\frac{A_1}{A_3}\right)^2 + \frac{\theta}{\sigma^2}}_{\text{flow acceleration effects}} + \underbrace{\frac{K_c + K_e \theta}{\sigma^2} \frac{\theta}{\theta - 1}}_{\text{inlet and exit effects}}, \quad (7)$$

where $K_c \equiv K_c' + K_c''$ and $K_e \equiv K_e' + K_e''$. According to these definitions, the loss coefficient K_c represents the aerodynamic losses within the tower shell before the heat exchanger, but including the heat exchanger inlet effect, and the loss coefficient K_e represents the heat exchanger exit effect combined with the aerodynamic losses within the tower shell after the heat exchanger.

The equation for the effective draft height Z is derived in Appendix 2:

$$Z \equiv Z_D + \frac{g_c}{g} c_p T_1 \frac{T_2}{T_F} \frac{\dot{W}_F \eta_F}{\dot{q}} \quad (8)$$

For natural-draft tower, Z is identical to Z_D, and for mechanical-draft tower, $Z_D \sim 0$. An equivalent form of equation 7 is

$$Z = Z_E + Z_A + Z_\theta + Z_{K_c} + Z_{K_e}$$

where Z_E, Z_A, Z_θ, Z_{K_c}, and Z_{K_e} are draft height components corresponding to the heat exchanger drag, flow acceleration from the heat exchanger exit to the tower exit, flow acceleration in the heat exchanger, and inlet and exit effects, respectively.

Scaling Relationship. A useful scaling relationship can be derived by introducing a length scale ℓ defined by Moore [9, 10]

$$\ell \equiv \left(\frac{\dot{q}}{\sqrt{2g}\rho_1 c_p T_1}\right)^{2/5}$$

where ℓ has a length dimension and is a constant for a given thermal duty and ambient condition. The air approach velocity V_1 is related to the heat exchanger frontal area, air flow rate, and air density at the heat exchanger inlet. This relation is combined with the air-side energy equation, $\dot{q} = wc_p T_1 (\theta - 1)$, and the definition of ℓ from equation (9) to yield:

$$V_1 = \frac{\sqrt{2g\ell}}{A_1^*(\theta - 1)}$$

Substituting this equation for V_1 in equation (7) and neglecting the air flow acceleration in the heat exchanger as well as the inlet and exit effects results in

$$\frac{(\theta - 1)^3}{\theta^2} A_1^{*2} Z^* = \frac{\theta_m}{\theta} \frac{f}{\sigma^2} \frac{\overline{A}}{A_c} + \left(\frac{A_1}{A_3}\right)^2, \quad (10)$$

Downloaded 01 Jun 2010 to 171.66.16.58. Redistribution subject to ASME license or copyright; see http://www.asme.org/terms/Terms_Use.cfm

where

$$Z^* = Z/\ell,$$

$$A_1^* = A_1/\ell^2.$$

Moore [9, 10] presents the power expansion of a general gas dynamic equation and combines the zero-order terms to derive a scaling relationship which is the same as equation (10) except for the quantities θ^2 and θ_m/θ, which do not appear in the zero-order terms of Moore's expansion (see Appendix 3). Note that a typical magnitude for $\theta\theta_m$ is $1.1 \times 1.05 = 1.15$ and thus a 15 percent error is introduced by the zero-order treatment.

The first term on the right-hand side of equation (10) expresses the influence of heat exchanger drag, and the second term represents the air flow acceleration from the exit of the heat exchanger to the tower exit.[2] This latter effect can have a large impact on the size of the tower.

At first it seems desirable to reduce the area ratio A_1/A_3 so that the tower size is reduced (equation 10)). This, however, must be consistent with technical limitations associated with reducing the exit velocity below a certain value. As an illustration, laboratory experiments [11, 12] and field data [13] have confirmed that towers with lower exit velocities are more susceptible to wind and flow recirculation effects. Furthermore, an A_3 value which is too large (to reduce V_3) makes for a larger and perhaps more expensive tower shell structure.

It can be seen that the tower size parameter $(A_1^{*\,2}Z^*)$ in equation (10) is less sensitive to height than to lateral dimension. If one is specially anxious to reduce the height $Z = Z_D$, it is a happy circumstance that if height is reduced by a factor of two, the lateral dimensions must be increased only by a factor of $2^{1/4}$, or 19 percent. Of course, this idea must not be applied too enthusiastically, because a tower which is too low and too wide may suffer adverse internal flow problems leading to flow instability, nonuniformity, and separation. Under such circumstances, the flow within the tower may no longer be uniform and the assumption concerning one-dimensionality of the flow within the tower shell may no longer be valid.

Heat Transfer Surface Area. The quantity $\overline{A}/A_c$ in equation (5), which is a measure of heat exchanger depth d or the number of tube rows in the direction of the air flow, can be written as follows:

$$\frac{\overline{A}}{A_c} \equiv \frac{4d}{D_h} \equiv \frac{\alpha d}{\sigma} \equiv \frac{\alpha \ell_p}{\sigma} n_r \tag{11}$$

The first quantity is the definition of hydraulic diameter D_h; the last two quantities result from the definitions of α and σ and the equation $d = \ell_p n_r$.

The total heat transfer area requirement may be written according to the log mean rate equation:

$$\overline{A} = \frac{\dot{q}}{UF\Delta T_{\ell m}}$$

If the exchanger is actually a counterflow or a parallel flow unit, the nondimensional factor F is unity; for all other flow arrangements, F is less than unity. This factor has been calculated for a variety of flow configurations [14, 15].[3]

Fig. 2 shows the temperature notation appropriate for counterflow. The initial temperature difference, I, is the difference between the temperature of the hot water entering the cooler (T_{w1}) and that of the cooling air entering the exchanger (T_1). The water is then cooled through the range R^*I to a temperature T_{w2}, which is above T_1 by the amount of approach P^*I. The air, meanwhile, is warmed by an amount $\alpha_I^* I$, and it leaves the exchanger at T_2. The usual logarithmic mean temperature difference may then be written

$$\Delta T_{\ell m} = I \frac{1 - \alpha_I^* - P^*}{\ell n\,[(1 - \alpha_I^*)/P^*]}.$$

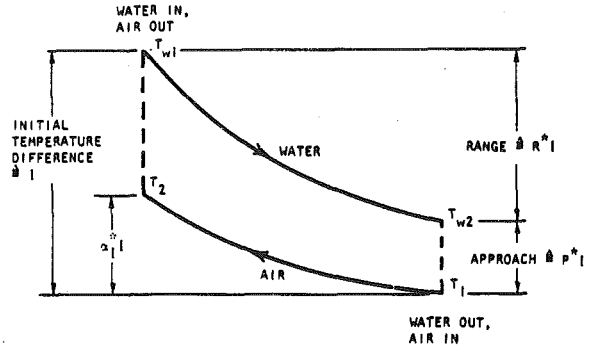


Fig. 2 Temperature diagram of counterflow heat exchanger defining terms and notations (drawn for $C_w < C_a$)

There is a one-to-one correspondence between the log-mean rate equation and the effectiveness-N_{tu} approach. It can be shown that [8]

$$F = \frac{N_{tu}\,(\text{counterflow for the same } \epsilon,\, C_{\min}/C_{\max})}{N_{tu}\,(\text{actual})}$$

Thus, F is a function of effectiveness (or P^*), capacity rate ratio (or α_I^*) and flow arrangement.

The parameters α_I^*, R^*, and P^* in Fig. 2 are related to effectiveness and capacity rate ratio as follows:

For $C_a > C_w$:
$$R^* = 1 - P^* = \epsilon$$
$$\alpha_I^* = \epsilon \frac{C_w}{C_a}$$

For $C_w \geq C_a$:
$$R^* = 1 - P^* = \epsilon \frac{C_a}{C_w}$$
$$\alpha_I^* = \epsilon$$

For either case:
$$\frac{R^*}{\alpha_I^*} = \frac{C_a}{C_w} \quad \text{and} \quad \frac{\Delta T_{\ell m}}{I} = \frac{1}{F}\frac{\epsilon}{N_{tu}},$$

The quantity $\overline{A}/A_c$ in equation (5) can be related to the thermal performance of the heat exchanger. This relationship is derived by appropriately combining the definitions of N_{tu}, St, λ, and the capacity rate:

$$\frac{\overline{A}}{A_c} = \frac{\lambda}{\text{St}} \cdot \frac{C_{\min}}{C_a} N_{tu}. \tag{12}$$

The quantity λ is the ratio of the overall thermal resistance to the convective resistance on the air side. It represents surface effectiveness, fouling, and film coefficients on the air and water sides; i.e.,

$$\lambda \equiv \frac{h}{U} = \frac{\text{I}}{\eta_0} + \frac{\alpha}{\alpha_w}\frac{h}{h_w} + \frac{\alpha}{\alpha_{\text{wall}}}\frac{h\delta_{\text{wall}}}{k_{\text{wall}}} + \frac{\alpha}{\alpha_w}\frac{h}{h_{d,w}} + \frac{h}{h_d} \tag{13}$$

where h_d and h_{dw} are heat transfer coefficients for fouling, accounting for scale formation on the air and water sides, respectively. When equations (5) and (12) are combined, they provide a link between the thermal performance and air-side pressure drop of the heat exchanger core.

The quantity N_{tu} in equation (12) is a function of effectiveness, capacity rate ratio, and flow arrangement (the results presented in this section are not restricted to any particular flow arrangement). The effectiveness-N_{tu} relations for various flow arrangements are given by Kays and London [8].[4] The heat exchanger flow arrangement in dry cooling towers is often a multipass cross counterflow type, with individual passes comprising the cross flow arrangement. The solution to the overall counterflow multipass configurations is given by Kays

[2] The latter term is sometimes called the tower exit effect.

[3] Reference [15] gives general approximate equations suitable for digital computer applications.

[4] Polynomial approximations of ϵ-N_{tu} relations are given by Wörsoé-Schmidt and Hogaard Knudsen [17] to accelerate convergence of the corresponding power series for large (greater than unity) values of N_{tu}. These relations are useful for digital computer applications.

Downloaded 01 Jun 2010 to 171.66.16.58. Redistribution subject to ASME license or copyright; see http://www.asme.org/terms/Terms_Use.cfm

and London [8], who postulate that the N_{tu} total is equally distributed between identical passes.

Water Pumping Power. The water pumping power requirement can be found using the energy and continuity equations. To enable visualization of the impact of the basic design parameters, water pumping power is given in terms of key design variables per unit of air-side heat transfer surface area (the derivation is given in Appendix 4):

$$\frac{\dot{W}k_P}{\overline{A}} = \left(\frac{\sigma_w k_\ell \rho_w}{2g_c \alpha D_i}\right)\frac{f_w V_w^3}{\eta_P}. \tag{14}$$

The quantity k_ℓ is based on the concept of the "hydraulic equivalent length," which is the ratio of total flow resistance to flow resistance due to straight heat exchanger tubing. This quantity is unity if flow resistance due to headers, valves, and other flow devices in the circuit is ignored. This ideal situation is of interest only if pumping power is used as a criterion against which a family of designs is compared.

Heat Exchanger Depth and Water Flow Length. In the design of so-called cross flow natural-draft dry cooling towers (Fig. 3), the heat exchanger modules are vertically placed around the periphery of the tower. The heat exchanger flow arrangement is generally multipass cross counterflow with water flowing in the vertical direction. In this case, H is the height of the heat exchanger module, which is given by the following equation (derived in Appendix 5):

$$\frac{H}{V_w} = \frac{\sigma_w \rho_w}{\alpha w_w}\frac{\overline{A}}{n}. \tag{15}$$

This equation is also applicable to other dry cooling tower and heat exchanger arrangements, where H is the length of the exchanger core in the direction of the water flow. The depth of the heat exchanger core in the direction of the air flow can be found from equation (11):

$$d = \frac{\sigma}{\alpha}\frac{\overline{A}}{A_c}. \tag{16}$$

Equation (16) is not restricted to a particular dry cooling tower or heat exchanger arrangement.

Skirt Diameter. The quantity D_s in cross flow natural-draft towers (Fig. 3) is the "skirt diameter" and can be calculated according to the following equation (derived in Appendix 5):

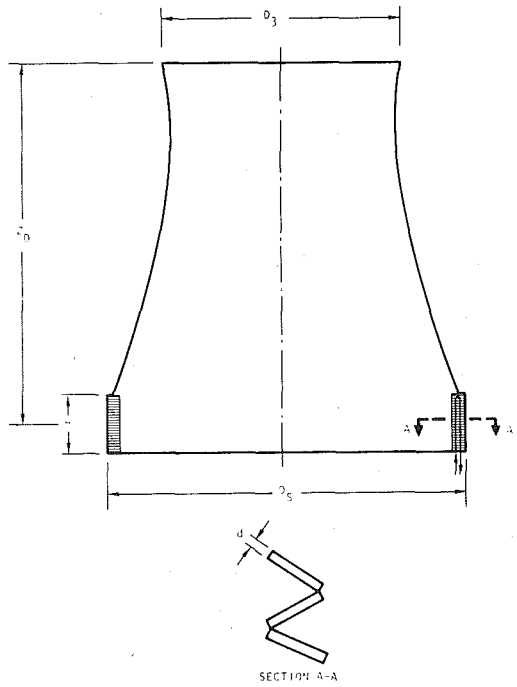


Fig. 3 Schematic arrangement of cross flow natural-draft dry cooling tower

$$\frac{D_s V_w}{w_w} = \frac{A_s/A_1}{\pi\rho_w \dfrac{\sigma\sigma_w}{\alpha}}\cdot\frac{n}{\overline{A}/A_c}, \tag{17}$$

where $A_s = \pi D_s H$, and A_1 is the heat exchanger frontal area. The ratio A_s/A_1 is generally less than unity owing to blockage and/or the arrangement of the heat exchanger modules, which in practice can be designed to form a V (referred to as Δ) configuration, as shown in Fig. 3.

Heat Exchanger Frontal Area. The energy and continuity equations on the air side can be combined to obtain the following equation, which relates heat exchanger frontal area, air approach velocity, and temperature rise ratio:

$$\frac{\dot{q}}{\rho_1 c_p T_1} = A_1 V_1(\theta - 1). \tag{18}$$

Air Temperature Rise Ratio. Air temperature rise through the heat echanger core is related to (1) heat exchanger effectiveness, (2) $\delta\ [\equiv (T_{w1}/T_1) - 1]$, and (3) capacity rate ratio $C_{\min}/C_a$ according to the following formula:

$$\theta - 1 = \frac{C_{\min}}{C_a}\epsilon\delta. \tag{19}$$

This equation is derived using the definition of effectiveness and the energy equation on the air side of the heat exchanger core.

Influence Coefficients

The equations derived so far provide a basis for the thermal design and the performance analysis of dry cooling towers. The high temperature fluid is assumed to be water, but the results are valid for other working fluids or direct condensation of steam, as in the case of a direct system. Thermal design of a dry cooling tower system is based on decisions which affect the overall cost of the system and are dependent upon:

1 Properties of the working fluids.
2 Surface geometry of the heat exchanger core and tower geometry.
3 Fluid velocities and heat transfer and flow friction behavior of the heat exchanger core.
4 Performance parameters of the tower.

The results given thus far are used to derive a set of alternative equations that are useful in quantifying the factors that affect the overall size and cost of the tower and the associated heat transfer system, and to establish the conditions that result in dry cooling tower cost reductions.

The drag of the heat exchanger core is represented by the first expression on the right-hand side of equation (7), which will be defined in nondimensional form as $Z_E/(V_1^2/2g)$. Introducing $\overline{A}/A_c$ from equation (12) into this expression and combining the result with equation (19) yields

$$\frac{Z_E}{V_1^2/2g} = \frac{f\lambda}{\mathrm{St}\sigma^2}\cdot\theta\theta_m\frac{N_{tu}}{\epsilon\delta}. \tag{20}$$

This relationship, known as the core velocity equation [8], is a coupling of the heat transfer and pressure drop of the heat exchanger core.

Introducing the definition of $\sigma\ (\equiv A_c/A_1)$ into equation (12) and combining the result with equations (18) and (19) enables the derivation of the following equation:

$$\frac{\overline{A}}{\dot{q}} = \frac{1}{\rho_1 c_p T_1}\cdot\frac{\lambda\sigma}{\mathrm{St}V_1}\cdot\frac{N_{tu}}{\epsilon\delta}. \tag{21}$$

To reduce the equation for heat exchanger height H to the desired form, the term $\overline{A}$ from equation (12) is substituted into equation (15). Introducing the definition of effectiveness and the energy equation on the water side result in

$$\frac{H}{V_w} = \frac{\rho_w c_w}{\rho_1 c_p}\frac{\sigma\sigma_w}{\alpha}\frac{\lambda}{\mathrm{St}V_1}\frac{R^* N_{tu}}{\epsilon n}. \tag{22}$$

Equations (12) and (16) are combined to yield the following equation for heat exchanger depth:

Downloaded 01 Jun 2010 to 171.66.16.58. Redistribution subject to ASME license or copyright; see http://www.asme.org/terms/Terms_Use.cfm

$$d = \frac{\sigma}{\alpha} \cdot \frac{\lambda}{\mathrm{St}} \frac{C_{\min}}{C_a} N_{tu}. \tag{23}$$

The derivation of the alternative equation for the skirt diameter involves the combination of several equations. First, the quantity $\overline{A}/A_c$ from equation (12) is substituted into equation (17), and the resulting equation is combined with equation (19) and the energy equation on the water side to yield

$$\frac{D_s V_w}{\dot{q}} = \frac{1}{\rho_w c_w T_1} \cdot \frac{A_s/A_1}{\pi \dfrac{\sigma\sigma_w}{\alpha}} \frac{\mathrm{St}}{\lambda} \frac{1}{(\theta - 1)\mathrm{R}^* \dfrac{N_{tu}}{n\epsilon}}. \tag{24}$$

Substituting $\overline{A}$ from equation (12) into equation (14) results in

$$\frac{\eta_p \dfrac{\dot{W k}_p}{\dot{q}}}{f_w V_w^3} = \frac{\rho_w}{2g_c \rho_1 c_p T_1} \cdot k_\ell \frac{\sigma\sigma_w}{\alpha D_i} \frac{\lambda}{\mathrm{St} V_1} \cdot \frac{N_{tu}}{\epsilon\delta}. \tag{25}$$

The right-hand sides of equations (20–25) are products of the following major quantities:

1 Property-dependent influence coefficients, i.e., quantities which depend on the thermodynamic properties of the working fluids.
2 Geometry-dependent influence coefficients, i.e., quantities which depend on tower and heat exchanger surface geometries. For a given heat exchanger surface geometry, these influence coefficients are constant.
3 Reynolds-number-dependent influence coefficients, i.e., quantities which depend on the Reynolds number and transport properties of the air and water components. For a given heat exchanger geometry and specific water-side conditions, these influence coefficients are dependent upon only the air-side Reynolds number or air approach velocity.
4 Capacity-rate-dependent influence coefficients, i.e., quantities which depend on the design operating conditions[5] and capacity rate of the air through the heat exchanger core. Once the design operating conditions have been established, these coefficients establish the air temperature rise through the tower.

The influence coefficients are listed in Table 1. These coefficients provide the tools for designing dry cooling towers and determining the optimum design conditions. They are also useful in quantifying the effects of various parameters on the design. To illustrate the latter application, it can be seen from Table 1 or equations (20, 21), and (25) that (1) draft height due to heat exchanger drag, (2) heat transfer surface area, and (3) water pumping power are proportional to $N_{tu}/\epsilon\delta = T_1/(F\Delta T_{lm})$, which suggests that all three can simultaneously be reduced by increasing the initial temperature difference and air-side capacity rate to maximize $\Delta T_{\ell m}$ and employing the counterflow option to maximize F.

The draft height components Z_A, Z_{Kc}, and Z_{Ke} in Table 1 and the heat exchanger frontal area can be reduced by increasing the air temperature rise through the heat exchanger. In general, a small air temperature rise causes a reduction in overall heat exchanger surface area, but results in a large air flow rate and decreased buoyancy, both of which cause the size (both height and diameter) of a natural-draft tower to increase. A small air temperature rise in a mechanical-draft tower increases the number of fans required and results in large heat exchanger frontal area.

Concluding Remarks

The fundamental design equations for forced- and natural-draft dry cooling tower systems have been derived in closed form to give explicit relations for salient design variables. These equations, summarized in Table 1, provide a basis for the design and optimization

[5] The design operating conditions are (1) water inlet and outlet conditions; (2) heat transfer rate or water flow rate; (3) ambient conditions.

Table 1 Influence coefficients

Design Parameter	Property-Dependent Coefficients: Air	Property-Dependent Coefficients: Water	Geometry-Dependent Coefficient	Reynolds-Number-Dependent Coefficient	Capacity-Rate-Dependent Coefficient	Reference Equation
Z_F	1	1	$\frac{1}{\sigma^2}$	$\frac{f\lambda}{\mathrm{St}} \frac{V_1^2}{2g}$	$\theta\theta_m \frac{N_{tu}}{\epsilon\delta}$ [c]	(20)
Z_A	1	1	$\left(\frac{A_1}{A_3}\right)^2$	$\frac{V_1^2}{2g}$	$\frac{\theta^2}{\theta - 1}$	Part of flow acceleration component of (7)
Z_{K_e}	1	1	$\frac{1}{\sigma^2}$	$K_e \frac{V_1^2}{2g}$	$\frac{\theta^2}{\theta - 1}$	Exit-effect component of (7)
Z_{K_c}	1	1	$\frac{1}{\sigma^2}$	$K_c \frac{V_1^2}{2g}$	$\frac{\theta}{\theta - 1}$	Inlet-effect component of (7)
Z_θ	1	1	$\frac{1}{\sigma^2}$	$\frac{V_1^2}{2g}$	θ	Part of flow acceleration component of (7)
$A_1/\dot{q}$	$\frac{1}{\rho_1 c_p T_1}$	1	1	$\frac{1}{V_1}$	$\frac{1}{\theta - 1}$	(18)
$\overline{A}/\dot{q}$	$\frac{1}{\rho_1 c_p T_1}$	1	σ	$\frac{\lambda}{\mathrm{St} V_1}$	$\frac{N_{tu}}{\epsilon\delta}$	(21)
d	1	1	$\frac{\sigma}{\alpha}$	$\frac{\lambda}{\mathrm{St}}$	$\frac{C_{\min}}{C_a} N_{tu}$	(23)
H/V_w	$\frac{1}{\rho_1 c_p}$	$\rho_w c_w$	$\frac{\sigma\sigma_w}{\alpha}$	$\frac{\lambda}{\mathrm{St} V_1}$	$\frac{R^* N_{tu}}{n\epsilon}$	(22)
$\frac{\eta_p \dot{W k}_p/\dot{q}}{f_w V_w^3}$	$\frac{1}{\rho_1 c_p T_1}$	$\frac{\rho_w}{2g_c}$	$\frac{\sigma\sigma_w}{\alpha D_i} k_\ell$	$\frac{\lambda}{\mathrm{St} V_1}$	$\frac{N_{tu}}{\epsilon\delta}$	(25)
$\frac{D_s V_w}{\dot{q}}$ [b]	$\frac{1}{T_1}$	$\frac{1}{\rho_w c_w}$	$\frac{A_s/A_1}{\pi\,\sigma\sigma_w/\alpha}$	$\frac{\mathrm{St}}{\lambda}$	$\frac{1}{(\theta - 1)R^* N_{tu}/n\epsilon}$	(24)

[a] The results given in this table are applicable to natural-draft and mechanical-draft dry cooling towers. Except for the last row ($D_s V_w/\dot{q}$), which is applicable to the configuration in Fig. 3, the results are independent of the shape and configuration of the dry cooling tower.
[b] Applicable to cross flow natural tower (Fig. 3).
[c] Notice that $N_{tu}/\epsilon\delta = 1/F\Delta T_{\ell m/T_1}$.

Downloaded 01 Jun 2010 to 171.66.16.58. Redistribution subject to ASME license or copyright; see http://www.asme.org/terms/Terms_Use.cfm

of dry cooling towers. Table 1 also defines the influence coefficients for quantifying the effects of various key design variables for dry cooling towers. Each of the equations in Table 1 is the product of five independent expressions. These expressions, called the influence coefficients, are related to (1) thermodynamic properties of the two working fluids (property-dependent influence coefficients); (2) geometries of the heat exchanger surface and tower shell (geometry-dependent influence coefficients); (3) Reynolds numbers of the working fluids (Reynolds-number-dependent influence coefficients); and (4) conditions and capacity rates of the hot and cold fluid components (capacity-rate-dependent influence coefficients).

A future presentation will concentrate on the use of influence coefficients for optimization of dry cooling towers and in the evaluation and selection of heat exchanger surface or in directing research and development efforts toward manufacturing of improved heat transfer surfaces for dry cooling tower applications.

Acknowledgments

The encouragement and technical guidance of Professor A. L. London of Stanford University is gratefully acknowledged.

References

1 "A review and Comparison of Selected United States Energy Forecasts," Battelle Memorial Institute Report, Dec. 1969.

2 "Considerations Affecting Steam Power Plant Site Selection," U.S. Office of Science and Technology, 1968.

3 Hauser, L. G., "Growing Water Requirements for the Growing Thermal Generating Additions of the Electric Utility Industry," *Proceedings of the American Power Conference*, Vol. 31, 1969.

4 "Waste Heat From Steam Electric Generating Plants Using Conventional Nuclear Steam Turbine Generators with Dry Cooling Systems," Paper Presented at the Winter Annual Meeting of the ASME, Detroit, Nov. 11–15, 1973.

5 Rossie, J. P., and W. A. Williams, Jr., "The Economics of Using Conventional Nuclear Steam Turbine Generators with Dry Cooling Systems," Paper Presented at the Winter Annual Meeting of the ASME, Detroit, Nov. 11–15, 1973.

6 Rossie, J. P., E. A. Cecil, and R. D. Young, "Cost Comparison of Dry-Type and Conventional Cooling Systems for Representative Nuclear Generating Plants," USAEC Report TID-26007, March 1972.

7 Englesson, G. A., M. C. Hu, and W. C. Savage, Wet/Dry Cooling for Water Conservation," Paper presented at teh Waste Heat Management and Utilization Conference, Miami Beach, May 9–11, 1977.

8 Kays, W. M., and A. L. London, *Compact Heat Exchangers*, 2nd ed., McGraw-Hill, New York, 1964.

9 Moore, F. K., "On the Minimum Size of Large Dry Cooling Towers with Combined Mechanical and Natural Draft," ASME *Journal of Heat Transfer*, Aug. 1973.

10 Moore, F. K. "Scaling Law for Dry Cooling Towers with Combined Mechanical and Natural Draft," Cornell University Report 72-19, Aug. 1972.

11 Christopher, P. J., and V. T. Forster, "Rugeley Dry Cooling Tower System," *Proceedings of the Institute of Mechanical Engineers*, Vol 184, Part 1, No. 11, 1969–70, pp. 197–222.

12 Hansen, E. P., "Dry Towers and Wet/Dry Towers for the Indirect Power Plant Cycle," Paper Presented at the Winter Annual Meeting of the ASME, Detroit, Nov. 11–15, 1973.

13 Baker, D. R., "Developing Cooling Tower Recirculation Factors from Field Test Data," ASME Paper No. 70-WA/HT-22.

14 Bowman, R. A., D. C. Mueller, and W. M. Nagle, "Mean Temperature Differences in Heat Exchanger Design," *Transactions of the ASME*, Vol. 62, 1940.

15 Roetzel, W., and F. J. L. Nicole, "Mean Temperature Difference for Heat Exchanger Design—A General Approximate Explicit Equation, ASME *Journal of Heat Transfer*, Feb. 1975.

16 McAdams, W. H., *Heat Transfer*, 3rd ed., McGraw-Hill, New York, 1954.

17 Wörsoé-Schmidt, P., and H. J. Hogaard Knudsen, "Thermal Modeling of Heat Exchangers for simulation purposes," in *Proceedings of the 1976 Heat Transfer and Fluid Mechanics Institute*, Stanford University Press.

18 "Characteristics of the Standard Atmosphere," Extension of *ICAO Std. Atmos.*, 1958.

APPENDIX 1

General Draft Equation

This appendix presents the general draft equation for the induced-draft tower for one-dimensional, steady state, steady flow conditions. A similar method can be used to derive the draft equation for the forced-draft tower. Either equation can be reduced to a form suitable for the natural-draft tower.

Fig. 1 shows the schematic arrangement of the induced-draft tower. The equations in this appendix are based on the one-dimensional laws of gas dynamics. Between Sections 0 and 1, the air accelerates from stagnation ambient conditions to the inlet section of the heat exchanger, resulting in a small pressure difference caused by the changes in elevation and air velocity. This process is assumed to take place reversibly,[6] adiabatically, and with negligible density change subject to the following equation:

$$\frac{p_0 - p_1}{\rho_1} = \frac{V_1^2}{2g_c} + \frac{g}{g_c}(Z_1 - Z_0) \tag{26}$$

As the air passes through the heat exchanger it undergoes a pressure drop Δp_E caused by viscous friction, form drag, flow acceleration, and heat exchanger inlet and exit effects:

$$\Delta p_E \equiv p_1 - p_2. \tag{27}$$

As the air flows from Section 2 to A it undergoes a further pressure drop owing to a change of elevation. There is also a possibility of flow acceleration (or deceleration) which is caused by the flow area change. This process is assumed to take place reversibly, adiabatically, and with negligible density change:

$$\frac{p_2 - p_A}{\rho_2} = \frac{V_A^2 - V_2^2}{2g_c} + \frac{g}{g_c}(Z_A - Z_2). \tag{28}$$

As the air passes through the fan it undergoes a pressure rise Δp_F:

$$\Delta p_F \equiv p_B - p_A, \tag{29}$$

and as it leaves the fan it is assumed to proceed through the outlet duct under adiabatic and reversible conditions and with negligible density change. Thus,

$$\frac{p_B - p_3}{\rho_B} = \frac{V_3^2 - V_B^2}{2g_c} + \frac{g}{g_c}(Z_3 - Z_B). \tag{30}$$

By neglecting the variations of ambient density with elevation, the ambient pressure difference $p_0 - p_3$ can be written in terms of the tower height:

$$p_0 - p_3 = \frac{\rho_0 g}{g_c}(Z_3 - Z_0) \tag{31}$$

The ambient density and pressure of the standard atmosphere are given by [18] and are presented in Fig. 4 for the first 3000 m above sea level. Fig. 4 also shows the calculated ambient pressure using equation (31) in a stepwise evaluation employing 213-m-high intervals. Table 2 lists the pressure difference between the specified elevation and an elevation 213 m above using both equation (31) and the standard atmosphere data given by [18]. The percentage deviation between these two sets of values is also listed in Table 2, indicating that equation (31) predicts the pressure difference between the top and bottom of a 213-m-high tower with an error of less than 2 percent. At the present time, technical and aesthetic considerations limit the height of natural-draft cooling towers to 150 m. Thus, equation (31) can be used for predicting the variation of ambient pressure with elevation with sufficient accuracy in the absence of atmospheric disturbances such as wind and atmospheric inversions.

The effect of neglecting the variations of ambient density with elevation in equation (31) tends to somewhat cancel the effect of neglecting the variation of air density with elevation inside the tower shell.

Equations (26–31) can be combined to give the draft equation for the induced-draft tower. To derive this equation, it is necessary first to eliminate the pressure terms by multiplying both sides of equations (26–31) by appropriate factors and summing the results. Next, the intermediate velocities must be eliminated by introducing appropriate continuity equations. To simplify the resulting equation, it is assumed that $A_1 = A_2$, $A_A = A_B$, and the fan zone from A to B and the heat

[6] Although the flow within the tower shell is idealized as reversible in this derivation, the aerodynamic losses within the tower shell are accounted for in the final results.

Downloaded 01 Jun 2010 to 171.66.16.58. Redistribution subject to ASME license or copyright; see http://www.asme.org/terms/Terms_Use.cfm

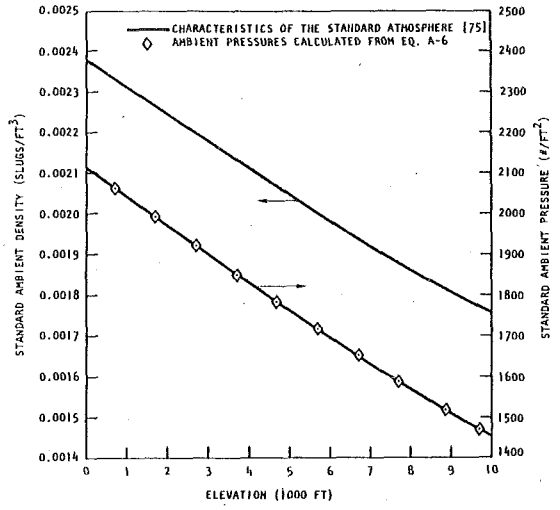


Fig. 4 Ambient density and pressure of the standard atmosphere as a function of elevation

exchanger zone from 1 to 2 are negligibly thin compared with tower height. The final result can be written in the form given by equation (1) where a pressure drop Δp_T is included to account for the aerodynamic losses within the tower shell.

APPENDIX 2

Effective Draft Height

By introducing the following definition for the effective draft height,

$$Z \equiv Z_D + \frac{g_c}{g} \cdot \frac{\Delta p_F/\rho_2}{\rho_E^* - 1}, \tag{32}$$

the draft equations for natural-draft and mechanical-draft towers equations (3) and (4), respectively, can be written in a single form as follows:

$$\left(1 - \frac{1}{\rho_E^*}\right)\frac{Z}{V_1^2/2g} = \frac{\Delta p_E}{\rho_1 \dfrac{V_1^2}{2g_c}} + \rho_E^*\left(\frac{A_1}{A_3}\right)^2 - (\rho_E^* - 1). \tag{33}$$

Because the pressure ratio across the heat exchanger is very close to unity, θ can be substituted for ρ_E^*, since $\rho_E^* \sim \theta$. Then Δp_E from equation (5) is introduced into equation (33), and equation (7) is obtained.

The Δp_F term in equation (32) can be written in terms of the fan power requirement according to the following equation:

$$\Delta p_F = \frac{\dot{Wk}_F}{w}\rho_{F\eta F}.$$

Then the energy equation on the air side and the $\rho_E^* \sim \theta$ approximation are introduced to find the following equation for the effective draft height:

$$Z = Z_D + \frac{g_c}{g} c_p T_1 \frac{\rho_F}{\rho_2}\frac{\dot{Wk}_F \eta_F}{\dot{q}}. \tag{34}$$

Noting that $\rho_F/\rho_2 \sim T_2/T_F$, equation (8) results.

APPENDIX 3

Tower Size Function

The purpose of this appendix is to derive an equivalent expression for the Moore's tower size function ψ in terms of effectiveness, capacity rate ratio and N_{tu}, and to compare equation (10) with the zero-order scaling relationship proposed by Moore. Moore [9, 10] presents the power expansion of a general gas dynamic equation and combines the zero-order terms to derive the scaling relationship:

Table 2 Comparison of Ambient Pressure Differences Calculated from Equation (31) and Standard Atmosphere Data [18] for 213-m-High Intervals

Elevation (m)	Standard Atmospheric Conditions: Density (kg/m³)	Standard Atmospheric Conditions: Pressure (MPa)	Pressure Difference[a] (kPa): Based on the Standard Atmosphere Data	Pressure Difference[a] (kPa): Calculated Using Equation (31)	Deviation (percent)
0	1.224	1.1013	2.516	2.565	1.9
300	1.189	0.0977	2.448	2.489	1.7
600	1.154	0.0942	2.379	2.420	1.7
900	1.120	0.0908	2.310	2.344	1.5
1200	1.087	0.0875	2.248	2.275	1.2
1500	1.055	0.0843	2.179	2.206	1.3
1800	1.024	0.0812	2.110	2.144	1.6
2100	0.993	0.0782	2.041	2.075	1.7
2400	0.963	0.0753	1.979	2.013	1.7
2700	0.933	0.0725	1.910	1.944	1.8

[a] This pressure difference is defined as the atmospheric pressure difference between the specified elevation and an elevation 213 m above.

$$\delta^3 A_3^{*2} Z^* = \frac{f\lambda\psi}{\mathrm{St}}\left(\frac{A_3}{A_c}\right)^2 + \frac{1}{\alpha_1^{*2}}. \tag{35}$$

The quantity ψ is the size function, which is defined according to the following equation

$$\psi \equiv \frac{\ell n\left(\dfrac{1-\alpha_I^*}{P^*}\right)}{\alpha_I^{*2} F(1 - P^* - \alpha_I^*)}, \tag{36}$$

where α_I^* and P^* are defined in Fig. 2.

The factor F in equation (36) can be written as $F = N_{tu,cf}/N_{tu}$ [8]. Substituting α_I^* and P^* in terms of ϵ and C^* into equation (36) and introducing the ϵ-N_{tu} relationship for counterflow yields

$$\psi = \frac{N_{tu}}{\left(\dfrac{C_{\min}}{C_a}\right)^2 \epsilon^3}. \tag{37}$$

Introducing equation (19) into equation (35) and substituting ψ from equation (37) yields

$$(\theta - 1)^3 A_1^{*2} Z^* = \frac{f}{\mathrm{St}}\frac{\lambda}{\sigma^2}\frac{C_{\min}}{C_a} N_{tu} + \left(\frac{A_1}{A_3}\right)^2.$$

To compare the above equation with equation (10), it is necessary to introduce equation (12) into the above equation, which yields

$$(\theta - 1)^3 A_1^{*2} Z^* = \frac{f}{\sigma^2}\frac{\overline{A}}{A_c} + \left(\frac{A_1}{A_3}\right)^2.$$

Here we see an identity with equation (10) providing θ^2 and θ_m/θ are treated as unity. Apparently, this is the case for the zero-order terms in the power expansion used by Moore. Note that a typical magnitude for θ-θ_m is $1.1 \times 1.05 = 1.15$ and that a 15 percent error is introduced by this zero-order treatment.

APPENDIX 4

Water Pumping Power

The equation for water pumping power is

$$\dot{Wk}_p = \frac{w_w \Delta p_w}{\eta_p \rho_w} \tag{38}$$

where

$$\Delta p_w = f_w \rho_w \frac{L_w}{D_i}\frac{V_w^2}{2g_c}, \tag{39}$$

and L_w is the total equivalent length based on the heat exchanger tubing geometry. The total length of straight heat exchanger tubing in an n-pass heat exchanger design is equal to nH, where H is the

Downloaded 01 Jun 2010 to 171.66.16.58. Redistribution subject to ASME license or copyright; see http://www.asme.org/terms/Terms_Use.cfm

length of the heat exchanger module in the direction of the water flow. Because of flow obstructions due to headers, fittings, and flow devices in the water circuit, the quantity k_ℓ, defined as

$$k_\ell \equiv \frac{L_w}{nH}, \tag{40}$$

is always greater than unity. The quantity k_ℓ is based on the concept of the "total equivalent length," which is the ratio of total flow resistance to flow resistance due to straight exchanger tubing. Thus, k_ℓ is unity if flow resistance due to headers, valves, and other flow devices in the circuit is ignored. This idealized situation is of interest only if pumping power is used as a criterion against which a family of designs is compared. The total volume of the heat exchanger core is equal to nHA_w, where A_w ($\equiv A_{cw}/\sigma_w$) is net water-side frontal area per pass; the total volume is equal to $\overline{A}/\alpha$. Therefore,

$$H = \frac{\overline{A}}{\alpha n A_w}. \tag{41}$$

An expression for A_w is found using the continuity equation on the water side:

$$A_w = \frac{w_w}{\rho_w \sigma_w V_w}. \tag{42}$$

Combining equations (38–42) yields

$$Wk_p = \frac{f_w \rho_w}{D_i} \frac{V_w^3}{2g_c} \frac{\sigma_w}{\alpha} k_\ell \frac{\overline{A}}{\eta_p}. \tag{43}$$

APPENDIX 5

Heat Exchanger Depth, Height, and Skirt Diameter

This appendix considers the case of a natural-draft dry cooling tower in which the heat exchanger modules are vertically arranged around the tower periphery (Fig. 3). The depth of the heat exchanger core in the air flow direction is

$$d = n_r \cdot \ell_p, \tag{44}$$

where n_r and ℓ_p are number of tube rows and longitudinal tube spacing, respectively. Substituting $\alpha\, \ell_p n_r/\sigma$ for $\overline{A}/A_c$ from equation (11) into equation (12) yields

$$n_r = \left(\frac{\sigma}{\alpha \ell_p} \frac{\lambda}{\mathrm{St}}\right) \frac{C_{\min}}{C_a} N_{tu}. \tag{45}$$

For a vertical tube arrangement, the height of the heat exchanger core can be found by substituting A_w from equation (42) into equation (41):

$$\frac{H}{V_w} = \frac{\sigma_w}{\alpha n} \frac{\rho_w \overline{A}}{w_w}. \tag{46}$$

Substituting H from equation (46) into the geometric relation $H = A_s/(\pi D_s)$ results in equation (17).

Downloaded 01 Jun 2010 to 171.66.16.58. Redistribution subject to ASME license or copyright; see http://www.asme.org/terms/Terms_Use.cfm

D. Adler[1]
NAVAIR Chair Visiting Professor,
Turbopropulsion Laboratory,
Department of Aeronautics,
Naval Postgraduate School,
Monterey, CA 93940

Status of Centrifugal Impeller Internal Aerodynamics

Part I: Inviscid Flow Prediction Methods

Recent developments in inviscid prediction methods of internal flow fields of centrifugal impellers and related flows are critically reviewed. The overall picture which emerges provides the reader with a state-of-the-art perspective on the subject. Restricting simplifying assumptions of the various methods are identified to stimulate future research. Topics included in this review are: two-dimensional subsonic and transonic inviscid flows as well as three-dimensional inviscid flows.

Introduction

The rising fuel costs put continuous pressure on designers to develop prime movers with reduced specific fuel consumption and smaller weight. In the case of small or medium sized gas turbines the demand for low weight focused increased attention on the centrifugal compressor with the requirement for improved efficiencies to achieve the reduction of specific fuel consumption. In the case of reciprocating engines the demand for reduced weight and reduced fuel consumption led to new concepts, like the turbo-compound and the adiabatic turbo-compound [1], as well as to increased interest in turbo-charging. These, in turn, also increased the attention paid to centrifugal compressors.

Both the gas turbine and the reciprocating engine, have to be efficient over a wide spectrum of points of operation. If variable compressor geometry is to be avoided (because of increased costs, weight, reliability and maintenance problems) the compressor must have a wide range of operation in which efficiencies are good, and surge or choke do not occur. This demand contradicts the requirement for high stage pressure ratios.

The evaluation of the optimal compromise between maximum pressure ratio, maximum efficiency at the design point and wide range of operation with fixed geometry, is a difficult task. Only deeper understanding resulting from improved capabilities for experimental observation and better predictive techniques for the internal flow will enable a fulfillment of this task.

It is the objective of this paper to review the recent developments and the present state-of-the-art of centrifugal compressor internal aerodynamics. In view of the great amount of published material, selectivity is unavoidable. Therefore, the paper is focused on inviscid centrifugal impeller flow. Experimental results and viscous flow problems will be discussed in a subsequent article. Inlet and diffuser flows, as well as flow in axial machines, are mentioned only as much as they affect the centrifugal impeller flow, or are connected to its flow problems.

Inviscid Flow Models

The flow in conventional centrifugal impellers is extremely complex. Clearly, the complexity is the result of the impeller geometry and the fact that it is rotating. Therefore, the impeller cannot be designed aerodynamically such that the real fluid behavior is properly accounted for. Improved aerodynamic design procedures and better performance predictions, however, both require the development of techniques to properly analyze the flow through the impeller. Such an analysis must contend with the adverse pressure gradient which is imposed on the flow, and the presence of turbulent viscosity variations which are strongly influenced by mean flow conditions, curvature of the stream lines and the Corriolis acceleration. As will be discussed in a subsequent article, a comprehensive mathematical model describing reality is too difficult to solve with the current state-of-the-art. The simplest approach certainly, is to calculate the flow field in the impeller by assuming that the fluid is inviscid. Even with this assumption the task is formidable, and raises the immediate query as to whether the effort is justified in view of the big differences obtained sometimes between inviscid predictions and measured results [2–5]. The answer however is affirmative: inviscid solutions can be useful in describing backswept impeller flow where the jet-wake flow does not exist at the design point, in describing the upstream regions of radial exit impellers and generally to predict the inviscid uncorrected core of any intra-impeller flow.

Existing methods for the prediction of inviscid centrifugal impeller flows are classified into four groups: (I) solutions on the hub-to-shroud (H-S) stream surface, (II) solutions in the blade-to-blade (B-B) stream surface, (III) transonic B-B solutions and (IV) three-dimensional (3-D) solutions. In each of these groups models can be reclassified into (1) streamline curvature methods, (2) partial differential methods.

1 *Streamline curvature methods* are based on a first order ordinary differential equation describing the force balance in the direction of the quasi-orthogonals to the streamlines. The equation is solved along these quasi-orthogonals marching forward along the passage from inlet to exit. The continuity equation is integrally satisfied along quasi-orthogonals. This is basically a nonelliptic procedure. The elliptic character of the flow is retained somehow by the curve fitting of the streamlines which link upstream to downstream points along the passage. The curve fitting also determines the streamline curvature. The accuracy of the results and the ellipticity of the solution depend strongly on which curve fitting method is used; this is the "non-natural" or "artificial" ingredient of the streamline curvature technique. The non-ellipticity of the technique also lies in the indirect manner in which downstream boundary conditions and backpressure are satisfied, and in the way their upstream effects on the entire flow field are predicted.

[1] Permanent Address: Department of Mechanical Engineering, Technion, Israel Institute of Technology, Haifa, Israel.

Contributed by the Gas Turbine Division for publication in the JOURNAL OF ENGINEERING FOR POWER. Manuscript received at ASME Headquarters May 7, 1979.

Copyright © 1980 by ASME
Downloaded 01 Jun 2010 to 171.66.16.58. Redistribution subject to ASME license or copyright; see http://www.asme.org/terms/Terms_Use.cfm

An early and extremely simple example of this approach is the method of Adler and Ilberg [6], where the assumption of linear variation of streamline curvature from hub to shroud along the quasi-orthogonals allowed integration of the quilibrium equation in the direction of the quasi-orthogonals. The method enabled the flow field to be obtained without the use of a computer.

2 *Partial differential methods* are based on the solution of the partial differential equations of the inviscid steady flow. Momentum equilibrium, energy conservation, and continuity are satisfied at a point, and the elliptic nature of the subsonic flow is well preserved both in the form of the partial differential equations and, consequently in the way the boundary conditions can be specified. The formulation is based in most cases on the classical work of Wu [7] or on equations similar to those given by Wu. Wu defined "special derivatives" valid only on H-S or B-B stream surfaces. These special derivatives allow an enormous simplification of the problem by splitting the 3-D formulation into two mathematically "two-dimensional" formulations. These are, however, interconnected by the "stream sheet thickness" thus retaining the three dimensionality of the physical situation. The partial differential equations can be solved either by finite differences or by finite element methods. These will be described later.

After having briefly explained the streamline curvature and the partial differential approaches let us continue the review along the classification into H-S, B-B and 3-D groups. Due to the large number of methods known, only a brief description can be given here. After this the various methods will be compared to each other and to experiments.

H-S Solutions. Historically, streamline curvature methods were the first to be developed. They required more modest computer storage and simpler computational techniques were needed because they involved only first order, ordinary differential equations. A frequently used streamline curvature program is Katsanis' early development [8]. Katsanis expressed the equation of motion of the H-S flow in terms of curved coordinates based on the streamlines and quasi-orthogonals. The resulting equation was solved simultaneously with the continuity equation in its integral form along the quasi-orthogonals. The numerical solution iterated on the constant mass flux between neighboring streamlines. The curvature of the streamlines was modified from iteration to iteration until convergence was achieved.

An additional method based on the streamline curvature technique was developed by Novak [9, 10]. As in the previous method the equation of motion was expressed in terms of the streamline curvature and the solution iterated on the constant mass flux between two successive streamlines. Unlike Katsanis, Novak modified his initially assumed streamlines along radii, rather than along quasi-orthogonals. This simplified the method but restricts its application to axial flow machines only. Davis [11] compared both Katsanis' and Novak's methods to a method developed by himself. He concluded that all three versions of the streamline curvature method were essentially identical. A general analysis of the streamline curvature approach can be found in a paper by Smith [12].

As mentioned above the partial differential methods are based in most cases on Wu's formulation [7] or its derivatives. An early finite difference solution was given by Wu [13] and later Marsh [14] used a modified version of Wu's model to obtain a solution of the flow field in the H-S surface. Later, in 1973, Davis published his technique [15] which was essentially similar to Marsh's. It was developed for axial machines but could be applied also to centrifugal compressors in an analogous way to Katsanis' and McNally's evolutionary work. Katsanis and McNally developed a finite difference method [16] which in its early version was limited to flows up to 45 deg from the axis. Their later version [17] extended the application to radial flows as well. Both methods, those of Davis and Katsanis and McNally, were based on the use of the stream function equations. The equations were solved with a finite difference technique, and the basic method was limited to subsonic flows. Locally supersonic flows could only be handled by a combination of the stream function solution and a velocity gradient (streamline curvature) technique [29].

A second way to solve the partial differential equations of the H-S flow is the finite element technique. The basic equations solved are essentially identical to those used in the finite difference solutions based on Wu's model, except for modifications introduced for the convenience of the technique. The first finite element solution was completed in 1974 by Adler and Krimerman [18]. This was followed in 1975 by Oates, et al. [19] and in 1976 by Hirsch and Warzee [20]. A basic difference between the finite element and the finite difference techniques is that the discretization of the continuous flow field in finite difference form is geometrically restricted by the coordinate system chosen for the problem (unless complicated and time consuming transformations are applied) while in finite element form no restriction is imposed on the location of the nodal points in the grid. The freedom in location of grid points enabled Adler and Krimerman [18] to locate their grid points on streamlines. This allowed a simpler satisfaction of the energy equation which, along streamlines, could be used in its integrated form. Further, the fact that grid points were located on streamlines made the incorporation of the solution into a fully 3-D solution easier. It was with this recognition that Adler and Krimerman choose the finite element technique for their solution.

Oates, et al. [19] applied a variational principle, producing, in effect, the integral of the H-S momentum, to create a system of nonlinear algebraic equations. The system of equations was solved using the Newton-Raphson technique. To formulate their method Oates, et al. used the well-known actuator disc method. The technique was fundamentally different from that of Adler and Krimerman who did not use a variational principle specially derived for their principal equation. Rather, they used the variational principle of Poisson's equation, giving their governing equation an artificial shape of a Poisson equation. This in turn required an iterative procedure. Further Adler and Krimerman did not use the actuator disc approach at all.

Hirsch and Warzee [20] used a weighted residual Galerkin procedure. Like Adler and Krimerman they gave their governing equation the shape of a Poisson equation, avoiding in this way the problem of deriving a variational principle for their governing equation. They also introduced NASA correlations into their technique to specify losses and deviation angles. It should be pointed out here that all these techniques were initially applied to axial flow compressors. There is, however, no special reason to believe that these techniques will fail when used to predict the flow in centrifugal impellers. In fact, Adler and Krimerman used their technique [18] successfully to analyze Eckardt's impeller [4] without any difficulties. This will be discussed later.

No systematic comparison of the simultaneous application of all these techniques has been reported. Further, no systematic comparison of the predictions of the various methods with the results of experiments has appeared. There are, however, isolated comparisons between two or three techniques or between a numerical solution and an experiment to be found in literature. Davis compared his streamline curvature method to those of Katsanis and Novak and found them to be essentially identical [15]. In 1972 Frost [21] presented a streamline curvature technique and compared its results to Marsh's method [14]. The agreement between the two techniques was very good but both do not agree too well with experimental results (see Fig. 1). Differences were observed not only in velocity magnitude and direction but also in velocity profile shapes, indicating a fundamental problem; perhaps the effect of viscosity?

Adler and Krimerman [18] compared their results calculated using a finite element method to Wu's results [13] which were evaluated with a finite difference method. The two results agreed fairly well and showed the same trends in the distributions of velocity and static pressure along the casing and the hub. When compared to experimental data both analytical techniques gave static pressure distributions showing trends similar to the measured profiles (see Fig. 2). Adler and Krimerman's results were closer to the measured profile when blade thickness effects and a total loss coefficient were included in the calculations.

In 1974 Davis and Millar [22] reported a comparison between finite difference and streamline curvature methods. Their comparison is illustrated in Fig. 3 where test results of a NASA single stage transonic

Downloaded 01 Jun 2010 to 171.66.16.58. Redistribution subject to ASME license or copyright; see http://www.asme.org/terms/Terms_Use.cfm

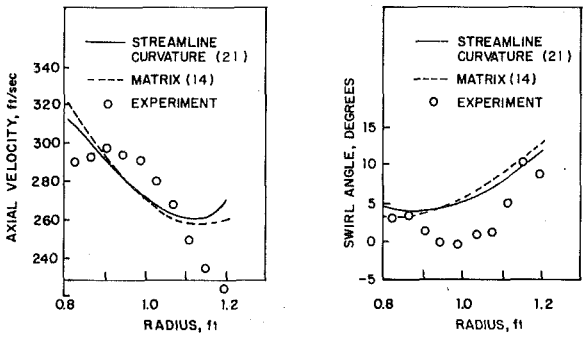


Fig. 1 Comparison between experiments, Marsh's H-S matrix method [14] and Frost's streamline curvature method [21]. The example is an axial turbine taken from [21]

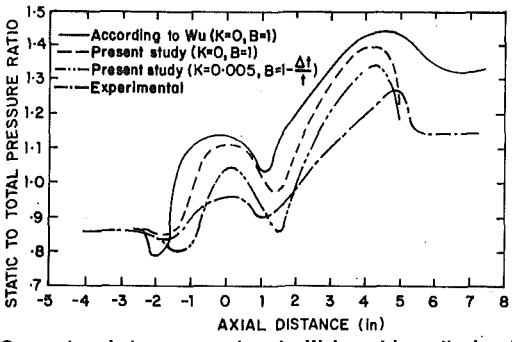


Fig. 2 Comparison between experiments, Wu's matrix method and Adler and Krimerman's H-S finite elements method [18]. The example is a mixed flow compressor taken from [18]. (K is a total pressure loss coefficient, B is the dimensionless circumferential stream sheet thickness, t is the impeller pitch, Δt is the blade thickness.)

compressor rotor are also shown. The two calculations predict similar velocity, pressure and total temperature distributions and agreement with experiments is reasonable. Finally in 1976 Hirsch and Warzee's finite element method was compared to experimental data obtained in a single stage NASA compressor (see Fig. 4). Agreement seems to be exceptionally good for an inviscid theory.

A final word of explanation and caution should be added here. Most of the H-S flow prediction methods mentioned so far and the comparisons discussed were carried out for axial flow machines (Figs. 1–4). The methods themselves, however, are of interest to centrifugal impeller flow studies.[2] But it should always be kept in mind, that three dimensional and viscous effects in centrifugal impellers are considerably more significant than in axial rotors, especially if a jet-wake flow is present. Therefore, in the case of conventional centrifugal impellers inviscid H-S techniques will give results which are further from reality than the comparisons in Figs. 1 to 4 would suggest. Further, all the H-S methods reviewed so far assume axisymmetric flow. In the higher loaded centrifugal impellers this assumption could lead to big discrepancies as will be shown later in this paper.

B-B Solutions. As in the case of the H-S surface solution the formulation of the B-B stream surface flow solution is somewhat artificial in that the assumed surface does not exist physically in the centrifugal impeller. The B-B solutions, however, serve to analyze trends required to be known for passage optimization rather than predict exact flow fields. Further, they can serve as essential "building blocks" in the development of more complete 3-D and viscous methods. Basically, the two groups of solutions on the H-S and the B-B stream surfaces have much in common. However, the most pronounced difference between the two is the lack of well defined boundaries at the inlet to, and the exit from the blade passages on the B-B surface. These boundaries are given on the H-S surface by the hub and shroud extensions in the upstream and downstream directions, and are therefore considered to be input data. In contrast, the boundaries, in form of the leading—and trailing edge stagnation

[2] For example the method of [18] was used unalteread in centrifugal radial exit impellers.

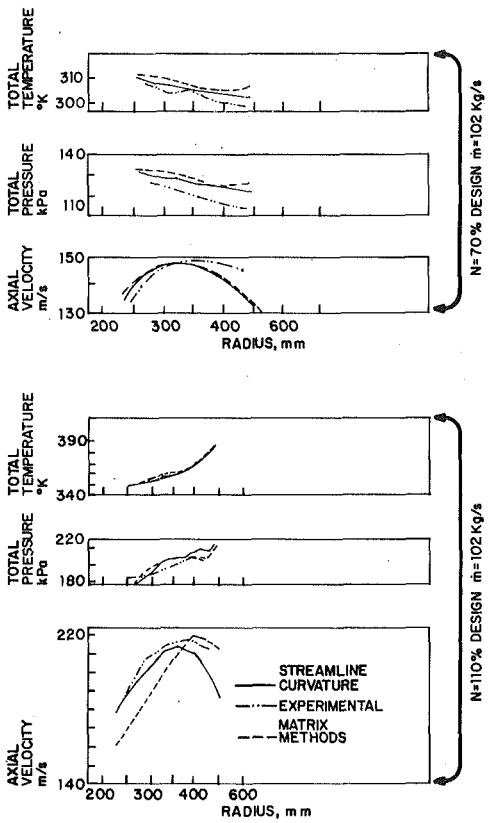


Fig. 3 Comparison between experiments, a H-S matrix method and a H-S streamline curvature technique according to Davis and Millar [22]. The example is an axial compressor taken from [22]

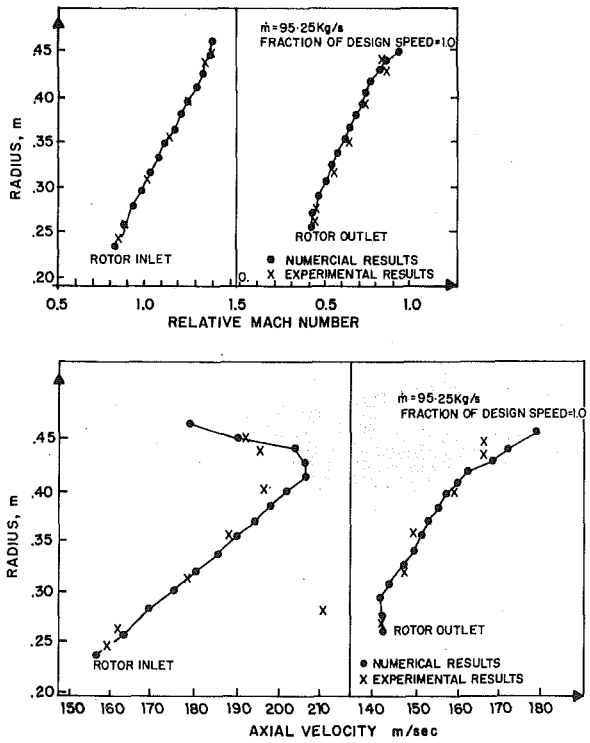


Fig.4 Comparison between experiments and Hirsch and Warzee's H-S finite elements calculations [20]. The example is an axial compressor taken from [20]

Downloaded 01 Jun 2010 to 171.66.16.58. Redistribution subject to ASME license or copyright; see http://www.asme.org/terms/Terms_Use.cfm

streamlines, are determined on the B-B surface in the course of the solution.

An approach to the B-B problem not used on the H-S surface is the method of singularities applied in all cases on a surface of revolution [23–28]. The surface is the center of a stream sheet which, in reality, is of varying thickness because of continuity with compressibility. The method has problems at the leading edge and the trailing edge, and the ways to overcome them are not always general enough. Martensen's [23] and Ogawa's [27, 28] methods, for example, develop difficulties when the blades are very thin (a common case in centrifugal impellers) or when the trailing edge is thick and rounded (again common in centrifugal impellers). It is reported that Wilkinson [24] was able to solve this problem; however, for an axial machine. In a centrifugal compressor, where viscous effects on deviation angle (and slip) are more significant, this problem is not yet solved. A severe problem in the application of the singularities technique in centrifugal impellers is the strongly varying streamsheet width. Ogawa and Murata [28] solved this problem by approximating the width variation by an analytical expression and, in a more exact manner by a numerical solution of their equations. From their work, it appeared that in spite of a large stream sheet variation, the solution yielded acceptable results.

As on the H-S surface, the streamline curvature method can be applied to the B-B surface flow prediction. It has been used less often however, probably because of the stagnation streamlines problem. One of the first methods was developed by Katsanis [29]. The method was based on an equation for the velocity gradient along quasi-orthogonals between the blades and was similar to the method of quasi-orthogonals on the H-S surface. The solution was carried out on a surface of revolution generated by rotating a previously calculated H-S streamline around the axis. Later, Katsanis used this streamline curvature technique in the supersonic regions of a transonic finite difference method which he developed. Wilkinson also developed a streamline curvature method [30]. He gave much attention to the location and shape of leading- and trailing edge stagnation streamlines, which is essential in this type of calculation. Wilkinson, who carried out basic work on streamline curvature techniques, their accuracy and convergence characteristics as affected by the curve fit procedures [31], was able to optimize the techniques as to the number of iterations required until convergence by deriving an optimum damping factor. Comparison of his results with experiments is given in Fig. 5.

Most frequently used in the B-B flow problem solution are finite difference techniques. Stanitz, a pioneer in this field, published a finite difference method as early as 1948 [32–34]. He determined the flow field by solving stream function equations. Stanitz also calculated off-design B-B flow fields and predicted pressure side separations (see Fig. 6) which, as is now well known, do not exist because of the important effect of viscosity on flow field. Stanitz's results illustrate clearly that inviscid methods are not able to predict, even approximately, off-design flow fields on the B-B stream surface. They should be used only at design point, and even here they will not be able to predict the jet-wake flow which has been measured by many investigators.

In 1968 Katsanis published a finite differences method to predict the B-B flow field [35]. Like most B-B flow calculation techniques, Katsanis' also suffered from the inaccuracy introduced by the sensivity of the results to the location and shape of the leading edge stagnation streamlines. To improve the accuracy of the prediction and to enable more detailed information in this critical part of the flow field, Katsanis and McNally [36] developed a method to predict the details of the flow field near the leading edge of the blades. They further developed their technique to handle splitter blades in centrifugal compressors [37]. The programs of Katsanis and McNally are popular and widely used but they also have the deficiency from which all inviscid B-B programs suffer; they can not predict the jet-wake flow, which is essentially a viscous phenomenon. This is a severe drawback of all inviscid B-B methods.

To complete the list of finite difference methods, the work of Smith and Frost should be noted [38]. Smith and Frost developed a finite

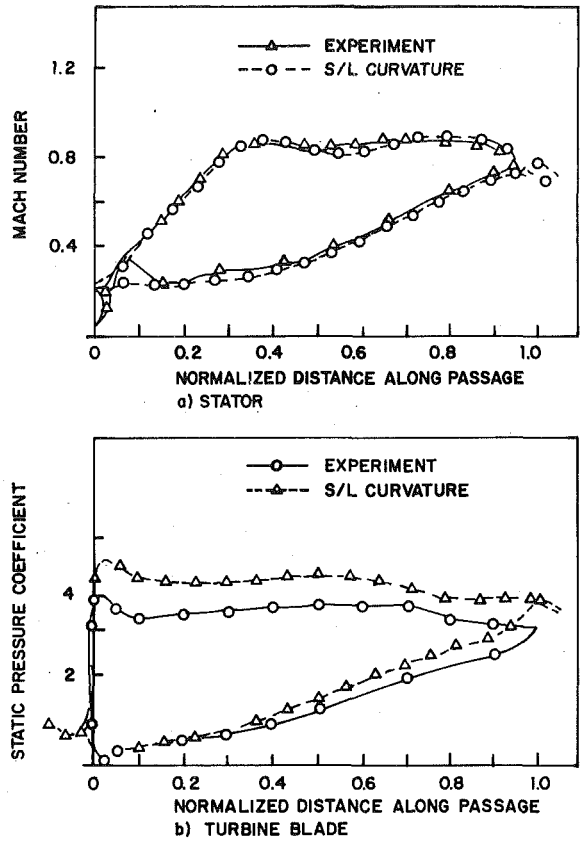


Fig. 5 Comparison between experiments and Wilkinson's B-B streamline curvature calculations [30]. The examples are an axial compressor and an axial turbine taken from [30]

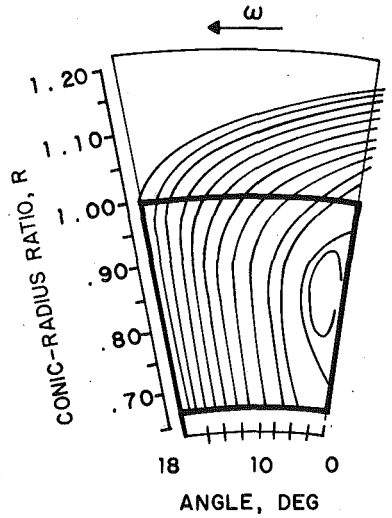


Fig. 6 Streamlines inside the rotating impeller as calculated by Stanitz [32]. The predicted inviscid pressure side separation is well visible on the right side. *Taken from [32]*

difference technique based on Wu's formulation [7]. They programed a solution using Marsh's scheme [14], and also programed a streamline curvature technique similar in its general features to those already mentioned. Using the two computer programs, Smith and Frost compared the two techniques by carrying out calculations for identical problems. In the case of an axial compressor a fair degree of agreement was achieved, except on the suction side leading edge where the velocity distribution computed by streamline curvature was oscillating. Smith and Frost believed that a finer mesh would have eliminated this problem. In the case of an axial turbine the streamline curvature technique behaved badly, and velocity oscillations were encountered both at the leading and the trailing edges, caused probably by difficulties in evaluation of streamline curvatures. This problem did not

Downloaded 01 Jun 2010 to 171.66.16.58. Redistribution subject to ASME license or copyright; see http://www.asme.org/terms/Terms_Use.cfm

exist in the finite difference solution. Generally it can be said that the streamline curvature technique required less computer storage than the finite difference technique, but the computing time was longer. In contrast to the finite difference method, the streamline curvature technique was not restricted by the local Mach number and could therefore be used in cases with local supersonic regions.

A general problem in numerical techniques is how to optimize convergence, accuracy and computation time. To demonstrate that the convergence and execution time of early programs can probably be improved in many cases, one can cite Deshpande's work [39]. Deshpande developed a new successive overrelaxation algorithm to improve Katsanis' original algorithm [35]. The new algorithm reduced execution time by a factor of 2.5 for a typical blade configuration. Further, Deshpande's algorithm enabled convergence for cases in which Katsanis' algorithm did not converge at all. Application of Deshpande's new algorithm in Katsanis' programs [35–37] required only minor modifications and is reported by Deshpande to have reduced computing costs considerably.

Davis and Millar [40] showed very clearly how complex the finite difference stencils can become in cases of unusual boundary geometry or with irregular grids imposed by the coordinate system. This problem can be removed by using the finite elements method.

Blade-to-blade finite element methods were published by Adler and Krimerman in 1977 [41], followed by Prince in 1978 [42]. Adler and Krimerman's approach was very similar to that taken in their H-S solution [18]. The main difference was that special care was taken to predict correctly the leading- and trailing edge stagnation streamlines. This was done by imposing the conditions of periodicity and constant angular momentum on the approaching flow field. The downstream stagnation streamline was evaluated using the Kutta-Jukowski condition and flow field periodicity. As in the H-S finite element solution, the B-B solution took advantage of the freedom to choose the location of grid points. Consequently, grid points were always located on streamlines, thus allowing again the use of the integrated energy equation. The model solved was Wu's B-B formulation [7], which was again given the artificial form of a Poisson equation to overcome the lack of a variational principle to Wu's principal equation. A comparison of Adler and Krimerman's results with experiments and with calculations by Stanitz, is shown in Fig. 7.

Prince [42] followed a somewhat different approach. He used a Galerkin variational analysis to satisfy the continuity equation for steady potential flow. He then used a Newton-Raphson method to solve the resulting system of nonlinear algebraic equations. Prince used continuity conditions to evaluate the upstream and downstream stagnation streamlines. To do this he used a distribution of stream sheet thickness which was required to be known a priori. Prince's calculated results compared well with experiments as is shown in Fig. 8.

Transonic B-B Flows. The case of transonic B-B flow is treated separately because the nature of this type of flow changes from elliptic when the Mach number is less than unity to hyperbolic when the Mach number is greater than unity. The difficulty in transonic solutions is that elliptic flow equations are solved with numerical techniques which differ considerably from the numerical techniques used in the solution of hyperbolic partial differential equations. The problem becomes even more complicated because the boundaries between the elliptic—and the hyperbolic regions of the flow (on which the equations are parabolic) is not known a priori but must be determined during the computation.

An early transonic solution was again derived by Katsanis [43]. Katsanis' method can be applied to any impeller geometry (axial or centrifugal). The solution was obtained as a combination of a finite difference technique, a stream function solution and a velocity gradient method. The finite difference solution, carried out at a reduced flow rate, provided information required for the velocity gradient method. For flow which was totally subsonic the finite difference method was used. In supersonic parts of the flow field, the streamline curvature technique was employed. Katsanis used different numerical techniques to obtain the solution in the different regions which required automatic detection of the region type and, accordingly, a

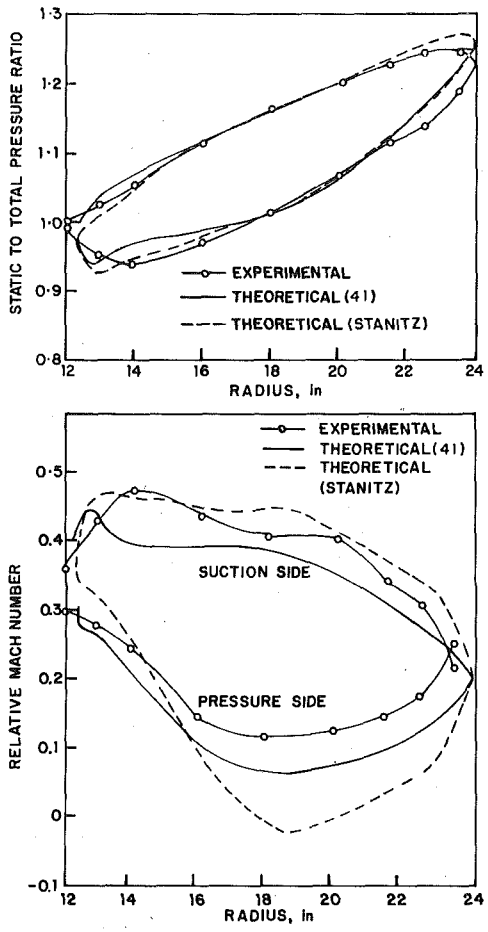


Fig. 7 Comparison between experiments, Stanitz's B-B calculations and Adler and Krimerman's B-B calculations [41]. The example is a centrifugal impeller taken from [41]

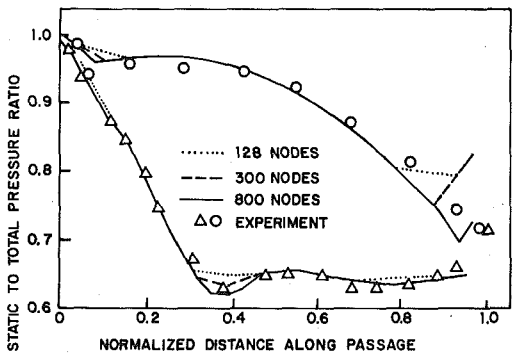


Fig. 8 Comparison between experiments and B-B calculations by Prince [42]. The example is an axial turbine stator taken from [42]

switch over from technique to technique. These complications could be overcome if a single solution could handle both sub- and supersonic regions of the transonic flow field.

Although the equations for steady flow are hyperbolic for supersonic flows and elliptic for subsonic flows, for unsteady flow the equations are hyperbolic both for super- and for subsonic flows. Therefore, if the time dependent equations of continuity, momentum and energy are used, a single solution technique is applicable for both types of flow. The steady flow, including both super- and subsonic regions, can then be regarded as the final steady state of the time dependent flow. This concept leads to a unified method used identically in the two flow regimes. Generally an approximate flow field is used as an initial condition and then the equations are integrated forward in time until the final steady solution is reached. The technique is known as the "time marching" method. In some cases, severe stability problems are encountered. They can often be solved, however, by reducing the time steps or by using an artificial viscosity

Downloaded 01 Jun 2010 to 171.66.16.58. Redistribution subject to ASME license or copyright; see http://www.asme.org/terms/Terms_Use.cfm

which has a damping effect.

In 1971, Marsh and Merryweather [44] described a stable time marching technique which was based on finite differences and did not rely on the use of artificial viscosity to achieve stability. It was found that several stable procedures could be developed for flow in convergent-divergent nozzles. The characteristic feature of the stable schemes was that the derivatives of all quantities other than pressure were approximated by backward differences, while the derivative of pressure contained a forward element. The computer program developed by Marsh and Merryweather [44] was relatively slow, some 2700 iterations being required to obtain a solution to an accuracy of 0.01 percent. Further work by Daneshyar and Glynn [45] was based on the method of characteristics which led to a much faster method of calculation. The method has been extended by Glynn to deal with cascade flows.

In 1971, McDonald [46] used a time marching method to calculate the pressure distribution around aerofoils in a cascade. The problem was formulated in terms of a finite area approach which led to the conservation equations in an integral form. The flow was assumed to be isentropic on the grounds that only weak shocks were normally encountered in cascades. McDonald obtained very good agreement between his calculated pressure distribution and that measured experimentally in a cascade. The use of the isentropic flow assumption is interesting in that Marsh and Merryweather had tried the same assumption for purely subsonic flows and had experienced a severe numerical instability. In impellers, where the flow is certainly not isentropic, these methods [44–46] have to be modified.

Also in 1971, Gopalakrishnan and Bozzola [47] published a time marching transonic technique. They used a predictor-corrector, two step, time splitting method to solve the partial differential formulation of the transonic flow problems. The method had stability problems unless the time step was smaller than a value predicted through a linear analysis, but even this was not always sufficient to give stable computation. To overcome this difficulty, a spatial smoothing procedure could be used. Excessive smoothing, however, caused inaccuracies in the results, as would be expected, and the problem then is the prediction of the negative effect of the smoothing.

In 1974, Denton [48] proposed a time marching scheme for cascade flows using a simpler grid than that of McDonald. Denton's grid consisted of quasi-streamlines and straight lines across the blade passage. The conservation equations for mass, momentum and energy were derived for a control volume. Instead of assuming isentropic flow, Denton assumed constant stagnation enthalpy, an assumption which became exact when the solution converged to the steady state flow. In Denton's scheme, the pressure at the central point of an element was assumed to act on the upstream face of the element, whereas the velocity at the center controlled the flow through the downstream face. The maximum time step for this scheme was found to be larger than for the method of Marsh and Merryweather [44].

Denton has applied his time marching method to calculating the blade-to-blade flow in several cascades and has obtained encouraging results. He has also extended the method to three-dimensional flows, although this did require a large amount of storage in the computer. The predictions obtained with this program have been compared with experiments performed with a rectangular duct having 60 deg of turning. Good agreement was obtained between the calculated and experimental pressure variations for the four corners of the duct. It should be possible to extend the time marching scheme to deal with three-dimensional flow in cascades.

It is noted again that Denton's technique and some of the other methods mentioned were developed for axial flow stator cascades. The methods can, in principle, be modified to handle the flow in centrifugal impellers. It simply has not yet been done. A computational technique to solve the flow in axial rotors was developed in 1975 by Kurzrock and Novick [49] in an approach similar to that of Gopalakrishnan and Bozzola [47]. They solved the Navier-Stokes equations using the time marching technique. The method was based on a time splitting finite difference technique, using a two step numerical evaluation of the time derivatives of the partial differential equations, together with a predictor-corrector technique. The spatial derivatives were numerically evaluated by backward differences for the predictor step and by forward differences for the corrector step. Fig. 9 illustrates the good agreement found between Kurzrock and Novick's results, and experimental measurements.

A completely different approach to the problem was introduced by Sobieczky, et al. [50]. Their method was developed for single airfoils but can be extended to stationary or rotating cascades [51]. Sobieczky, et al. developed a technique which enabled the design of shock free transonic aerofoils, in principle eliminating the losses associated with shocks and shock-boundary layer interactions. Their procedure was based on the use of any numerical method for subsonic, compressible isentropic flow. The algorithm of the selected method was modified so that if the flow became hyperbolic, the basic equations in that region were altered, using a "fictitious gas" concept, such that the system of equations reverted to elliptic behavior. In this way the complete flow field over a given configuration was first calculated using an elliptic procedure. The calculation served to define sonic surfaces. Outside the sonic surface the solution obtained satisfied the correct unmodified equations, and the potential at infinity had the correct value for the circulation. The second step in the procedure was to modify the surface geometry inside the sonic surface, using a hyperbolic procedure for the real gas, to generate a shock-free supersonic flow with the same conditions along the sonic line. Here a problem arises as it is well known that shock free, two or three dimensional irrotational near-sonic flows are physically and mathematically isolated. Any small change in flow—or boundary conditions might in practice lead to the formation of shock waves. However, if the shock waves are very weak the method will have practical significance. While Sobieczky's method was developed for inviscid flow, the same procedure can be employed iteratively with a boundary layer calculation to achieve shock free viscous designs.

3-D Inviscid Solutions. The prediction techniques previously described were all two dimensional. Their relevance to describing real impeller flows must be questioned, especially in the case of highly loaded centrifugal impellers where three dimensional effects are much more significant than in axial rotors or cascades. The answer to this question can be obtained in two ways: (1) comparison to experiments, (2) comparison between 2-D and 3-D solutions both carried out for a given impeller at the same operating conditions. First, currently available methods which can predict 3-D centrifugal impeller flow (or related axial rotor flow) will be reviewed.

An early attempt to predict the 3-D inviscid impeller flow was made by Schilhansl [52]. The work was restricted to incompressible flow and was developed with the severely restrictive assumption that all stream surfaces were surfaces of revolution. The method was based

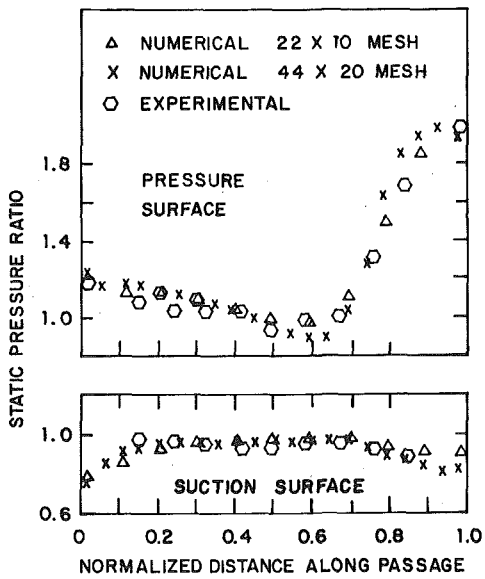


Fig. 9 Comparison between transonic experiments and Kurzrock and Novick's B-B calculations [49]. The example is an axial compressor cascade taken from [49]

Downloaded 01 Jun 2010 to 171.66.16.58. Redistribution subject to ASME license or copyright; see http://www.asme.org/terms/Terms_Use.cfm

on cascade theories then available in 1965. In fact the method of singularities used by Schilhansl restricted the application even further to irrotational flow, a severe limitation in turbomachinery flows. No results were reported in Schilhansl's paper [52] but the work illustrated very clearly what the difficulties were in the solution of 3-D flows. Six years later, in 1971, Katsanis published a 3-D compressible flow prediction method [53]. Katsanis used the ordinary differential equations of the streamline curvature technique, which define the values of velocity gradients along quasi-orthogonals. The continuity equation was integrally satisfied as is normally done in the streamline curvature methods. Katsanis solved the H-S and the B-B velocity gradient equations simultaneously, with the condition that either the weight flow was specified or that the flow was choked, to determine the velocity distribution over the blade surfaces. The method incorporated a number of assumptions, some of which could affect considerably the accuracy of the results in extreme geometries or flow conditions. The most restrictive assumptions were, (1) that there was either a linear variation of curvature or of radius of curvature along an orthogonal, (2) that there was no change in radius along a B-B orthogonal, and (3) that the flow angle along a B-B orthogonal was constant.

In 1972 Senno and Nakase published a quasi-3-D method [54]. The method included again the limitation that the blade-to-blade stream surfaces were axisymmetric. (In reality these stream surfaces are highly twisted and distorted.) Senoo and Nakase's method was based on two interacting procedures; one, a streamline curvature H-S procedure and the other a partial differential blade-to-blade technique developed by Senoo and Nakase a year earlier [55]. To achieve a final solution the method iterated from H-S to B-B and back, but the B-B stream surfaces were unaltered during the process and remained surfaces of revolution. The H-S method was rather conventional while the B-B solution was based on Prasil's independent variable transformation. The transformation simplified the method, but required the B-B stream surfaces to be axisymmetric. A comparison between Senoo and Nakase's calculated results and experiments is given in Fig. 10.

Six years later, two further works were published; Bosman and El-Shaarawi [56] and Novak and Hearsey [57]. Bosman and El-Shaarawi used Wu's approach to provide the mathematical model. They worked iteratively with the solutions obtained alternately on the H-S and B-B stream surfaces. However, the B-B surface was again always a surface of revolution and the H-S surface was calculated for an averaged mass flux. In reality the H-S surfaces and the mass flux through them change considerably across the passages. Thus their method was not truly three-dimensional. The solution of the principal equations was obtained using Marsh's matrix inversion method rather than by a relaxation method, because comparative studies carried out by Hill [58] and Bosman [59] showed that the matrix inversion method was considerably faster than the relaxation method. No comparison with experimental results was given in Bosman and El-Shaarawi's paper. But the differences between a 2-D computed flow field and their quasi-3-D results are demonstrated to be significant enough in the case of a typical centrifugal compressor impeller to justify the more elaborate quasi 3-D computation.

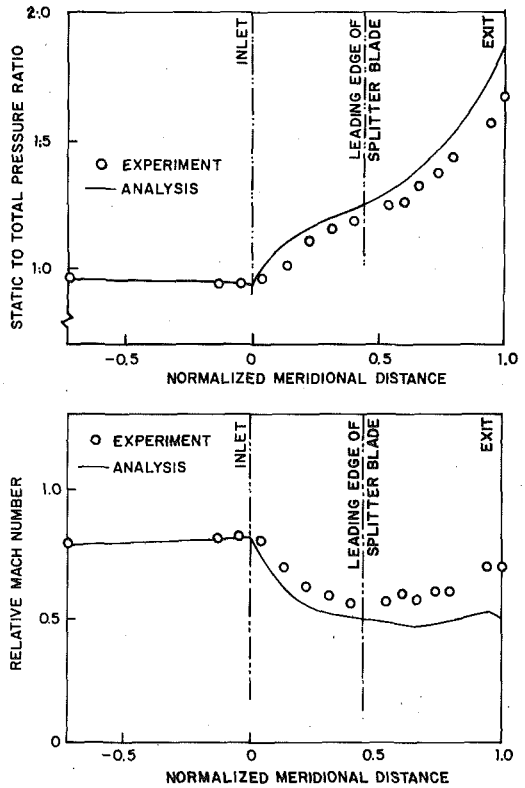


Fig. 10 Comparison between experiments and Senoo and Nakase's quasi-3-D calculations [54]. The example is a centrifugal impeller taken from [5]

Novak and Hearsey [57] also used two 2-D methods, one on the H-S surface and the other on the B-B surface to generate quasi 3-D results. Both 2-D component methods used the streamline curvature technique. The two programs were coordinated to yield a quasi 3-D solution, but as in the previous example, the B-B surfaces were surfaces of revolution, and the H-S surfaces were stream sheets roughly parallel to the blades. In other words, the H-S surfaces, which in reality vary from pressure side to suction side of the rotating passage, are represented in Novak's and Hearsey's work by a single surface. Comparisons with experimental measurements were given for an axial nozzle passage and an axial compressor cascade, and agreement was good. Centrifugal compressor flows were not analyzed, and therefore the accuracy of the technique in this case of more distorted flow is not known.

In 1978 two new 3-D inviscid methods were published, Hirsch and Warzee [60] and Krimerman and Adler [61] developed quasi-3-D methods based on Wu's approach. The method of Hirsch and Warzee [60], again used H-S and B-B formulations which were combined iteratively to yield a quasi 3-D flow. In Hirsch and Warzee's method the interaction between the H-S and the B-B solutions was stronger than in the previous methods because the stream sheet thickness and the streamline angles were transfered from the H-S solution to the B-B solution. Further, the fluctuation terms (as defined by Hirsch and Warzee [20]) were determined by a number of successive B-B solutions and then transfered to the H-S calculation. This was a step toward a more three-dimensional calculation; but nevertheless the B-B stream surfaces were always axisymmetric and the H-S solution, although corrected by computed fluctuation terms resulting from the B-B results, was still carried out on a single surface. As in their first method [20] Hirsch and Warzee used the finite elements technique for their solution.

Krimerman and Adler's method [61] was based on H-S and B-B solutions which they developed earlier [18, 41], and used the finite elements method of solution. However, in contrast to the previous methods in Krimerman and Adler's approach the B-B surface was not required to be axisymmetric and the real stream sheet thickness was taken into account as a spatially three-dimensional function. Further, the H-S flow was not represented any more by a single stream surface but was calculated on an arbitrary number of H-S surfaces which varied in shape from pressure side to suction side across the passage. Krimerman and Adler solved Wu's model, which they modified slightly. They began by calculating a single mean H-S solution. Then they calculated a number of axisymmetric B-B solutions between the hub and the shroud. As a third step, a number of H-S solutions were carried out, giving the circumferential variation of the flow field from pressure-to suction side. The fourth step was to calculate a number of B-B solutions in which the real variation of the H-S flows from pressure side to suction side of the passage was accounted for. Steps three and four were iteratively repeated until convergence was achieved. In this method [61] all the quantities and stream surface geometries were truly three-dimensional. No restricting assumptions about stream surface geometries are made and no pitch averages or fluctuation terms were required. The results were restricted only by the inviscid nature of the fluid and by the fact that corner streamlines

Downloaded 01 Jun 2010 to 171.66.16.58. Redistribution subject to ASME license or copyright; see http://www.asme.org/terms/Terms_Use.cfm

were fixed by the boundary conditions to be identical with the geometrical passage corners. In reality streamlines are not necessarily identical to the geometrical corners of the passage. Fig. 11 shows a sample of the results obtained by Krimerman and Adler for the flow in a centrifugal impeller. In Fig. 11, the intersection lines of quasi-orthogonal planes and the computed H-S and B-B surfaces are shown for four selected planes. The departure of the B-B surfaces, computed by the 3-D method from the axisymmetric B-B surfaces used previously is seen to be considerable. Fig. 11 also shows the variation of the H-S stream surfaces from pressure side to the suction side of the passage. In previous methods this variation was either not taken into account or it was represented by pitch averages and fluctuation terms. Fig. 12 shows how the method converged from the initial steps to the final 3-D solution.

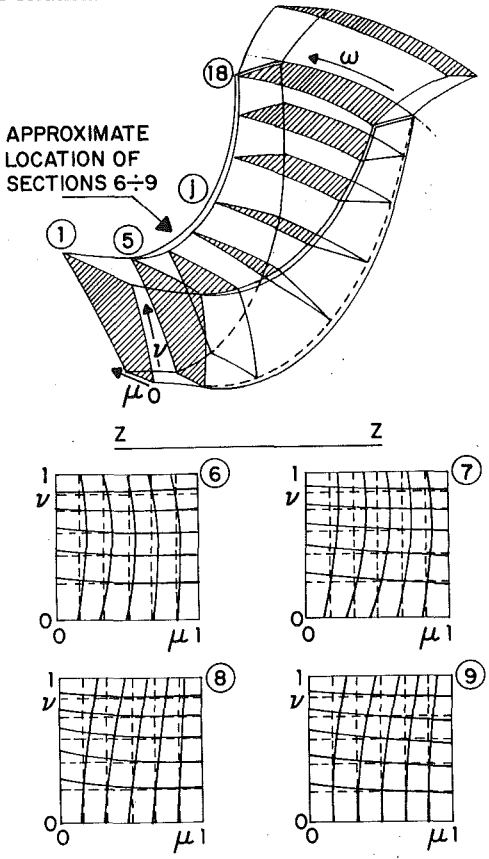


Fig. 11 The difference between the traces of 2-D surfaces (dashed lines) and 3-D stream surface traces, calculated by Krimerman and Adler [61]. The example is a centrifugal impeller taken from [61]. (The sections 6 to 9 shown are located in the inducer and beyond, in the region where the flow undergoes a double-change of direction both in the tangential direction and from axial to radial.)

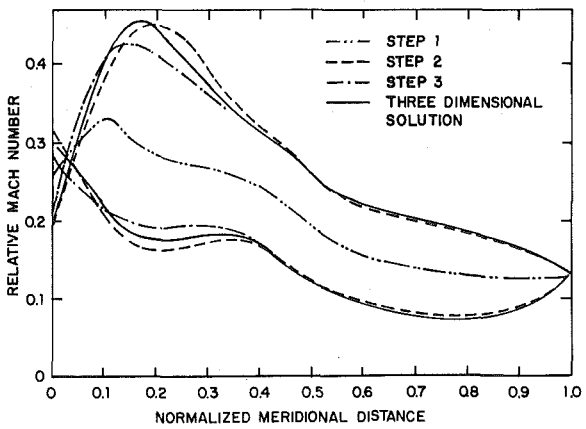


Fig. 12 The convergence into the 3-D solution of the relative-velocity Mach number distribution around a centrifugal compressor blade, according to Krimerman and Adler's calculations [61]. Example taken from [61]

The comparisons between the predictions of various inviscid techniques and the results of Figs. 2–9 are encouraging. Only in Figs. 1 and 10 are discrepancies clearly evident. The comparison shown in Fig. 13 fits well into this encouraging scene except for the data near the impeller exit, where the measured average pressure is far from the prediction. Is this a failure of the analysis or a measurement error? This question must be examined with greater care.

Adler and Krimerman [62] also used the technique described in [61], to calculate the flow in Eckardt's impeller [4], using the geometry reconstructed by Moore [63]. The results for some selected blade-to-blade sections in the center of the passage are given in Fig. 14. The predictions appear to be good except perhaps near to the exit. How-

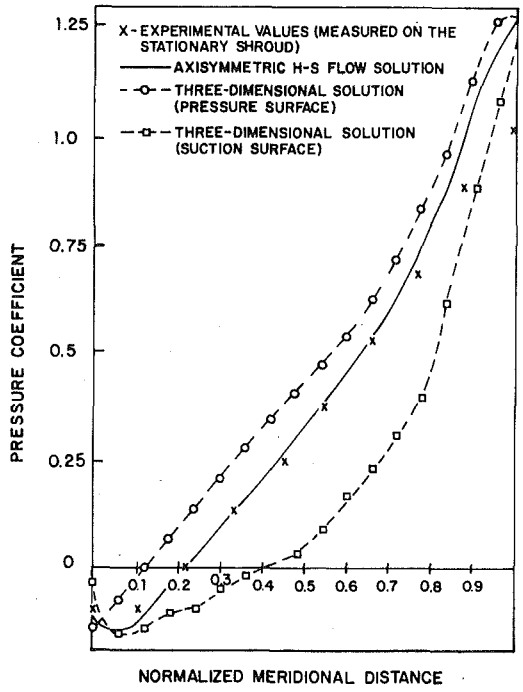


Fig. 13 Comparison between experiments and 3-D inviscid calculations by Krimerman and Adler [61]. The example is a centrifugal radial exit impeller taken from [61]

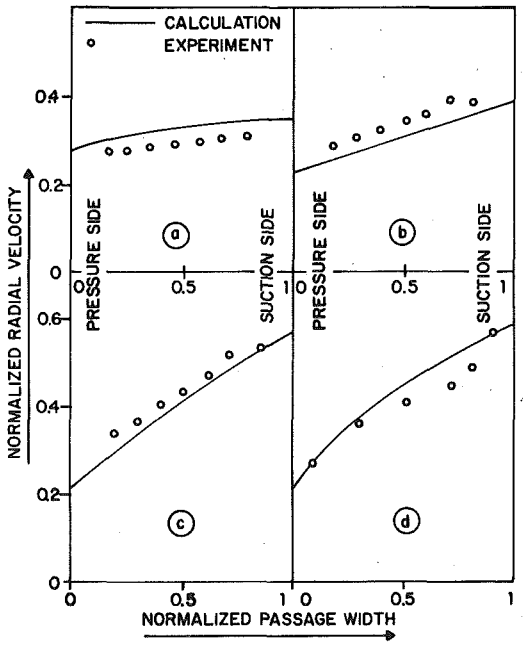


Fig. 14 Comparison between Eckardt's measurements at the passage center [4] and 3-D calculations by Krimerman and Adler [61]. (a) immediately after inlet; (b, c) about mid passage location; (d) close to exit

Downloaded 01 Jun 2010 to 171.66.16.58. Redistribution subject to ASME license or copyright; see http://www.asme.org/terms/Terms_Use.cfm

ever, Fig. 15 gives the comparison between calculations and measurement in the same impeller but close to the shroud where Eckardt detected the wake. Here the prediction is seen to be poor. The reason for the poor agreement between calculation and experiment seen in Fig. 16 and at the exit regions in Fig. 13 and Fig. 14, is almost certainly the effect of viscosity which was eliminated in the analytical models.

The failure of the inviscid models to predict the flow in centrifugal impellers is manifested when a jet-wake flow is present. The situation in this case is quite different from that found in axial flow machines and is reminiscent of the inadequacy which is found in applying inviscid models in cases of separated flows. The wake is probably similar to a separated flow, although different in that it must be influenced by the strong centrifugal and the Coriolis acceleration fields which are present in rotating passages. These features will be discussed in a subsequent article [64]. Inviscid models are acceptable for the prediction of the flow only in impellers with fully attached flow.

Another major limitation of the inviscid models described in the previous paragraphs is their inability to predict correctly secondary flows, which are to a large extent dominated and initiated by viscous effects. The secondary flows, so well described by Eckardt [4], can have a significant effect on the impeller flow field and consequently on the impeller performance. Secondary flow effects must be included in a really representative prediction method.

Comparison of Computation Times

The solution techniques mentioned in this review require numerical methods. A comparison of their drawbacks and merits is not complete without consideration of their demands for computer time and computer storage. For most numerical techniques the storage requirements are not published, though the particular computer model used can sometimes indicate what might be required. Table 1 gives an approximate indication of computation times for some of the techniques mentioned in this review. An exact accounting, however, is not possible as some authors mention virtual execution time, and others indicate a total time which includes compilation of the program. Some authors even neglect to define the time that they quote. Furthermore, the time stated depends strongly on the problem solved and the accuracy obtained in the results. The accuracy, in turn, is affected by mesh size and convergence criterions adopted. The values given in the following table should therefore, be treated as an order of magnitude indication only. Table 1 classifies the techniques according to the following abbreviations: SC = streamline curvature, FD = finite differences, and FE = finite elements.

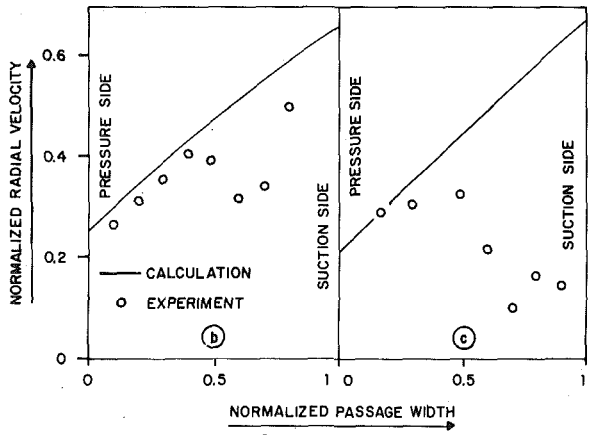


Fig. 15 Comparison between Eckardt's measurements [4] near the shroud and 3-D calculations by Krimerman and Adler [61]. (*b, c*) about mid passage location

Acknowledgments

The research for this report was partly conducted while the author was a Visiting Consultant to Cummins Engines Company Inc., Columbus, Indiana. The study was completed and the report written while he was NAVAIR Chair Visiting Professor at the Turbopropulsion Laboratory of the Naval Postgraduate School, Monterey, California.

The author is grateful for the support he received from Dr. W. T. Lyn, Vice President and Head of the Research Division at Cummins, for sponsorship by the Naval Air Systems Command under the cognizance of Dr. H. J. Mueller, and for the considerable help given by professors M. F. Platzer and R. P. Shreeve, Naval Postgraduate School.

References

1 Stang, J. H., "Designing Adiabatic Engine Components", SAE paper 780069, 1978.

2 Fowler, H. S., "The Distribution and Stability of Flow in a Rotating Passage," ASME JOURNAL OF ENGINEERING FOR POWER, Vol. 90, 1968, pp. 229–236.

3 Moore, J., "A Wake and an Eddy in a Rotating Radial Flow Passage," ASME JOURNAL OF ENGINEERING FOR POWER, Vol. 95, 1973, pp. 205–219.

4 Eckardt, D., "Detailed Flow Investigation within a High Speed Centrifugal Compressor Impeller," *Journal of Fluid Engineering*, Vol. 98, 1970, p. 390.

5 Senoo, Y., Hayami, H., Kinoshita, Y., and Yamasaki, H., "Experimental Study on Flow in a Supersonic Centrifugal Impeller," ASME JOURNAL OF ENGINEERING FOR POWER, Vol. 101, 1979, pp. 32–41.

6 Adler D., and Ilberg, M., "A Simplified Method for Calculation of the Flow Field at the Entrance of a Radial or a Mixed Flow Impeller," ASME Paper No. 70-FE-36, 1970.

7 Wu, C. H., "A General Theory of Three-Dimensional Flow in Subsonic and Supersonic Turbomachines of Axial Radial, and Mixed Flow Types," NACA TN 2604, 1952.

8 Katsanis, T., "Use of Arbitrary Quasi-Orthogonals for Calculating Flow Distribution in the Meriodional Plane of a Turbomachine," NASA TN D-2546, 1964.

9 Novak, R. A., "Stream Line Curvature Computing Procedures for Fluid Flow Problems," Trans ASME, 1967.

10 Novak, R. A., "The Mean Stream-Sheet Momentum Continuity Solution

Table 1 Comparison of approximate computation times

Author	Ref. No.	Computer Used	Time (Mins)	Flow	Technique
Katsanis	[8]	IBM 360	10	H-S inviscid	SC
Marsh	[14]	KDF 9	10–15	H-S inviscid	FD
Katsanis/McNally	[16]	IBM 360	30	H-S inviscid	FD
Katsanis/McNally	[17]	IBM 360	3–15	H-S inviscid	FD
Adler/Krimerman	[18]	IBM 370	1.5	H-S inviscid	FE
Frost	[21]	SDS 90/300	10–15	H-S inviscid	SC
Davis/Millar	[22]	?	1	H-S inviscid	SC
Davis/Millar	[22]	?	.5	H-S inviscid	FD
Wilkinson	[30]	IBM 360	.5	B-B inviscid	SC
Katsanis/McNally	[36]	IBM 360	30	B-B inviscid	FD
Adler/Krimerman	[41]	IBM 370	2	B-B inviscid	FE
Katsanis	[43]	IBM 360	10	B-B transonic/inviscid	SC/FD
Senoo/Nakase	[55]	Facom 230-60	cpu 10 (sec)	B-B inviscid	FD
Katsanis	[53]	IBM 360	2	3-D inviscid	SC/FD
Senoo/Nakase	[54]	Facom 230-60	16	3-D inviscid	SC/FD
Bosman/Shaarawi	[56]	CDC 7600	3.5	3-D inviscid	FD
Novak/Hearsey	[57]	CDC 6600	1.5	3-D inviscid	SC
Hirsch/Warzee	[60]	CDC 6500	cpu 1	3-D inviscid	FE
Krimerman/Adler	[61]	IBM 370	5	3-D inviscid	FE

Downloaded 01 Jun 2010 to 171.66.16.58. Redistribution subject to ASME license or copyright; see http://www.asme.org/terms/Terms_Use.cfm

Techniques for Turbomachinery," Iowa State University, July 15–25, 1975.
11 Davis, W. R., "A Comparison of Different Forms of the Quasi-Three-Dimensional Radial Equilibrium Equation of Turbomachines," Carleton University Report No. ME/A 68-1, 1968.
12 Smith, L. H., "The Radial Equilibrium Equation of Turbomachinery," ASME JOURNAL OF ENGINEERING FOR POWER, Vol. 88, 1966, pp. 1–12.
13 Wu C. H., and Curtis, A., et al., "Analysis of Flow in a Subsonic Mixed Flow Impeller," NACA TN-2749, 1952.
14 Marsh, H., "A Digital Computer Program for the Through-Flow Fluid Mechanics in an Arbitrary Turbomachine Using a Matrix Method," R&M No. 3509, 1968.
15 Davis, W. R., "Axial Flow Compressor Analysis Using a Matrix Method," Carleton University, Report No. MW/A 73-1, 1973.
16 Katsanis, T., McNally, W. D., "Fortran Program for Calculating Velocity and Streamlines on the Hub-Shroud Mid Channel Flow Surface of an Axial- or Mixed Flow Turbo-machine," NASA TN D-7343, 1973.
17 Katsanis T., and McNally, W. D., "Revised Fortran Program Calculating Velocities and Streamlines on the Hub-Shroud Mid Channel Stream Surface of an Axial, Radial, or Mixed Flow Turbomachine of Annular Duct," NASA TN D-8430/1, 1977.
18 Adler D., and Krimerman, Y., "The Numerical Calculation of the Meridional Flow Field in Turbomachines Using the Finite Elements Method," *Israel Journal of Technology*, Vol. 12, 1974, pp. 268–274.
19 Oates, B. C. Knight C. J., and Carey, G. F., "A Variational Formulation of the Compressible Through Flow Problem," ASME Paper No. 75-GT-32, 1975.
20 Hirsch Ch., and Warzee, G., "A Finite Element Method for Through Flow Calculation in Turbomachines", *Journal of Fluids Engineering* Vol. 98, 1976, p. 403.
21 Frost, D. H., "A Streamline Curvature Through Flow Computer Program for Analyzing the Flow Through Axial Flow Turbomachines", *Aero. Res. Council*, R&E No. 3687, 1972.
22 Davis W. R., and Millar, D. A. J., "A Comparison of the Matrix and Streamline Curvature Methods of Axial Flow Turbomachinery Analysis from a User's Point of View," ASME Paper No. 74-WA/GT-4, 1974.
23 Martensen, G. E., *Juris Verlag*, Prom. No. 3042, 1964.
24 Wilkinson, D. H., Aeronautical Research Council, R&M 3545, 1968.
25 Rauchman B. S., "Blade Cascade on Axisymmetric Flow Sheet of Variable Thickness of Subsonic Flow," *Energomachinostroenie* N11, 1972 (in Russian).
26 von Der Braembussche, "Transonic Flow in Turbomachinery," von Karman Institute Lecture Series, Lecture 59 (1973).
27 Ogawa T., and Murata, S., "On the Flow in the Centrifugal Impeller with Arbitrary Airfoil Blades," *Bulletine of the JSME*, Vol. 17, 1974, p. 713.
28 Ogawa T., and Murata S., "On the Flow in the Centrifugal Impeller with Arbitrary Airfoil Blades," *Bulletine of the JSME*, Vol 17, 1974, p. 723.
29 Katsanis, T., "Use of Arbitrary Quasi-Orthogonals for Calculating Flow Distribution on a Blade-to-Blade Surface in a Turbomachine," NASA TN D-2809, 1965.
30 Wilkinson, D. H., "Calculation of Blade-to-Blade Flow in a Turbomachine by Streamline Curvature," Aeronautical Research Council, R&M No. 3704, 1972.
31 Wilkinson, D. H., "Streamline Curvature Methods for Calculating the Flow in Turbomachines," English Electric Co., Report No. W/M (3F), 1969.
32 Stanitz, J. D., "Two-Dimensional Compressible Flow in Conical Mixed Flow Compressors," NACN TN 1744, 1948.
33 Stanitz, J. D., "Two-Dimensional Compressible Flow in Turbomachines With Conical Flow Surfaces," NACA TO 935, 1949.
34 Stanitz J. D., and Ellis, G. O., "Two-Dimensional Compressible Flow in Centrifugal Compressors with Straight Blades," NACA TR 954, 1950.
35 Katsanis, T., "Computer Program for Calculating Velocities and Streamlines on a Blade-to-Blade Stream Surface of a Turbo-machine," NASA TN D-4525, 1968.
36 Katsanis T., and McNally, W. D., "Fortran Program for Calculating Velocities in a Magnified Region on a Blade-to-Blade Stream Surface of a Turbomachine," NASA TN D-5044, 1969.
37 Katsanis T., and McNally, W. D., "Fortran Program for Calculating Velocities and Streamlines on a Blade-to-Blade Stream Surface of a Tandem Turbomachine," NASA TN D-5044, 1969.
38 Smith D. J. L., and Frost, D. H., "Calculation of the Flow Past Turbomachine Blades," *Proc. Institution of Mechanical Engineers*, Vol. 184, part 3G (II), 1969/70.
39 Deshpande, R. B., "A New Algorithm for the Solution of Turbomachinery Flow Problems," *Journal of Fluids Engineering*, Vol. 97, 1975, pp. 372–374.
40 Davis W. R., and Millar, D. A. J., "A Matrix Method Applied to the Analysis of the Flow Past Turbomachine Blades," Carleton University Report ME/A72-7, 1972.
41 Adler D., and Krimerman Y., "Calculation of the Blade-to-Blade Compressible Flow Field in Turbo Impellers Using the Finite-Element Method," *Journal of Mechanical Engineering Science*, Vol. 19, 1977, pp. 108–112.
42 Prince, T. C., "Prediction of Steady Inviscid Compressible Flow on a Blade-to-Blade Surface by Finite-Element Method," AIAA paper 78-244, 1978.
43 Katsanis, T., "Fortran Program for Calculating Transonic Velocities on a Blade-to-Blade Stream Surface of a Turbomachine," NASA TN D-5427, 1969.
44 Marsh H., and Merryweather, H., "The Calculation of Subsonic and Supersonic Flow in Nozzles," Institution of Mechanical Engineers, Symp. on Internal Flows, paper 22, 1971.
45 Daneshyar H., and Glynn, D. R., "The Calculation of Flow in Nozzles Using a Time Marching Technique Based on the Method of Characteristics," *International Journal of Mechanical Eng. Science*, 1973, p. 921.
46 McDonald, R. W., "The Computation of Transonic Flow Through Two-Dimensional Gas Turbine Cascades," ASME Paper 71-GT-89, 1971.
47 Gopalakrishran S., and Bozzola, R., "A Numerical Technique for the Calculation of Transonic Flows in Turbomachinery Cascades," ASME Paper No. 71-GT-42, 1971.
48 Denton, J. D., "A Time Marching Method for Two- and Three-Dimensional Blade-to-Blade Flows," Aeronautical Research Council, 35567, 1974.
49 Kurzrock J. W., and Novick, A. S., "Transonic Flow Around Rotor Blade Elements," ASME Paper No. 75-FE-24, 1975.
50 Sobieczky, H., Fung K. Y., and Seebass, A. R., "A New Method for Designing Shock Free Transonic Configurations," AIAA Paper 78-144, 1978.
51 Sobieczky H., "Design of Shock Free Transonic Flow in Turbomachinery," USN Naval Postgraduate School Report NPS 67-78-005, 1978.
52 Schilhansl, M. J., "Three-Dimensional Theory of Incompressible and Inviscid Flow Through Mixed Flow Turbomachines," ASME JOURNAL OF ENGINEERING FOR POWER, Vol. 87, 1965, pp. 361–373.
53 Katsanis, T., "Fortran Program for Quasi-Three-Dimensional Calculation of Surface Velocities and Choking Flow for Turbomachine Blade Rows," NASA TN D-6177, 1971.
54 Senoo Y., and Nakase, Y., "An Analysis of Flow Through a Mixed Flow Impeller," ASME JOURNAL OF ENGINEERING FOR POWER, Vol. 94, 1972, pp. 43–50.
55 Senoo Y., and Nakase, Y., "A Blade Theory of an Impeller with an Arbitrary Surface of Revolution," ASME JOURNAL OF ENGINEERING FOR POWER, Vol. 93, 1971, pp. 454–460.
56 Bosman C., and El-Shaarawi, M. A. I., "Quasi-Hsec-Dimensional Numerical Solution of Flow in Turbomachines," *Journal of Fluids Engineering*, Vol. 99, 1977, pp. 132–140.
57 Novak R. A., and Hearsey, R. M., "A Nearly Three-Dimensional Interblade Computing System for Turbomachinery," *Journal of Fluids Engineering*, Vol. 99, 1977, pp. 154–166.
58 Hill, M. J., "Numerical Solutions for Mixed Flow Turbomachines," University of Manchester Institute of Science and Technology, Ph.D. Thesis, 1977.
59 Bosman, C., "Computation Aspects of Fluid Flow Through a Turbomachine," University of Manchester Institute of Science and Technology, Ph. . Thesis, 1977.
60 Hirsch Ch., and Warzee, G., "An Integrated Quasi-3-D Finite Element Calculation Program for Turbomachinery Flows," ASME JOURNAL OF ENGINEERING FOR POWER, Vol. 101, 1979, pp. 141–148.
61 Krimerman Y., and Adler, D., "The Complete Three-Dimensional Calculation of the Compressible Flow Field in Turbo Impellers," *Journal of Mechanical Engineering Science*, Vol. 20, 1978, pp. 149–158.
62 Adler D., and Krimerman, Y., "On the Relevance of Inviscid Subsonic Flow Calculations to Real Centrifugal Impeller Flow" (to be published).
63 Moore, J., "Eckardt's Impeller—a Ghost From Ages Past," University of Cambridge Report CUED/A-Turbo/TR 83, 1976.
64 Adler, D., "Status of Centrifugal Impeller Internal Aerodynamics: Part II: Experiments and Influence of Viscosity," ASME JOURNAL OF ENGINEERING FOR POWER, Vol. 102, No. 3, pp. 738–746.

Downloaded 01 Jun 2010 to 171.66.16.58. Redistribution subject to ASME license or copyright; see http://www.asme.org/terms/Terms_Use.cfm

D. Adler[1]
NAVAIR Chair Visiting Professor,
Turbopropulsion Laboratory,
Department of Aeronautics,
Naval Postgraduate School,
Monterey, CA 94940

Status of Centrifugal Impeller Internal Aerodynamics

Part II: Experiments and Influence of Viscosity

Recent developments in internal viscous aerodynamics of centrifugal impellers and related flows are critically reviewed. The overall picture which emerges provides the reader with a state-of-the-art perspective on the subject. Gaps in understanding are identified to stimulate future research. Topics included in this review are: experimental work carried out in the last decade, the structure of turbulence in curved rotating passages and solution of viscous flow problems in impellers.

Introduction

Inviscid flow prediction methods in centrifugal impellers were reviewed in a previous article [1]. It was found that the comparison between the predictions by a number of inviscid techniques with experiments [2–8] was satisfactory. However, in the comparison given in [9] and [10], discrepancies were clearly evident. The comparison between the prediction in [11] and experimental results fitted well into this encouraging picture except for data near the impeller exit, where the measured average pressure was far from the prediction. Is this a failure of the analysis or a measurement error? This question will be examined with greater care in this article.

The technique described in [11] was used to calculate the flow in Eckardt's impeller [12], using the geometry reconstructed by Moore [13]. The results for some selected blade-to-blade sections in the center of the passage are given in Fig. 1. The predictions appear to be good except perhaps near to the exit. However, Fig. 2 gives the comparison between calculations and measurement in the same impeller but close to the shroud where Eckardt detected the wake. Here the prediction is seen to be poor. The reason for the poor agreement between calculation and experiment seen in Fig. 2 and at the exit regions in Fig. 3 and Fig. 1 is almost certainly the effect of viscosity which was eliminated in the analytical models used.

The failure of the inviscid models to predict the flow in centrifugal impellers is manifested when a jet-wake flow is present. The situation in this case is quite different from that found in axial flow machines and is reminiscent of the inadequacy which is found in applying inviscid models in cases of separated flows. The wake is probably similar to a separated flow, although different in that it must be influenced by the strong centrifugal and the Coriolis acceleration fields which are present in rotating passages. Inviscid models are acceptable for the prediction of the flow only in impellers with fully attached flow.

The aim of this article is to discuss these effects of viscosity in the light of experimental observations. Further, the state-of-the-art of viscous impeller flow prediction methods will be described, thus completing the picture given in [1].

Experimental Observations

For a long time centrifugal impellers were designed with the concept of a full passage flow. The classical approach of infinite number of blades of zero thickness combined with a correcting slip factor is an example of this approach. However, the full passage flow concept was already challenged as early as 1923 by Carrard [14], who calculated a neutral zone in the impeller passage. He was probably the first to propose a calculation method for this type of flow which about three decades later was called the jet-wake flow.

The full passage concept could survive for a long period only because experimental insight into the impeller flow was hampered by the fact that it is, unfortunately, rotating. The wake in a rotating impeller was visualized or detected by a number of investigators [15–18] but no detailed velocity mapping was available until 1957, when Acosta and Bowerman [19] measured the flow field inside a centrifugal pump impeller with backswept blades ($\beta = 23.5$ deg) using manometer tubes which were rotating with the impeller. They did not detect a jet-wake flow, which probably did not occur in the type of strongly backswept impeller which they used. Their results, therefore, did not challenge the full passage flow concept. A year later, in 1958, Fujie [20] published results measured inside a radial exit ($\beta_2 = 90$ deg) centrifugal compressor impeller using a low speed "pneumatic slip ring," or pressure transfer cell. Fujie's experiments were carried out at a number of tip speeds ranging from 37 m/s to 105 m/s. Although "pockets" of lower relative velocities were detected in the vicinity of the passage suction side, no well developed wake region, like those found by later investigators, was detected. This is surprising, but furthermore, Fujie's comparison of the measurements to calculated inviscid irrotational and incompressible velocity profiles [20] (Fig. 14 [20]) revealed that viscous effects now recognized and fully appreciated, were smaller in his results than one would have expected.

Ten years passed, until in 1968, Fowler [21] published results taken in a radial exit impeller at low speed (30 to 60 rpm). Fowler used hot wire anemometers for his measurements. The impeller had to rotate very slowly because a technician, rotating with the impeller in a special cage, monitored the readings. The tip velocity in this experiment is estimated to have been 2.5 m/s to 5 m/s (Fowler did not publish the exact geometry and diameter of his impeller), but despite this low tip speed, Fowler detected a flow having the main features of the jet-wake structure. In fact, he measured, in all through-flows from fully open flow to 50 percent reduced flow rates, a suction side velocity that was

[1] Permanent Address: Department of Mechanical Engineering, Technion, Israel Institute of Technology, Haifa, Israel.

Contributed by the Gas Turbine Division for publication in the JOURNAL OF ENGINEERING FOR POWER. Manuscript received at ASME Headquarters May 7, 1979.

Copyright © 1980 by ASME
Downloaded 01 Jun 2010 to 171.66.16.58. Redistribution subject to ASME license or copyright; see http://www.asme.org/terms/Terms_Use.cfm

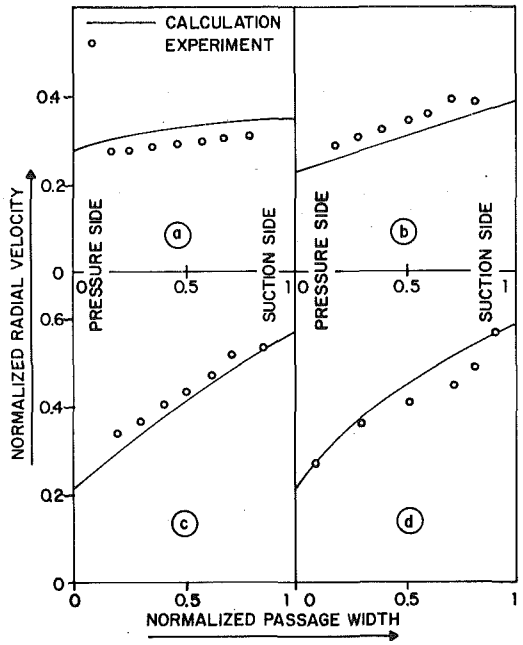


Fig. 1 Comparison between Eckardt's measurements at the passage center [12] and 3-D calculations by Krimerman and Adler [11]. (*a*) immediately after inlet; (*b, c*) about mid passage location; (*d*) close to exit

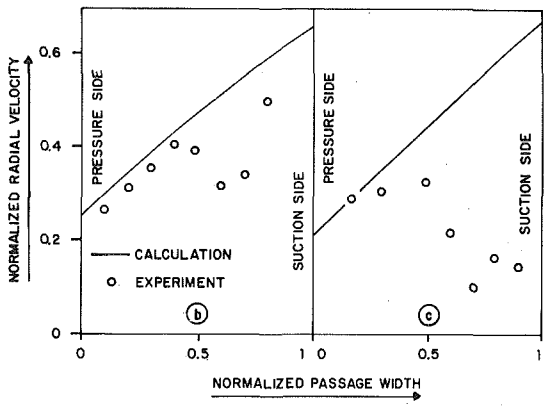


Fig. 2 Comparison between Eckardt's measurements [12] near the shroud and 3-D calculations by Krimerman and Adler [11]. (*b, c*) about mid passage location

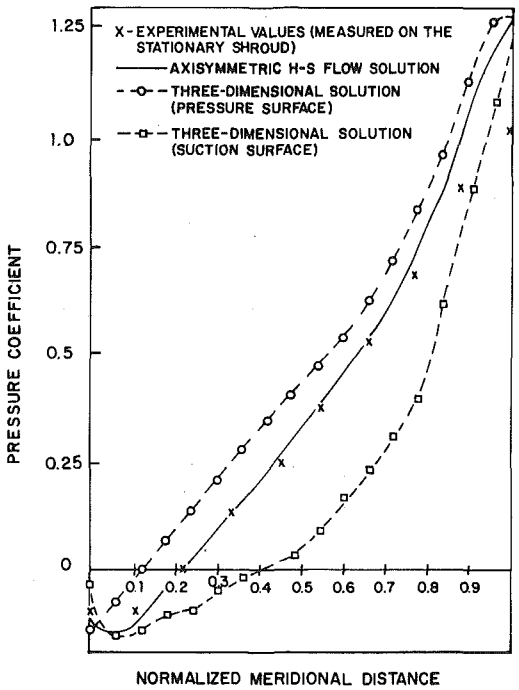


Fig. 3 Comparison between experiments and 3-D inviscid calculations by Krimerman and Adler [11]. The example is a centrifugal redial exit impeller taken from [11]

much lower than pressure side velocity, in contrast to inviscid flow predictions. Fowler did not detect the shear layer which separates the wake from the jet, and in which the velocity gradients are exceptionally large. However, his measurements showed that for radial exit centrifugal impellers, even at very low speeds, the inviscid flow models were not able to describe the real flow with sufficient accuracy.

In 1973, Moore [22] published his results obtained in a radial exit rotating single passage. The results were reported in detail, including secondary flows, and were the first published data that describe the shear layer between a jet and wake in a rotating passage. They were detailed enough to allow a quantitative analysis of a jet wake flow. The jet wake structure observed by Moore was well developed despite the small peripheral tip speed of about 20 m/s and the fact that the fluid was pushed through the passage. Moore's experiments were carried out at a number of flow rates, and it is interesting to point out that in contrast to that of Fowler, Moore's jet-wake structure weakened considerably as the flow rate was reduced until it disappeared completely and wake filled up with healthy flow. Unfortunately this weakening of the jet-wake flow with flow rate was not discussed in detail. A possible explanation could be that Moore reduced his flow rate more than others did.

In 1975 Howard and Kittmer presented measurements carried out inside a backswept centrifugal impeller ($\beta_2 = 22$ deg) with and without a rotating shroud [23]. Their impeller pumped water, and the velocity field was measured with a miniature hot film probe. Like Acosta [19] and in contrast to Moore [22] and Fowler [21], Howard and Kittmer did not detect a jet-wake flow though all these experiments were carried out under imcompressible low speed flow conditions. The full passage flow in Howard's experiments was present in both the closed and the open impeller versions, an indication that in this case the blade tip clearance flow did not affect the flow stability. Acosta [19] and Howard [23] measured in back swept impellers and they did not detect a jet-wake flow. Fowler [21] and Moore [22] measured in radial exit impellers and they found a jet-wake structure. Is this observation significant, taking into account that all these experiments were low speed and incompressible?

Later, in 1976, Eckardt published his paper [12] on the optical measurement of flow in a high speed open radial exit centrifugal impeller, close to its design point. The tip velocity was about 300 m/s. Eckardt used Schodl's L2F technique [24] and was able to obtain the internal impeller flow field details. His results showed the development of a well established jet-wake structure from an almost uniform inlet flow field into a highly distorted exit flow field. Unfortunately, the geometry of Eckardt's impeller was not published by him, so that his results could not be used for analysis by other investigators. Luckily the missing information was furnished by J. Moore [13] who reconstructed Eckardt's flow passage using available data.

Also in 1975, Mizuki, et al. published a very detailed report [25] on measurements in an open radial exit centrifugal impeller at a number of points of operation. The impeller rotated at a tip speed of 60.8 m/s and readings were taken inside the impeller with four-hole yaw probes and taken out by means of mechanical seals. Further, static pressures were measured along the stationary shroud with high frequency transducers and gas velocities were measured at the impeller exit with a hot wire anemometer. Their results are interesting because like Fowler [21] and Moore [22] they extend over a relatively wide range of flow coefficient from $\varphi = 0.11$ to $\varphi = 0.33$. Unfortunately, these points are not identified on the compressor map so that their relation to the choke and surge lines is not known. Like previous investigators Mizuki et al. identified a jet-wake structure, the wake being located as usual close to the suction side-shroud corner, though a little displaced from the boundary. As in Fowler's experiments, and even more so in Moore's, the intensity of the wake was decreasing with reduced through-flow probably because of a general reduction of intensity of the flow field. This was verified by Mizuki both in his internal measurements at the impeller exit and his stationary measurements in

Downloaded 01 Jun 2010 to 171.66.16.58. Redistribution subject to ASME license or copyright; see http://www.asme.org/terms/Terms_Use.cfm

the diffuser immediately after the impeller exit. An important conclusion to be drawn from Mizuki's experiments is that the jet-wake flow is verified to persist over a wide range of operation. Another interesting result from Mizuki's work was that a separation bubble was identified in the impeller inlet near the shroud. The bubble did not exist at the high flow rate ($\varphi = 0.33$) but was initially detected at medium flow rates ($\varphi = 0.22$) and became more intense at low flow rates ($\varphi = 0.11$). The separation bubble was not detected at all by Eckardt probably because it did not exist in his apparatus because of the inlet geometry, or because he operated at a higher flow rate.

The passages which were mapped by Fowler [21], Moore [22], Eckardt [12] and Mizuki [25] were all radial at their exits. The jet-wake structures detected in these passages were likely the result of a complicated nonlinear combination of the effects of impeller speed, exit angle of the blades, curvature of the blades, number of blades, existence of a shroud cover, rate of flow deceleration through the impeller and flow rate. The effect of each of these parameters certainly can not be explored in a few experiments. However, a comparison of Fowler [21], Moore [22], Eckardt [12] and Mizuki [25] to Acosta [19] and Howard [23] suggested that the jet-wake flow was most dominantly affected by the sweep-back of the blades. This argument prompted Adler and Levy [26] to measure inside a closed centrifugal impeller with swept back straight blades, in which a full passage flow was anticipated to occur at the design point. To show that this was the case (and to explore the feasibility of optical measurements through a rotating window) they carried out laser doppler measurement in a closed backswept centrifugal impeller. They did not find a jet-wake structure. The impeller displayed, as anticipated, a full passage flow. This result led them to hypothesize that the jet-wake flow is weakened up to total disappearance as both impeller speed and blade sweep-back angle are reduced. This view is represented graphically in Fig. 4. As the boundary between the full passage flow and the jet-wake flow is dominantly though not solely influenced by the tip speed and the sweepback angle, a border region rather than a border line is shown in Fig. 4.

Adler and Levy's experiments were the first in which laser doppler measurements were carried out through a rotating window. They showed that a rotating window is not a severe obstacle for laser doppler velocimetry though special attention must be given to window glass quality, flatness and cleanliness.

All the experiments described above concentrated on the measurement of the flow field inside the rotating impeller. Some insight into the flow inside the impeller can also be gained, though to a much more limited extent, from measurements at the impeller exit; and in the case of open impellers, from measurements along the stationary shroud. Examples of this approach, which results in a somewhat simpler experimental set-up can be found in the measurements of Eckardt [27] and Senoo, et al. [28]. Eckardt [27] carried out measurements at three points of operation of the stage investigated in [12]; one on the choke line, the second at peak efficiency and the third about half way between peak efficiency and surge. He used high frequency pressure transducers on the open stationary shroud as well as a high frequency directionally insensitive impact tube and a hot wire directional probe after the impeller exit. His measurements showed again that the jet-wake flow at the impeller exit persisted over the entire operation range investigated, though it was somewhat reduced with reducing flow rate. Further, a possible separation immediately behind the inlet near the suction side was detected. But in contrast to Mizuki [25] this separation bubble appeared not at low flow rates, but rather at high flow rates. These two results are contradictory and require additional investigation. A third, interesting result of this work was the mapping of total pressure fluctuations at the impeller exit. Inside the wake the fluctuations reached a relative value of 14 percent to 18 percent while in the jet they were less intense, having a value of 10 percent to 12 percent. This may throw some light on the distribution of losses and turbulent viscosity inside a rotating passage.

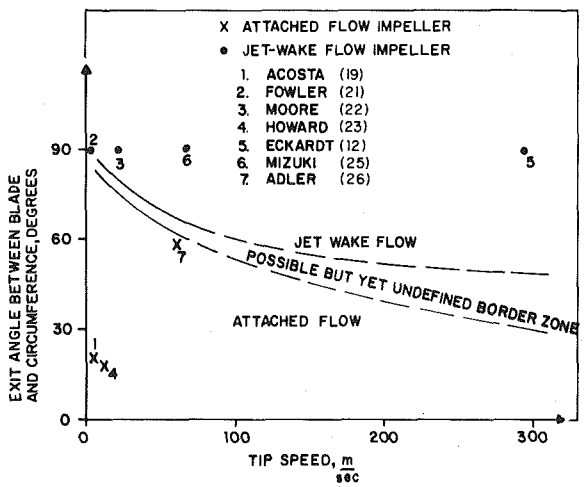


Fig. 4 Possible flow regime classification in centrifugal impellers (The location and width of the border zone are assumed and have yet to be verified.)

A recent work was published by Senoo, et al. [28]. Using stationary shroud taps to analyze the flow in a supersonic impeller, they were able to establish the shock wave pattern inside the impeller. In addition, they discovered a new longitudinal slip band occurring in the subsonic flow regime. This slip band was located in the middle between the blades, and its thickness increased with flow rate reduction. It became thinner as flow rate was increased until it disappeared altogether. Senoo did not give an explanation for this flow behavior, nor did he comment on its effect on compressor performance. Evidently this newly discovered slip band should be further explored in more detail using optical techniques, and correlated with impeller characteristics.

The experimental observations reviewed here lead to a number of imported conclusions:

1 The larger the rotor exit flow angle (β_2) and the higher the rotor speed, the more likely is the development of a jet-wake flow towards the impeller exit.

2 The jet-wake flow when present at the design point, exists also over a wide range of operation points.

3 The jet-wake flow departs so much from inviscid flow predictions that inviscid flow calculation are representative only for small β_2 impellers, or in case of large β_2 impellers, for inlet and mid passage regions only.

4 Small β_2 impellers generally deliver a more uniform flow field into the diffuser. This could explain their better efficiencies and wider range of operation between choke and surge.

The Structure of Turbulence and the Turbulent Viscosity in Rotating Passages

A conclusion in the previous paragraph and in [1] was that viscosity can be a dominant influence in centrifugal impellers and that in many cases inviscid methods must fail to predict reality. The role of viscosity is influential, not only because of the adverse pressure gradients present but also because viscosity variations caused by curvature and Coriolis accelerations can be large. Because the flow in most practical impellers is turbulent, work on laminar viscous flows in centrifugal impellers are not in general reviewed here. One result however is noted. Grundmann's study [29] showed that in laminar flow, centrifugal and Coriolis acceleration terms and the additional curvature terms had a strong influence on the location predicted for the separation point using boundary layer theory. If the centrifugal acceleration exceeded a certain limit, the solution scheme failed. This makes the use of boundary layer theory doubtful for this class of flows.

Most practical impeller flows are turbulent, and the pattern of these flows is, among other factors, the result of significant turbulent viscosity gradients. The aim of this paragraph is to review the main reasons for the viscosity gradients, the nature of viscosity in rotating passages and the effect of viscosity gradients on the flow field. The literature on this subject has increased considerably in recent years. On the basis of reported studies it appears that the viscosity variation in the flow field inside a centrifugal impeller is the result of the in-

Downloaded 01 Jun 2010 to 171.66.16.58. Redistribution subject to ASME license or copyright; see http://www.asme.org/terms/Terms_Use.cfm

teraction between a body force field and the velocity field. The viscosity variation depends on the relation between these two fields and is greatest at locations where velocity gradients are large. For the purpose of this review the literature will be classified into three groups: (1) effects of curvature, (2) effects of rotation, and (3) combined effects and application.

Curvature Effect. In 1969 Bradshaw described an analogy between streamline curvature- and buoyancy effects on turbulent viscosity [30]. He showed that there was a similarity between thermally stratified turbulent viscous flows, (which were by then better explored, especially in meteorological problems) and turbulent viscous flow along curved streamlines. He also discussed, briefly, effects of rotation. His major conclusion was that the effects of curvature, either concave or convex, on the viscosity were large if the thickness of the shear layer exceeded 1/300th of the radius of curvature of the streamline. These effects increased with increasing Mach number. Later, in 1973 and 1975, So and Mellor studied experimentally the effects of curvature on turbulent viscosity [31, 32]. They found that, along a convex wall, the Reynolds stress was decreased so strongly that it vanished in the middle of the boundary layer. In other words, they found that the boundary layer was "laminarized" and that turbulence was suppressed. In contrast, they found that along a concave wall the turbulent intensities inside the boundary layer were substantially increased. These phenomena have a striking effect on centrifugal impeller flows. In 1975, So [33], derived a formula for the variation of the turbulent velocity scale with the Richardson number for curved shear flows. He used the Reynolds stress equations and assumed that production of turbulent energy balanced the viscous dissipation. This provided a first quantitative account of the phenomenon. In the same year Irwin and Smith [34] also published a quantitative prediction of curvature effects. They verified that even small amounts of streamline curvature have a surprisingly strong effect on the eddy viscosity. Using data from curved boundary layers, they were able to predict the curvature effect properly if the curvature terms were included in the model. It is important to note the considerable effect of even small curvatures. It can explain some observed impeller flow field characteristics, such as suction side separation and pressure side attachment, which are contrary to inviscid theory predictions.

Recently Shivaprasad and Ramaprian published two experimental studies [35, 36] which again verified that turbulent viscosity was considerably affected by an even small curvature of the streamlines. Convex curvature decreased both the length and velocity scales of turbulent motions, whereas concave curvature caused the opposite. The effect of small curvature was found to be much larger than one would expect from a linear interpolation between the effects of zero and strong curvatures. That is to say, the effect is nonlinear, and is strong even at small curvatures. They also observed that curvature had a relatively larger influence on the turbulent shear stress than on the turbulent kinetic energy. Another important conclusion was that convex curvature had a stronger effect on the behaviour of the boundary layer than concave curvature of the same magnitude, (this conclusion is again important in the understanding of impeller flows, especially the onset of the wake on the convex suction side of the blades). In addition Shivaprasad and Ramaprian provided a way to calculate these effects using a correction factor to existing phonomenological methods.

A simple description can be given for the mechanism of the curvature effect. A flow is considered to be stable[2] if a fluid particle, on being perturbed perpendicularly to the average flow, encounters a net restoring force and decelerates. In flows over curved surfaces, the centrifugal force is largely balanced by a normal pressure gradient. If a fluid particle is displaced away from the wall into a region of higher mean velocity, its movement in this direction is on the average reduced if it flows along a convex surface. This is because in its perturbed position the centrifugal force acting on the fluid particle will be smaller than the mean normal pressure force existing in the flow field. The result is a net restoring force. The opposite is true for flow along concave walls. Similar considerations also hold for particle displacement towards the wall. The effects of rotation on turbulence are similar, with the difference that the centrifugal acceleration due to curvature is replaced by the component of the Coriolis acceleration normal to the blade surface.

Effects of Rotation. As in flow along curved streamlines, the influence of rotation is a result of the relation between pressure forces and inertia forces in the flow. Here the inertia forces are caused by the Coriolis acceleration. In turbomachines the Coriolis acceleration has only two components, radial and circumferential. The circumferential component, which causes the main effect of rotation on turbulence since it is almost perpendicular to the blade surface, is very small in axial flow machines because the radial component of the relative velocity is small. In centrifugal machines, on the other hand, the circumferential Coriolis component has a considerable magnitude, and therefore effects of rotation on turbulence play a major role. Johnston [37] pointed out that there are two basic effects associated with boundary layers on rotating surfaces: (1) If a component of the Coriolis acceleration exists parallel to the solid wall, secondary flows will tend to develop in the mean flow field of the boundary layer. This effect is present both in axial flow and in radial flow machines; (2) If a component of the Coriolis acceleration exists perpendicular to a solid surface, damping or amplifying effects are observed in the structure of turbulence. Because of geometrical reasons this effect is not very strong in axial machines. In radial machines, however, it is of dominant importance.

In 1972 Johnston, et al. [38] published experimental results from a slowly rotating water channel. They concluded that three different effects can be distinguished in rotating boundary layers; (1) The reduction of turbulent wall layer streak bursting rate in locally stabilized layers. In a centrifugal impeller these layers are on the suction side of the rotating passage. The opposite is true for locally destabilized layers, which in a centrifugal impeller are located on the pressure side; (2) production of turbulence is totally suppressed in locally stabilized layers; (3) roll cells are developed on the destabilized side of the channel. These three mechanisms were correlated to the gradient Richardson number and to the rotation number as defined in [38]. Later, in 1973, Johnston extended his observations to derive a predictive method for this type of boundary layer flow [39]. Using the Eddy Reynolds number, Johnston tried to predict the rotating boundary layers using a mixing length correction that accounts for rotation. Lack of sufficient data prevented verification of his results. On the other hand, application of the eddy Reynolds number criterion to the prediction of transition, also observed experimentally, was quite successful. Johnston's results were derived for rotating passages of constant cross section.

To approximate more closely the conditions in centrifugal impellers, where the passage cross section section increases in the flow direction, Rothe and Johnston carried out experiments in rotating diffusers [40]. Their experiments demonstrated that rotation strongly enhanced the tendency of a diffuser to stall. This stall, however, appeared only on the suction side of the rotating diffuser, and was highly steady and two-dimensional. The appearance of the suction side stall was correlated by Rothe and Johnston to the rotation number, and a stall regime map was drawn to enable stall prediction in rotating diffusers. It is noted that the appearance of stall on the suction side only is fully consistent with previous observations of the effect of rotation on the structure of turbulence and is explained by them. In 1976 Rothe and Johnston published more data to provide a quantitative account of the onset of flow separation in rotating diffusers [41]. The conclusions were similar to the conclusions in the previous work [40]. It was, however, emphasized in addition that the suppression of turbulent mixing and shear stress by the Coriolis acceleration was powerful even when fully turbulent upstream wall layers were present, and even at small rotation numbers relative to those typical of centrifugal impellers. This conclusion is analogous to the observation that even very small streamline curvatures have a relatively strong effect on turbulent viscosity.

Very recently Koyama, et al. [42] reported a study confirming the observations made thus far. They contributed additional information

[2] Stable here refers to the stability of turbulent fluctuations and not the stability of the averaged flow to resist possible separation.

Downloaded 01 Jun 2010 to 171.66.16.58. Redistribution subject to ASME license or copyright; see http://www.asme.org/terms/Terms_Use.cfm

on the quantitative effect of rotation on the skin friction coefficient, and on the Monin Oboukhov coefficient, to enable more reliable predictions.

Combined Effects of Surface Curvature and Rotation and Their Application. So far the effects of streamline curvature without rotation and of rotation without streamline curvature were discussed. In reality, however, they occur together and must be so treated. The effects of the impeller rotation and the curvature of its blades on the stability and structure of the internal boundary layers must be properly described if the flow pattern in a centrifugal impeller is to be predicted correctly. Especially affected by curvature and rotation is the onset of boundary layer separation and stall in the impeller. The regions of stalled or low velocity flow (wakes) reduce efficiency, reduce operating range, and distort the flow delivered at the impeller outlet.

Johnston and Eide [43] devised a method, using previous experimental information, to include the effects of curvature and rotation in an existing differential method for turbulent boundary layer calculation; namely a slightly modified version [44] of STAN 5 [45]. STAN 5 was based on Patankar and Spalding's computing scheme [46]. Johnston and Eide modified the turbulent viscosity model in STAN 5 to include the effects of curvature and rotation. They assumed that the mixing length for the boundary layer on a flat wall with zero rotation must be multiplied by a correction factor F given by

$$F = 1 - \beta_c \mathrm{Ri}_c - \beta_\Omega \mathrm{Ri}_\Omega \quad (1)$$

where β_c and β_Ω are empirical constants for curvature and rotational effects, Ri are the corresponding Richardson numbers. This simple correction factor, which assumes that the effects of curvature and rotation are linearly combined, was tested on a number of boundary layers. Unfortunately, all the available cases were either curved or rotating and the combination of the two effects could not be checked. The agreement between the description provided by equation (1) and the experiments was good in cases where the thin-shear-layer approximation was applicable.

In 1977 Launder, et al. [47] published a method which was applied to spinning cones. It is nevertheless of interest here. Again Patankar and Spalding's approach [46] was used for the boundary layer calculation in an adapted version of the GENMIX program. They corrected the turbulent viscosity for curvature and rotation effects using a model of turbulence kinetic energy and its local rate of dissipation. The direct effect of curvature in the model was limited to a single empirical coefficient whose magnitude was directly proportional to a Richardson number based on a time scale of the energy-containing eddies. They carried out computations for shear flows on curved or spinning surfaces. They found that the turbulent kinetic energy-dissipation rate model did describe the experimental results, provided that the transport equation for dissipation was modified to include an extra term to account for curvature and swirl effects. The success on curved surfaces was better than on spinning surfaces, where the predictions obtained were only marginally superior to those obtained with a mixing length model [48]. They concluded that when a mixing length profile can be predicted with reasonable certainty, its use would be advantageous for spinning flows because of the smaller computing time required to obtain a solution.

The present knowledge on turbulence in rotating passages allows, at least, qualitative understanding of many of the internal passage flow mechanisms. It can explain the occurrence of the jet-wake flow. It can explain why inviscid pressure side separations like the one shown in Fig. 5 were never detected experimentally. It can also provide qualitative justification for observed three dimensional flow effects. However, the present knowledge is not sufficient to allow accurate quantitative predictions to be made of the turbulent viscosity and incorporation of those predictions in the three-dimensional viscous computing techniques now under development.

Computing techniques, once reliable, would allow for example a detailed study to be carried out of the influence of blade sweepback and curvature on stage efficiency and range of operation. Presently, the effects of blade sweepback are qualitative inferred from an examination of global overall information such as stage performance

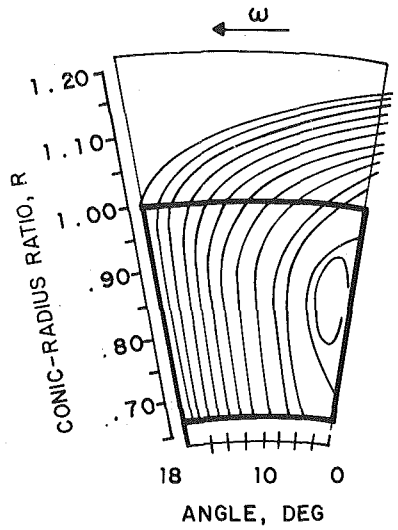


Fig. 5 Streamlines inside the rotating impeller as calculated by Stanitz [49]. The predicted inviscid pressure side separation is well visible on the right side. Taken from [49]

maps, which correlate blade geometry with efficiency and range, but always leave the internal flow details in the dark. A detailed analytical study could, for example, examine the apparently large and harmful effects of even a small amount of convex suction-side blade curvature on the onset of jet-wake flow, and might correlate this information with observations of the triggering of surge. Also, viscous computations with correct viscosity models could be used to create diagrams like the one in Fig. 1, and give a better understanding of the processes causing jet-wake flow.

Inner-Outer Solution Combinations (Patching Techniques)

A standard approach to solving for a complete flow field, is first to divide the flow field into regions. In each region, a different simplifying assumption is made in order to allow an easy solution to be obtained. The regions are connected by common boundary conditions on common boundaries. The classical example of this approach is boundary layer theory. In centrifugal impellers a similar approach was used by a number of investigators in a very simplified way to attack the problem of the jet-wake flow.[3] The problem is of course complicated by the fact that the region boundaries are not known a-priori. Consequently, the techniques are either iterative or depend strongly on empirical results. At present, the information quoted above on turbulent viscosity variation in curved rotating passages is not directly incorporated in viscous flow field calculations, and some methods avoid viscosity altogether.

In 1973 Moore [50] published a method of calculating the jet-wake flow in a rotating radial flow passage. Moore divided the flow field into four parts; (1) potential flow; (2) top and bottom wall boundary layers; (3) corner flows, and (4) side wall boundary layers. Moore calculated the potential core flow accounting for the displacement and acceleration of the potential flow by the wake on the suction side wall. The development of the cross flows on the top and bottom walls was computed on the basis of Moses' strip integral method [51] modified to include the three dimensional and rotational terms for steady incompressible flow in rotating passages. Thus on top and bottom the wall boundary layers as well as radial and tangential flows were predicted. The corner flows were modeled by assuming that continuity holds over the corner cross section, and that the fluid turning through the corner maintains its momentum in the radial direction. The side wall boundary layers were computed with an analysis which included a Coriolis' acceleration term associated with velocities normal to the

[3] There are also a number of works published on boundary layers and secondary flows in impellers. Though relevant, these studies are not included in order to keep this review within reasonable limits.

Downloaded 01 Jun 2010 to 171.66.16.58. Redistribution subject to ASME license or copyright; see http://www.asme.org/terms/Terms_Use.cfm

wall and a Coriolis term affecting the pressure gradient normal to the wall. The model gave a momentum integral equation similar to the one derived by Moon [52]. However, it was applied with irrotational potential flow at the edge of the boundary layer, and retained the terms which arose due to the two Coriolis effects. Moore calculated the wake assuming that it started at a point where the shape factor was 3.0. Subsequent flow was considered to consist of similarity profiles, including a cross flow entrainment into the wake from the corners. These four partial flows were combined to yield a good agreement between calculations and experiment (Fig. 6).

In 1975 Sturge and Cumpsty developed a two dimensional method to predict the incompressible jet-wake flow [53,54]. For simplicity, they avoided the direct modelling of viscous effects, which led to major drawbacks in their method. The method was later extended to compressible flows [54]. The two dimensional blade to blade passage was divided into two regions; (1) a jet region where the flow was assumed to be inviscid and irrotational; (2) a wake region where there was no flow. The boundary between the two regions was treated as a free shear layer without mixing between the two regions, similar to an air-water interface. The position of the shear layer was characterised by the condition that there was no change in static pressure across it, and that in the wake the pressure was governed only by hydrostatic effects due to the centrifugal acceleration field. The flow in the jet was analysed using irrotationality and continuity and defining a stream function, and was solved numerically with the shear layer between the jet and the wake as one of the boundaries. This required an iterative process which was shortened by a variable transformation which left the stream function as one of the independent variables. The resulting second order partial differential equation was solved using a finite difference technique. Besides the fact that the method was restricted to irrotational flow, a much more disturbing feature was that the separation point on the suction side could not be predicted, but had to be known a-priori or assumed. (This was the penalty for not modelling the viscous effects.) Though a separation criterion based on a velocity ratio between separation and the highest velocity attained on the suction side was suggested by Sturge and Cumpsty the method was still not predictive unless the calculation of a separation point on the suction side was incorporated. Another drawback of the technique was that no flow was assumed in the wake. This is not in accordance with Eckardt's observations [12]. Eckardt measured significant velocities inside the wake. The magnitude of the velocities was about 30 percent of the jet velocities. No comparison to experiments were given in Sturge and Compusty's work.

Howard and Osborne [55] developed a further simplified method to predict the jet-wake flow. The method was based on Katsanis' streamline curvature inviscid method on the H-S stream surface [56] combined with an extremely simplified calculation on the B-B surface [57]. In contrast to Sturge and Cumpsty's method the analysis did not determine an exit flow angle and required a separate correlation for this purpose. The wake was treated, as in the previous method, as an additional blockage in the passage. The inviscid calculation was carried out in the jet only with the mid passage H-S surface, moved towards the pressure side by one-half the wake width. Subsequently, the B-B analysis was carried out in the region of the jet only. The continuity equation at each quasi-orthogonal was adjusted to account for growth of the wake width. The wake width and the jet flow angle, required in the calculation, were not predicted by the technique but had to be established either by empirical correlations or from measured data. The ability of the method to be really predictive depended on the accuracy and the generality of this empirical information. Although some three dimensional aspects of the jet-wake flow were included, they were possibly oversimplified by the assumption that the wake was evenly distributed along the suction side of the passage from shroud to hub. This is not consistent with Eckardt's observations [12].

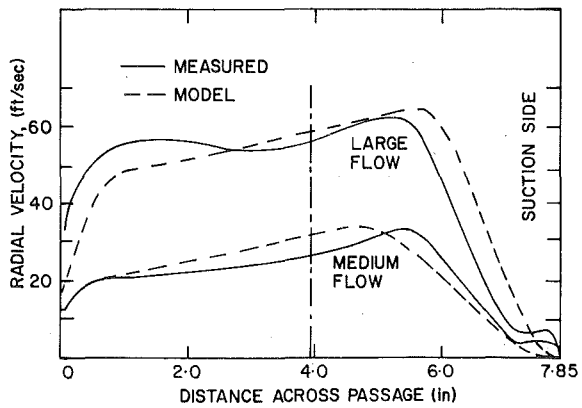


Fig. 6 Comparison between the experiments and the calculations of Moore [50]

The problem of calculating the jet-wake flow properly is formidable. Only three attempts have been reported so far, and none was based on a partial differential approach. Two (Sturge and Cumpsty, and Howard and Osborne) avoided viscosity altogether by replacing the wake with a region without flow. Moore, in a more detailed model, applied an integral boundary layer technique. The full task is still not accomplished and further attempts are anticipated.

Fully Viscous Solutions

A large volume of work on the solution of viscous flows was published in the past few years and a complete review will not be attempted. Of direct interest here are solutions for flows which are both rotating and turbulent. A number of relevant works will be chronologically reviewed.

In 1975 Walitt, et al. published a technique [58], to predict the viscous flow field on the B-B stream surface. It was the first phase of a technique developed to solve the steady three-dimensional compressible Navier-Stokes equations in rotating curvilinear coordinates. Any turbulence model could be incorporated in the method which was applied (in Phase I) to laminar flow and to turbulent flow described by a simple mixing length correlation not incorporating rotation and curvature effects. In 1978 the second phase of the work, solving the flow on cross sectional surfaces prependicular to the direction of the primary flow, was published [59]. The full technique solved the equation of motion by iterations. The solution started from a zeroth iteration which was a three-dimensional inviscid solution; Katsanis' method [56] was used. The solution marched alternately from hub to shroud (solving on B-B surfaces) and from inlet to outlet (solving on cross-sectional surfaces). The cross-sectional iteration employed the B-B flow field as the previous iterate. The method was an explicit two dimensional time marching scheme extended to three-dimensional flows using the equivalence principle of Hayes. In its original derivation, the equivalence principle states that for slender bodies at hypersonic speeds the three-dimensional steady equations of motion for inviscid flow reduce identically to unsteady equations in two space dimensions. An extension of the principle was used in forming an analytical model which calculated the viscous cross flow with a known flow from a previous iterate in the marching direction. The coordinate in the marching direction was made proportional to a time like variable by forming the product with a characteristic velocity.

The method was used to predict the flows in a radial exit, and in a backswept compressor impeller. In the radial exit impeller a separation zone was predicted on the suction side of the passage close to the outlet. The flow in the backswept impeller was attached. No conclusions can be drawn with regard to the effectiveness of sweepback in reducing or eliminating the jet-wake flow because the radial exit impeller was calculated with a laminar viscosity model, and the backswept impeller was calculated with a turbulent mixing length model for steady flows along straight surfaces. No comparison to experiments was given, but in [59] a qualitatively correct jet-wake pattern was predicted.

In 1976 Briley, et al. published a method developed for stationary axial turbomachinery passages [60]. It is included here becuase it can in principle be extended to rotating centrifugal passages. The method was based on an approximate formulation which was solved in a forward marching technique in a primary spacial direction. The complete

Downloaded 01 Jun 2010 to 171.66.16.58. Redistribution subject to ASME license or copyright; see http://www.asme.org/terms/Terms_Use.cfm

flow was obtained in a sequence of two dimensional calculations, resulting in a substantial saving of computer time and storage over that which would be required for the solution of the full, elliptic Navier-Stokes equations. Essential to the method was the derivation of a particular coordinate system. One coordinate direction was identified with the primary flow direction along which the solution was to march, while the two remaining coordinate directions could be associated with secondary flows. The full elliptic flow model was simplified by a number of assumptions. For high Reynolds numbers, viscous effects were negligible except in the boundary layers on all four walls. The method was an extension of three-dimensional boundary layer methods, but the approximate equations were also used in the inviscid core flow. For entirely supersonic flows the equations, together with initial and boundary conditions, could be solved by forward marching in the primary direction without any assumptions about the pressure field. For subsonic, however, where the inviscid core was elliptic, downstream boundary conditions were required to enable a solution. This problem was overcome by imposing on the solution, an entirely inviscid pressure field which was calculated a priori with proper elliptic boundary conditions. The pressure field then had to be corrected as part of the solution procedure. The viscous pressure drop in the primary direction was treated separately as a function of the distance in this direction only, and was computed with the forward marching integration using integral mass conservations in that direction. No assumptions were made concerning the pressure gradients in the secondary flow directions. The turbulence model incorporated in the method was based on the solution of conservation equations for turbulent kinetic energy and dissipation, and as the technique was developed for stationary passages, rotation effects were not included. Curvature effects were also neglected.

Another viscous computation technique for stationary turbomachinery ducts was reported by Dodge [61]. Again the model was not based on the full Navier-Stokes equations in order to save computer time and storage space. The method was based on separating the momentum and continuity equations into coupled elliptic and parabolic parts which were then solved iteratively. Dodge separated the velocity into a viscous and a potential component. Substitution of the decomposed velocity into the equation of motion yielded a simpler equation of motion from which the pressure gradient was eliminated using the velocity potential. The velocity potential in turn was expressed using the continuity equation. The simplified equation of motion was parabolic with a primary direction in the flow direction, and was solved using a marching technique similar to those used in boundary layer theories. The equation for the potential was elliptic and was solved with a relaxation technique. Since both equations contained coupling terms, iteration was required between the two. Dodge developed and used his technique for stationary passages; consequently his turbulence model did not include effects of rotation. He also did not correct the turbulence model for curvature effects despite the presence of curvature in the passages which were analysed. The turbulent viscosity was calculated using a mixing length concept near the walls (including van Driest's wall shear correction and Cebeci-Smith pressure correction) and a constant free stream viscosity away from the walls. A nearly constant viscosity was used in wakes. Dodge's technique failed in the presence of reversed flow, the forward marching differences then becoming unstable. By replacing the variation of the dependent variable in the normal direction by a spectral series [62] this problem was overcome. A number of comparisons with the experiments of Schubauer and Klebanoff revealed good agreement.

In 1977 a paper [63] was published by Majudmar, et al. which described a method based on Patankar and Spalding's boundary layer calculation [64]. The method of Patankar and Spalding for parabolic flows is based on the uncoupling of the pressure; using in the momentum equation for the primary direction (the radial direction) a pressure value which is averaged over the cross section. In the method of Majudmar, et al. the model reported in [64] was modified through addition of a Coriolis term in the circumferential momentum equation and both a centrifugal and a Coriolis term in the radial momentum equation. The turbulence model used was not corrected for rotational and curvature effects; it was based on Launder's and Spalding's kinetic energy-dissipation concept [65]. The model was solved in a single forward marching sweep from inlet to outlet in the following steps:

1 The pressure distribution in a cross section perpendicular to the primary direction, and the average value of the pressure in that cross section were assigned preliminary guessed values.

2 The three momentum equations at a downstream position were solved, using flow properties at an upstream position, to yield a first approximation to the velocity distribution.

3 The mean cross sectional pressure was corrected to give new radial velocity components which satisfied continuity. This was done using a linearized radial momentum equation.

4 A corrected pressure field on the cross section surface was computed using an elliptic equation derived from continuity, and two linearized momentum equations in that surface. The cross-sectional velocities were corrected according to this pressure field.

5 A new turbulent viscosity distribution was evaluated from a solution of the kinetic energy and dissipation equations.

Fig. 7 illustrates the good agreement obtained between this technique and Moore's experiments [22].

Majumdar, et al. concluded, however, that their parabolic technique was only accurate for low values of $\Omega B/\overline{w}$ (where Ω is the angular velocity, B is the circumferential width of passage, and $\overline{w}$ is the bulk mean velocity). For high values of $\Omega B/\overline{w}$, partially parbolic procedures [66, 67] in which the pressure uncoupling was abandoned yielded more accurate results. Both the partially parabolic technique and the parabolic technique [63] were based on identical mathematical and turbulence models. The difference was in the method of solution. While in the parabolic technique a single marching sweep was carried out from inlet to outlet, the partially parabolic technique was necessarily iterative. A number of marching sweeps, each similar to the single sweep of the parabolic method, were required. In each sweep, or iteration, the pressure field was corrected until convergence was achieved. Thus through the pressure field, downstream effects were transmitted into the flow field and the solution was given a radially, or streamwise, elliptic character. Results for secondary flows were given in [67] and compared to measurements of Wagner and Velkoff [68]. Agreement was good in some cases, but significant disagreements were found in others.

Very recently Bosman, et al. published a finite difference technique which was simple and probably not expensive to run [69]. The model was, however, subjected to a number of restrictions which limited its application to two dimensional flows in radial surfaces which were absolutely plane and perpendicular to the axis of rotation. The flow had to be incompressible and the viscosity constant in the entire flow field. Further, the technique utilized a nondimensional slip parameter to represent the blade surface shear stresses. The slip parameter was assumed to be constant along the blades from inlet to outlet, and reliable information was not given on its evaluation. Using the incompressible equations of continuity and momentum and a stream function, the flow was formulated with two coupled partial differential elliptic equations. This was the distinctive feature of this technique in contrast to the parabolic, or partially parabolic nature of the forward marching methods. The unknown functions to be evaluated were the stream function and the relative vorticity. The equations were solved with a relaxation technique with finite difference approxi-

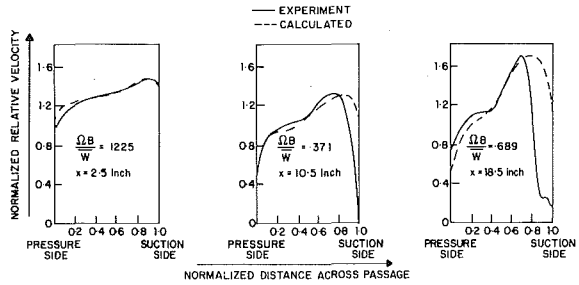


Fig. 7 Comparison between the experiments of Moore [22] and Majumdar's, et al. calculations [63]

Downloaded 01 Jun 2010 to 171.66.16.58. Redistribution subject to ASME license or copyright; see http://www.asme.org/terms/Terms_Use.cfm

mations. Central differences were used for diffusion terms and upwind differences for convection terms. The two equations were solved iteratively until convergence was achieved. The results were compared to measurements carried out in a water rig [70, 71] and to results of an inviscid calculation based on Wu. At the design point of the impeller, agreement between the experiments, the inviscid calculation, and the viscous calculation was not bad. This is not surprising in view of the fact that the impeller was two dimensional and strongly backswept. In such a configuration, viscous effects are not very strong (see Fig. 4) and inviscid calculations should give fairly accurate results. The situation at off design points, with positive or negative inlet incidence angles, was not much different downstream and close to the impeller exit. At upstream positions, closer to the inlet, the agreement between experiments and viscous results was better than agreement between experiments and inviscid results. This again is not surprising in view of the fact that inviscid theories should not be used at all at off design conditions since they can not represent properly the viscous effects associated with the inlet shock. The technique of Bosman, et al. [69], when further developed to remove some of its restrictions could become a useful design aid.

Also in 1978 Goulas and Baker [72] published a method for calculating the viscous flow on either the H-S or on the B-B stream surfaces. The method was not three dimensional thus far, but the author's stated intention was to couple the two solutions in an iterative sequence to obtain the three dimensional flow field. The published method was based on the usual conservation equations written for a stream surface. Introducing a stream function, the two equations of motion for the stream surface were combined into a Poisson like equation, $\nabla^2\psi = q(r,\phi,Z)$, in which the function q was not known. The function q contained all the differences between incompressible irrotational flow and real viscous compressible flow under consideration. The solution by finite differences on a stream surface was carried out in the following steps:

1 A stream function distribution was assumed from which the initial two components of the velocity on the surface were calculated. The third velocity component was calculated using the geometry of the stream surface.

2 With this information the turbulent viscosity was computed using Launder's and Sapldings's kinetic energy-dissipation model [65]. A set of linear equations was formed and solved simultaneously for each quasi-orthogonal line. Starting from the inlet where the kinetic energy and dissipation were known as initial values, the solution proceeded downstream to the exit.

3 The streamwise momentum equation was integrated along streamlines, using the calculated turbulent viscosity, to yield an entropy field.

4 With velocities, entropy and density known, the function q was calculated, and Poisson equation for the stream function was then solved.

The process was iteratively repeated until convergence of the stream function was achieved.

Results were compared with the inviscid solution of the flow field in a turbocharger compressor and viscous effects were qualitatively clearly visible [72]. No comparison with experiments was given.

Comparison of Computation Times

The solution techniques mentioned in this review require numerical methods. A comparison of their drawbacks and merits is not complete without consideration of their demands for computer time and computer storage. For most numerical techniques the storage requirements are not published, though the particular computer model used can sometimes indicate what might be required. The following table gives an approximate indication of computation times for some of the techniques mentioned in this review. An exact accounting, however, is not possible as some authors mention virtual execution time, and others indicate a total time which includes compilation of the program. Some authors even neglect to define the time that they quote. Furthermore, the time stated depends strongly on the problem solved and the accuracy obtained in the results. The accuracy, in turn, is affected by mesh size and convergence criterions adopted. The values given in the following table should therefore, be treated as an order of magnitude indication only.

Table 1 Comparison of approximate computation times

Author	Reference	Computer Used	Time (Min)	Flow
Wallit/Harp/Liu	[58]	CDC 6400	3000	3-D viscous
Dodge	[61]	CDC 6400	60	3-D viscous
Dodge/Lieber	[62]	CDC 6400	7	3-D viscous
Dodge/Lieber	[62]	CDC 7600	0.5	3-D viscous
Madjumar/Pratap	[63]	CDC 6600	2.5	3-D viscous
Madjumar/Spalding	[66]	CDC 6600	2.5	3-D viscous

Acknowledgments

The research for this report was partly conducted while the author was a Visiting Consultant to Cummins Engines Company Inc., Columbus, Indiana. The study was completed and the report written while he was NAVAIR Chair Visiting Professor at the Turbo-propulsion Laboratory of the Naval Postgraduate School, Monterey, California.

The author is grateful for the support he received from Dr. W. T. Lyn, Vice President and Head of the Research Division at Cummins, for sponsorship by the Naval Air Systems Command under the cognizance of Dr. H. J. Mueller, and for the considerable help given by Professors M. F. Platzer and R. P. Shreeve, Naval Postgraduate School.

References

1 Adler, D., "Status of Centrifugal Impeller Internal Aerodynamics, Part I, Inviscid Flow Prediction Methods," ASME JOURNAL OF ENGINEERING FOR POWER, Vol. 102, No. 3, pp. 728–737.

2 Adler, D., and Krimerman, Y., "The Numerical Calculation of the Meridional Flow Field in Turbomachines Using the Finite Elements Method," *Israel Journal of Technology*, Vol. 12, 1974, pp. 268–274.

3 Davis, W. R., and Millar, D. A. J., "A Comparison of the Matrix and Streamline Curvature Methods of Axial Flow Turbomachinery Analysis from a User's Point of View," ASME Paper No. 74-WA/GT-4, 1974.

4 Hirsch, Ch., and Warzee, G., "A Finite Element Method for Through Flow Calculation in Turbomachines," *Journal of Fluids Engineering*, Vol. 98, 1976, p. 403.

5 Wilkinson, D. H., "Calculation of Blade-to-Blade Flow in a Turbomachine by Streamline Curvature," Aeronautical Research Council, R&M No. 3704, 1972.

6 Adler, D., and Krimerman, Y., "Calculation of the Blade-to-Balde Compressible Flow Field in Turbo Impellers Using the Finite-Element Method," *Journal of Mechanical Engineering Science*, Vol. 19, 1977, pp. 108–112.

7 Prince, T. C., "Prediction of Steady Inviscid Compressible Flow on a Blade-to-Blade Surface by Finite Element Method," AIAA paper 78-244, 1978.

8 Kurzrock, J. W., and Novick, A. S., "Transonic Flow Around Rotor Blade Elements," ASME Paper No. 75-FE-24, 1975.

9 Frost, D. H., "A Streamline Curvature Through Flow Computer Program for Analyzing the Flow Through Axial Flow Turbomachines," *Aero. Res. Council* R&E No. 3687, 1972.

10 Senoo, Y., and Nakase, Y., "An Analysis of Flow Through a Mixed Flow Impeller," ASME JOURNAL OF ENGINEERING FOR POWER, Vol. 94, 1972, pp. 43–50.

11 Krimerman, Y., and Alder, D., "The Complete Three-Dimensional Calculation of the Compressible Flow Field in Turbo Impellers," *Journal of Mechanical Engineering Science*, Vol. 20, 1978, pp. 149–158.

12 Eckardt, D., "Detailed Flow Investigation within a High Speed Centrifugal Compressor Impeller," *Journal of Fluid Engineering*, Vol. 98, p. 390, 1970.

13 Moore, J., "Eckardt's Impeller—a Ghost From Ages Past," University of Cambridge, Report CUED/A-Turbo/TR 83, 1976.

14 Carrard, A., "On Calculations for Centrifugal Wheels," *La Technique Moderne*, T. XV-No. 3, Feb. 1923.

15 Oertli, H., "Untersuchungen der Wasserstromungdurch ein rotierendes Zellen-Kreiselrad," Dissertation E.T.H. No. 317, 1923.

16 Prasil, P., "Verschiedene Stromungserscheinungen," Second International Congress for Applied Mechanics, Zurich, 1926.

17 Fischer, K., and Thoma, D., "Investigation of the Flow Conditions in a Centrifugal Pump," Trans. ASME, HYD-54-8, 1932.

18 Keanton, W. J., "Influence of the Number of Impeller Blades on the Pressure Generated in a Centrifugal Compressor and on its General Performance," *Proc. Fust. Mech Engs.*, Vol. 124, 1933 pp. 481–568.

19 Acosta, A. J., Bowerman, R. D., "An Experimental Study of Centrifugal Pump Impellers," Trans. ASME, Vol. 79, 1957, pp. 1821–1839.

Downloaded 01 Jun 2010 to 171.66.16.58. Redistribution subject to ASME license or copyright; see http://www.asme.org/terms/Terms_Use.cfm

20 Fujie, K., "Three-Dimensional Investigation of Flow in Centrifugal Impeller with Straight-Radial Blades," *Bulletin of JSME,* Vol. 1, 1958, pp. 42–49.

21 Fowler, H. S., "The Distribution and Stability of Flow in a Rotating Passage," ASME JOURNAL OF ENGINEERING FOR POWER, Vol. 90, 1968, pp. 229–236.

22 Moore, J., "A Wake and an Eddy in a Rotating Radial Flow Passage," ASME JOURNAL OF ENGINEERING FOR POWER, Vol. 95, 1973, pp. 205–219.

23 Howard, J. H. G., Kittmer, C. W., "Measured Passage Velocities in a Radial Impeller with Shrouded and Unshrouded Configuration," ASME JOURNAL OF ENGINEERING FOR POWER, Vol. 97, 1975, pp. 207–213.

24 Schodl, R., "A Laser Dual-Beam Method for Flow Measurements in Turbomachines," ASME Paper No. 74-GT-157, 1974.

25 Mizuki, S., Hattore, T., Arign, I., and Watanabe, I., "Reversed Flow Phenomena within a Centrifugal Compressor Channels at Lower Flow Rates," ASME Paper No. 76-GT-86, 1976.

26 Adler, D., Levy, Y., "Laser Doppler Flow Investigation Inside a Backswept Closed Centrifugal Impeller," *Journal of Mechanical Engineering Science,* Vol. 21, No. 1, 1979.

27 Eckardt, D., "Instantaneous Measurements in the Jet-Wake Discharge Flow of a Centrifugal Compressor Impeller," ASME JOURNAL OF ENGINEERING FOR POWER, Vol. 97, 1975, pp. 337–346.

28 Senoo, Y., Hayami, H., Kinoshita, Y., Yamasaki, H., "Experimental Study on Flow in a Supersonic Centrifugal Impeller," ASME JOURNAL OF ENGINEERING FOR POWER, Vol. 101, 1979, pp. 32–41.

29 Grundmann, R., "Two-Dimensional, Laminar, Compressible Boundary Layer Calculation in Turbomachines," *DFVLR* DLR-FB 76-38, 1976.

30 Bradshaw, P., "The Analogy Between Streamline Curvature and Buoyancy in Turbulent Flow," *Journal of Fluid Mechanics,* Vol. 36, 1969, pp. 177–191.

31 So, R. C., and Mellor, G. L., "Experiment on Convex Curvature Effects in Turbulent Boundary Layers," *Journal of Fluid Mechanics,* Vol. 60, 1973, pp. 43–62.

32 So, R. C., and Mellor, G. L., "Experiment on Turbulent Boundary Layers on a Concave Wall," *The Aeronautical Quarterly,* Vol. 26, 1975, pp. 25–40.

33 So, R. C., "A Turbulence Velocity Scale for Curved Shear Flows," *Journal of Fluid Mechanics,* Vol. 70, 1975, pp. 37–57.

34 Irwin, H. P. A. M., and Smith, P. A., "Prediction of the Effect of Streamline Curvature on Turbulence," *The Physics of Fluids,* Vol. 18, 1975, pp. 624–630.

35 Shivaprasad, B. G., and Ramaprian, B. R., "Turbulence Measurements in Boundary Layers Along Mildly Curved Surfaces," ASME Paper No. 77-WA/FE-8, 1977.

36 Ramaprian B. R., and Shivaprasad, B. G., "The Structure of Turbulent Boundary Layers Along Mildly Curved Surfaces," *Journal of Fluid Mechanics,* Vol. 85, 1978, pp. 273–303.

37 Johnston, J. P., "The Effects of Rotation on Boundary Layers in Turbomachine Rotors," Stanford University Report MO-24, 1970.

38 Johnston, J. P., Halleen, R. M., and Lazins, D. K., "Effects of Spanwise Rotation on the Structure of Two-Dimensional Fully Developed Turbulent Channel Flow," *Journal of Fluid Mechanics,* Vol. 56, 1972, pp. 533–557.

39 Johnston, J. P., "The Suppression of Shear Layer Turbulence in Rotating Systems," *Journal of Fluids Engineering,* Vol. 95, 1973, pp. 229–236.

40 Rothe, P. H., and Johnston, J. P., "Stall in Rotating Two-Dimensional Diffusers," *Journal of Fluids Engineering,* Vol. 97, 1975, pp. 252–253.

41 Rothe P. H., and Johnston, J. P., "Effect of System Rotation on the Performance of Two Dimensional Diffusers," *Journal of Fluids Engineering,* Vol. 98, 1976, pp. 422–430.

42 Koyama, H., Masuda, S., Ariga, I., and Watanbe, I., "Stabilizing and Destabilizing Effects of Cariolis Force on Two-Dimensional Laminar and Turbulent Boundary Layers," ASME JOURNAL OF ENGINEERING FOR POWER, Vol. 101, 1979, pp. 23–31.

43 Johnston J. P., and Eide, S. A., "Turbulent Boundary Layers on Centrifugal Compressor Blades: Prediction of the Effects of Surface Curvature and Rotation," *Journal of Fluids Engineering* Vol. 98, 1976, pp. 374–381.

44 Eide, S. A., and Johnston, J. P., "Prediction of the Effects of Longitudinal Wall Curvature and System Rotation on Turbulent Boundary Layers," Stanford University Report PD-19, 1975.

45 Crawford, M. E., and Kays, W. M., "STAN5—A Program for Numerical Computation of Two-Dimensional Internal/External Boundary Layer Flows," Stanford University Report HMT-23, 1975.

46 Patankar, S. V., and Spalding, O. B., "A Finite Difference Procedure for Solving the Equations of the Two-Dimensional Boundary Layer," *International Journal of Heat and Mass Transfer,* Vol. 10, 1967, pp. 1389–1412.

47 Launder, B. E., Priddin, C. H., and Sharma, B. I., "The Calculation of Turbulent Boundary Layers on Spinning and Curved Surfaces," *Journal of Fluids Engineering,* Vol. 99, 1977, pp. 231–239.

48 Koosinlin, M. L., Launder, B. E., and Sharma, B. I., "Prediction of Momentum Heat and Mass Transfer in Swirling Turbulent Boundary Layers," ASME *Journal of Heat Transfer,* Vol. 96, 1974, p. 204.

49 Stanitz, J. D., "Two-Dimensional Compressible Flow In Conical Mixed Flow Compressors," NACN TN 1744, 1948.

50 Moore, J., "A Wake and an Eddy in a Rotating Radial Flow Passage, Part 2: Flow Model," ASME JOURNAL OF ENGINEERING FOR POWER, Vol. 95, 1973, pp. 213–219.

51 Moses, H. L., "A Strip Integral Method for Predicting the Behavior of Turbulent Boundary Layers," Stanford University Symposium on Turbulent Boundary Layers, Aug. 1968.

52 Moon, I. M., "Effects of Coriolis Force on the Turbulent Boundary Layer in Rotating Fluid Mechanics," M.I.T. Gas Turbine Laboratory, Report No. 74, 1964.

53 Sturge, D. P., and Cumpsty, N. A., "Two-Dimensional Method for Calculating Separated Flow in a Centrifugal Impeller," *Journal of Fluids Engineering,* Vol. 97, 1975, pp. 581–597.

54 Sturge, D. P., "Compressible Flow in a Centrifugal Impeller with Separation: A Two-Dimensional Calculation Method," *Journal of Fluids Engineering,* Vol. 100, 1978, pp. 37–46.

55 Howard, J. H. G., and Osborne, C., "A Centrifugal Compressor Flow Analysis Employing a Set-Wake Passage Flow Model," *Journal of Fluids Engineering,* Vol. 99, 1977, pp. 141–147.

56 Katsanis, T., "Use of Arbitrary Quasi-Orthogonals for Calculating Flow Distribution in the Meridional Plane of a Turbomachine," NASA TN D-2546, 1964.

57 Stanitz, J. D., and Prian, V. D., "A Rapid Approximate Method for Determining Velocity Distributions on Impeller Blades of Centrifugal Compressors," NACA TN 2421, 1951.

58 Wallitt, L., Harp, J. L., and Liu, C. Y., "Numerical Calculation of the Internal Flow Field in a Centrifugal Compressor Impeller," NASA CR-134984, 1975.

59 Walitt, L., Liu, C. Y., and Harp, Jr., J. L.,"An Alternating Direction Explicit Method for Computing Three-Dimensional Viscous Flow Fields in Turbomachines," SAE Paper 781001, 1978.

60 Briley, W. R., Kreskovsky, J. P., and McDonald, H., "Computation of the Three-Dimensional Viscous Flow in Straight and Curved Passages," United Technologies Center Report R76-911841-9 for NAVAIR Systems Command, 1976.

61 Dodge, P. R., "A Numerical Method for 2-D and 3-D Viscous Flows," AIAA Paper No. 76-425, 1976.

62 Dodge, P. R., and Lieber, L., "A Numerical Method for the Solution of the Navier-Stokes Equations with Separated Flow," AIAA Paper 77-170, 1977.

63 Majumder, A. K., Pratap, V. S., and Spalding, D. B., "Numerical Computation of Flow In Rotating Ducts."

64 Patankar, S. V., and Spalding, D. B., "A Calculation Procedure for Heat, Mass and Momentum Transfer in Three-Dimensional Parabolic Flows," *International Journal of Heat and Mass Transfer,* Vol. 15, 1972, pp. 1787–1806.

65 Launder, B. E., and Spalding, D. B., "The Numerical Computation of Turbulent Flows," *Computer Methods in Applied Engineering,* Vol. 3, 1974, pp. 269–289.

66 Majumdar, A. K., and Spalding, D. B., "A Numerical Investigation of Flow in Rotating Radial Diffusers," *Imperial College of Science and Technology* Report HTS/76/4, 1976.

67 Majumdar, A. K., and Spalding, D. B., "A Numerical Investigation of Three-Dimensional Flows in a Rotating Duct by a Partially-Parabolic Procedure," ASME Paper No. 77-WA/FE-7, 1977.

68 Wagner, R. E., and Velkoff, H. R., "Measurement of Secondary Flows in a Rotating Duct," ASME JOURNAL OF ENGINEERING FOR POWER, Vol. 94, 1972, pp. 261–270.

69 Bosman, C., Chan, K. C., and Hatton, A. P., "A Calculation Method for Incompressible, Blade-to-Blade Flow through Radial Turbomachines with Log-Spiral Blade Surfaces," ASME Paper No. 78-GT-195, 1978.

70 Cartwright, W. G., "The Determination of the Static Pressure and Relative Velocity Distribution in a Two-Dimensional Radially Bladed Rotor," Institution of Mechanical Engineers Conference, University of Warwick, April 1973.

71 Unwala, J. K., "Velocity Distribution in the Rotor of a Radial Turbomachine," University of Manchester Institute of Science and Technology, M.Sc. Thesis, 1972.

72 Goulas, A., and Baker, R. C., "Through Flow Analysis of Centrifugal Compressors," ASME Paper No. 78-FT-110, 1978.

Downloaded 01 Jun 2010 to 171.66.16.58. Redistribution subject to ASME license or copyright; see http://www.asme.org/terms/Terms_Use.cfm